Pore Scale Mechanisms of Carbonated Water Injection in Oil Reservoirs

By

Masoud Riazi

BSc., MSc.

Submitted for the degree of **Doctor of Philosophy** in

Petroleum Engineering

Heriot-Watt University

Institute of Petroleum Engineering

January 2011

ABSTRACT

Concerns over the environmental impact of carbon dioxide (CO_2) have led to a resurgence of interest in CO_2 injection (CO_2I) in oil reservoirs, which can enhance oil recovery from these reservoirs and store large quantities of CO_2 for a long period of time. Oil displacement and recovery by CO_2I has been studied and applied in the field extensively. However, CO_2I lacks acceptable sweep efficiency, due to the large viscosity contrast between CO_2 and resident reservoir fluids. Various CO_2I strategies e.g. alternating (WAG) or simultaneous injection of CO_2 and water have been suggested to alleviate this problem. An effective alternative strategy is carbonated (CO_2-enriched) water injection. In carbonated water, CO_2 exists as a dissolved as opposed to a free phase, hence eliminating the problems of gravity segregation and poor sweep efficiency. In this thesis, the results of an integrated experimental and theoretical investigation of the process of carbonated water injection (CWI) as an injection strategy for enhanced oil recovery (EOR) with the added value of CO_2 storage are described. High-pressure micromodel technology was used to physically simulate the process of CWI and visually investigate its EOR potential, at typical reservoir conditions. Using the results of these flow visualisation experiments, the underlying physical processes and the pore-scale mechanisms of fluid-fluid and fluid-solid interactions during CWI were demonstrated to be oil swelling, coalescence of the isolated oil ganglia, wettability alteration, oil viscosity reduction and flow diversion due to flow restriction in some of the pores as a result of oil swelling and the resultant fluid redistribution. A mathematical model was developed that accounts for the pore-scale mechanisms observed during the micromodel experiments. In this study, some of the micromodel experimental observations were interpreted and the impact of some of the pertinent parameters on CWI and CO_2I processes was studied. The results predicted by the model were linked to the results obtained using a new relationship developed based on the dimensional analysis technique. To examine and investigate the effect of CWI on wettability, micromodel experiments, designed only to observe possible variation of contact angles and spontaneous imbibition displacement mechanisms due to CW, were performed. Contact angle measurements were also conducted to quantify different tendencies of CW and water to wet solid surfaces, using three different solid plates with different salinity of the aqueous phase, under different pressure and temperature conditions. Two other important parameters affecting the performance of CWI, i.e. CO_2 solubility in water and its CO_2 diffusion coefficient, were also experimentally studied and estimated. A mathematical model was developed to estimate CO_2 diffusion coefficient from the corresponding experimental results. The results of this research show that CWI is an effective and efficient injection strategy that offers great potential for enhanced oil recovery and at the same time a unique solution to the problem of reducing CO_2 emission.

DEDICATION

To

My parents, my wife

and

my kids

(Hasti and Mohammad)

for their patient and continuous support throughout

my study

ACKNOWLEDGEMENTS

I would like to express my sincere appreciation to my supervisors Dr. Mahmoud Jamiolahmady and Dr Mehran Sohrabi for their outstanding technical guidance. Their extensive knowledge on this area and constant encouragement has been invaluable for the successful completion of this thesis. The best thing I enjoyed about working with them was that they were always available to guide my research while encouraging me to follow independent ideas.

The financial support of Heriot-Watt University during my study through a full scholarship is highly appreciated. This thesis is the outcome of the first phase of Carbonated Water Injection JIP at Heriot-Watt University, which was equally sponsored by the UK Department of Energy and Climate (DECC), Total, Petrobras, Dong Energy and Statoil. Their support is also gratefully acknowledged.

I also want to thank Mr Shaun Ireland, Mr Christopher Brown, Mr Jack Irvine, Mr Jim Alisson, Mr David Weir, Mr Ken Malcolm, Mr Graeme Robertson, Ms Claire McMillan and everyone in the Heriot-Watt University for helping me with lab equipment related and study issues, which made my research possible. Thank you very much to Prof. Adrian C. Todd and Dr. M.R. Fassihi for accepting to be my examiners and also for their constructive comments.

Thanks to Mr Alireza Emadi, Ms Nor Idah Kechut, Mr Hamidreza Shahverdi, Prof Dabir Tehrani and Dr. Jerald Hamon for their time for the discussion and providing valuable comments.

I would like to thank Mr Moradali Hashemi, Dr Manochehr Haghighi, Dr Alireza Bahramian, Dr Mohammadreza Rasaie, Prof M. Mosavian, Prof Patrick Corbett and in particular many thanks to my supervisor Dr Mahmoud Jamiolahmady for providing this opportunity to study my PhD at Heriot-Watt University.

The support of the Iranian Ministry of Science, Research and Technology and my dear friend Dr. Hojjat Mahdiyar for providing an opportunity for my future career during my study is also sincerely acknowledged.

My thanks also go to all my friends especially Mr. Mohammadreza Rahmanian, Mr. Hamidreza Hamdi, Dr Hojjat Mahdiyar, Dr Arfan Ali and Mr Alireza Kazemi with whom I had pleasant time in Edinburgh.

I also would like to thank Ms Jenifer Spencer for her useful feedback on my writing style related issues.

My last (but not least) and special deepest thanks is due to all members of my family in particular my wife for her kindness and outstanding patience throughout all my studies from undergraduate to PhD, who constantly believed that I could progress further.

ACADEMIC REGISTRY
Research Thesis Submission

Name*:*	Masoud Riazi		
School/PGI:	Institute of Petroleum Engineering		
Version: *(i.e. First, Resubmission, Final)*	Final	Degree Sought (Award **and** Subject area)	PhD of Petroleum Engineering

Declaration

In accordance with the appropriate regulations I hereby submit my thesis and I declare that:

1) the thesis embodies the results of my own work and has been composed by myself
2) where appropriate, I have made acknowledgement of the work of others and have made reference to work carried out in collaboration with other persons
3) the thesis is the correct version of the thesis for submission and is the same version as any electronic versions submitted*.
4) my thesis for the award referred to, deposited in the Heriot-Watt University Library, should be made available for loan or photocopying and be available via the Institutional Repository, subject to such conditions as the Librarian may require
5) I understand that as a student of the University I am required to abide by the Regulations of the University and to conform to its discipline.

* *Please note that it is the responsibility of the candidate to ensure that the correct version of the thesis is submitted.*

Signature of Candidate*:*		Date:	

Submission

Submitted By *(name in capitals):*	
Signature of Individual Submitting:	
Date Submitted:	

For Completion in Academic Registry

Received in the Academic Registry by *(name in capitals):*			
Method of Submission *(Handed in to Academic Registry; posted through internal/external mail):*			
*E-thesis Submitted (**mandatory for final theses from January 2009)***			
Signature:		Date:	

NOMENCLATURE

A	Cross sectional area (Chapter 7), [m^2]
A	Hamaker constant (Chapter 4)
C_{CO_2}	CO_2 concentration, [kmol m^{-3}]
$\left[C_{co_2}(t)\right]_{ave}^{V}$	Volumetric average CO_2 concentration
C_{CO_2-O}	CO_2 concentration in the oil phase, [kmol m^{-3}]
C_{CO_2-W}	CO_2 concentration in the water phase, [kmol m^{-3}]
C_s	Spreading coefficient
D_{CO_2}	Diffusion coefficient of CO_2 in oil or water, [m^2 s^{-1}]
$d_{sh\text{-}sw}$	The difference of shrinkage and swelling (i.e. shrinkage- swelling), [%]
E_a	Areal sweep efficiency, [-]
E_m	Microscopic displacement efficiency, [-]
E_v	Vertical sweep efficiency, [-]
E_t	Total sweep efficiency, [-]
F_v	Viscous forces, [N]
F_c	Capillary forces, [N]
h	Film thickness (in Equation 4.3)
H	Mean curvature
$K_{CO_2-w/o}$	Water/oil-CO_2 partition coefficient, [-]
K_h	Hydration equilibrium constant (in Equation 2.1)
K_H	Henry's constant, [atm m mol^{-1}], (in Equation 2.1)
K_{a1}	dissociation constant (for the dissociation of carbonic acid into the bicarbonate, in Equation 2.1)
L_o	Oil thickness, [m]
L_w	The shielding water thickness separating oil and carbonated water, [m]
Mw_{CO_2}	CO_2 molecular weight, [kg $kmol^{-1}$]
$n_{co_2}(t)$	Number of moles of CO_2, [kmol]
N_{ca}	Capillary number, [-]
P_c	Capillary pressure, [psi]

P_{nw}	non-wetting phase pressure at the interface, [psi]
P_w	wetting phase pressure at the interface, [psi]
p_{co_2}	Partial pressure of CO_2 (in Equation 2.1), [atm]
r	Radius of pore, [m]
R	Gas constant, [m^3 psi K^{-1} mol^{-1}]
R_s	Dissolved gas GOR, [scf/STB]
S_{or}	Residual oil saturation, [%]
t	Time, [s]
T	Temperature, [K]
$V_{CO_2}(t)$	CO_2 volume dissolved in oil at time t, [m^3]
V_{oil}	Initial oil volume, [m^3]
$V_{oil+co_2}(t)$	Total oil plus CO_2 volume, at time t, [m^3]
v	Interstitial velocity (Darcy's velocity), [$m.s^{-1}$], (in Equation 3.1)
v	Molar average velocity, [$m.s^{-1}$], (in Equation 7.22)
$x(t)$	Length, [m]
Z	CO_2 compressibility factor, [-]
ρ_{CO_2}	CO_2 density, [kg m^{-3}]
μ_{OD}	Viscosity of gas-free oil, cP
μ_{oil},	Oil viscosity, [Pa.s]
μ_w	Water viscosity, [mPa.s]
Π_d	Disjoining pressure, [psi]
δ_{co_2w}	CO_2/water interfacial tension, [Nm^{-1}]
δ_{ow}	oil/water interfacial tension, [Nm^{-1}]
δ_{co_2o}	CO_2/oil interfacial tension, [Nm^{-1}]
δ_{nw-s}	Interfacial tensions (IFT) between solid and non-wetting phase, [Nm^{-1}]
δ_{w-s},	IFT between solid and wetting phase, [Nm^{-1}]
δ_{nw-w}	IFT between wetting and non-wetting phases, [Nm^{-1}]
θ	Contact angle measured through the wetting drop

Subscripts

CO_2	Carbon dioxide
eq	denotes the value of the quantity at the equilibrium conditions
i	denotes the value of the quantity at the interface
O	refers to oil phase
nw	non-wetting
s	solid
sh	shrinkage
sw	swelling
w	wetting
W	refers to water phase

1. Chapter 1: Introduction

1.1 Introduction

Worldwide energy demand has grown substantially from the late 1970s and early 1980s (Smith, 2001). Growth in population and rising standard of living mainly contribute to such energy demands (Energy Information Administration 2003). Hydrocarbon fluids are considered as one of the major sources of energy. However, there is a rapid decline of many of the world's existing conventional oil fields (Schroeder, and Pena, 2002), These suggest shifting our focus towards methods to increase oil recovery and/or exploiting new resources that are generally located in harsh, isolated, and politically unstable regions (Schroeder, and Pena, 2002).

At the same time, with the continued increase in use of fossil fuels (as one of the main sources of energy), there is an increase in undesired CO_2 emission from burning of the fossil fuels. On the other hand, the increased international awareness and commitment drives the need for substantial reductions in CO_2 emissions levels. In other words, there are three main challenging issues here; i.e. continued increase in energy demand, continued decline in production from current oil reservoirs, and responsibility for reduction of CO_2 emissions. This thesis is aimed at describing an injection strategy into oil reservoirs that addresses some of these issues.

This chapter starts with a brief discussion on different hydrocarbon displacement and sweep efficiencies. As the main target of the injection strategy described here is the residual oil left after primary and secondary recovery methods, some of the general concepts related to hydrocarbon recovery, oil entrapment mechanisms, increased oil recovery methods by mobilising these remaining oils, will be described. Then, (CO_2-enriched) carbonated water injection (CWI) as an enhanced oil recovery (EOR) method, which is the main focus of this study, is introduced.

1.1.1. Hydrocarbon reserve

Reserve is referred to recoverable petroleum from the discovered reservoirs under the established and existing technologies at economic conditions on the specified date (Lake, 1989). So discovering new fields and reservoirs increases, whereas oil production reduces the reserves. Furthermore, changes in the economic of the production technology can redefine the reserves. Declining the reserve to production ratio, which is in the line with the growth in energy demand, has been also reported several times (Basic Petroleum Data Book, 1991).

The oil production period of a reservoir can be mainly divided into three stages including; primary, secondary and tertiary oil recovery. In the primary recovery period, oil is produced as a result of the natural drives such as solution gas drive, aquifer inflow, expansion of the gas cap and gravity segregation. The second stage of oil recovery operation, secondary recovery, is implemented after or during declining the primary recovery period. In this stage usually water flooding and/or gas injection are applied to maintain the pressure of the reservoir.

However, after primary and secondary recoveries a major part of the initial oil in place remains un-recovered in the reservoir. The amount of this un-recovered (residual) oil saturation mainly depends on the reservoir conditions and oil type. To recover parts of the remaining oil, enhanced oil recovery (EOR) methods are applied. EOR is an oil recovery process in which a fluid or more than one fluid is injected into oil reservoirs to displace the remaining oil towards the production wells. Many EOR processes have been proposed since the end of World War II (Green and Wilhite, 1998), when oil producers recognized that significant amount of oil remained unrecovered after the initial oil recovery periods (i.e. primary and secondary oil recovery).

The major EOR methods can be classified into three categories (Lake, 1989): thermal (e.g. Steam, In situ combustion, Hot water), chemical (e.g. Miceller polymer, Polymer, Alkaline) or solvent (e.g. Hydrocarbon miscible, CO_2 miscible, CO_2 immiscible, Nitrogen, Flue gas). The efficiency of EOR methods could be different for different reservoir conditions, rock and oil types. Thus, to achieve the most benefit of an EOR method the conditions of the target (i.e. unrecovered oil) as well as the production mechanisms of the EOR processes should be well understood and studied.

The main focus of this thesis is to investigate the process and feasibility of carbonated (CO_2-enriched) water injection as an EOR method. Therefore, some of the basic concepts, past experiences related to this oil recovery method and the needs for and benefits of this study are discussed in this chapter after describing some of the basic general concepts related to EOR process.

1.1.2. Target of unrecovered oil for EOR processes

The performance of an EOR method is addressed by a factor known as total or overall sweep efficiency. This factor can be divided into three different sweep efficiencies that control the performance of an EOR method. The projected 2-D area of the region swept by the displacing fluid would never become equal to the area of the entire reservoir, since there are always some dead zones, which are not swept by the displacing fluid. So the ratio of the swept area over the reservoir area is referred to as the areal sweep efficiency (E_a). Some parts of the reservoir will not be invaded by the displacing fluid if there are vertical heterogeneities within the reservoir, so a vertical sweep efficiency (E_v) which is less than unity should be considered to account for the vertical heterogeneity as well. In addition to these two factors, which determine the volumetric sweep efficiency, there is microscopic displacement efficiency (E_m), which describes the displacement efficiency at the pore level. Microscopic displacement efficiency is controlled by the balance of gravity, capillary and viscous forces and also pore size distribution, geometry and aspect ratio of pores (i.e. pore to throat effective diameter ratio) in the porous medium.

Based on these three sweep efficiencies, the total sweep efficiency (E_t) is defined by the following equation:

$$E_t = E_a \times E_v \times E_m \qquad (1.1)$$

Generally two main oil resources are considered as a target for EOR processes as the swept and un-swept residual oil (Green and Wilhite, 1998). Residual oil saturation typically is about 20-35% in swept region. This remained oil mainly is in the form of isolated and trapped oil ganglia in the pores for water wet conditions or films around the rock particles for oil wet conditions. On other hand, the un-swept residual oil exists in high saturation (50-60%) with high oil mobility (i.e. high oil relative permeability).

EOR methods that are selected to mobilize these oil resources, which are trapped through different mechanisms, can be different. Polymer injection can be considered as a proper EOR method to mobilize the un-swept residual oil, because, in this EOR strategy the apparent permeability of the high permeable zone, which is swept first, is reduced and consequently flow direction is diverted into un-swept area, which usually has a lower permeability. On the other hands, miscible gas injection, which increases the microscopic displacement efficiency can be chosen to recover the residual oil in swept area.

One of the main objectives of the current study is a pore level investigation of an EOR method, the impact of some of the pertinent parameters on oil displacement efficiency and oil entrapment mechanisms at pore scale will be discussed in the following section.

1.2 Oil Entrapment Mechanism at the Pore Scale

The oil trapping mechanisms in the swept region strongly depend on the physical properties of the fluids and the porous media and their mutual interactions.

Based on the tendency of immiscible fluids within the porous medium to wet the surface of pores, the fluids (for two phases) are classified into wetting and non-wetting phases. A wetting phase is the more strongly attracted phase to the solid surface compared to the non-wetting phase (Green and Wilhite, 1998). The wettability can be quantitatively expressed by assessing the interfacial forces. The following equation, which is known as Young's equation, defines the balances of the forces caused by a droplet of a wetting phase on a dry surface in which surrounded by non wetting phase.

$$\delta_{nw-s} - \delta_{w-s} = \delta_{nw-w} \cos\theta \qquad (1.2)$$

where δ_{nw-s}, δ_{w-s}, δ_{nw-w} are interfacial tensions (IFT) between solid and non-wetting phase, solid and wetting phase, and wetting and non-wetting phases, respectively, and θ is the contact angle measured through the wetting drop.

The pressure difference across the interface of two static immiscible fluids in a pore, which is caused by tension of interfaces and known as capillary pressure, is defined by Young–Laplace equation.

$$P_c = P_{nw} - P_w = \frac{2\delta_{nw-w}\cos\theta}{r} \tag{1.3}$$

where P_c, P_{nw}, P_w are capillary pressure, non-wetting phase pressure at the interface and wetting phase pressure at the interface, respectively, and r is the radius of the pore. For a simple system of oil and water in a water wet porous medium, two simple models have been suggested to show the trapping mechanisms for the non-wetting phase (oil) at the pore scale (Lake, 1989) as described below.

1.2.1. Pore doublet model

In a double pore or pore doublet model at least two parallel pores are considered (Figure 1). As can be seen from this image, flow path sizes are not the same for these two parallel pores. Assuming a capillary dominated flow regime, the wetting phase prefers to be established and move faster in the smaller pore due to having higher capillary pressure (Figure 1A). As a result of this tendency of the wetting phase, a part of the non-wetting phase is trapped in the larger pore (Figure 1B). It is known that lowering the capillary forces and local heterogeneity will reduce the amount of oil trapping by this mechanism.

The mechanism of oil trapping in the pore doublet model has been theoretically and experimentally investigated by several researchers (Moore and Slobod, 1956; Laidlaw and Wardlaw, 1983; Chatzis and Dullien, 1983; Rose and Witherspoon, 1956).

1.2.2. Snap-off model

It should be noted that pore channels in reservoir rocks are unevenly shaped rather than smooth and straight. So usually, due to channel geometry, the non-wetting phase (oil) does not entirely seal the channel. In these conditions the second wetting phase (water) can bypass the oil phase inside the single pore, Figure 2. In other words the pore surface is wetted with a continuous thin film layer of the wet phase (water), whereas the main pore body is occupied with the non-wet phase (oil). Due to variation of capillary pressure with position in the flow path the thickness of the wetting layer across the flow

differs, i.e. it is thin where the pore is wide and it is thick where the pore is narrow. For some specific pore geometry, the displacement potential of the wetting phase across the pore channel can be insufficient to force the non-wetting phase to pass the pore throat. In these conditions, where the capillary pressure is greater than the potential displacement gradient, the non-wetting phase is snapped-off into oil ganglia and remains as trapped oil in the pore body of the channel.

The snap-off mechanism is a function of capillary pressure (i.e. interfacial tension (IFT), wettability and aspect ratio (pore to throat effective diameter ratio), see equation 3). The aspect ratio necessary for snap-off (critical aspect ratio) at strongly water wet conditions (advancing contact angle =0) has been reported to be in the range of 1.5-3.65 by different authors in the literature. Li and Wardlaw (1986); Mohanaty, (1981); Lenormand, et al. (1983) and Roof (1970) reported critical aspect ratios for strongly water wet conditions of 1.5, 2.0, 2.3 and 3.65, respectively. These data have been published based on experimental investigations.

Figure 2 shows the snap-off model with different cross section areas and various degrees of heterogeneity. As can be seen from this image, for a pore geometry with low aspect ratio (Figure 2A), oil is completely displaced by water without any entrapment. However, Figure 2B shows oil entrapment as a result of snap-off mechanism in the pore path with a higher aspect ratio compared to Figure 2A.

1.3 Gas Injection as an Enhanced Oil Recovery Method

In the previous section, two main oil trapping mechanisms at the pore scale were discussed. It should be noted that this trapped oil would not be recovered by secondary recovery method, i.e. such as injection of water with water being the wetting phase. Thus, EOR methods should be applied to maximise oil recovery.

Gas injection is widely applied to displace the resident oil after water flooding. As mentioned earlier, the microscopic displacement efficiency (E_m) is one of the key parameters affecting total sweep efficiency. The properties of the displacing gas are of great importance in controlling the displacement efficiency. Injected gas can be miscible or immiscible with the oil reservoir. In a miscible injection, which yields

better oil displacement performance than immiscible injection, oil trapped due to capillary forces is targeted by engineering the properties of the displacing fluid. The main standard methods of miscible drive are: I) high pressure gas injection, II) enriched gas injection and III) liquefied petroleum gas (LPG) slug injection.

Miscible gas injection can be involved with two different displacement processes (first-contact and multiple-contact miscible) depending on the pressure, temperature and oil/gas compositions (Green and Wilhite, 1998). In the first-contact miscible (FCM) process the injected gas is miscible with the oil in the first contact. In this condition initially a slug of expensive miscible gas is injected, followed by less expensive second slug. The second slug is not directly miscible with the oil but should be miscible with the first slug to avoid trapping the primary slug during displacement process. Determining the slug sizes in this injection process is important from economical point of view, which requires following careful optimisation procedures. In multiple-contact miscible (MCM) process the gas and oil are not miscible in the initial contact but the miscibility develops in the reservoir through mass transfer between injected gas and the reservoir oil. Green and Wilhite (1998) have classified the multiple contact processes as vaporizing-gas, condensing and condensing/vaporizing-gas displacements.

In the vaporizing process, the injected gas contains mainly methane and low molecular weight hydrocarbons or some inert gases such as nitrogen. In the vaporisation mechanism, the oil components evaporate into the gas and the injected gas is enriched in composition. This continued enrichment results on miscible displacement at some point in the reservoir. It is well known that extraction, which results in the vaporisation mechanism, is highly dependent on the gas density.

In the condensing process, the injected gas is more expensive as it contains intermediate molecular weight hydrocarbon. In this process the oil gradually becomes enriched by the intermediate components that condense out of the injected gas. Once the oil sufficiently modified in composition the miscible displacement develops.

Some gas/oil systems can also develop dynamic miscibility by both the condensing and vaporising mechanisms (Zick, 1986). In this process, intermediate components condense from the injected gas into the oil phase. Vaporisation of heavier intermediates

from the enriched oil to the injected gas also occurs. The injected gas, enriched with heavier intermediates from the oil, moves forward to contact fresh oil and undergoes the condensing/vaporisation process again. At some point in this process the compositions of the gas and oil become similar so that miscibility develops.

1.4 CO_2 Injection as an Enhanced Oil Recovery Method

In the context of gas injection, CO_2 injection into the oil reservoirs can be very attractive. CO_2I for EOR is a well-established technology (Orr and Taber, 1984). The solubility of CO_2 in oil results in improving oil recovery by primarily swelling of the oil, reduction of the oil viscosity and possible vaporisation and extraction of intermediate components.

Grigg et al. (1997) reported that density of CO_2 can vary by a factor of three (0.2 to 0.6 g/cc) at 100 °F over a relatively small pressure range (1005 to 1345 psi) near the critical temperature. However, the lean-gas density varies only by a factor of two (0.162 to 0.252 g/cc at 230 °F) over a much wider pressure range (2000 to 4430 psi). As the behaviour of the CO_2 injection (CO_2I) process is analogous to the vaporizing process (Green and Wilhite, 1998), the higher solvent power of CO_2 due to its higher density develops miscible condition faster, consequently results in more economically oil recovery.

In addition to this vital advantage of CO_2 over the other gases, higher solubility of CO_2 in water compared to the other hydrocarbon components causes more oil swelling in water shielded oil ganglions, (Bijeljic et al. 2002; MacGuire and Stalkup, 1992). Figure 3A compare the solubility of different gases in water. Figure 3B shows the same data but scaled to the total amount of dissolved gases given in Figure 3A. As can be seen from these graphs, CO_2 solubility in water is copious compared to other gases such as C_1H_4, C_2H_4 and C_2H_6. The solubility of CO_2 in water favourably changes the physical properties of water and interfacial tension between oil and water, which affects directly the microscopic displacement efficiency.

These properties of CO_2 as well as the environmental advantages of CO_2 storage as part of a CCS (carbon capture and storage) programme make CO_2 a very suitable medium for injection into the oil reservoirs.

However, low sweep efficiency due to its high mobility and gravity segregation in the reservoir is a problem for conventional CO_2I. Hence, injection strategies like water alternating gas (WAG) and simultaneous water and gas (SWAG) injections have been proposed and used to ease this problem. One of the main reasons behind these combinations of water and gas is to improve the displacement efficiency by reducing the mobility of gas. WAG also improves oil production due to hysteresis effect during displacement (Sohrabi et al., 2000), which its impact is reflected in the relative permeability values.

Although WAG injection can improve sweep efficiency to some extent, it can result in significant oil trapping, which adversely affects oil recovery (Lin and Huang, 1990). Tiffin et al. (1991) reported that during the WAG process the oil in place is shielded from the injected solvent by the mobile water in water wet porous media. Presence of water reduces the gas/oil interfacial area hence reducing mass transfer. Wylie and Mohanaty (1997) showed experimentally that at high water saturations islands of oil will be isolated by water and consequently the mass transfer rate between the CO_2 and oil will be reduced. This so-called water shielding or water blocking effect can prevent direct contact of oil and gas (CO_2) both in WAG and tertiary CO_2 injection. This effect has also been studied theoretically by other researchers (Grogan and Pinczewski, 1987; Grogan et al., 1988; Do and Pinczewski, 1993; Bijeljic, et al. 2002). Lin and Huang, (1990) specifically investigated the effect of rock wettability on water blocking during miscible displacement. They introduced a simulator capable of modelling viscous fingering and water-blocking effects during the miscible flooding processes, and proposed an equation for estimating the amount of trapped oil due to the water blocking effect.

CO_2 foam injection has also been considered as another alterative method for direct CO_2I. Foam is an accumulation of gas bubbles, separated from each other by thin films of liquid. The viscosity of foam is higher than those of the gas and liquid of which it is composed. Hence, injection of foam into the reservoir leads to lower mobility ratio

therefore yields better oil displacement. The aim of this method, like the previous applications, is, mainly, the reduction of the gas mobility and subsequently improving the gas displacement efficiency (Khalil and Asghari, 2006). Low injectivity and stability of thin films of water in foam are two main practical issues that should be considered for this method.

In summary, direct injection of CO_2 (both continuous flooding and WAG) might not result in economically significant amounts of additional oil recovery. It should be also added that in terms of CO_2 storage potential, poor sweep efficiency implies a lower storage capacity for CO_2. However, with the new global interest in CO_2 injection, many other alterative scenarios are being considered for CO_2 injection in oil reservoirs. Another alternative injection strategy in which CO_2 is used more efficiently (compared to conventional CO_2 injection) is carbonated water (CO_2-enriched water) injection (CWI). In CWI, CO_2 is delivered to a much larger part of the reservoir compared to direct CO_2 injection due to a much improved sweep efficiency. In CWI CO_2 is used efficiently and much less CO_2 is required compared to conventional CO_2 flooding and hence the process is particularly attractive for those reservoirs with limited access to large quantities of CO_2 (offshore reservoirs or reservoirs far away from inexpensive natural CO_2 resources). It could also serve as a water-based EOR method for watered-out oil reservoirs in which high water saturations adversely affects the conventional CO_2 injections. As carbonated water (CW) delivers CO_2 compared to pain water injection, it can provide more efficient displacement process. The main pore level mechanisms in CWI in which results in better displacement method compared to plain water will be shown and demonstrated in this study.

CWI as a method for enhanced oil recovery is the main focus of this thesis. The added value of CO_2 storage is also considered to some extent. High-pressure transparent porous media (micromodel) technology was used to simulate physically the process of CWI and visually investigate its EOR potential at typical reservoir conditions. Using the results of a series of high-pressure flow visualisation experiments, the author reveals the underlying physical processes and the pore-scale mechanisms of fluid-fluid and fluid-solid interactions during CWI. Based on the results of the flow visualisation, a mathematical model was developed that accounts for the pore-scale mechanisms observed during the experiments.

The results of a mathematical model developed in this study addressing some of the experimental observations and a sensitivity analysis, which was carried out to investigate the impact of the key pertinent parameters, are also discussed. Following some qualitative investigation of wettability alteration during micromodel experiments, some contact angle measurements were also conducted to quantify the observed different tendencies of CW and water to wet solid surfaces. Some experimental measurements on CO_2 solubility in water and CO_2 diffusion coefficient, as two important parameters affecting the performance of CWI, were also performed. The experimental results together with the features of another mathematical model that was developed to estimate CO_2 diffusion coefficient from the experimental results are discussed.

In the next sections a literature review of the application of this method based on the coreflood experimental data and field scale experiences available in the literature is presented. Some operational problems associated with this process and the difference and advantage of the approach and the methodology of this study compared to those in the literatures are presented.

1.5 Carbonated Water Injection

1.5.1. Literature review of CWI core experiments

As discussed above, carbonated water may have a better performance over direct CO_2 injection because of its better sweep efficiency. In water flooded reservoirs, CWI can alleviate the adverse effect of high water saturation and the water shielding effects as a result of mixing with the resident water. This might in turn increase the rate of CO_2 diffusion and the subsequent oil swelling. It has been shown that in direct CO_2 injection, due to low sweep efficiency and gravity segregation, the time scale of diffusion can be several years (Solomon, 2007). In terms of CO_2 storage, in CWI, CO_2 is dissolved in water (and later in oil) rather than as a free phase, thereby providing a safer method of CO_2 storage compared to direct CO_2 injection. However, CWI in the literature has been considered mainly as an enhancing oil recovery method. Thus, its CO_2 storage potential has been considered as an additional advantage rather than being the main drive as it would be in a CCS program.

There are a few studies that can be found in the literature on CWI:

CWI as an EOR method was studied using coreflood experiments by Martin (1951). He reported that CWI reduced the initial oil saturation from 30% to 8% of pore space, whereas ''*the estimated residual oil after removal of all oil economically recoverable by any present methods was 23%*''. He investigated the impact of several parameters such as the effect of natural gases, organic components and wetting agents on oil recovery when they are combined with CW or CO_2. For instance, he showed that CO_2 promotes the solubility of natural gases in the crude oils.

In the same year Saxon et al. (1951) conducted several coreflood laboratory tests with CO_2 and CW. Although unlike Martine's results, no significant difference between water and CW was reported in this study, the impact of brine and dissolved natural gas on oil swelling was evident. For instance, he showed that when natural gas is dissolved in the crude oil a greater carbon dioxide saturation pressure is required to produce the same volume change.

Johnson et al. (1952) continued Saxon et al.'s (1951) study and investigated the effect of CWI on oil recovery using coreflood experiments. They presented charts showing no recovery from brine injection but substantial recoveries when carbonated water was injected. Additional oil recovery was also reported during the subsequent depressurisation period at the end of the CWI stage. They also showed more oil recovery by CWI at a lower temperature, which could be due to higher CO_2 solubility in oil at a lower temperature, causing a greater expansion in oil volume and consequently greater oil recovery. They demonstrated that as the percentage of light hydrocarbons (C_3 and higher) was increased, the volume expansion became greater. They also reported that ''*carbonation of outlet water never quite reached that of the injection water even after 130 pore volumes had been passed through the core*''. Based on material balance they showed that the difference was about 7% of the total carbon dioxide, which indicated the process of taking up CO_2 by the retained oil in the porous media continued for some time.

Further coreflood CWI experiments were performed by Holm (1959). These experimental results demonstrated the modification of the permeability of a dolomite

core, based on the amount of injected CW into the core. Contrary to the results of the previous studies he showed that ''*dissolved or free gas, up to 20% hydrocarbon pore volume does not have any appreciable effect on the efficiency of the CO_2-carbonated water flooding*''. The results of Holm's study and the statements of Martin (1951) and Saxon et al. (1951), taken together, indicate that there should be a critical swelling factor due to dissolution of CO_2 for a typical system in order to have additional oil recovery. The dependency of oil recovery on the CO_2 content of a system is theoretically and experimentally investigated in this research (Chapter 3 and Chapter 7).

During CO_2I the lighter fractions of oil would usually be removed and the heavier fractions including waxes, asphalts, etc. would remain within the oil and retard or prevent any further recovery of oil. Martin and Tuckahoe (1959) suggested that to alleviate this problem and to avoid having carbon dioxide as a free gas, it is necessary that water or brine be carbonated to a critical concentration, which will be stable at the reservoir temperature and pressure conditions.

During the CWI process two different main mechanisms of oil recovery take place i) swelling and coalescence of trapped oil drops, which lead to improved sweep efficiency and ii) oil viscosity reduction as a result of diffusion and partitioning of CO_2 from carbonated water into oil. This also improves sweep efficiency by changing the mobility ratio between the oil and water phases. The former, swelling and coalescence of trapped oil drops, is expected to be the dominant mechanism in lighter oil types, due to higher CO_2 solubility in these kinds of oil, and the latter to be the main mechanism in heavier and more viscous oil type due to significant reduction in viscosity as a result of dissolved gas in oil. Thus, in this framework, CWI was suggested by Winston (1983) for recovery of viscous oils. The impact of these mechanisms on oil displacement and recovery will be visually and quantitatively presented (in Chapter 3) later. As one of the purposes of this study was screening of oil samples for CWI application, in this study three different oil types were used.

Another effect of the dissolved CO_2 in CW could be wettability alteration (also see Appendix A) of the porous media, which can affect oil recovery. Several reports of laboratory experiments that have been performed to compare the oil recovery by water or by CW imbibition were found in the literature. The first study in this line of work

was carried out by Panteleev and Tumasyan (1972). They used a natural consolidated sandstone, crude oil and water for this study. They claimed that carbonated water imbibition took place faster and recovered more oil than plain water, i.e. 37.3% oil recovery by CW imbibition compared to 26.5% oil production by water imbibition. They also showed that both oil recovery and imbibition rate increased as the concentration of CO_2 in the water increased.

Perez et al. (1992) also investigated the imbibition mechanisms, by CW using limestone core samples. They also confirmed that the CO_2 dissolved in water increased both the oil recovery rate and the ultimate oil recovery by imbibition mechanism compared to unadulterated water. A similar study was also carried out by Cardoza et al. (1992) in the same year.

Flumerfelt and Li (1993) followed the work of Perez et al. (1992) using two different oil types (kerosene and crude oil) and low permeability fractured dolomite rock samples. They also investigated the effect of surfactants on the performance of CWI. They reported that the additional oil recovery by CW with surfactant was 50% whereas that by CW alone was 20%, both compared to water injection.

Although the last group of experimental studies showed the benefit of CW on oil recovery by imbibition mechanism compared to plain water, the sub-mechanisms of this additional oil recovery were not comprehensively evaluated and the physics involved in the imbibition mechanism is still not well understood. Thus, the impact of contact angle variation, which affects wettability, by CW compared to plain water on a number of solid plates were investigated in this study and will be discussed in Chapter 5 of this thesis.

Application of Carbonated Water as Wetting Agent

Surfactants are chemical materials that are used in some EOR methods. Surfactants can be classified as IFT reducers and wetting agents. Surfactants, basically, by reduction the capillary forces affecting the displacement process of oil. Martin et al. (1959b) presented another benefit of CW when it is combined with using some surface active agents. They showed that the most effective way of introducing the surface active agent into a formation is by CW. For instance, they showed that CW removes the non-ionic surface active agent more rapidly than un-carbonated water. It was also shown that

more un-carbonated water than carbonated water was required to recover the adsorbed/absorbed non-ionic surface agent. They also reported more improvement of oil recovery by carbonated water than un-carbonated water with the same amount of wetting agent.

1.5.2. Theoretical Study on carbonated water injection

The CWI process and the imbibition mechanisms by CW have also been theoretically studied by several researchers (Nevers, 1963; Ramesh and Dixon, 1973; Shenawi et al., 1994). Shenawi and Wu (1994b), in another publication, presented the simulation of CW imbibition in naturally fractured reservoirs using a compositional simulator (COMABS). It should be noted this simulator, COMABS, allows the partitioning of CO_2 from the injected water phase into the oil phase based on the CO_2 solubility in each phase. The results of simulation indicated that CW enhances the water imbibition rate close to the imbibing core face.

1.5.3. Use of co-solvent to increase CO_2 solubility in water

Although as described above, CO_2 solubility in water is significant compared to other gases such as C_1H_4 and C_2H_4 (Figure 3), compared to conventional CO_2 injection the amount of CO_2 delivered by carbonated water is low. As will be shown later, CO_2 content is an important parameter for the performance of CWI. Low CO_2 content can adversely affect the CWI performance. However, the solubility of CO_2 in water can be improved by adding chemicals to the water phase. In the literature, the use of some of these chemicals, which are known as co-solvent materials, has been reported.

Winston (1983), in a patent, suggested that to increase the amount of CO_2 available for reducing oil viscosity, first a slug of CW containing a CO_2 solubility promoter to increase the amount of dissolved CO_2 in water should be injected into the formation. Then a slug of a CO_2 solubility demoter should be injected into the formation to decrease the solubility of the CO_2 in the aqueous slug in order to release CO_2 from CW. The CO_2 solubility promoter reacts with the CO_2 in the CW and increases CO_2 solubility. The CO_2 solubility promoters that were suggested by him include: mono-ethanolamine, diethanolamine, ammonia, sodium carbonate, potassium carbonate, sodium hydroxide, potassium hydroxide, potassium phosphate, diaminoisopropanol,

methyl diethanolamine, triethanolamine or other weak base chemicals, and the CO_2 solubility demoters include any weak acids, preferably acids commonly used for well stimulation in the petroleum industry such as hydrochloric, acetic and hydrofluoric acids.

Winston (1984), in another patent, suggested that after injection of CW, which contains CO_2 solubility promoter, a heated fluid can be injected to release CO_2 from the injected carbonated water instead of using CO_2 demoters.

It should be noted that CO_2 co-solvents can be divided into two groups: physical and chemical absorbent agents. Chemical absorption is characterized by the occurrence of a chemical reaction between the gas (CO_2) component and a component in the liquid (water) phase. The chemical materials proposed by Winston (1983) fall into this group. However, use of such co-solvents (chemical absorption) would not readily allow CO_2 to diffuse into the oil phase; thus as Winston suggested either a slug of demoter or heated fluid would be needed to release CO_2 from the carbonated water.

A physical absorbent on the other hand, does not react chemically with the absorbed CO_2 and hence allows the partitioning of CO_2 when it comes in contact with oil. Below are some examples of physical absorbent materials for CO_2 (Vitaly and Suphat 1999; Jodecke et al., 2004, 2007; Hu and Adeyiga 2004; Keskes et al. 2006; Williams et al., 2002; Blance et al., 1979; Kamps et al., 2000):

- Tributyl phosphate (TBP)
- Propylene carbonate (PC)
- Normal Methyl Pyrrolidone (NMP)
- Dimethyl Ether of Polyethylene Glycol (Selexol)
- Mixture of Polyethylene Glycol Dialkyl Ethers (Sepasolv)
- Methanol
- Acetone
- Hexamethyl phosphorotriamide
- Alkanes such as n-C_4 and n-C_{10} for the oil phase

Some preliminary experiments to study the impact of one of these materials on improving the CO_2 solubility in water were performed and are reported in Chapter 8 and Appendix D. However, it was concluded that systematic investigation of this issue, was beyond the scope of this study. Hence, working in this area is suggested as a future work. The current study concentrates on establishing whether CWI can be used as a successful EOR method.

1.5.4. CWI field experience

As already discussed, the advantages of CWI compared to plain water injection for oil recovery improvement have been shown with coreflood experiments carried out previously and reported in the literature. Despite some encouraging core test results, only a few EOR field applications were found in the literature. Some of its applications were for well stimulation, whilst others were applied to clean up the ground water from oil based contamination. In the following sections, details of some of these experiences are discussed.

CWI for EOR Purposes

The first reported CWI field trial took place in Allegany County near Richburg, New York in 1947 (Martin and Tuckahoe 1959). The production data for this field showed a significant improvement of the production rate from 92 barrels/acre/year to 1260 barrels/acre/year as a result of injection of CW instead of water.

The other CWI field experience was found in a field located 10 miles north of Bartlesville, Oklahoma. CWI in this field, which is known as the K&S project, was started in 1958 (Hickok et al., 1960). A substantial improvement in water injectivity was reported in all injection wells of this field during CWI period. It was also reported that the additional oil production obtained in 1959 was more than the oil production during the entire primary production life (29 years) of the field.

Increases in oil recovery and water injectivity and also shorter flood life have been reported for CWI application compared to plain water injection in Oklahoma, Texas and Kansas and projects elsewhere (Hickok and Ramsay, 1962; Christensen, 1961; Scott, and Forrester, 1965).

In another field scale application (Tumasyan et al., 1973), the oil recovery improvement by CWI compared to WI was reported to be 14 to 16%. The effect of water saturation was experimentally investigated by the same authors demonstrating that water saturation had an adverse effect on the oil recovery performance of CWI.

CWI for Well Stimulation

When CO_2 is dissolved in water, carbonic acid will be formed. The injected carbonated water will react with the carbonate materials in the rock to form bicarbonates, which are much more soluble, especially in the vicinity of the wellbore, and results in improved permeability thus improving water injectivity (Ramsay and Small, 1964; Hickok and Ramsay, 1962). Therefore, in some fields, CWI was applied with the purpose of well stimulation (Kraus et al., 1970). The results of this application in the Aleksandrovsk (Tuimazy) field, for instance, show a significant improvement in the water intake rate of the wells after CWI (Kislyakov, et al., 1967).

CWI for Cleaning Up the Ground Water from Contaminations

Another application of carbonated water is cleaning up the ground water from oil based contamination. In a very recent study, (Nelson et al., 2009), CWI was conducted in a pilot field scale trial to evaluate the recovery of volatile, light non-aqueous phase liquids from ground water. In this technique, CW is injected into the subsurface; as a result, the nucleation of CO_2 bubbles at and away from the injection point takes place. The nucleating bubbles coalesce, rise and volatilize residual oil ganglia. A 78% and 50% recovery of the pentane and less volatile hexane, respectively, were reported using this technique.

CW Application for Other Purposes

It is interesting to note that the effect of carbonated water on soil modification in the agriculture field has also been investigated. Novero et al., (1991), studied the effect of carbonated water application under mulched and un-mulched conditions using tomatoes. They reported a total fruit yield improvement of 15.9%, using carbonated water compared to water.

Although some promising results for CWI process, both on core and field scales, have been obtained and reported, the application of this process has been relatively limited mainly due to lack of sufficient understanding of the mechanisms involved in the

process. Operational problems of CWI process could also be one of the contributing reasons for this. In the following section some of the important operational issues of CWI are discussed.

1.6 Operational Issues of CWI

1.6.1. Preparing CW

Perhaps one of the main practical issues is preparing CW at the large scale and desired pressure and temperature conditions with safety and economic considerations. One of the well known technologies to make carbonated water is the gas infusion (GI) generator. The GI generator uses thousands of hydrophobic micro-hollow fibres to dissolve CO_2 gas into water at elevated pressures (Li, et al., 2007).

1.6.2. Corrosion

The other important practical issue associated with CWI is corrosion of the facilities due to formation of carbonic acid (H_2CO_3) as a result of CO_2 dissolution in water (De Waard et al., 1993). The acid will lower the pH and, in sufficient quantities, may promote corrosion of carbon steel. The critical factors in this process are partial pressure of CO_2, temperature, pH of the CW and velocity of the fluid within the pipes (De Waard et al., 1995). The De Waard-Milliams equation (De Waard and Milliams 1975) is used to predict the rate of aqueous CO_2 corrosion of carbon steel based on the partial pressure of CO_2, temperature and injection rate.

However, it should be noted that as the carbonated water passes through the formation, it becomes saturated with bicarbonates, loses its acidic nature and the reaction will lessen. Despite the concerns that carbonic acid may cause localized corrosion of steel (Browning, 1984), Hickok and Ramsay (1962) reported no evidence of further corrosion in the production wells, flow lines or tank batteries of the first commercial K&S carbonated waterflood project apart from what would be observed for the normal waterflood case. The CO_2 injection lines were re-used several times during the staging of the CO_2 injection. It was hypothesized that the limited proportion of CO_2 forms sufficient amounts of alkali earth carbonates and bicarbonates and these salts act as buffers, which prevent the corrosion of the steel (Martin, 1951). Blackford (1987) studied the impact of CWI on equipment used during a CWI pilot test performed by the Amoco production company in the Slaughter field, Texas. It was reported that stainless

steel and aluminum bronze material showed no deterioration during the test period. However, injection wells, compared to production wells, should generally be protected from corrosion caused by carbonated water.

1.6.3. Scale formation and asphaltene precipitation

As a result of the dissolved CO_2 in water, some operational problems such as precipitation of asphaltene and paraffins and calcium sulfate scale formation may take place (Brownlee and Sugg, 1987). These changes during CWI cause blockage in the reservoir and pipeline facilities and consequently affect the fluid flow processes.

1.6.4. Water weakening effect

The water weakening effect refers to the deformation of reservoir layers (especially for chalk layers) during water flooding. This effect causes several issues, such as reservoir compaction and seabed subsidence. For instance, about 9 meters of seabed subsidence at the Ekofisk field has been reported due to this effect (Spencer et al., 2008).

The effect of dissolved CO_2 in water on rock–fluid interaction has been studied by different research groups (Sayegh et al., 1990; Hiorth, et al. 2008). Korsnes et al., (2008) showed that water weakening is enhanced by adding CO_2 in water and stated that ''*it is probably linked to higher $CaCO_3$ solubility and precipitation of $CaSO_4$ (s), which will promote enhanced chalk dissolution*''.

1.7 Scope and Methodology of the Study

Generally in terms of the scale of study, the investigation of the fluid flow process in the porous media can be divided into three classes:

I) **Reservoir scale**: Here simulation of particular production and EOR methods at the field scale or for a single-well model is investigated mainly using developed commercial softwares. However, sometimes an in-house simulator is developed for a single-well study.

II) **Core scale**: This is a much smaller investigation scale than the previous one. A piece of rock is considered and the effect of different parameters such as

rock type, pressure, temperature, oil type and so on, on different fluid flow mechanisms is experimentally and/or theoretically investigated.

III) **Pore scale**: The finest scale to study a displacement process is at the pore scale. Understanding the fluid flow and recovery mechanisms at the pore scale using visualisation experiments provides vital information needed for interpretation of the core and field scale displacements. It is interesting to note that at this scale of study the capillary pressure and relative permeabilities curves, which are needed for simulation, can also be obtained from a pore network model, which could be linked to visualisation experiments.

As mentioned in the previous sections, several laboratory experiments have been conducted at the core scale by different research groups to investigate the performance of the CWI process. Some of the data found in the literature (Martin, 1951; Johnson et al., 1952) showed that CWI significantly improves oil recovery, compared to plain water injection. However, Saxon, et al., 1951 reported no significant difference between CWI and WI. These contradictory results indicate that the impact of pertinent parameters on the CWI performance is not well understood. Some of the key parameters controlling the fluid distribution and its flow, include rock type, temperature, pressure, salinity of brine, oil composition and the type of oil trapping. Different investigators conducted experiments at different prevailing conditions, hence reporting different results. Thus, to obtain the benefit of CWI process it is necessary to choose a reservoir suitable for this process.

As discussed above, the initial studies of this process were started at core and field scales. It should be noted that although conventional coreflood experiments are very useful for quantification of the performance of CWI and the level of additional oil recovery due to this injection strategy, the black-box nature of coreflood experiments means that the underlying physical processes involved in CWI cannot be identified and studied by these experiments. High-pressure visualisation experiments of CWI, which provide a very useful tool to directly investigate and visualise the pore-scale mechanisms and events taking place during the flooding process, have not been reported previously. Such information is essential in achieving an in-depth understanding of the

impact of pertinent parameters in order to maximise the benefit of a CWI process. Hence, in this study the main focus is on generating such pore level information by conducting pore scale visualisation experiments and developing the relevant mathematical models in order to simulate important mechanisms of events during the CWI process.

In CWI, it is expected that injection of CO_2-enriched water causes the oil to swell and the viscosity of the oil to drop. It can reduce water-oil interfacial tension and can also favorably affect wettability of the reservoir (See Appendix A). Oil swelling due to CWI after waterflood can reconnect the discontinuous residual oil and results in additional oil recovery. An additional oil recovery process could be the in situ release of CO_2 subsequent to CWI by pressure blow-down of the reservoir. A subsequent waterflooding may also further reduce the amount of residual oil, which has been redistributed during the CWI period.

In the experimental section of this study, CWI process is investigated at pore scale, using a high-pressure transparent porous medium (glass micromodel) as one of the visualising tools to observe and interpret oil recovery, displacement mechanisms and the interaction of CW with the resident fluid phases. It should be noted that such visual observation of fluid flow and the data generated are very important and useful input for modelling of flow mechanisms at the pore scale, which constitutes another element of this study. Although the main purpose of running visualisation experiments is to achieve qualitative information, the results obtained from these experiments can also be processed using image analysis techniques to obtain some useful quantitative information.

1.8 Thesis Content

This thesis was planned to conduct a comprehensive experimental and theoretical studies of the CWI process through conducting flow visualisation and mathematical modelling at the pore level. A series of multiphase (two and three phases) fluid flow experiments were performed using high-pressure two-dimensional glass micromodel. A list of all the experiments conducted in this study is shown in a table in Appendix B. A number of mathematical models have also been developed, investigating the dynamics

of CO_2 diffusion from a CO_2 source into an oil phase destination. Detailed descriptions of these exercises are discussed in five chapters as described below.

Chapter 2 introduces the experimental facilities and the fluid system used in this study. The image analysis technique, which was used to quantify fluid saturation in the micromodel, is also explained in this chapter.

In Chapter 3, the author addresses the lack of pore level information on CWI by performing 14 micromodel displacement experiments. These experiments carried out to visually investigate and demonstrate the physical process of CWI as an EOR injection strategy and also to generate pore level information for developing mathematical model. In this chapter, the results of CWI as both secondary (pre waterflood) and tertiary oil recovery (post waterflood) processes are discussed. The impacts of cyclic injection of water/CW and blow down mode after CWI on fluid redistribution within the porous medium and on oil recovery are also presented. The impact of CO_2 concentration in carbonated water on the performance of CWI is investigated. In this chapter, three different oil types were used. The visualization results also include a detailed discussion of the observed pore scale mechanisms of oil displacement by CWI.

In Chapter 4, first the impact of water shielding and water saturation on the performance of (supercritical) CO_2 injection is studied. Then, the impact of CWI prior to CO_2 injection on mitigation the water shielding effect is investigated. The results of 8 micromodel experiments for two different oil types are presented to support the benefits of CWI in conjunction with CO_2I.

Chapter 5 addresses the lack of sufficient understanding on CW imbibition mechanisms in the literature. In this chapter, the results of the experiments conducted to investigate the impact of CW on rock wettability and carbonated water spontaneous imbibition are presented. Two micromodel tests were designed to observe the spontaneous imbibition displacement mechanisms due to CW. Some contact angle measurement tests were also performed to quantify the tendency of CW and water to wet different solid surfaces as described in this chapter.

Lack of sufficient diffusion coefficient data for CO_2 in water at high pressure is an outstanding issue, which has partly been addressed in Chapter 6. The effects of the blue dye used in the majority of the micromodel experiments on CO_2 solubility and diffusion coefficient of CO_2 in water were also experimentally investigated, in this chapter. A mathematical model, which has been developed to estimate diffusion coefficient of CO_2 in water and blue water based on the results of the relevant experiments, is also discussed in this chapter.

In Chapter 7, the lack of theoretical studies on CWI at pore level is addressed. A mathematical model, simulating the dynamic process of swelling of an oil ganglion when it comes in direct contact with CWI or is separated from the CO_2 source by water layers (indirect contact), has also been developed in this study. The structure of the model, including the underlying assumptions, governing equations, boundary conditions, and solution technique are discussed in this chapter. The results of this model including a comprehensive sensitivity study of the impact of pertinent parameters and those results that support some of the experimental observations are discussed next in this chapter. Two simple equations have also been derived using the results of the developed mathematical model, one of which can be used for simulation of diffusion processes, as it directly relates the amount of CO_2 dissolved to the CO_2 diffusion coefficient. The other one can be used to estimate the amount of oil swelling from the CO_2 concentration in water. The results predicted by the model have been also linked to the results obtained using a new relationship developed based on the dimensional analysis technique.

The main conclusions of this study with some suggestions for future work are given in Chapter 8.

A comprehensive bank of experimental data, correlations and theoretical concepts (obtained from the literature) related to the physical properties of oil, water and rock when it comes in contact with CO_2 at different pressure and temperature conditions are presented in Appendix A.

For more interested readers a more detailed description of some of the results the micromodel experiments described in Chapter 3 are included in Appendices B and C.

In Appendix D the results of two preliminary micromodel experiments, which were performed to investigate the impact of co-solvent on CWI performance, are discussed.

In Appendix E a list of the publications of this study is given.

1.9 References

Basic Petroleum Data Book, 1991: Petroleum Industry Statistics, Washington, D. C., American Petroleum Institute, January.

Bijeljic B. R., Muggeridge A. H., Blunt M. J., 2002: ''Effect of Composition on Waterblocking for Multicomponent Gas floods'', SPE 77697, SPE annual Technical Conference and Exhibition held in San Antonio, Texas, 29 Sep-2Oct 2002.

Blackford, T. A., 1987: ''Carbonated Waterflood Implementation and Its Impact on Material Performance in a Pilot Project'', SPE Paper 16831.

Blance, C., Chenard J.Y., Delpuech J.J., Oliveau O., 1979: ''Physical Solvent Absorption of Carbon Dioxide and Hydrogen Sulphide for the Deacidification of Industrial Gaseous Mixtures'', United State Patent 4162903 Jul.31, 1979.

Browning, D.R, 1984: ''CO_2 Corrosion in the Anadarko Basin", SPE12608, SPE Deep Drilling and Production Symposium, 1-3 April 1984, Amarillo, Texas

Brownlee, M. H. and Sugg, L.A., 1987: ''East Vaccum Grayburg-San Andres Unit CO_2 Injection Project: Development and Result to Date'', 82nd Annual Technical Conference Exhibition of the Society of Petroleum Engineers held in Dallas. TX September 27-30. SPE paper 16721.

Cardoza, J. M.P., Sharif, Q.J. and Poston, S.W., 1992: ''Carbonated Water Imbibition Flooding: An Enhanced Oil Recovery Process for Fractured Reservoirs,", paper SPE/DOE 24164 presented at the SPE/DOE 8th Symposium on Enhanced Oil Recovery, Tulsa, Oklahoma, April 22-24.

Chatzis. I. and Dullien F. A. L., 1983: ''Dynamic Immiscible Displacement Mechanisms in Pore Doublets: Theory versus Experiment'', J. Colloid Interface Sci. 91, 199-222 (1983).

Christensen, R. J., 1961: ''Carbonated Waterflood Results—Texas and Oklahoma'', Paper SPE 66.

De Waard, C. and Milliams, D.E., 1975: ''Carbonic acid corrosion of steel'', Corrosion 31, 5 (1975), p 177

De Waard, C and Lotz, U., 1993: ''Prediction of CO_2 corrosion of carbon steel'', CORROSION/1993, Paper No. 69, NACE International

De Waard, C, Lotz, U. and Dugstad, A., 1995: ''Influence of liquid flow velocity on CO_2 corrosion: a semi-empirical model'', NACE CORROSION/1995 paper 128.

Do H.D., Pinczewski W.V., 1993: ''diffusion controlled swelling of reservoir oil by indirect contact with injection gas'', Chemical engineering science Vol.48, No18, PP. 3243-3252, 1993.

Energy Information Administration, Annual Energy Outlook 2003.

Flumerfelt R,W. and Li X., 1993: ''A Cyclic Surfactant-Based Imbibition/Solution Gas Drive Process for Low-Permeability, Fractured Reservoirs'', 68th Annual Technical Conference and Exhibition of the Society of Petroleum Engineers held in Houston, Texas, 3-6 October 1993., SPE paper 26373.

Green D. W. and Willhite G. P., 1998: ''Enhanced Oil Recovery'', SPE Textbook Series Vol. 6.

Grigg R. B., Gregory M. D., Purkaple J. D., 1997: ''Effect of pressure on improved oilflood recovery from tertiary gas injection'' Reservoir Engineering, August, SPE paper 35426.

Grogan A.T., Pinczewski W.V., 1987: ''The Role of Molecular Diffusion Processes in Tertiary CO_2 Flooding'', JPT, SPE 12706.

Grogan A.T., Pinczewski W.V., Ruskauff G. J., Orr Jr F.M., 1988: ''Diffusion of CO_2 at Reservoir Conditions: Models and Measurements'', SPE 14897.

Hickok, C. W., Christensen R. J. and Ramsay, H. J., 1960: ''Progress Review of the K&S Carbonated Waterflood Project'', Journal of Petroleum Technology, December 1960, 20-24, SPE 1474-G.

Hickok, C. W. and Ramsay, H. J., 1962: ''Case Histories of Carbonated Waterfloods in Dewey-Bartlesville Field'', paper SPE 333-MS, SPE Secondary Recovery Symposium, 7-8 May 1962, Wichita Falls, Texas.

Hiorth A., Cathles L. M., Kolnes J., Vikane O., Lohne A., Korsnes R. I., Madland M. V., 2008: ''A Chemical Model for the Seawater-CO_2- Carbonate System – Aqueous and Surface Chemistry'', International Symposium of the Society of Core Analysts held in Abu Dhabi, UAE 29 October-2 November, Paper SCA2008-18.

Holm, L. W., 1959: ''Carbon dioxide solvent flooding for increased oil recovery'', SPE paper 1250-G.

Hu L. and Adeyiga A. A., 2004: ‘‘Carbon Dioxide Separation by Phase Enhanced Gas-Liquid Absorption’’, Annual Project Progress Report, May 2004, DOE Award Number: DE-FG26-02NT41668

Jodecke, M., Xia, J., Kamps, A. P.-S., and Maurer, G., 2004: ‘‘Solubility of Carbon Dioxide in Aqueous, Salt-Containing Solution of Methanol or Acetone’’, Chem. Eng. Technol. 27, 1 P 31-34.

Jodecke, M., Kamps A. P.-S., and Maurer G., 2007: ‘‘Experimental Investigation of the Solubility of CO_2 in (Acetone + Water) Michael’’, Journal of Chemical and Engineering Data, Vol. 52, No. 3, 2007, P 1003-1009.

Johnson, W. E., Macfarlane, R. M., Breston, J. N. and Neil, D. C., 1952,: ‘‘Laboratory experiments with carbonated water and liquid carbon dioxide as oil recovery agents’’, Producers Monthly (Nov) 17, No. 1, 15.

Kamps, A. P.-S., Sing, R., Rumpf, B., and Maurer, G., 2000: ‘‘Influence of NH4Cl, NH4NO3, and NaNO3 on the Simultaneous Solubility of Ammonia and Carbon Dioxide in Water’’, Journal of Chemical and Engineering Data, Vol. 45, No. 5, 2000 P-796-809.

Keskes, E., Adjiman, C. S., Galindo, A., and Jackson, G., 2006: ‘‘A Physical Absorption Process for the Capture of CO_2 From CO_2-Rich Natural Gas Streams’’, AIChE 2006 Annual Meeting San Francisco also in Internet.

Kislyakov, Y. P., Kovalenko, K. I., Babalyna, G. A., 1967: ‘‘Treatment of well-Bore Area of Injection Wells with Carbonated Water’’, Neft Khoz, Vol. 45, No. 4 P. 41-44.

Khalil, F. and Asghari, K., 2006: ‘‘Application of CO 2-Foam as a Means of Reducing Carbon Dioxide Mobility’’, Journal of Canadian Petroleum Technology, May 2006, Volume 45, No. 5.

Korsnes, R.I., Madland, M.V., Vorland, K.A.N, Hildebrand H., T., Kristiansen, T.G., and Hiorth, A., 2008: ‘‘Enhanced Chemical Weakening of Chalk Due to Injection of CO_2 Enriched Water’’, International Symposium of the Society of Core Analysts held in Abu Dhabi, UAE 29 October-2 November, Paper SCA2008-24.

Kraus, A. D., Mendoza, C. M. and Cortes, M. C., 1970: ‘‘Injection of Acidulated Water of Carbonated Water’’, ING Petrol, Vol. 10, No. 1, P. 17-21.

Laidlaw W. G. and Wardlaw N. C., 1983: ‘‘A Theoretical and Experimental Investigation of Trapping in Pore Doublets’’, the Canadian Journal of Chemical Engineering, Volume 61. October 1983

Lake L.W., 1989: Enhanced oil Recovery, Prentic Hall, Englewood Cliffs, New Jersey 07632.

Li, T.M.W., Ioannidis, M., and Chatzis, I., 2007: ‘‘Recovery of Non-aqueous Phase Liquids from Ground Sources”, U.S. Patent 7,300,227 B2, issued Nov. 27.

Lin E. C. and Huang E.T.S., 1990: ‘‘The effect of rock wettability on water blocking during miscible displacement’’, Reservoir Engineering, May, SPE paper 17375.

MacGuire, P. L. and Stalkup, F. I., 1992: ‘‘Performance analysis and optimisation of the Prudhoe Bay miscible gas project’’, SPE/DOE 27746 proceeding of the SPE International Meeting on Petroleum Engineering, Beijing, China, 719-728.

Martin, J. W., 1951: ‘‘Additional oil production through flooding with carbonated water’’, Producers Monthly (July) 15, No. 9, 18.

Martin, J. W., Tuckahoe, N. Y., 1959: ‘‘Process of recovering oil from oil fields involving the use of critically carbonated water’’ U.S Patent 2875833, Mar. 3.

Martin, J. W., Tuckahoe, N. Y. and Frederick A., 1959b: ‘‘Dissemination of wetting agents in subterranean hydrocarbon-bearing formations’’, U.S Patent 2875831, Mar. 3.

Moore, T. F. and Slobod, R. L., 1956: ‘‘The Effect of Viscosity and Capillarity on the Displacement of Oil by Water’’, Prod. Mon. 20, 20.

Nelson, L., Barker, J., Li, T., Thomson, N., Ioannidis, M., Chatzis, J., 2009: ‘‘A field trial to assess the performance of CO_2-supersaturated water injection for residual volatile LNAPL recovery’’, Journal of Contaminant Hydrology 109, 82–90.

Nevers, N. D., 1963: ‘‘A Calculation Method for Carbonated Water Flooding’’, Society of Petroleum Engineers Journal, March 1964, 9-20, SPE paper 569.

Orr, F. M. Jr and Taber, J. J., 1984: ‘‘Use of Carbon Dioxide in Enhanced Oil Recovery’’, Science Vol. 224 No. 4649 PP. 563-569.

Panteleev, V. G. and Tumasyan, A. B., 1972: ‘‘Capillary Imbibition of Carbonated Water into an Oil-Saturated Porous Medium’’, Neft Khoz, No. 5 PP. 64-66.

Perez, J.M., Poston, S.W and Sharif Q. J., 1992: ‘‘Carbonated Water Imbibition Flooding: An Enhanced Oil Recovery Process for Fractured Reservoirs’’ SPE/DOE eighth symposium on enhanced oil recovery held in Tulsa, Oklahomas, April 22-24, 1992. SPE paper 24164.

Ramesh A. B. and Dixon T. N., 1973: ‘‘Numerical simulation of Carbonated Waterflooding in a Hetrogeneous Reservoir’’, Third Numerical Simulation of

Reservoir Performance Symposium of the Society of Petroleum Engineers of AIME to be held in Houston, Tex. Jan. l0-12. SPE Paper 4075.

Ramsay, H.J.J. and Small, F.R., 1964: ‘‘Use of Carbon Dioxide for Water Injectivity Improvement’’, Journal of Petroleum Technology, 25, 1964.

Rose, W. and Witherspoon P. A., 1956: ‘‘Trapping Oil in a Pore Doublet’’, Prod. Mon. 21. 32.

Saxon, J., Jr., Breston, J. N. and Macfarlane, R. M., 1951: ‘‘Laboratory tests with carbon dioxide and carbonated water as flooding mediums’’, Producers Monthly (Nov. 1951) 16, N. 1, 8.

Sayegh, S.G., Krause, F.F., Marcel, G., Cornellus, D., 1990: ‘‘Rock/Fluid Interactions of Carbonated Brines in a Sandstone Reservoir: Pembina Cardium, Alberta, Canada’’, SPE Formation Evaluation, December, SPE paper 19392.

Schroeder, A.J and Pena, E., 2002: ‘‘Energy and the Environment - a Global View’’, Offshore Technology Conference, 6-9 May 2002, Houston, Texas.

Scott, J. O. and Forrester C. E., 1965: ‘‘Performance of Domes Unit Carbonated Waterflood - First Stage’’, Journal of Petroleum Technology, December, P1379-1384, SPE Paper 1126.

Shenawi, S.H., Wu, C.H, and Luan Z.A., 1994: ‘‘A New Iterative Mathematical Model for the Analysis of Imbibition Carbonated Waterflood in Naturally Fractured Reservoirs’’, SPE Permian Basin Oil and Gas Recovery Conference held in Midland, Texas, 16-18 March. SPE paper 27717.

Shenawi, S.H and Wu C.H, 1994b: ‘‘Compositional Simulation of Carbonated Waterfloods in Naturally Fractured Reservoirs’’, SPE/DOE Ninth Symposium on Improved 0i1 Recovery held in Tulsa, Oklahoma, U.S.A., 17-20 April. SPE paper 27741.

Smith, J.R. 2001: ‘‘Energy Demand Creates New Opportunities and Challenges for Drilling’’, JCPT, May, Volume 40, No. 5.

Sohrabi, M., Henderson, G.D., Tehrani, D.H. and Danesh, A., 2000: ‘‘Visualisation of Oil Recovery by Water Alternating Gas (WAG) Injection Using High Pressure Micromodels - Water-Wet System’’, SPE Annual Technical Conference and Exhibition held in Dallas, Texas, 1–4 October 2000, SPE paper 63000.

Solomon, S., 2007: ‘‘The Bellona Foundation- Fact sheet: CO_2 Storage’’ Bellona Report May 2007. http://www.bellona.org/factsheets/1191921304.33

Spencer, A.M., Briskeby, P.I., Christensen, L.D., Foyn, R., Kjølleberg, M., Kvadsheim, E., Knight, I., Larsen, M.R., Williams, J., 2008: ‘‘Petroleum geoscience in Norden exploration, production and organization’’. Episodes, 31, 115-124.

Tiffin, D. L., Sebastian, H. M. and Bergman, D. F., 1991: ‘‘Displacement Mechanism and water shielding phenomena for a rich-gas/crude-oil system’’, Reservoir Engineering, May, SPE paper 17374.

Tumasyan, A. B., Babalyan G. A., Panteleev, B. G., Khalimov, E. M., Murzagildina, I, Sh. and Ionov, V. I., 1973: ‘‘Results of Field Experiment on Pumping Carbonated Water in the Stratum’’, Neft Khoz, No 12, pp 31-35.

Vitaly, A., and Suphat, W., 1999: ‘‘Equation of state mixing rule based on activity coefficient model: explicit solution for ‘finite pressure approach’’, Fluid Phase Equilibria, Volume 158-160, June 1999, Pages 259-269

Williams, L. L., Mas, E. M., and Rubin, J. B., 2002: ‘‘Vapor-Liquid Equilibrium in the Carbon Dioxide-Propylene Carbonate System at High Pressures’’, Journal of Chemical and Engineering Data, Vol. 47, No. 2, 2002, P 282-285

Winston, R. S., 1983: ‘‘Carbonated waterflooding for viscous oil recovery using a CO_2 solubility promoter and demoter’’, U.S Patent 4415032, Nov. 15.

Winston, R. S., 1984: ‘‘Carbonated waterflooding for viscous oil recovery’’, U.S Patent 4441555, Apr. 10, 1984.

Wylie, P., and Mohanaty, K. K., 1997: ‘‘Effect of water saturation on oil recovery by near-miscible gas injection’’, Reservoir Engineering, November, SPE paper 36718.

Zick, A. A., 1986: ‘‘A combined condensing/vaporizing mechanism in the displacement of oil by enriched gases’’, SPE paper 15493 presented at the SPE Annual Technical Conference and Exhibition, New Orleans, Oct 5-8.

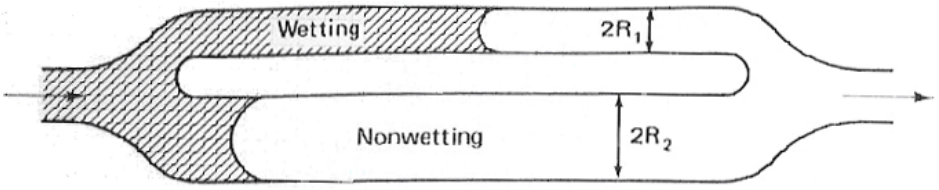

A

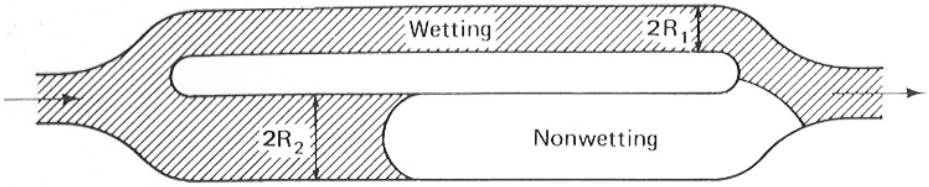

B

Figure 1-1: Schematic of the pore doublet model A) before trapping B) after trapping (Pictures are from Lake, 1989)

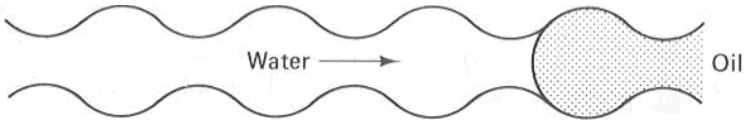

A

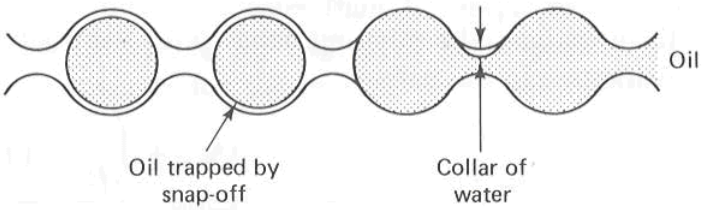

B

Figure 1-2: Various geometries of the pore snap-off model A) Low aspect ratio B) High aspect ratio (Pictures are from Lake, 1989)

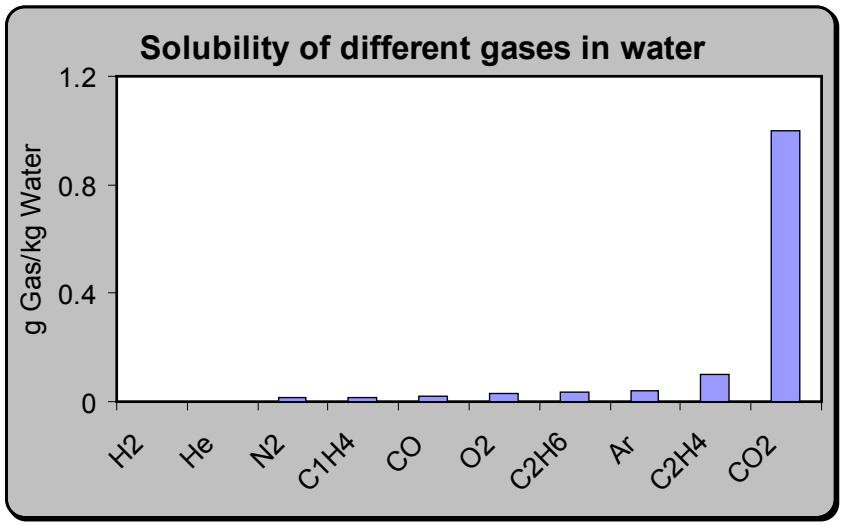

A

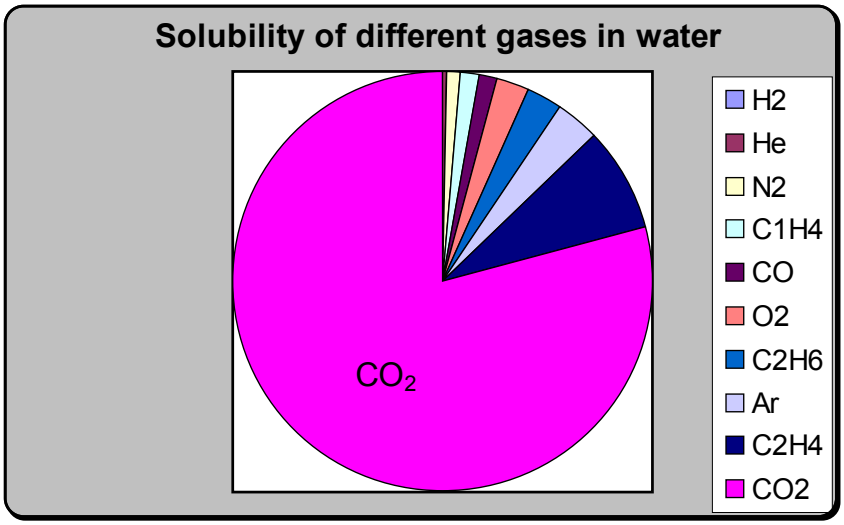

B

Figure 1-3: Comparison of solubility of different gases in water at 40 °C and atmospheric pressure conditions (www.engineeringtoolbox.com). Data of Figure 3B are the data of Figure 3A scaled to total amount of dissolved gases given in Figure 3A.

2 Chapter 2: Experimental Facilities, Fluid Systems and Method of Image Analysis

In this chapter, the experimental facilities and the fluid system used for performing micromodel tests and the image analysis method employed to quantify the micromodel experimental results are introduced.

2.1 Experimental Facilities

A modified high-pressure micromodel rig was used, in this study, for performing carbonated water injection (CWI) tests. The rig can operate at pressures as high as 5000 psia and at a temperature of 100 °F (38 °C). The micromodel rig is shown schematically in Figures 1 and 2. Figure 3 shows an illustration of this rig in the laboratory. It should be noted that different elements of this high pressure rig are made of titanium, instead of steel, to avoid the corrosion problem when working with the carbonated water (CW) acidic fluid. The rig consists of a number of major components as described below.

2.1.1 Fluid Storage Oven

A temperature-controlled air oven is used to store the injection fluids, lines and connections at constant temperature. In this part of the rig there are six storage cells, five of which are for injection of (1) CO_2 in equilibrium with water (gas), (2) carbonated water, (3) plain water, (4) oil and (5) overburden fluid (glycerol) and the remaining one is used to retract the fluids from the bypass and micromodel outlet.

2.1.2 Micromodel Oven

Another temperature-controlled air oven is used to maintain the overburden chamber, which houses the micromodel. This chamber can be turned to allow flow tests to be performed at any desired degree of orientation, including vertical and horizontal. This is particularly important for inclusion or exclusion of gravity effects.

2.1.3 Low Rate Pumps

To inject fluid into the system (micromodel and overburden chamber) two low rate pumps are used. A third pump is used to pull back the fluids and collect them into the retract cell. The pumps are capable of working at pressures up to 5000 psia with a flow rate in the range 0.001 to 14 $cm^3 h^{-1}$.

2.1.4 Manual Camera Mount System

A manual camera mount and positioning system is used, which allows a camera and its magnifying lens to be positioned at any part of the micromodel. It is also used to scan the micromodel for video and still image recording. Figure 4 and Figure 5 show a schematic diagram of the optical system of the rig and an illustration of a part of this system in the laboratory, respectively.

2.1.5 Glass Micromodel

A transparent porous medium (micromodel) was used which consists of two glass plates. A two dimensional (2-D) pore pattern, which was generated by random sampling from a normal pore size distribution, was etched onto the surface of a glass plate, which was otherwise completely flat. A second glass plate is then placed over the first one, covering the etched pattern and thus creating an enclosed pore space. This second plate, the covering plate, has an inlet hole and an outlet hole drilled at either end, allowing fluids to be displaced through the network of pores (Figure 6). Because the structure is only one pore deep, and the containing solid walls are all glass, it is possible to observe the fluids as they flow along the pore channels and interact with each other. It is also possible to observe how the geometry of the pore network affects the patterns of flow and trapping. Figure 7 shows an image of the whole micromodel, which was used in this study. This water wet micromodel consists of pores with relatively simple geometry albeit with some single and multiple dead end pores. The micromodel dimensional characteristics are shown in Table 1. As these data show the range of the pore diameters, which is one of the main parameters controlling aspect ratio (i.e. pore to throat effective diameter ratio), are quite large (i.e. 30-500 μm). Aspect ratio, which is an indication of the degrees of heterogeneity of the porous medium at the pore level, in addition to wettability and interfacial tension promotes the snap-off mechanism. This in

turn increases residual oil saturation (oil trapping) during water and carbonated water flooding.

Li and Wardlaw (1986); Mohanaty, (1981); Lenormand, et al. (1983) and Roof (1970) reported different critical aspect ratios (below which snap-off is minimal) of 1.5, 2.0, 2.3 and 3.65, respectively. All these experimental studies were for strongly water wet conditions (advancing contact angle = 0). Considering the large variation in the pore size of the micromodel, it is expected that snap-off mechanism would be significant in the micromodel used in this study, something which was visually confirmed by looking at the results of the conducted displacement experiments (see Chapter 3).

The impact of the amount and distribution of residual oil saturation, which are controlled by heterogeneity of the micromodel, on the CWI process will be discussed in Chapter 3. It will also be discussed that in one of the micromodel displacement test with initial oil saturation of 79.1% a residual oil saturation of 53.9% was obtained. These values are comparable to those of the core experiments conducted in our laboratory (Kechut, et al. 2010) for the same oil type. Therefore, it can be concluded that the heterogeneity of the current micromodel, to some extent, could be comparable to a real porous medium.

2.2 Fluid System

The fluid system used in the micromodel experiments consisted of distilled water, carbon dioxide, normal decane, a viscous mineral oil and a sample of a real crude oil. To distinguish between the mineral oils and the aqueous phase, the water colour was changed to blue using a water-soluble dye (Water Blue $C_{37}H_{27}N_3Na_2O_9S_3$) with 0.6 weight percent dye concentration. In some of the preliminary experiments the colour of the oil was altered to red using hydrocarbon soluble red dye (Sudan Red with 0.6 weight percent dye concentration). The dyed fluids were filtered using fine filter papers to remove any un-dissolved dye particles. Blue-dyed water, having been degassed by vacuum pump to remove its air content, was mixed with CO_2 in a rocking cell at 100 °F and 2000 psia. Figure 8 shows the rocking cell used for making carbonated water, with more details. The content of the rocking cell was mixed for a long period of time (i.e. several days) while its pressure was monitored. Obtaining constant pressure during

mixing is a good indication that the fluids inside the cell are at equilibrium and the pressure can be considered as the equilibrium pressure. Finally, the equilibrium phases are transferred into their storage vessels and maintained at the test pressure and temperature.

2.2.1 Oil Properties

A viscous mineral oil and high purity normal decane ($C_{10}H_{22}$) were used as the model oils. The properties of the former are given in Table 2. As can be seen from this table, the dynamic viscosity of this oil at test temperature of 38 °C (100 °F) and atmospheric pressure is 16.47 cP (highlighted in **Bold**). The viscous oil composition includes C_{10}, C_{20}, C_{35} and C_{60} components. This oil is used to calibrate the viscometer and is known as ISO 17025. The viscosity of normal decane, which was used as a lighter oil compared to the viscous mineral oil, is 0.83 mPa.s (cP) at 2000 psia and 38 °C (National Institute of Standards and Technology).

In addition to the mineral oils a real dead crude oil-A was also used. The properties of this oil are shown in Table 3.

2.2.2 Carbonated Water Properties

Viscosity and Density of Carbonated Water

Viscosity of carbonated water is estimated to be 1.3 cP based on CO_2 solubility at 2000 psia and 38 °C (Baviere, 1991). Density of carbonated water based on a correlation developed by Hebach, et al. (2004), was estimated at 1011.3 kg m^{-3} at the experimental pressure and temperature conditions. It should be mentioned that the density of distilled water is about 998.9 kg m^{-3} under the same conditions (National Institute of Standard and Technology).

pH Measurement

As a result of dissolution of carbon dioxide in water, carbonic acid is formed. The pH factor for carbonated water can be obtained through the following approximate formula, which requires CO_2 concentration (Wikipedia).

$$pH \approx \log(10^{-14} + \frac{K_h K_{a1}}{K_H} p_{co_2})^{1/2} \qquad (2.1)$$

Partial pressure of CO_2 (p_{co_2}) and CO_2 concentrations are related by the following equation:

$$C_{co2} = \frac{p_{co_2}}{K_H} \tag{2.2}$$

where for the following reaction at 25 °C:

$H_2CO_3 \Leftrightarrow HCO_3^- + H^+$

K_h is the hydration equilibrium constant and its value at 25 °C; is 1.70×10^{-3}.

K_H is the Henry's constant and its value at 25 °C; is 29.76 atm/(mol/L).

K_{a1} is the dissociation constant (for the dissociation of carbonic acid into the bicarbonate) and its value at 25 °C; is 2.5×10^{-4}

The literature data (See Table 4) shows that the pH of CW fully saturated with CO_2 is reduced considerably even at low CO_2 partial pressure (Donald, 1982 and Crawford, et al. 1963)

2.3 Image Analysis of the Micromodel Experimental Results

Although the main purpose of running visualised experiments is to achieve qualitative information about fluid flow mechanisms in the porous media, the results can also be processed using image analysis techniques to obtain some useful quantitative information as reported here.

To show the changes quantitatively, the oil saturation of the porous section of the micromodel was estimated using an image analysis computer program, i.e. Adobe Photoshop CS. In this method the fluid saturation was estimated, based on the number of pixels representing each phase. In this procedure the depth of pores in the entire micromodel was assumed uniform.

The accuracy of this technique was investigated using a simple example of fluid distribution, which is shown in Figure 9. Figure 10 shows this image in the Adobe Photoshop media. As can be seen from this image, *Magic Word Tool (W)* was used to estimate the pixel numbers of each phase. Table 5 shows the porosity and saturation measurements of this configuration using the image analysis technique and simple

geometrical equations. A comparison of the results (highlighted in **Bold**) of these two methods, confirms the high accuracy of the image analysis technique.

The same image analysis technique was used to monitor the swelling process of an oil ganglion during CWI tests reported in this work.

2.4 References

Baviere, M., 1991: ‘‘Basic concepts in enhanced oil recovery processes’’, Published for SCI by Elsevier Applied Science, in London and New York.

Crawford, H.R., Neill, G.H., Bucy, B.J. and Crawford, P.B., 1963: ‘‘Carbon Dioxide- A Multipurpose Additive for Effective Well Stimulation’’, J. Pet. Tech. (March 1963) 237-242.

Donald R. G., 1982: ‘‘The dissolution Effect of Carbonated Water on Oil Reservoir Carbonates- a Study under High Pressure Carbon Dioxide Flood Conditions’’, PhD Thesis, Heriot Watt University, Edinburgh, June 1982.

Hebach, A., Oberhof, A. and Dahmen, N., 2004: ‘‘Density of Water + Carbon Dioxide at Elevated Pressures: Measurements and Correlation’’, Journal of Chemical and Engineering Data, Vol. 49, No. 4.

Kechut, N.I, Riazi, M., Sohrabi, M. and Jamiolahmady, M., 2010: ‘‘Tertiary Oil Recovery and CO_2 Sequestration by Carbonated Water Injection (CWI)’’, SPE paper 139667.

Lenormand, R., Zarcone, C. and Sarr, A., 1983: ‘‘Mechanisms of the displacement of one fluid by another in a network of capillary ducts’’, Journal of Fluid Mechanics , Volume 135, 337.

Li, Y., and Wardlaw N. C., 1986: ‘‘The Influence of Wettability and Critical Pore-Throat Size Ratio on Snap-off’’, Journal of Colloid and Interface Science, Vol. 109, No. 2, Feb.

Mohanaty, K. K., 1981: ‘‘Fluids in Porous Media: Two Phase Distribution and Flow,’’ PhD thesis University of Minnesota.

National Institute of Standard and Technology Website: http://www.nist.gov/srd/, date accessed 15 March 2009.

Roof, J.G., 1970: ‘‘Snap-Off of Oil Droplets in Water-Wet Pores’’, Society of Petroleum Engineering journal , 10, 85, SPE paper 2504-PA.

Wikipedia: http://en.wikipedia.org/wiki/Carbonic_acid, date accessed 23 April 2010.

Height cm	Width cm	MM PV cm^3	Porosity %	Ave. Pore depth μm	Pore Dia. Range μm
4	0.7	0.01	62	50	30-500

Table 2-1: Dimensional characteristics of the micromodel.

Temperature		Viscosity		Density
		Kinematic	Dynamic	
(°C)	(°F)	mm^2s^{-1}, cSt	mPa.s, cP	g/ml
20	68	42.61	36.25	0.8508
25	77	33.54	28.42	0.8474
37.78	**100**	**19.62**	**16.47**	**0.8392**
40	104	18.05	15.12	0.8379
50	122	12.78	10.63	0.8315
80	176	5.732	4.658	0.8126
98.89	210	3.922	3.14	0.8005
100	212	3.847	3.076	0.7997

Table 2-2: Viscosity and density of the viscous mineral oil at different temperature and atmospheric pressure, [Paragon Scientific Ltd].

Parameters		Unit
Oil Density (at surface conditions)	58.801	lb/ft^3
Oil Density (at reservoir conditions)	55.717	lb/ft^3
Oil Gravity	18.73	API
Oil Viscosity at 2000 psi and 38 °C	145	mPa*s

Table 2-3: Physical properties of dead crude oil A.

CO_2 partial pressure (bar)	Solution pH
1	3.7
1.7	3.5
2.5	3.4
5.4	3.3
33.3	3.3

Table 2-4: The impact of CO_2 on pH of water at 25 °C and different pressures. (Donald, 1982 and Crawford, et al. 1963).

	Method of evaluation		
	Area (cm^2) (I)	Area (Pixels) (II)	Equation
A (gray)	75	99006	10*10-B-C
B (blue)	17.93	23028	5*5-C
C (white)	7.07	9064	$(3/2)^2$*3.14
Porosity (%)	25.0	24.5	(B+C)/(A+B+C)
So (%)	**28.28**	**28.24**	C/(B+C)
Sw (%)	**71.72**	**71.76**	B/(B+C)

Table 2-5: Porosity and saturation values of the fluid distribution shown in Figure 9 using (I) simple geometrical equation and (II) image analysis software.

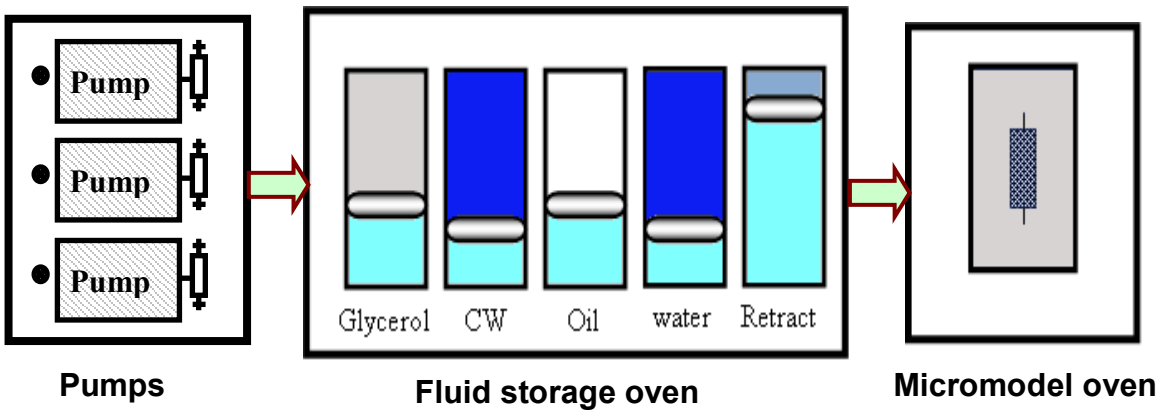

Figure 2-1: An overall schematic diagram of the micromodel rig.

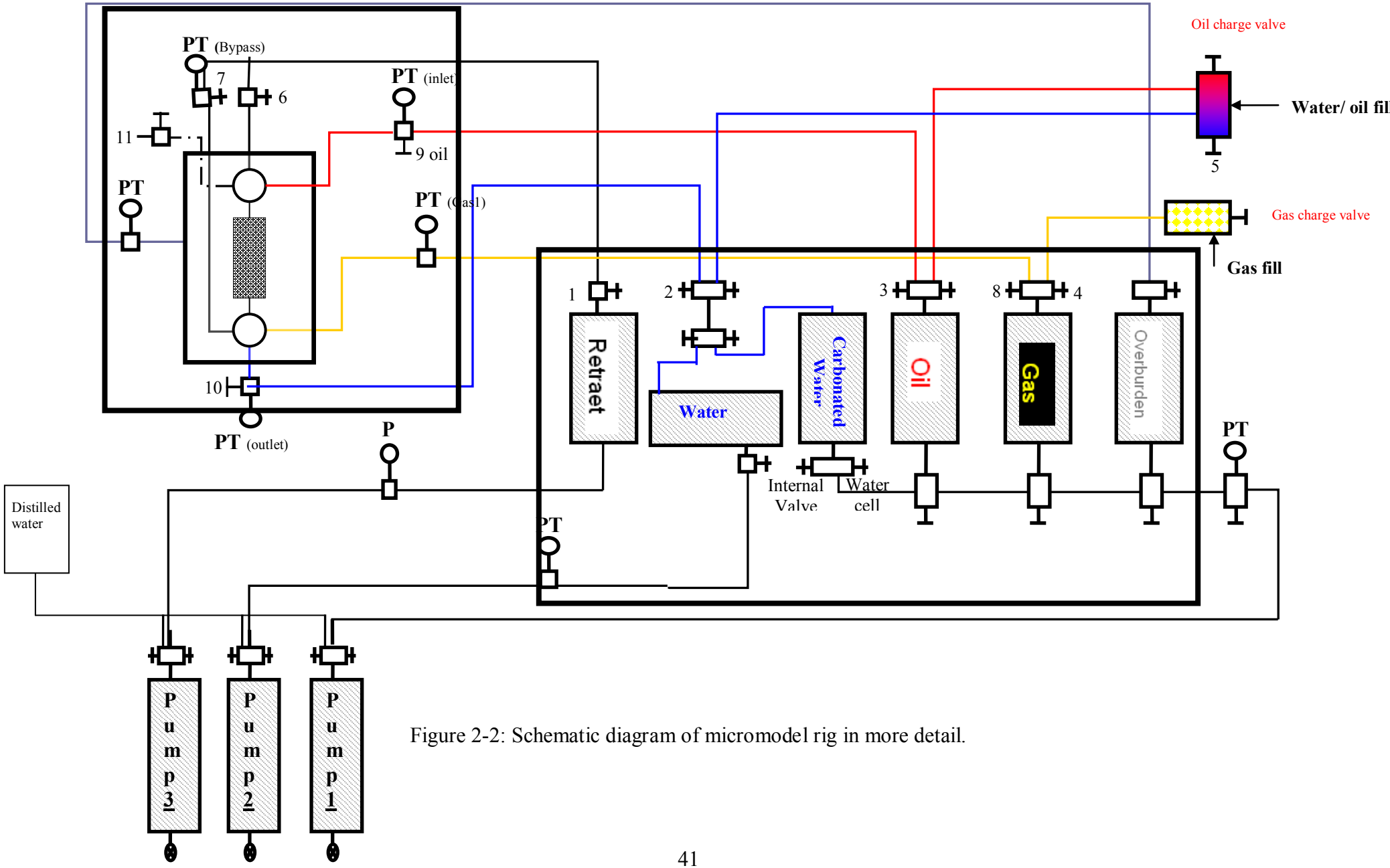

Figure 2-2: Schematic diagram of micromodel rig in more detail.

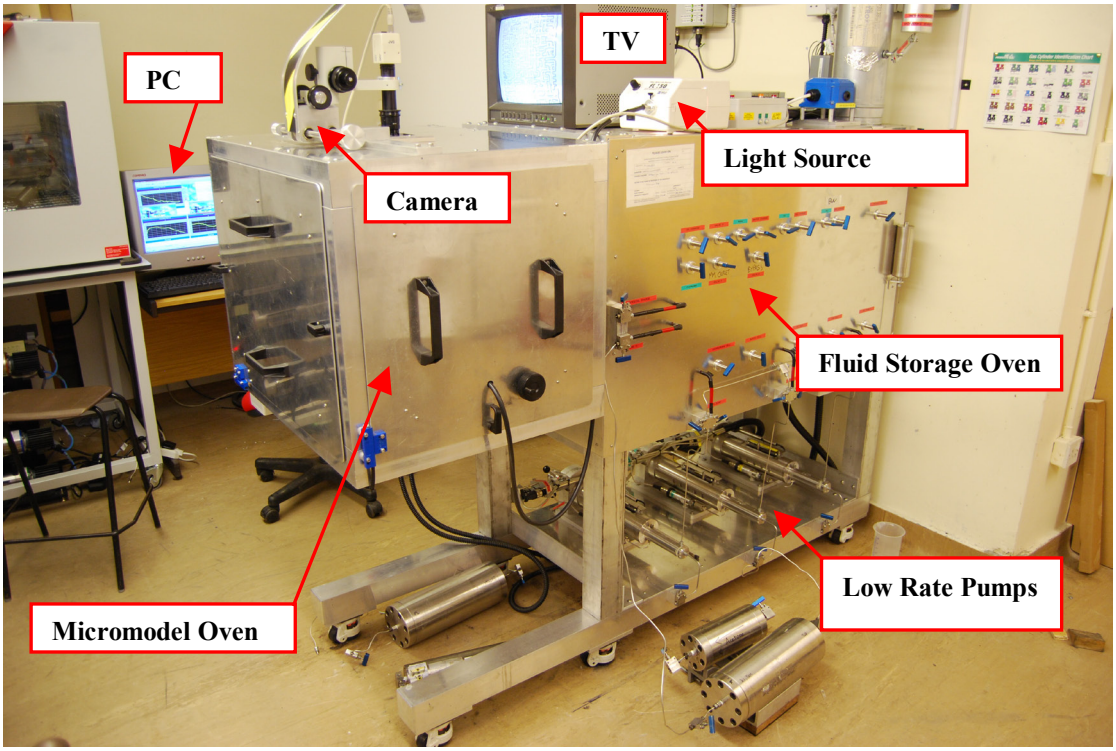

Figure 2-3: A Picture of the micromodel rig in the laboratory.

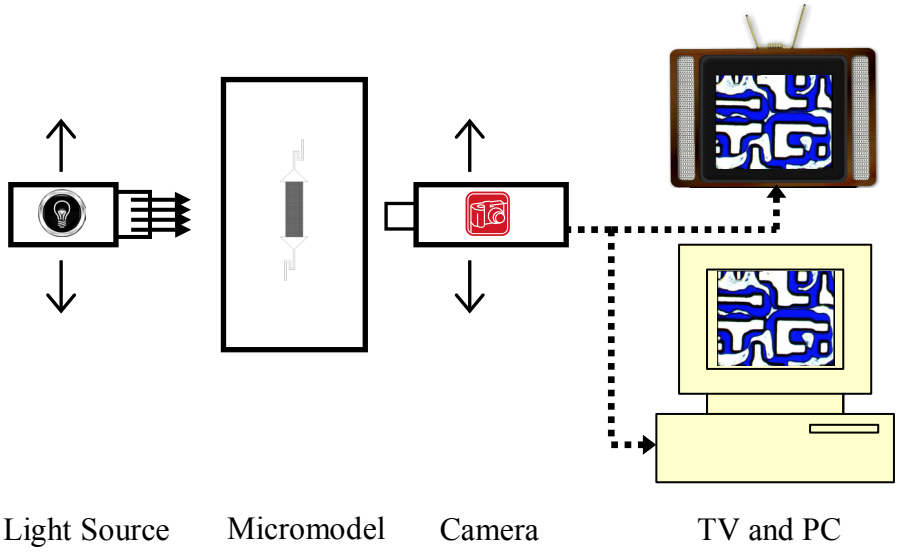

Figure 2-4: A schematic diagram of the visual system.

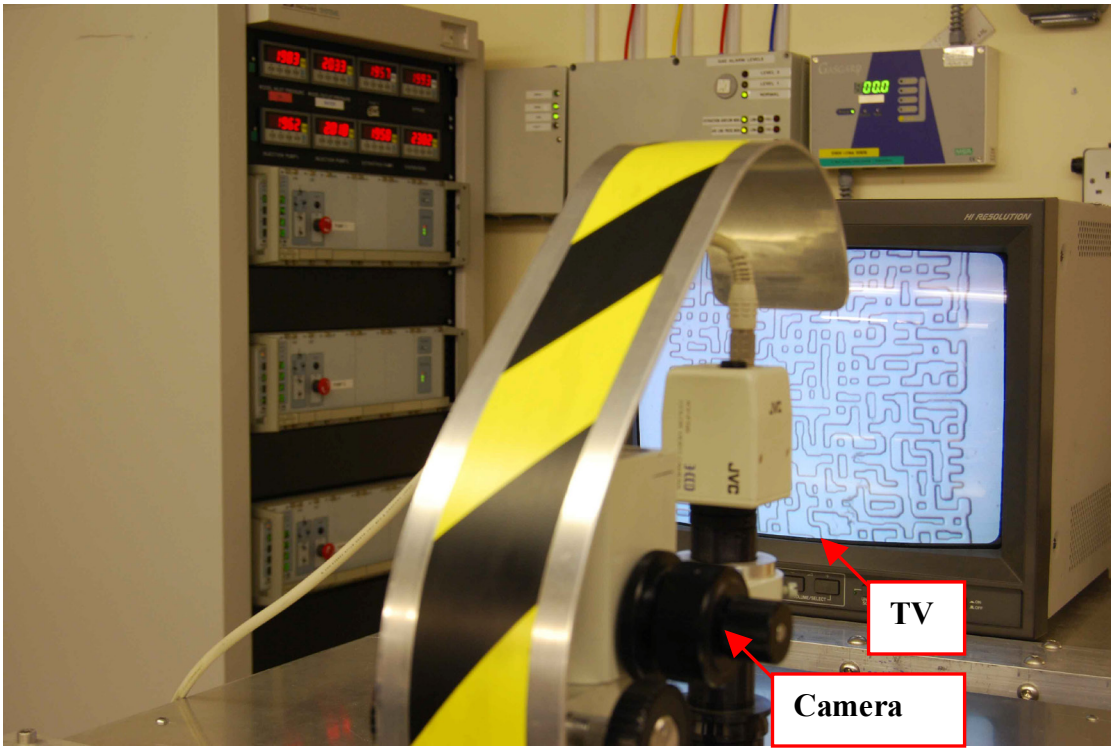

Figure 2-5: A picture of a part of the optical system of the rig in the laboratory.

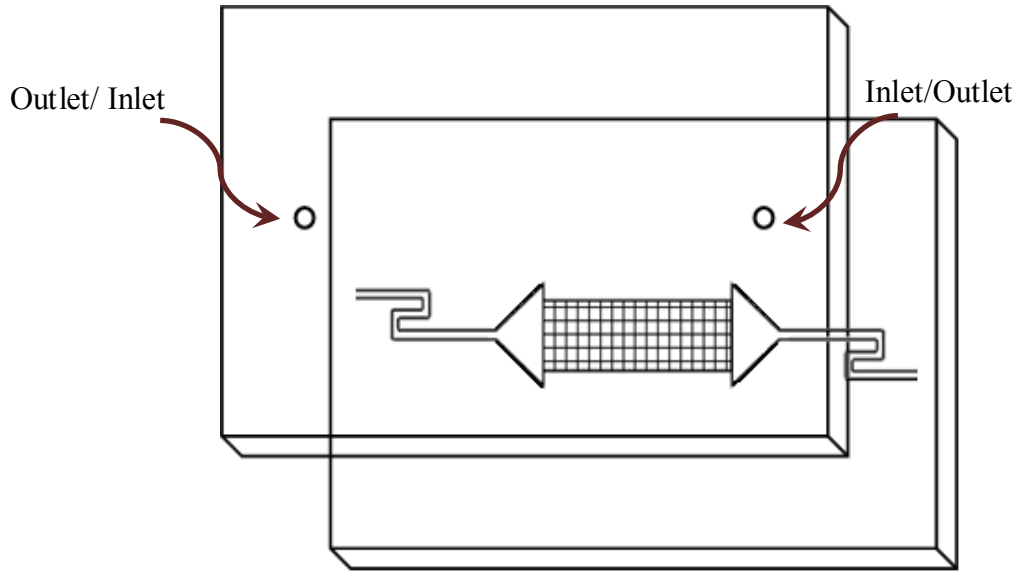

Figure 2-6: A schematic picture of two (pore pattern etched and cover) plates of the micromodel: transparent porous medium.

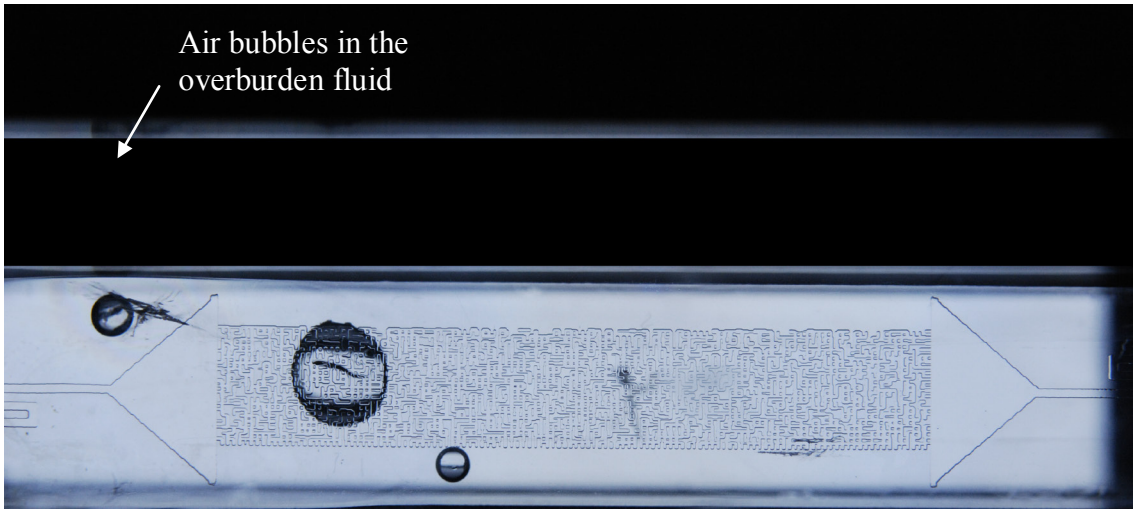

Figure 2-7: An image of the pore pattern and the two inlet and outlet triangles of the micromodel.

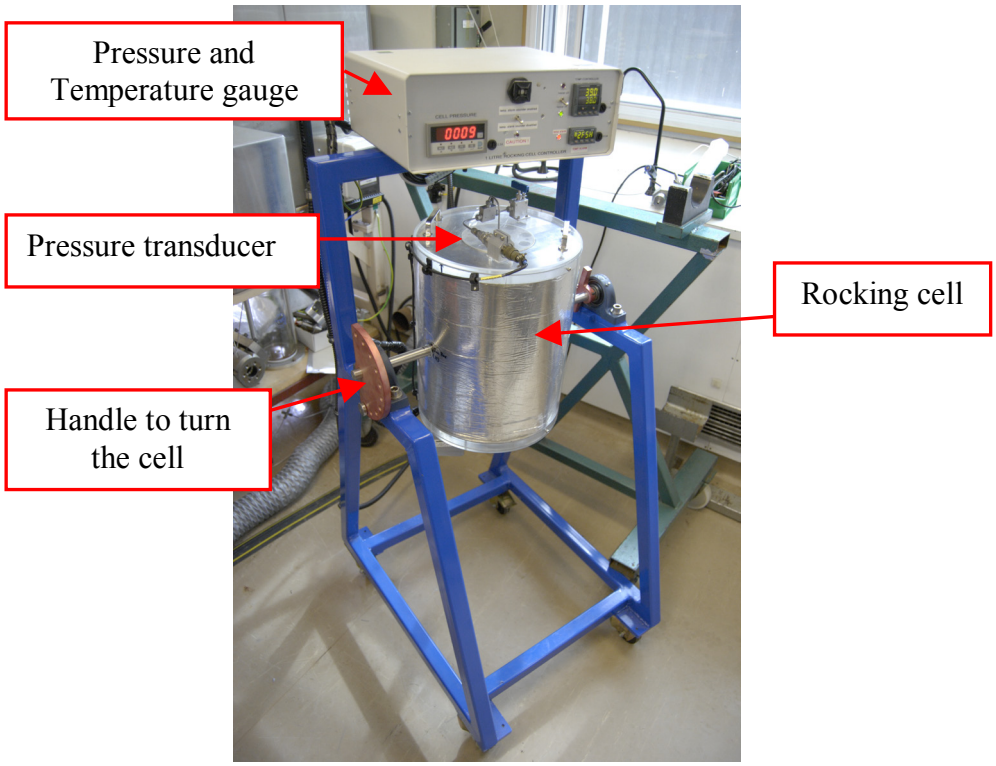

Figure 2-8: Picture of the rocking cell used to prepare carbonated water.

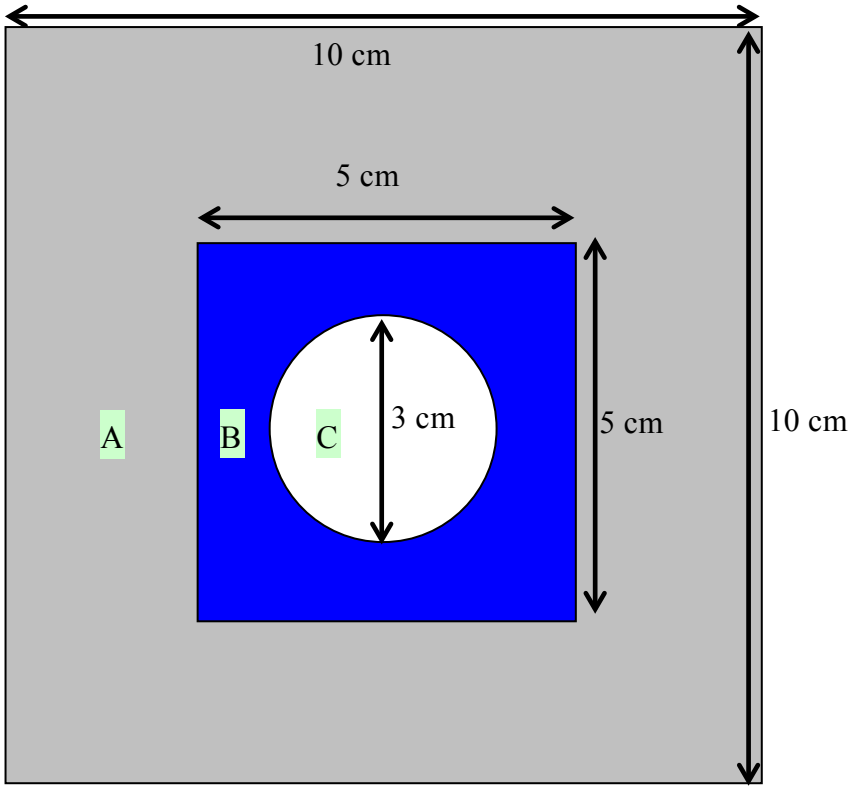

Figure 2-9: A simple example of fluid distribution: gray (A), blue (B) and white (C) areas are representative of grain, water and oil in the model, respectively.

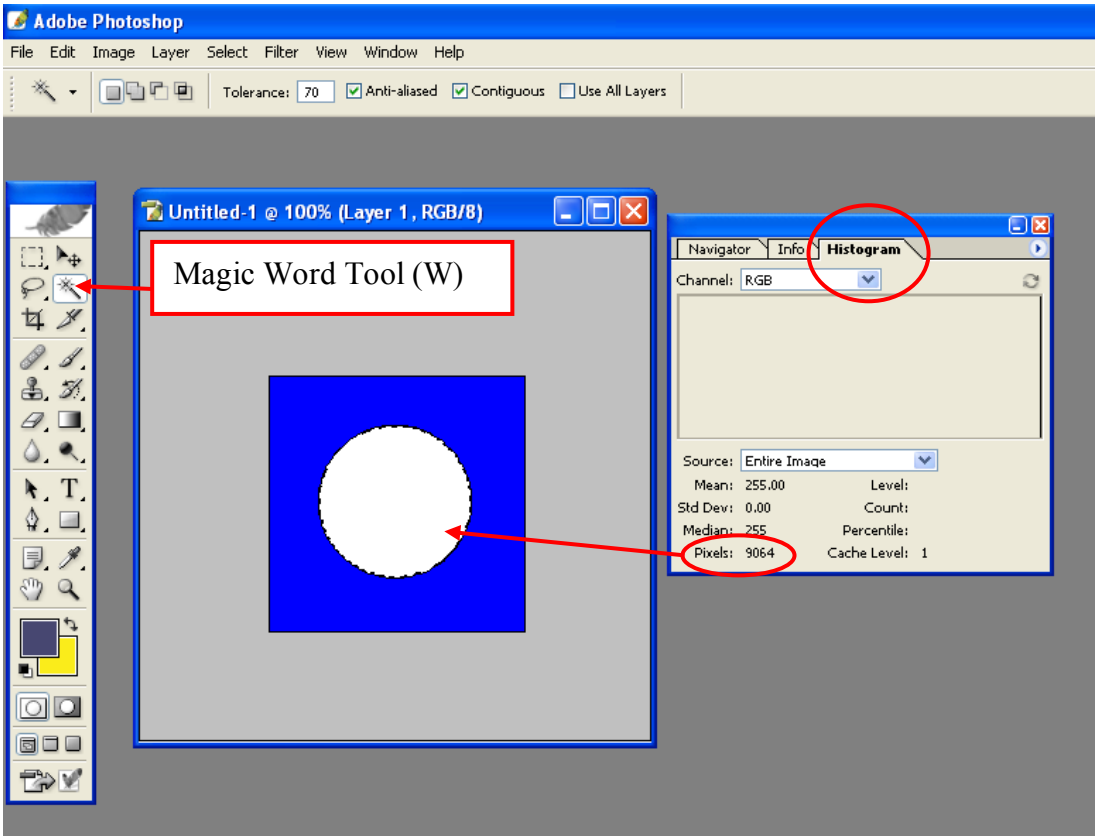

Figure 2-10: Image analysis using Adobe Photoshop.

3 Chapter 3: Experimental Results of Carbonated Water Injection

3.1 Introduction

Injection of CO_2-enriched water is expected to cause oil swelling and viscosity reduction. This can reduce water-oil interfacial tension and also favourably affect wettability of the reservoir. In waterflooded reservoirs, swelling of oil can reconnect the discontinuous residual oil resulting in additional oil recovery. An additional oil recovery process could be the in situ release of CO_2 subsequent to carbonated water injection (CWI) by pressure blow-down of the reservoir. Cyclic injection of carbonated water (CW) and water in porous media might also further reduce the amount of residual oil, which has been redistributed during the oil swelling and shrinkage processes. As mentioned previously one of the main objectives of this study was to investigate such processes and to address the lack of pore level information on CWI by conducting pore scale visualisation experiments through which the underlying physical processes involved in CWI can be identified and studied

This chapter describes the results of an experimental investigation of the process of CWI as an injection strategy for enhanced oil recovery (EOR) with the added value of CO_2 storage. A high-pressure micromodel experimental facility was used to simulate the CWI process and visually investigate its EOR potential at typical reservoir conditions.

The broad objective of these high-pressure micromodel experiments is to view and record processes such as fluid displacement and redistribution, alteration of wettability, oil swelling and CO_2 diffusion within the porous medium. Image analysis of such information can be used to identify and study important pore-scale mechanisms involved in oil mobilisation and recovery. This will improve our understanding of displacement principles underlying such processes in the reservoir. These images can

also be used in the development of mathematical models simulating the relevant processes.

Different mechanisms that occur at the pore level during CWI and cause oil recovery improvement are presented and discussed in this chapter by direct comparison between the performance of CWI and that of water injection (WI). In these experiments CWI was conducted as both a secondary and a tertiary oil recovery method with different CO_2 content. The results of the experiments are also analysed to evaluate the impact of blowdown mode subsequent to CWI and cyclic injection of plain water (without CO_2) and CW on oil recovery. In this chapter the effect of oil type on the performance of CWI is also studied by using two different mineral oil types and a real crude oil.

3.2 Rig Modification and Commission

One of the existing high-pressure micromodel rigs at Heriot-Watt University was modified and adapted to perform the required and planned experiments to investigate the process of CWI for oil recovery. For compatibility with CO_2, the existing stainless steel high-pressure storage cells were replaced with titanium cells to guard against possible corrosion issues and ensure safe operation. The rig was re-plumbed and leak tested at a pressure of 2500 psia. This was followed by a series of commissioning tests in a water-wet micromodel.

3.3 Experimental Procedure

All the experiments in this study were carried out using a 2-D glass micromodel with a semi-geometrical pore pattern. Since the micromodel is fragile and its pore volume is extremely small (0.01 cm^3), running the required experiments at high pressure conditions requires special care in the operational procedure, compared to conducting the core flooding experiments. Before setting micromodel, both the glass plates were thoroughly cleaned and polished using an ultrasonic Decone bath. Then they were flushed with plenty of distilled water. After the cleaning stage, the flat glass plate was placed over the etched one in order to cover the pore pattern and connect the input and output holes of the flat plate to the inlet and outlet path lines of the etched plate. Silicon rubber compound-flowable fluid was used to seal the groove between the plates.

Failure to achieve a perfect seal would result in failure of the experiments due to leakage of the overburden fluid into the porous medium. At this stage the sealed micromodel was mounted on the rig and overburden pressure was applied and maintained at around 300-400 psi above the pore pressure within the micromodel. In all the experiments reported here, the micromodel was mounted horizontally and kept motionless to minimise the gravity effect. Then the micromodel pressure (pore pressure) was increased gradually by injecting distilled water. After establishing the desired pressure and temperature, distilled water was replaced with degassed blue-dyed distilled water. Figure 1 shows the micromodel at the beginning of a typical experiment when it is fully saturated with blue water. The illustration shows the pore pattern as well as the triangular sections at both ends of the porous section, which have been designed to evenly distribute the fluids in the porous medium. Figure 2 shows a section of the micromodel (the red rectangular section highlighted in Figure 1) at higher magnification to show the pore pattern of the micromodel used in this study in more details. The full micromodel contains about 10 frames of images at this size. In both of these two figures, the blue areas represent the pores and the white areas are un-etched glass representing rock grains in real rocks. As can clearly be seen, these images show the semi-geometrical pore pattern of the model. This pore pattern was selected to be able to develop a mathematical model based on the micromodel results. The dimensions of the porous section as well as the size of the pores are given in Table 2-1.

After saturating and pressurising the micromodel with water, the experiments are commenced. To simulate the primary drainage of water and the initial migration of oil in a reservoir, the injection of the oil was carried out at a rate of 0.1 $cm^3\ h^{-1}$, for the majority of the experiments, to ensure realistic connate water saturation is established in a short period of time. The injection of oil stopped when the oil front reached the other end of the micromodel. This procedure was followed in some of the experiments whilst in others the oil was circulated through the by-pass line. This difference between these two exercises will be discussed later in this chapter.

Figure 3, shows fluid distribution in a section of the micromodel at the end of the oil (*n*-decane) injection period. To better differentiate between the un-etched glass and the oil, (both in white in the original image) in this image, the un-etched glass is shown as hatched areas. Figure 3 shows the relative positions of the wetting phase (blue water)

and continuous non-wetting phase (*n*-decane) in the porous medium. Water in the water-wet micromodel occupies the smaller and dead-end pores and also as layers on the walls of the oil-occupied pores. Figure 4 shows a magnified section of a part of Figure 3 showing the shape and the direction of the water-oil interfaces, which are also good indications of water-wet conditions within the micromodel.

After establishing the initial oil and water saturations, blue-dyed water was injected into the micromodel at a low injection rate of 0.01 $cm^3\ h^{-1}$ into the micromodel, to simulate more realistic flow velocities. Based on the time that it took for the water front to travel from the inlet of the porous section of the micromodel to its outlet and the length of this section of the micromodel, the actual velocity of water was estimated as around 3 $m\ d^{-1}$. A relatively similar velocity value was obtained for all the experiments reported here, which on its own is a good indication of a well-controlled fluid injection

One of the dimensionless parameters used to analyse the fluid flow mechanisms is capillary number, which is a ratio of viscous to capillary forces. Equation 1 was used to calculate capillary number in these experiments.

$$N_{ca} = \frac{F_v}{F_c} = \frac{v\mu_w}{\sigma_{ow}} \tag{3.1}$$

Where

N_{ca}: Capillary number,-.

F_v: Viscous forces, N.

F_c: Capillary forces, N.

v: Interstitial velocity (Darcy's velocity) = actual velocity * porosity*(1-S_{or}), $m.s^{-1}$.

S_{or}: Residual oil saturation, %.

μ_w: Viscosity of the displacing fluid, pa.s.

σ_{ow}: Interfacial tension between the displaced and displacing phases, Nm^{-1}.

Based on the estimated velocity in the experiments, capillary number values of 2.20E-7 and 2.86E-7 were calculated when using viscosity of water and carbonated water, respectively, in Equation 1. Using another method, based on the injection rate and cross sectional area, Darcy's velocity was estimated to recalculate capillary numbers. Using this method, capillary number values of 1.59E-7 and 2.06E-7 were calculated for water

injection (WI) and CWI, respectively. Although there are some minimal differences between the results of these two methods, the order of magnitude of capillary number for all of them is 1E-7. Table 1 shows the N_{ca} values for WI and CWI processes using these different methods. These low N_{ca} values confirm a capillary dominated flow regime within the micromodel.

Table 2 summarises the flooding procedure and the rate of different injections of 14 micromodel experiments reported in this chapter.

3.4 Carbonated Water Injection Experiments Using Refined Oils

3.4.1 Using Decane as the Oil Phase

Before the main experiments, some preliminary experiments were performed to evaluate the impact of colouring the fluids on the results and post processing image analysis exercise.

Preliminary Experiment No.1

In the first preliminary experiment, the red-dyed oil and blue-dyed water were used. Figure 5 illustrates the initial oil and water saturations in a selected frame of the model. As can be seen, the quality of the image is quite good.

Preliminary Experiment No.2

In the second preliminary experiment clear water, clear CW and red-dyed decane were used as the fluid system.

During this experiment, some evidence of wettability alteration of the micromodel was observed. The micromodel was water-wet at the beginning but during the experiment its wettability changed to less water-wet or even oil-wet at some parts of the model. Figures 6 and 7 show magnified image of a section of the micromodel before and after CWI, respectively. It is noted that before CWI all water-oil interfaces seem to be water-wet (Figure 6), whilst after CWI, in the same part of the micromodel, different wettability conditions can be identified from the shape of the water-oil interfaces in Figure 7. Wettability alteration is one of the most important factors controlling fluid flow and oil recovery. These results suggest that the red dye, which is a surface active

hydrophobic particle, was gradually adsorbed on to the glass surface and consequently changed the wettability of the system. Therefore the use of red dye in the next experiments was avoided.

Preliminary Experiment No.3

Since dyes make the image analysis possible and improve the quality of images, after ensuring that blue dye did not have adverse effect on diffusivity and concentration of CO_2 in the water phase, it was decided to use blue-dye in water. The results of solubility and diffusion coefficient experiments using clear and blue dyed water will be fully discussed in Chapter 6. However, as mentioned earlier, due to the adverse effect of red-dye in oil on the wettability of the system, its use in this experiment was avoided.

Figure 8 illustrates the initial oil saturation after oil flooding period. Comparison of this figure with Figure 5 shows that the initial oil saturation is almost equal for both experiments, with a very similar fluid distribution. This is another indication of a well-controlled fluid injection and good repeatability. After selecting the fluid system and ensuring that the results of the experiments would be repeatable the main experiments commenced.

Experiment No.1-Tertiary CWI- Decane

The first experiment was conducted with the purpose of studying the impact of CWI as a tertiary oil recovery method (post waterflood) on oil recovery. The interactions of CW with the resident fluids and micromodel were monitored by recording and verifying the pore scale mechanisms during this CWI process.

In Experiment No.1, initially the micromodel was fully saturated with degassed blue-dyed water and pressurised to 2000 psi at 38 °C (Figure 9A). Then, *n*-decane was injected at the rate of 0.1 $cm^3\ h^{-1}$ (Figure 9B) and stopped when the oil front reached the other end of the micromodel. The oil distribution in Figure 9B indicates a good connectivity of the pores in this micromodel. Figure 10 shows a selected section of the micromodel at the end of this oil injection period. The initial oil saturation in the micromodel was estimated to be 67.1%, using image analysis technique as described in Chapter 2.

After the establishment of the initial oil and connate water saturation, Figure 9B, WI commenced at low rate of 0.01 $cm^3 h^{-1}$. Figure 9C and Figure 11 show the whole image and the selected frame of the micromodel at the end of WI, respectively. Figure 11 shows the growth of the water film in positions highlighted with a circle and square during the WI when compared with the corresponding locations in Figure 10. Water films surrounding the oil in the pores were observed to grow in thickness, which indicates the film/layer flow mechanism. This is a direct result of the low rate of WI (capillary dominated) and strongly water-wet characteristics of the micromodel. As Figure 11 shows, capillary continuity (hydraulic connectivity) of the oil phase has been lost as a result of WI and the induced film flow. WI continued until steady-state conditions were achieved, where no more oil production or changes in the distribution of fluids within the micromodel could be detected. The residual oil saturation after this initial waterflooding stage was estimated at 49.1%, which showed 18.0% oil production with a 26.8% oil recovery factor compared to the initial oil saturation.

The oil production during waterflooding took place mainly before the water breakthrough (BT). After BT, the flood water passed through the porous medium via the water films that had already been formed and left the model without any further oil recovery or fluid re-distribution. Thus, the only way to produce more oil after waterflooding is either by increasing the injection rate dramatically or somehow reconnecting the isolated and trapped oil ganglia to each other. Since the former is not practical in a real reservoir conditions, in this study the feasibility of the latter is investigated by applying CO_2-enriched water injection. Hence, CWI as a tertiary recovery method was begun at the same rate as the previous WI.

Figure 12 shows the fluid distribution in the micromodel an hour after CWI. A comparison of Figure 12 with Figure 11 shows that as a result of CWI, swelling of the oil took place due to the partitioning of CO_2 from the injected CW and its diffusion and dissolution into the oil phase. The red rectangle highlights swelling of oil in a part of Figure 12 when it is compared with the same position in Figure 11. As shown in Figure 12 (red arrows), this oil swelling caused re-connection of two isolated oil ganglia left behind after the waterflooding stage. More swelling and reconnection was observed as CWI continued. Compared with Figure 12, Figure 13 shows more oil swelling (highlighted by the red rectangle) and consequently oil reconnection (highlighted by the

red arrow) after about 3 hrs of CWI. As a result of the oil swelling and reconnection, the remobilisation and recovery of part of the oil could be expected. Figure 14, when compared with Figure 13, demonstrates the second oil displacement after about 6 hrs of CWI. As a consequence of oil displacement, more oil was recovered. Furthermore, it should be noted that swelling and reconnection began to take place after CWI and continued through out the CWI process. For this reason, oil production as a result of swelling and coalescence occurred gradually during the course of CWI.

In Experiment No.1 (Tertiary CWI- Decane), the swelling of an isolated oil ganglion was also monitored. This enabled us to monitor the full mass transfer process. The quantified data for the swelling process of this oil ganglion will be discussed later in this chapter. Figures 9D and 15 show the final fluid distribution in the micromodel after one week of CWI. The remaining (swollen) oil saturation at the end of this stage was estimated at 64.3%, which was close to the initial (dead) oil saturation, 67.1%, prior to the preceding water flooding.

Since the remaining oil in the micromodel contains dissolved CO_2, direct comparison between this stage and the plain water (without CO_2) injection stage to determine the additional oil recovery is not valid. In order to establish the amount of the actual recovered oil by CW, a second WI period followed CWI to obtain the black oil equivalent volume of the remaining oil after the CWI by stripping the dissolved CO_2 from the oil. This remaining oil can be considered as the residual oil saturation at the end of the CWI and can be compared with what was obtained after the initial WI period. Figure 9E shows the residual oil saturation in the micromodel after this second period of WI. Comparison of this image with Figure 9D, illustrates significant oil shrinkage and/or displacement. Comparing the oil saturation after the second WI (Figure 9E) with the residual oil saturation at the end of the first WI (Figure 9C) reveals significant oil production during CWI and the subsequent WI (2^{nd} WI period). The oil saturation at this stage is estimated at 33.4%, which indicates 15.7% additional oil production during the first cycle of CW and WI. Figures 16 and 17 show some fragmented and disconnected oil ganglia resulted from the shrinkage of the oil during the 2^{nd} WI 3.7 and 6.5 hrs after WI, respectively. The red arrows highlighted in these figures indicate disconnected locations compared to their corresponding previous stages.

The first experiment continued by injecting a second cycle of CW/water with the purpose of investigating the impact of additional cycle of CW/WI on oil recovery and displacement.

Figures 18A and 18B show the results of fluid distribution in the whole micromodel at the end of the 2nd CWI and the 3rd WI periods. The oil saturation at the end of the 2nd CWI and the 3rd WI was estimated at 60.0% and 33.0%, respectively. The comparison of the oil saturation values, Table 3, shows very small oil recovery in the second cycle, 0.4%, compared to the additional oil recovery in the first cycle, 15.7%.

The experimental results so far show that alternating injection of water and CW brings about favourable oil redistribution and more oil production. However, the additional oil recovery in the first cycle, 15.7%, is much more than that in the second cycle, 0.4%. This shows that the potential of the first cycle is significantly higher than that of the second cycle. This difference could be mainly due to having higher (dead) oil saturation within the micromodel before the first CWI compared to that before the second CWI.

Based on the values of oil saturation reported in Table 3 and neglecting the oil produced in the second cycle and also assuming the same oil swelling factor (the validity of this assumption is discussed later, in the discussion section) at the end of the first and the second CWI, it can be concluded that out of the total of 15.7% additional oil recovery observed after the first cycle of CWI and WI, about 13.0% was recovered during the CWI period and about 2.0% ((64.2-60.0)*(1-swelling factor)) during the subsequent WI period (the 2nd WI). The oil production during the 2nd WI subsequent to the 1st CWI can be linked to another pore scale mechanism, local flow diversion, and also to different swelling and shrinkage rates during CWI and WI, respectively. These two most likely reasons are discussed in more details in the discussion section of this experiment.

Discussion

Local flow diversion

As shown earlier, oil swelling as an initial important mechanism results in more oil recovery during CWI compared to unadulterated WI. In addition to causing coalescence of the isolated oil ganglia, oil swelling also affects the flow path at the pore level. That is, swelling of the oil due to diffusion of CO_2, blocks some of the pores in

the porous medium. This pore blockage, either partially or completely, would cause local flow diversions and velocity alteration at the pore level, which could in turn cause fluid redistribution and oil recovery. It should be mentioned this pore blockage is one of the important oil recovery mechanisms in polymer injection. Figure 19 shows two small oil ganglia before and after CWI demonstrating the swelling of the oil due to CO_2 dissolution and hence how this swelling could restrict the flow of CW around these pores and cause flow diversion.

Diffusion rate during different stages of the experiment

An oil ganglion far away from the other oil ganglia was selected in order to avoid reconnection. This oil ganglion, which is shown in Figure 20, was monitored during the different stages of the first experiment. Comparison of Figure 20B (oil shape at the end of the first CWI) and 20A (isolated oil after the first WI) demonstrates a considerable swelling of the oil and displacement of the water phase by both co-current and counter current flow mechanisms, within the pores as a result of oil swelling process during CWI.

The first conclusion that can be drawn, based on the different shape and distribution of the oil ganglia both after WI (Figures 20A, 20C and 20E) and after CWI (Figures 20B and 20D), is that the swelling and shrinkage process are not exactly the reverse of each other.

To investigate the CO_2 diffusion rate during the swelling and shrinkage processes, the volume (area in 2D) of the oil ganglion, at different times during CWI and WI, was estimated and plotted, using image-processing technique.

The oil volume versus time has been plotted in Figures 21 for different stages of Experiment No.1. Based on these data, the estimated swelling of *n*-decane is around 100% at the conditions of the experiment i.e., 2000 psi and 38°C. This plot shows that the swelling rates for the first and second CW floods are almost the same. These data also shows the same diffusion rate for the second and third WI periods.

As can be seen from Figure 21, there is a significant difference between swelling and shrinkage rates in both the first and the second cycles. Some likely reasons for this observation will be discussed based on the developed mathematical model in Chapter 7.

Combination of the observed significant difference between the oil swelling and shrinkage rates and the local flow diversion, which causes fluid redistribution within the porous medium to some extent, explains the oil recovery during the second WI.

Wettability alteration

Another important observation that should be mentioned and highlighted, before ending the discussion of this experiment, is the settling water layer between the oil and the glass (micromodel) during CWI stages (Figures 20B and 20D) compared to their previous and subsequent plain WI stages (Figures 20A, 20C and 20E). This point, which has been highlighted by a brown arrow in Figure 20B can be an evidence of wettability alteration during CWI towards more water wet conditions.

Another interesting point in Figure 20C and 20E is the fact that the oil ganglia on the left side of the micromodel appear to wet the surface, i.e., the ganglia are very small, not rounded and appear to thin towards their edges. This observation could be due to non-uniform geometry of the oil ganglion, non-uniform plain water source, different local flow rate around the oil ganglia and consequently the non-uniform shrinkage rate on different sides of the oil. In other words, during the shrinkage process the oil would be disconnected, with a very thin layer of oil remaining in the pores surrounded by blue water due to the above reasons, as shown in Figure 22. The second likely explanation for this observation could be wettability alteration from (strongly) water wet to weaker water wet condition during WI subsequent to CWI stage. This observation was a starting point for the author to consider wettability alteration by CWI compared to plain (without CO_2) WI. Wettability alteration by CW will be discussed comprehensively and in detail in Chapter 5, both qualitatively and quantitatively.

Experiment No.2- Secondary CWI- Decane

The visual and quantified data of Experiment No.1 (Tertiary CWI- Decane) show additional oil recovery by CWI in the tertiary recovery mode compared to the plain waterflooding. The relevant oil displacement mechanisms by CWI at the pore level

were also visually shown in the previous experiment. Experiment No.2 was carried out at the same pressure and temperature as the previous experiment, with the primary purpose of investigating the performance of CWI as a secondary (pre-waterflood) oil recovery method. In fact, Experiment No.2 was originally designed to compare the performance of CWI process as a secondary mode with the tertiary one (in the previous experiment).

In the second experiment (Secondary CWI- Decane), as in the first experiment, to simulate primary drainage of water, decane was injected at a low rate of 0.1 $cm^3 h^{-1}$, but unlike Experiment No.1 (Tertiary CWI- Decane), the injection of the oil was continued and circulated through the bypass to displace all the plain water in the lines. It should be noted that although the length of the line and the amount of water is very small, for the secondary mode replacing all the plain water in the line is essential, otherwise once CW has entered the micromodel it brings a bank of plain water, separating oil and CW, consequently the results will be similar to the tertiary recovery method.

Since the displacement mechanism during CWI is not completely pistonwise, some oil remains behind in the inlet line. Figure 23 shows the lower side (input section) of the micromodel, illustrating some oil ganglia in the inlet line after passing the front of CW. If this oil enters the porous section of the micromodel during water or CW injection, the final results will not be comparable with tertiary and therefore makes the analogy dubious.

Figure 24 shows the initial (A) and final (B) fluid conditions of one of the successful secondary experiments in the micromodel whole-image (see Appendix B for the results of the intermediate stages of this test).

The same section of the micromodel as that shown in Figure 10 (in Experiment No.1, Tertiary CWI- Decane) was selected (highlighted by a red rectangle in Figure 24) to compare the results of these two experiments. See Table 2 for the details of different injection stages of these two experiments.

The mechanisms observed for oil recovery and displacement during CWI were both film flow and piston type displacements identical to the WI in the first experiment.

Discussion

Secondary vs. Tertiary oil recovery by CWI:

The results of these two experiments show that the main oil recovery mechanism during CWI is oil swelling as a result of CO_2 diffusion from CW into the oil phase, which causes reconnection of the isolated oil ganglia and fluid redistribution during the flooding process.

Figures 25A and 25B show the dead oil saturation at the end of the first CWI period in the first experiment, and the second experiment, respectively. To highlight this difference, the colour of the oil was altered to red in both images. Comparison of these images shows the lower residual dead oil saturation (red area) after CWI as the secondary recovery mode (Figure 25B) compared to CWI as the tertiary recovery mode (Figure 25A). Quantified data based on image analysis show 30% less residual oil in the secondary mode (Figure 25B) compared to the tertiary mode (Figure 25A).

The results of these two experiments demonstrated that CWI increases oil recovery for both secondary and tertiary recovery scenarios. However, the results of both the visual and quantified data indicate that CWI results in much higher overall recovery when injected prior to waterflooding i.e. as a secondary oil recovery method.

Based on the results of these two experiments, switching a WI plan to CWI, which can improve oil recovery from reservoirs, can be considered. This action is also important in terms of CO_2 storage, especially nowadays when the huge CO_2 producers such as power stations have been committed to developing sustainable solutions in response to the challenge of continued use of fossil fuels, climate-change and compliance with national and international commitments to reduce CO_2 emissions.

Swelling rate during CWI as secondary or tertiary recovery methods

Higher oil recovery when CWI takes place before WI rather than after WI is likely to be due to better oil connectivity when CW enters the micromodel before WI. Another possible reason for this important difference could be lower water saturation in the porous medium before CWI in the secondary mode compared to that in the tertiary mode, which affects the effective CO_2 concentration in the CW phase and also the mass transfer rate. These possibilities are discussed here in part, based on the visual

observations, and further explanation in this regard, will come in Chapter 7 based on the results of the developed mathematical model.

Figure 26 compares the swelling rate of oil during CWI in the first experiment (Tertiary CWI- Decane) with that in the second one (Secondary CWI- Decane). The data show that the degrees of swelling adequately match each other, thereby demonstrating, to some extent, the reliability of the image analysis process and repeatability of the results.

The initial part of the quantified date (highlighted by the brown rectangle), however, shows slightly higher swelling rate during CWI as secondary than as tertiary mode. Figure 27 shows this part of the data at higher magnification. The higher swelling rate at the beginning of the second experiment, which keeps connectivity of the oil phase in the porous medium better (when the oil saturation in the model is still high), could be the most likely reason for the noticed difference in oil recovery in these two different flooding strategies. It should be also mentioned that this difference is more pronounced at early times.

3.4.2 Using Viscous Mineral Oil as the Oil Phase

Experiment No.3- Tertiary CWI- Viscous oil

In Experiment No.1, the impact of CWI in tertiary recovery mode and that of alternating injection of CW and water on the recovery of *n*-decane as light oil was investigated. In Experiment No.3 a similar procedure was carried out but viscous mineral oil was used instead of *n*-decane to investigate the impact of oil type on the performance of CWI process. In Experiment No.3 again, similarly to Experiment No.1 (Tertiary CWI- Decane), two cycles of water and CWI were carried out.

The visual data of this third experiment (see Appendix B) like the results of Experiment No.1 indicate that the alternating injection of CW and water brings about redistribution of fluids in the porous medium. In both tests, the redistribution and displacement of the oil was observed to happen mainly in the first cycle.

The dead oil saturation in the micromodel at different stages of this experiment (No.3) was estimated. Table 4 contains the oil saturation values, including the initial oil saturation and that after the three WI stages. The data show that as a result of the first

WI period, the initial oil saturation reduced from 76.4% to 56.7%, which shows 19.7% oil production with a 25.8% oil recovery factor. Table 4 also shows that during the subsequent first cycle of alternating injection of CW and water, 6.7% more oil was recovered. However, the additional oil recovery in the second cycle of CWI followed by WI was only 0.7%.

Discussion

Oil recovery: light oil versus viscous oil

Based on the results of CWI into *n*-decane and the viscous oil, the performance of the CWI process for these two different kinds of oil can be compared. For this purpose, the initial and final fluid conditions (after two cycles of CW/W injection) in the middle frame of the micromodel are studied. Figures 28 and 29 show the initial oil saturation (left hand side images) and the final dead oil saturation conditions (right hand side images) for the CWI into the viscous oil and *n*-decane, respectively.

Comparison of the initial oil saturation and distribution (left hand side images) of viscous oil in Experiment No.3 (Tertiary CWI- Viscous oil, Figure 29) with the corresponding one in Experiment No.1 (Tertiary CWI- Decane, Figure 28) shows a very similar fluid distribution within the micromodel. Nevertheless, a higher initial oil saturation value was achieved for the viscous oil (76.4 %) compared to the experiment with *n*-decane (67.1 %). Higher oil saturation in Experiment No.3 is due to larger viscous force because of higher oil viscosity (16.47 cP as opposed to 0.83 cP). The injected non-wetting fluid (oil) with higher viscous force would overcome easier the capillary forces within the pores preventing the displacement of the wetting phase, i.e. lower resident water saturation.

Comparison of the right hand side images in Figure 28 and 29 shows lower residual dead oil saturation (white area) after CWI using *n*-decane (Figure 28) compared to that using the viscous oil (Figure 29). The higher oil recovery observed during the light oil CWI experiment is mainly attributed to the observed higher oil swelling and coalescence in this oil compared to the viscous oil.

In addition to the visual results of these two experiments, the quantified (saturation) data can also provide further vital information to investigate the effect of oil type on oil

recovery. Figure 30 and Figure 31 show a summary of the oil saturations estimated at the end of the different stages with the corresponding recovery factors with respect to their previous stages in the first and the third experiments, respectively. The data show that, for both *n*-decane (light oil) and the viscous oil, the injection of CW resulted in more oil recovery over and on top of what had already been recovered during the preceding waterflooding. However, the recovery factor for *n*-decane (32.7%) was much greater than the viscous oil (11.8%).

Swelling factor: light oil versus viscous oil

Figure 32 shows snapshots of a viscous oil ganglion before and after CWI. The swelling factor from these images is estimated at about 23%. The higher swelling factor for *n*-decane (100%) compared to the viscous oil is consistent with the expected higher CO_2 solubility in the lighter oil.

The higher production of *n*-decane during CWI, as was noted in the previous section, can be linked to the higher oil swelling and coalescence in this oil compared to the viscous oil.

Although the quantified data indicate that the swelling of the viscous oil is less compared to that of decane, the experiments' images (see Appendix B) show that it is significant enough to cause coalescences of the trapped oil. However, greater viscosity reduction, known as another oil recovery mechanism, for this viscous oil compared to that for decane is also expected to play a role. The effect of viscosity reduction will be later investigated and discussed by performing some CWI experiments with lower CO_2 content.

CO_2 storage capacity: light oil versus viscous oil

As discussed in Chapter 1, in addition to enhanced oil recovery, CWI can also be considered as part of a carbon capture and storage programme. Therefore, the amount of stored and trapped CO_2 within micromodel was estimated.

At final equilibrium test conditions after CWI, the relative volume of stored CO_2 in the residual oil saturation, was estimated around 18.7 Vol%, of the viscous oil saturation, and 50 Vol%, of *n*-decane. The corresponding value in the water phase is around 7

Vol%. Table 5 compares these values and the corresponding oil and water saturations in these two experiments (No.1 and No.3). These data reveal that the total amount of CO_2 stored (which is equal to oil swelling times oil saturation plus water swelling times water saturation) in the experiment using *n*-decane (34.5%) is higher than the corresponding value in the experiment using the viscous oil (14.2%). As the tabulated data reveals, this difference is mainly due to higher CO_2 solubility in *n*-decane compared to the viscous oil. At reservoir scale this amount of CO_2 storage is significant.

It should also be added that, based on the recent UK Production Data Release (1 April 2008), the total injected water in all the oil fields in the UK, offshore and land oil fields, in 2007 was about 7.1E+7 tons. A rough estimate shows that if CW had been used instead of water, assuming the same level of CO_2 solubility observed in our experiments, we would have had about 4.97E+6 tones of CO_2 injected. Some of this CO_2 might be produced by oil and water production streams, which can then be re-injected back into the reservoir.

3.4.3 Carbonated Water Injection with Lower CO_2 Content

In the previous experiments (No.1 to 3), two main mechanisms of oil recovery during CWI were discussed. They were i) oil swelling and the subsequent flow diversion and coalescence of the trapped oil ganglia and ii) the reduction in oil viscosity. The former is the dominant mechanism for light oils with their high CO_2 solubility and the latter is more relevant for viscous oils with a significant reduction in their viscosity as a result of CO_2 dissolution. The results of the visualisation experiments of two oil types illustrated this effect, to some extent. To further evaluate the impact of these two displacement mechanisms for these two oil types some more experiments with lower CO_2 content in the CW were performed

It is worth mentioning that in practical terms to avoid the formation of free gas in reservoir as a result of pressure and temperature change, which could drastically reduce the injectivity and relative permeabilities of fluids and consequently affect the oil recovery, it is recommended to make CW with lower CO_2 content than the fully saturated concentration conditions. Furthermore, it should be noted that as CW front progresses it loses its CO_2 content whilst coming in contact with the oil free from CO_2.

Therefore in the next set of experiments the effect of CO_2 concentration in CW on the performance of the CWI process was investigated to cover these issues. That is, in the previous experiments, the carbonated water was in equilibrium with CO_2 at the experimental pressure and temperature conditions, i.e. the full CO_2 concentration (33 CO_2 sm^3/water sm^3) was used, but in these experiments CW was sub-saturated by half under the same pressure and temperature conditions.

Experiment No.4- Tertiary CWI- Viscous oil- Low CO_2 Concentration in CW

In Experiment No.4 a similar procedure was carried out as Experiment No.3 (Tertiary CWI- Viscous oil), with the only difference being that CW with a lower CO_2 content (17.8 CO_2 sm^3/water sm^3) was used.

Figures 33A and 33B show the fluid distribution, after the first CWI (with residual dead oil saturation), in Experiments No.3 and No.4, respectively. These figures reveal significantly greater residual oil saturation in Experiment No.4 (Figure 33B) compared to that in Experiment No.3 (Figure 33A). This indicates better oil recovery by CW with higher CO_2 concentration. The additional oil recovery by CW in Experiment No.4, 2.6%, estimated to be less than that in Experiment No.3, 6.7%. This difference is attributed to the lower CO_2 content of CW in Experiment No.4, that is, the degree of coalescence of the isolated oil ganglia during CWI mainly depends on the amount of oil swelling, which is a function of the CO_2 content in CW. This dependency will be further investigated in Chapter 7 using the developed mathematical model.

Experiment No.5- Tertiary CWI- Decane- Low CO_2 Concentration in CW

In Experiment No.4, the impact of lower concentration of CO_2 in CW on recovery of the viscous oil was investigated. In Experiment No.5 a similar procedure was carried out with the only difference that *n*-decane, as the light oil, was used.

The visualisation results of this test can be found in Appendix B. The oil saturation of the porous section of the micromodel was estimated, and plotted versus time (Figure 34). The green line in Figure 34 shows the oil recovery after the first WI, which took place in a relatively short period of time compared to the rest of this experiment. The blue line indicates the second stage of this test, which corresponds to the main swelling as a result of CWI. At the end of this stage some oil (estimated as around 2.3 %) was

produced. Because these graphs have been prepared based on oil volume in the porous section of the micromodel (disregarding the inlet and outlet triangles), so the amount of oil recovered out of the porous section has been shown as a brace in the plot. The brown line is a representation of the shrinkage process during the second WI. The amount of oil produced at the end of this stage has been estimated as around 1.5%.

The quantified data show that the additional oil recovery by CW and the subsequent WI in Experiment No.5 (Tertiary CWI- Decane- Low CO_2 Concentration in CW), 3.8%, was significantly less than that in Experiment No.1 (Tertiary CWI- Decane), 15.7%.

This considerable difference in oil recovery can also be visually observed and confirmed by comparing the visualisation results of the experiments. Figures 17 and 35 show the final remaining oil saturation in a selected frame of the micromodel for Experiments No.1 and No.5, respectively. Comparison of these two images illustrates the high impact of the level of dissolved CO_2 in CW on oil recovery. Another point that should be mentioned is that in Experiment No.1, oil production took place continually at the early stages of CWI, whereas in Experiment No.5, oil production was just observed once and at a late stage of CWI. This discrepancy, which is also believed to be attributed to oil swelling, will be discussed in the following section.

Oil swelling factor: high carbonation level versus low carbonation level

The swelling factor of *n*-decane in Experiment No.5 is estimated to be 23.6 % which is significantly less than 100% observed during the first test. It should be noted that the carbonation level of the CW in this experiment was about half of that in Experiment No.1. However, the swelling factor reduction was considerably more. Figure 36 shows this difference visually, during the whole process. The reason for this observation will be discussed theoretically in Chapter 7.

Oil recovery mechanisms: oil swelling and coalescence vs. oil viscosity reduction

To further evaluate the relevant displacement mechanisms in different oil types, the final quantified data, (swelling factor and oil recovery factor (RF) for the CWI period compared to the preceding WI stage) of the discussed visualisation experiments have been tabulated in Table 6 and plotted in Figure 37. These data indicate that the oil recovery increases when the swelling factor is increased for both *n*-decane and the

viscous oil. A higher swelling factor results in more oil reconnection; hence more oil displacement and recovery is achieved. An important conclusion can be drawn from the comparison of the results of the third and the fifth experiments, which are presented in bold in Table 6. These data show a higher oil recovery factor for the viscous oil in Experiment No.3 (Tertiary CWI- Viscous oil) with CW fully saturated with CO_2, 11.8%, compared to *n*-decane in Experiment No.5 with reduced level of carbonation, 4.4%, although based on the fluid conditions almost the same swelling has been achieved. If we neglect the effect of viscosity reduction of *n*-decane during CWI on oil recovery compared to that in the viscous oil, it can be concluded that about 63% ([11.8-4.4]/11.8) of the recovered viscous oil has been due to the viscosity reduction mechanism and the rest, 37% (=4.4/11.8), is due to the swelling and coalescence mechanisms.

To this effect, Figure 37 also shows that with increased oil swelling there is an increased level of oil recovery. This figure shows an almost linear dependency of oil recovery factor on swelling factor for the limited available data. Furthermore, this plot shows two sets of data with two different slopes (steeper slope for the viscous oil). As mentioned earlier, this difference could be due mainly to different impacts of the two oil recovery mechanisms for different oil types during the CWI process.

Experiment No.6- Secondary CWI- Decane-Low CO_2 Concentration in CW

Experiment No.6 was carried out at the same pressure and temperature and with the same oil and CW as the previous experiment with the only difference being that in Experiment No.6 CW was injected as a secondary (pre waterflood) oil recovery method to compare the performance of the CWI process as a secondary mode with the tertiary mode (Experiment No.5), both with lower CO_2 concentration in CWI (i.e. lower oil swelling).

In this experiment (No.6) a depressurisation period was also performed after the CWI period, to investigate the potential benefits of a blowdown period on oil recovery and fluid redistribution within the porous medium.

Discussion

Secondary vs. tertiary oil recovery:

The oil saturation values for the whole micromodel versus time are shown in Figure 38. These data can be divided into three parts: 1) main oil displacement up to the BT of CW, 2) oil swelling of the remaining oil phase during CWI, 3) coalescence of the isolated oil ganglia as a result of the swelling and the resultant fluid redistribution and oil production.

It should be pointed out that just as in the WI period in the previous experiment (No.5, Figure 34), the duration of the first part of this experiment (No.6) was significantly shorter than that of the second part. This point suggests that the displacement rate is considerably faster than the diffusion rate. Generally, the additional oil recovery obtained during CWI can be divided into two stages: (i) direct displacement and (ii) CO_2 diffusion. It is expected that the performance of CWI would be enhanced if the injection rate was lowered to allow more CO_2 diffusion before the oil became disconnected by the advancing front.

Comparison of the quantified oil saturation data of this secondary experiment (Figure 38) with the corresponding values of the previous tertiary experiment (Figure 34) reveals that although CWI recovered extra oil after BT both as secondary and tertiary recovery methods, the additional oil recovery was greater in the secondary (3.2%) than tertiary mode (2.3%). The extra oil was also recovered faster in the secondary (40 hrs of CWI) rather than the tertiary mode (100 hrs of CWI) showing the advantage of CWI as the secondary mode is greater than that as the tertiary mode. These data confirmed the results of the first and the second experiments that had shown that CWI results in much higher overall recovery when injected prior to waterflooding.

Depressurisation stage:

During CWI, a significant amount of CO_2 is dissolved in oil and water. This dissolved CO_2 can provide a source of energy for additional oil recovery in a pressure blowdown mode subsequent to CWI. This blowdown phase following CWI can also cause significant redistribution of the fluids within the reservoir. Therefore, in this experiment (No.6), after CWI the micromodel went through a depressurising period in

which the pressure of the system (both micromodel and overburden pressure) was reduced slowly by a depletion rate of 50 psi/hr (average value). In Experiment No.6 (Secondary CWI- Decane-Low CO_2 Concentration in CW), gas started to nucleate when pressure dropped below 485 psi.

The distribution of the fluids after this depressurisation period is shown in Figure 39(B). The yellow colour in this figure shows the free gas phase that has been formed during the pressure blowdown period. The CO_2 was digitally coloured in yellow, using an image analysis computer program to distinguish the colourless CO_2 from the clear oil phase. This figure reveals that the gas bubbles are in the oil phase rather than in the water. This could be due to the fact that interfacial tension (IFT) between CO_2 and *n*-decane compared to that between CO_2 and water is lower: hence, CO_2 bubbles stay in the oil rather than in water to reach more stable conditions of minimum energy level after the gas nucleation and expansion stages. This observation is in line with the IFT data reported in the literature for a heavier oil-water-CO_2 system, (Yang and Gu 2004a and 2004b).

Comparison of the remaining oil volume in Figure 39B in which the pressure is 180 Psia with the oil volume at the early stages of CWI period (Figure 39A) shows that there is a significant amount of fluid redistribution and additional oil recovery. This additional oil recovery was as a result of both CWI (because of CO_2 diffusion) and the subsequent blowdown period. It should be noted that the comparison of the value of the remaining oil in these two figures is open to question to some extent, because there is no dead oil volume in these two figures. However, because of the relatively low quantity of dissolved CO_2 at the conditions shown in both figures, the difference is not expected to significantly affect the results. The low amount of dissolved CO_2 in the former (Figure 39B) has been obtained by lowering the pressure and in the latter (Figure 39A) is due to a short CWI.

Oil swelling factor: Fully saturated versus partially saturated CW,

Another purpose of performing Experiment No.6 (Secondary CWI- Decane-Low CO_2 Concentration in CW) was verifying the oil (*n*-decane) swelling factor by comparing it with what was observed in Experiment No.5 (Tertiary CWI- Decane- Low CO_2 Concentration in CW).

As Figure 40 shows, the amount of oil swelling was estimated to be 23.8 %, which is in a very good agreement with the corresponding value estimated for the same oil during CWI in Experiment No.5.

As mentioned earlier, the purpose of depressurising the fluid system was investigating the feasibility of blowdown mode, subsequent to the CWI stage, on additional oil recovery. However, two more experiments (Experiment No.7 and No.8) were carried out with the main purpose of monitoring the gas nucleation and detecting the exact pressure of liberation of the gas from the liquids (oil and water) within the porous medium during the depressurisation period. The results of these two experiments, which have been discussed in Appendix C, confirm the gas nucleation below 485 psi.

3.5 Carbonated Water Injection Experiments Using Crude Oil

3.5.1 Using Crude Oil-A as the Oil Phase

Holm (1986) claimed that there can be substantial differences between the flow behaviour of refined oils and crude oils that could be due to the effect of rock wettability alteration by the crude oil. Therefore, in this study, three more micromodel experiments were performed using a crude oil sample to compare the performance of CWI into porous media saturated with mineral oils. In these experiments a real reservoir crude oil (crude oil A) was used to investigate the pore-scale mechanisms of oil recovery by CWI and the interactions between CW and oil/water/solid under more realistic conditions.

The fluid system used consisted of distilled water, carbonated water (fully saturated) and crude oil A. The crude oil properties are shown in Table 2.3. The blue dye in the water phase was eliminated, since the crude oil was already brown in the model and the interfaces were clearly visible to differentiate the phases.

Experiment No.9- Secondary CWI -Crude oil

In Experiment No.9, the performance of the CWI process as a secondary oil recovery method was investigated. The procedure of this test has been summarised in Table 2. The visualisation results of this experiment are presented in Appendix B.

In this test, different sections of the micromodel were examined during and after the oil injection period to identify possible wettability change. The static shape and direction of the water-crude oil interfaces in one of these sections is demonstrated in Figure 41. This figure shows that both water-wet and neutral-wet conditions can be identified when the real crude oil is used. It should be noted that this micromodel showed strongly water wet conditions in the presence of the mineral oils in the previous experiments (No.1 to 6).

Figures 42A and 42B shows another magnified section of the micromodel at the end of the oil injection period and at the BT of CW (fully CO_2-enriched water), respectively. As the comparison of these two images shows, the displacement mechanism during CWI was observed and recorded to be completely pistonwise and no film flow was observed. One of the most likely reasons for this different displacement mechanism is having less water wet conditions in this experiment (No.9), compared to that in the previous experiments (No.1 to 6).

Table 7 summarises the initial oil saturation and the oil saturation at the BT of CW and after the subsequent WI stages of this test.

Experiment No.10- Tertiary CWI -Crude oil

In Experiment No.10, CWI (fully CO_2-enriched water) was conducted as a tertiary oil recovery method. See Table 2 and Appendix B for more details about the procedure and the visualisation results.

The dead oil saturation values of different stages of this experiment have been tabulated in Table 8.

Discussion

Oil colour change:

In both Experiments No.9 (Secondary CWI -Crude oil) and 10 (Tertiary CWI -Crude oil), changes in the colour of the crude oil were observed during different stages of the experiment.

Figure 43 shows a sequence of magnified images of a section of the micromodel at different stages of Experiment No.10. It is noted that dark spots appear in the oil phase as the first WI continues. Figures 43A and B clearly show both the original and the modified colour of the crude oil after BT and after 67 hours of WI. As will be discussed later, it is believed that these dark spots are micro droplets of water in the oil and on the pore surfaces.

In Figure 43C (at the end of the CWI period), compared to Figures 43A and 43B (after WI), a significant change in the oil colour is observed. These three images (43A-C) show two different oil colours, dark and light brown. That is, as can be seen from these figures, there are dark spots in the oil that appeared to grow in size with time. In this figure there is also a section where the oil colour is lighter than the original colour. This change of colour of the crude oil from dark brown to light brown is attributed to the transfer and dissolution of CO_2 in the oil from CW. The crude oil discolouring is also a good indication of the modification of the crude oil physical properties (i.e. reduction of the oil viscosity, oil density and oil/water interfacial tension) during the CWI process.

The last figure in this sequence, 43D, shows the colour of the oil at the end of the second WI. The second WI was continued until there was no more shrinkage and change in the oil size due to CO_2 transfer out of the oil. The red circles in Figure 43A and 43D highlight a dead oil ganglion. Comparison of the size of this oil ganglion after the first and the second WI shows this oil ganglion has not returned to its original size. Its larger size after stripping the dissolved CO_2 at the end of the experiment suggests that micro droplets and emulsion of water in the oil phase have been formed. Since this was not observed for the viscous mineral oil, one hypothesis could be that they have been probably been formed as a result of the change of the wettability of the surface, due to contact with the crude oil. The formation of these micro bubbles merits further investigation but is beyond the scope of this study (See the first recommendation in Chapter 8).

Secondary CWI vs. tertiary CWI:

The results of these two experiments (No.9 and 10) have clearly shown that injecting CW instead of water increases oil recovery. Comparing Figure 44A (at the BT of CW, Experiment No.9) with Figure 44B (at the BT of W, Experiment No.10) shows that

CWI has displaced more crude oil. Visual comparison of these two figures clearly indicates a better oil displacement by CWI than WI. It should be noted that the actual oil recovery by CWI is even higher than what can be observed from these figures because part of the oil phase in the micromodel during CWI (Figure 44A) contains the dissolved CO_2. That is, for evaluating the performance of CWI, the final dead oil saturation conditions should be compared.

Continuation of CWI after BT, led to more oil recovery. The results of image analysis show that the continuation of secondary CWI after BT reduced the oil saturation from 47.2% at the BT of CW to 40% at the end of the subsequent WI. The total oil recovery achieved during this secondary CWI experiment was 48.9% of the initial oil in place.

Tertiary CWI was also successful in increasing oil recovery and led to the remobilisation and recovery of part of the waterflood trapped oil. The oil saturation dropped from 53.9% at the end of waterflooding to 46.3%, due to the subsequent tertiary CWI. The total oil recovery achieved in the tertiary experiment was 40.7% of the initial oil in place which, compared to 48.8% recovery in the secondary experiment, reveals that significantly higher oil recovery has been achieved during secondary CWI than that during tertiary CWI. The magnified images in Figure 45 also show the lower residual dead oil saturation after CWI as secondary recovery mode (Figure 45A), compared to that after CWI as tertiary recovery mode, Figure 45B.

The estimated oil recovery factors for different stages in the secondary and tertiary CWI have been summarised and tabulated in Table 9.

As mentioned in the first chapter, the main objective of using 2D transparent porous media in the direct flow visualisation experiments was to understand the underlying pore-scale mechanisms of oil recovery and displacement in the CWI process and also to demonstrate the interactions of CW with the resident fluid phases (formation brine and oil). Thus, this approach results in a qualitative analysis of the dominant mechanisms in the CWI process. Furthermore, it has been discussed that although the visualised results can be quantified, core flood experiments should be carried to assess the efficiency of this process quantitatively. Generally, for the core experiments, a plot of oil recovery versus pore volume injected is used to address the implication of the results in a real

field situation. Such a plot can be generated using the quantified results of the micromodel experiments.

Figure 46 summarises and compares the results of the plain water injection, secondary and tertiary CWI in such a plot. The results of the experiments, in which crude oil A was used as the oil phase, have been used for this plot. All the key points of these three displacement processes are highlighted in this Plot. They are: i) At BT, CWI recovers more oil than WI. ii) The ultimate oil recovery is greater for secondary CWI than that for tertiary process, confirming the better performance of CWI when it is performed prior to plain WI. iii) Continued injection of (plain) water after BT does not produce more oil. iv) CW recovers additional oil after BT, however, additional oil recovery in the secondary CWI is greater than in the tertiary CWI method. Although this plot clearly compares the performance of different flooding processes, the scale of the PV injected could drastically differ from those of the core experiments. For instance, it has been reported by Kechut, et al. 2010 that the ultimate oil recovery during CWI would be obtained by injecting a couple of PVs, whereas in the micromodel experiments tens of PVs should be injected to get to the end of the test. Significant differences such as, 2-D structure of the micromodel with lower connectivity compared to the 3-D system of the core with higher CWI-oil contact and large ratio of the volume of the pipes and that of the porous medium for the micromodel, are the main contributors of this difference. Hence, to quantitatively assess the efficiency of the CWI process, core flood experiments data is needed.

3.5.2 The Impact of Oil Saturation on the Performance of CWI on Oil Recovery.

Experiment No.11- Tertiary CWI -Crude oil- low oil saturation at BT

It has been shown that the reconnection of the isolated oil ganglia after BT as a consequence of oil swelling is one of the main mechanisms for oil recovery during CWI. In addition to oil swelling, which yields coalescence of disconnected oil ganglia and is a function of pressure, temperature and oil type, the distance between the oil ganglia also is of great importance. The extent of oil saturation and its distribution within the porous medium affect the distance from one another at which the oil ganglia settle after BT. To study and investigate the role of oil saturation and distribution on the performance of CWI another test similar to Experiment No.10 (Tertiary CWI -Crude oil) was performed, but with a different initial oil saturation. That is, in this experiment,

unlike the previous one the oil injection, was stopped as soon as the oil front reached the other end of the micromodel, and WI commenced with a rate about twice as high as that in Experiment No.10. Figure 47 shows a sequence images of the fluid distribution within the micromodel during this test.

Discussion

Oil colour change

Alteration of oil colour in this experiment similar to that in Experiment No.10 was also observed. Figure 48 shows a sequence of images of an oil ganglion in the micromodel at different stages of this experiment (No.11). These images show growth of the dark spots in the oil through time. The highlighted area in Figure 48D (red rectangle) shows some white (clear) spots which seem to be some small water droplets. It is likely that these white droplets, which are big enough to let light to pass through, would have been generated as a result of aggregation of the dark spots in the oil, which were suspected to be micro droplets of water in oil. This observation further strengthens the idea of the formation of micro droplets of water in the oil.

Low oil saturation vs. high oil saturation:

Table 10 and Figure 49 show and compare the values of oil saturation at different stages of Experiments No.10 and No.11. As these data reveal, the initial oil saturation in the former (Experiment No.10) is slightly greater than the latter (Experiment No.11), because of shorter period of oil injection in Experiment No.11. Since the porous medium (micromodel) had been initially saturated with the wetting phase (water), injection of the non-wetting phase (oil) for a longer time is expected to displace more water, mainly by the piston type displacement mechanism up to the oil BT, and afterwards by film flow.

Comparison of the amount of the retained oil saturation after the first WI period shows significantly higher oil saturation in Experiment No.10 than that in Experiment No.11. This difference in oil saturation, is due to the difference in the initial oil saturation and water injection rates.

Comparison of the quantified data shows that the oil saturation as a result of CWI has reduced from 53.9% to 46.9% showing 7.0% oil recovery for Experiment No.10 and

from 40.0% to 38.4% showing 1.6% oil recovery for Experiment No.11. Based on these results one can conclude that the greater the oil saturation before CWI in the porous medium, the higher additional oil recovery by CWI. This difference has been visually shown in Figure 49 as well.

Based on the results of these two experiments, a critical oil saturation can be expected below which CWI does not result in any additional oil recovery. Generally, this critical oil saturation should be a function of the properties of the porous media, oil type, pressure, temperature and carbonation level. Assuming a linear dependency between the oil recovery (after the first WI and during CWI) and the oil saturation (before CWI) the critical oil saturation was estimated at about 36%. It should be noted that the assumption of linear dependency is not necessarily valid and more data points are needed to estimate this parameter for a specific system

The effect of oil saturation on oil recovery can be eliminated, to some extent, by dividing the amount of the recovered oil during CWI (fifth row of Table 10) by the oil saturation before injectionn of CW (third row of Table 10). The oil recovery factor (RF) during CWI compared to the corresponding previous WI stage has been tabulated in Table 10 (last row). The estimated data shows RF of 13% against 4%, for CWI in the experiments with high and low oil saturation before CWI, respectively. The rather large difference between these RF values indicates that another parameter also affects the CWI process. The visualisation results show that, in addition to the oil saturation, the oil distribution, which is controlled mainly by the heterogeneity of the porous medium, also affects the performance of CWI. Figure 47 shows that the additional oil recovery in Experiment No.11 took place mainly from the top of the micromodel. Although oil swelling and shrinkage during CWI and plain WI occurred throughout the micromodel, oil displacement from other parts of the micromodel was not detected. This observation highlights the importance of fluid distribution within the porous medium on the CWI process, particularly when it is conducted as a tertiary mode. It is also expected that for lower oil saturation, the impact of the oil distribution on the process of oil recovery by CWI would be greater.

3.6 Summary and overall discussion:

In this study, to investigate and demonstrate the pore-scale mechanisms involved in carbonated water injection (CWI) process, a series of visualisation experiments was carried out. A list of these experiments, through which three different oil types were used, has been summarised and shown in Figure 50. High-pressure micromodel technology was used to physically simulate the process of CWI and visually investigate its EOR potential, at typical reservoir conditions. Using the results of these flow visualisation experiments, the underlying physical processes and the pore-scale mechanisms of fluid-fluid and fluid-solid interactions during CWI were demonstrated to be oil swelling, coalescence of the isolated oil ganglia, wettability alteration, oil viscosity reduction and flow diversion due to flow restriction in some of the pores as a result of oil swelling and the resultant fluid redistribution.

In the micromodel experiments discussed in this chapter, the impact of important pertinent parameters on the performance of CWI was studied under different displacement processes. These parameters and displacement processes include, I) the oil type, II) the level of oil saturation in the porous medium before CWI, III) the level of carbonation of carbonated water (CW), IV) CWI before (secondary) and after (tertiary) water injection, V) cyclic injection of CW and water, VI) the in situ release of CO_2 subsequent to CWI. In addition to investigation of these parameters, the performance of CWI was also compared with that of unadulterated water (CO_2 free) injection. The classification of the experiments, which were used to assess the impact of these factors on CWI process, is shown in Figure 51.

Using the visualisation results (i.e. micromodel images, e.g. Figure 25), trend graphs (e.g. Figures 37 and 46), bar charts (e.g. Figures 30 and 49) and quantified data (e.g. Tables 3 and 4), the impact of the abovementioned parameters was analysed. The results showed that, compared to unadulterated water injection, CWI improves oil recovery in both secondary and tertiary injection modes. The improvement is, however, higher when carbonated water is injected before water flooding. Both mineral (light and heavy) and real crude oil were used in the experiments. The mechanisms and degree of oil recovery observed for light oil were vastly different from those for heavy oil. In light oil, significant swelling of the oil was observed during CWI, which brought about reconnection of the isolated oil ganglia and, in turn caused, remobilisation and recovery

of the trapped oil. In heavy oil the amount of swelling was much less than that in light oil. However, the degree of oil viscosity reduction in heavy oil was much greater than that in the light oil, leading to the mobilisation and recovery of the trapped oil. An additional oil recovery process was achieved as a result of the in situ release of CO_2 subsequent to CWI, by pressure blow-down of the model. A possible increase in oil recovery as a result of cyclic injection of CW and water in porous media was also observed. The quantified and visualisation results indicated that the oil recovery increases when the CO_2 concentration in carbonated water is increased for both *n*-decane and the viscous oil. However, it was shown that the level of additional oil recovery as a result of the added CO_2 content strongly depends on the oil type. It was demonstrated that the greater the oil saturation before CWI in the porous medium, the higher additional oil recovery by CWI would be achieved.

3.7 Conclusions

- Three main observed mechanisms of oil recovery during CWI were; the swelling and subsequent coalescence of trapped oil ganglia, local flow diversion and reduction of the oil viscosity.
- CWI as tertiary recovery method (post waterflood) increased oil recovery compared to the corresponding plain waterflooding both for the light (*n*-decane) and viscous oil. However, this increase was higher for the light oil (32.7%) than the viscous oil (11.82%). This was mainly due to a higher swelling factor observed in *n*-decane.
- CW increases oil recovery, both as a secondary and tertiary recovery method. However, this increase was higher in the secondary flood scenario. The poorer connectivity of the oil phase and higher water saturation in the tertiary mode than the secondary one were the main reasons for this difference.
- Alternating injection of water and CW brings about a favourable oil redistribution and more oil production; however, the additional oil recovery in the first cycle, was significantly higher than that in the second cycle. This shows that the potential of the first cycle is significantly higher than that of the second cycle.
- The results showed that oil swelling during CWI and oil shrinkage during the subsequent WI period do not happen at the same rate for the first and second

cycles. This difference contributed to the oil redistribution during alternating injection of CW and water, which resulted around 2% additional oil recovery during the WI period subsequent to CWI in the first test.

- The performance of CWI was shown that strongly is a function of the carbonation level. It was, the higher the CO_2 concentration in water the greater the oil swelling and consequently the higher the additional oil recovery.
- Some evidence of wettability alteration, towards more water-wetness, was observed during CWI. More experimental results will be presented in Chapter 5 to verify this observation.
- Blowdown of the micromodel subsequent to a period of CWI showed that residual oil saturation can be further reduced and more oil can be recovered during this process.
- In the series of micromodel experiments using crude oil A, there was clearly a tendency for the porous medium to become mixed-wet or weakly water-wet compared to the experiments in which mineral/model oil had been used. This demonstrates the ability of the crude oil to alter the wettability of the porous medium. As a result, the oil displacement mechanism with water and CW was mainly piston wise as opposed to layer and film flow, which was observed in the experiments with mineral oils.
- Similarly to the results of the previous experiments using decane and mineral oil, CWI increased the recovery of crude oil A, in both the secondary and tertiary injection modes. The additional oil recovery was also higher in secondary mode.
- The colour of the crude oil was observed to change during both WI and CWI. In some locations, the oil colour became darker, which is believed to be due to the formation of small water droplets in the oil. There was also oil with a lighter colour compared to the original oil colour which was caused by CO_2 dissolution in the oil phase.
- Comparison of the size of an oil ganglion after the first WI (before CWI) and the second WI period (after CWI) in Experiment No.10 (Tertiary CWI -Crude oil) showed that the oil did not return to the original size, even after stripping all the dissolved CO_2. The larger oil size, which was darker in colour at the end of the

experiments, would support the formation of a micro emulsion of water in the oil phase.

- It has been shown visually that a higher oil saturation before CWI in the porous medium results in higher additional oil recovery by CWI.
- The impact of the oil distribution within the porous medium shown that has important impact on oil displacement during CWI.

3.8 References

Holm, L. W., 1986: ''Mobilization of Waterflood Residual Oil by Miscible Fluids'', SPE Reservoir Engineering, July, SPE paper 13216.

Kechut, N., Riazi, M., Sohrabi, M., Jamiolahmady, M. 2010: ''Tertiary Oil Recovery and CO_2 Sequestration by Carbonated Water Injection (CWI)'', SPE paper 139667, SPE International Conference on CO_2 Capture, Storage and Utilization held in New Orleans, Louisiana, USA, 10-12 November.

UK Production Data Release, Department for Business, Enterprise and Regulatory Reform Energy Group, released data 01 April 2008. https://www.og.dti.gov.uk/pprs/pprsindex.htm.

Yang, D., Gu, Y., 2004a: ''Visualization of Interfacial Tension of Crude Oil-CO_2 Systems under Reservoir Conditions'', SPE 89366.

Yang, D., Gu, Y., 2004b: ''Interfacial Interactions of Crude Oil-Brine-CO_2 Systems under Reservoir Conditions.'', SPE 90198.

Method of estimating velocity, v		μ_w (pa.s)	σ_{ow} interfacial tension, (Nm^{-1})	S_{or} at breakthrough. (%)	v ($m.s^{-1}$)	N_{ca} (-)
Actual velocity	WI	0.0010	5.0 E-2	49	1.10E-5	2.20E-7
	CWI	0.0013	O/W value was used	49	1.10E-5	2.85E-7
Flow rate/ cross sectional area	WI	0.0010	5.0 E-2	-	7.94E-6	1.59E-7
	CWI	0.0013	5.0 E-2	-	7.94E-6	2.06E-7

Table 3-1: Capillary number (N_{ca}) in water and CWI processes.

EXP No.	Oil type	CW type	Flooding Procedure	Rate of injection $cm^3\ h^{-1}$						psi h^{-1}
				OI	WI	CWI	WI	CWI	WI	BD
P1	n-C_{10}	-	OI	0.1	-	-	-	-	-	-
P2	n-C_{10}	-	T-CWI	0.1	0.01	0.01	-	-	-	-
P3	n-C_{10}	-	OI	0.1	-	-	-	-	-	-
1	n-C_{10}	FS	T-CWI	0.1	0.01	0.01	0.01	0.01	0.01	
2	n-C_{10}	FS	S-CWI	0.1	-	0.01	0.01	-	-	-
3	Viscous oil	FS	T-CWI	0.1	0.01	0.01	0.01	0.01	0.01	-
4	Viscous oil	PS	T-CWI	0.1	0.01	0.01	0.01	-	-	-
5	n-C_{10}	PS	T-CWI	0.1	0.01	0.01	0.01	-	-	-
6	n-C_{10}	PS	S-CWI/BD	0.1	-	0.01	-	-	-	50
7	n-C_{10}	PS	S-CWI/BD	0.1	-	0.01	-	-	-	50
8	CW	PS	BD	-	-	-	-	-	-	10
9	Crude oil	FS	S-CWI	0.1	-	0.008	0.008	-	-	-
10	Crude oil	FS	T-CWI	0.1	0.008	0.008	0.008	-	-	-
11	Crude oil	FS	T-CWI	0.1	0.016	0.008	0.008	-	-	-

Table 3-2: List of the micromodel experiments discussed in Chapter 3.

BD: Blow down (depressurisation) | CO_2: Carbon dioxide | CW: Carbonated water
FS: Fully saturated | I: injection | O: oil
P: Preliminary test | PS: Partially saturated | R: Repeat
S: Secondary | T: Tertiary | W: Water

Micromodel	Time	So (%)
Figure 9A-initial conditions		0.0
Figure 9B-Soi		67.1
Figure 9C-after the1st WI		49.1
Figure 9D-after the 1st CWI	167 hrs	64.3
Figure 9E-after the 2nd WI	70 hrs	33.4
Figure 18A-after the 2nd CWI	142 hrs	60.0
Figure 18B-after the 3rd WI	117 hrs	33.0

Table 3-3: Tabular data of oil saturation at different stages of Experiment No.1 (Tertiary CWI- Decane).

Different stages	Oil saturation (%)
Initial oil saturation	76.4
Residual oil saturation after first WI	56.7
Residual oil saturation after second WI	50.0
Residual oil saturation after third WI	49.3

Table 3-4: Quantified value of dead oil saturation at different stages of Experiment No.3 (Tertiary CWI- Viscous oil).

	First test (*n*-decane)	Third test (the viscous oil)
Oil Saturation (%)	64.0	61.4
Water Saturation (%)	36.0	38.6
CO_2 percentage in the oil phase (%) (S_o*18.7% or*50.0%)	32.0	11.5
CO_2 percentage in the water phase (%) (S_w*7.0%)	2.5	2.7
Percentage of CO_2 in the micromodel (%)	34.5	14.2

Table 3-5: Estimated CO_2 storage in the micromodel for both tests.

Test Number	**Oil Type**	**Swelling Factor (%)**	**RF (%) Compared to the first WI period**
1	*n*-decane	100.0	28
5	***n*-decane**	**23.5**	**4.4**
3	**viscous oil**	**22.8**	**11.8**
4	viscous oil	11.5	5.5

Table 3-6: Recovery factor data for CWI with respect to the preceding WI, for different oil types and swelling factors.

Different Stages	So (%)
Initial Condition	0.00
Initial oil saturation (S_{oi})	78.2
Oil saturation (So) at BT of CWI	47.2
Sor at the end of WI	40.0

Table 3-7: Tabular data of oil saturation at different stages of Experiment No.9 (Secondary CWI -Crude oil).

Different Stages	So (%)
Initial Condition	0.00
Soi	79.1
So at BT of the 1st WI	53.9
Sor at the end of the 2nd WI	46.9

Table 3-8: Tabular data of oil saturation at different stages of Experiment No.10 (Tertiary CWI -Crude oil).

CWI mode	R.F at BT (%)	Total R.F (%)
Secondary	39.6	48.9
Tertiary	31.9	40.7

Table 3-9: Oil recovery factors at different stages for secondary and tertiary CWI, Experiments No.9 (Secondary CWI -Crude oil) and No.10 (Tertiary CWI -Crude oil).

Micromodel	So (%), Exp. No.10	So (%), Exp. No.11
IC	**0.0**	**0.0**
Soi	**79.1**	**76.7**
So after the 1st WI	**53.9**	**40.0**
So after the 2nd WI	**46.9**	**38.4**
Recovered oil during CWI	**7.0**	**1.6**
Oil recovery factor of CW compared to the previous WI stage.	**13.0**	**4.0**

Table 3-10: Tabular data of oil saturation at different stages of Experiment No.10 (Tertiary CWI -Crude oil) and Experiment No.11 (Tertiary CWI -Crude oil- low oil saturation at BT).

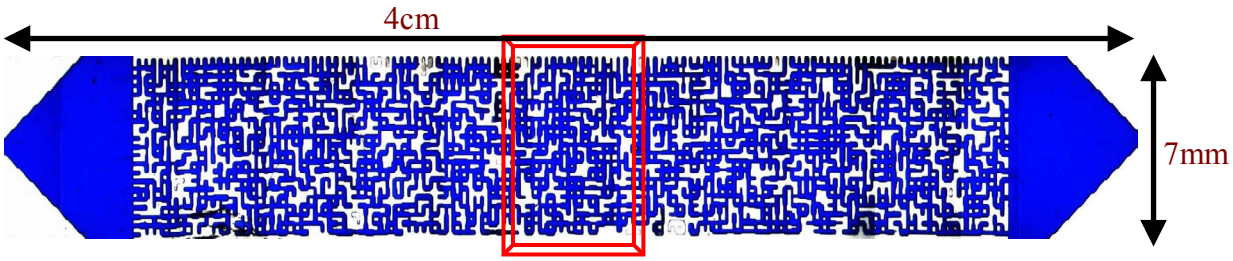

Figure 3-1 : Image of the micromodel when fully saturated with blue-dyed water.

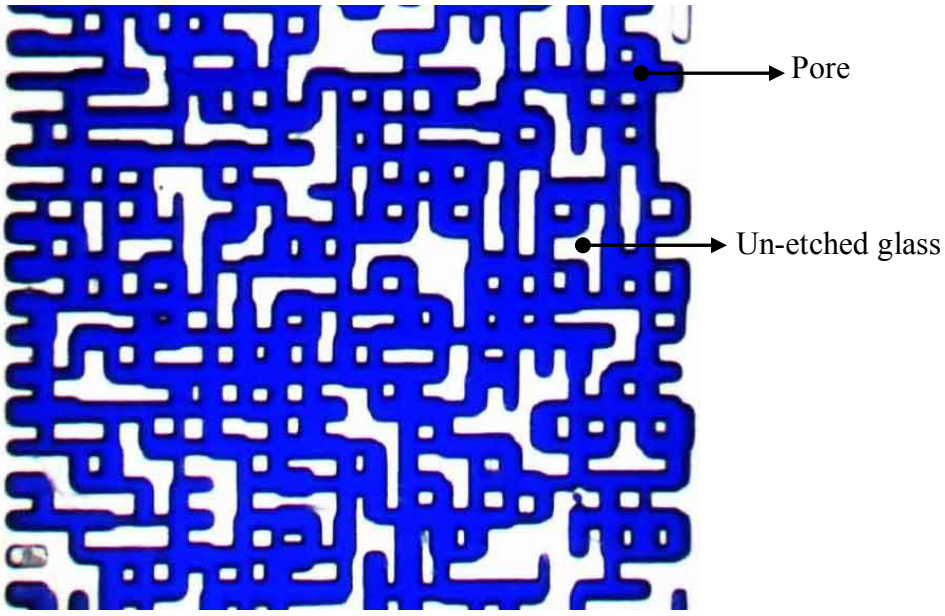

Figure 3-2 : Pore pattern of the micromodel shown in Figure 1.

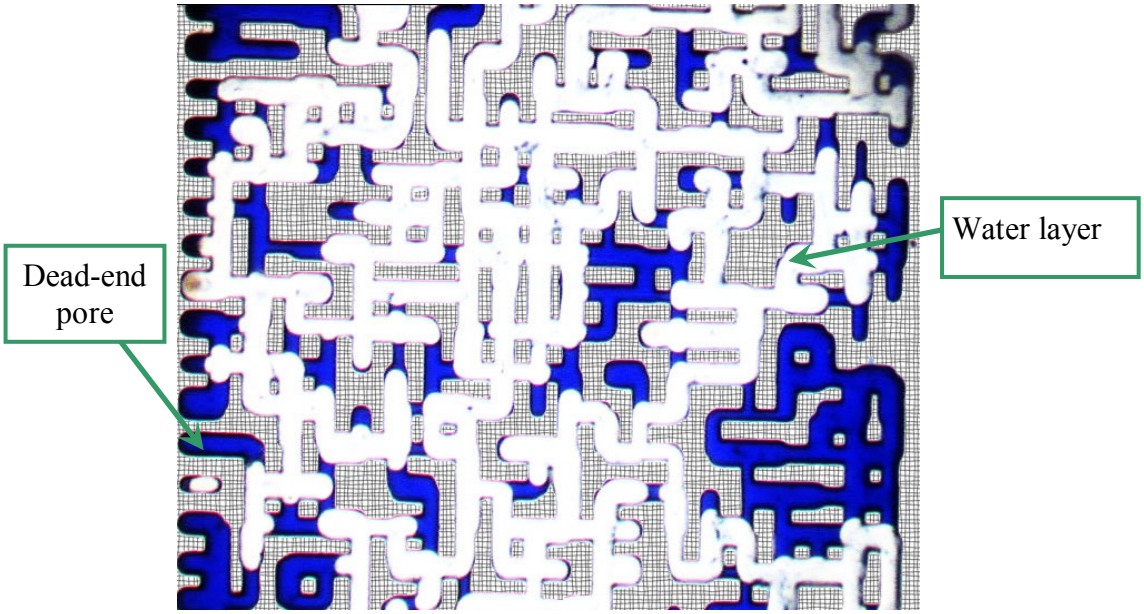

Figure 3-3: Initial oil saturation within a section of the micromodel, light oil at S_{wi}.

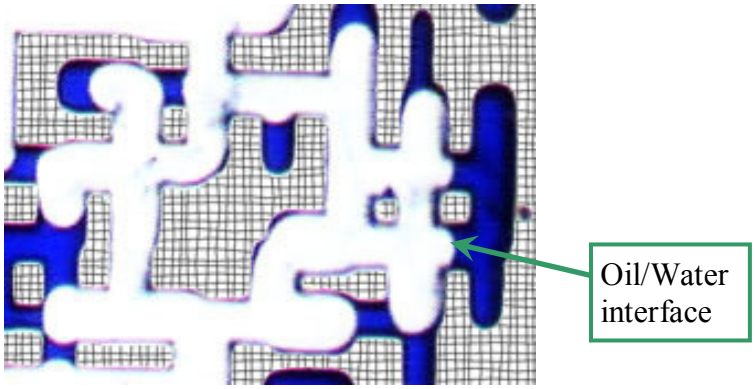

Figure 3-4: The shape and direction of the water-oil interfaces in the water-wet micromodel.

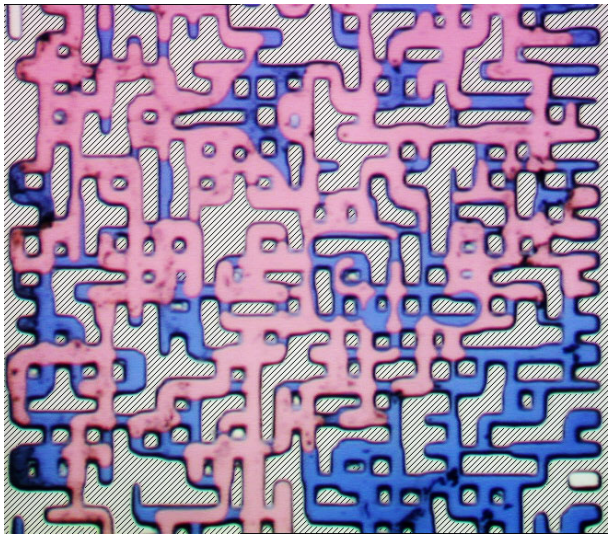

Figure 3-5: Initial oil (pink) and water (blue) saturation in a selected frame of the micromodel, Preliminary Experiment No.1 (red oil and blue water were used).

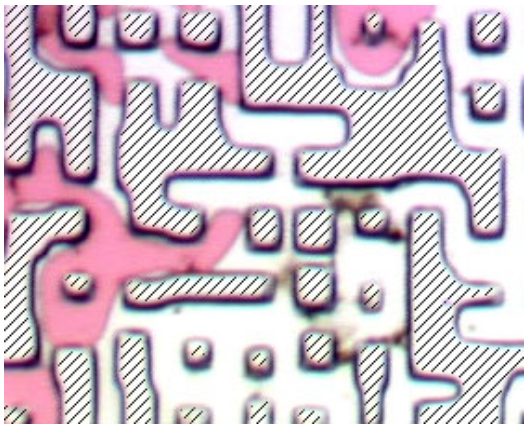

Figure 3-6: A close-up of a section of the micromodel after water injection, Preliminary Experiment No.2 (red oil and clear water were used).

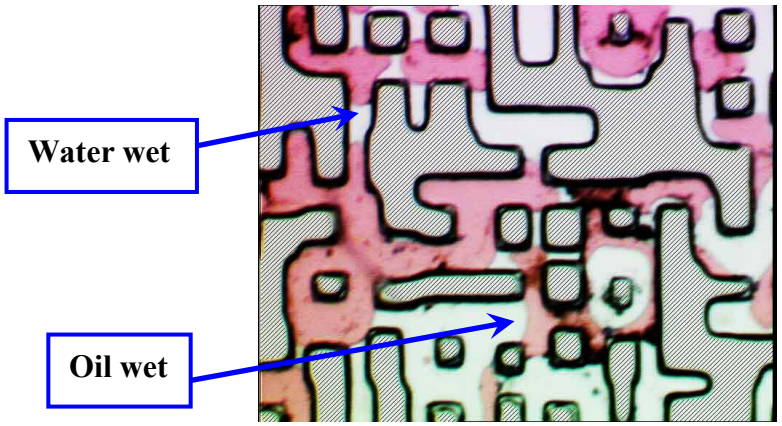

Figure 3-7: The same section of the micromodel as Figure 6 after CWI, which shows two types of wettability in the micromodel, Preliminary Experiment No.2 (red oil and clear water were used).

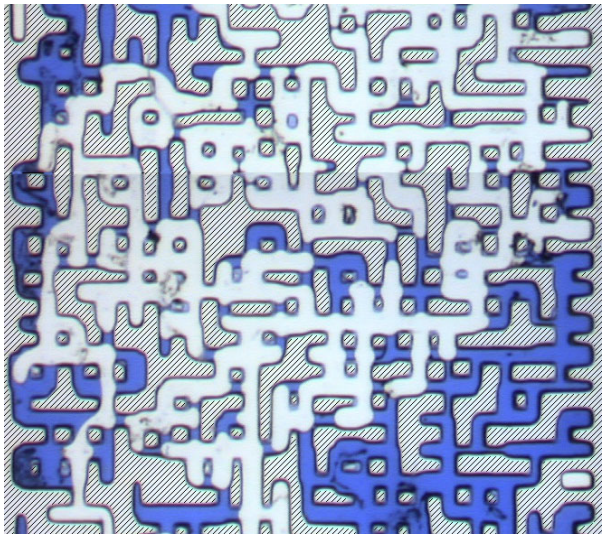

Figure 3-8: Initial oil (white) and connate water (blue) saturation in the same frame as Figure 5, Preliminary Experiment No.3 (clear oil and blue water were used).

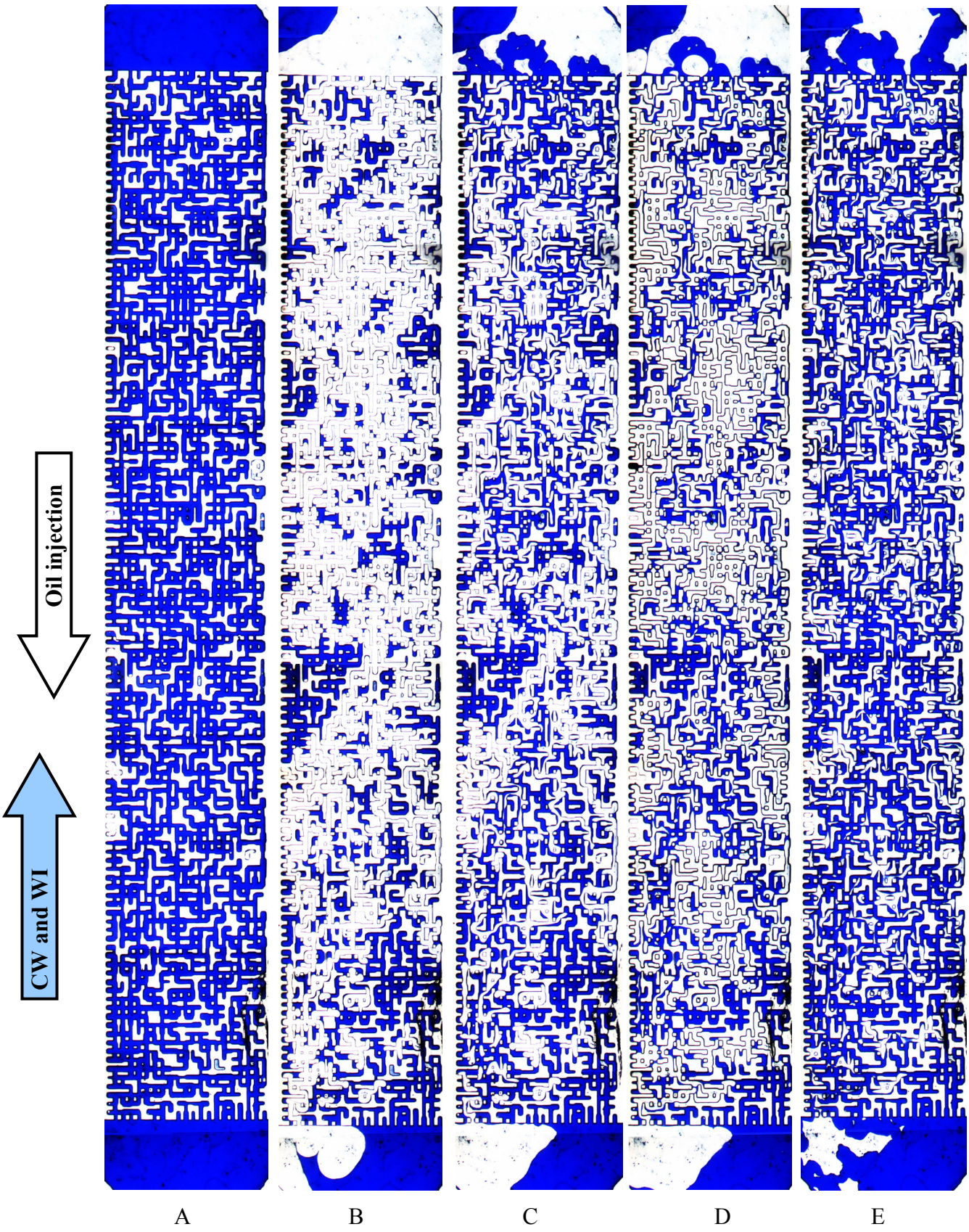

Figure 3-9: Whole images of the micromodel: A) Fully saturated with water; B) Initial oil saturation; C) Sor (residual oil saturation) after the first WI; D) Fluid distribution at the end of the 1st CWI; E) Sor after the 2nd WI, Experiment No.1 (Tertiary CWI-Decane).

Figure 3-10: Initial oil saturation in Experiment No.1 (Tertiary CWI- Decane) after the first drainage stage.

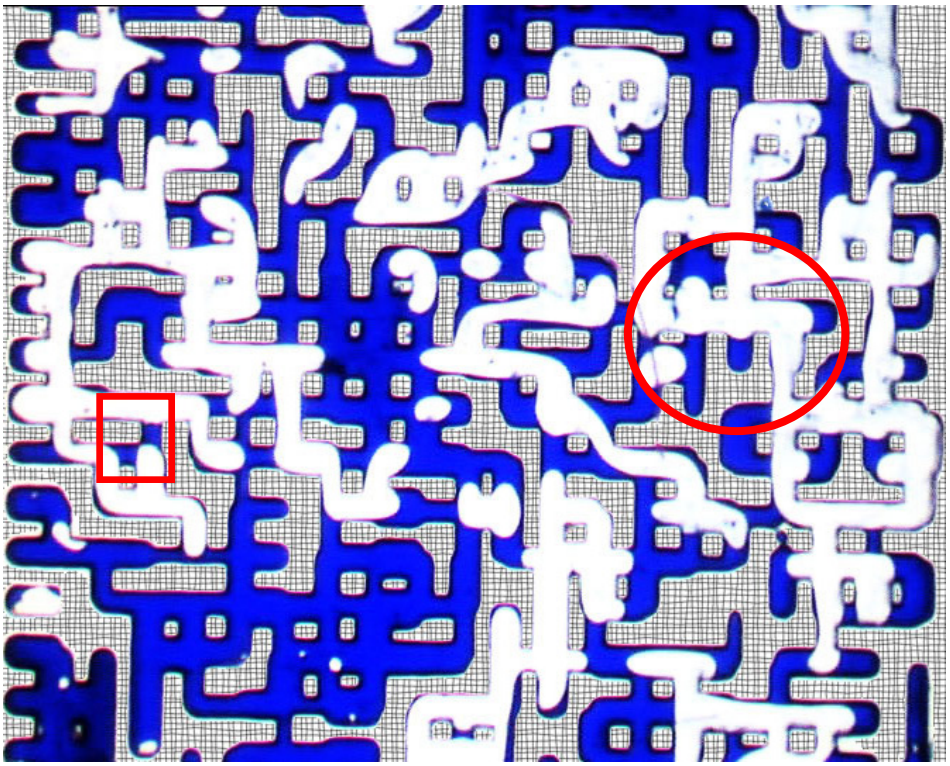

Figure 3-11: Established waterflood residual oil saturation in Experiment No.1 (Tertiary CWI- Decane) after the 1st WI.

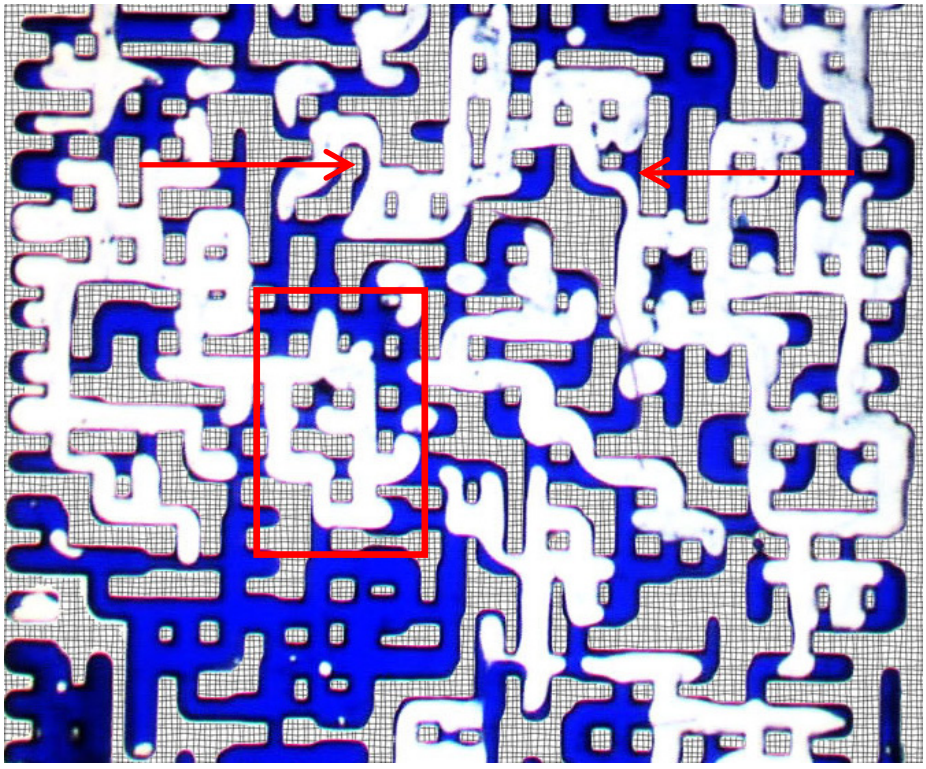

Figure 3-12: Swelling of the oil phase in Experiment No.1 (Tertiary CWI- Decane), 1 hr after CWI.

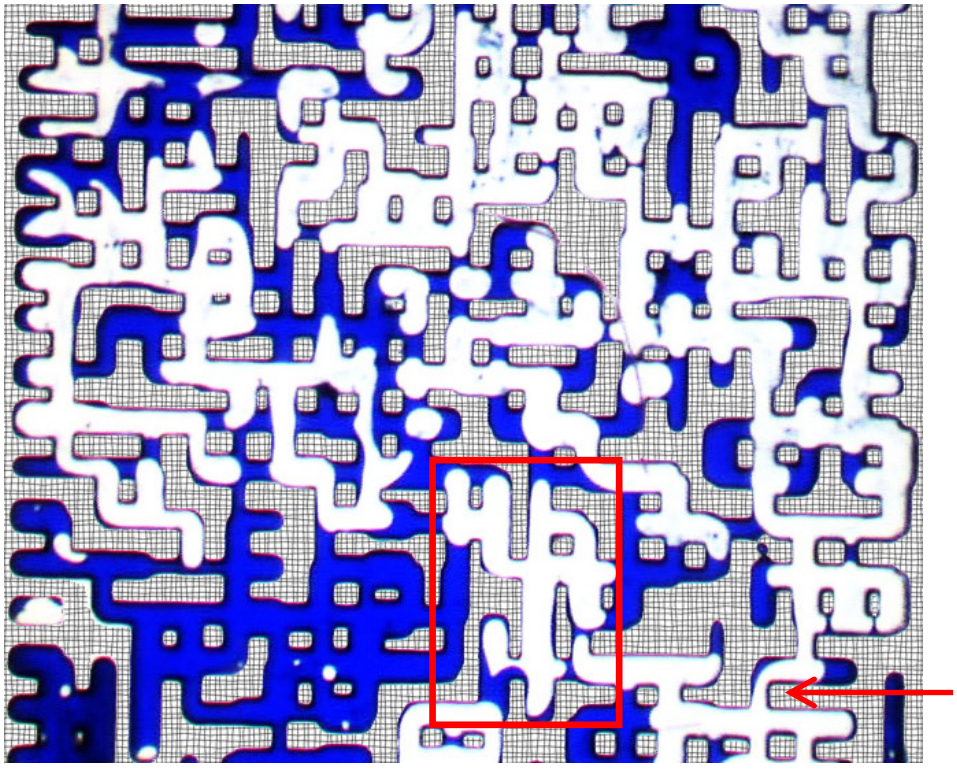

Figure 3-13: Swelling, coalescence and displacement of oil in Experiment No.1 (Tertiary CWI- Decane), 3.3 hrs after CWI.

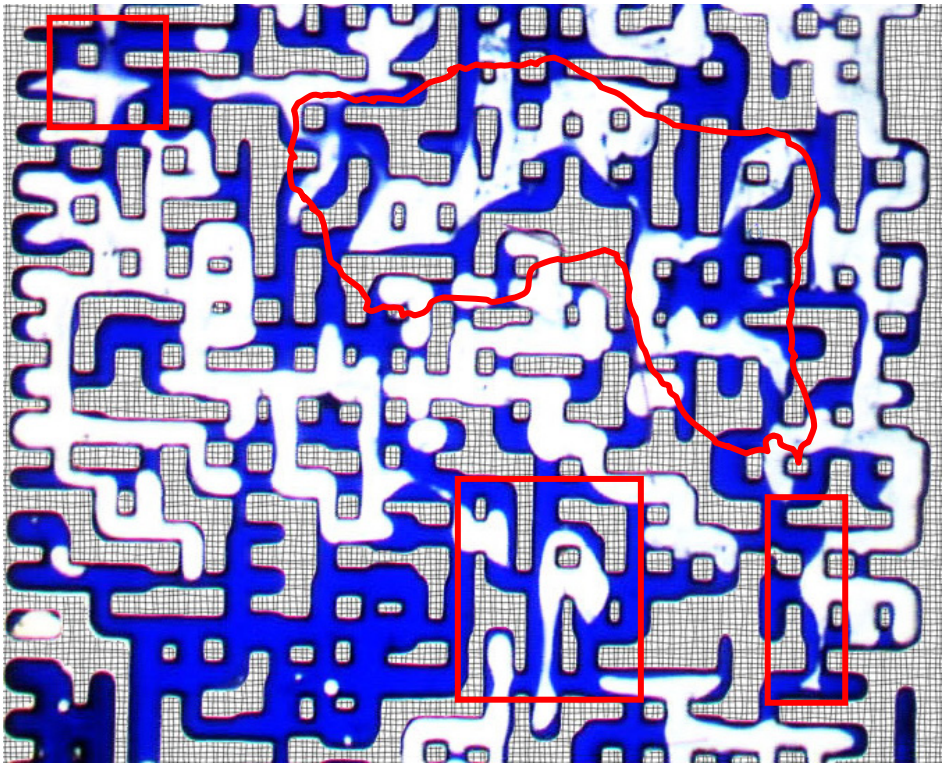

Figure 3-14: Compared to Figure 13, significant oil displacement after 6.3 hrs of CWI.

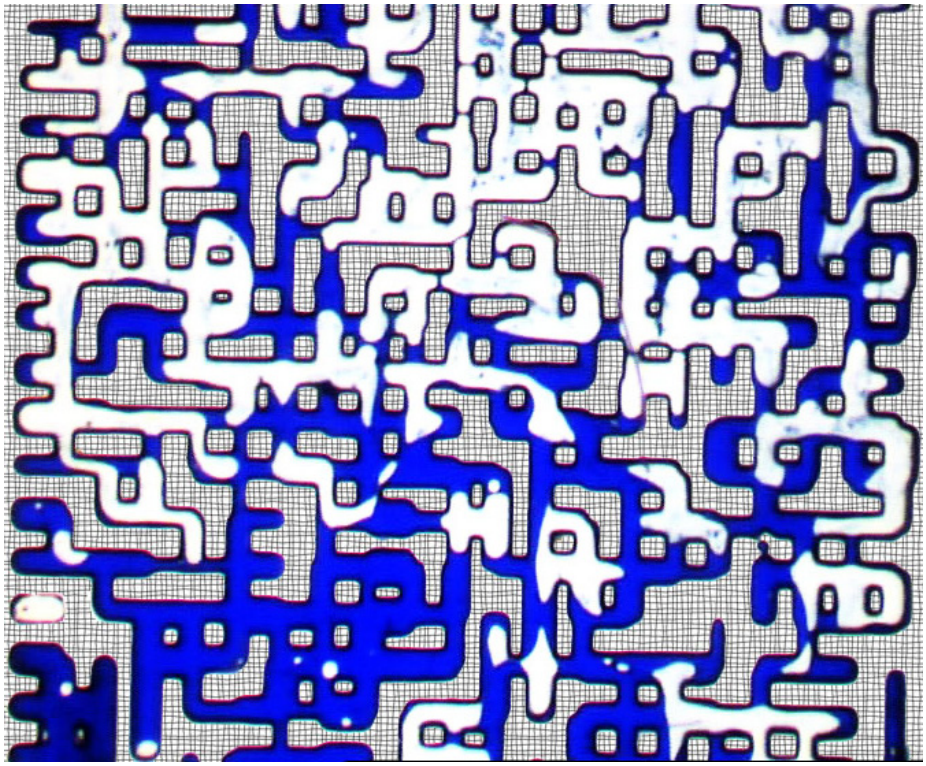

Figure 3-15: Swelling and displacement of oil after 143.6 hrs of CWI.

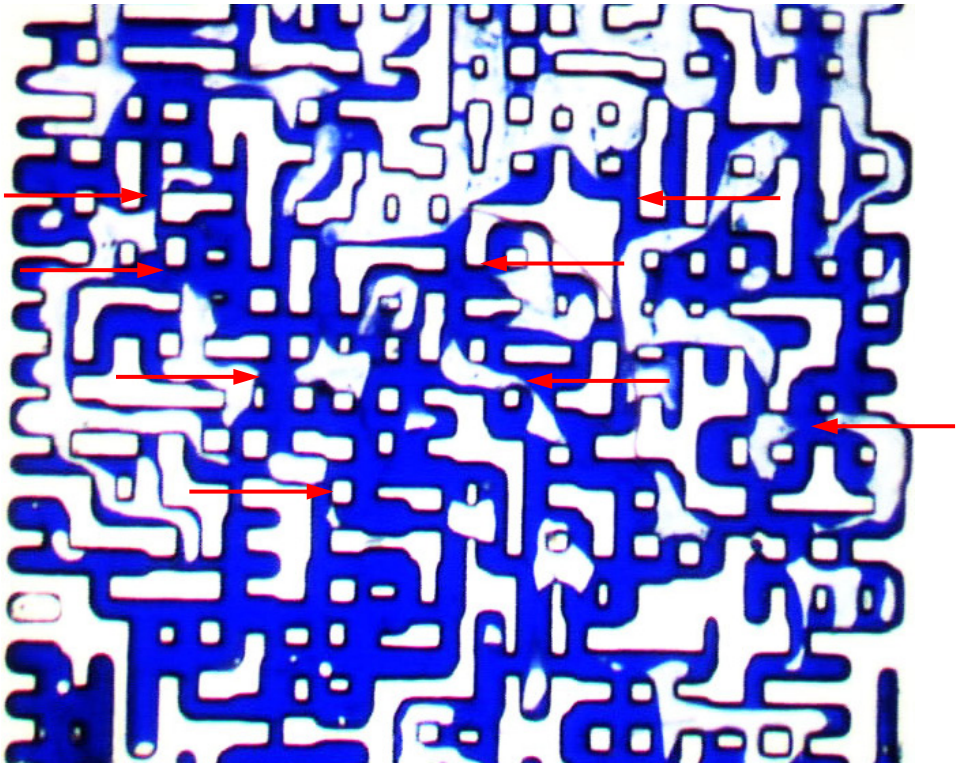

Figure 3-16: Shrinkage and disconnection of oil ganglia as a result of stripping CO_2 away by plain water, after 3.7 hrs of the 2nd WI.

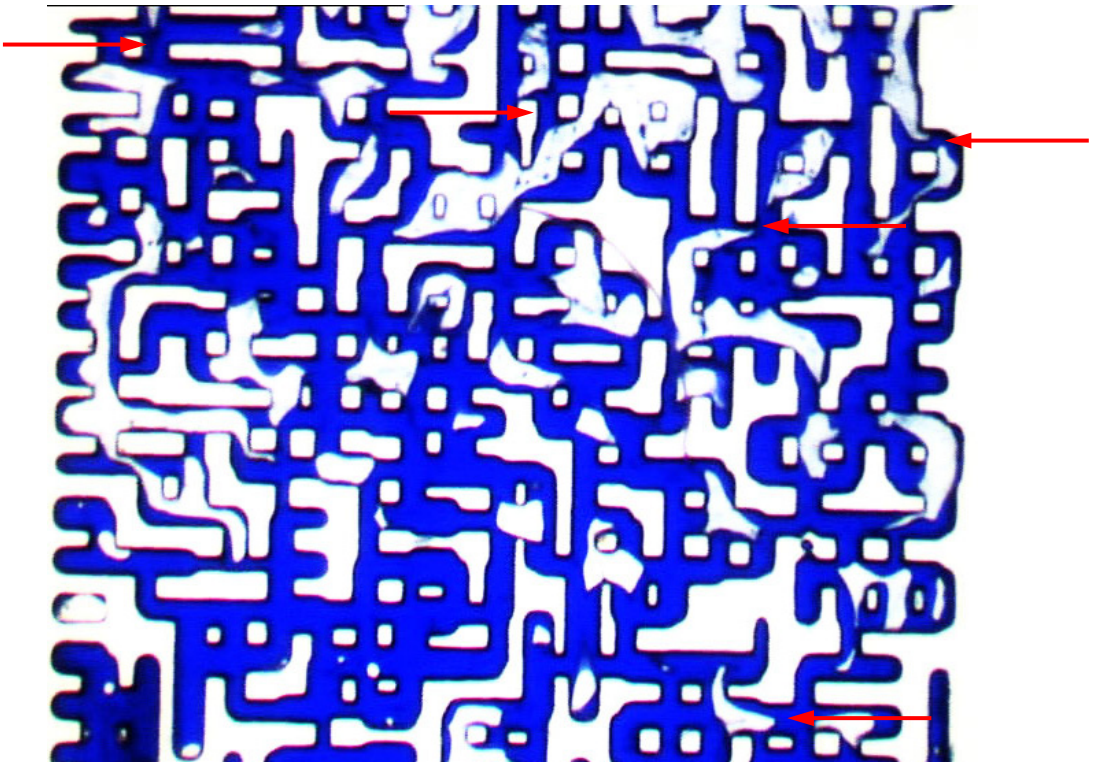

Figure 3-17: More oil shrinkage and disconnection after 6.5 hrs of the 2nd WI.

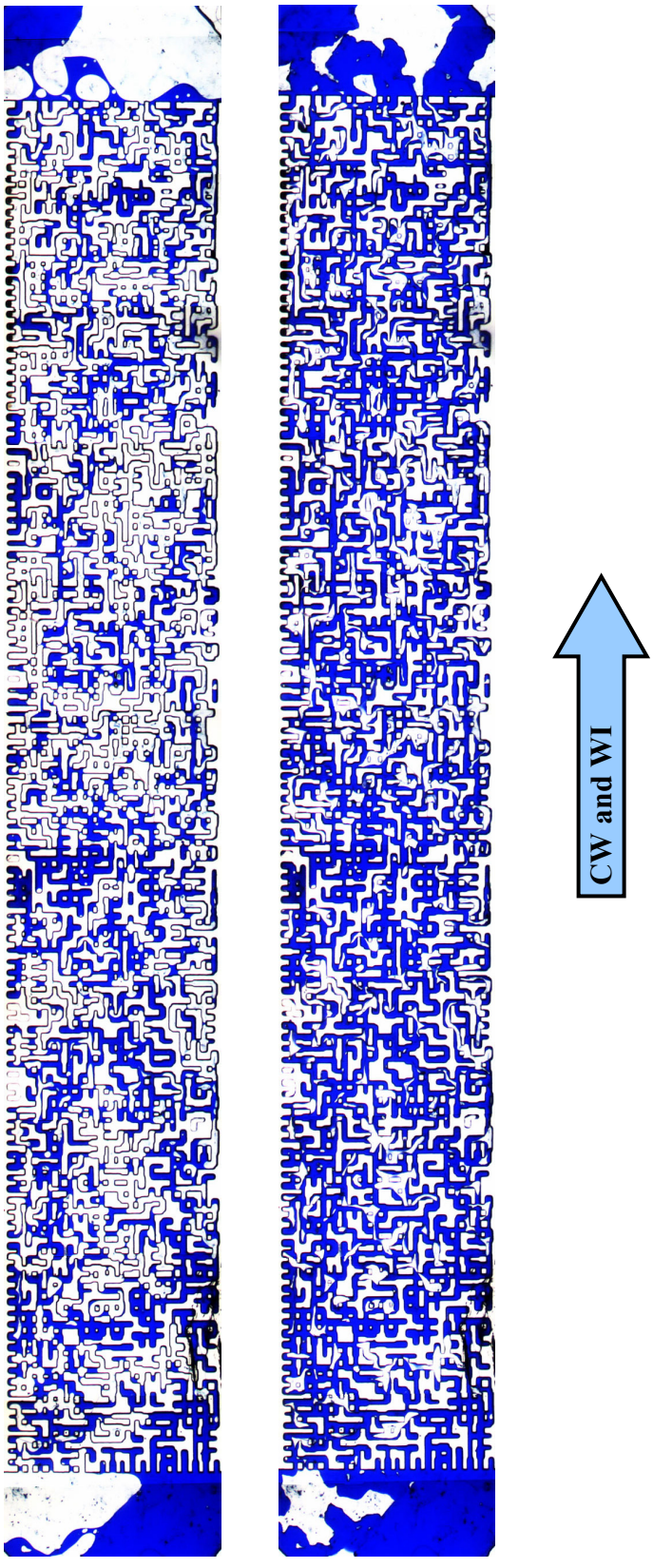

Figure 3-18: The results of the second cycle of CW and WI: A) Fluid distribution after the 2nd CWI; B) Sor after the 3rd WI, Experiment No.1 (Tertiary CWI- Decane).

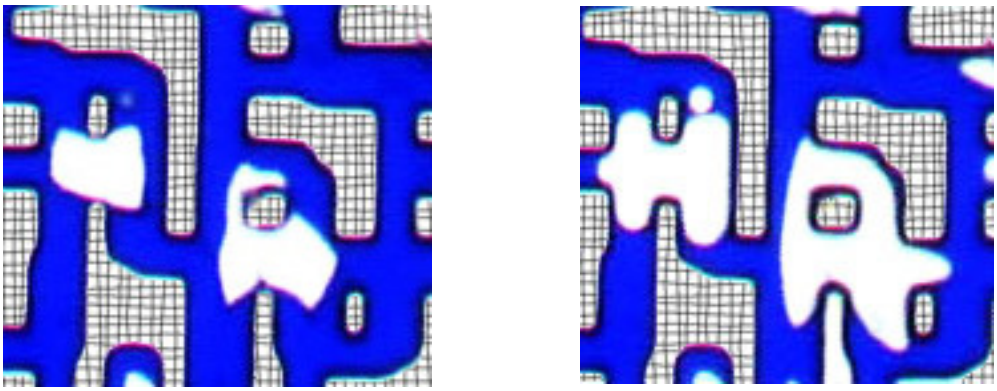

A B

Figure 3-19: Partial and complete pore blockage as a result of swelling of oil droplets: A) Free gas oil droplets; B) Swollen oil droplets, as a result of dissolved CO_2.

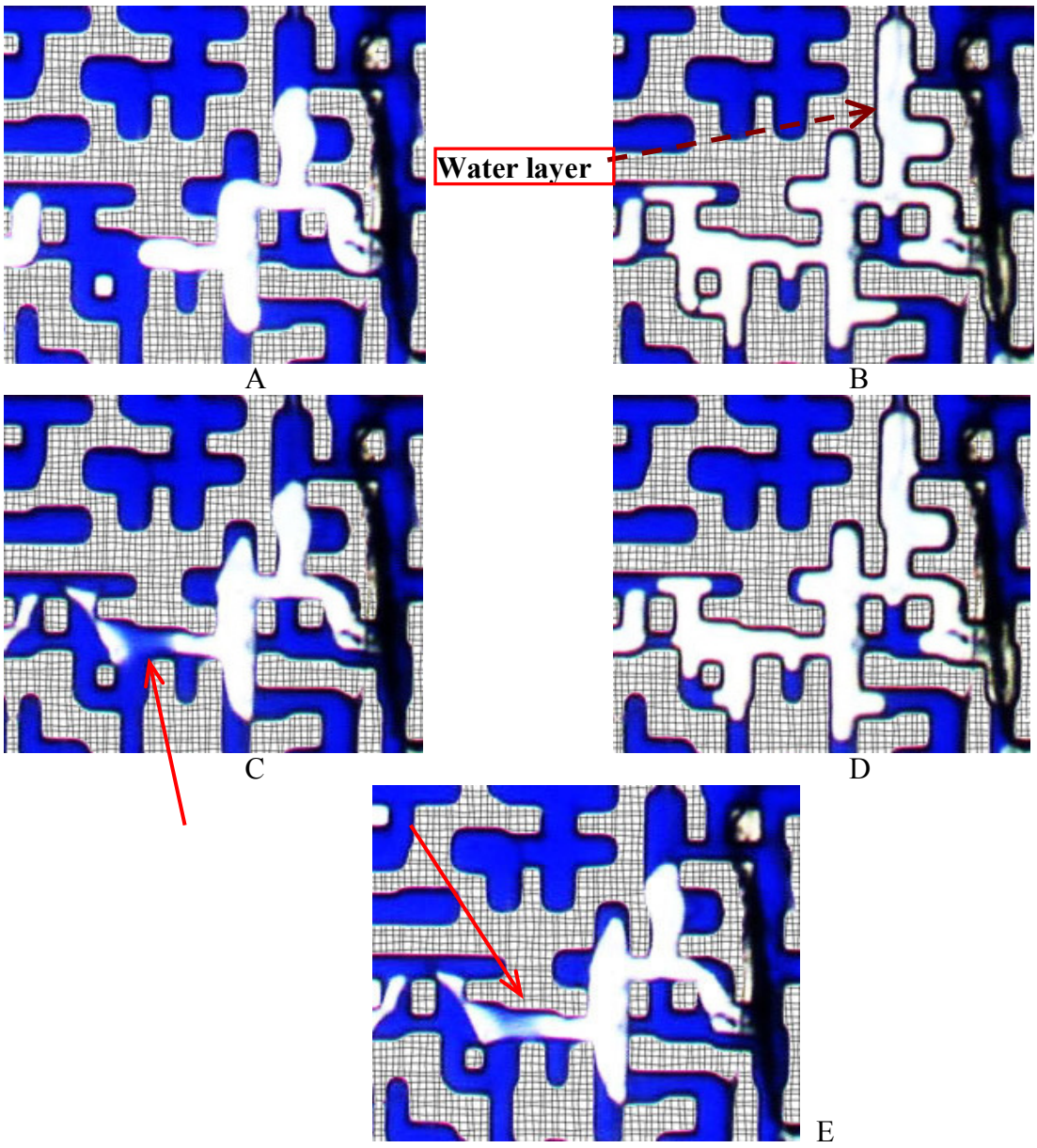

Figure 3-20: The oil ganglion at different stages of Experiment No.1 (Tertiary CWI-Decane): A) after the 1st WI; B) At the end of the 1st CWI; C) After the 2nd WI; D) At the end of the 2nd CWI; E) After the 3rd WI.

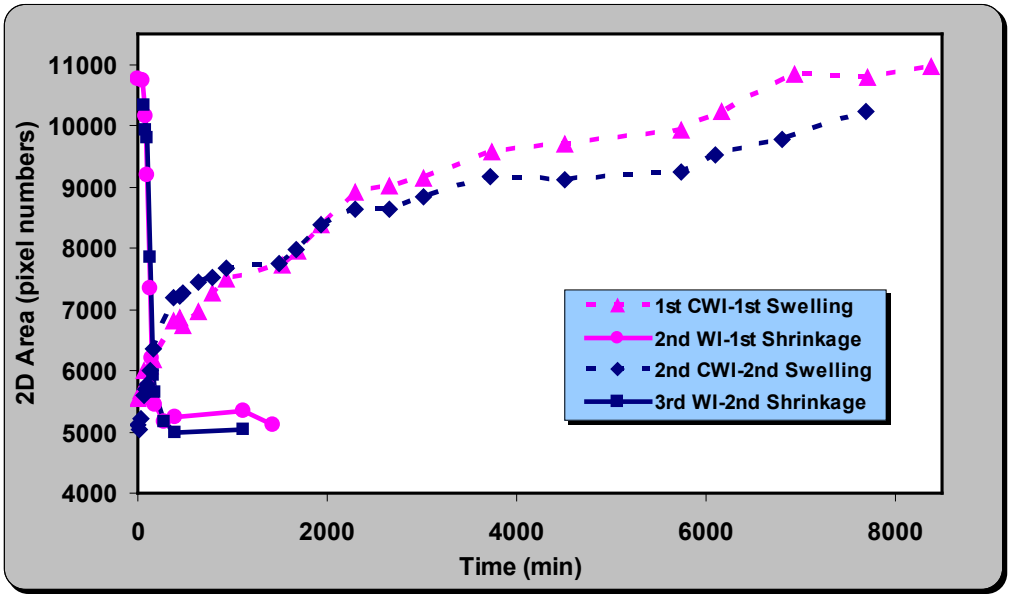

Figure 3-21: Comparison of swelling and shrinkage rates during the first and second cycle of CW and W injection, Experiment No.1 (Tertiary CWI- Decane).

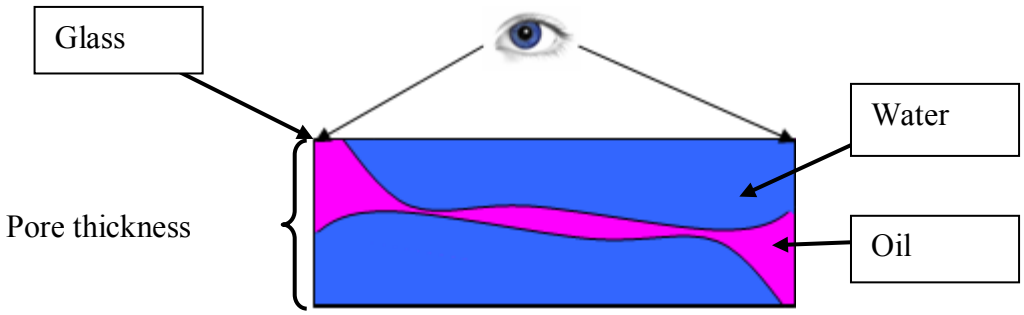

Figure 3-22: Oil layer surrounded by blue water.

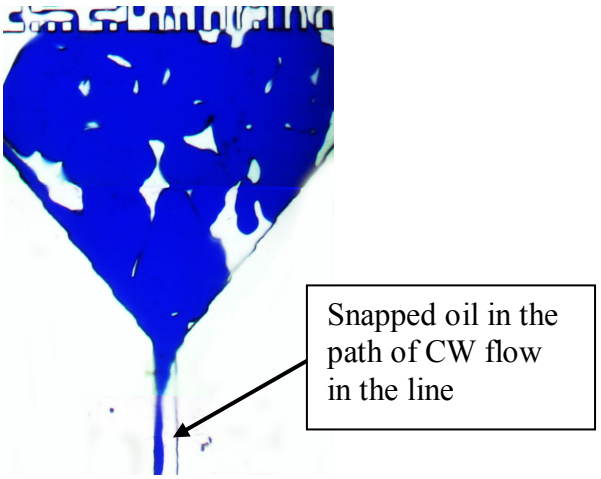

Figure 3-23: Inlet part of the micromodel during CWI in Experiment No.2 (Secondary CWI- Decane).

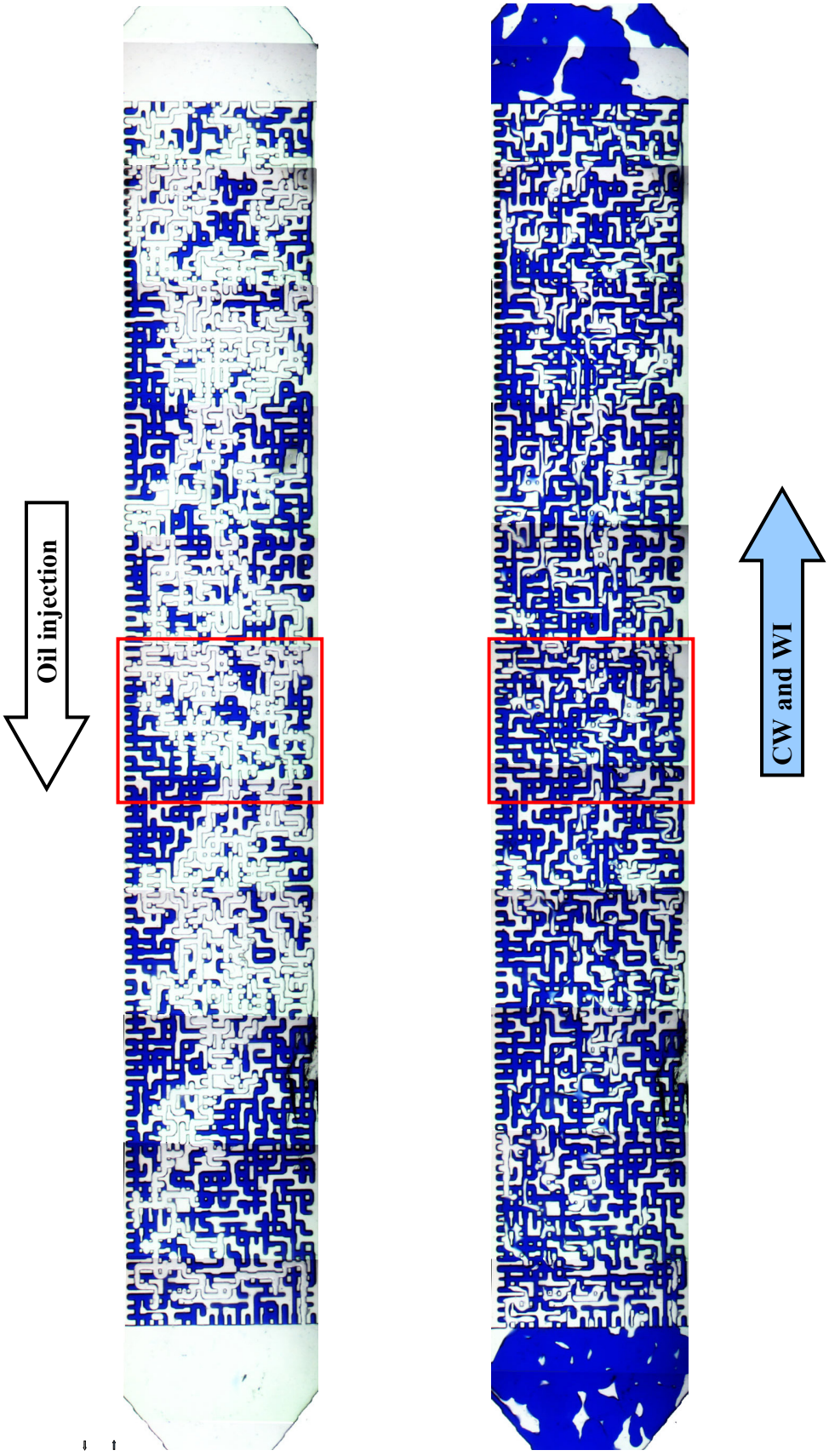

Figure 3-24: Whole images of the micromodel: A) Initial oil saturation; B) Sor after WI subsequent to CWI, Experiment No.2 (Secondary CWI- Decane).

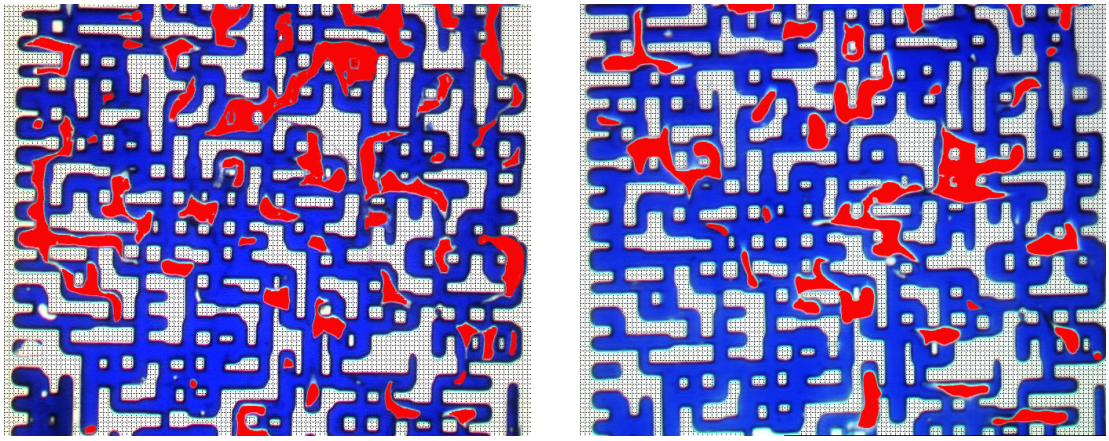

A B

Figure 3-25: Dead oil (CO_2 free) saturation condition at the end of the first CWI period: A) as a tertiary oil recovery mode, Experiment No. 1 (Tertiary CWI- Decane); and B) as a secondary oil recovery method, Experiment No. 2 (Secondary CWI- Decane).

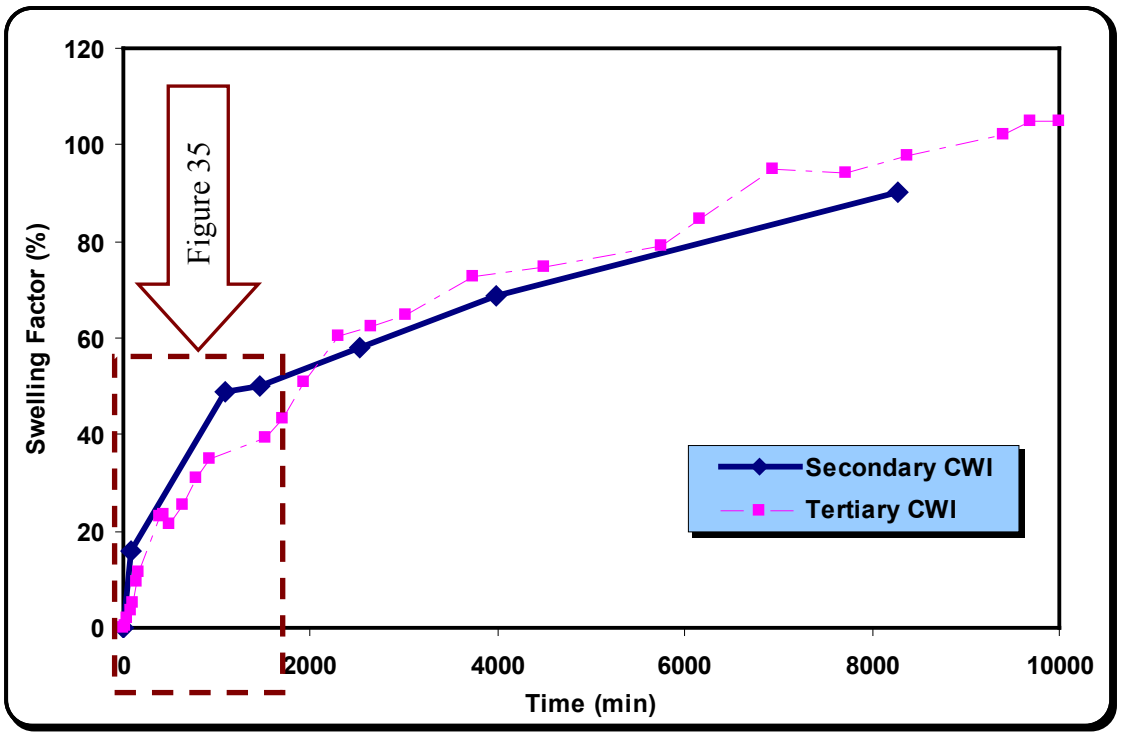

Figure 3-26: Swelling of oil (*n*-decane) during the first CWI in Experiment No.1 (tertiary) and in Experiment No.2 (secondary).

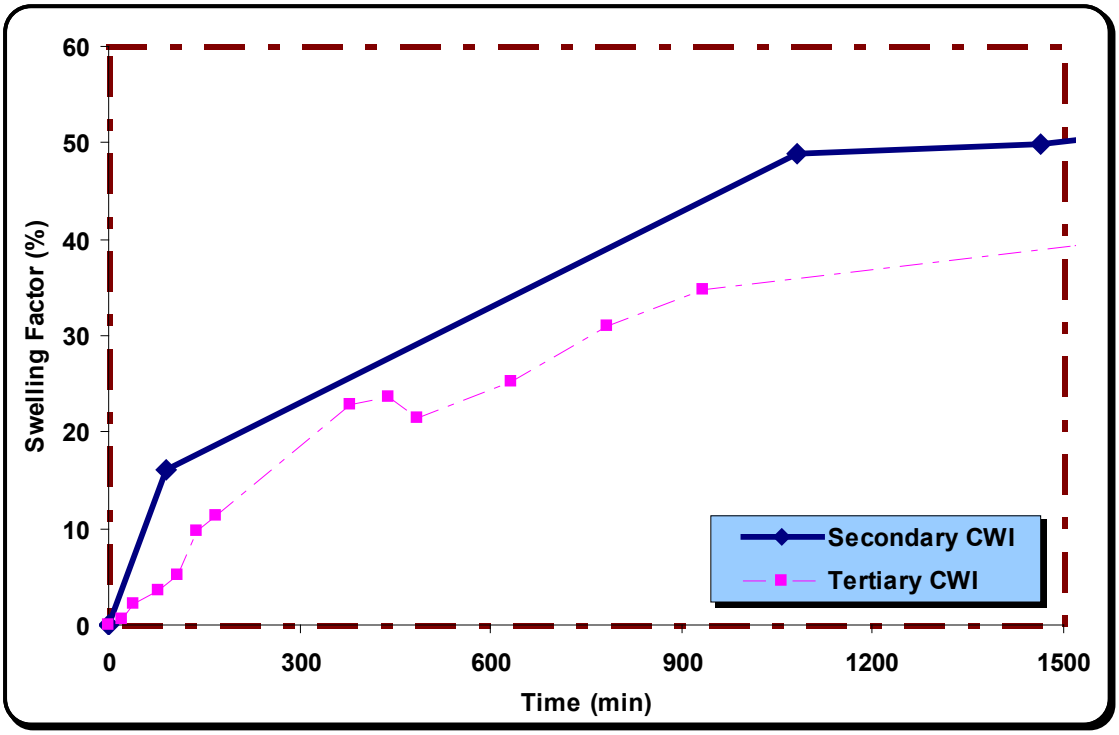

Figure 3-27: Initial part of Figure 26 at higher magnification.

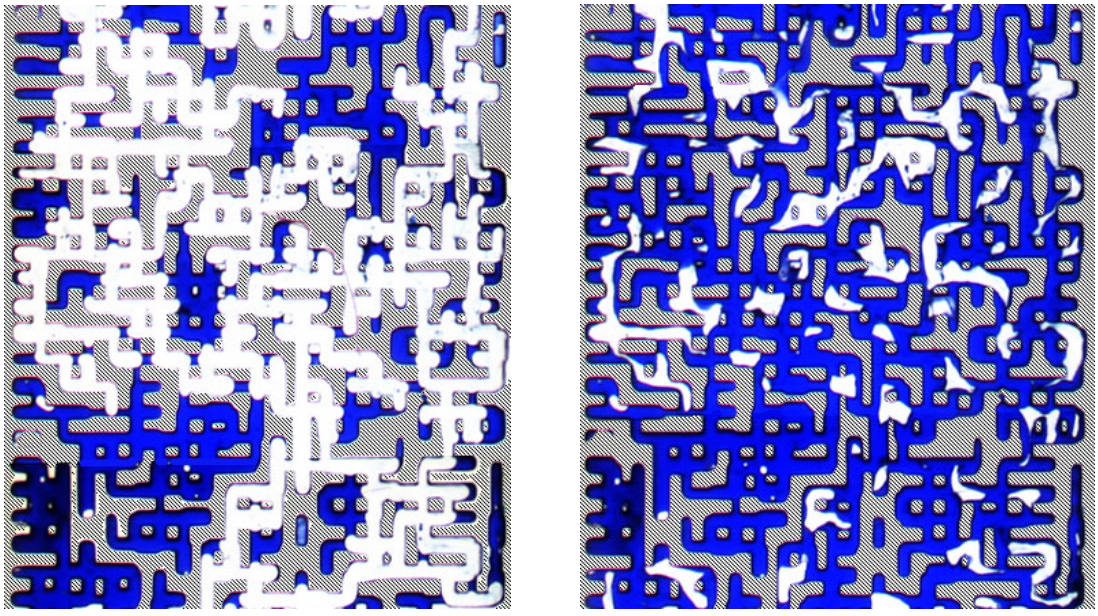

Figure 3-28: Initial oil (*n*-decane) saturation (left hand side image), residual oil saturation at the end of Experiment No.1, Tertiary CWI- Decane, (right hand side image).

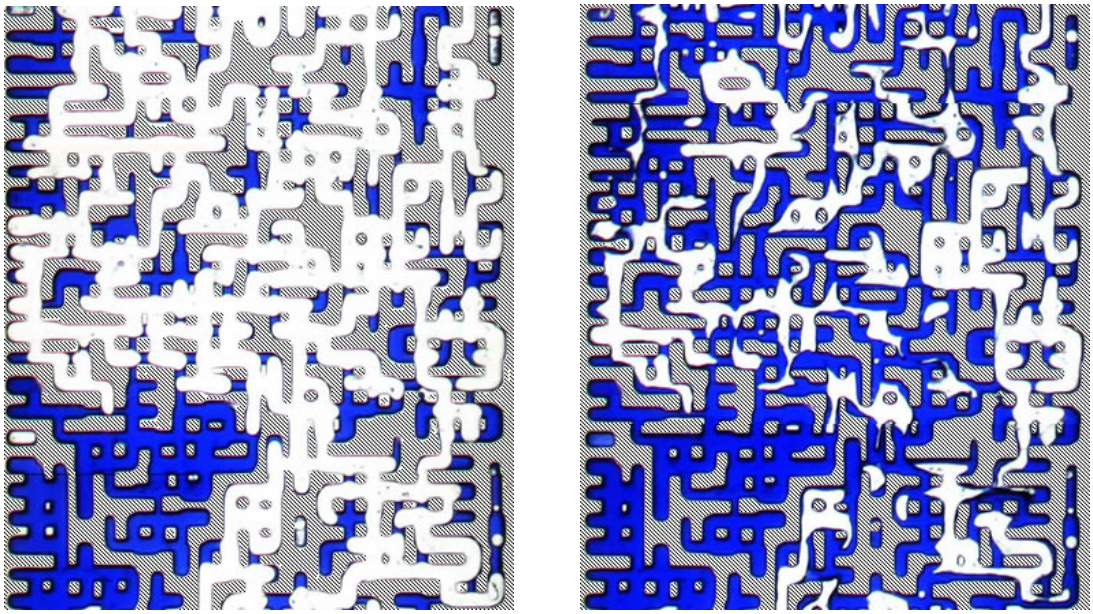

Figure 3-29: Initial oil (the viscous oil) saturation (left hand side image), residual oil saturation at the end of Experiment No.3, Tertiary CWI- Viscous oil, (right hand side image).

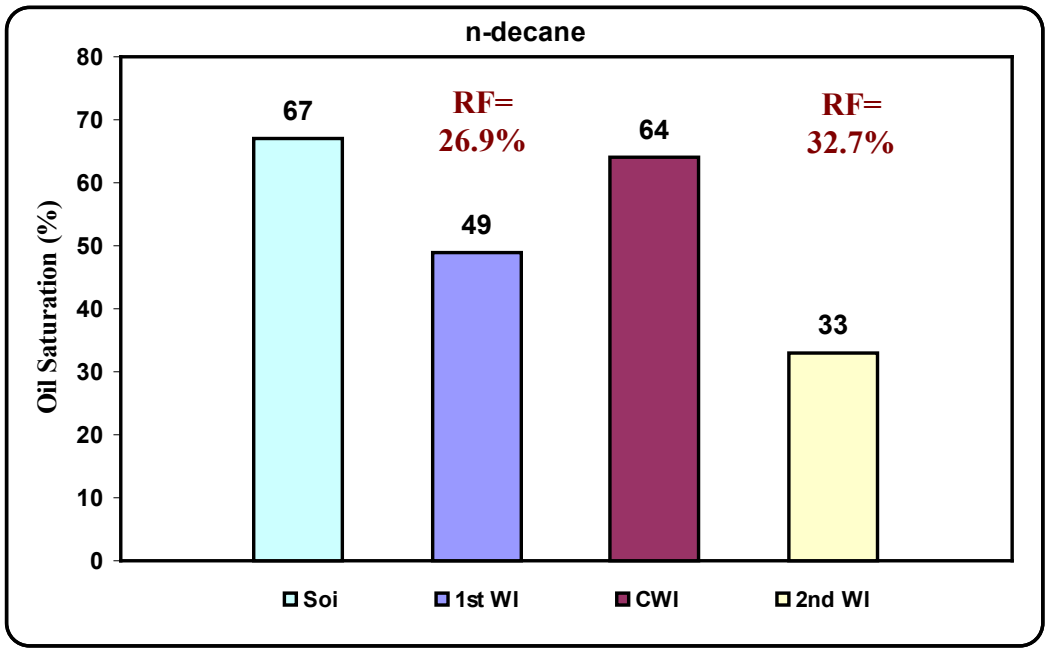

Figure 3-30: Oil saturation (*n*-decane) at different stages of the first test (Tertiary CWI-Decane).

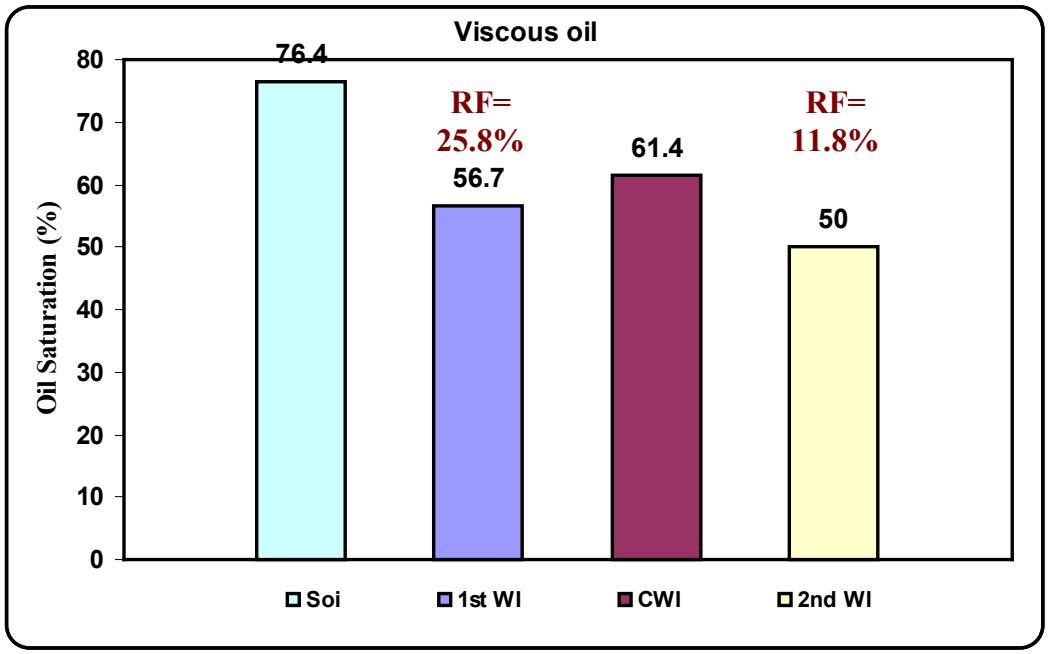

Figure 3-31: Oil saturation (viscous oil) at different stages of the third test (Tertiary CWI- Viscous oil).

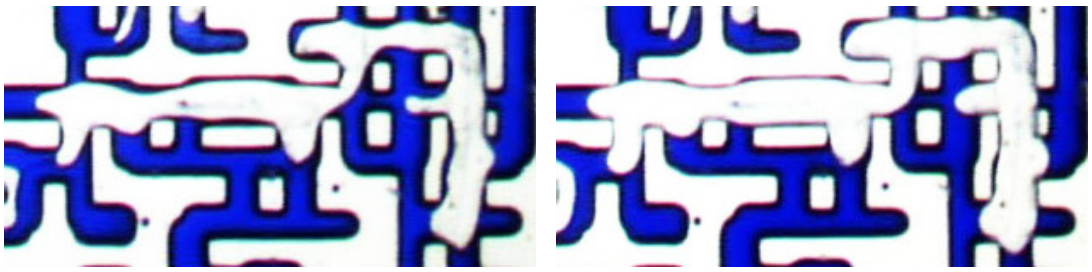

A B

Figure 3-32: An oil ganglion in Experiment No.3 (Tertiary CWI- Viscous oil): A) after the 1st WI; B) swollen oil at the end of the 1st CWI stage.

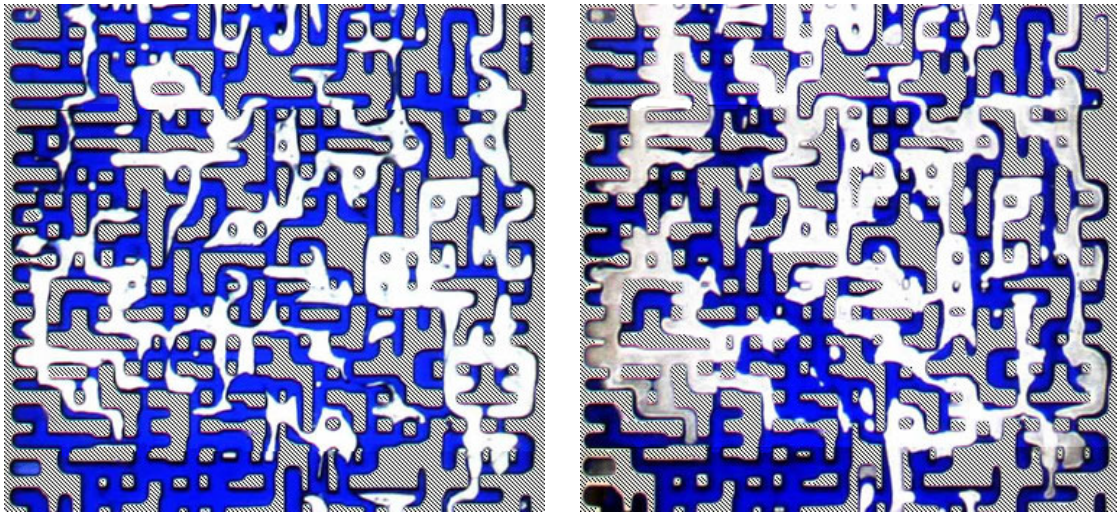

A B

Figure 3-33: Final dead residual oil saturation after (first) CWI: A) in Experiment No.3 (Tertiary CWI- Viscous oil) and; B) in Experiment No.4 (Tertiary CWI- Viscous oil- Low CO_2 Concentration in CW).

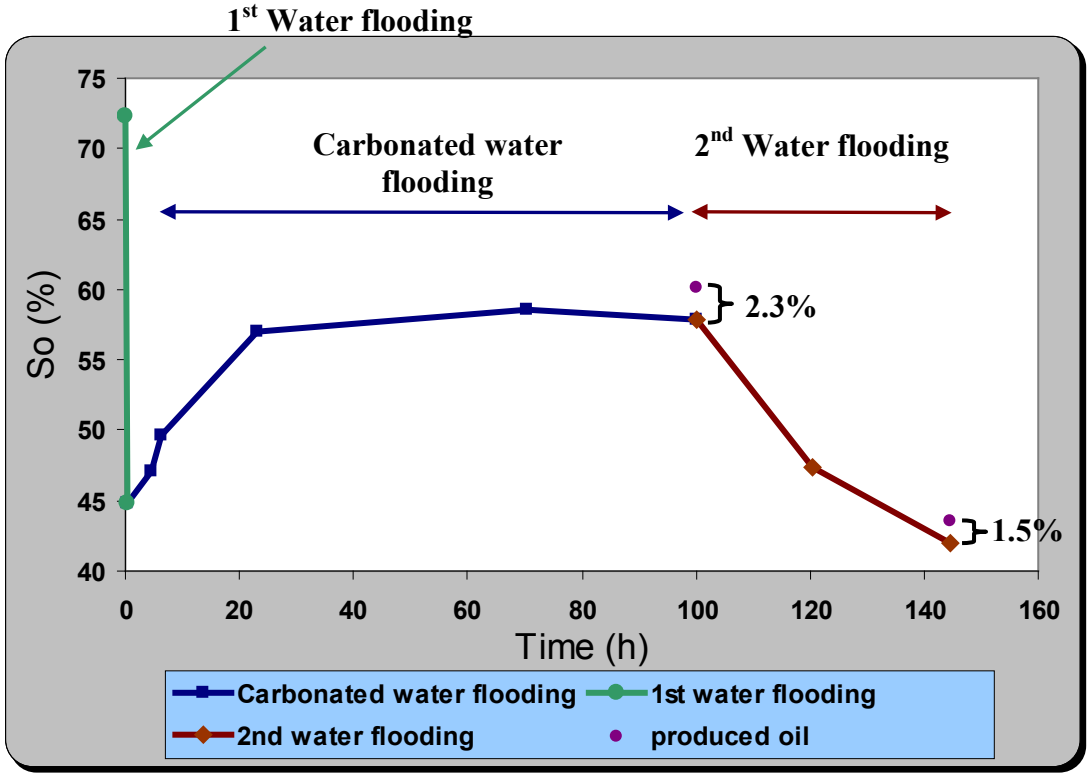

Figure 3-34: Oil, decane, saturation within micromodel (without triangular parts) versus time, Experiment No.5 (Tertiary CWI- Decane- Low CO_2 Concentration in CW).

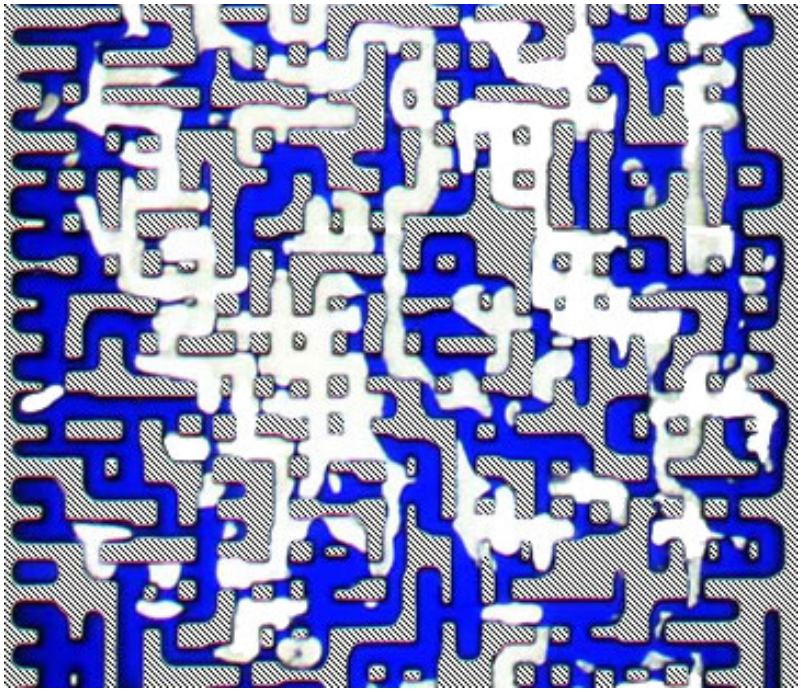

Figure 3-35: Residual dead oil saturation after the 2nd WI in Experiment No.5 (Tertiary CWI- Decane- Low CO_2 Concentration in CW) at the same section as Figure 17.

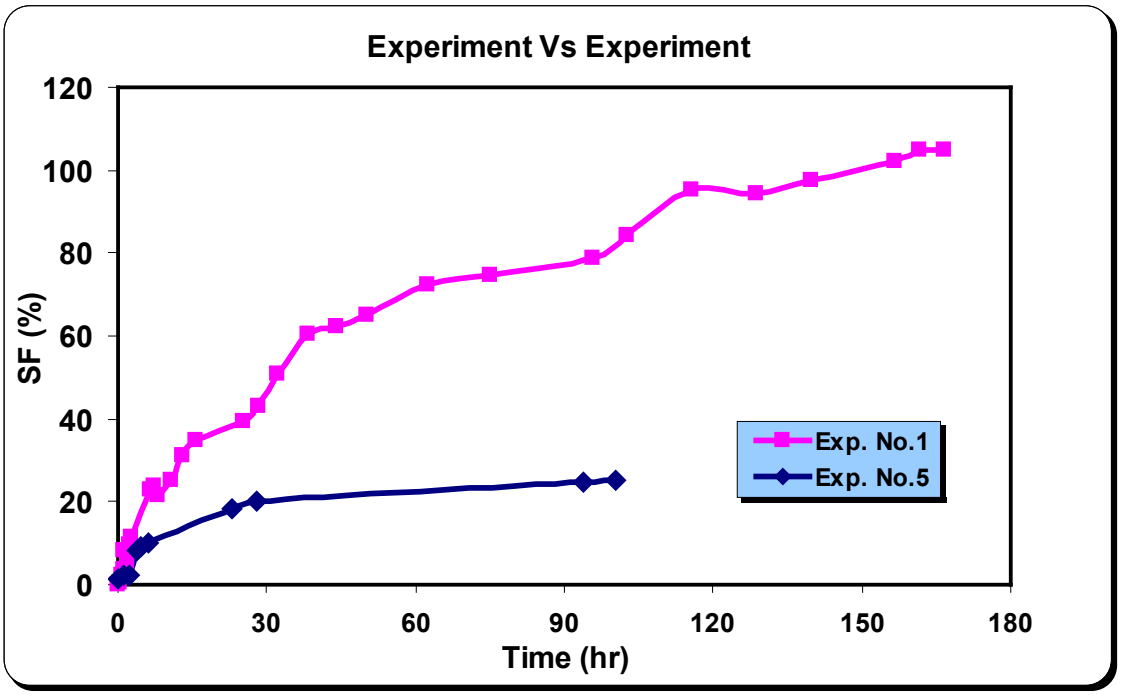

Figure 3-36: Swelling factor of *n*-decane during CWI: the first experiment (pink plot) vs. the fifth experiment (blue plot).

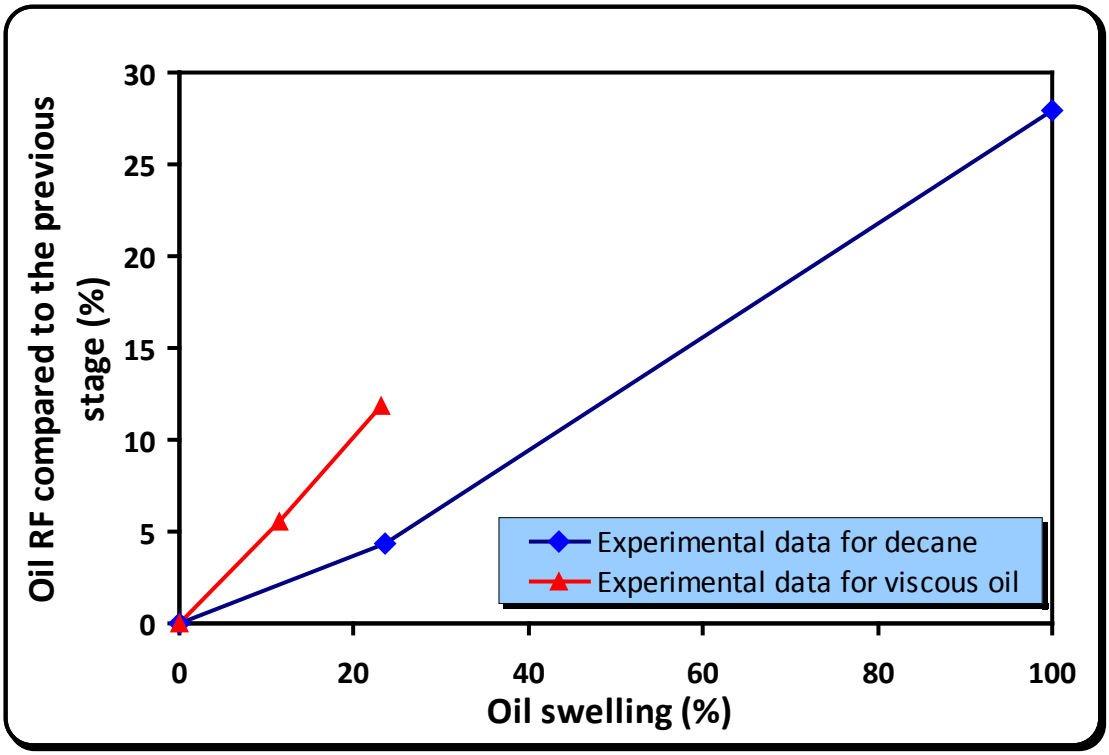

Figure 3-37: Oil recovery factor versus swelling factor of *n*-decane and the viscous oil.

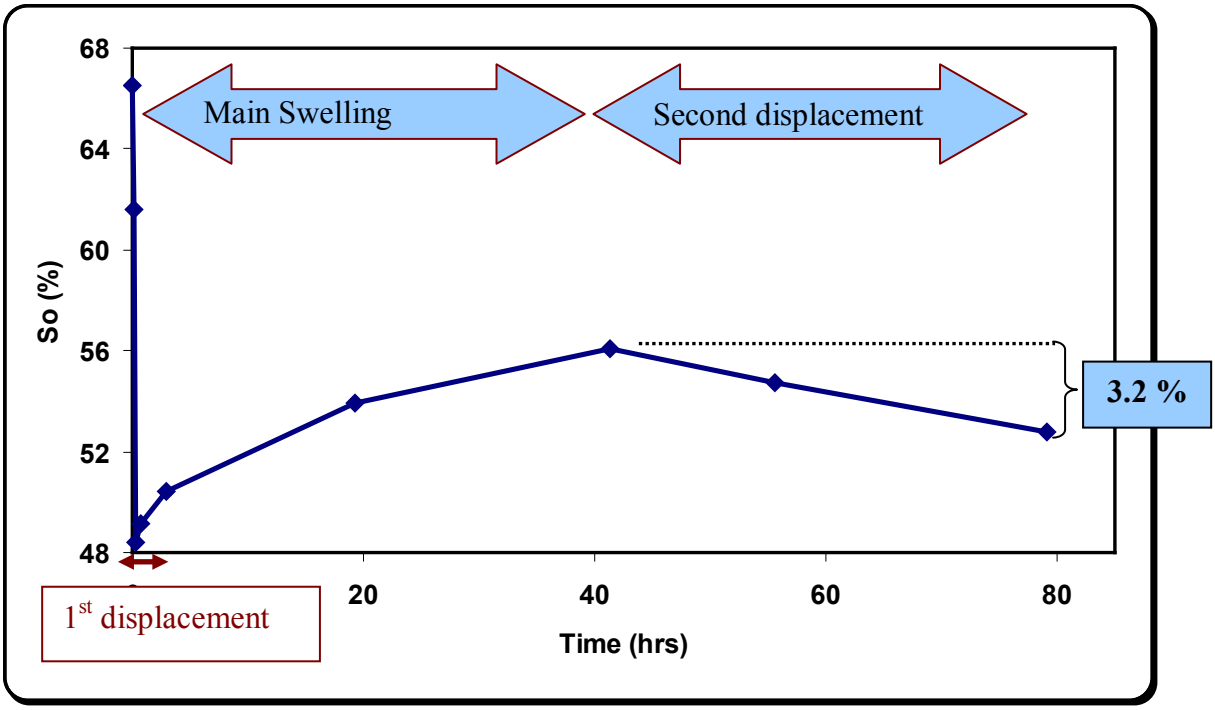

Figure 3-38: Oil saturation in the micromodel versus time, during CWI as a secondary recovery method, Experiment No.6, (Secondary CWI- Decane-Low CO_2 Concentration in CW).

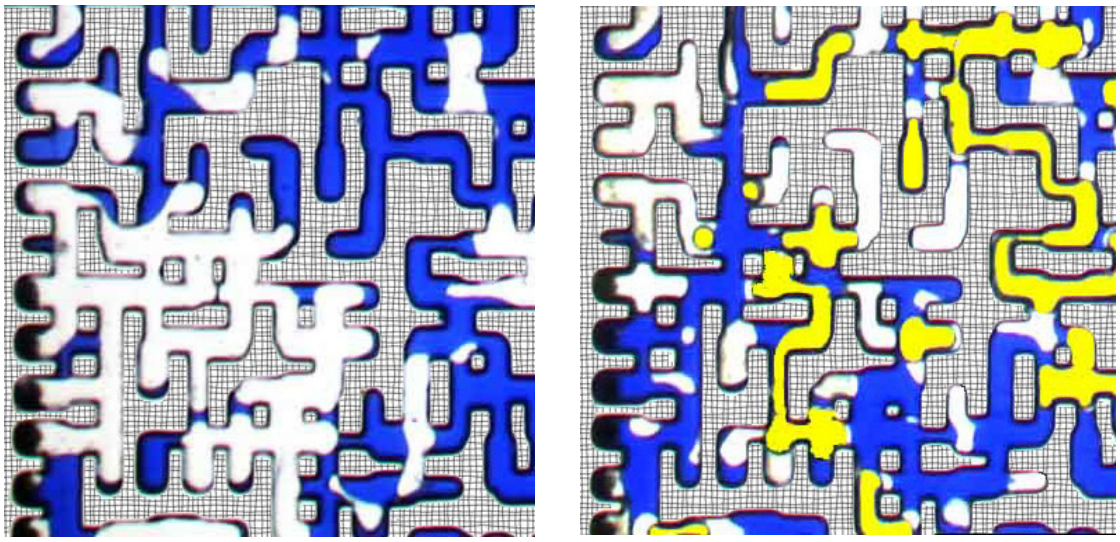

A B

Figure 3-39: Fluid distribution in a selected frame of the micromodel in Experiment No.6 (Secondary CWI- Decane-Low CO_2 Concentration in CW), A) oil saturation at BT of CW after 0.68 hrs. B) oil recovery and displacement during the depressurisation stage, when pressure reached 180 Psia.

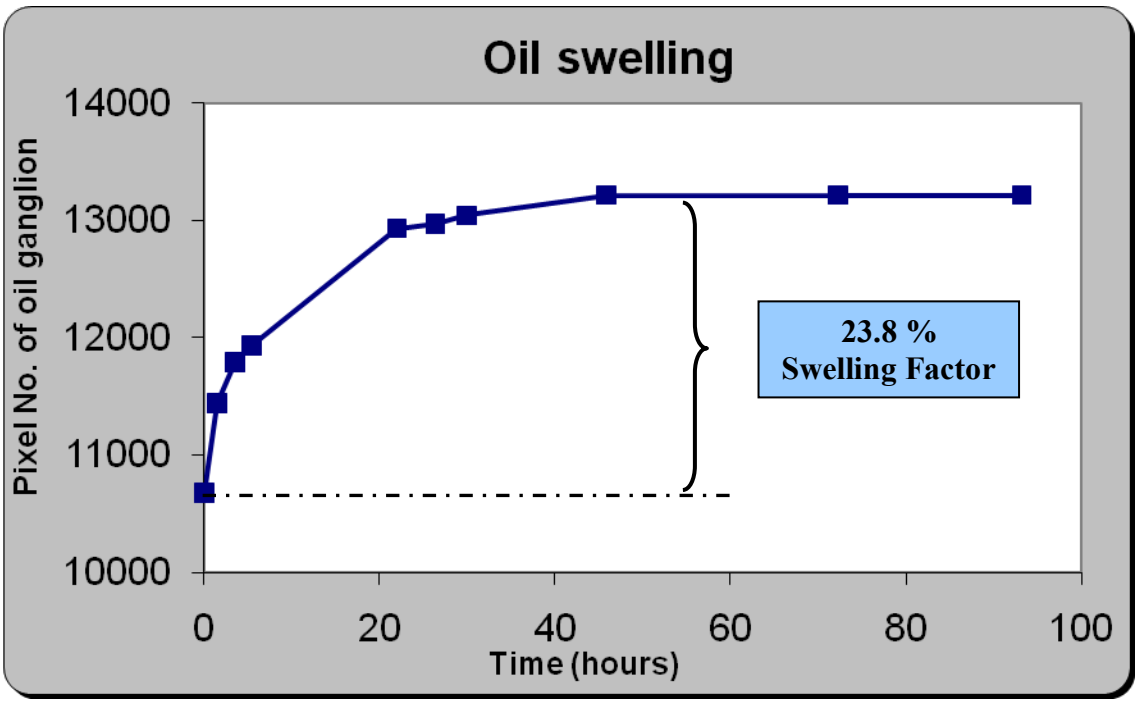

Figure 3-40: Variation of volume of an oil droplet Experiment No.6, (Secondary CWI-Decane-Low CO_2 Concentration in CW).

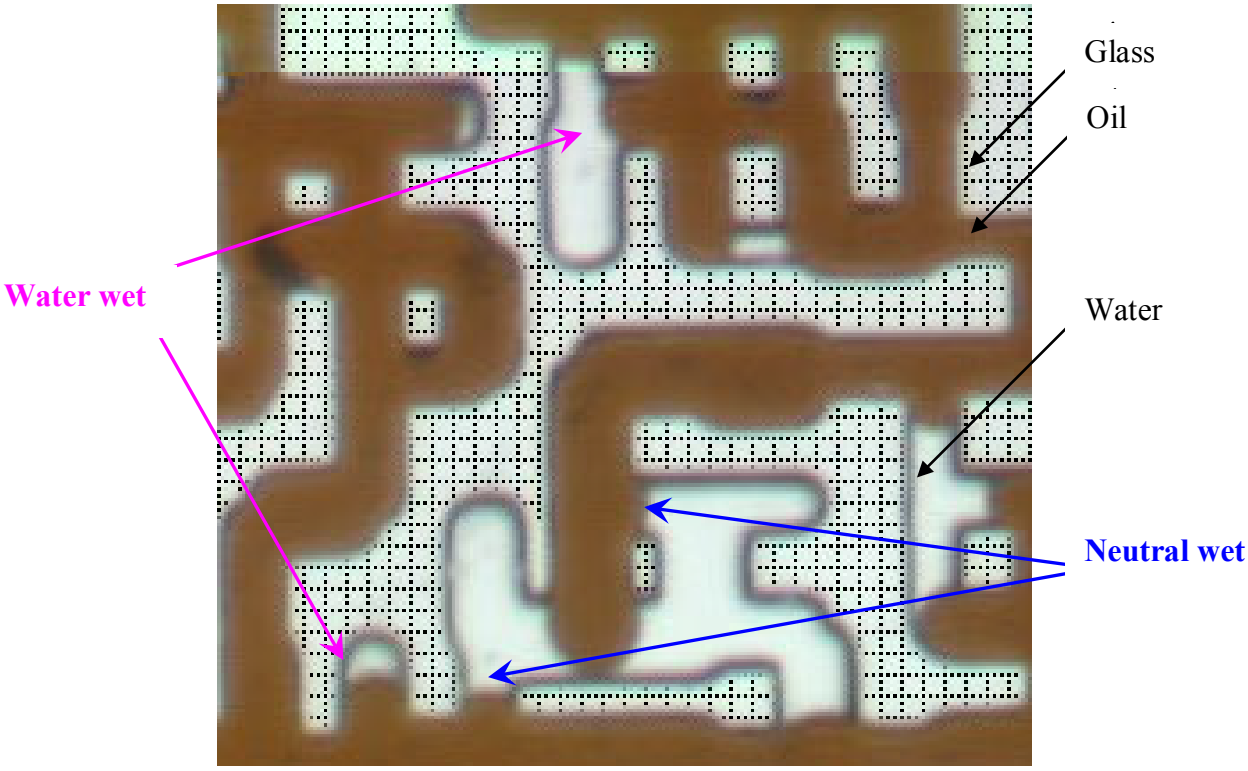

Figure 3-41: Water-wet and neutral-wet conditions within the micromodel, Experiment No.9 (Secondary CWI -Crude oil).

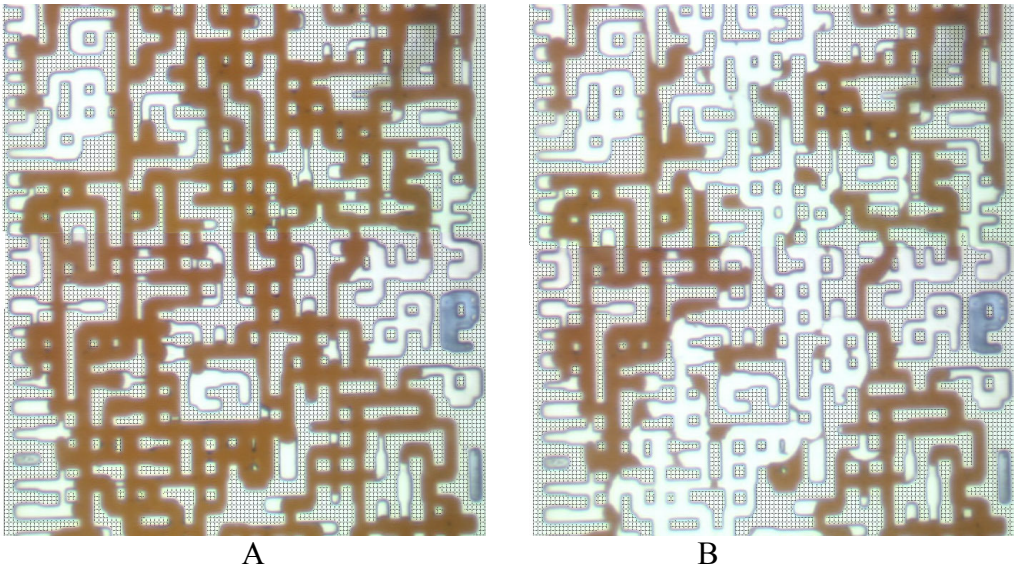

A B

Figure 3-42: A) Initial oil saturation at S_{wi} in a selected section of the micromodel after the first drainage stage, B) Fluid distribution at the BT of CW, Experiment No.9 (Secondary CWI -Crude oil).

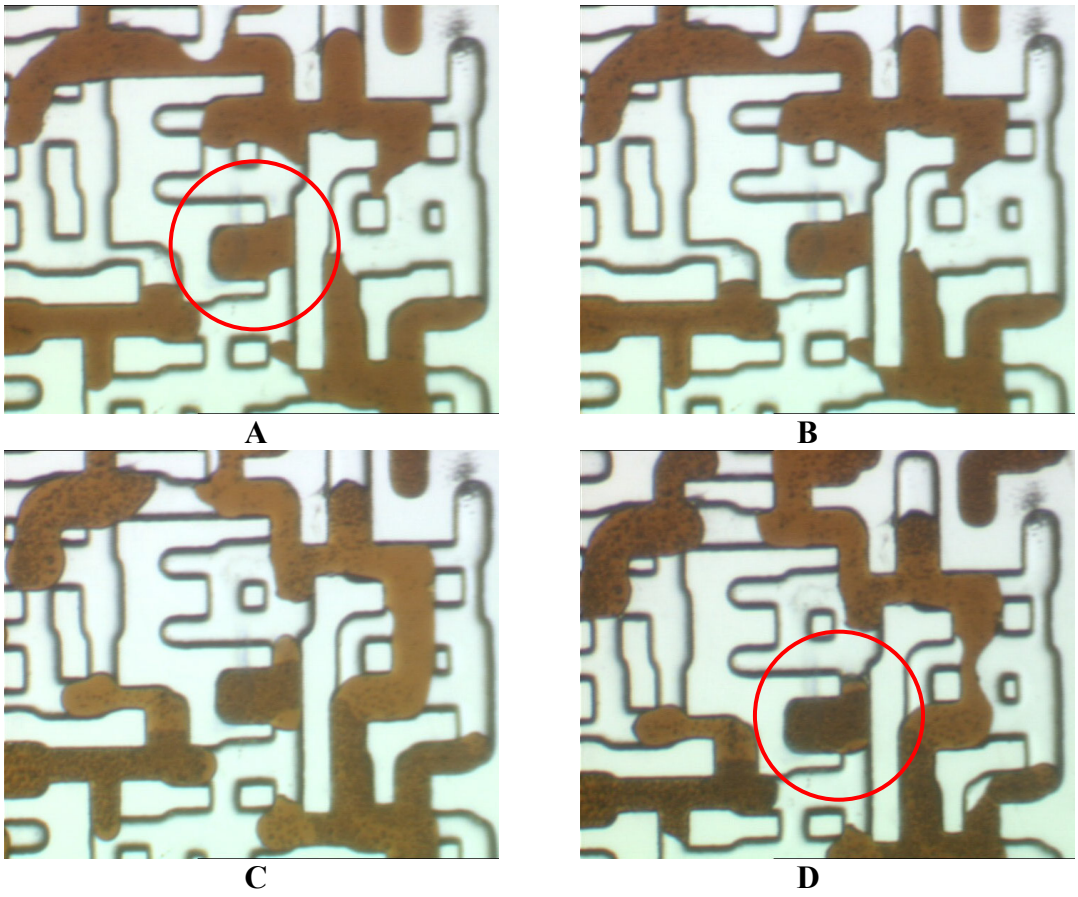

A **B**

C **D**

Figure 3-43: The state of oil ganglia, in a selected section of the micromodel, at different stages of Experiment No.10 (Tertiary CWI -Crude oil): A) at B.T. of the 1st WI; B) At the end of the 1st WI, 67 hrs; C) At the end of the CWI, 147 hrs; D) At the end of the 2nd WI, 67 hrs.

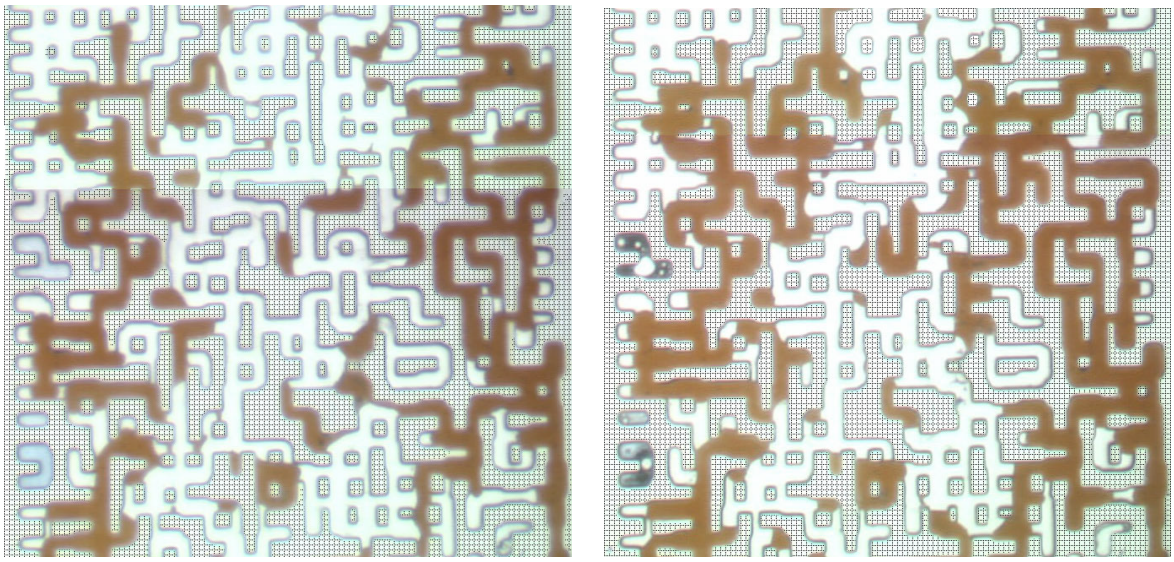

A **B**

Figure 3-44: Fluid distribution: A) at the BT of CWI in Experiment No.9 (Secondary CWI -Crude oil); B) at the BT of the WI in Experiment No.10 (Tertiary CWI -Crude oil).

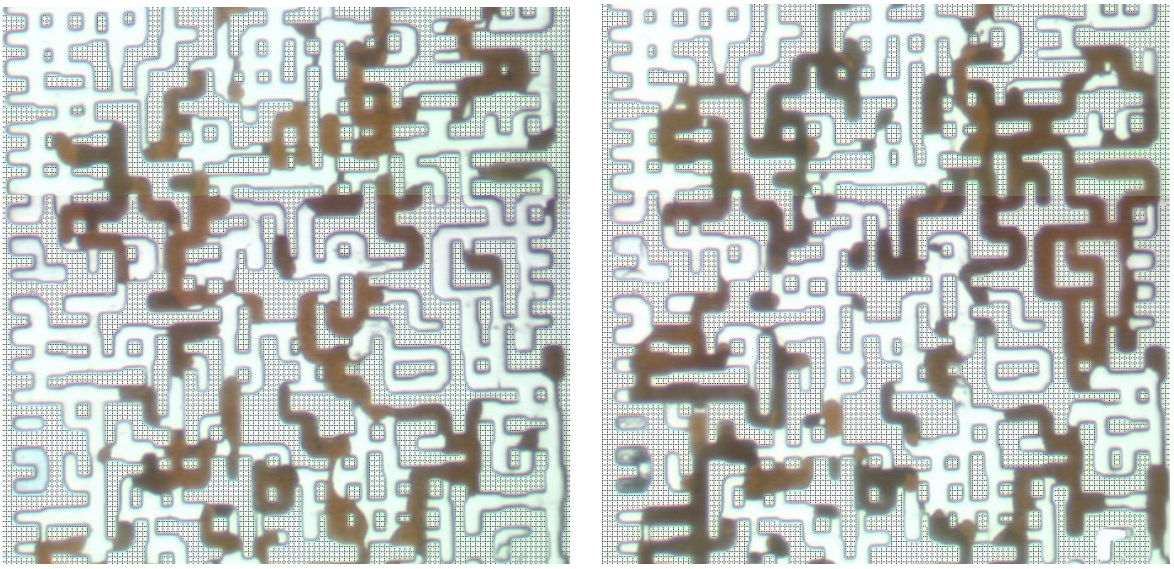

A **B**

Figure 3-45: Dead oil saturation condition: A) at the end of Experiment No.9 (Secondary CWI -Crude oil); B) at the end of Experiment No.10 (Tertiary CWI -Crude oil).

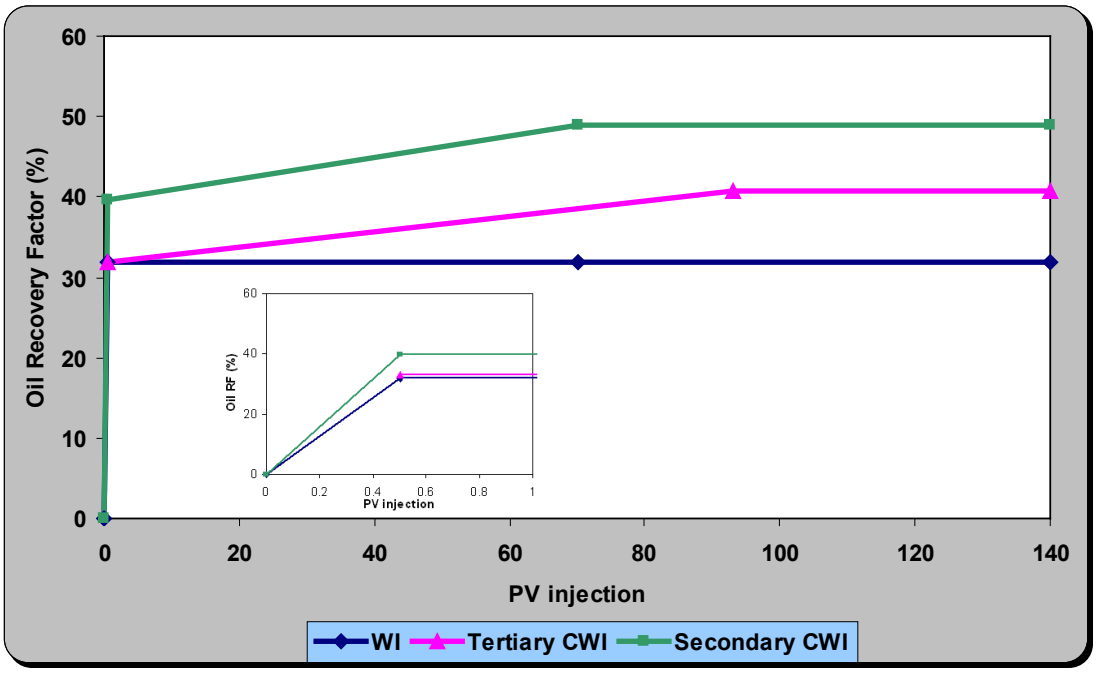

Figure 3-46: Oil (Crude A) recovery versus pore volume injected for plain water injection, tertiary CWI (Experiment No.10) and secondary (Experiment No.9).

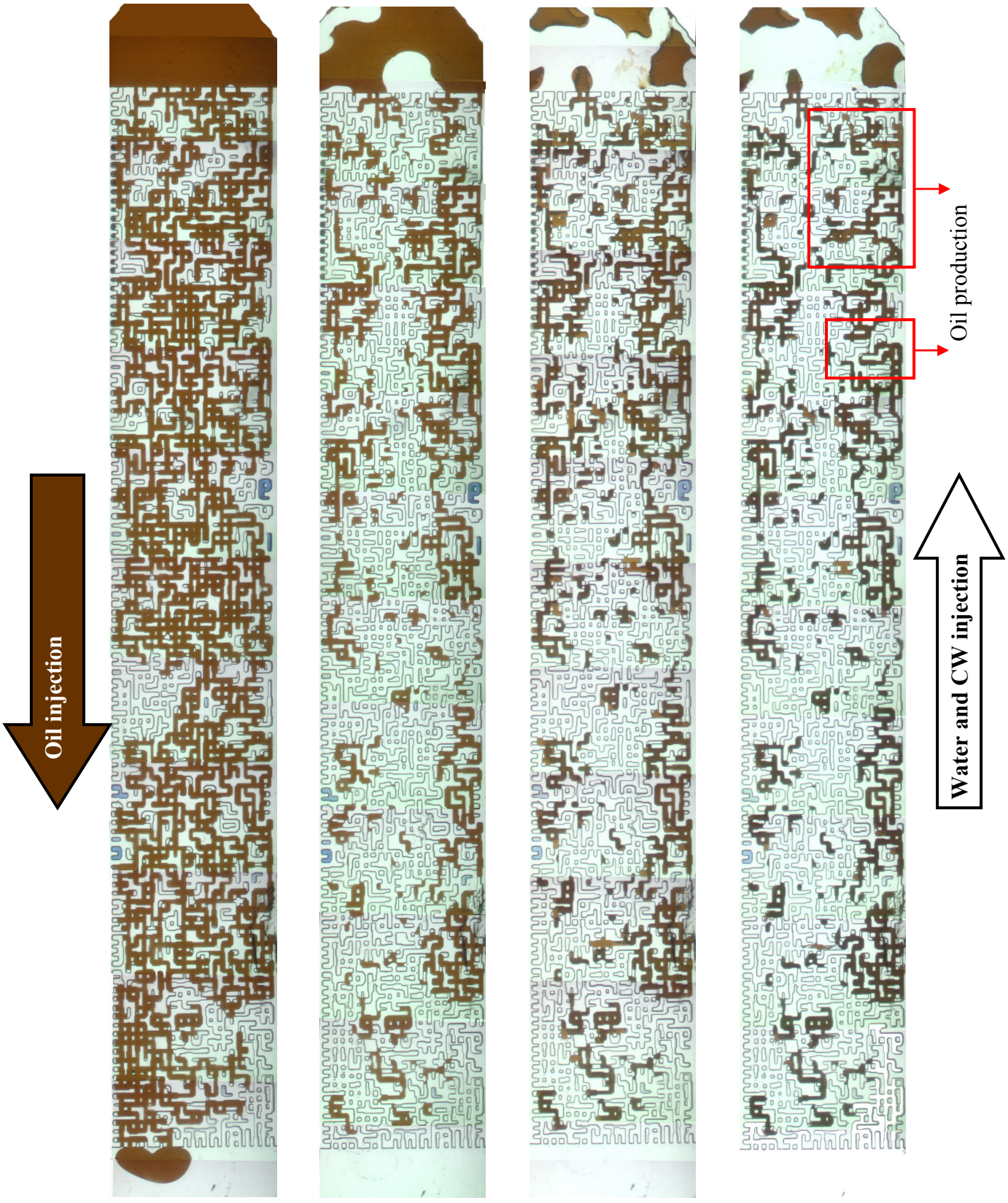

Figure 3-47: A sequence images of the micromodel during Experiment No.11 (Tertiary CWI -Crude oil- low oil saturation at BT): A) Initial oil saturation condition; B) Established residual oil saturation after the 1st WI; C) Established fluid distribution after CWI, 140 hrs; D) Residual oil saturation after 2nd WI, 19.5 hrs.

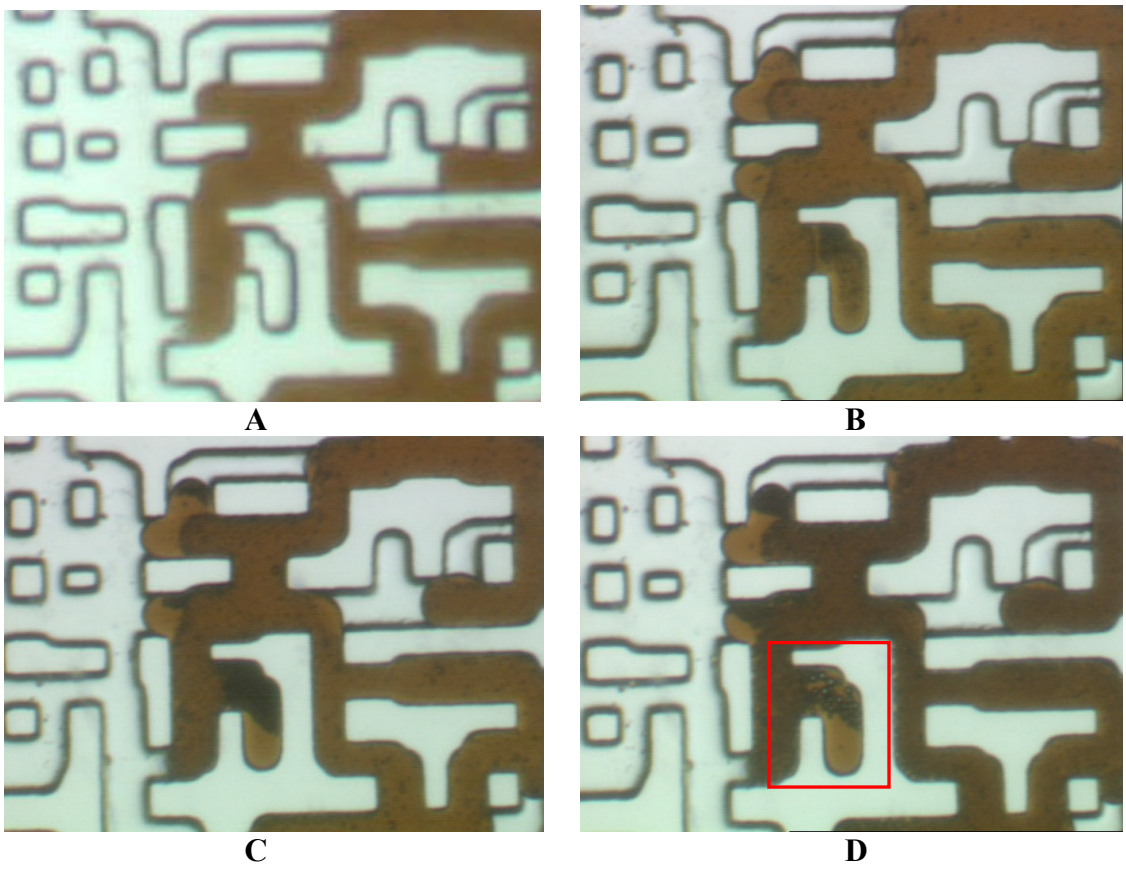

Figure 3-48: A sequence of images of a section of the micromodel during Experiment No.11 (Tertiary CWI -Crude oil- low oil saturation at BT): A) after BT of the 1st water injection; B); C) and D) after 19, 43 and 140 hrs of CWI, respectively.

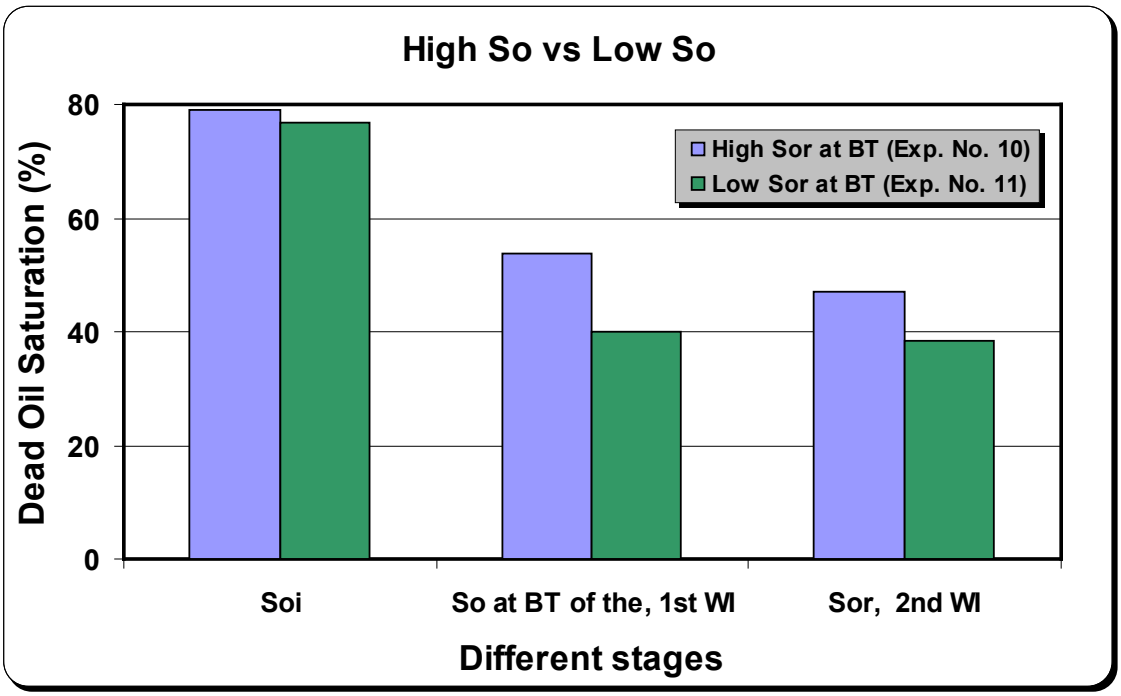

Figure 3-49: Dead oil saturation at different stages of Experiment No.10 (Tertiary CWI -Crude oil) vs. Experiment No.11 (Tertiary CWI -Crude oil- low oil saturation at BT).

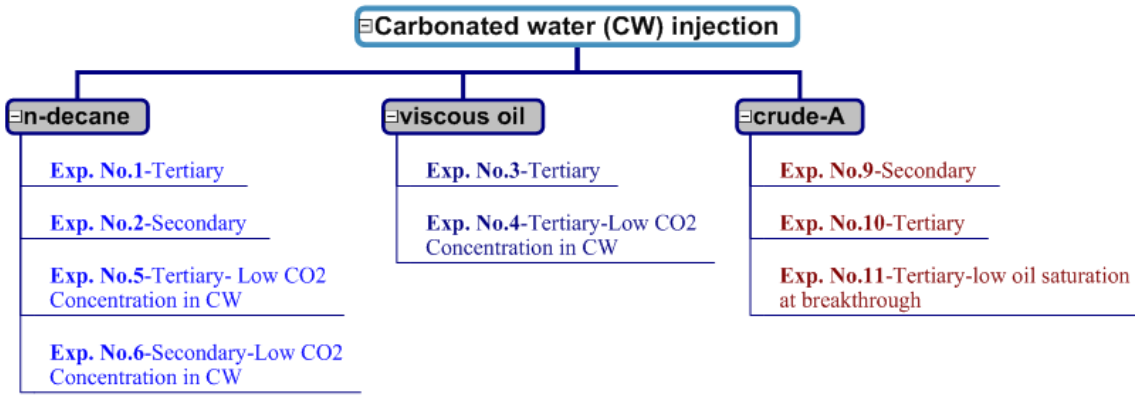

Figure 3-50: Classification of the micromodel experiments based on the oil type used.

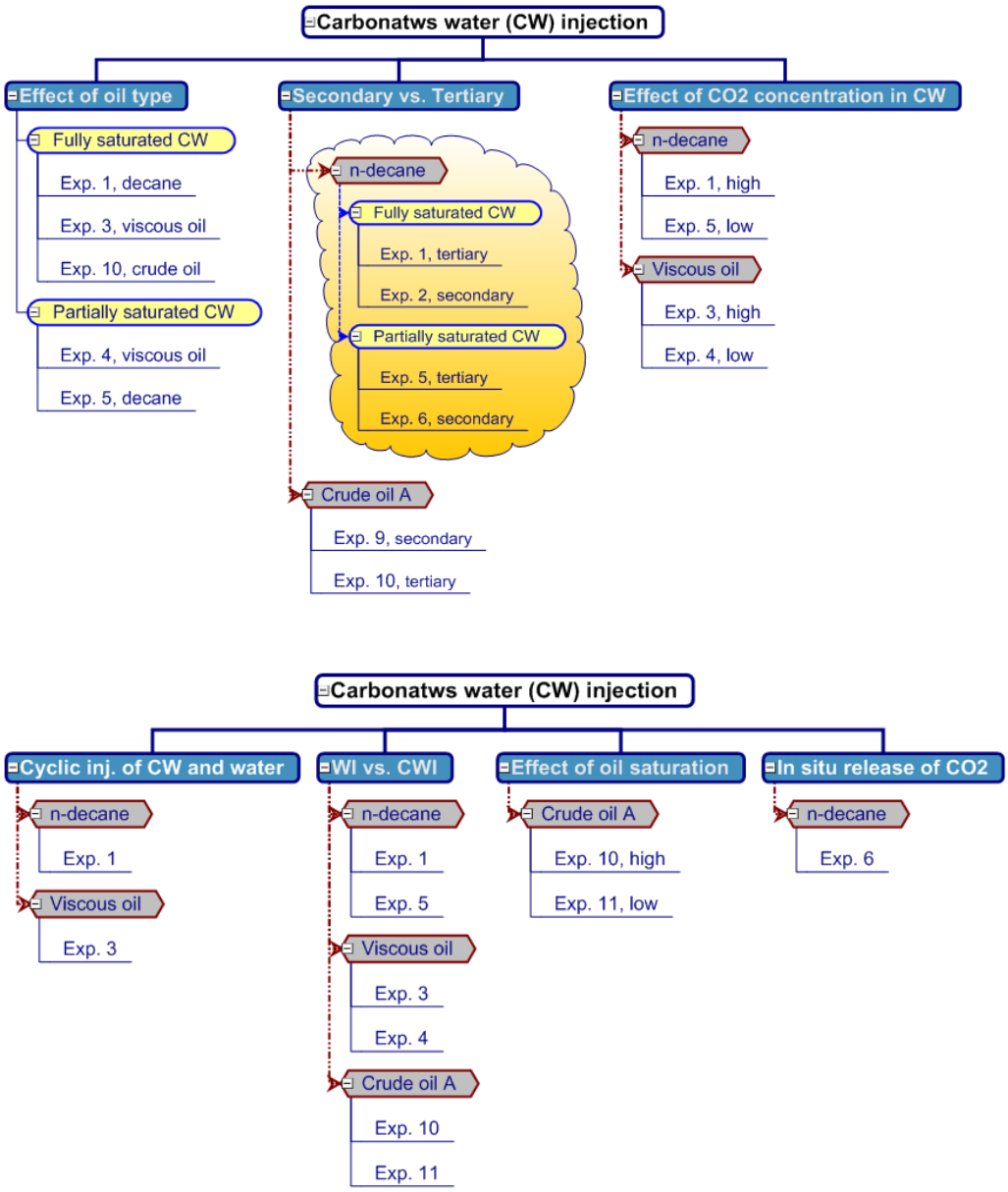

Figure 3-51: Classification of the micromodel experiments based on the effect of different parameters and process pertinent to CWI.

4 Chapter 4: Impact of Carbonated Water Injection on CO_2 Injection

4.1 Introduction

Carbon dioxide (CO_2) and hydrocarbon gas injections are usually conducted after water flooding. Under these conditions, the gas phase may not contact all the oil phase directly and replace the trapped and residual oil behind the water layers. Water shielding effect in which water layers prevent direct contact of oil and gas (CO_2) has been experimentally observed by several researchers (Campbell and Orr 1985; Wylie and Mohanaty 1997; Tiffin et al. 1991; Lin and Huang 1990; Holm 1986). The results of these studies have shown that if the oil swelling as a result of partitioning and diffusion of the gas component from the water barrier into the oil is enough to rupture the water layer then that trapped oil will be produced; otherwise, the swollen trapped oil remains as the unrecoverable phase. The rate and the amount of oil swelling, as two key parameters in rupturing the water layer, are highly dependent on the pressure and temperature conditions of the system, salinity of the water layer and oil composition. Furthermore, the stability of the water layer between CO_2 stream and the oil phase can control the rupturing process of the water layer.

Based on the above discussion, injection strategies that can increase the contact between CO_2 and oil would improve oil recovery and alleviate the adverse effect of water shielding.

The main purpose of this chapter is the investigation of the effect of carbonated water injection (CWI) instead of plain water injection (WI) prior to carbon dioxide injection (CO_2I) on oil displacement mechanisms and recovery. This comparison will be shown here for the viscous mineral oil and crude oil A. Two preliminary tests were also performed to investigate the interaction of CO_2 with the resident fluids and the displacement mechanisms of CO_2I when the micromodel is saturated with water or

mineral oil and compare them with the case when both oil and water are present in the system. Table 1 summarises different stages of each test in this chapter.

4.2 CO_2I into Water and/or Mineral Oil

Experiment No.12- CO_2I into the porous medium fully saturated with water

Experiment No.12 the horizontal micromodel was initially fully saturated with blue-dyed plain water (Figure 1A). Then supercritical CO_2, which had been pre-equilibrated with water, at 2000 psia and 38 °C (100 °F), was injected at a low rate of 0.01 cm^3h^{-1} into the micromodel. This test could represent CO_2 storage in aquifer. To distinguish the colourless CO_2 from the colourless glass, CO_2 was digitally coloured in yellow. Figure 1B, which shows the distribution of CO_2 at the breakthrough (BT) of CO_2, will later be compared with the cases when the micromodel is fully saturated with oil and when both oil and water are in the porous medium before CO_2I. CO_2 BT happened after 0.5 hours (hrs) of CO_2I. This figure shows that CO_2 has channelled through the micromodel, due to the high adverse viscosity ratio between CO_2 and water (i.e. $\mu_{CO2}/\mu_{water} = 0.098 << 1.0$).

As this image shows, CO_2 is more or less a continuous stream in the porous section, apart from a few locations at the outlet of the micromodel, which have been highlighted by red arrows. This has occurred due to the end effect and discontinuity in capillary pressure at the outlet section of the micromodel. This observation, which is an example of the capillary trapping mechanism, may reflect the impact of reservoir heterogeneity on CO_2 flow and trapping mechanisms.

The water is not initially in thermodynamic equilibrium conditions with CO_2. However, through time, as a result of mass transfer, they eventually reach equilibrium conditions. The required equilibrium time is a function of different parameters, such as diffusion coefficient, CO_2 solubility and saturation and distribution of CO_2. Although investigation of this issue is not the main aim of conducting this test, here, to some extent, the effect of mass transfer on fluid distribution can be visually demonstrated. Figure 1C shows the fluid distribution (CO_2 in yellow and water in blue) within the micromodel two hours after CO_2 BT time. Comparison of this figure with Figure 1B

indicates that shrinkage of CO_2 occurred, as a result of mass transfer. Some of these differences have been highlighted by red rectangles in Figures 1B and 1C.

However, the extent of CO_2 dissolution and the resultant water imbibition were not significant enough (during the 2 hrs time scale) to cause the snap off of CO_2 at the pore level and hence, capillary discontinuity of the CO_2 stream. As more time passes after the injection of CO_2, it is expected that the dissolution of CO_2 in water continues and eventually causes disconnection and trapping of the CO_2 phase. Fluid distribution, 20 hours after CO_2I, is shown in Figure 1D. As this image shows, a higher dissolution of CO_2 in water, especially at the upper side of the micromodel, where water was in less contact with CO_2 can be observed. However, the extent of CO_2 dissolution is not still enough to cause the capillary discontinuity. This is attributed to the low CO_2 solubility in water, high CO_2 saturation and also the slow diffusion process.

Experiment No.13- CO_2I into the porous medium fully saturated with the viscous mineral oil

To investigate the displacement mechanism of CO_2 in the porous medium containing oil, in this test the micromodel was initially fully saturated with the mineral oil without any initial (connate) water saturation (S_{wi}=0). Figure 2 shows the fluid distribution in the whole of the micromodel at different stages of this test. The CO_2 BT in this test happened after 0.45 hrs of CO_2I. By comparing the location of the gas–oil interfaces in this figure, it can be seen that as a result of continued CO_2I, the area occupied by CO_2 has become larger and the volume of the oil ganglia contacted by CO_2 has shrunk.

Flow diversion and piston type displacement within the pores

Comparison of different parts of the porous section of the micromodel in this test indicated that as CO_2I continued the flow path of the gas stream changed. Examples of this behaviour have been highlighted by red rectangles in Figure 2. Figures 3A and 3B show this observation in a highly magnified image of the upper side section of the micromodel.

Different stages of this flow diversion process can be illustrated using a simple multiple pore model, displayed in Figure 4. This model can demonstrate the displacement process of oil (in white) by CO_2 (in yellow). Figure 4A shows that the gas stream in

pore No.1, when reaching the intersection of this pore with pores No.2 and No.3, chooses the larger pore size (pore No.2) with its lower capillary pressure, i.e. less flow resistance against the flow of gas, as the non-wetting phase. Figure 4B shows that the oil in pore No.3 has been displaced by gas. This displacement could be due to mass transfer i.e. evaporation of oil into the CO_2 stream. At this stage the gas interface encounters a larger pore (No.4) than pore No.2, which is easier for gas to flow through. Figure 4C illustrates that CO_2 mainly flows through this pore rather than its previous flow path. Such a change in flow path during injection could drastically redistribute the fluid within the porous medium, as observed in Figure 3B.

Figure 2C, compared to Figure 2B, shows the impact of such flow diversion after BT of CO_2 on a large oil ganglion produced in the upper triangle. The resultant oil production for such flow behaviour is an indication of piston type displacement by CO_2. As will be discussed in the next experiment, this piston-type displacement mechanism after BT is the main difference between this test and the one, where there is a water phase in the porous medium, together with the oil phase, where the presence of water layers between the oil and gas stream, impede the mass transfer process.

4.2.1 CO_2I after WI

Experiment No.14- WI followed by supercritical CO_2I with S_{wi}-The viscous mineral oil

This experiment (No.14) and the next one are designed to correspond to CO_2I into depleted oil reservoirs. Hence, in this test, after saturating the porous medium with 100% blue-dyed water, the mineral oil was injected from one end of the micromodel and continued until oil reached the other end of the micromodel. WI began after this initial oil injection stage. Figure 5 and Table 1 shows the visualisation results and the details of different stages of this test, respectively. Figure 5C shows CO_2 channelled through the micromodel due to the high adverse viscosity ratio between CO_2 and the resident fluids. In this test CO_2 BT happened after 0.35 hrs of CO_2I, Figure 5C.

Figures 6-8 show a magnified image of the same section of the micromodel at the end of the waterflooding, after CO_2 BT and after about 3 hrs of CO_2I, respectively. The direction and the shape of the interfaces in this three-phase fluid flow test indicated water-wet conditions. It also showed that oil is the intermediate wetting phase and CO_2

is the non-wetting phase. For this three-phase system, the spreading coefficient of oil on water in presence of CO_2 is defined as a balance of interfacial tensions (IFT), (Adamson, 1960; Sohrabi, 2001) as below:

$$C_s = \delta_{co_2w} - (\delta_{ow} + \delta_{co_2o}) \quad (4.1)$$

where δ_{co_2w} , δ_{ow} and δ_{co_2o} are the CO_2/water, oil/water and CO_2/oil interfacial tensions, respectively.

In the water-wet porous medium, when C_s is positive (C_s>0) the oil tends to spread as a film between water and CO_2, whereas when C_s is negative (C_s<0) the three phases meet at some points.

Since, initially, no oil film separated water and CO_2 in this test, the spreading coefficient should be negative, C_s<0. As will be shown later, as the test progressed, the IFT values changed and the spreading coefficient became positive.

A comparison between Figure 7 and Figure 6 shows that CO_2 flooding has changed the fluid distribution. These two images also indicate that CO_2 displaced mainly water rather than oil. The lower part of the micromodel in Figure 5C provides clear evidence of CO_2 by-passing the oil and passing through the water phase.

The likely reason for this phenomenon could be the higher viscosity of oil (about 16 cP) compared to water (about 1cP). The other reason could be that the water layer separating oil and CO_2 phases did not rupture. As will be demonstrated in the next test, when a CWI prior to CO_2I was conducted, this water layer ruptured and more oil was displaced.

During this test even at CO_2 BT, swelling and even oil re-connection could be seen in some parts of the micromodel. The red rectangles in Figure 7 highlight swelling and oil reconnection, compared to the same positions in Figure 6.

Figure 8 shows fluid distribution about three hours after CO_2 BT. By comparing the gas/oil interfaces in Figures 7 and 8, it is noted that the area occupied by CO_2 has increased and the volume of the oil ganglia, which had been in contact with the CO_2 has

shrunk (highlighted with red circles). This displacement of oil was mainly due to the extraction of oil components by the fresh flow of CO_2 stream. However, some indications of the film flow mechanism of oil were also observed. Figure 9 shows a section of the micromodel, demonstrating shrinkage of the bypassed oil, which was accompanied by the widening of the CO_2 stream, and its flow alongside the flowing CO_2.

Swelling of some of the oil ganglia, which were not in direct contact with the CO_2 stream can also be observed. The red rectangle in Figure 8 shows displacement of the water layer as a result of swelling of an oil ganglia, which is produced by CO_2 later on during the test, as shown in Figure 10. These images highlight how water layers between oil and CO_2 prevents oil production.

The other point that should be highlighted, here, is that in Figures 8 and 10 there are some oil films, which are positioned between the water and the gas phase. These locations have been highlighted by red arrows in these figures. This observation indicates a possible change of IFT of the fluids with time and a shift of the spreading coefficient from negative to positive (Equation 1). The shape of a lens of oil highlighted by a red rectangle in Figure 9B compared to that in Figure 9A shows, the tendency of the oil to spread over the water in the presence of CO_2. The dynamic process of the spreading of oil is as a consequence of mass transfer and IFT modifications during CO_2I.

<u>The impact of resident fluids on the efficiency of CO_2I</u>

The results of Experiment No.14 (CO_2I after WI-The viscous mineral oil) can be compared with the results of the previous experiments (No.12 (CO_2I into the porous medium fully saturated with water) and No.13 (CO_2I into the porous medium fully saturated with the viscous mineral oil)) to investigate the impact of the resident fluids on fluid distribution within the porous medium during CO_2I.

A comparison of the required time to BT in Experiment No.14 (0.35 hrs) with the corresponding time in Experiment No.13 (0.45 hrs) and in Experiment No.12 (0.5 hrs) indicates that BT in this test took place faster. This difference could be explained by comparing the fluid distribution within the micromodel in these tests.

It is noted that in Experiment No.14 (CO_2I after WI), CO_2 has channelled through a single pore path (Figure 5C) whilst in Experiments No.12 and No.13, the CO_2 stream has occupied a number of pores across the main flow path (Figures 1B and 2B).

These figures also show that CO_2 saturation in Experiments No.12 (Figure 1B, CO_2I into 100% water) and No.13 (Figure 2B, CO_2I into 100% oil) is more or less the same. The minimal difference between CO_2 distribution in Figure 1B and Figure 2B could be due to different fluid properties of water and oil, such as IFT between resident fluid and CO_2 and different wettability conditions, which directly affect the capillary forces within the porous medium. Although the IFTs of CO_2-oil and CO_2-water in this study have not been measured experimentally, the literature data shows that the IFT between water and CO_2 is generally higher than the IFT between oil and CO_2. For instance Yang and Gu (2004) experimentally showed that IFT of CO_2-a typical crude oil varies from 27-5 dyne/cm whereas IFT of CO_2-brine varies from 70-30 for the same range of pressure and temperature. In other hands the curvature of the interfaces in Figures 1B (CO_2-water) and Figure 2B (CO_2-oil) as well as the fluid distribution in Figure 5C (CO_2-water-oil) indicate that the porous medium is more water wet compared to the oil. Theoretically point of view, it is lower contact angle for the system of CO_2-water-glass with higher cosine value than the system of CO_2-oil-glass. Having known the dependency of capillary pressure on contact angle and IFT indicates higher capillary pressure (P_c) for the former system (Figure 1B) than the latter one (Figure 2B). Since the pore size distribution of the micromodel is quite wide (30-500 μm), diversity of capillary pressure, which plays as a resistance against the flow, affects the fluid distribution during CO_2I. This effect for higher capillary pressure system (Figure 1B) and when the displacing fluid is gas with high compressibility factor is expected to be greater. Having less gas fingering in Figure 2B than that in Figure 1B is a good indication of this mechanistic fact.

It should also be pointed out that in Experiment No.14 (CO_2I after WI-The viscous mineral oil), where the porous medium contains both oil and water, CO_2 distribution (Figure 5C) is drastically different from that observed in the experiments with the micromodel fully saturated with only one of these two fluids. In Experiment No.14, CO_2 channelled only through a single pore then the stream widened over time, whilst in

Experiments No.12 and No.13 widening of the CO_2 stream took place during CO_2I before its BT. Having a larger number of oil/water interfaces in the path of the CO_2 front significantly reduces the mobility of the resident phases and acts as a resistance to the CO_2 flow and its propagation in the porous medium.

The results of Experiment No.14 (CO_2I after WI)show that the three-phase conditions, which act as a barrier against the CO_2 flow, can readily limit the displacement efficiency (for EOR) and consequently reduce the sequestration capacity (for CCS), due to poor sweep efficiency and early BT.

Comparison of the location of the gas–oil interfaces in Figures 2B and 2D with those in Figures 5C and 5D, respectively, demonstrates that as CO_2I continued, the area occupied by CO_2 has widened, the volume of those oil ganglia, which have been contacted by the CO_2 has shrunk, and more oil has been recovered. It is also noted that the area of the CO_2 widened faster in the former (Figure 2D) than the latter (Figure 5D), due to the presence of the water layer in the test with S_{wi}, which slows down the mass transfer process between CO_2 and oil. This highlights the negative impact of water shielding on the diffusion process.

4.2.2 CO_2I after CWI

Experiment No.15- CO_2I after CWI-The viscous mineral oil

The purpose of this test was investigation of CO_2I performance after CWI, rather than CO_2I after WI, which was the case in Experiment No.14.

The initial stages of this test were similar to those in Experiment No.14 except in this test a slug of carbonated water (CW) was injected before CO_2I. Figure 11 shows fluid distribution in the micromodel during different stages of this test.

Figure 11C shows gas channelling in the micromodel, just after the CO_2 BT, which took place after 0.37 hrs of CO_2I. Comparison of this image with Figure 5C (showing fluid distribution after the CO_2 BT following a WI process, Experiment No.14), reveals significant differences in the CO_2 distribution within the porous medium.

Figure 11C shows that there are oil films between CO_2 and the water phase even at the beginning of CO_2I. This indicates a positive spreading coefficient (C_s>0) at the beginning of CO_2I, something that was not observed in the previous test. A similar observation was noted in Experiment No.14 (CO_2I after WI-The viscous mineral oil), long after CO_2 entered the micromodel.

The spreading characteristic of a three-phase flow system plays a key role in CO_2I and displacement efficiency. Vizika and Lombard (1996) experimentally showed that for water wet conditions, in Brine-Soltrol 170 (+isobutanol)-air system, a positive spreading coefficient results in higher oil recovery and displacement efficiency compared to the case of negative spreading coefficient conditions. This difference is explained on the basis of the microscopic displacement mechanisms. That is, for C_s>0 the spreading oil films, which cover the water surface, maintain the hydraulic connectivity of the oleic phase. This connectivity throughout the porous medium results in higher oil production during gas injection, down to very low oil saturation. For C_s<0, on the other hand, early disconnection of the oil films leads to trapping of the oil phase. The impact of CWI prior to CO_2I on oil recovery efficiency will be quantitatively analysed, later in this chapter.

Since the initial fluid properties and the rate of CO_2I during these two experiments were the same; the difference in fluid distribution (Figure 5C compared to Figure 11C) should be related to the altered physical properties of oil and water before CO_2I in Experiment No.15 (CO_2I after CWI) compared to Experiment No.14 (CO_2I after WI). Lower oil viscosity after CWI (Figure 11B), due to CO_2 dissolved in the oil phase, compared to the original oil viscosity after plain WI (Figure 5B) could be one of the reasons for the difference observed in the CO_2 flow displacement mechanisms. The change in spreading nature of the system discussed above, could be another reason. Another point that should be considered is greater oil connectivity after CWI compared to that after WI, which can affect the displacement process. That is, as a result of swelling, the trapped oil ganglia coalesce with each other; consequently, oil connectivity in the micromodel increases.

The single displacement mechanism of oil by CO_2 also occurred in this test (Experiment No.15) as the water layer separating these two phases ruptured at early stages. For

instance, although the oil ganglion in the lower (or upper) triangle in this test (Figure11C) was displaced by CO_2 the same oil drop in Experiment No.14 (Figure 5C) was by-passed. A change in the disjoining pressure of the aqueous layer could contribute to this observation.

The concept of disjoining pressure (denoted by Π_d) was introduced by Derjaguin and Churaev in 1974. Π_d tends to separate or join the two interfaces in thin fluid films. Disjoining pressure results from intermolecular forces such as van der Waals, electrostatic and structural forces (e.g. hydrogen bonding) (Hirasaki, 1991). A positive Π_d, which corresponds to a lower pressure in the thin film rather than the same fluid in the bulk conditions, separates the two interfaces. This condition promotes the spontaneous thickening of the layer. However, a negative Π_d attracts the two interfaces and prevents the thickening of the layer.

The Young-Laplace equation including Π_d, takes the following form:

$$P_c = \Pi_d + 2\delta H \tag{4.2}$$

where δ is the interfacial tension, H is the mean curvature and P_c is the capillary pressure. For a thick layer $\Pi_d = 0$ and Equation 2 reduces to the normal Young-Laplace equation. On other hand, for a flat solid, the second term in Equation 2 becomes zero, since the mean curvature is zero. In this case, Equation 2 reduces to $P_c = \Pi_d$.

The following equation has been proposed to estimate Π_d (Argento, and French, 1996; Tadmor, and Pepper, 2008):

$$\Pi_d \propto \frac{A}{h} \tag{4.3}$$

where A (Hamaker constant) is a coefficient that relates the disjoining pressure as a result of van der Waals interaction to distance between the two interfaces of a fluid film (i.e. h is the film thickness). Hirasaki, (1991) reported that the Hamaker constant of a three-phase system strongly depends on the materials. Thus, the Hamaker constant for the oil-water-CO_2 system (Experiment No.14, CO_2I after WI) is expected to be different from the oil-CW-CO_2 system (Experiment No.15, CO_2I after CWI).

Most importantly, a comparison of the lower triangular sections of Figures 11B and 11C reveals that, once connected to that big oil ganglion in the upstream section, CO_2 has moved the oil phase and has formed an oil bank, whereas in Experiment No.14, CO_2 channelled mainly through the water phase and did not form an oil bank. The recorded video clips of these two CO_2I processes clearly show that some of the oil phase was replaced by CO_2 in Experiment No.15 (after CWI), whereas no oil was produced in Experiment No.14 (after WI) at BT of CO_2.

Experiment No.16 and No.17- Repeated Tests of Experiment of No.14 and No.15

The results of the previous two experiments showed that one of the advantages of CWI prior to CO_2I is to alleviate the adverse effect of water shielding on oil recovery. To confirm these results, those two experiments were repeated to confirm this important observation. As in the previous experiments, the results of the repeated experiments showed that contrary to the case of CO_2I after WI, after CWI, CO_2 channelled through micromodel via the oil phase. The CO_2 stream position and its distribution after CWI were again almost completely different from the one after WI.

4.3 CO_2I into Real Crude Oil

In the previous section it was demonstrated that performing a CWI period after WI and before CO_2I (Experiment No.15) resulted in different fluid flow and displacement mechanisms compared to the case where CO_2I was carried out straight after WI (Experiment No.14). This observation was further investigated by using a real crude oil, rather than model oil, which was used previously.

4.3.1 CO_2I after WI

Experiment No.18- CO_2I after WI-The Crude Oil A

Figure 12 and Table 1 show fluid distribution and injection rates during different stages of this test. The video clip recorded during CO_2I indicates that CO_2 displaced mainly water, which is in line with the results of Experiment No.14 (CO_2I after WI). The blue arrow in Figure 12B highlights that CO_2 has clearly flowed through the water layer between the two large oil ganglia.

However, unlike the Experiment No.14, some oil displacement by CO_2 also took place during this CO_2I stage. The red circle in Figure 12B highlights a location in the micromodel, which shows oil displacement compared to the same position in Figure 12A. This observation indicates that the displacement of residual crude oil by CO_2 compared to that of mineral oil is more efficient. Holm (1986) presented the same results for miscible solvent injection through coreflood experiments. He attributed this to having a crude oil wetted surface, in which provides better access to contact with an injected miscible fluid. As shown, in Chapter 3, the wettability of the micromodel changed from strongly water wet, for mineral oils (Figure 3-4), to less water wet and neutral wet, for crude oil (Figure 3-41). This observation explains the different CO_2 displacement efficiencies between crude oil and mineral oil.

Figure 12B also shows the swelling of both oil ganglia, which had been shielded by water from CO_2 (highlighted by the red arrow labelled 1) and those, which had been directly connected to the CO_2 stream (highlighted by the red arrow labelled 2). This observation confirms that for this relatively viscous crude oil, the predominant mechanism during CO_2I was mass transfer from CO_2 stream into the oil phase (CO_2 dissolution) for both the direct and indirect contact of CO_2 with oil.

The red rectangle in Figure 12C (compared to Figure 12B) shows displacement of oil during the subsequent WI.

After the first cycle of CO_2-water injection, the second cycle was started by performing another period of CO_2I. In the second CO_2I period, similarly to the first one, CO_2 mainly displaced the water phase rather than the oil phase (for instance the blue arrow in Figure 12D). Comparison of Figure 12D with Figure 12C shows a small quantity of additional oil recovery (highlighted by the blue oval).

Figure 12E shows the final dead oil saturation after the 3rd WI at the end of this test. In the 3rd WI, similarly to the 2nd WI period, some oil displacement was observed (for instance within the blue rectangle in this figure).

Table 2 shows the oil saturation values at various stages of this experiment (No.18), obtained from the images shown in Figure 12. The data show that during the first cycle of alternating injection of CO_2 and water (W) (1st CO_2 and the 2nd WI), 7.9% more oil

was recovered (over what had been recovered in the initial WI) with a 21.1% oil recovery factor (compared to the oil saturation after first WI). However, the additional oil recovery in the second cycle of CO_2-W injection (2^{nd} CO_2 and the 3^{rd} WI) was only 4.8% with a 16.2% oil recovery factor (compared to the oil saturation after the 2^{nd} WI). The first cycle has therefore been more efficient and effective than the second cycle. This was mainly due to the higher remaining oil saturation and better oil connectivity in the first cycle.

4.3.2 CO_2I after CWI

Experiment No.19- CO_2I after CWI -The Crude Oil A

The purpose of this test was to investigate the effect of injecting CW before injecting CO_2 on the performance of alternating injection of CW and CO_2 and compare the results with the previous experiment in which water was used rather than CW.

Figure 13 shows the fluid distribution in the whole of the micromodel during different stages of this test. Table 1 summarises the required information about the injection rates of different stages of this test.

Figure 13B shows fluid distribution after about two hours of the first CO_2I following the CWI stage. The videos recorded during the CO_2I period indicate that the CO_2 mainly flowed through the oil phase, contrary to the previous test, where it passed mainly through the water phase. As a result of the invasion of the oil-filled pores by the CO_2 in this test, a bank of oil was formed, which moved ahead of the CO_2 front in the porous medium and led to the production of some oil at the BT of CO_2. The formation of the oil bank and recovery of oil at the BT of CO_2 had not been observed in the previous experiment (No.18). The blue rectangles in Figure 13B, compared to the same positions in Figure 13A, show significant oil displacement and recovery from the micromodel. The quantified data (Table 3) suggest that the oil saturation was reduced from 41.0% (at the end of 1^{st} CWI period, Figure 13A) to 26.7% (at the end of 1^{st} CO_2I, Figure 13B). The corresponding values for the previous tests were 37.5% and 35.3%. It should be mentioned that the maximum swelling of this oil at the conditions of the experiment was estimated to be around 15%. Based on the estimated maximum swelling factor, it can be concluded that the performance of the CO_2I after CWI in Experiment No.19 was better than the performance of CO_2I after WI (Experiment

No.18). That is, 12.2% oil recovery ((41.0%-26.7%)*0.85=12.2%) for the former, compared to 7.5% oil recovery ((37.5%-35.3%*0.85%=7.5%) for the latter.
As mentioned previously for the case of mineral oil, lower oil viscosity and interfacial tension between CO_2 and oil after CWI, due to dissolution of CO_2 in the oil phase, could be two main reasons for the observed improvement in the performance of CO_2I. Another reason that can be considered for the crude oil case could be the change in the wettability of the system caused by CWI, which will be discussed in more detail in the next chapter. The oil film flow mechanism was also observed during the CO_2I test carried out after CWI (Experiment No.19). Oil films and layers were observed to cause break up of the CO_2 flow several times within the porous medium, before the CO_2 breakthrough. It should be emphasised that in the previous test (Experiment No.18, CO_2I after WI-The Crude Oil A) no film flow of oil or subsequent snap off of the flowing CO_2 stream took place. This film flow could be attributed to wettability and IFT change during CWI, which could change the capillary forces within the porous medium.

To examine the performance of alternating injection of CW and CO_2 and compare it with the performance of alternating injection of (plain) water and CO_2, a second CWI period at the end of the first CO_2I period was commenced (Figure 13C). During this CWI period, some of the CO_2 was displaced and part of it broke up into smaller pieces. The movement of these broken up pieces of CO_2 caused redistribution of fluids and also resulted in some oil displacement and recovery. The blue rectangles in this figure highlight the places within the micromodel where oil recovery has taken place. Comparison of Figure 13C with Figure 12C shows that when CW was injected after CO_2, even after long injection times, there is still free CO_2 phase in the porous medium whereas when water was injected after CO_2, since the water was not saturated with CO_2, all of the CO_2 phase was dissolved by the flood water. The existence of this free CO_2 phase during CWI resulted in more fluid redistribution and increased the amount of oil recovery.

Figure 13D and E shows the fluid distribution in the micromodel after two hours of the second CO_2I and after the third CWI, respectively. The positions highlighted with the blue rectangles in these two figures, when compared with the same positions in their corresponding previous stages of the test, indicate oil displacement.

Some reconnection of the separated oil ganglia was observed during the final WI stage (e.g., in the red rectangle in Figure 13F). This was caused by the dissolution of the CO_2, which had been separating the oil ganglia and caused the coalescence of the oil.

The quantified data (Table 3) shows that as a result of the two cycles of alternating injection of CO_2 and CW, the residual oil saturation to waterflood reduced from 35.3% to 21.4%. This shows 13.9% oil production with a 40% oil recovery factor compared to the first WI period, whereas the additional oil recovery during the alternating injection of CO_2-water in the previous test was estimated to be around 33%. The difference in the oil recovery factor, 7%, is considerable, which demonstrates the benefit of CWI prior to CO_2I. The improvement in the performance of CO_2I in the second test, Experiment No.19 (CO_2I after CWI -The Crude Oil A), is mainly due to the invasion of the oil-filled pores by the injected CO_2, compared to the situation in Experiment No.18 where CO_2 mainly flowed through the water-filled pores. This observation will be further discussed in the next section, where an analysis of the time taken for CO_2 flow through the oil and oil-filled pores during various stages of the experiment is presented.

4.3.3 Quantification of the impact on CWI on CO_2/oil contact

The video clips recorded during the 1st and the 2nd CO_2I in Experiments No.18 and No.19 were analysed, in order to measure the time that it took for the CO_2 front to flow through the oil-filled pores in these tests. Table 4 shows the total required time for CO_2 to travel through the porous section of the micromodel and also the time during which CO_2 flowed in the oil during CO_2I stages of the tests. The last column of Table 4 indicates the percentage of the time that CO_2 spent flowing through the oil phase compared to total BT time. The data confirms that the CO_2 front spent much longer time flowing through the oil phase in Experiment No.19 (CO_2I after CWI) compared to Experiment No.18 (CO_2I after WI). It also shows that, in both tests, the CO_2 flowed through the oil for a longer time in the first CO_2I period than in the second CO_2I. This can be explained by the higher oil saturation in the first CO_2I period. That is, the higher the oil saturation in the micromodel, the more contact between the CO_2 and the oil.

During CWI, as a result of the transfer of CO_2 from CW into the oil, swelling of the oil phase takes place and hence its volume increases. The question here could be whether

the reason for CO_2 to invade more oil-filled pores when CW is injected before CO_2I is due to the increased saturation of the oil caused by CWI. To answer this question, the data in Table 4 has been plotted against the saturation of the oil in the porous medium at the beginning of CO_2I for both Experiments No.18 and No.19, as shown in Figure 14. The fact that there is a higher contact time between CO_2 and oil at higher saturation in both tests confirms that the contact time is a function of the oil saturation. However, as can be seen from this figure, even for the same oil saturation, the time that CO_2 flows through the oil phase is much longer for the case where CW has been injected into the porous medium before CO_2I. This suggests that in addition to oil saturation, which is generally higher in the test with CW, there should be other parameters contributing to the observed increased oil recovery in Experiment No.19 (CWI before CO_2I). In other words, in addition to oil swelling, modifications in the physical properties of the oil, IFT between CO_2 and oil and wettability alteration could have also contributed to increasing the contact between the injected CO_2 and the oil during CO_2I in Experiment No.19 compared to that in Experiment No.18.

4.4 Conclusions:

- Using viscous mineral oil in Experiment No.14, (CO_2I after WI- viscous mineral oil) CO_2 displaced mainly water, whereas in Experiment No.15 (where CO_2I followed CWI- viscous mineral oil), CO_2 mainly displaced oil. In other words, performing a CWI after WI and before CO_2I (Experiment No.15) results in a completely different fluid flow displacement compared to the case of CO_2I after WI (Experiment No.14). This is mainly due to the changes of oil (and water) viscosity and IFT during CWI. It also seems that CO_2 ruptures the CW film separating oil and gas more easily, facilitating the single-oil displacement by CO_2 in Experiment No.15 compared to Experiment No.14, with a water film separating oil and CO_2 phases.
- During CO_2I after WI (Experiment No.14), initially there was no oil film separating water, the spreading coefficient was negative, but as the test progressed, the IFT values changed and, in some locations, the spreading coefficient became positive, i.e., there was an oil film between water and gas. In Experiment No.15, CO_2I after CWI, there were oil films between the CO_2 and

the water phase, even at the beginning of the CO_2I. This indicates that at the earlier stage of Experiment No.15, CWI changed the IFT values before CO_2 coming into contact with the oil phase.

- In the case of using crude oil A, similarly to the viscous mineral oil cases, injection of CW prior to CO_2 altered the fluid flow pattern and increased oil recovery.
- The first cycle of the alternating injection of CO_2 and water (or CW) resulted in more additional oil recovery compared to its second cycle, mainly because of higher oil saturation prior to the first cycle.
- Injecting CW instead of plain water before CO_2 led to improved oil recovery, as the contact between CO_2 and oil increased and the CO_2 front invaded more oil-filled pores. The positive impact of CWI on the performance of CO_2I was verified both by direct flow visualisation (comparison of Experiments No.18 (CO_2I after WI-The Crude Oil A) and No.19 (CO_2I after CWI -The Crude Oil A)) and by quantifying the time for which CO_2 travelled through the oil phase rather than the water phase.

4.5 References:

Adamson, A.W., 1960: ‘‘Physical Chemistry of Surfaces’’, Interscience Publishers Inc., New York.

Argento, C. and French, R.H., 1996: ‘‘Parametric tip model and force-distance relationship for Hamaker constant determination for atomic force microscopy’’, J. Applied Physics, 80 (11), 1-December, pages 6081-6090

Campbell B. T., Orr, Jr F. M., 1985: ‘‘Flow Visualization for CO_2/Crude-Oil Displacements’’, SPE paper11958.

Derjaguin, B.V. and Churaev, N.V., 1974: ‘‘Structural component of disjoining pressure’’, J. of Colloid and Interface Science, Volume 49, Issue 2, No.vember, pages 249-255

Hirasaki, G.J., 1991: ‘‘Wettability: Fundamentals and Surface Forces’’, SPE Formation Evaluation Journal, June, pages 217-226, SPE paper 17367.

Holm, L. W., 1986: ‘‘Mobilization of waterflood residual oil by miscible fluids’’, SPE Reservoir Engineering, July 1986, SPE paper 13216.

Lin C. E. and Huang T. S. E., 1990: ‘‘The effect of rock wettability on water blocking during miscible displacement’’, Reservoir Engineering, SPE paper 17375.

Sohrabi, M., 2001: ‘‘Water alternating gas (WAG) injection studies’’, PhD Thesis, Heriot-Watt University.

Tadmor, R. and Pepper, K. G., 2008: ‘‘Interfacial Tension and Spreading Coefficient for Thin Films’’, Langmuir 2008, 24, pages 3185-3190

Tiffin, D. L., Sebastian, H. M. and Bergman, D. F., 1991: ‘‘Displacement Mechanism and water shielding phenomena for a rich-gas/crude-oil system’’, Reservoir Engineering, SPE paper 17374.

Vizika, O. and Lombard, J.-M., 1996: ‘‘Wettability and Spreading: Two Key Parameters in Oil Recovery with Three-Phase Gravity Drainage’’, SPE Reservoir Engineering, February 1996, pages 54-60.

Wylie P. and Mohanaty K. K., 1997: ‘‘Effect of water saturation on oil recovery by near-miscible gas injection’’, Reservoir Engineering, SPE paper 36718.

Yang, D. and Gu, Y., 2004. ‘‘Interfacial Interactions of Crude Oil-Brine-CO_2 Systems Under Reservoir Conditions’’, paper number SPE 90198.

EXP No.	Oil type	Rate of injection $cm^3\ h^{-1}$						
		OI	WI	CWI	CO_2I	(C)WI	CO_2I	(C)WI
12	-	-	-	-	0.01	-	-	-
13	Viscous oil	2	-	-	0.01	-	-	-
14	Viscous oil	0.1	0.01	-	0.01	-	-	-
15	Viscous oil	0.1	0.01	0.01	0.01	-	-	-
16 (R14)	Viscous oil	0.1	0.01	-	0.01	-	-	-
17 (R15)	Viscous oil	0.1	0.01	0.01	0.01	-	-	-
18	Crude oil A	0.1	0.008	-	0.01	0.01	0.01	0.01
19	Crude oil A	0.1	0.008	0.01	0.01	0.01	0.01	0.01

Table 4-1: List of the micromodel experiments reported in Chapter 4. Experimental condition was 2000 psi and 38 °C.

CO_2I: Carbon dioxide injection

CWI: Carbonated water injection

OI: Oil injection

WI: Water injection

R: Repeat

Experimental stage	So (%)
1st WI	**37.5**
1st CO_2	**35.3**
2nd WI	**29.6**
2nd CO_2	**26.7**
3rd WI	**24.8**

Table 4-2: Tabular data of oil saturation at different stages of Experiment No.18 (CO_2I after WI-The Crude Oil A).

Experimental stage	So (%)
1st WI	**35.3**
1st CWI	**41.0**
1st CO_2	**26.7**
2nd CWI	**23.9**
2nd CO_2	**26.2**
3rd CWI	**24.1**
2nd WI	**21.4**

Table 4-3: Tabular data of oil saturation at different stages of Experiment No.19 (CO_2I after CWI -The Crude Oil A).

Video clip	Total time (min)	Time in oil (min)	Time in oil (%)
1st CO_2I- Experiment No.18	2':55''	1':15''	**42.8**
2nd CO_2I- Experiment No.18	7':23''	2':10''	**29.3**
1st CO_2I- Experiment No.19	2':58''	2':29''	**83.7**
2nd CO_2I- Experiment No.19	4':55''	2':35''	**52.5**

Table 4-4: The time that it took CO_2 to travel through the porous section of the micromodel and that to pass through oil saturated pores, also see Figure 14.

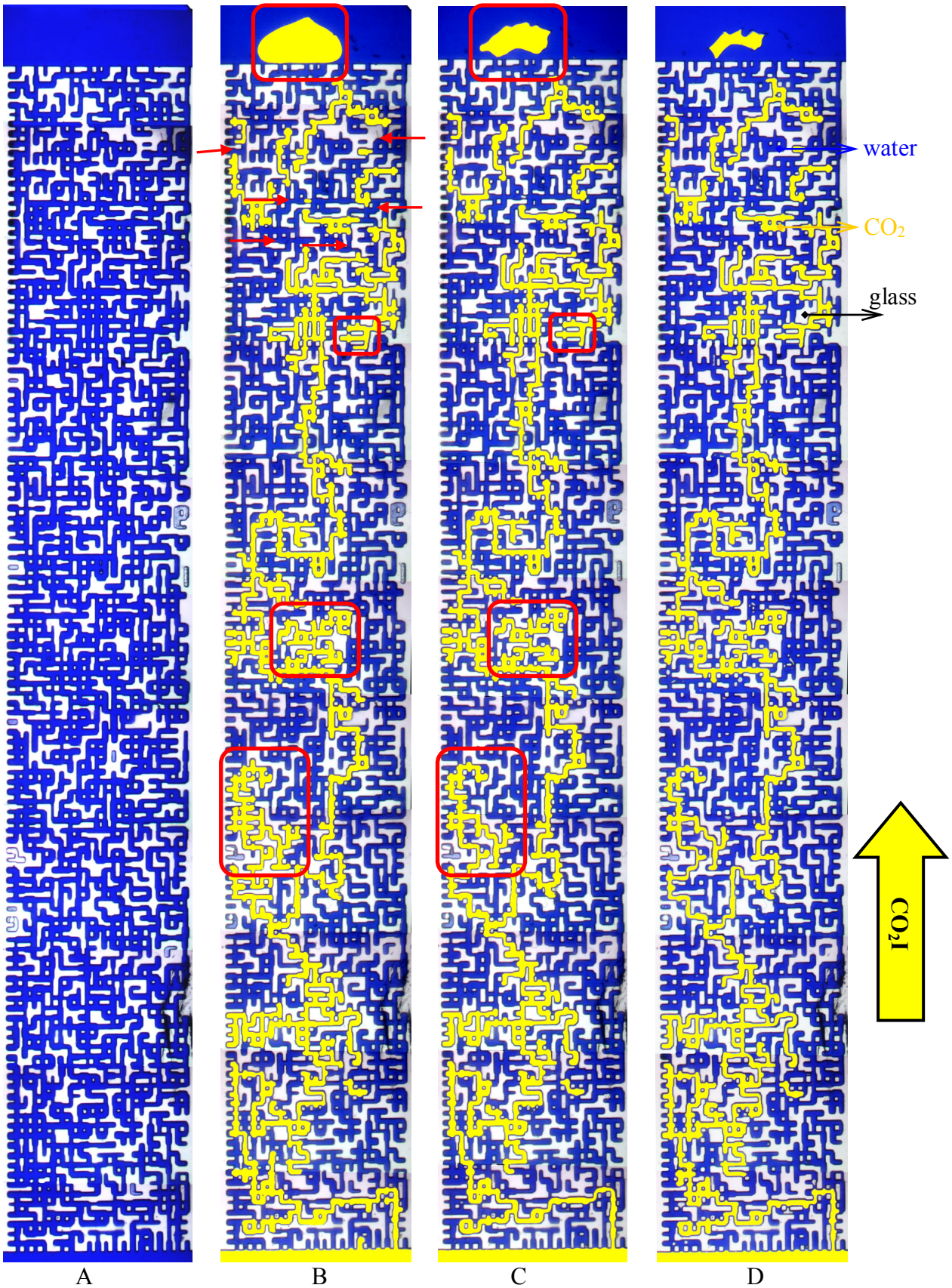

Figure 4-1: The full micromodel image: A) fully saturated with blue-dyed water; B) at CO_2 BT; C) and D) 2 and 20 hrs after BT of CO_2, respectively.

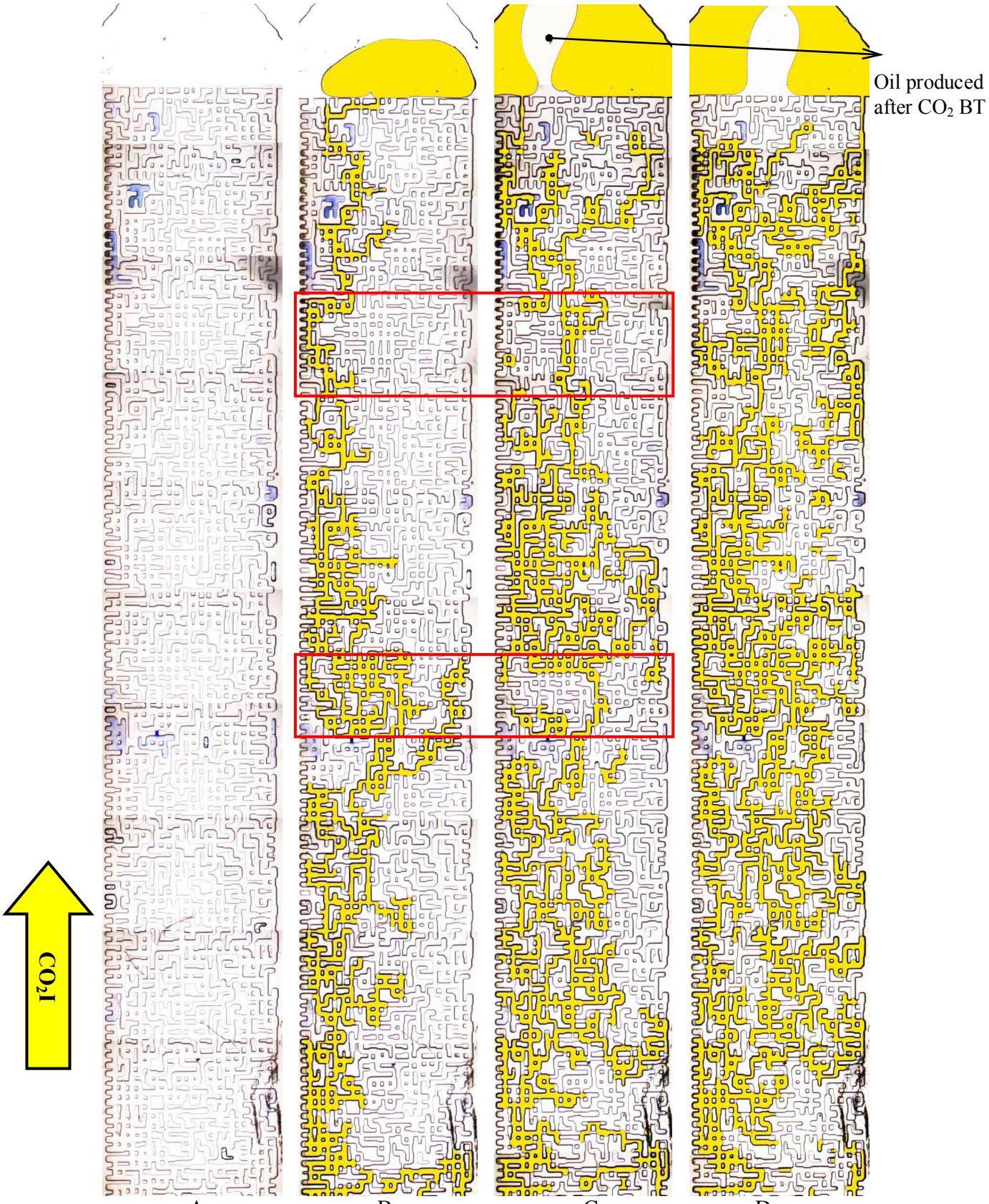

Figure 4-2: Fluid distribution within the micromodel at different stages of Experiment No.13 (CO_2I into the porous medium fully saturated with the viscous mineral oil): A) Soi=100%; B),C) and D) after 0.45, 1 and 3 hrs of CO_2I, respectively.

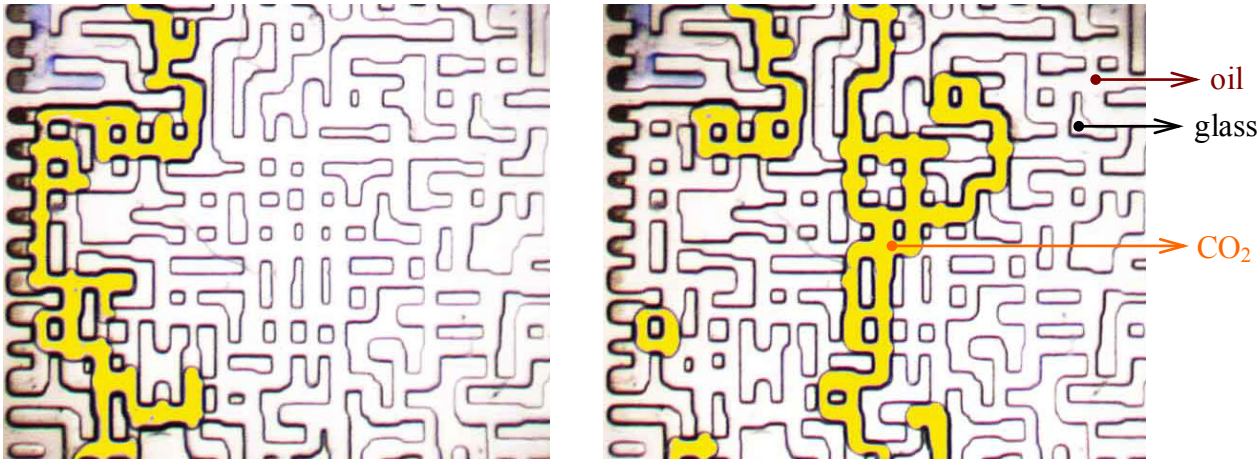

Figure 4-3: Highly magnified images of a section of the micromodel: A) and B) corresponding to 0.45and 1 hrs after CO_2I, respectively.

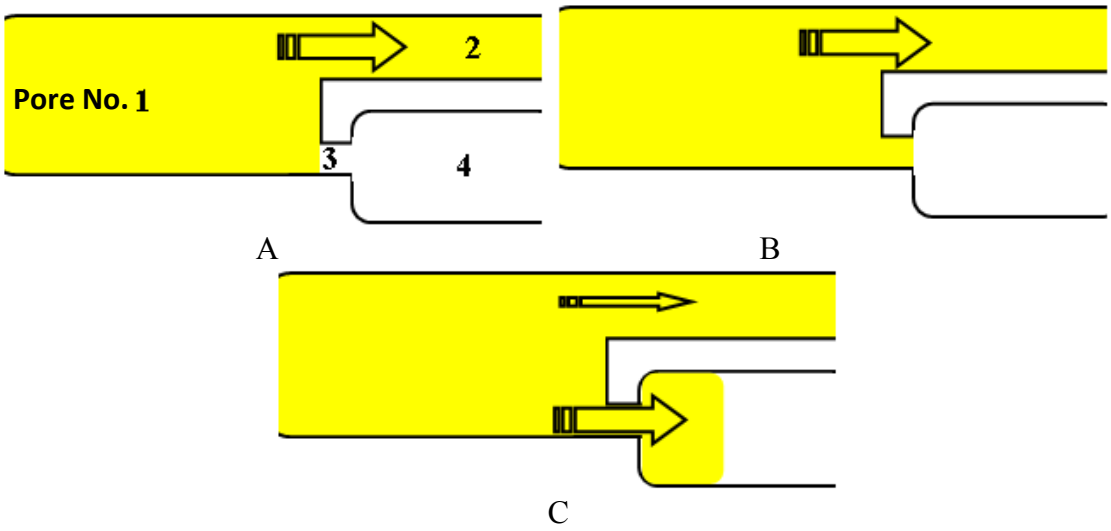

Figure 4-4: A demonstration of a change in the flow path of the CO_2 stream: A) CO_2 selects the larger pore ahead (pore No.2 compared to pore No.3) with lower capillary pressure; B) Oil in pore No.3 evaporates; C) CO_2 flows thorough the larger pore (pore No.4 compared to pore No.2).

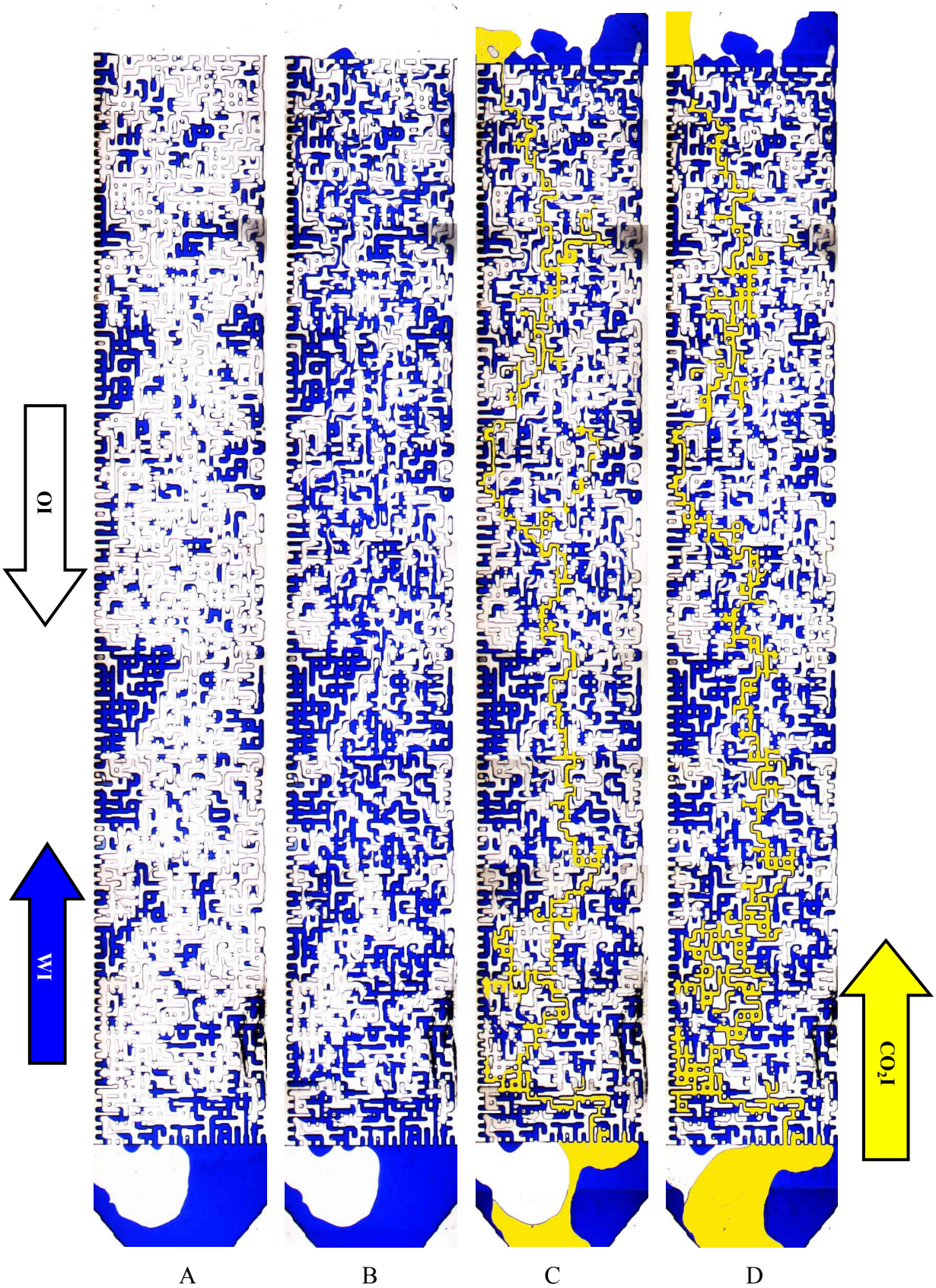

Figure 4-5: Fluid distribution in Experiment No.14 (WI followed by supercritical CO_2I with S_{wi}-The viscous mineral oil): A) viscous oil with Swi; B) residual oil saturation after waterflooding; C) at CO_2 BT time, 0.35 hrs.

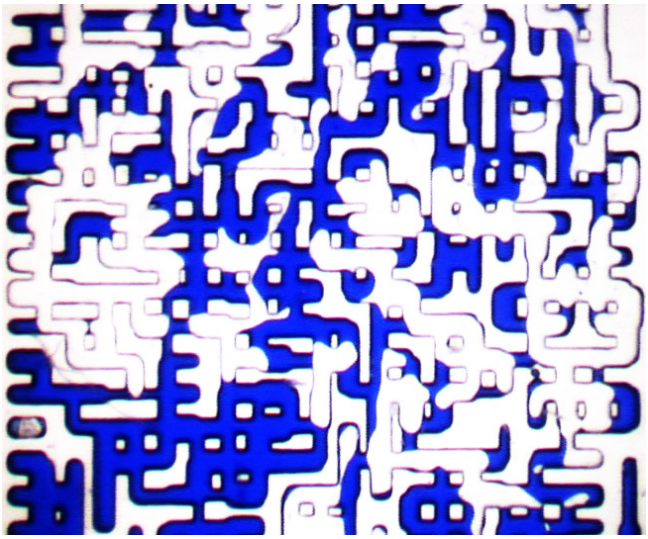

Figure 4-6: Fluid distribution in a selected frame of the micromodel after WI, Experiment No. 14 (WI followed by supercritical CO_2I with S_{wi}-The viscous mineral oil).

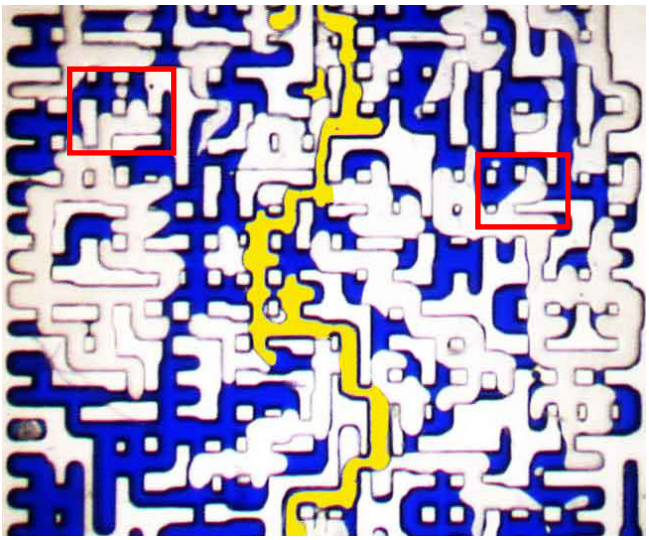

Figure 4-7: Fluid distribution in the same frame (as in Figure 6) after 0.35 hrs of CO_2I, Experiment No. 14 (WI followed by supercritical CO_2I with S_{wi}-The viscous mineral oil).

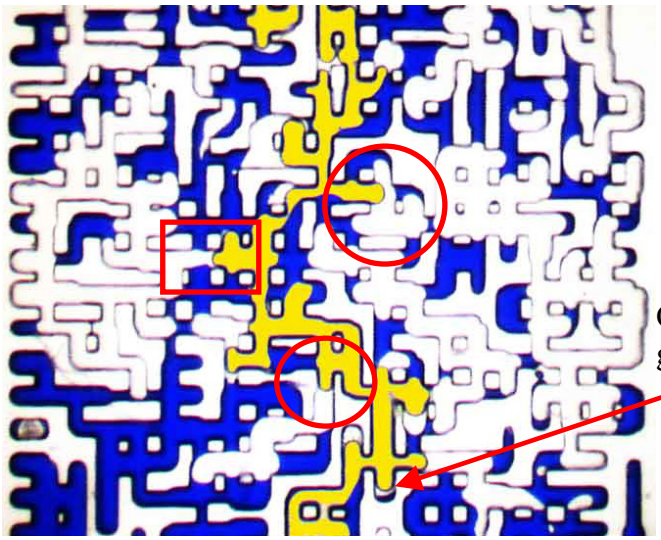

Figure 4-8: Fluid distribution in the same frame (as in Figure 6) after 3.4 hrs of CO_2I, Experiment No. 14 (WI followed by CO_2I with S_{wi}-The viscous mineral oil).

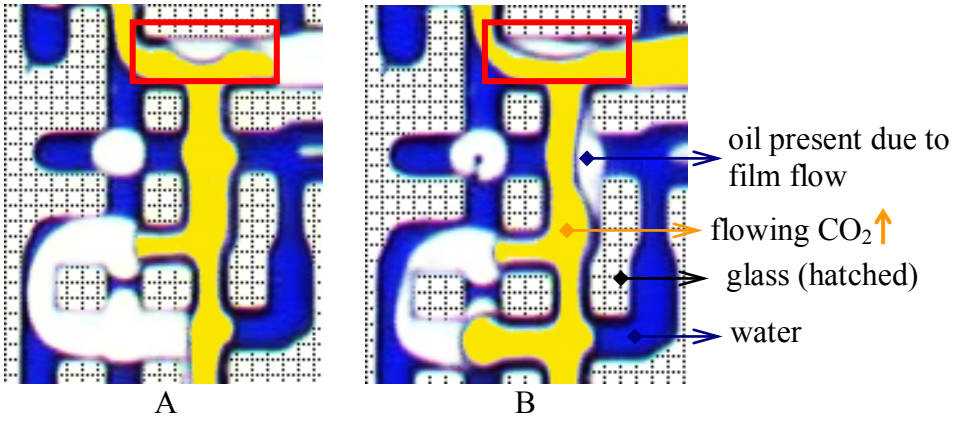

Figure 4-9: Fluid distribution in a highly magnified section of the micromodel: A) at CO_2 BT and B) 1 hr after CO_2I. They demonstrate the shrinkage of the bypassed oil and its flow alongside the flowing CO_2.

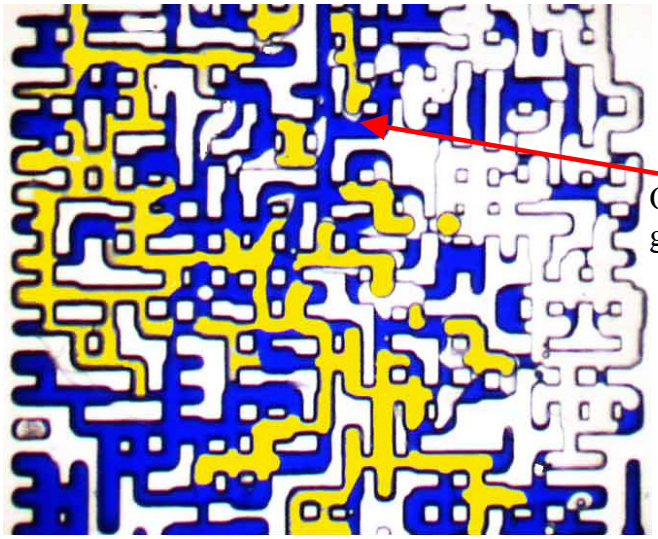

Figure 4-10: Fluid distribution in the same frame (as in Figure 6) after 23 hrs of CO_2 flooding, Experiment No. 14 (WI followed by CO_2I with S_{wi}- viscous mineral oil).

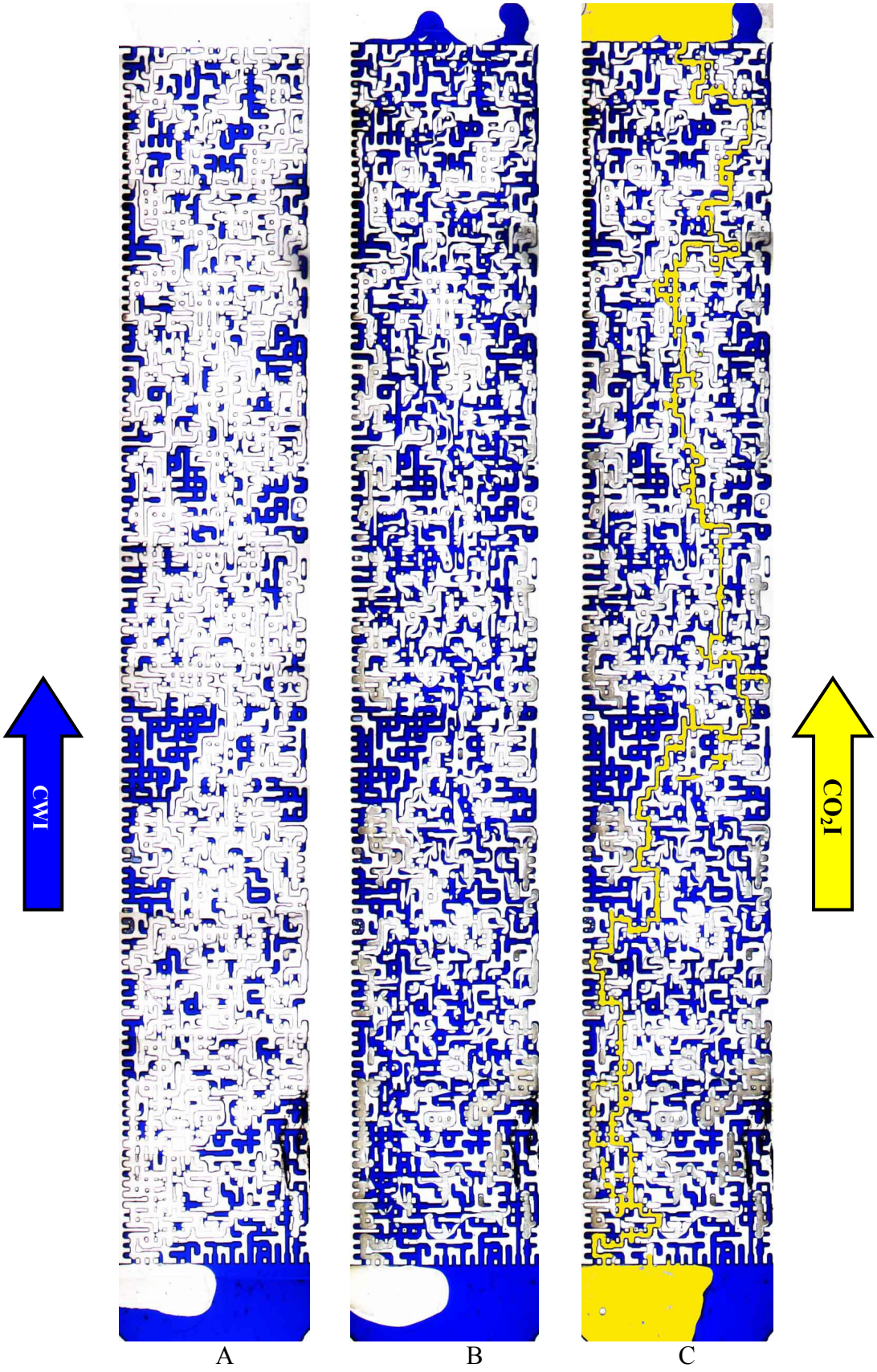

Figure 4-11: Fluid distribution in Experiment No.15 (CO_2I after CWI-The viscous mineral oil): A) Viscous oil with S_{wi} ; B) fluid distribution after a week of CWI; C) fluid distribution after CO_2I at BT time of CO_2, 0.37 hrs.

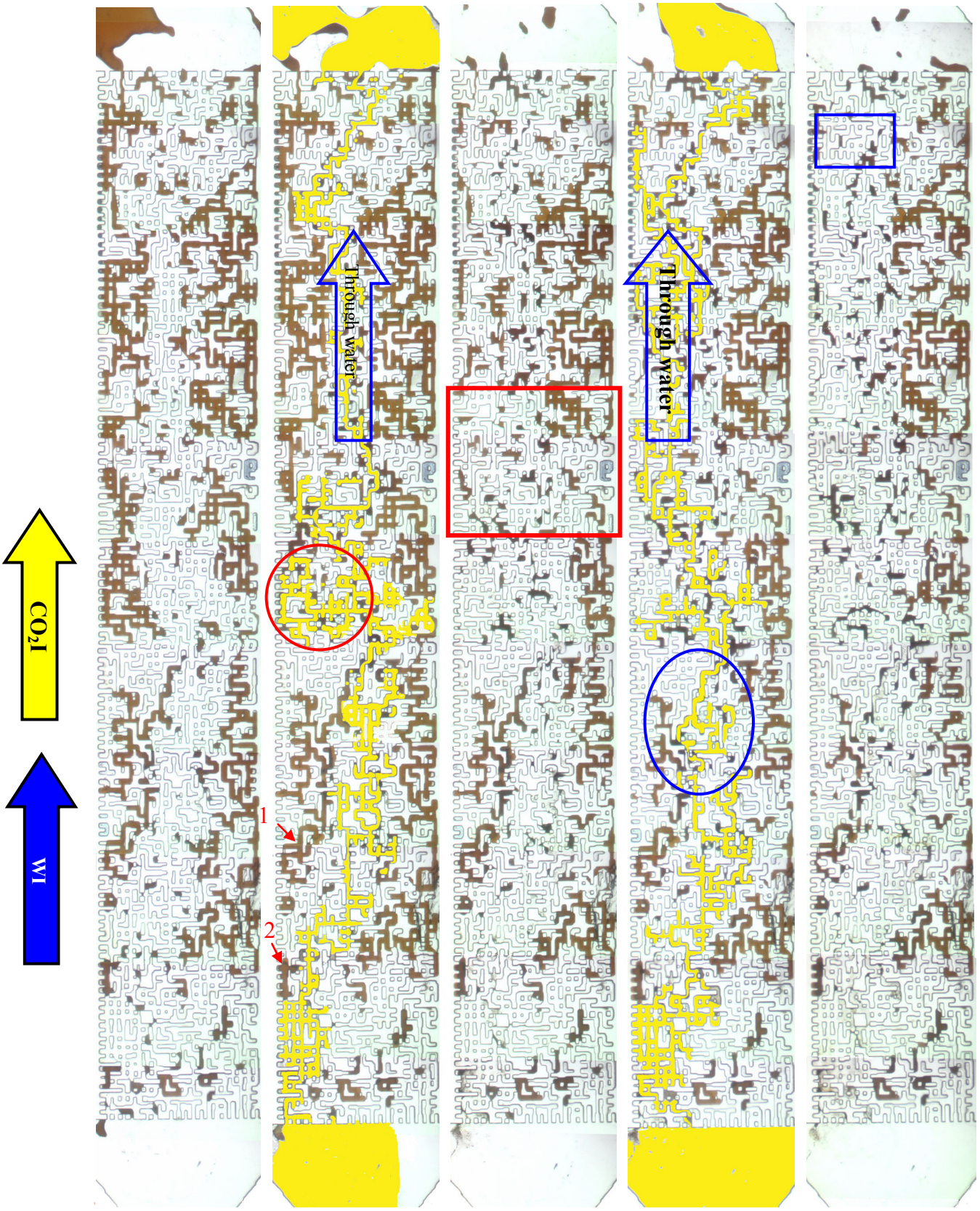

Figure 4-12: Fluid distribution in the micromodel during Experiment No.18 (CO_2I after WI-The Crude Oil A), A) at the end of the first WI; B) after 2 hrs of the first CO_2I; C) after the second WI; D) after 2 hrs of the second CO_2I; E) after the 3rd WI.

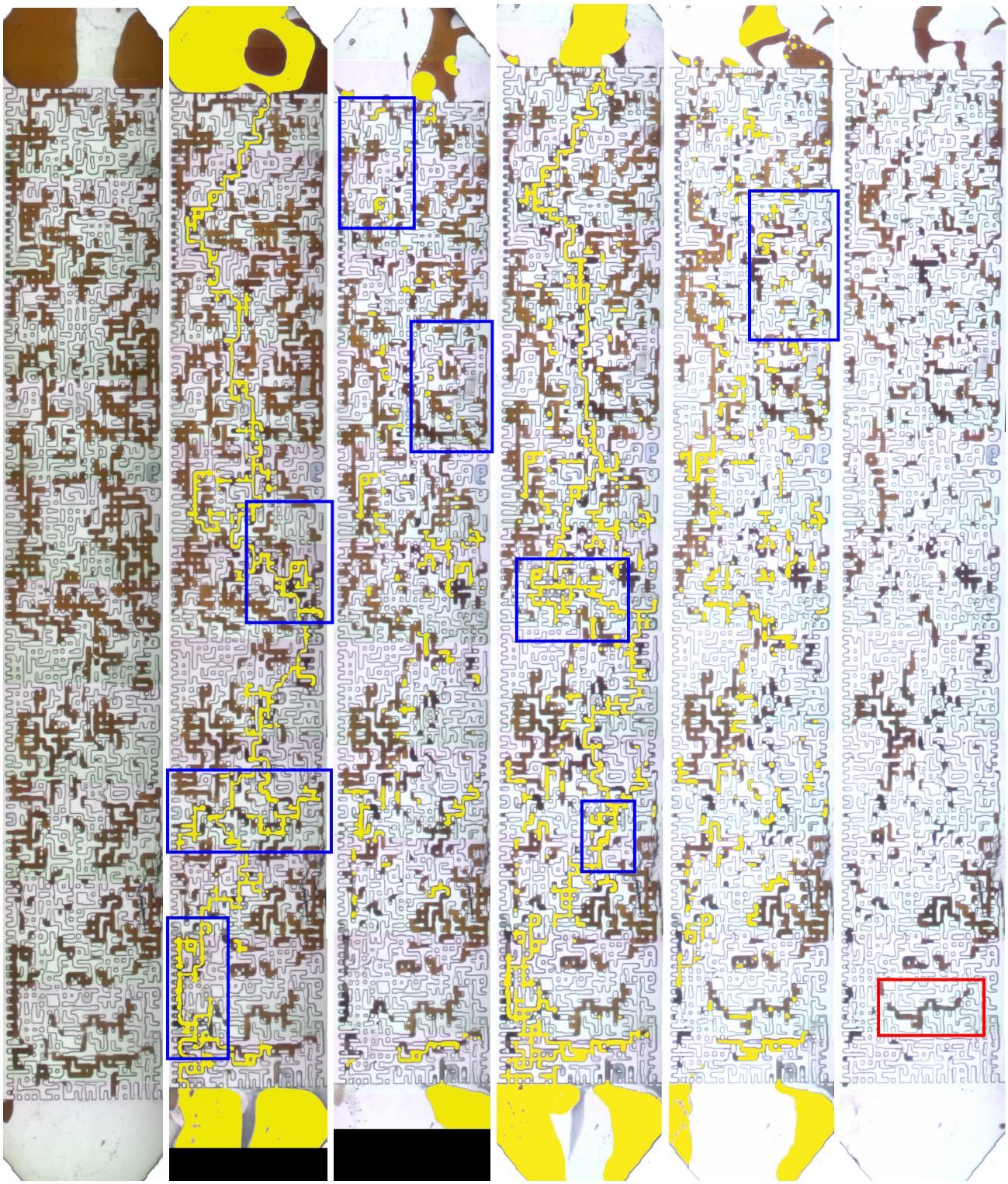

Figure 4-13: Fluid distribution in the whole micromodel, during Experiment No.19 (CO_2I after CWI -The Crude Oil A): A) swollen oil after 88 hrs of CWI; B) 2 hrs after the first CO_2I; C) after the second CWI; D) after 2 hrs of the second CO_2I; E) after the 2nd CWI and; F) dead oil saturation condition after the 2nd WI.

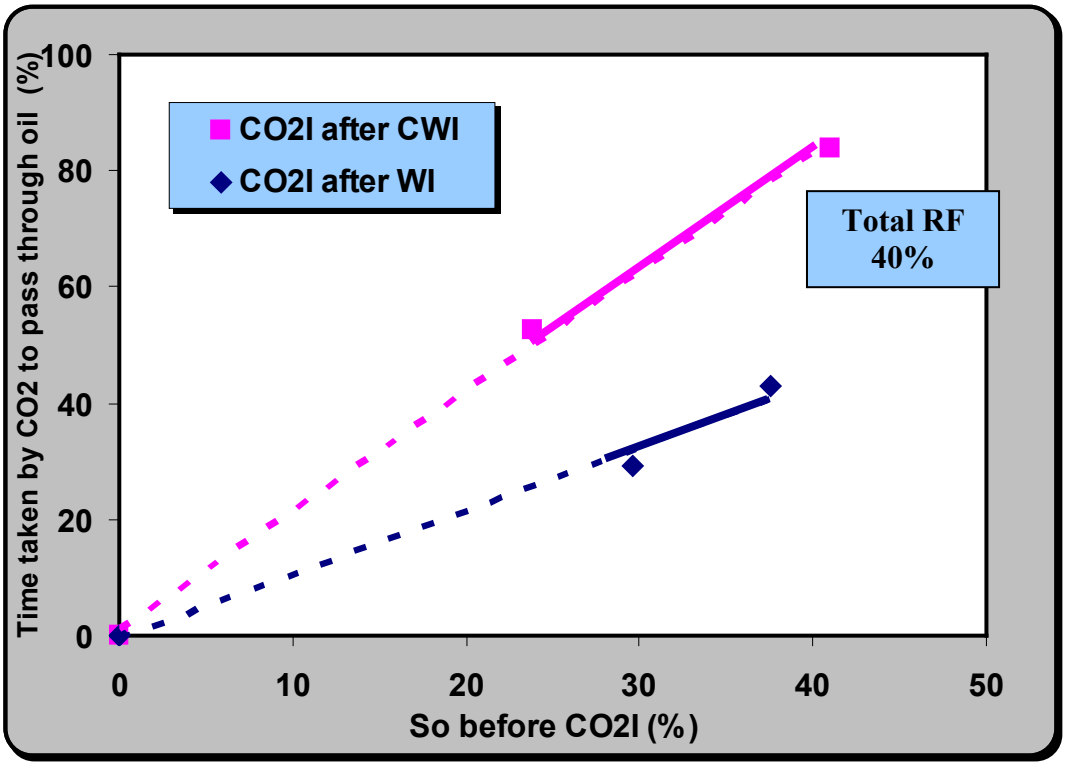

Figure 4-14: The time that it took CO_2 to travel through the porous section of the micromodel and that to pass through oil saturated pores. Also see Table 4.

5 Chapter 5: Wettability Studies

5.1 Direct Visualisation (Micromodel) Experiments

5.1.1 Introduction

In the previous chapters, a series of micromodel experiments were reported, demonstrating the performance of carbonated water injection (CWI) for oil recovery. However, the impact of CWI on rock wettability was not fully investigated.

Rock wettability is an important parameter in petroleum reservoirs and influences fluid distribution and multi-phase flow within the porous medium by affecting the capillary pressure and relative permeability curves. In enhanced oil recovery processes, wettability is one of the factors controlling residual oil saturation and oil recovery.

Wardlaw (1980) reported that in strongly wetted porous media, the amount of trapped saturation of the non-wetting phase is highly dependent on the geometric and topological properties of the pore system such as:

- Pore throat size ratio
- Type and degree of heterogeneity in the arrangement of pores
- Coordination number or connectivity
- Composition of pore surface
- Degree of roughness of pore surfaces

Under conditions of intermediate wetting, however, the effect of geometric properties is reduced and displacement efficiency is greater. Therefore, it is important to understand the rock wettability.

In the literature, different experimental methods have been introduced and proposed for quantifying the wettability of rocks (Adamson 1982).

In the qualitative methods, the distribution of fluids, the shape and direction of interfaces between fluids and also fluid flow displacement mechanisms are compared. These indicators can be visualised, recorded and investigated using transparent porous media (micromodel). In the previous chapters, the degree of wettability of the micromodels used in the CWI experiments in comparison with water injection (WI) tests was discussed and compared, to some extent. The important observation was the different affinity of water and carbonated water (CW) towards wetting the glass surface in the presence of oil. In the following sections, some of these qualitative direct observations are discussed and compared in more detail. To further examine and investigate the effect of CWI on wettability, two more micromodel experiments were performed. These two experiments were designed to observe possible variation of contact angles and spontaneous imbibition displacement mechanisms due to CWI in the micromodel.

Following these qualitative investigation of wettability, some contact angle measurements were also conducted to quantify the observed different tendency of CW and water to wet solid surfaces.

These results will be used to draw some conclusions on the impact of CWI on rock wettability and on oil recovery by CWI instead of WI.

5.1.2 Wettability Alteration

During the micromodel experiments, some indications of wettability alteration during CWI were observed. These observations prompted the author to investigate possible change of wettability by performing contact angle measurements. In this section, first some indications of wettability alteration observed during micromodel experiments are discussed. These will be followed by the results of contact angle measurements.

First Observation: Experiment No.1-Tertiary CWI-Decane.

Figure 1 shows a magnified image of an isolated oil ganglion in the experiment after the first WI (Figure 1A) and the same oil ganglion at the end of a subsequent CWI stage (Figure 1B). This experiment was conducted at 2000 psia and 38 °C using *n*-decane as the oil phase. In these two pictures, the shaded areas are un-etched glass representing rock grains and the blue coloured areas are pores occupied by water, (Figure 1A) or CW

(Figure 1B). Comparison of the colour contrast close to the walls of pores occupied by the oil, highlighted by red rectangles in these two pictures, indicates that a thicker water layer exists between oil and glass after CWI (Figure 1B) than that after WI (Figure 1A). This observation was attributed to the micromodel being more water-wet during CWI than during WI.

Second Observation: Experiment No.4-Tertiary CWI-Viscous Mineral Oil.

Figure 2A shows a magnified section of the micromodel after the first WI in Experiment No 4, in which the viscous mineral oil was used as the oil phase. Figure 2B shows the same frame as that shown in Figure 2A, after about 16 hrs of CWI. Comparison of these two images shows the modification of the shape of oil ganglia during CWI as a result of transferring CO_2 from CW into oil: that is, the oil has a more rounded shape in the presence of CW, Figure 2B, compared to that in the presence of water, Figure 2A. The capillary forces change the shape of the fluids' interface in the porous medium conditions. Since the dimensions of pores are the same in both images, the effective parameters, which determine the shape of the interface, are wettability and interfacial tension (IFT) between the oil and the aqueous phase. The modification of the shape of the oil is unlikely to be due to an increase in IFT, because the IFT between oil/water decreases in presence of CO_2 (Yang et al., 2005). Thus there is no additional driving force to minimise the surface area. Hence, this change of shape was attributed to a change in the wettability of the glass surface. These visual data reveal that the micromodel has become less oil wet in the presence of CW than that of plain water. In other words, CW has made the surface more water wet, which is in line with the observations reported in Experiment No.1.

Third Observation: Low Rate CWI-Decane without S_{wi}

In one of the experiments conducted in this study, CW was injected after WI in the tertiary recovery mode, into the micromodel fully saturated with *n*-decane. The injection rate for both WI and CWI during this experiment was one order of magnitude less than the normal injection rate that had been used in the other experiments reported in this work, i.e. 0.001 $cm^3\ h^{-1}$ instead of 0.01 $cm^3\ h^{-1}$. Figure 3 shows three magnified images of a section of the micromodel at different stages of this experiment.

In this test, unlike the other micromodel experiments presented previously, water-wetness condition was not observed in the micromodel. Figure 3A shows that oil occupied the smaller and dead-end pores, which is the indication of the non-water wet conditions of the micromodel. The shape and the direction of the water-oil interfaces confirm the oil wet conditions within the micromodel. Figure 3A also shows no indication of establishment of water layers as a thin film between oil and glass during WI. However, the next two images show the growth of some water droplets inside the oil phase during CWI: i.e. the presence of CO_2 in water has resulted in the formation of these droplets by establishing continuous water wetting layers between the water droplets and the flowing CW stream. These water droplets have been highlighted by the red rectangles in Figure 3B and Figure 3C. This observation is further evidence supporting the idea of wettability alteration towards more water-wet conditions by CW.

Fourth Observation: Experiment No.10-Tertiary CWI-Crude oil.

In this experiment, CW was injected in the tertiary mode into the micromodel containing a crude oil (Crude-A) and connate water. As discussed in the previous chapters, changes in the colour of the crude oil were observed during different stages of the experiment. As mentioned in Chapter 3, this observed change of the colour of the crude oil was attributed to the formation of micro droplets of water in the crude oil and on the pore surfaces. Figure 4 shows a sequence of magnified images of a section of the micromodel at different stages of this experiment. As can be seen, the level of change of the oil colour during CWI (Figure 4D compared to 4C) was significantly greater than the observed level of the change during WI (Figure 4B compared to Figure 4A), for almost the same injection time. Again, this difference can be another indication of the surface of the micromodel becoming more water-wet during CWI and supplying more water between the oil and glass to form more micro droplets of water.

To further examine and investigate the effect of CWI on wettability alteration, two micromodel experiments were performed. In this section the results of these two visualisation experiments are presented. These two tests, Experiments No. 20 and No. 21, were performed using *n*-decane as the oil phase at 2000 Psia and 38 °C. In both experiments the micromodel was mounted horizontally to minimise the effect of gravity on the flow.

Experiment No. 20: Wettability in an n-decane/water system

In this test, the micromodel was initially fully saturated with plain (blue) water. Then oil, *n*-decane, was injected from one end of the micromodel, the inlet, until the front of the oil reached to other end of the micromodel, the outlet. Figure 5 shows a schematic diagram of the micromodel including the inlet/outlet lines. The position of a particular location in the lower line of the micromodel, referred to as point A, where the variation of the oil-water interface curvature was monitored during the experiment, is also shown in this image. In this test, after the oil/water interface reached point A, the valve number one (1), at the inlet, was closed and kept shut; however, the valve number two (2), at the outlet, remained open during the entire test.

Figure 6 shows magnified pictures of an n-decane/water interface in the lower pipe of the micromodel at different times. The shape and the curvature of the interface at point A indicate the water-wetting conditions of the micromodel. During this test, no noticeable change of the shape and curvature of the oil/water interface was observed, even 27 hours after establishing the initial oil and connate water saturation.

Fluid distribution in the whole micromodel was also monitored and scanned during the test at different times. Similarly to what was observed at point A, no alteration of the shape of oil/water interfaces in the porous section of the entire micromodel was detected after oil flood (establishment of Swi). Figure 7 shows initial oil saturation condition in the whole image of the micromodel, which remained unchanged for two days.

Experiment No. 21: Wettability in n-decane- carbonated water

In this test, an experimental procedure similar to the previous test was followed with the only difference being that CW was used instead of plain water.

Figure 8 compares the initial shape of the interface of oil/water (Figures 8A and 8C) with that of oil/CW (Figures 8B and 8D), with two different degree of magnification. These images indicate different contact angles between the glass surface and water compared to glass and CW.

In this test, similarly to the previous one, the distribution of fluids in the micromodel was monitored with time by repeatedly scanning the micromodel. Unlike the preceding

test, in this test fluid distribution changed within the porous medium, with time. This change of fluid distribution with time was a consequence of spontaneous imbibition of CW into the micromodel and the subsequent displacement of the oil phase. The driving force for spontaneous imbibition is the capillary pressure (Pc) and the rate of the imbibition depends on the magnitude of Pc. Based on what has been observed by the results of these two experiments, it is believed that wettability alteration was the main parameter affecting capillary pressure. In these two tests the same porous medium was used and the variation of IFT was not expected to cause this difference and hence, the observed spontaneous imbibition for CW was attributed to the change of wettability of the micromodel when in contact with CW compared to water.

Figure 9 shows fluid distribution in this horizontally placed (i.e. no gravity segregation) micromodel at different times after establishing the initial oil saturation and stopping fluid injection. Figure 9A and 9B shows the oil distribution in the micromodel at the end of oil flooding stage and just over 3.9 hrs after establishing the initial oil and water saturations, respectively. Figures 9C and 9D show the oil and CW distribution after 18.9 and 44.8 hrs, respectively. Comparison of these images reveals that the oil phase has been displaced and produced by the spontaneous imbibition mechanism, as can be seen by thick water layers surrounding oil in the pores. This observation is yet further evidence that the micromodel became more water-wet when in contact with CW instead of water.

Based on the time that it took for the CW front to travel from the inlet of the porous section of the micromodel to its outlet end and the length of this section of the micromodel, the actual velocity of CW was estimated at around 0.022 m d^{-1}. This value, which corresponds to the spontaneous imbibition process, is two orders of magnitude slower than the corresponding value of the normal displacing rate in the previous reported micromodel experiments (i.e. 3 m d^{-1}).

A section of the micromodel, which is highlighted with a red rectangle in Figure 9D, has been magnified to show the spontaneous imbibition mechanism and its effect on fluid distribution in more detail. Figures 10A, 10B and 10C show these magnified images after 3.9, 18.9 and 44.8 hrs of oil injection, respectively.

Figure 10B illustrates that water films in this section of the micromodel have thickened after 18.9 hrs and, as a result, a part of the oil produced. The last image, Figure 10C, shows the snapping off of oil, due to imbibition, after 44.8 hrs.

In summary, based on the results of these two micromodel experiments and also other visual evidence that was presented earlier in this chapter, it can be concluded that CW, compared to plain water, has a stronger affinity to wet the surface of the porous medium.

These micromodel results demonstrated qualitatively that CW affects the wettability of the porous medium. To further investigate this effect and to quantify the degree of wettability alteration by CW, a series of direct contact angle measurements have been carried out. In the next section, some of the results of contact angle measurements are presented and discussed.

5.2 Contact Angle Measurement Experiments

5.2.1 Introduction

As discussed above, micromodel results demonstrated that the wettability of the micromodel was altered when CW was used instead of water. The dissolution of CO_2 in water reduces the pH of water, which can, in turn, affect the electric charges on water/solid interfaces and hence change the wettability characteristics of the surface. The contact angle measurement is one of the well established experimental methods to quantify wettability. In this study to investigate the extent of wettability alteration by CW, a series of contact angle measurements were performed. It is known that the wetting phenomenon is controlled by the outermost layer of molecules (Morrow, 1990). Therefore, contact angle measurements need to be conducted accurately to ensure that fluids and solids are not contaminated.

5.2.2 Experimental Facilities

Contact Angle Measurement Rig

A newly manufactured (2008) high-pressure high-temperature rig was used for performing contact angle measurements in this study. The rig can operate at pressures as high as 7500 psia and at a temperature up to 180 °C. The metallic parts of the rig are

made of Hastelloy C 276, PTFE, to make the rig compatible with brine and CO_2 at high pressure and temperature conditions. The picture of the contact angle measurement rig is shown in Figure 11. It mainly consists of the following components:

1) High pressure viewing chamber with a sight glass at either side.
2) Heater and temperature controller.
3) Two piston pumps.
4) A video system with camera, optical system, prism, prism tilt and light source.
5) Software (DSA1 v 1.9) capable of analysing the shape of droplet to determine the drop parameters such as volume, contact angle, interfacial tension, area and base diameter.
6) Computer and monitor

5.2.3 Solid Substrates

Three different mineral substrates were used in this study. These are: Glass, Quartz and Mica:

Microscope glass slides (ground edges) with 25*75*1.2-1.4 mm dimensions were sourced from Breukhoven and cut into dimension of 25*28 mm. Average roughness of the glass slide, as measured using the DekTak Profilometer, is less than 1100 Å.

Quartz slides were provided by UQG Ltd (UK optical manufacturer) with 30*30*1 mm dimensions. Quartz is one of the main minerals of sandstones.

High quality optical grade Mica sheets (Ruby V-1 Mica Scratch free) were obtained from S&J Trading Company with dimensions of 25 mm*25mm*300 Microns and were fixed to glass plates. Mica was selected since it can be found in some shale and clay materials.

5.2.4 Fluid System

The fluid system used in the contact angle experiments consisted of brine, *n*-decane, carbon dioxide and distilled water. Brine with salinity of 10000 PPM was made by dissolving 16gr NaCl and 4gr $CaCl_2$, $6H_2O$ in 2 litres of distilled water. The purities of carbon dioxide and n-decane are 99.995% and 99.0%, respectively.

5.2.5 Experimental Procedure

The procedure for measuring the contact angle is briefly described here:

Cleaning and preparation:

Brand new substrates were used for these measurements and prior to each measurement, the substrate was thoroughly cleaned by rinsing with copious amounts of acetone and then with plenty of distilled water. Before placing the substrate in the viewing chamber and as the final stage of cleaning, it was immersed in an ultrasonic bath filled with distilled water or brine, for half an hour.

Transferring fluids:

After the cleaning process, the substrate was placed in the viewing chamber to perform the contact angle measurement. Figure 12 shows the position of the needle, which is upside down, with the substrate placed above it, within the viewing chamber.

The cell is then partially filled with the brine, by injecting from the bottom of the cell until the brine level completely covers the substrate. During this stage, care should be taken not to move the substrate out of its position. Then CO_2 is injected into the cell from the top while the discharging valve (see Figure 11) is opened, to displace the trapped air inside the chamber. Finally the system is pressurised to the desired pressure of the measurement by shutting the valve. It should be noted that the temperature is adjusted by switching the heater and the temperature controller on, at the start of this stage of the test.

At this point CO_2 and brine start transferring mass, as CO_2 dissolves in brine. As a result of this mass transfer, the pressure of the chamber drops. Hence, some time should be given to allow the system to reach equilibrium conditions. Pressure stabilisation is a good indication that the fluids inside the cell are at equilibrium and the final stable pressure can be considered as the equilibrium pressure of the system. Figure 13 shows pressure decay data versus time for the experiment with initial pressures of 430. Although this graph can be later used for determining the diffusion coefficient of CO_2 in brine at different experimental conditions, at this stage they provide a good indication of the equilibrium time when the oil droplet should be placed on the surface.

Once equilibrium conditions have been achieved, an oil drop is slowly introduced onto the surface of the substrate to analyse its shape and measure the corresponding contact angle.

5.2.6 Analysis of the Shape of the Oil Drop

The contact angle is determined using the images of the settled drop on the surface of the substrate. The contact angle measurement rig is equipped with software that determines the actual shape of the drop by analysis of the pixels of the image. The contact line (baseline) with the surface can also be determined by the same method or manually by the user. Then the drop shape is fitted to a mathematical model, which is then used to calculate the contact angle.

5.2.7 Results and Discussion

In this study, as Figure 14 shows, the values of the contact angle, which was measured in the aqueous phase, are reported and compared. A smaller contact angle indicates stronger tendency for the aqueous phase to wet the substrate.

Glass/n-decane/distilled carbonated water system at 38 °C

In the first set of experiments, contact angles were measured between n-decane and (distilled) carbonated water on a glass substrate at 38 °C. The values of these contact angles as a function of pressure are shown in Figure 15. This figure also shows the measured contact angle data for the carbonated brine (CB)/n-decane/glass system, which will be discussed in the next section. As this plot shows, for this system, the contact angle initially increases and then decreases by pressure. If we divide the data into two parts, the data in the first part (at lower pressures, i.e. below 1200 psi) shows that the system becomes less aqueous wet as the pressure increases. However, in the second part (at higher pressures, i.e. above 1200 psi) the system becomes more aqueous wet as the pressure increases. Such a trend has also been observed in data reported by Yang et al. (2008) for a crude oil/carbonated brine/reservoir rock system at 27 °C. However, they have not highlighted this behaviour and hence no explanation has been put forward.

Figure 16 shows and compares the shape, the projected wetted line and the observed contact angles of an oil drop when the equilibrium pressure of the system changed from

about 400 psi to 2000 psi. As these digital images show, the wettability has clearly been affected and altered the shape of the oil drop. The projected wetted line by oil, which is one of the most important parameters for defining the shape of the oil drop, has been outlined in yellow in this figure. This image shows that the projected wetted line is greater at the lower pressure. As can be seen, the CW phase is less wetting when the pressure is 400 psi (Figure 16A) compared to the case when pressure is 2000 psi (Figure 16B). In other words, the oil has more tendency to wet the glass when pressure is reduced from 2000 psi to 400 psi.

Glass/n-decane/carbonated brine system at 38 °C

These series of contact angle measurements were carried out again, using glass substrate and n-decane as the oil phase. However, carbonated brine with salinity of 10000 PPM was used instead of carbonated distilled water as in the previous measurements.

As can be seen in Figure 15, the same trend as that observed for distilled CW case has been obtained. The repeated trend to some extent confirms the validity of the observed trends in these two sets of results. To examine the repeatability of the measured data, the first and last data points were repeated. The results of the repeated measurements showed a very small variation of less than 1 degree confirming the repeatability of the measured contact angle values.

Glass/n-decane/distilled water vs. brine system at 38 °C

The following points can be highlighted from Figure 15.

I) All the contact angles measured using both carbonated brine and carbonated (distilled) water tests are less than 65 ($\theta < 65°$). This indicates that, as expected, the aqueous phase, rather than the oil, remains the wetting phase for glass.

II) The presence of salt (10000 PPM) in water makes water a more wetting phase compared to distilled water, i.e. the contact angle decreases with salinity by about 3-10°. This trend is consistent with the literature data for low range of salinities, in which about 20° reduction in contact angle in water has been reported when salinity increases from 0.01 M NaCl (584 PPM) to 0.1 M NaCl (5844 PPM) in brine/CO_2/quartz and brine/CO_2/mica systems (Chiquet and Broseta, 2005). However, the influence of brine

salinity on contact angle has been reported to be different at high salinity ranges. That is, increasing the salinity by almost the same order of magnitude from 0.1 M NaCl (5840 PPM) to 1 M NaCl (58440 PPM) has increased θ (Chiquet and Broseta, 2005).

III) For both carbonated distilled water and carbonated brine, the contact angle initially increases up to a maximum value (turning point) then decreases as the pressure increases.

IV) For the two reported sets of data, the turning point (maximum contact angle) for carbonated distilled water corresponds to a higher pressure of 1200 psi compared to that for carbonated brine (800 psi).

V) The range of wettability alteration by pressure in carbonated water decreases by adding salt. That is, the difference between the maximum and minimum values of the measured contact angles in the experiments with carbonated distilled water (63.05-49.3=13.75°) is greater than the corresponding value in experiments with carbonated brine (53.18-46=7.18°). Reduction of solubility of carbon dioxide in brine by salt is well known (Chang et al., 1998; Baviere, 1991; Koschel et al., 2006). This reduction might be one of the reasons for this observed trend.

Quartz/n-decane/CB system at 38 °C

In this set of experiments CB and n-decane were used as the aqueous and oleic phases, respectively. The main reason for using quartz here was because quartz forms the main mineral of sandstones and also the obtained data can be compared with data available in the literature.

Figure 17 shows the values of the contact angles measured for carbonated brine and n-decane on a quartz slide versus pressure. A similar trend as that observed for the glass substrate, is also observed here. However, to verify the accuracy of the measurements, some of the measured data on quartz were repeated, which are plotted in this figure labelled as series 2. There is a very good agreement between the two measured data series (blue shows original and pink repeated data) confirming both the accuracy and repeatability of the data.

Comparing these measured data with the data available in the literature for quartz shows that only the trend of the first part (increasing contact angle with increasing pressure) is

consistent with the set of measurements reported in the literature (Chiquet and Broseta, 2005). As will be described below, the date reported by Chiquet and Broseta, (2005) were not measured at sufficiently high pressure to observe this behaviour. That is, the pH of CW and CB, which alters at higher pressures, can be used to explain the observed non-monotonic behaviour of measured contact angle values. It has been reported that the tendency of the rock to have a positively or negatively charged surface, which affects its wettability, can be altered by pH, i.e. at different pH, the rock surface could have different wettability tendencies. That is, for instance silica surface is negatively charged above pH of 2 and positively charged below pH of 2, whereas this critical pH for calcite surface is about 9.5 (i.e. calcite surface is negatively charged above pH of 9.5 and positively charged below it) (Buckley et. al., 1998). It has also been shown that the pH of carbonated water reduces by increasing the pressure of the system (Donald, 1982 and Crawford, et al. 1963). Therefore, it is hypothesised that by increasing the pressure, pH reduces below the critical value, the surface become positively charged and the surface become more water wet afterwards, i.e. contact angle decreases.

Quartz/n-decane/CB vs. plain brine system at 38 °C

To better understand the impact of dissolved CO_2 on wettability and to have a basis for comparison, the contact angle between n-decane and plain brine (brine without dissolved CO_2) was also measured.

Figure 18 summarises both series of contact angle data corresponding to CB and plain brine. As these data demonstrate, for all the pressure conditions, without any exception, a higher contact angle for brine has been measured compared to carbonated brine. The differences between these two systems are between 8-24°. It is noted that there is no clear dependency between pressure and the extent of these differences. The size of the arrows (in Figure 18) displays this point visually. This comparison demonstrates that dissolved CO_2 in brine makes quartz more aqueous (water) wet. This conclusion is consistent with the observations made during the preceding micromodel experiments.

Quartz/n-decane/CB system at 58 °C

Here the impact of temperature on wettability is addressed. Both salinity and temperature affect CO_2 solubility and hence both parameters are expected to affect the modification of wettability due to carbonated water. The fluid system (carbonated brine

and n-decane) and the substrate (quartz) in this set of contact angle measurements were the same as the previous one, with the only difference being the higher temperature of these measurements, i.e. 58 °C compared to 38 °C corresponding to the previous measurements.

Figure 19 show the values of contact angles measured using both brine and carbonated brine at higher temperature and at different pressures. The measured data at 58°C shows the same trends as those observed at 38 °C, shown in Figures 18. Based on the comparison of the measured contact angles for quartz with and without CO_2 at this higher temperature of 58 °C, the same conclusion as that reached for the lower temperature of 38 °C, was achieved, i.e. CO_2 dissolved in brine makes quartz more water–wet compared to plain brine. Similar results for a crude oil/reservoir brine/reservoir rock system at 58 °C have been presented by Yang et al. (2008). In their experiments the rock sample was limestone. Perez, et al. (1992) also investigated the effect of dissolved CO_2 on oil recovery by imbibition mechanisms using limestone core samples. They showed that the dissolved CO_2 in water increases the oil recovery rate and ultimate oil recovery by the imbibition mechanism.

Quartz/n-decane/CB system 38 °C vs. 58 °C

Figure 20 compares the measured contact angle data in a CB system at two different temperature conditions (T=38 and T= 58 °C). This plot illustrates that the pressure of the turning point (maximum contact angle) measured at higher temperature (blue curve) is significantly lower, 800 psi, than that measured at the lower temperature (pink curve), 1300 psi. It was also previously shown that salinity reduces the pressure of the turning point. Reduction of the pressure of the turning point and CO_2 solubility in water, by increasing both salinity and temperature, could suggest a dependency between the turning point and the CO_2 content of brine. That is, the charges induced by carbonic acid can change the balance of charges on the interfacial surfaces and consequently alter the wettability. However, more experimental data is required to verify such a conclusion.

As mentioned earlier, the reported data by Chiquet and Broseta, (2005) correspond to the trend observed for the first part of the observed data in this study (before reaching the turning point) where increasing the pressure increases the contact angle. This

reported observation, as explained already, could be due to their relatively low working pressure because their measurements were at lower temperature of 35 °C. In other words, they have not examined high enough pressures to observe the turning point that was repeatedly observed in the measured data here.

Effect of oil swelling on wettability

All the reported contact angle data presented here for both carbonated distilled water and carbonated brine were measured immediately after introducing the oil droplet on the surface of the substrate. Therefore, the CO_2 dissolved in the CW started to dissolve into the oil droplet as soon as the droplet was placed on the substrate, which was immersed in CW. As a result of this mass transfer, the volume of the oil drop increased with time.

As a consequence of oil swelling, the projected wetted contact line and the position of the three-phase line as well as the physical properties of oil and interfacial tension between oil and water, change with time. As a result of a change in the size and the shape of the oil droplet with time, the contact angle value could be different if it was measured during the swelling of oil. It should also be noted that the heterogeneity of the substrate, such as different mineralogy and roughness of surface (1100 Å for the substrate glass, for instance) can also cause some degree of variation of the measured contact angle during the oil swelling period. In this section some of these issues are investigated and discussed.

Oil droplet size dependency on contact angle

The modified Young equation, Equation 1, expresses the dependency of contact angle to the drop size. This equation initially was developed for a sessile liquid drop on an ideal solid surface in contact with air by Boruvka and Neumann (1977).

$$\cos\theta = \cos\theta_{\infty} - \frac{\sigma}{\gamma_{lv}}\frac{1}{R} \qquad (5.1)$$

where θ_{∞} is defined based on the classical Young equation at equilibrium conditions. θ_{∞} satisfies the following equation:

$$\cos\theta_{\infty} = \frac{\gamma_{sv} - \gamma_{sl}}{\gamma_{lv}} \qquad (5.2)$$

θ is the equilibrium contact angle corresponding to the three-phase contact circle with a radius of R.

θ_∞ is the equilibrium contact angle corresponding to an infinitely large drop size, R.

σ is defined as line tension of the three-phase contact circle and, like the surface tension, which tends to minimise the interfacial area, it tends to minimise the length of the three-phase contact circle.

γ_{sl}, γ_{sv} and γ_{lv} are the interfacial tension of solid/liquid and surface tension of solid/vapour and liquid/vapour, respectively.

The dependency of the contact angle on the oil droplet size has been investigated by Gu (2001) for a solid/oil/water system. He reported a decrease of about 7° for the equilibrium contact angle when the radius of oil droplet increases from 0.0205 to about 0.24 cm. However, no significant change was observed for relatively big oil droplets (the radius of an oil droplet from 0.24 cm to 0.4684 cm).

In this study, the dependency of contact angle on oil droplet size was also observed. Figure 21 shows two oil droplets with significantly different sizes. As the data on this image show, the contact angle in water increases from 26.4° to 42.3° when the base contact circle diameter (BCD) increases from 0.0589 cm to 0.2014 cm. These diameters correspond to the oil volume of 1.15 μL and 12.05 μL, respectively.

In this study, oil swelling and the effect of oil droplet size on wettability alteration was simulated and investigated by eliminating the CO_2 from the system. The size of the oil droplet was changed by adding oil to the oil droplet settled on the substrate in brine. This would give a more direct and accurate estimation of the effect of oil droplet size on the contact angle, as the variation of interfacial tensions due to CO_2 dissolution is eliminated. Figure 22 shows the contact angle in brine at pressure and temperature of 1627 psi and 58 °C, respectively, when the oil droplet size was increased from 11.23 μL to 21.13 μL. These oil droplet sizes correspond to the base contact circle diameter of 0.2244 and 0.2818 cm, respectively.

The measured contact angle for different oil droplet sizes have been plotted and shown in Figure 23. It is noted that this type of measured angles can also be referred to as apparent contact angle to differentiate it from the advancing and receding angles, which are discussed in the next section. In Figure 23 a horizontal line has also been drawn, representing the average value of the contact angle. As this plot reveals, the contact angle has not been influenced by oil droplet size, i.e. the variation of measured contact angle compared to the average value is small. The lack of dependency of contact angle of oil drop size in the range of oil droplet sizes investigated here (0.2244 -0.2818 cm) is consistent with the Gu's (2001) experimental data obtained for relatively big oil droplets in a completely different solid substrate-fluid system.

Contact angle hysteresis

Contact angle hysteresis is a well established phenomenon and is considered as one of the sources of hysteresis in capillary pressure and relative permeability curves, i.e. having a different flow path for drainage and imbibition processes. The contact angle hysteresis is expressed by dynamic contact angles. One of the methods to measure dynamic contact angles is increasing and decreasing the volume of the oil drop and measuring advancing and retreating contact angles, respectively. In this method, the needle (used for forming oil droplets) is slightly inside the drop throughout the whole measurement process. Furthermore, for measuring the advancing and its corresponding receding contact angle, the contact area during increasing and decreasing oil volume should be the same.

Figure 24 shows the position and the shape of the oil droplet at the advancing and receding conditions in one of such experiments. The difference between these two angles is used to make a statement on the heterogeneities of the surface. Neumann and Good (1972) and Li and Neumann (1992) have shown that the advancing contact angle for a heterogeneous surface would be representative of the dominant material on the surface, while the receding contact angle reveals the properties of mineral impurities.

Figure 25 also shows the measured advancing, 45.6°, and receding, 58.7°, contact angles as well as the apparent contact angles previously plotted in Figure 23. The difference between these two values, 13.1°, is referred to as hysteresis. This plot also shows a small difference of 2.5° between the apparent contact angles and the advancing

ones, which could be due to the effect of the needle in deforming the shape of the oil droplet. The close agreement between the reported contact angles and the corresponding advancing contact angles, which is representative of the dominant material on the surface, is further evidence of the reliability of the data reported here.

Mica/n-decane/CB system at 38 °C

In the last set of contact angle measurements that was carried out in this study, the wettability of mica in contact with the carbonated brine and n-decane was investigated at a number of pressures. These measurements (Figure 26) were carried out at 38 °C, which demonstrated the general trend of the data for glass and quartz, i.e. it went through a maximum value at turning point.

Mica vs. quartz in n-decane/CB system at 38 °C

Figure 26 also compares the measured data for mica with those obtained for quartz (Figure 17) using the same fluid system and at the same temperature of 38 °C. As can be seen, the turning point pressure for both systems is almost the same. However, these data distinctly show that the variation of the contact angle with pressure for mica, 100.4°-43°=57.4°, is greater than that for quartz, 36.7°-28°=8.7. The difference between mica and quartz contact angle measurements for CO_2/brine/mica and CO_2/brine/quartz systems has been previously reported elsewhere (Chiquet and Broseta 2005). The observed contact angle variation, for the first part of this data, before the turning point, in these experiments is in agreement with the measured advancing contact angle data (in brine with 0.1M NaCl) reported in the literature (Chiquet and Broseta 2005). The corresponding values available in the literature for mica and quartz are about 50° and 16°, respectively.

Mica/n-decane, CB vs. brine systems at 38 °C

The measured advancing contact angles for n-decane/brine on mica have been compared with the corresponding data for CB (shown in Figure 26) and shown in Figure 27. The data in this plot, contrary to the data obtained for quartz in Figure 18, highlights that at all pressures dissolved CO_2 makes mica less water wet. The difference between contact angles in brine and carbonated brine varies from 17° to 74.2° for the minimum and maximum contact angle points, respectively.

To demonstrate the effect of dissolved CO_2 (carbonated water) on wettability of mica, Figure 28 has been prepared. This figure shows the shape of an oil drop at different pressure conditions and at 38 °C on mica, using brine (28A) and carbonated brine (28B and 28C). This figure clearly shows a significant change in contact angle and hence wettability of mica, when in contact with carbonated brine. The high contact angle (measured in water) shown in Figure 28C, 100.4°, is consistent with the results of adhesion test conducted as described below.

Adhesion and Non-adhesion

Adhesion refers to tendency of different (dissimilar) molecules to cling together due to attractive forces. Cohesion, on the other hand, is due to intermolecular attraction between similar molecules within a substrate. The interaction of cohesive (liquid/liquid) and adhesive (solid/liquid) forces determines the wettability. That is, strong adhesion and weak cohesion result in a high degree of wetting and conversely, weak adhesion and strong cohesion result in poor wetting.

Four general types of chemical bonds are recognized to affect adhesion and cohesion; i) electrostatic, ii) covalent, iii) metallic and iv) van der Waals. Based on the relative strength of the bonds, the first three ones are classified as primary bonds and the last one is categorized as a secondary bond. Electrostatic or polar bonds are the types holding together the atoms in common salts. Covalent bonds act to hold together the atoms of carbon, hydrogen and other elements in organic compounds. Metallic bonds are the types, which hold the atoms of metals together. When such primary bonds are formed, the negative and positive charges of atoms are not completely neutralized. Thus there are residual energies which provide attractive forces known as van der Waals' forces. (Reinhart, 1954)

The competition of cohesion and adhesion can in general be used to explain phenomena related to surface forces such as wettability, surface tension and meniscus. Adhesion tests have been performed to study the wettability behaviour of various systems (Buckley et. al., 1989). To further study the impact of carbonated water on wettability, a series of adhesion tests were also carried out in this study.

In these tests, an oil droplet is introduced through a needle on a solid plate in the presence of water. Once the oil droplet settled on the surface, it is pulled back from the surface. If the oil was disconnected from the needle and remained on the surface it represents a positive adhesion point on the adhesion map prepared by varying the test pressure and temperature.

In adhesion tests conducted here on glass and quartz, it was possible to place oil droplets on the surface of these solids. However, this was not the case when mica was used with the same fluid system (brine, n-decane) under the same conditions. Because of the non-adhesion property of oil on mica in brine, only the advancing contact angles for this system could be reported (Figure 27).

Figure 29 shows different stages of introducing an oil drop onto the mica surface immersed in CB, during one of the adhesion tests.

Adhesion of oil for the system with brine instead of CB was also examined for a wide range of pressure, 400-2000 psi, and temperature, 21, 38, 58 °C but the oil drop did not adhere to the surface of mica. Figure 30 shows different stages of attaching and detaching the same oil drop in this system. As these images show, there is not enough tendency for the oil to wet the surface of mica in order to cling to it. The stability of the water layer settled between oil and mica could be one of the possible reasons for this behaviour as described in the next section. This distinctly different behaviour is a good indication of different wettability response of mica to brine and CB.

Effect of oil layer on contact angle

Some visualisation (micromodel) experiments in this study were carried out, in which the micromodel was initially fully saturated with oil without any connate water. The results of these experiments showed different wettability conditions for the micromodel compared to similar experiments in which connate water was present in the porous medium. The wettability of the former was less water wet and more towards neutral and sometimes oil-wet conditions, whereas the wettability of the latter was strongly water wet.

Here, two tests were performed using a quartz substrate. In one of the tests, the surface was initially wetted with the brine and in the other one with the oil, then the oil/water contact angle was measured. Figure 31 shows the shape of the oil droplets and their corresponding measured contact angles at these two different conditions. As can be seen the surface of quartz pre-wet with water remained strongly water-wet, whilst that pre-wet with oil became oil wet. These results are consistent with the observations of the micromodel experiments without connate water and also in line with the reported data by Hirasaki (1991), which confirms that if no water layer exists on the surface the dehydrated quartz surface will be oil wet. One of the likely reasons for this observation has been discussed by Hirasaki (1991), based on the role of the van der Waals forces on the stability of thin layers between different phases. That is, in the case of pre-wetting the surface of quartz with water, electric charges at the interfaces between the oil and aqueous phases and between the aqueous phase and the solid could have the same polarity, which enhances the repulsive electrostatic forces between the interfaces, and results in the stability of the water film layers between oil and surface, i.e. the surface remains water wet.

5.3 Conclusions

The following conclusions can be drawn from the reported contact angle experiments and micromodel visualisation experiments:

- CW makes the glass micromodel more water-wet compared to plain water at conditions tested in the visualisation experiments (2000 psi and 38 °C). Oil displacement by spontaneous imbibition was observed when CW was present but no evidence of spontaneous imbibition was observed for experiments with plain water.
- Compared to plain water, carbonated water alters wettability of minerals tested in this study. Compared to a CO_2-free system, dissolved CO_2 makes the quartz slide more water wet at both 38 and 58 °C. However, contrary to the obtained data for quartz, dissolved CO_2 makes the mica surface less water wet (at 38 °C).
- For all the contact angle measurements carried out with CB, the angle initially increased with increasing pressure up to a maximum value and then decreased

with increasing pressure. Reduction of the pressure of the turning point (maximum contact angle) by both salinity and temperature was also observed.

- The measured contact angle data for mica and quartz show that the turning point for both systems is almost the same. However, the variation of wettability (contact angle) for mica (43°-100.4°) with pressure compared to quartz (28°-36.7°) is considerably greater.
- Due to the non-adhesion property of the oil in brine/mica system, no oil drop was formed on the surface of mica over a wide range of pressure (400-2000 psi) and at various temperature conditions (21, 38, 58 °C).

5.4 References

Adamson, A.W., 1982: ''Physical chemistry of surfaces'', fourth edition, Wiley, New York.

Baviere, M., 1991: ''Basic concepts in enhanced oil recovery processes'', Published for SCI by Elsevier Applied Science, in London and New York.

Boruvka, L. and Neumann, A. W., 1977: ''Generalization of the classical theory of capillarity'', J. Chemical Physics, 66, 5464.

Buckley, J.S., Takamura, K. and Morrow, N.R., 1989: ''Influence of electrical surface charges on the wetting properties of crude oils,'' SPE Reservoir Eng. 332.

Buckley, J.S., Liu, Y. and Monsterleet, S., 1998: ''Mechanisms of Wetting Alteration by Crud Oils'', SPE Journal, March, P 54-61, SPE paper 37230.

Chang, Y. B., Coats B.K. and Nolen J.S., 1998: ''A Compositional Model for CO_2 Floods Including CO_2 Solubility in Water'' SPE 35164.

Chiquet, P. and Broseta, D., 2005: ''Capillary Alteration of Shaly Caprocks by Carbon Dioxide.'', SPE 94183.

Crawford, H.R., Neill, G.H., Bucy, B.J. and Crawford, P.B., 1963: ''Carbon Dioxide- A Multipurpose Additive for Effective Well Stimulation'', J. Pet. Tech. (March 1963) 237-242.

Donald R. G., 1982: ''The dissolution Effect of Carbonated Water on Oil Reservoir Carbonates- a Study under High Pressure Carbon Dioxide Flood Conditions'', PhD Thesis, Heriot Watt University, Edinburgh, June 1982.

Gu, Y., 2001: ‘‘Drop size dependence of contact angles of oil drops on a solid surface in water’’ Colloids and Surfaces A: Physicochemical and Engineering Aspects 181, 215-224.

Hirasaki, G. J., 1991: ‘‘Wettability: Fundamental and Surface Forces’’, SPE Formation Evaluation, SPE 17367.

Koschel, D., Coxam, J. Y., Rodier, L., Majer, V., 2006: ‘‘Enthalpy and solubility data of CO_2 in water and NaCl (aq) at conditions of interest for geological sequestration’’, Fluid Phase Equilibria 247, 107–120.

Li, D. and Neumann, A. W., 1992: ‘‘Surface heterogeneity and contact angle hysteresis’’, Colloid and Polymer Science, 270, 498.

Morrow, N. R., 1990: ‘‘Wettability and its Effect on Oil Recovery’’, JPT, 1476-84, SPE paper 21621.

Neumann, A. W., Good R. J., 1972: ‘‘Thermodynamics of contact angles. I. Heterogeneous solid surfaces’’, Journal of Colloid and Interface Science, Volume 38, Issue 2, Pages 341-358.

Perez, J.M., Poston, S.W, and Sharif Q. J., 1992: ‘‘Carbonated Water Imbibition Flooding: An Enhanced Oil Recovery Process for Fractured Reservoirs’’ SPE/DOE eighth symposium on enhanced oil recovery held in Tulsa, Oklahoma, April 22-24, 1992. SPE paper 24164.

Reinhart F.W., 1954: ‘‘Survey of Adhesion and Types of Bonds Involved’’, preceding of Adhesion and Adhesives Fundamental and Practice, 1954, page 9-15.

Wardlaw, N. C., 1980: ‘‘The effect of pore structure on displacement efficiency in reservoir rocks and in glass micromodels’’, SPE paper 8843.

Yang, D., Tontiwachwuthikul P., and Gu Y, 2005: ‘‘Interfacial Tensions of the Crude Oil + Reservoir Brine + CO_2Systems at Pressures up to 31 MPa and Temperatures of 27 °C and 58 °C’’, Journal of Chemical and Engineering Data, Vol. 50, No. 4.

Yang, D., Gu, Y. and Tontiwachwuthikul P., 2008: ‘‘Wettability Determination of the Crude Oil-Reservoir Brine-Reservoir Rock System with Dissolution of CO_2 at High Pressures and Elevated Temperatures’’, Energy Fuels, 22 (4), 2362-2371.

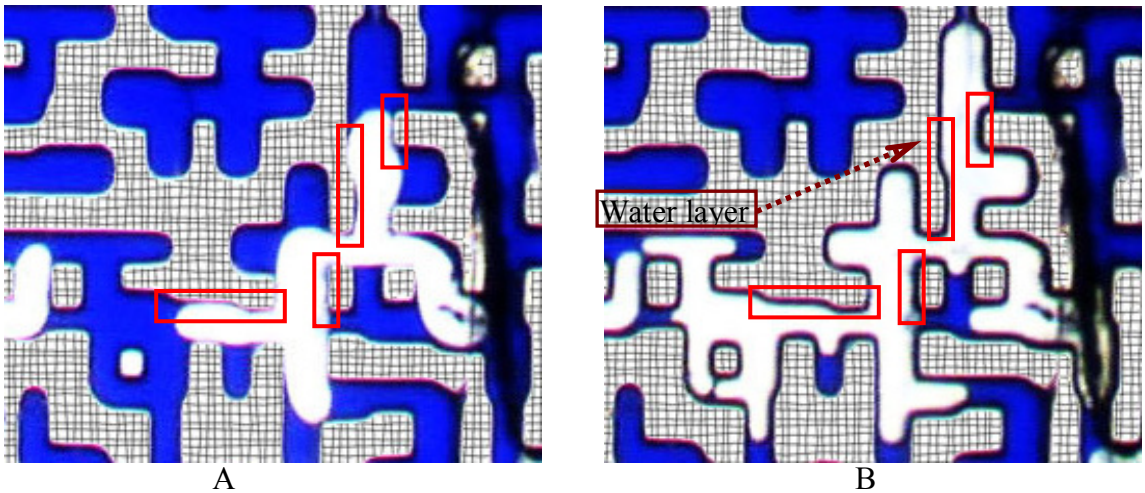

A B

Figure 5-1: An oil ganglion in a section of the micromodel during Experiment No. 1: A) after 1st WI; B) at the end of CWI.

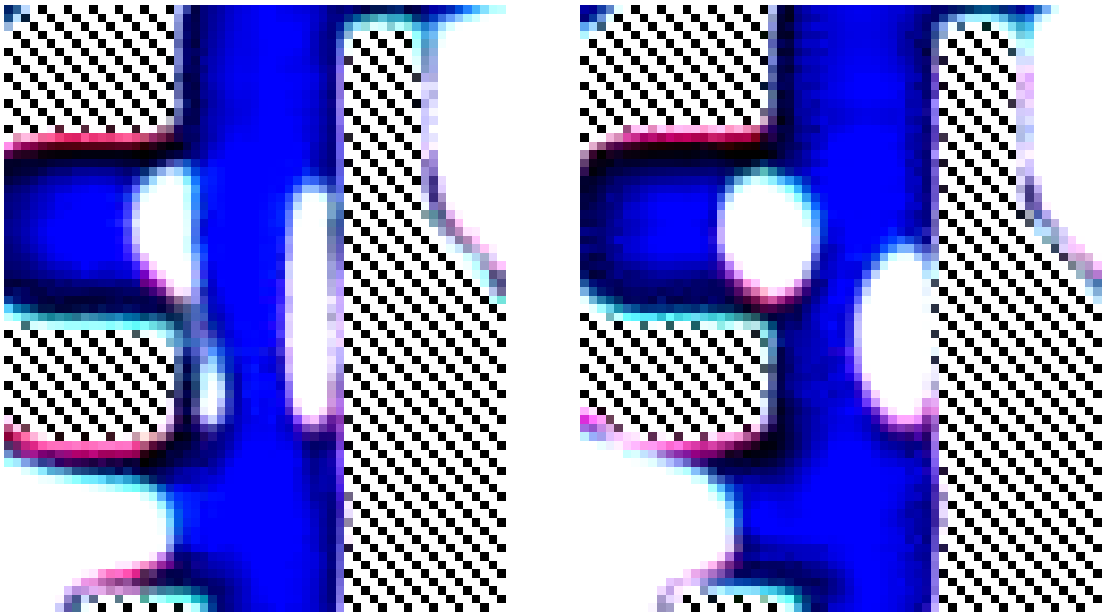

A B

Figure 5-2: A magnified image of a section of the micromodel, demonstrating different micromodel wettability during Experiment No. 4: A) more oil wet, after WI; B) less oil wet, after 15.8 hrs of CWI.

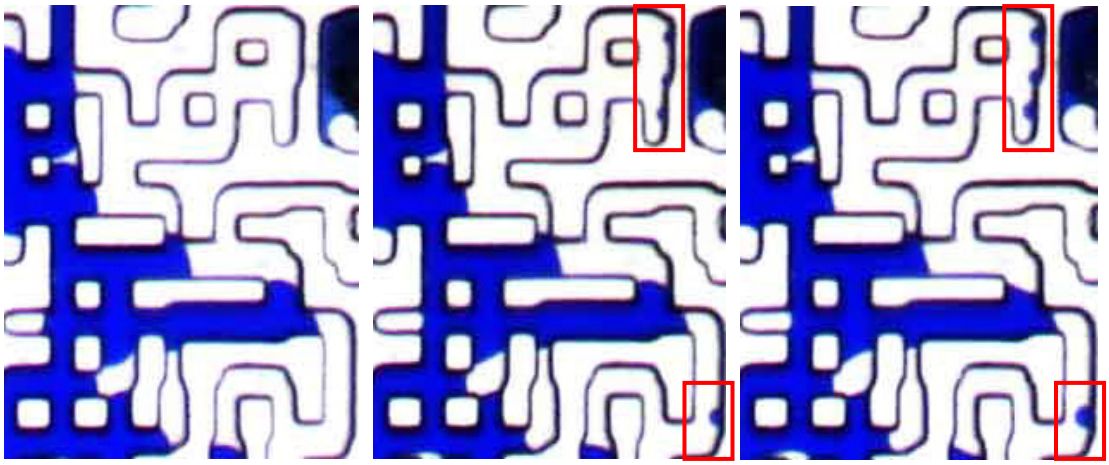

A B C

Figure 5-3: Establishment of carbonated water between oil and glass during carbonated water injection in a experiment with a low injection rate: A) after WI; B) and C) after 19.6 and 47.12 hrs of CWI, respectively.

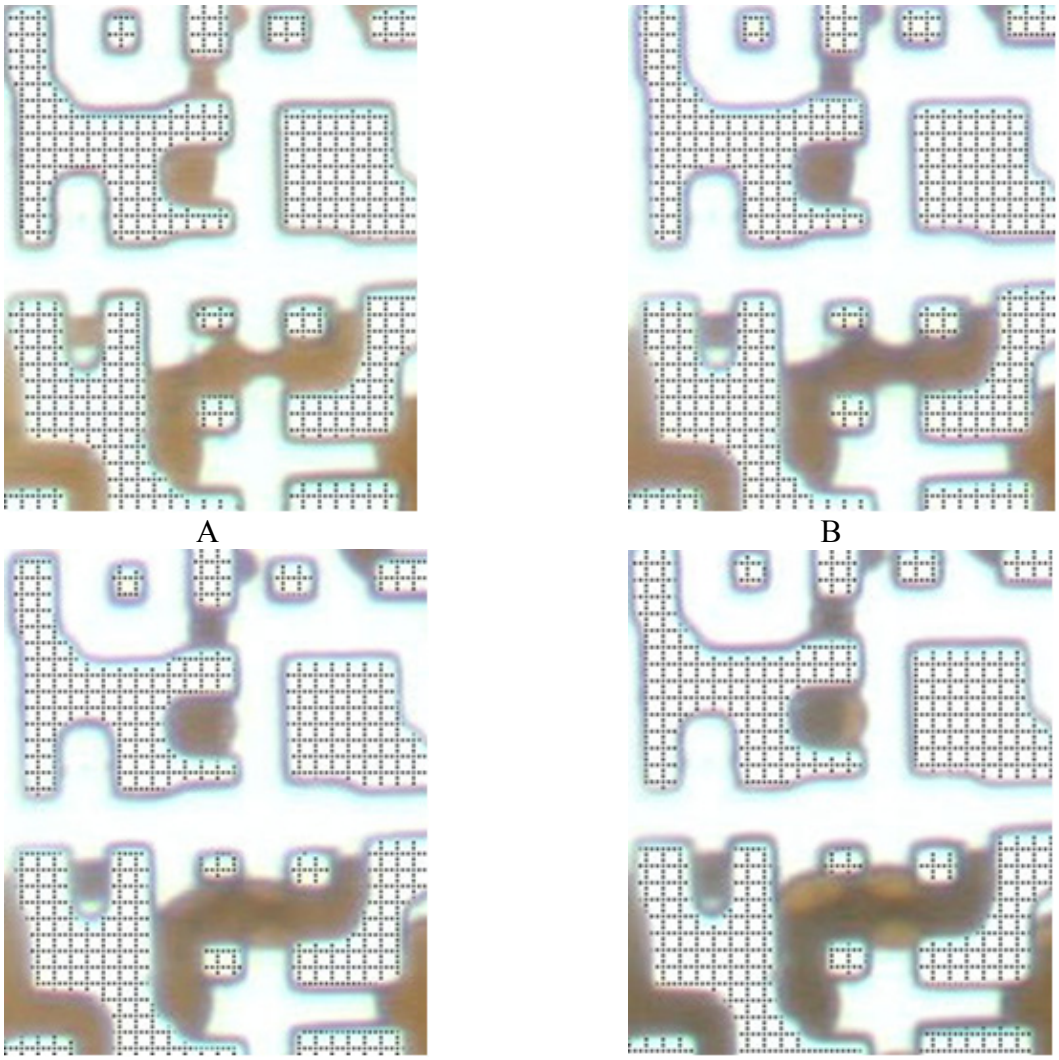

A B

C D

Figure 5-4: The state of an oil ganglion at different stages of Experiment No. 10: A) at BT of the 1st WI; B) At the end of the 1st WI, after 67 hrs; C) and D) after 20.5 and 93 hrs of the CWI, respectively.

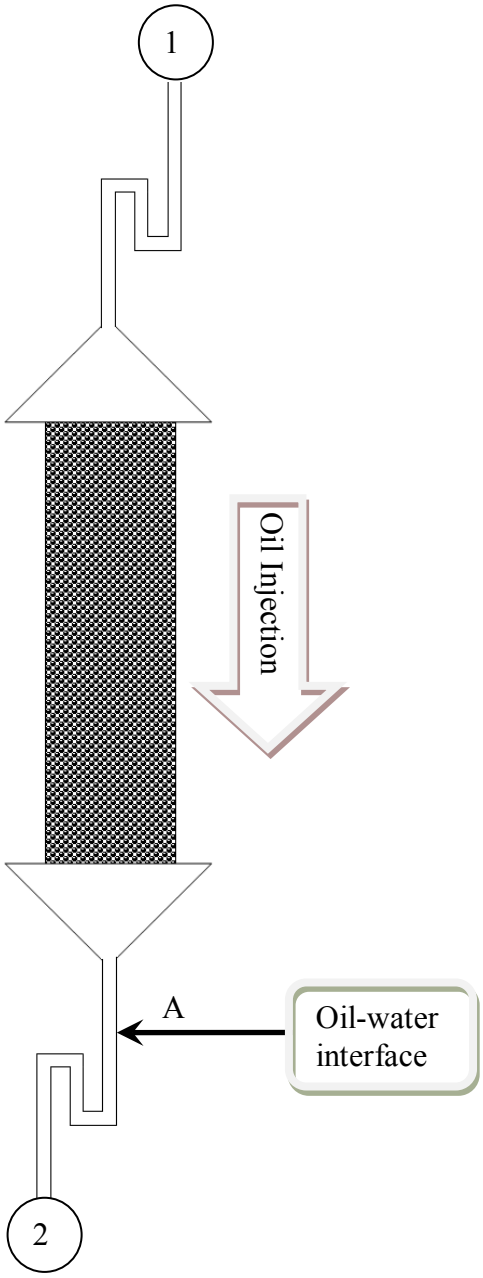

Figure 5-5: A schematic diagram of the micromodel showing position of the oil-water interface, valves, lines and triangular sections.

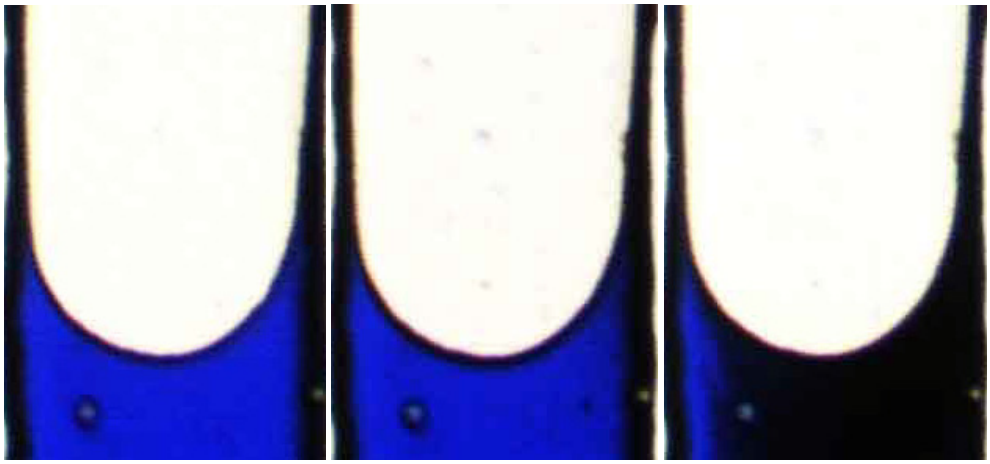

A B C

Figure 5-6: n-decane-water interface at point A of Figure 5-5 and different times: A) t=0; B) t=3; hrs C) t=27 hrs.

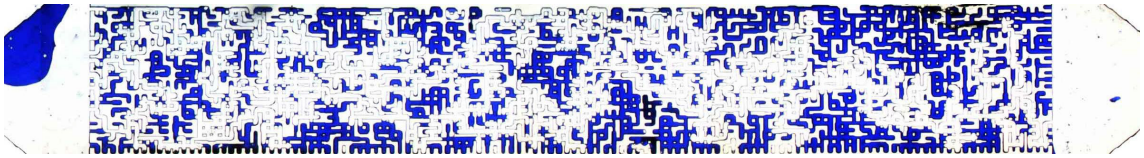

Figure 5-7: Initial oil saturation condition at 0<t<48 hrs (Experiment No. 20).

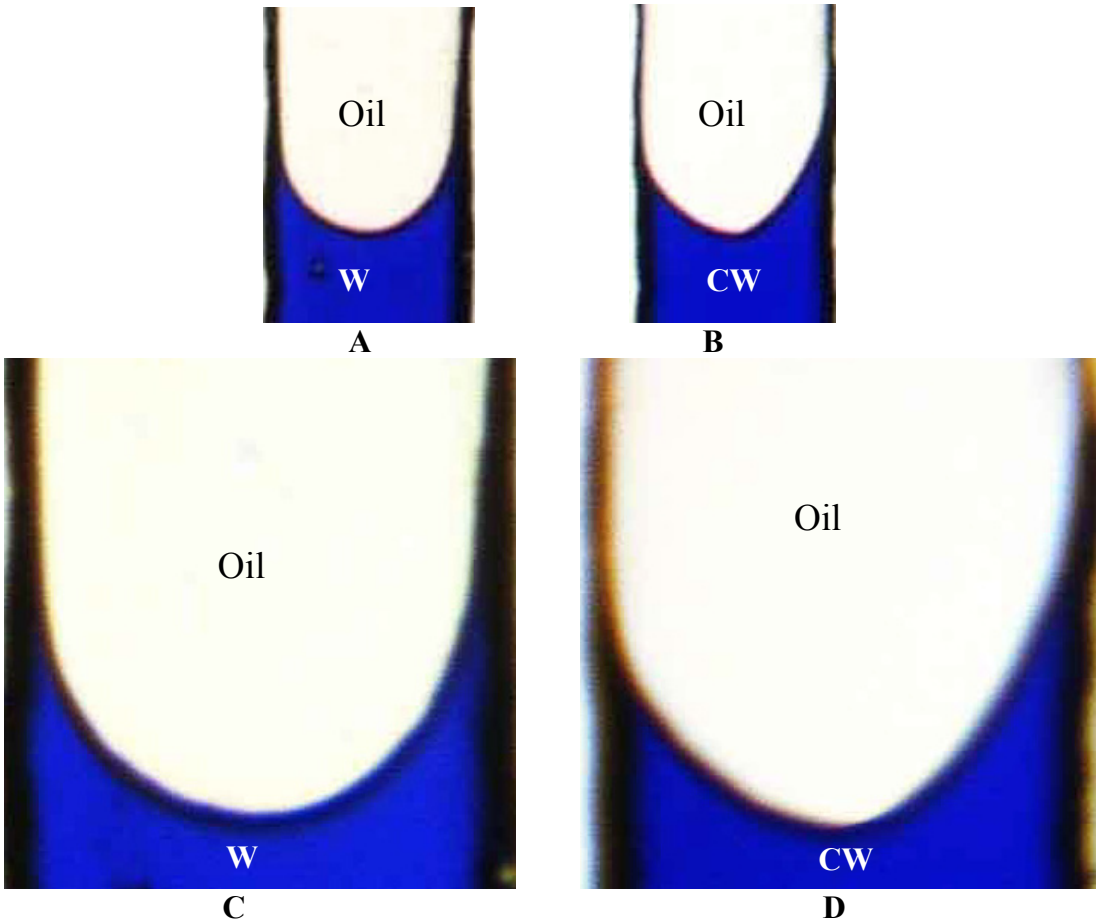

Figure 5-8 Interface of n-decane/water (A and C) and n-decane/carbonated water (B and D) systems at different magnification.

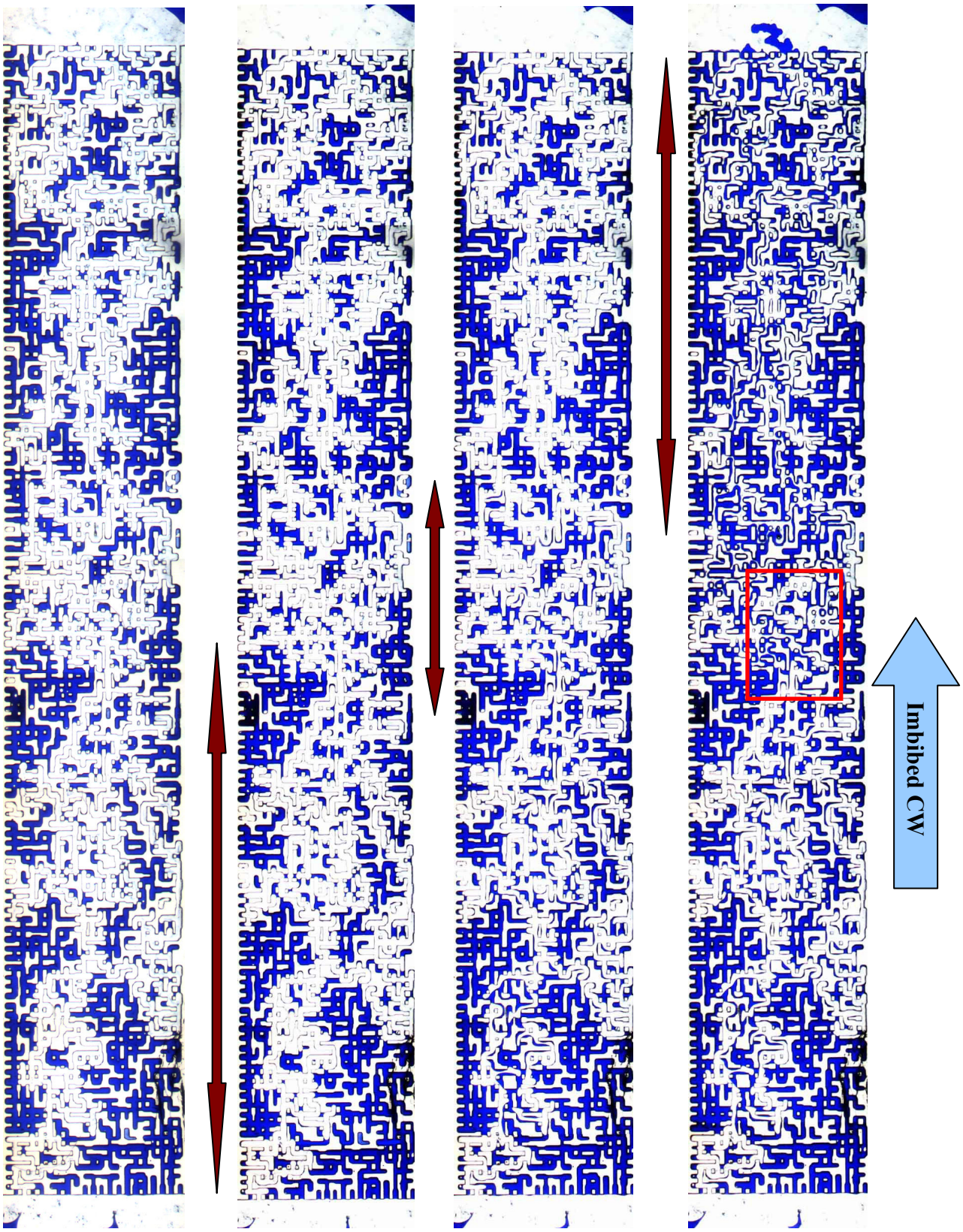

Figure 5-9: Fluid distribution as a result of spontaneous imbibition at t=0 and at different times: after A) 3.9 hrs; B) 18.9 hrs; and C) 44.8 hrs in Experiment No. 21. The brown arrows show the area invaded by spontaneous imbibiton of CW compared to their previous stages.

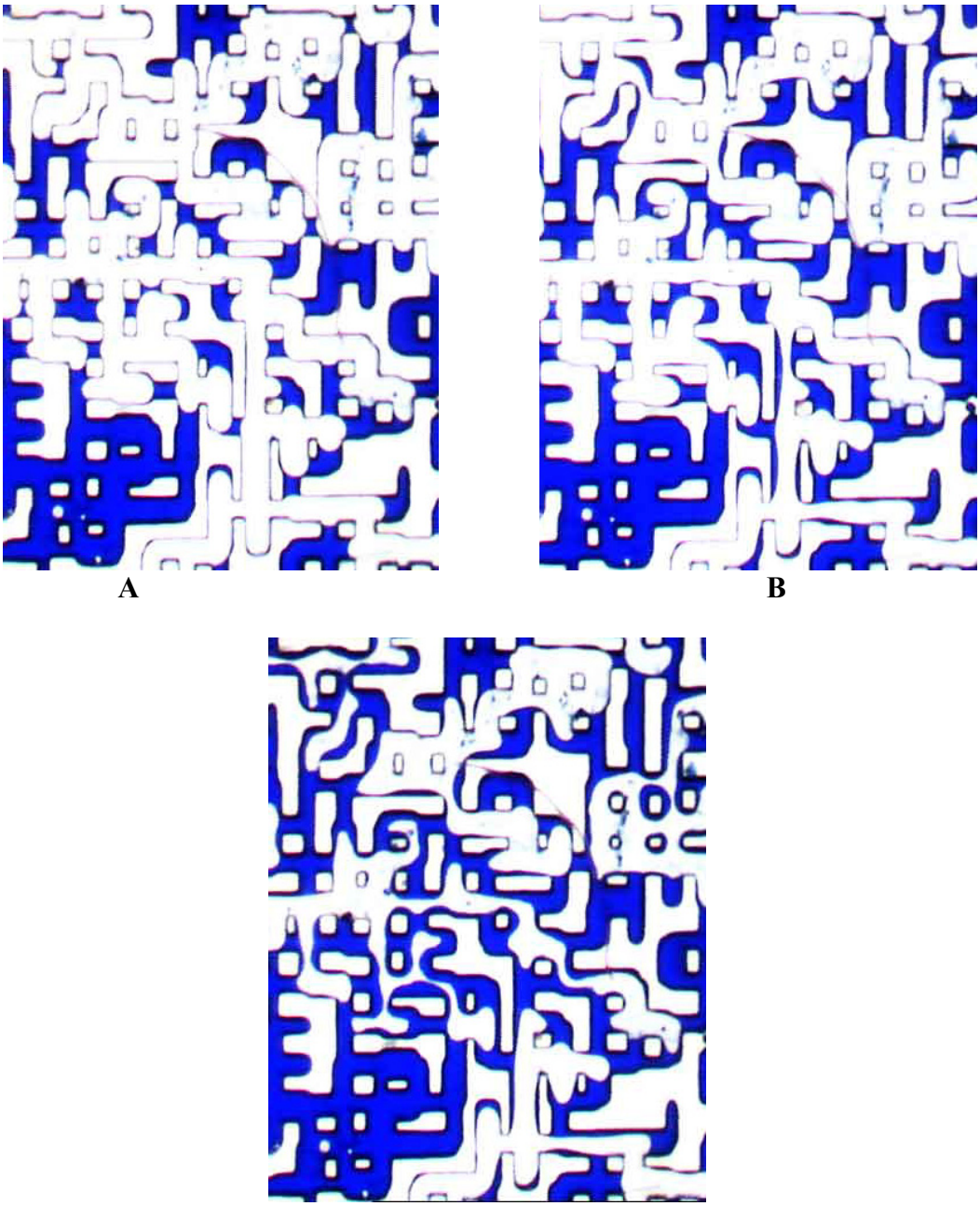

Figure 5-10: A) B) and C): Magnified images of a section of the micromodel during the observed spontaneous imbibition of CW (Experiment No. 21) into the micromodel after 3.9, 18.9 and 44.8 hrs of the first drainage period, respectively.

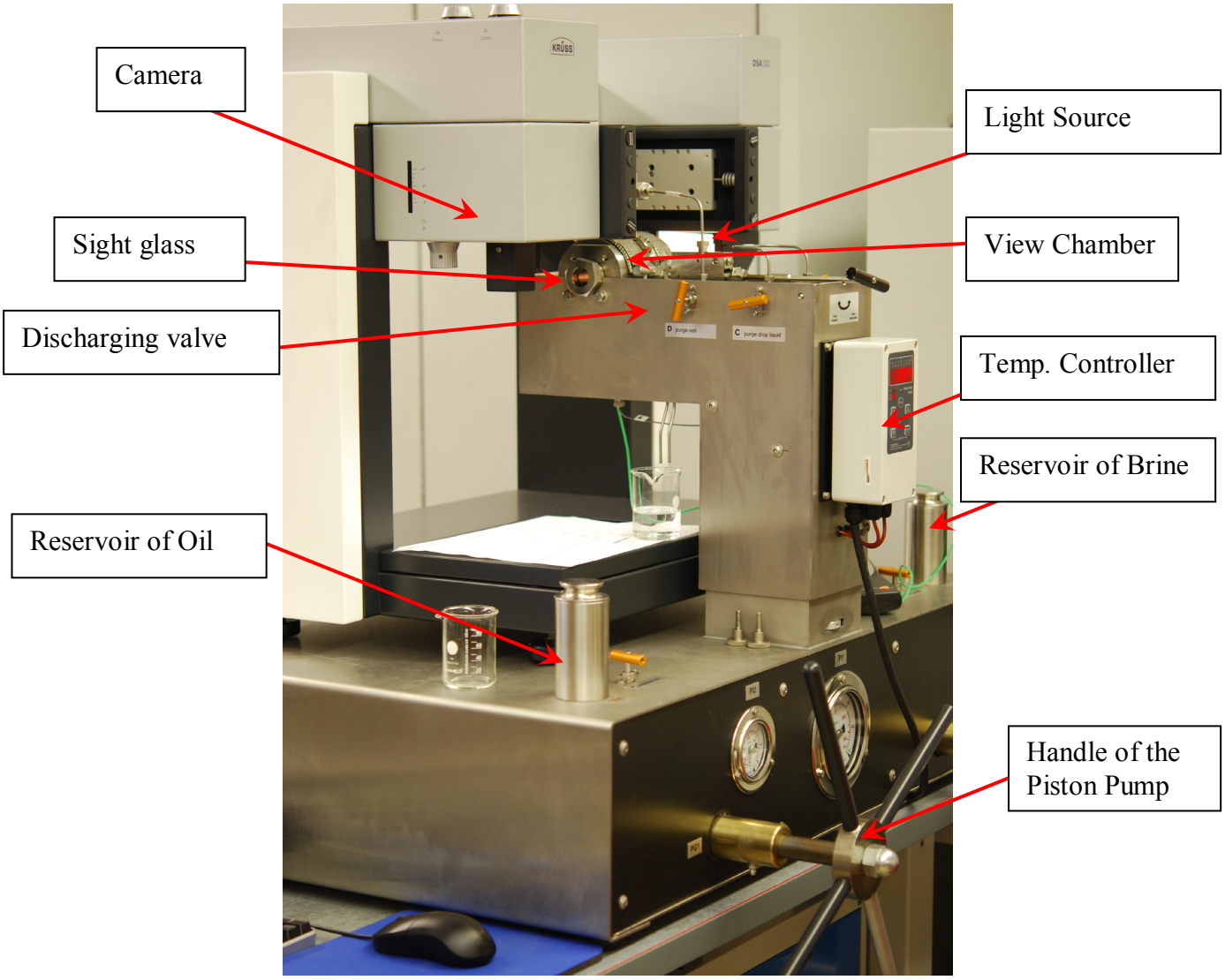

Figure 5-11: Photo of the contact angle measurement rig.

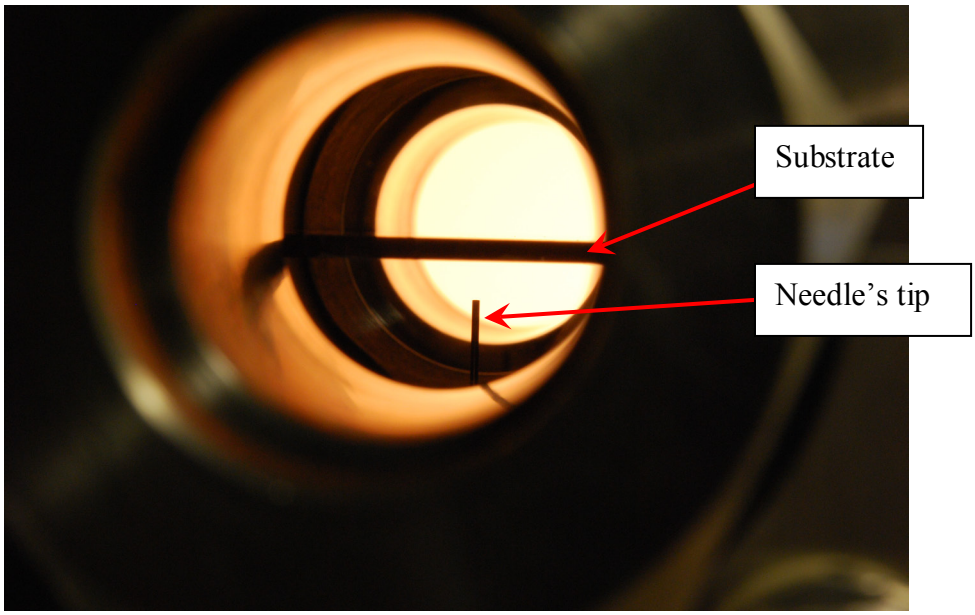

Figure 5-12: Position of the needle and substrate within the viewing chamber.

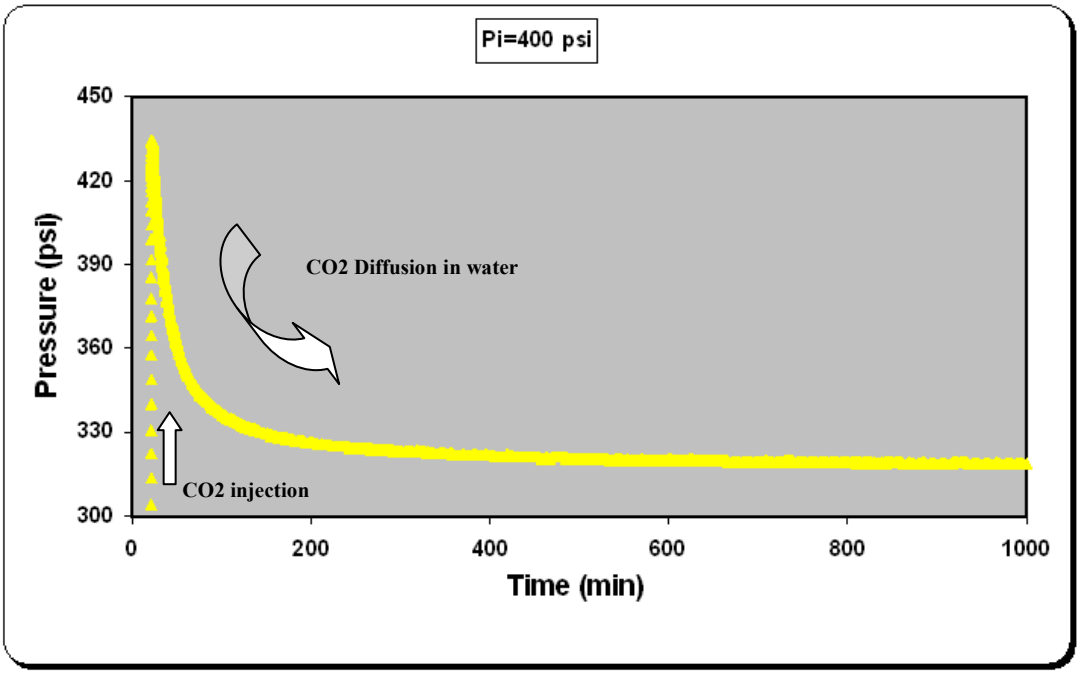

Figure 5-13: Pressure decay data versus time when initial pressure of the system is about 400 psi; T=38 °C.

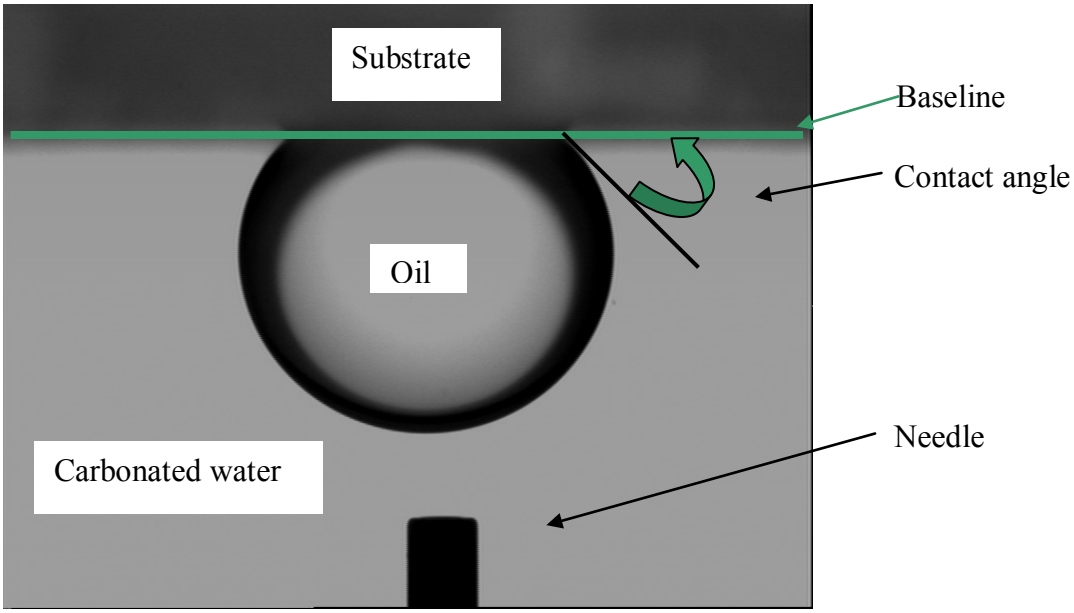

Figure 5-14: The contact angle measured within the aqueous phase.

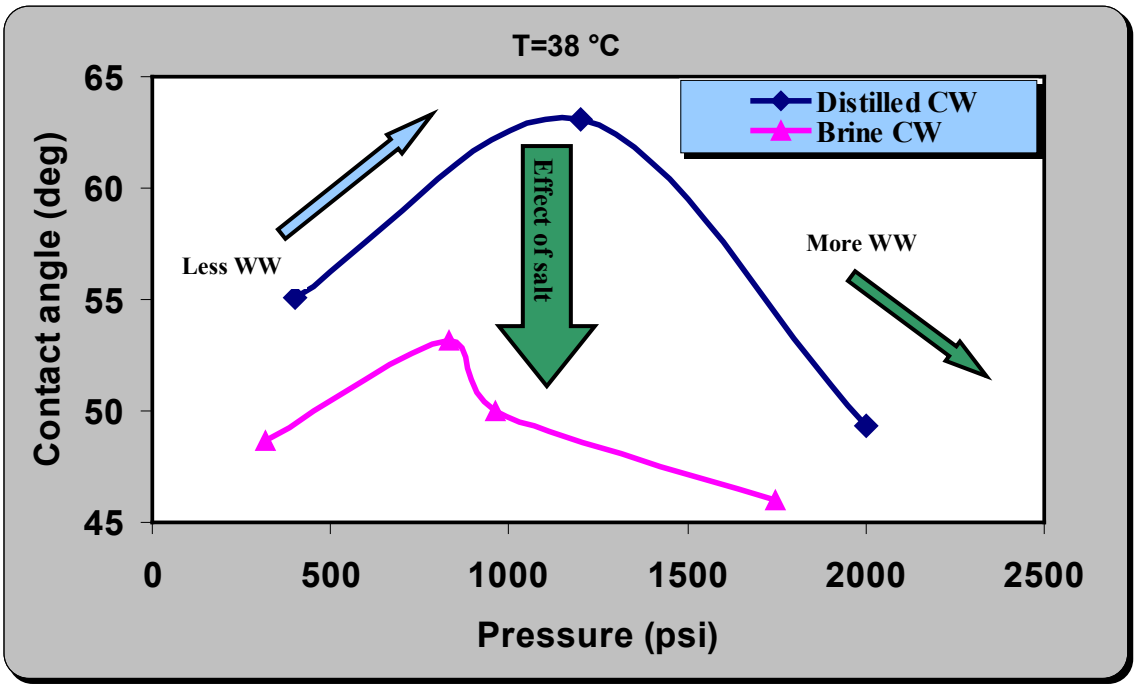

Figure 5-15: The oil/CW and oil/CB contact angles, measured on a glass slide immersed in carbonated distilled water, as a function of pressure at T=38 °C.

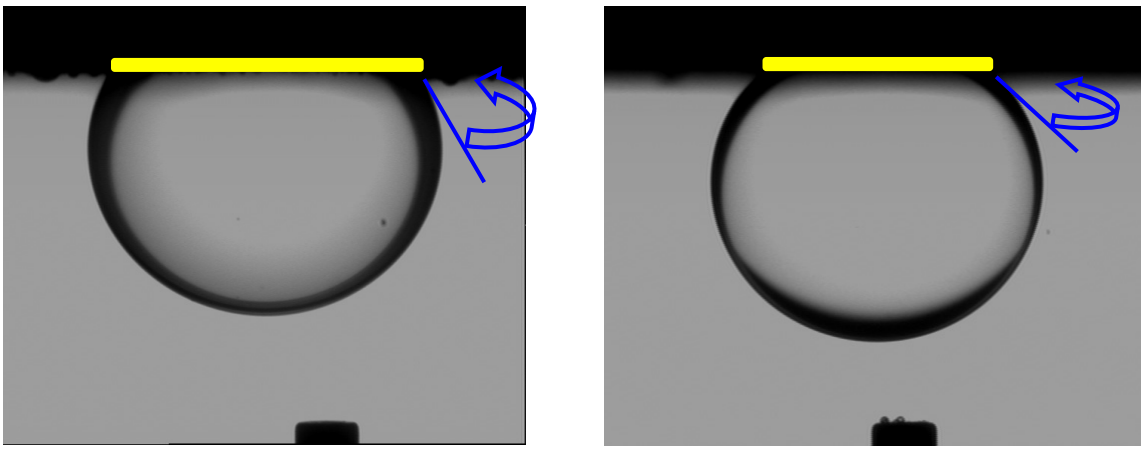

Figure 5-16: Digital images of oil drops on glass immersed in carbonated distilled water at: A) P=400 psi with θ=55.12° and B) P=2000 psi with θ=49.30°. The temperature of the system is 38 °C and the oil drop size is between 10-11 μL .

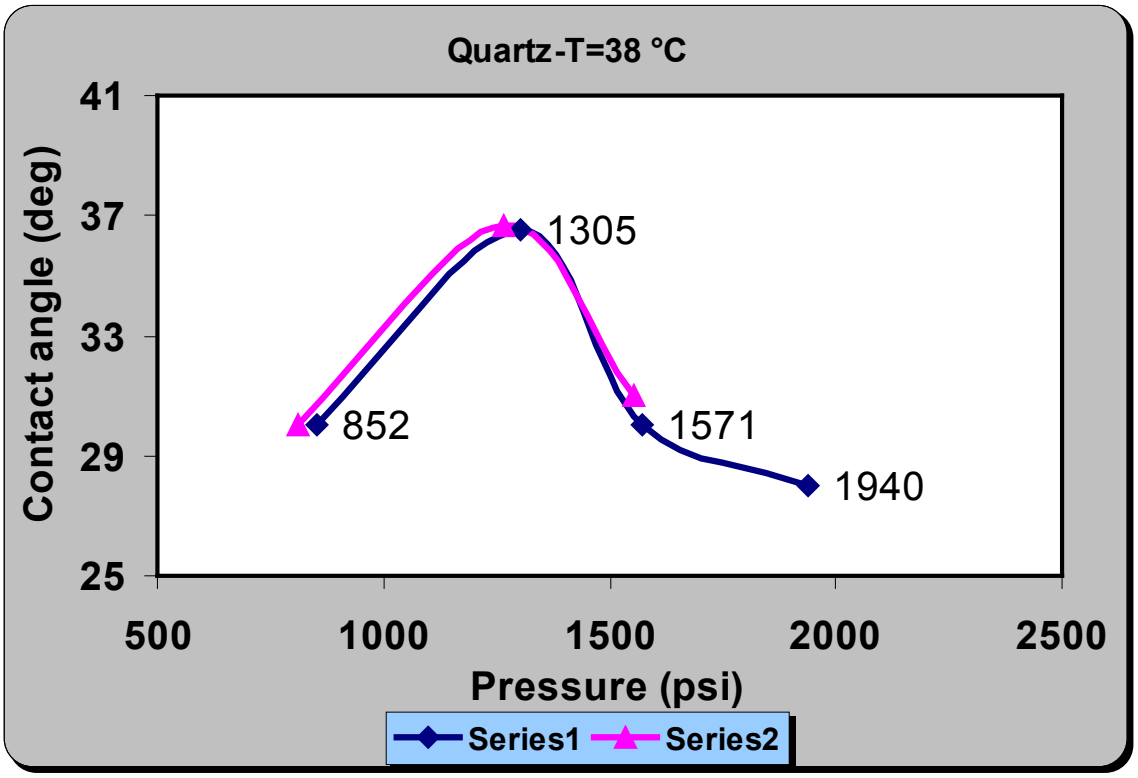

Figure 5-17: First vs. second series of oil/CB contact angles, measured on the quartz slide immersed in carbonated brine, as a function of pressure at T=38 °C.

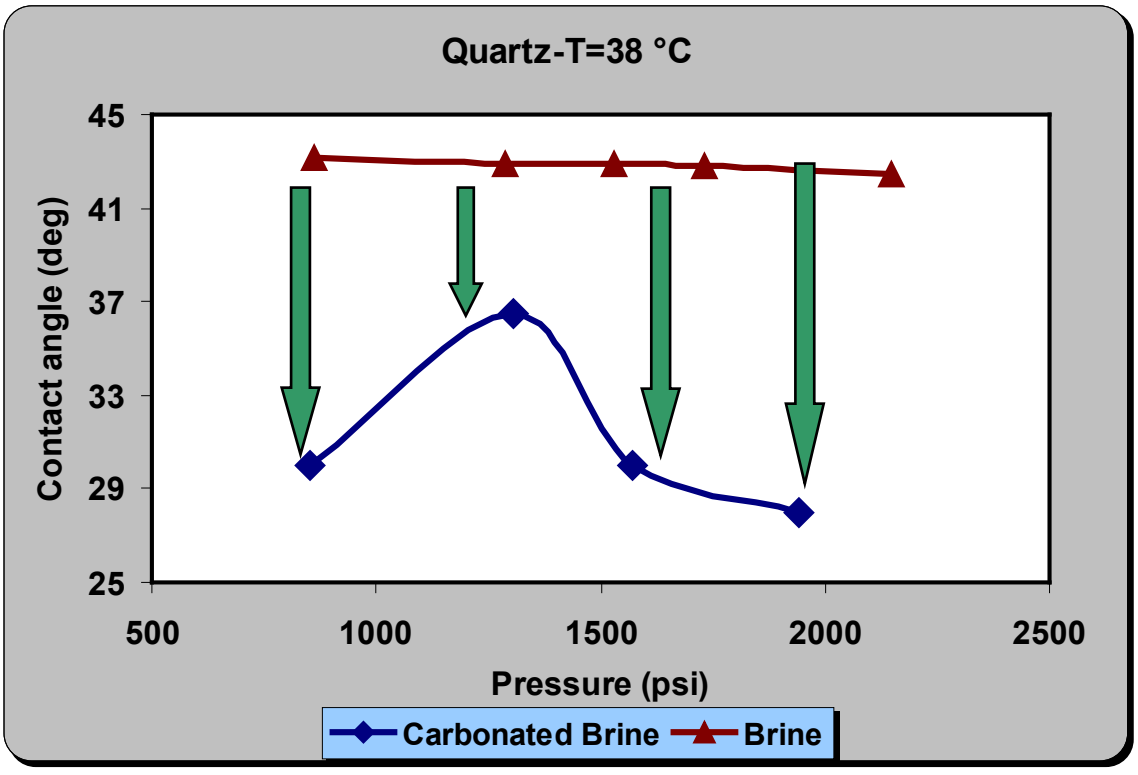

Figure 5-18: Contact angles measured between oil and carbonated brine, measured on a quartz slide immersed in carbonated brine (blue dots) versus those on a quartz slide immersed in plain brine (brown dots), as a function of pressure at T=38 °C.

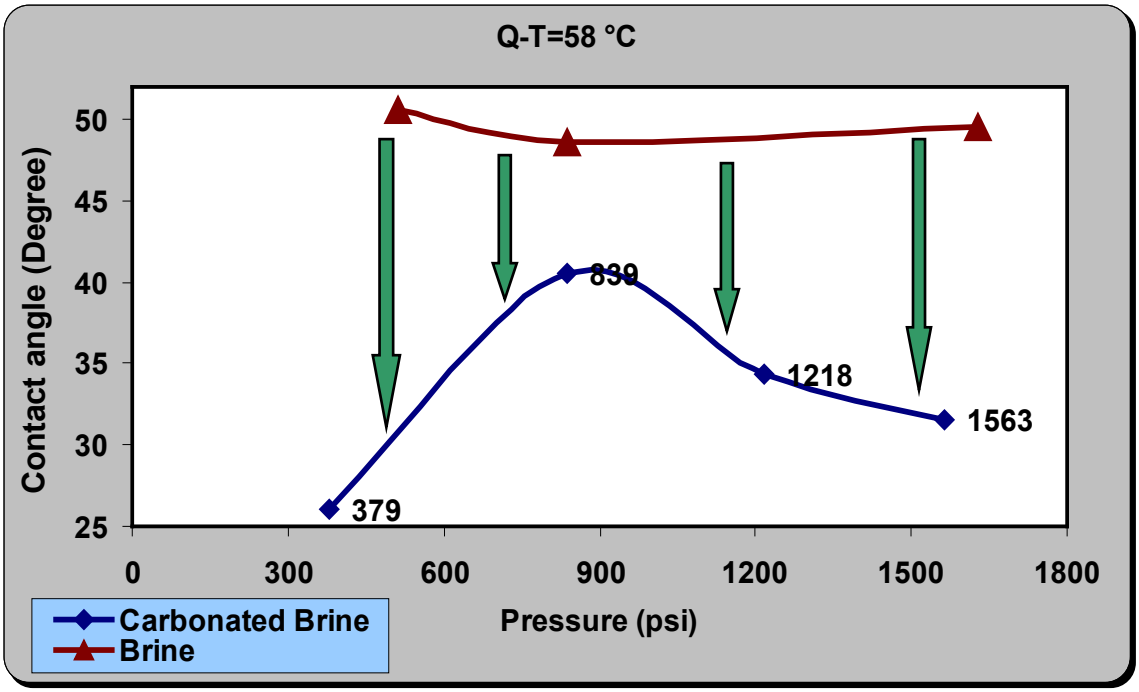

Figure 5-19: Contact angles measured between oil and the aqueous phase on a quartz slide immersed in carbonated brine (blue dots) and immersed in brine (pink points), as a function of pressure at T=58 °C.

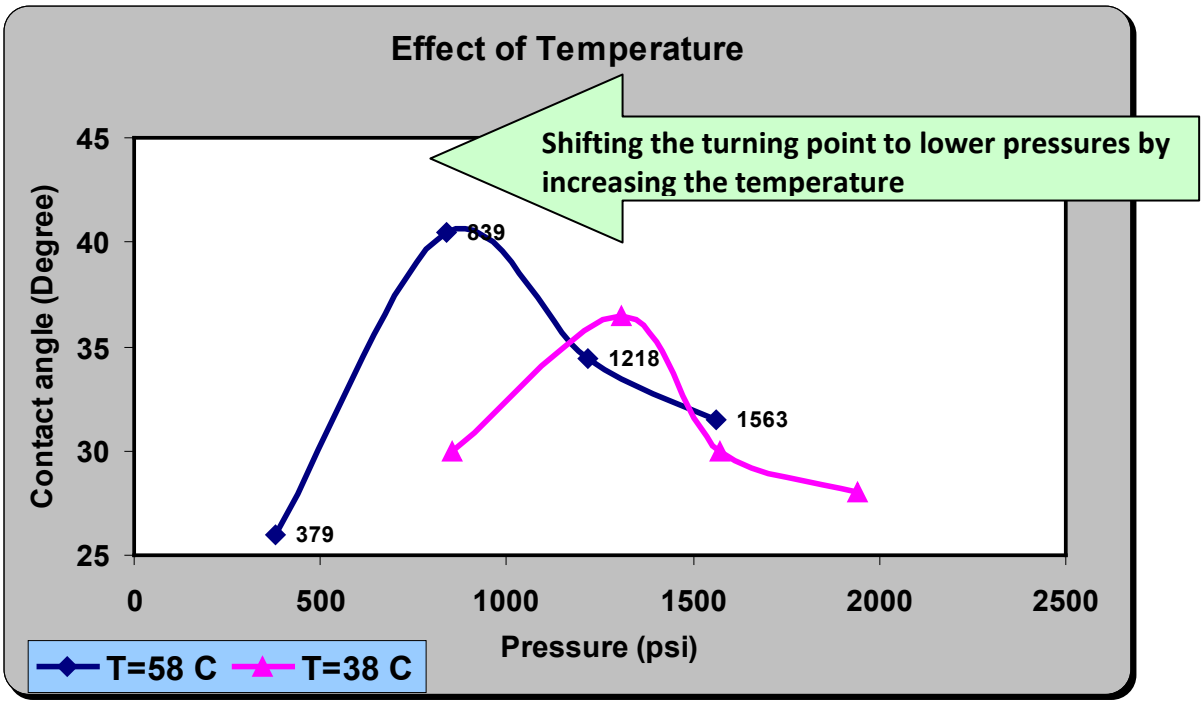

Figure 5-20: Comparison of contact angles measured between CB and oil on a quartz slide as a function of pressure at T=38 °C with T=58 °C.

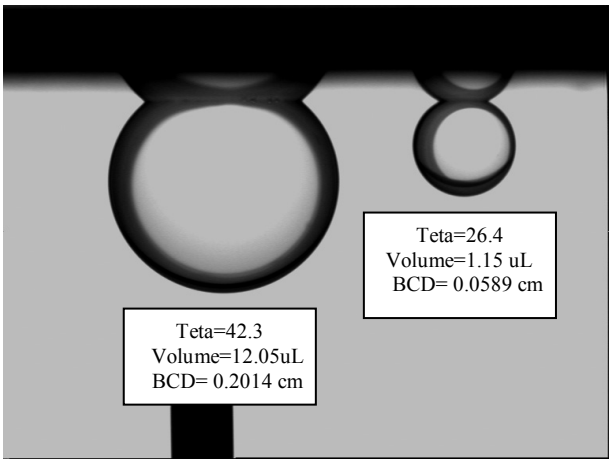

Figure 5-21: Measured the contact angle between oil and brine on a quartz slide (by applying Tangent Method 1 which is more accurate than Tangent Method 2 for smaller droplets in a frame), at 1615 psi and 38 °C.

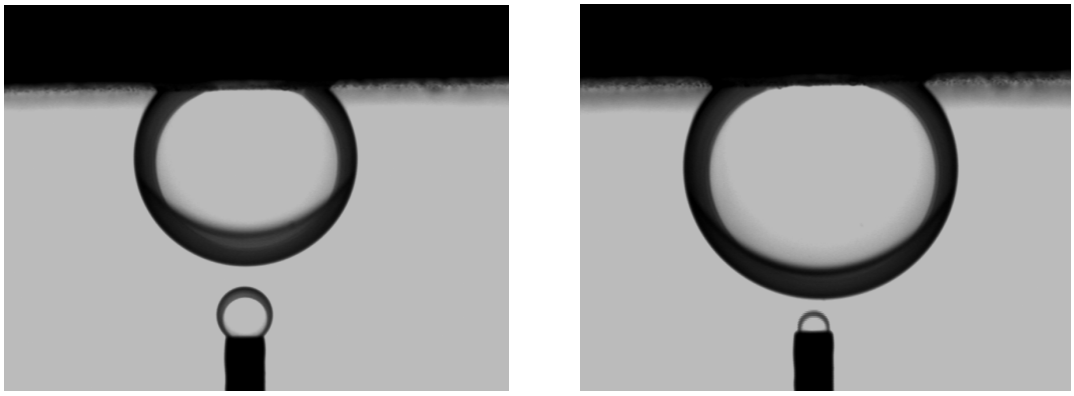

A B

Figure 5-22: Effect of oil droplet size on the contact angle in brine/n-decane/quartz system at P=1627 psi, T=58 °C, when oil droplet size is A) 11.23 μL, BCD=0.2244 cm, θ=49.5 and B) 21.13 μL, BCD=0.2818 cm, θ=49.0.

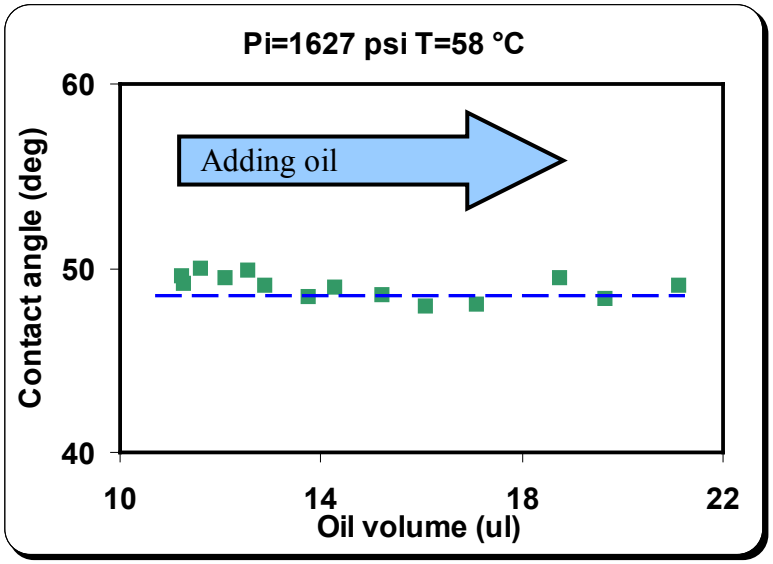

Figure 5-23: Dependency of the apparent contact angle on oil droplet size, quartz/brine/n-decane system.

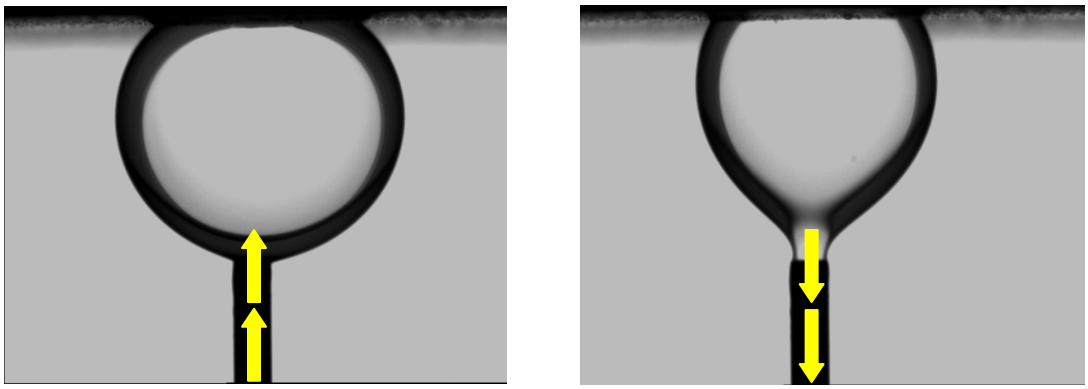

Figure 5-24: The position of an oil droplet and the needle to measure advancing (left hand side) and receding (right hand side) contact angles in a quartz/brine/n-decane system at 1627 psi and 58 °C.

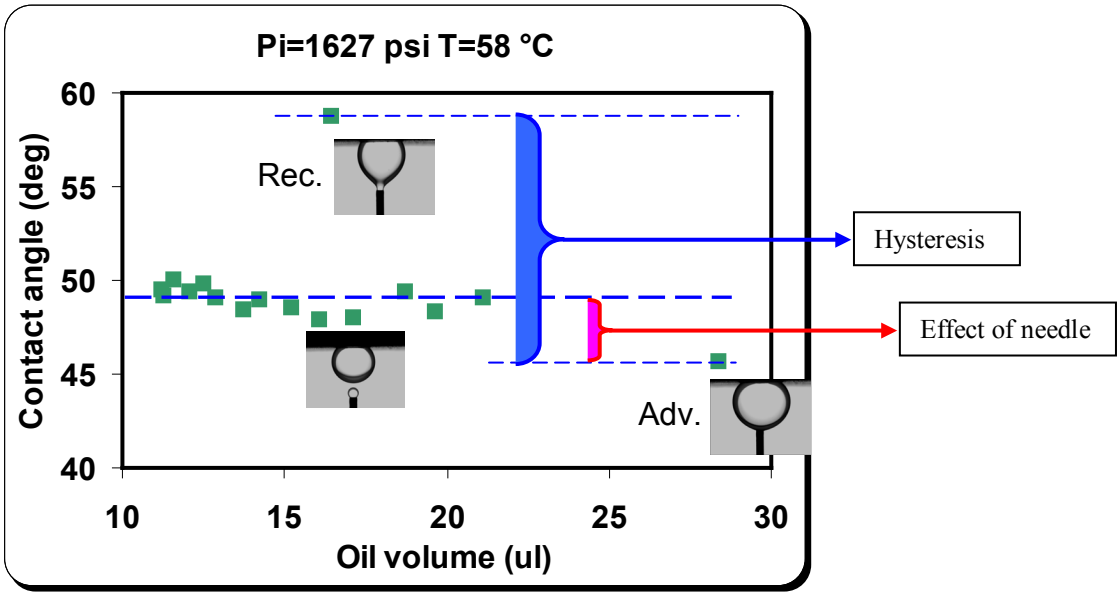

Figure 5-25: Measured advancing, receding and the apparent contact angles measured between oil and brine on a quartz slide at T=58 °C.

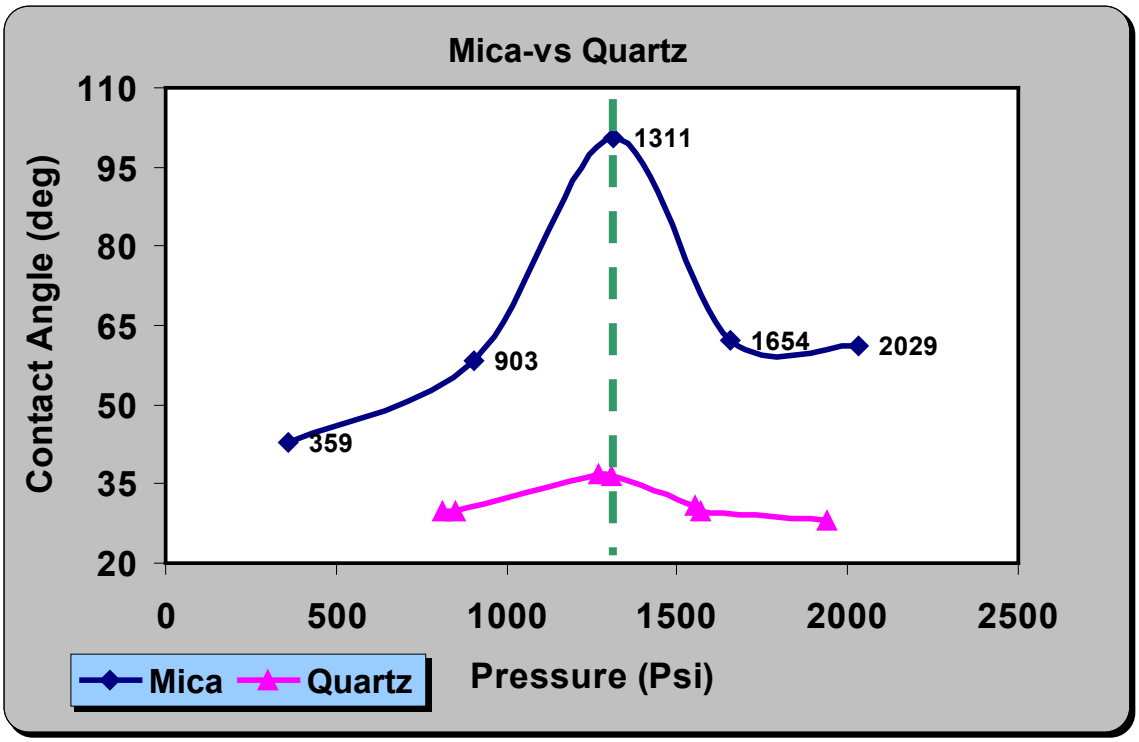

Figure 5-26: Contact angles measured between oil (n-decane) and carbonated brine on the Mica and Quartz slides, as a function of pressure at T=38 °C.

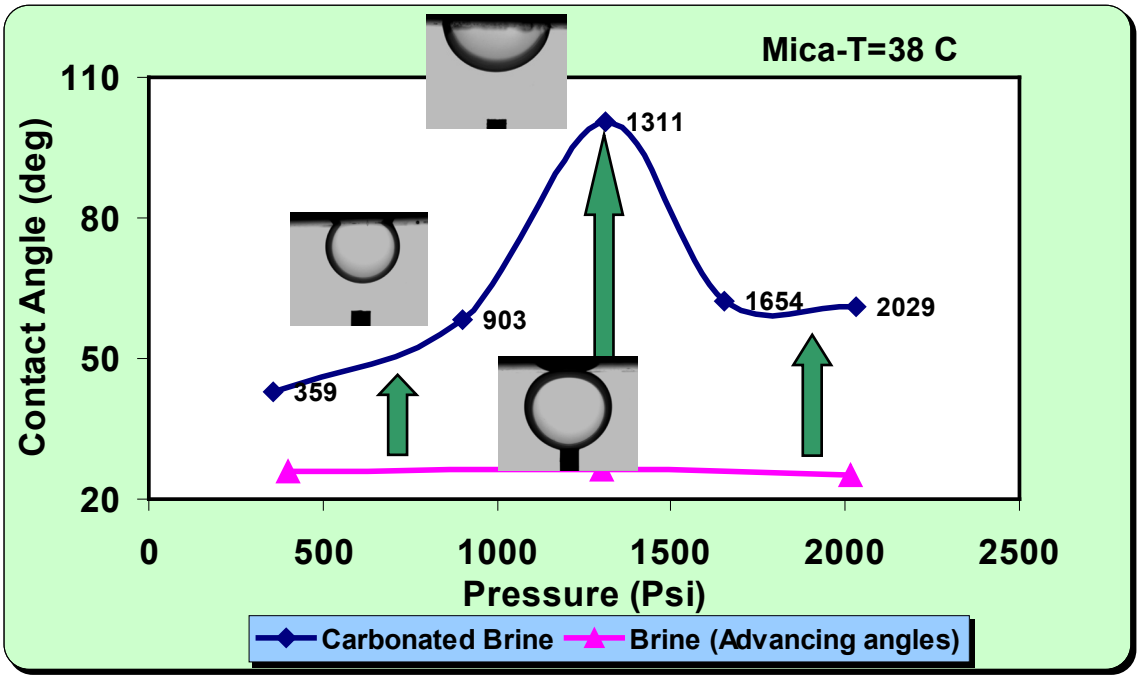

Figure 5-27: Contact angles measured between oil and aqueous phase on the mica slide in the carbonated brine (blue points) and brine (pink points), as a function of pressure at T=38 °C.

A **B** **C**

Figure 5-28: Different wettability behaviours at different conditions for mica at 38 °C: A) Advancing contact angle= 26.2°, in brine at 1300 psi; B) Contact angle= 58.2°, in carbonated brine at 903 psi; C) Contact angle= 100.4°, in carbonated brine at 1311 psi.

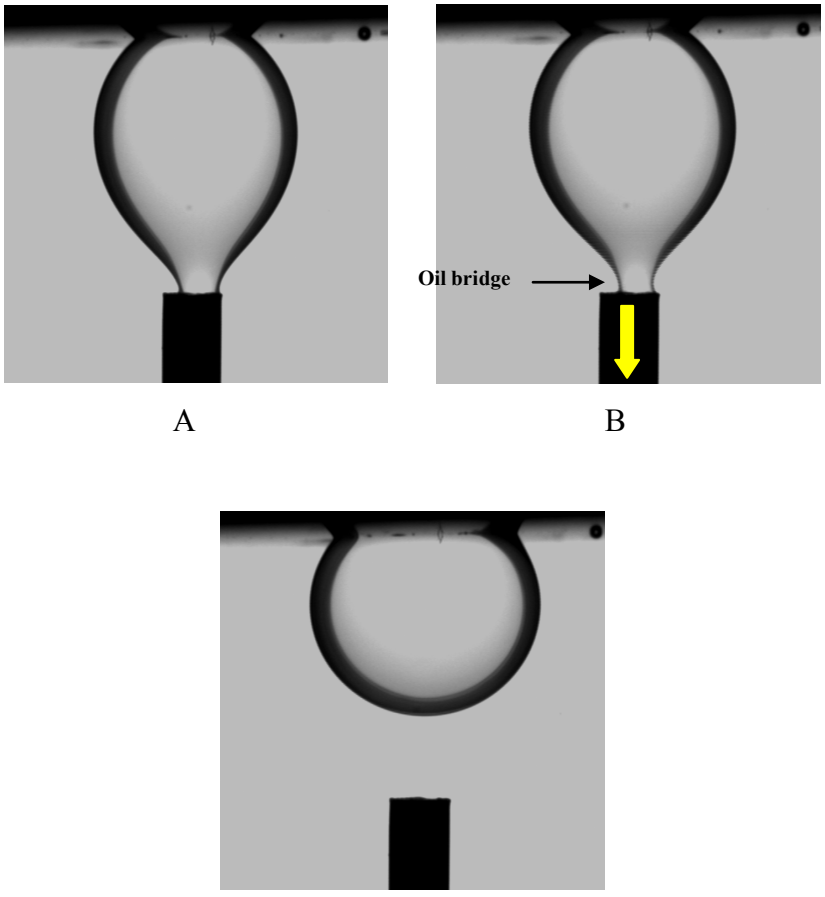

A B

C

Figure 5-29: position of oil droplet with the surface and needle when A) It is connected to the surface with high advancing contact angle in water; B) Bridge is about to break due to de-wetting process; C) After the oil bridge was ruptured. Mica-carbonated brine-n-decane system at 903 psi and 38 °C.

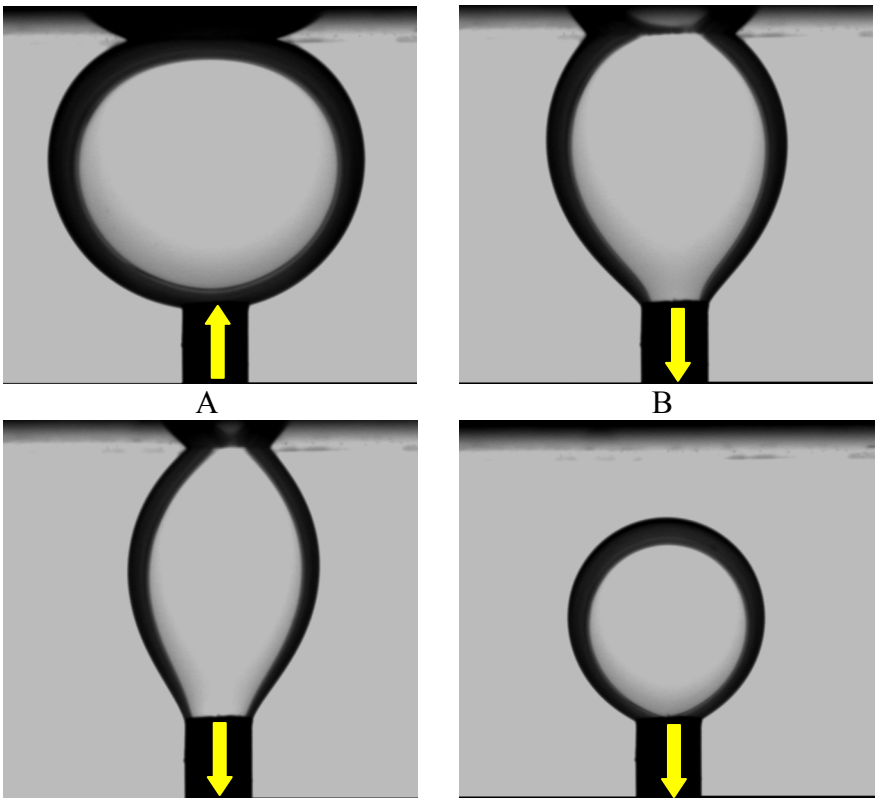

Figure 5-30: Position of oil droplet when A) it is connected to the surface with low advancing contact angle in water; B) and C) it is being detached from the surface during de-wetting process; D) is completely detached.

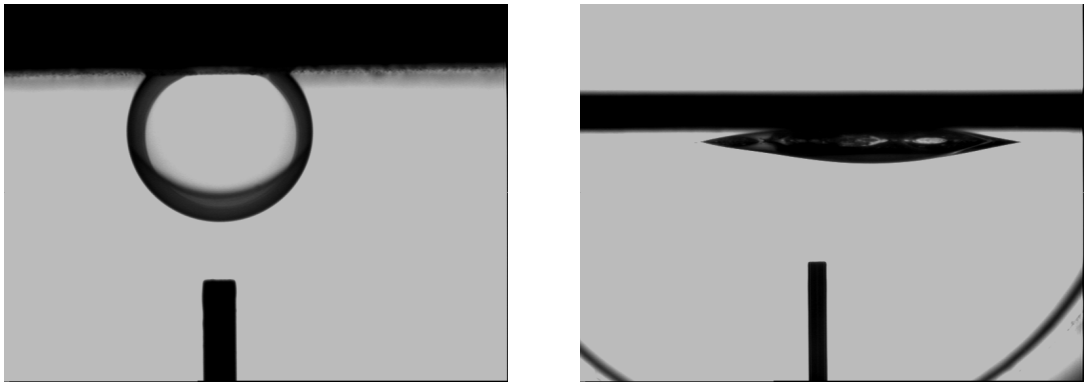

Figure 5-31: Different wettability conditions when quartz surface is initially wetted by A) brine (contact angle=49.5°); B) oil(contact angle=170°); at 1600 psi and 58 °C.

6 Chapter 6: Solubility and Diffusion Coefficient Measurement Experiments

6.1 Introduction

In the previous chapter, the impact of CO_2 dissolved in water on one of the important parameters of solid-fluid system (i.e. wettability) was studied. In this chapter, two other key parameters on CWI process are experimentally estimated. These are CO_2 diffusion coefficient and its solubility in water. The former controls the rate of mass transfer and the latter determines the amount of CO_2 delivered by carbonated water.

As pointed out already in the fluid system section (Chapter 2), to distinguish between the mineral oils and the aqueous phase, the colour of the water was changed to blue using a water-soluble dye (Water Blue $C_{37}H_{27}N_3Na_2O_9S_3$) with 0.6 weight percent dye concentration. One of the concerns in using this substance in water is changing these two physical properties, which consequently could affect the results of the micromodel experiments. In this chapter, the impact of blue dye on these two important parameters is also investigated.

6.2 Solubility Tests

Previously, the impact of CO_2 solubility in water as one of the important parameters on the performance of the CWI process was visually investigated (Chapter 3). Here, the question that is going to be addressed is whether this amount of blue dye changes the CO_2 solubility in water. One of the simple experimental methods to measure the amount of dissolved CO_2 in carbonated water is to drop the pressure down to atmospheric pressure to separate CO_2 from the water in order to collect and measure it later on.

6.2.1 Procedure of Solubility Test

The following procedure was carried out to estimate the CO_2 content in CW:

Figure 1 shows a schematic diagram of the system used for these measurements. One side of a piston cell was initially completely emptied by pushing the piston to one end, while the other side was pressurised by water to 2000 psi. After vacuuming the empty side a certain volume of CW (35 cc) at pressure and temperature conditions of the experiments was transferred into the piston cell. The other side of the cell was then connected to a hydraulic pump to drop the pressure. The volume of the pulled back water and the pressure of the system were recorded while dropping the pressure to the atmospheric conditions. In this set of experiments, the flow rate of the pump was changed several times, due to the change of the compressibility of the system as a result of gas liberation from CW. Finally, to double check the measured data, CO_2 was transferred to a gas meter to measure the gas volume. The remaining water in the CW side was collected and measured using a measuring tube. Eventually, the measured volume of CO_2 was divided by the volume of water to estimate the solubility of CO_2 in CW in the units of sm^3 of CO_2/sm^3 of water.

Figure 2 shows the recorded volume of the pump at different pressure during one of the solubility tests. As this plot shows, the retract rate has not been constant during the experiment and it was boosted several times to cope with the pressure drop rate.

6.2.2 Results and Discussion

Performing the procedure described above, the solubility of CO_2 in blue carbonated water at 2000 psi and 38 °C was estimated to be around 33 sm^3 CO_2/sm^3 water. This value is adequately consistent with the data reported in the literature with the same units (Baviere, 1991). Hence, based on the results of these experiments it can be concluded that the blue dye, at least with the concentration that was used here (6000 ppm), does not significantly change the CO_2 solubility in water.

Based on the results of these tests, the value for CO_2 content in the partially saturated CW, used in Experiments No.4-6, was estimated to be 17.8 CO_2 sm^3/water sm^3 at 2000 psi and 38 °C.

6.3 Diffusion Coefficient Measurement Experiments

As mentioned already, another important parameter that affects the performance of carbonated water injection (CWI) is the rate of CO_2 diffusion from the source to the oil phase, which is directly related to the CO_2 diffusion coefficient. This parameter determines the swelling rate of oil and oil recovery.

There are several experimental methods for measuring molecular diffusion coefficient. These can generally be categorized into direct and indirect methods. In the direct methods, which are based on compositional analysis, composition of gas diffused into the liquid phase at different times is measured. The drawback of this method is that it is time-consuming and expensive. Indirect methods, however, are simpler and cheaper. These methods are based on measuring certain parameters of the system, which change due to diffusion of gas into the liquid phase. These parameters could be pressure, the position and velocity of the gas-liquid interface, the conductivity of the liquid phase, the volume and the shape of the diffusing solute.

Zappe et al. (2000) presented a method based on measuring the electrical conductivity of a water drop, which increases by dissolving CO_2. The increase in conductivity by CO_2 dissolution is because of the formation of carbonic acid in the water phase.

Two more new methods developed by Yang and Gu (2003, 2005, 2006) for measuring gas diffusivity in heavy oil (HO) by dynamic pendant drop shape analysis (DPDSA) and by dynamic pendant drop volume analysis (DPDVA). In this method, during the diffusion process, the density of gas and HO drop varies with time and position. Interfacial tension reduction and oil swelling as a result of diffusion of the solute change the shape and the volume of the oil drop. These data are used to estimate diffusivity.

Riazi (1996) proposed a method known as the pressure decay method to determine diffusion coefficient of dense gases in liquids using a constant-volume constant-temperature PVT cell. In this method, which has been adopted here as described in the next section, the experimental data required to estimate diffusion coefficient are gas pressure and position of interface both versus time.

6.3.1 Procedure of Pressure Decay Experiments

In this study to estimate the diffusion coefficient of CO_2 in water ($D_{CO2\text{-}water}$)at the conditions corresponding to the micromodel experiments and to investigate the effect of the blue dye used in these experiments on $D_{CO2\text{-}water}$, two experiments using the Riazi's pressure decay method, were performed.

The experimental setup used for these experiments consists of a PVT cell placed in a constant-temperature oven at 38 °C. During the experiments, the height of the CO_2/water interface in the cell was observed through the glass window and recorded. The cell pressure was measured and recorded by a high-precision pressure gauge (Figure 3).

To minimise the error caused by the initial delay in recording the data, the modified procedure proposed by Tharanivasan et al. (2006) was used in the pressure decay tests. After leak testing the cell, CO_2 was first injected into the cell and pressurised to the desired test pressure (2000 psia). Water was then transferred in the cell and immediately the recording of the interface position and the cell pressure began. To avoid evaporation of water and subsequent shrinkage, prior to each test, CO_2 was hydrated with water in a rocking cell at the pressure and temperature of the test.

Two main tests, one with clear water and the other with blue-dyed water, were carried out at 2000 psi and 38 °C.

It should be mentioned that the density of water increases as a result of dissolution of CO_2 in water, (Hebach, et al., 2004). Hence, during the tests, some degree of free convection was also taking place because of the density gradient in this experimental setup. To alleviate this free convection effect, a small volume of water (short water height) was used, i.e. only around 7 cm^3 water or blue dyed water was transferred into the 100 cm^3 pressure cell in these experiments.

6.3.2 Results and Discussion

Figures 4 and 5 show the results of pressure decay data versus time for CO_2-clear water and CO_2-blue dyed water systems at 2000 psi and 38 °C, respectively.

For both tests shown in these figures, the trends of the pressure drop are quite similar. This suggests that the CO_2 diffusion coefficient in both the water and blue dyed water, which controls the rate of pressure drop, is similar. This is a qualitative observation of the impact of CO_2 diffusion coefficients in these two systems. However, to estimate the diffusion coefficient of CO_2 in water and in blue water, and to quantitatively compare this parameter in the different systems, a mathematical model was developed as described in the next section.

6.4 Mathematical Modelling

6.4.1 Introduction

Based on the proposed pressure decay method (Riazi, 1996), several researchers have estimated the diffusivity of gas components in water and crude oil (Sachs, 1998; Zhang et al., 2000; Civan and Rasmussen, 2002; Tharanivasan et al., 2004 and 2006; Sheikha et al., 2005). These authors have used analytical or graphical methods to analyse the data and estimate the diffusion coefficient. In these methods, major simplifying assumptions have been made. Solving this problem numerically eliminates these simplifying assumptions and allows us to obtain more accurate results consistent with the real experimental conditions. To the best of the author's knowledge this is the first time that numerical method has been applied to model pressure decay experiments since this method was proposed by Riazi (1996).

This section starts with a discussion on the statement of the problem including the underlying assumptions made in the model. The governing equations and the numerical solution technique, as well as initial and boundary conditions, are presented next, before reporting the modelling results simulating two pressure decay experiments conducted in the laboratory. Finally, this chapter ends with the conclusions of this study, highlighting the key findings of the pressure decay experiments and the developed mathematical modelling approach.

6.4.2 Problem Statement

Figure 6 shows the designed model with its mesh structure built using COMSOL multi-physics software to simulate the results of two experiments conducted in the PVT cell,

shown in Figures 4-5. This software is a powerful mathematical package, which is used to solve partial differential equations based on the finite element method.

In the developed model, CO_2 from the upper domain, the CO_2 phase, diffuses into the lower domain, the water phase. As a result of mass transfer into the water, the CO_2 pressure drops at a rate controlled by the CO_2 diffusion coefficient in the water phase ($D_{CO2\text{-}water}$). The equilibrium pressure is determined by the solubility of CO_2 in the liquid phase at the given temperature.

The following assumptions have been made to model this process:

1. No chemical reaction between water and CO_2.
2. No convection as a result of the density gradient in water.
3. No mass transfer from the water into CO_2.
4. No resistance against mass transfer at the CO_2/water interface.
5. No pressure gradient in the CO_2 phase.
6. No movement for the water/CO_2 interface, swelling of water due to CO_2 dissolution is negligible.
7. An isothermal process.
8. A constant diffusion coefficient.
9. The thermodynamic equilibrium at the CO_2/water interface is satisfied by Henry's law, (Equation 1). Hence, the concentration of the CO_2 in the water at the interface can be expressed in terms of pressure as follows:

$$P(t) = K_h C(t) \tag{6.1}$$

where

- $C(t)$ is the CO_2 concentration in the water, [kmol m^{-3}]
- K_h is the Henry's law constant, [Pa m^3 $kmol^{-1}$]
- $P(t)$ is the pressure of the gas phase, [Pa.]

It should be noted that all the variables in the model have been expressed and used in SI units.

6.4.3 Governing Equations

Based on the second Fick's law, CO_2 concentration in water is a function of time (t) and position (x, y and z); Equation 2 shows this relationship in this 1D (one dimensional) system:

$$\frac{\partial C_{CO2}(t,z)}{\partial t} = \frac{D_{CO2}\partial^2 C_{CO2}(t,z)}{\partial z^2}, \tag{6.2}$$

where

- C_{CO2} is the CO_2 concentration in water, [kmol m^{-3}],
- D_{CO2} is the diffusion coefficient of CO_2 in water, [m^2 s^{-1}].

Equation 2 is used to determine the CO_2 concentration in the water domain at any time and position.

The CO_2 pressure in the gas phase is related to its volume and number of moles by real gas law:

$$PV=ZnRT \text{ or } P=Z\,C'_{CO2}\,RT, \tag{6.3}$$

where

- C'_{CO2} is the CO_2 concentration in the gas phase, [kmol m^{-3}],
- R is the universal gas constant =8314 [J $kmol^{-1}$ K^{-1}],
- T is the absolute temperature of the PVT cell, [K],
- Z is the CO_2 compressibility factor [-].

The number of moles of CO_2 diffused into water is proportional to pressure change within the CO_2 phase. The mathematical form of this mass balance relationship, after differentiating with respect to time, assuming constant Z, can be obtained by:

$$\frac{dP}{dt} = ZRT.\frac{dC'_{CO2}}{dt} \tag{6.4}$$

The absolute value of CO_2 concentration in the CO_2 domain, C'_{CO2} , is related to the CO_2 concentration variation in water. With negligible volume change for the two domains, assumption six, this can be expressed as follows:

$$\frac{\partial C'_{CO2}(t)}{\partial t} = -\frac{\partial C_{CO2}(t)}{\partial t}\frac{H_L}{H_G}, \tag{6.5}$$

where

- H_G is the height of the gas column, CO_2, [m],
- H_L is the height of the liquid column, water, [m].

In Equation 5, $\frac{\partial C_{CO2}(t)}{\partial t}$ is the volumetric average of the CO_2 concentration gradient in water with respect to time, at any time, and is calculated using Equation 6.

$$\frac{\partial C_{CO2}(t)}{\partial t} = \frac{\int_0^{H_L} \frac{\partial C_{CO2}(t,z)}{\partial t} dz}{z(t)} \tag{6.6}$$

Although Z was assumed constant when deriving Equation 4, its variation with time during the simulation can be considered. To do so, it is noted that Z is related to the CO_2 density by the real gas law:

$$Z(t) = \frac{P(t)M_{CO2}}{\rho_{CO2}(t)RT} \tag{6.7}$$

Measured CO_2 density values obtained from the literature (NIST database) were plotted versus pressure at constant temperature of 311 K, as shown in Figure 7. A line, described by Equation 8, was fitted to the measured data points.

$$\rho_{CO2}(t) = 2E-5P(t) + 508.62 \tag{6.8}$$

In the model, CO_2 density is updated based on Equation 8. The updated density is used in Equation 7 to estimate Z(t). The updated Z(t) is then used to estimate pressure gradient with respect to time, using Equation 4.

6.4.4 Initial and Boundary Conditions

In this model, there are two domains, one for CO_2 and one for water. To solve the set of equations, two initial conditions (I.C.), one for each (CO_2 and water) domain, are needed.

These initial conditions are:

- At the beginning of the process, the concentration of CO_2 in water is equal to zero. Thus the first initial condition is given by:

$$C_{CO2}(z, t=0) = 0, \qquad 0 \le z \le H_L$$

- The initial pressure of CO_2 is known.

$$P(t=0) \cong Pi$$

The boundaries of the domains are labelled in Figure 6B. The corresponding boundary conditions are:

- For the lower boundary of the water domain, labelled 8, the mass transfer flux at any time is equal to zero. Therefore, the following Neumann (second type) boundary condition can be applied to this boundary:

$$\frac{\partial C_{CO2}(z=0,t)}{\partial z} = 0 \qquad t \ge 0$$

- At the CO_2/water interface, labelled 5 (Figure 6B), the CO_2 concentration in water is related to the CO_2 pressure using Henry's law (assumption 9):

$$C_{CO2}(z = H_L, t) = P(t) / K_h \qquad z = H_L, t \ge 0 \tag{6.9}$$

The CO_2 boundaries, labelled 1 to 3, and the left and right hand side boundaries of water, labelled 6-7, similarly to boundary labelled 8, are all no flow boundary conditions. Figure 8 shows the initial and boundary conditions and the equations used for the water domain to simulate this CO_2 mass transfer process.

6.4.5 Solution Technique

The partial (Equation 2 for water) and ordinary (Equation 4 for CO_2) differential equations together with auxiliary equations (Equations 5 to 8) and the associated boundary and initial conditions described above were solved using COMSOL multi-physics. A diffusion application mode, Equation 2, and a PDE application mode, Equation 4, are used. The volumetric average CO_2 concentration gradient with respect to time (Equation 6) was obtained by defining an integral variable on the water sub-domain.

6.4.6 Results

As mentioned previously, this model was developed to simulate the two pressure decay tests which were performed in the laboratory. In these two tests, the clear and blue

water phases were separately put in contact with CO_2 in the PVT cell. The results of these two experiments, Figures 4 and 5, were used to determine D_{CO2}. There are two parameters in the developed model, which affect the pressure decay curve, i.e. the equilibrium pressure and diffusion rate. The total amount of pressure drop, i.e. the final equilibrium pressure in the gas phase, is restricted by the Henry's law constant. The rate of pressure drop, i.e. the required time to get to the equilibrium condition is controlled by D_{CO2}. These two uncertain properties have been estimated to minimise the difference between the model and the test results.

Figure 9 shows that D_{CO2} =4E-8 m^2s^{-1} gives the same pressure decay curve in the model as that in the experiment conducted using clear water. The Henry's constant has been estimated as 8.1E5 pa m^3 $kmol^{-1}$. Figure 10 shows the variation of gas compressibility factor and CO_2 density with time in this model. As can be seen, both of them decrease with time.

The modelling results of the blue water test are shown in Figure 11. The best estimated values for the diffusion coefficient and Henry's constant for this test are 4E-8 m^2s^{-1} and 6.3E5 pa m^3 $kmol^{-1}$, respectively. Since the estimated diffusion coefficients of both clear and blue water are the same, it can be concluded that blue dye does not change this parameter.

Figure 12, like Figure 10, shows the reduction of the CO_2 compressibility factor and density with time in the blue water model. A summary of experimental conditions and estimated values of D_{CO2} and K_h are found in Table 1.

It should also be added that the estimated value of D_{CO2} , 4E-8 m^2s^{-1}, is in good agreement with the value estimated based on Zappe et al.'s (2000) results: 1.02E-8, which was obtained by analysing their data measured at 12.5 Mpa and 311K. Fjelde et al. (2008) also reported D_{CO2}=1.98E-8 m^2s^{-1} using a graphical method to analyse the results of a pressure decay experiment that they conducted. In their test, the pressure and temperature, 4718 psi and 328 K, respectively, were higher than those, in the experiments conducted here, i.e. 2000 psi and 311 K, respectively.

One reason for the difference between these two data could be related to the different experimental methods and models, which have been applied to estimate diffusion coefficient. It should be noted that Zappe et al. (2000) used a water droplet to monitor the change in electrical conductivity as a result of CO_2 dissolution. They then mapped the corresponding equations for change in electrical conductivity to that of mass transfer to obtain the mass transfer coefficient. They have also proposed an equation for calculation of the CO_2 diffusion coefficient following a similar analogy.

As mentioned already, the density of water increases as a result of dissolution of CO_2 in water, (Hebach, et al. 2004). Hence, there is some level of free convection, because of the density gradient in this experimental setup. The slightly greater value of diffusivity estimated from the pressure decay test than that from the literature data could also be due to this free convection effect in our experiment. Using a smaller volume of water, a shorter height of the water column, can alleviate this to some extent.

The estimated values for Henry's constant are also in good agreement with the recent literature data. Majer, et al. (2008) gave a table of ratios of this parameter at given pressures to the corresponding value at atmospheric pressure. The CO_2 Henry's constant in water at atmospheric conditions for the test temperature was measured by Alanezi, et al (2008). Using the reported data in these two publications, a value of 7.43E5 pa m^3 $kmol^{-1}$ for Henry's constant was estimated under the test conditions, which is in close agreement with the value obtained when matching the experimental pressure decay curve with that of the mathematical model.

6.5 Conclusions

- The results of the CO_2 solubility tests showed that the addition of the blue dye to water did not change CO_2 solubility considerably.
- The results of the CO_2 diffusion coefficient measurement tests showed that the addition of the blue dye to water did not change CO_2 diffusion coefficient.
- The pressure drop of CO_2 in the PVT cell as a result of diffusion into the water phase was successfully simulated.
- In pressure decay test there are two uncertain parameters that affect pressure decay curve differently. The final equilibrium state is determined by Henry's

constant in the model. The rate of the pressure change as a function of time depends on the rate of diffusion, i.e. the CO_2 diffusion coefficient in the water phase.

- Diffusion coefficient of CO_2 in both clear and blue water was estimated at 4E-8 m^2s^{-1}, which is in good agreement with the literature data.
- Henry's constant was estimated as 8.1E5 pa m^3 mol^{-1} for clear water and 6.3E5 pa m^3 mol^{-1} for blue water at 2000 psi and 38 °C. These values also are in good agreement with the literature data.

6.6 References

Alanezi, K., Somerfield, C., Mee, D., Hilal, N., 2008: ''Parameters affecting the solubility of carbon dioxide in seawater at the conditions encountered in MSF desalination plants'', Desalination 222 548-571.

Baviere, M., 1991: ''Basic concepts in enhanced oil recovery processes'', Published for SCI by Elsevier Applied Science, in London and New York.

Civan, F., and Rasmussen, M.L., 2002: ''Improved Measurement of Gas Diffusivity for Miscible Gas Flooding under Nonequilibrium vs. Equilibrium Conditions'', SPE paper 75135.

Fjelde, I., Zuta, J., Duyilemi O.V., 2008: ''Oil Recovery from Matrix during CO_2-Foam Flooding of Fractured Carbonate Oil Reservoirs'', SPE paper 113880, Italy 9–12 June 2008.

Hebach, A., Oberhof, A. and Dahmen, N., 2004: ''Density of Water + Carbon Dioxide at Elevated Pressures: Measurements and Correlation'', Journal of Chemical and Engineering Data, Vol. 49, No. 4.

Majer, V., Sedlbauer, J., Bergin G., 2008: ''Henry's law constant and related coefficient for aqueous hydrocarbons CO_2 and H2S over a wide range of temperature and pressure'', Fluid Phase Equilibria 272, 65-74.

National Institute of Standards and Technology Website: http://www.nist.gov/srd/, date accessed 23 April 2009.

Riazi, M.R., 1996: ''A new method for experimental measurement of diffusion coefficients in reservoir fluids'', Journal of Petroleum Science and Engineering 14, 235-250.

Sachs, W., 1998: ‘‘The diffusional transport of methane in liquid water: method and result of experimental investigation at elevated pressure’’, Journal of Petroleum Science and Engineering 21, 153-164.

Sheikha, H., Pooladi-Darvish, M., and Mehrotra A.K., 2005: ‘‘Development of Graphical Method for Estimating the Diffusivity Coefficient of Gases in Bitumen from Pressure-Decay Data’’, Energy & Fuels, 19, 2041-2049.

Tharanivasan, A.K., Yang C., and Gu Y., 2004: ‘‘Comparison of three interface mass transfer models used in the experimental measurement of solvent diffusivity in heavy oil’’, Journal of Petroleum Science and Engineering 44, 269-282.

Tharanivasan, A.K., Yang C., and Gu Y., 2006: ‘‘Measurement of Molecular Diffusion Coefficient of Carbon Dioxide, Methane and Propane in Heavy Oil under Reservoir Conditions’’, Energy & Fuels, 20, 2509-2517.

Yang, C. and Gu, Y., 2003: ‘‘Numerical Modeling of Solvent Diffusion in a Pendant Drop of Heavy Oil’’, Intl. Conference on Computational Heat and Mass Transfer, Banff, Canada.

Yang, C. and Gu, Y., 2005: ‘‘New Experimental Method for Measuring Gas Diffusivity in Heavy Oil by the Dynamic Pendant Drop Volume Analysis (DPDVA)’’, Ind. Eng. Chem. Res., 44, 4474.

Yang, C. and Gu, Y., 2006: ‘‘A New Method for Measuring Solvent Diffusivity in Heavy Oil by Dynamic Pendant Drop Shape Analysis (DPDSA)’’, SPE Journal 48-57. SPE paper 84202.

Zappe, J., Wesch, A., and Ebert, K. H., 2000: ‘‘Measurement of the Mass Transfer into Single Drops in the System of Water/Supercritical Carbon Dioxide’’, Journal of Colloid and Interface Science 231, 1–7.

Zhang Y.P., Hyndman C.L., and Maini B.B., 2000: ‘‘Measurement of gas diffusivity in heavy oils’’, Journal of Petroleum Science and Engineering 25, 37-47.

	Water height, H_L (mm)	CO_2 height, H_G (mm)	Initial pressure (psi)	Diffusivity of CO_2 in water, D (m^2s^{-1})	Henry's law constant, K_h ($pa.m^3mol^{-1}$)
Clear water	6.15	93.85	2000	4E-8	8.1E5
Blue water	6.15	93.85	2000.92	4E-8	6.3E5

Table 6-1: Experimental conditions and estimated parameters of two decay pressure tests at 38 °C.

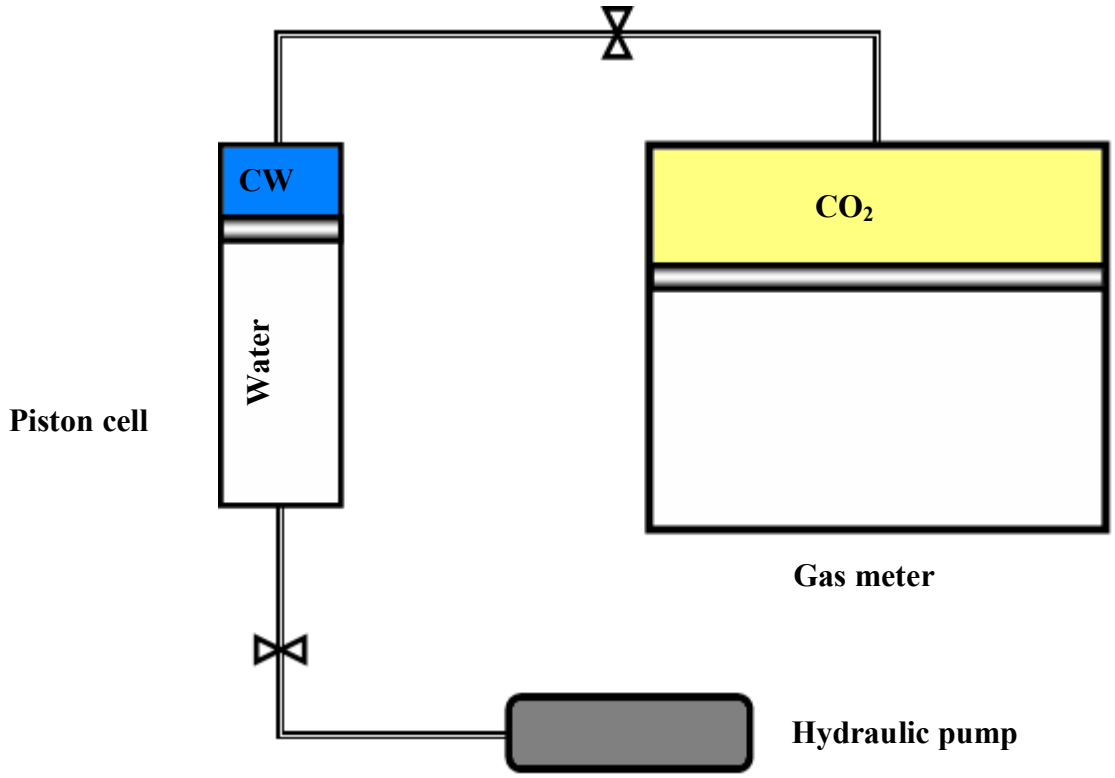

Figure 6-1: A schematic diagram of the system used to measure CO_2 solubility in CW.

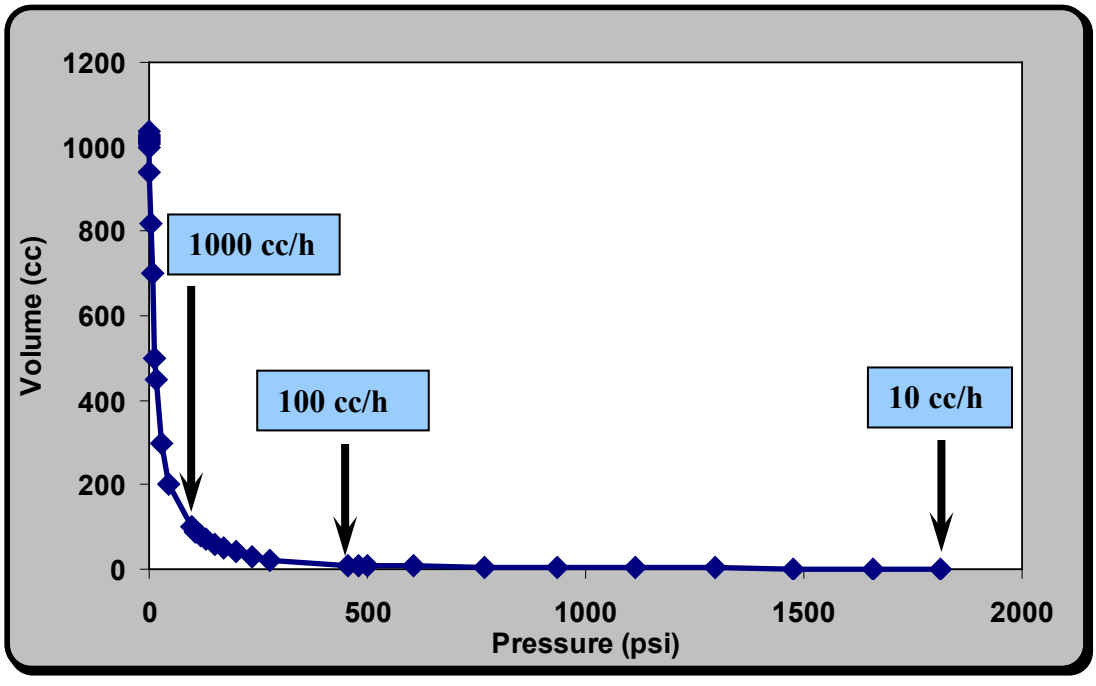

Figure 6-2: The recorded volumes at different pressure while pulling back the piston cell at different rates.

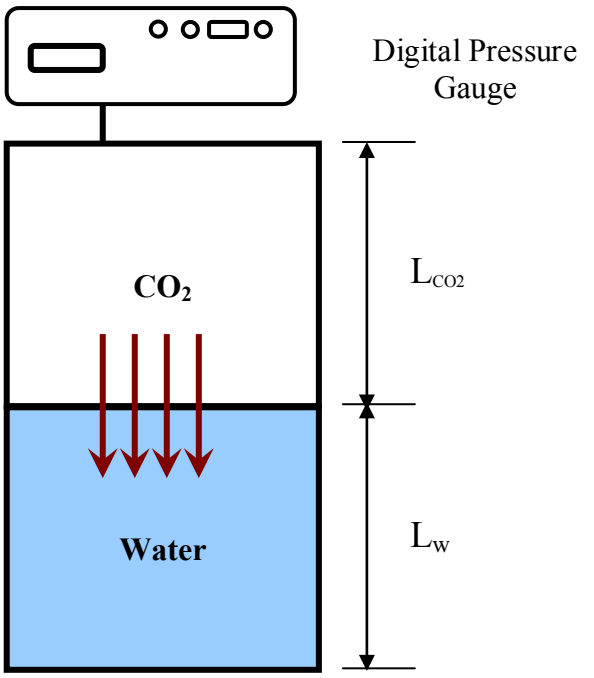

Figure 6-3: A schematic diagram of constant-pressure, constant-temperature PVT cell used for measuring the CO_2 diffusion coefficient in water during a pressure decay test.

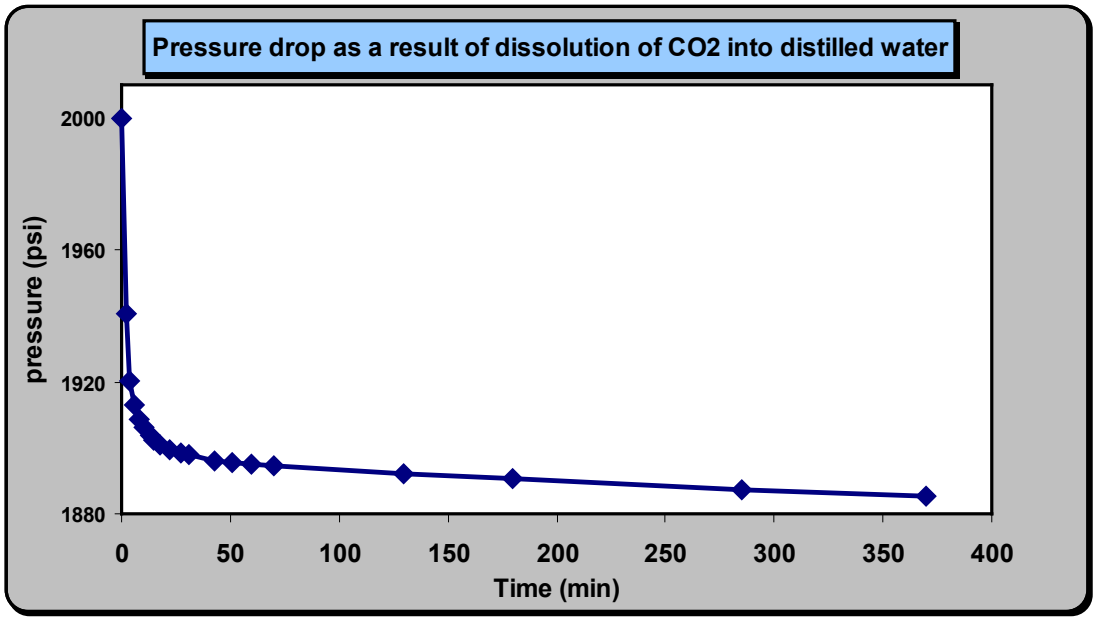

Figure 6-4: Measured pressure decay data versus time for clear distilled water.

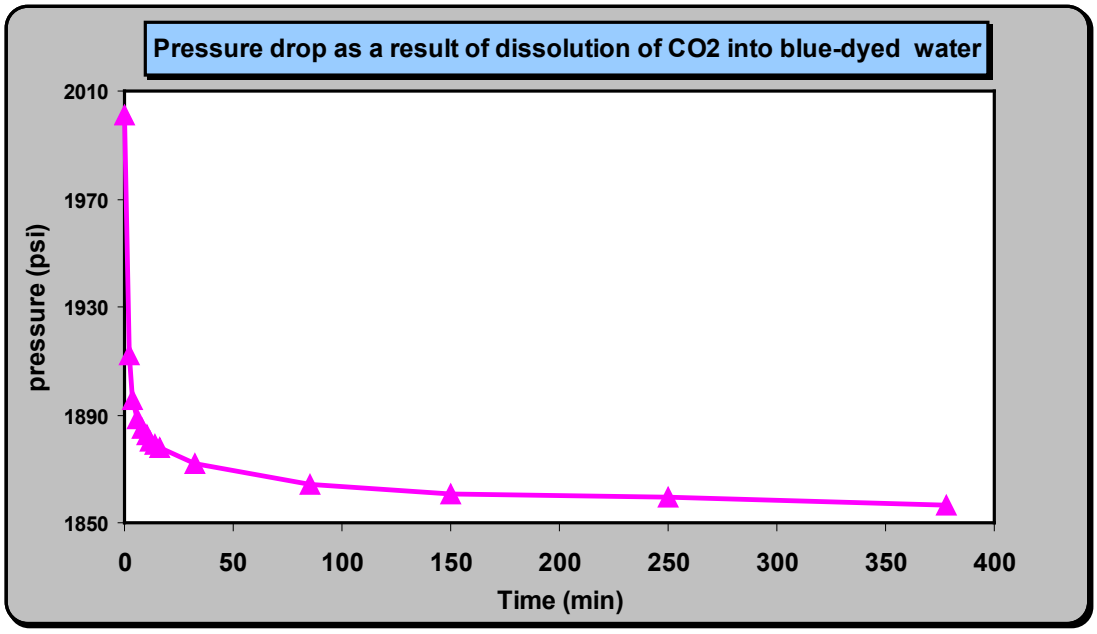

Figure 6-5: Measured pressure decay data versus time for blue-dyed water.

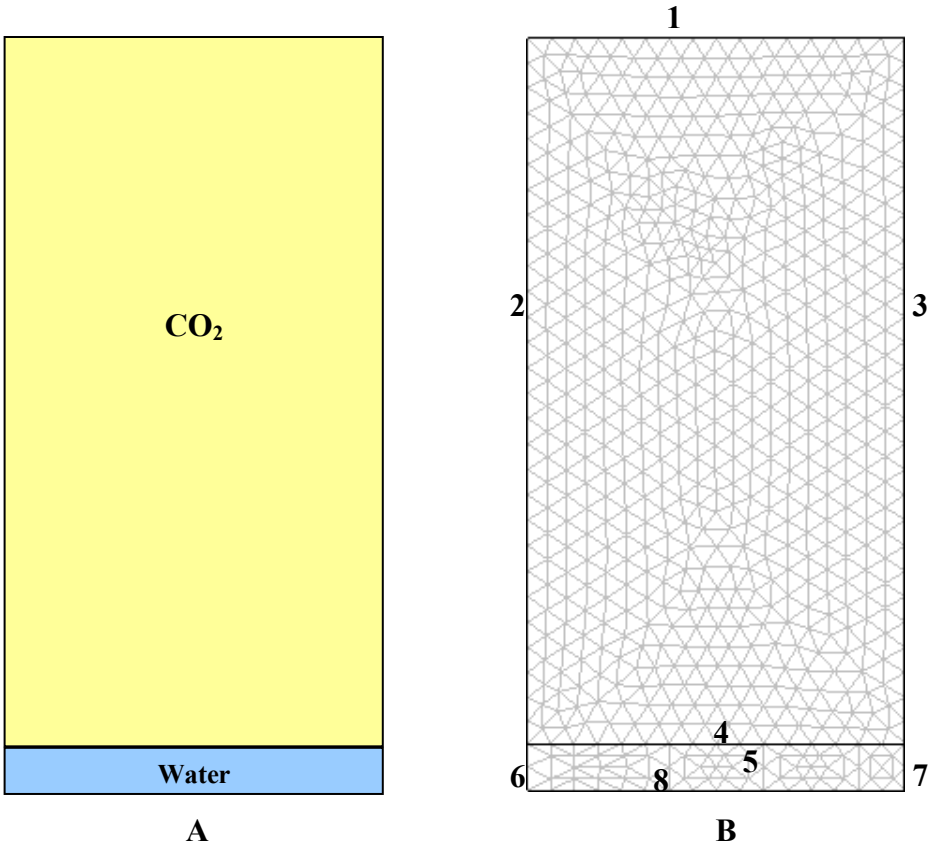

Figure 6-6: Mathematical model constructed in COMSOL Multiphysics to simulate the conducted pressure decay experiments.

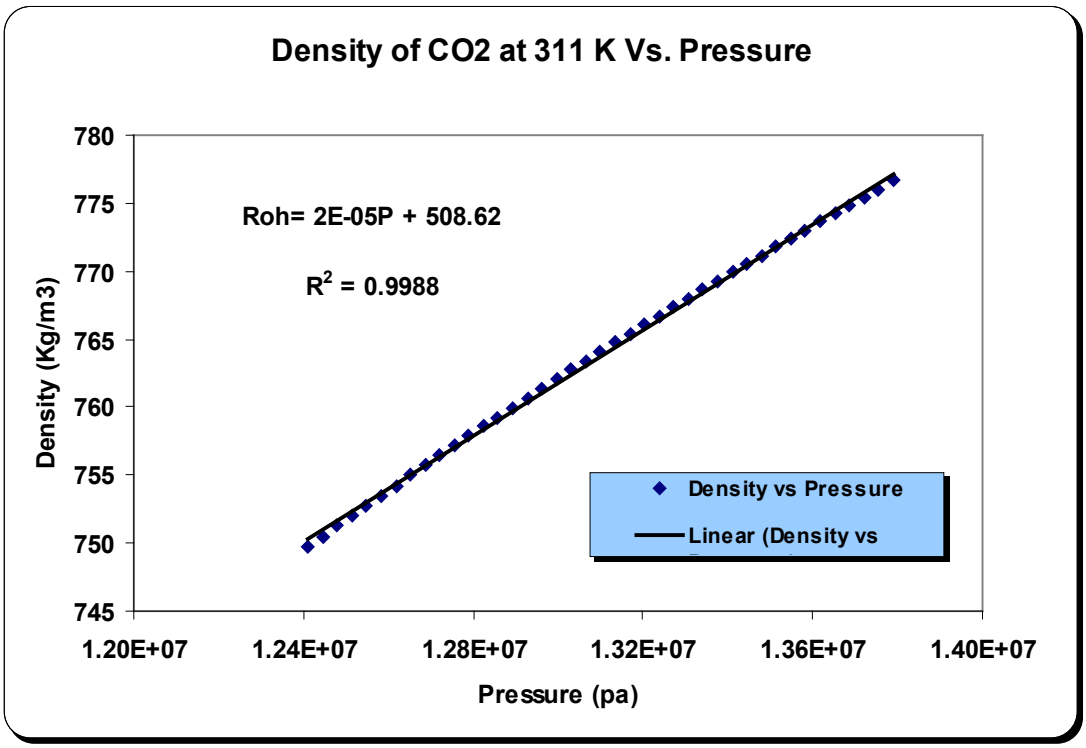

Figure 6-7: Variation of CO_2 density versus pressure at 311 K (National Institute of Standards and Technology, NIST.gov).

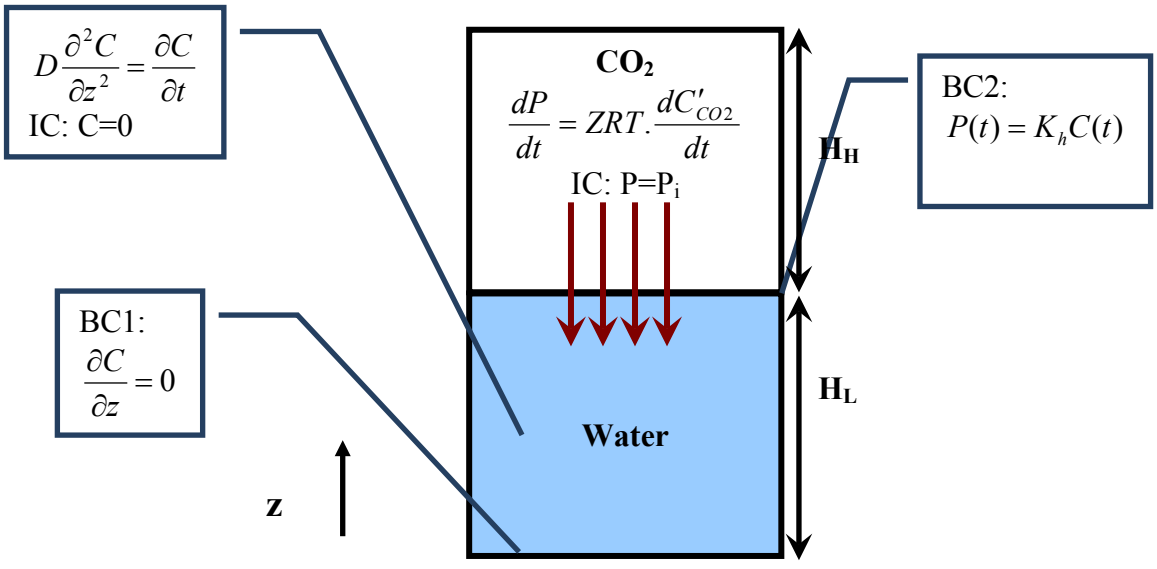

Figure 6-8: The set of equations used in solving the mass transfer problem of the gas component into the liquid phase including IC, and BCs.

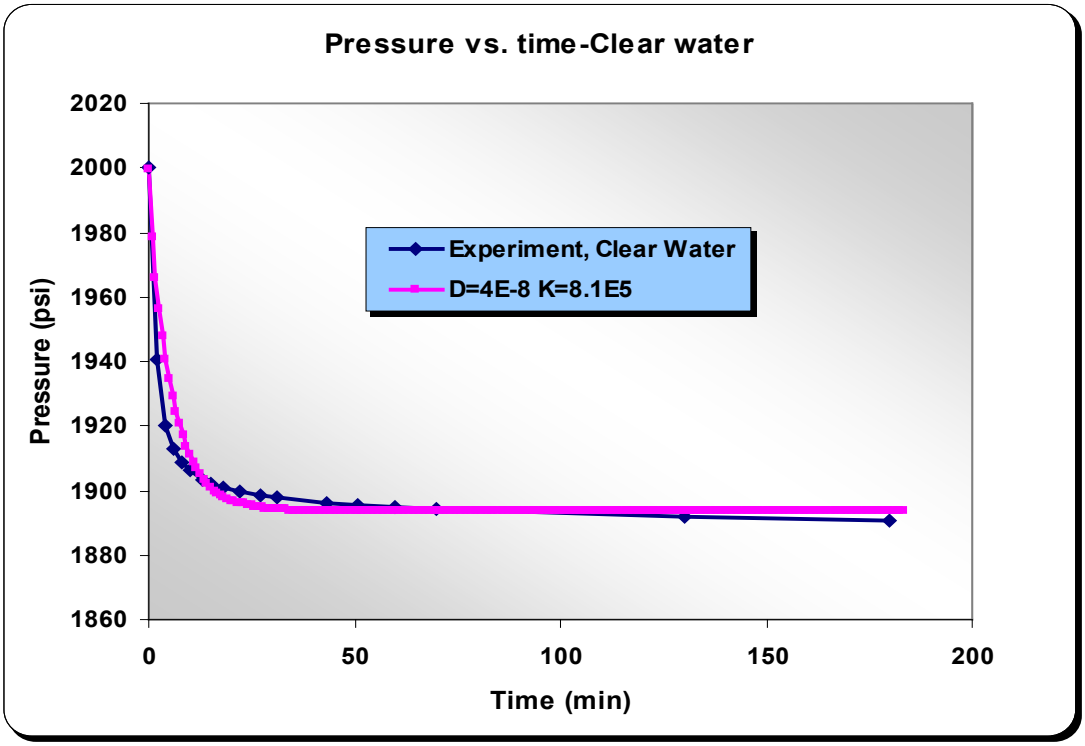

Figure 6-9: The measured (in the lab) and simulated (by the mathematical model) data of the pressure decay test: clear water.

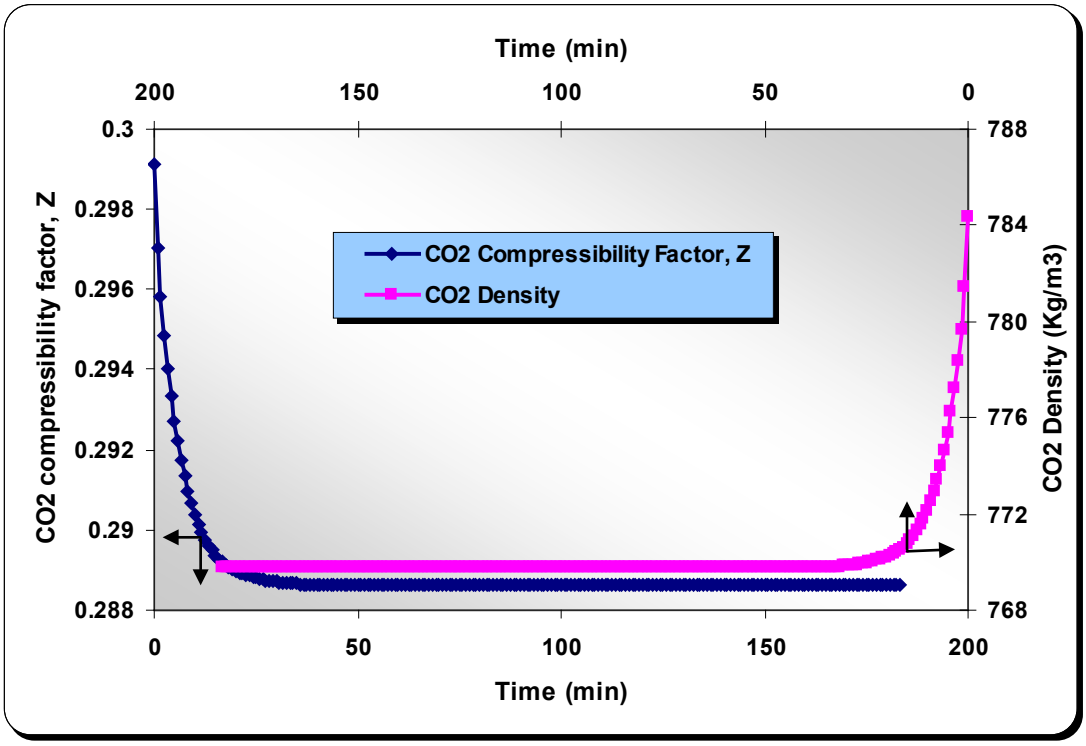

Figure 6-10: Variation of gas compressibility factor and density of CO_2 with time: mathematical model for clear water.

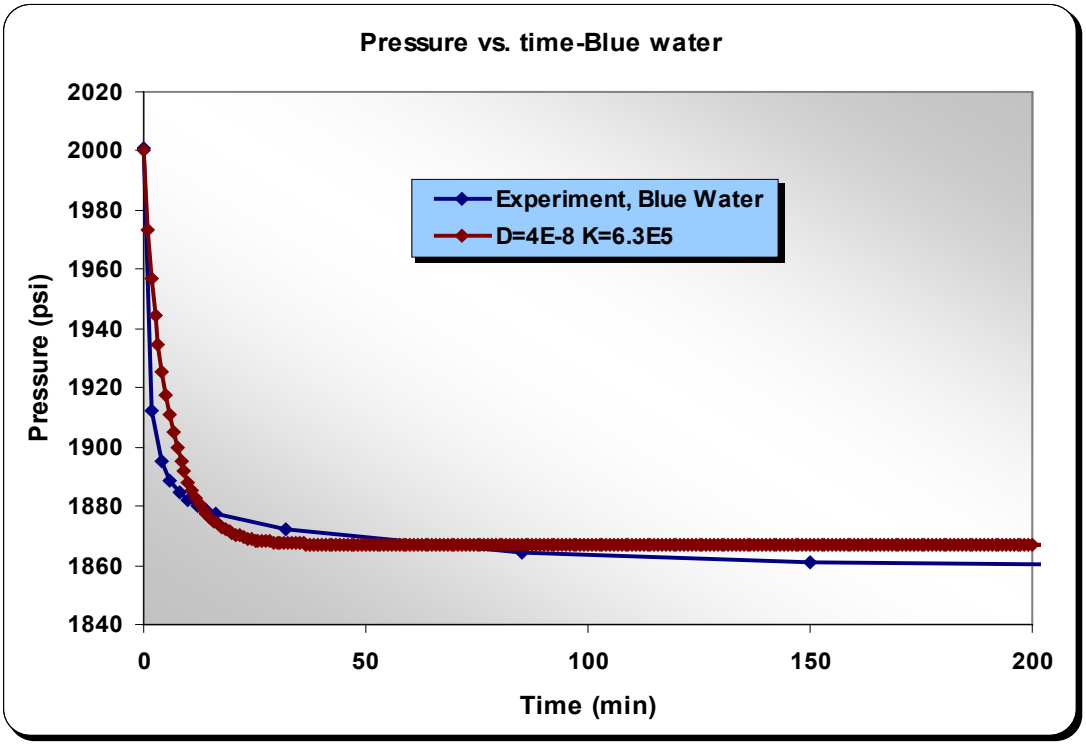

Figure 6-11: The measured (in the lab) and simulated (by the mathematical model) data of the pressure decay test: blue-dyed water.

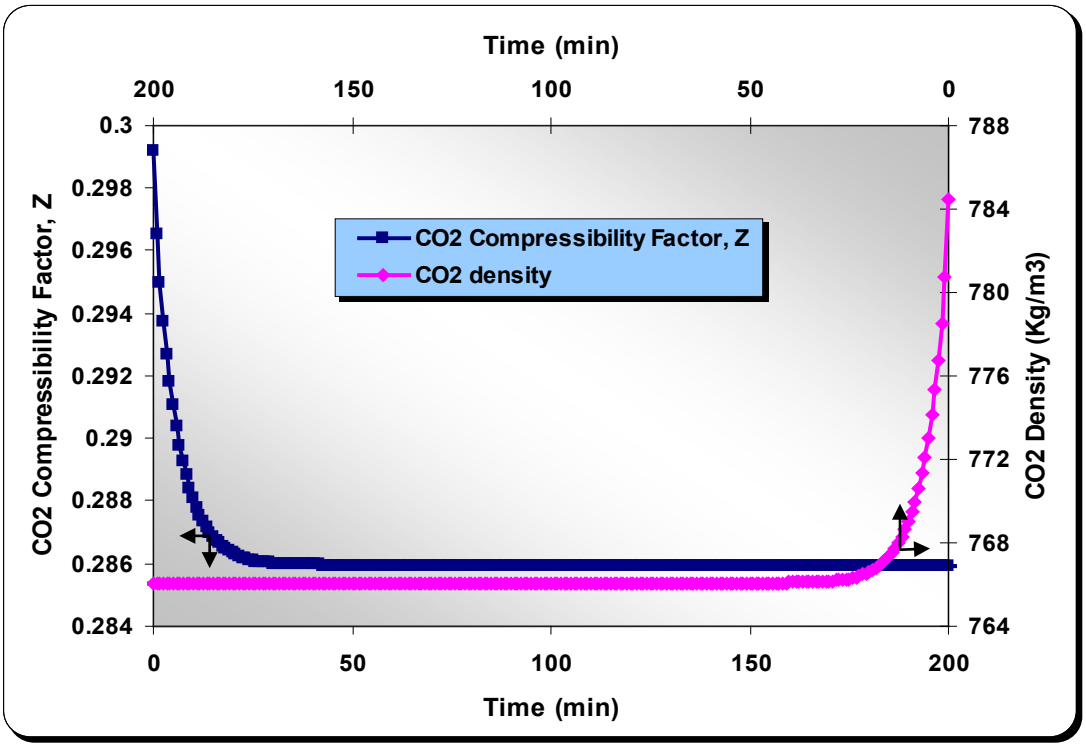

Figure 6-12: Variation of gas compressibility factor and density of CO_2 by time: mathematical model for blue dyed water.

7 Chapter 7: Mathematical Modelling

7.1 Introduction

In Chapter 3, results of visualisation experiments were reported, demonstrating swelling and remobilisation of isolated oil ganglia as a result of diffusion of CO_2 from carbonated water to oil as one of the most important mechanisms of oil recovery by carbonated water.

The impact of CO_2 diffusion in direct CO_2 injection, as a tertiary oil recovery mechanism, has been investigated before by several researchers (Grogan and Pinczewski, 1987; Grogan, et al., 1988; Campbell, and Orr, 1985; Do and Pinczewski, 1993; Bijeljic, et al., 2002).

Grogan and Pinczewski (1987) developed a 1-D mathematical model at the pore level to study the adverse effect of the presence of a water layer separating CO_2 from the oil, which is referred to as "water blocking". In the simulated process, the increased oil volume due to CO_2 diffusion reduced this volume of water, which was assumed to be transported without any resistance, as oil swelling continued. Based on the results of the sensitivity studies conducted, they identified the partition coefficient and diffusion coefficient of CO_2 in the water phase as the "bottlenecks" of this process. Partition coefficient relates the CO_2 concentration in the oil phase to that in the water phase at the water-oil interface.

Muller and Lake (1991) developed another 1-D pore level model simulating both diffusion of a solvent into oil and diffusional extraction of oil components by a solvent. The former process results in oil swelling, whilst the latter causes the oil to shrink. In their model, water separated the mobile solvent from the stagnant oil. As the oil swelled, the reduced water volume was transported by the flowing water phase. The stagnant oil phase expanded or shrank as a result of diffusion from or to the mobile solvent.

The results of their model showed that the two dimensionless parameters affecting production of oil in the presence of water blocking are the ratio of the stagnant water/oil volumes and the solvent equilibrium constants at the phase boundaries. Contrary to Grogan and Pinczewski's findings (1987), they concluded that the diffusion coefficient of the solvent has little effect on the results.

Bijeljic, et al. (2002) developed a 1-D diffusion based pore model studying the effect of water blocking on a multi-component tertiary gas flood. They assumed an ideal mixture (i.e., the total volume is the summation of the volumes of oil and CO_2) for oil phase and neglected the convection term in their equations. They also assumed a uniform gas concentration in the oil phase at any time and that the time required for the gas in the water phase to reach steady state conditions is negligible, i.e. applying the first Fick's law for this part of their model. They investigated the impact of swelling and/or shrinkage of the oil phase due to mass transfer from or to the gas phase in the presence of water blocking. They showed that the time required for the water layer to rupture as a result of oil swelling increases with a decrease in the ratio between the initial oil to water layer thicknesses. The pronounced effect of initial thickness of the water layer was highlighted, demonstrating that the rupture time increases with the square of initial thickness of the water layer (L_w^2).

All these theoretical studies provide useful information for the process of oil recovery by CO_2 injection. However, there is little information available on the impact of pertinent parameters on the process of oil recovery by carbonated water injection (CWI). Furthermore, the sensitivity of the pertinent parameters on the mass transfer process during direct CO_2I and CWI could be different. Therefore, to investigate the impact of pertinent parameters affecting this process and interpret some of the micromodel visualisation observations discussed in the previous chapters, a 1-D mathematical pore model was developed as described in this chapter. This model simulates the dynamic process of swelling as a result of partitioning of CO_2 from CW and its dissolution into an isolated oil ganglion at the pore level.

This chapter starts with a discussion on the statement of the problem, including the underlying assumptions made in the modelling approach to capture this multi-physics

phenomenon. Next, the governing equations and the numerical solution techniques are discussed. At this stage of study, the integrity of the modelling approach is verified by comparing some of its results with those of the literature for the same prevailing conditions and also by evaluating the validity of some of the simplified assumptions made. The results of the sensitivity study performed on the impact of parameters pertinent to this process are then presented. Some of the results are also compared with those obtained when simulating mass transfer during direct CO_2I. The impact of some of the pertinent parameters as predicted by the model is then linked to the results obtained using a new relationship developed, based on the dimensional analysis technique. The impact of the presence of a water layer separating the CO_2 source from the oil on swelling and shrinkage processes as well as the effect of CO_2 solubility in water on oil swelling are also studied. Two new formulas are also introduced in this part of the study; one of them can be used as a useful tool for simulation of diffusion process, as it directly related the amount of CO_2 dissolved in oil to its CO_2 diffusion coefficient. The second equation can be used to relate the equilibrium swelling factor of oil on the water CO_2 solubility. Finally the main conclusions of this study are summarised.

7.2 Problem Statement

Figures 1A and 1B show a schematic diagram of an isolated oil droplet in a dead-end pore for two different scenarios. In the first scenario (direct contact) oil is surrounded by flowing carbonated water (CO_2 source). In the second case (indirect contact) there is a water layer separating the CO_2 source from the oil phase. The former could represent carbonated water injection (CWI) as a secondary injection process, whilst the latter could simulate CWI as a tertiary (post-waterflood) injection strategy. It should be noted that, in this case, it is also likely that some of the water layers are miscibly displaced by CW. However, in direct CO_2 injection, the water layers surrounding oil ganglia are not displaced, which could slow down the CO_2 dissolution process and the subsequent oil swelling and recovery.

Figures 2A and 2B are demonstrations of CO_2 concentration profiles in water, oil and CO_2 source (CW) for the two above mentioned scenarios, respectively. CO_2 concentration in the flowing CW has been assumed to be constant. The CO_2

concentration in the oil phase at the interface was different from that in the water (or carbonated water) phase, due to its increased/decreased solubility. This value can be estimated assuming CO_2 concentrations in the two phases at equilibrium at the interface using partition coefficient as follows:

$$C_{CO2-O} = K_{CO2-w/o} C_{CO2-W}, \quad (7.1)$$

where $K_{CO2\text{-}w/o}$ is the water/oil-CO_2 partition coefficient, which is defined as the ratio of the equilibrium concentrations of a solute (C_{CO2} in this case) in two largely immiscible solvents. $C_{CO2\text{-}O}$ and $C_{CO2\text{-}W}$ are the CO_2 concentration in the oil and water phases, respectively.

The following further assumptions were made to simulate this process:

1. The effect of capillary force on the interface was neglected, i.e., the interfaces are flat. The impact of this assumption is on the size of the contact area between the CO_2 source and the solvent phase, i.e. the real interface area is slightly greater. However for the one dimensional system considered in this study using typical characteristic dimensions the impact would be minimal. Furthermore, the exact definition of curved interface and accurate modelling of such geometry is challenging and open to question.
2. CO_2 diffusion coefficients in oil and water were constant during the diffusion process. The impact of this assumption has been studied for different oil types as will be described later in this chapter.
3. The fluid system was an ideal mixture, that is, the total volume is the summation of volumes of oil and CO_2. The impact of this assumption, which affects the level of oil swelling or the amount of required CO_2 for the interface to reach a fixed position, will be discussed in this chapter.
4. The change in the volume of the water layer due to CO_2 diffusion was neglected, in the second scenario. As CO_2 solubility in water compared to that in oil, used in this study is much smaller, the impact of this assumption on the results would be minimal.
5. Oil, water, CO_2 and CW are at equilibrium conditions at the interfaces. Generally three different boundary conditions (BC) are considered; the so called equilibrium, quasi-equilibrium and non-equilibrium BC. Quasi-equilibrium BC is

usually considered for a system with varying pressure such as pressure decay method (Riazi, 1996), which as will be described in Chapter 6 is an indirect method to determine diffusion coefficient. Non-equilibrium BC is based on considering an interfacial resistance. In this case a concentration gradient within an extremely thin film around the boundary is considered, which slows down the diffusion process. The description of this resistance is not well defined and open to questions. Tharanivasan et al. (2004 and 2006) in their recent publications investigated the integrity of these three conditions for the system of CO_2-Crude oil and CH_4-Crude oil by simulating the pressure decay data versus time. Their results show that the non-equilibrium BC at the interface is most applicable at small diffusion time, whereas the quasi-equilibrium BC is the most valid one at large diffusion time. However, for the CH_4-Crude oil system, the experimental data are insensitive to the BCs. To the best of the author's knowledge, there has not been a similar study for carbonated water-oil system in the literatures. Later in the validation of the model section of this chapter the validity of this assumption will be further addressed.

6. Solubility of oil in water and water in oil are neglected. Considering these numbers, the impact of this assumption on the results would be minimal.

7. Convection due to diffusion was neglected. The validity of this assumption on the results has been studied and will be discussed later in this chapter.

8. In the model (Figure 2), the oil/water boundary in the second scenario and the oil/CW boundary in the first scenario move to the right hand side, due to oil swelling. The resultant displaced water and CW will be flowing with the main flowing stream, with no additional resistance. It should be noted that Figure 2 represents half of a symmetrical configuration where an oil ganglion is located in the main flow stream.

7.3 Governing Equations

A combination of the mass balance and first Fick's diffusion law, referred to as the second Fick's law, describes the CO_2 concentration profile in oil and water as a function of time (t) and position (x, y and z). Equation 2 shows this relationship in this one dimensional (1D) system:

$$\frac{\partial C_{CO_2}(t,x)}{\partial t} = \frac{D_{CO_2}\partial^2 C_{CO_2}(t,x)}{\partial x^2} \tag{7.2}$$

where

D: Diffusion coefficient or diffusivity, [m^2 s^{-1}]

C: Concentration, [kmol m^{-3}]

x: Length, [m]

t: Time, [sec]

Equation 2 describes the CO_2 concentration in the oil and water domains at any time and position.

In this system, total oil volume increases because of the increased CO_2 concentration (assumption 3). That is,

$$V_{oil+co_2}(t) = V_{oil} + V_{co_2}(t) = x(t) \times A, \tag{7.3}$$

where

V_{oil}: Initial oil volume, [m^3],

A: Cross sectional area, [m^2],

$V_{oil+co_2}(t)$: Total oil plus CO_2 volume, at time t, [m^3],

$V_{co_2}(t)$: CO_2 volume dissolved in oil at time t, [m^3],

$x(t)$: The displacement value of the right side boundary, [m].

The change in total volume as a result of CO_2 diffusion drives the interface to the right, i.e.

$$\frac{dV_{oil+co_2}}{dt} = \frac{dV_{co_2}}{dt} = A\frac{dx}{dt}. \tag{7.4}$$

CO_2 density in oil (ρ_{co_2}) is calculated by

$$\rho_{co_2} = \frac{m_{co_2}(t)}{V_{co_2}(t)} = \frac{Mw_{co_2} n_{co_2}(t)}{V_{co_2}(t)}, \tag{7.5}$$

where

Mw_{co_2} : CO_2 molecular weight, [kg/kmol],

$n_{co_2}(t)$: number of moles of CO_2, [kmol].

The volumetric average of the CO_2 concentration in the system is

$$\left[C_{co_2}(t)\right]_{ave}^{V} = \frac{n_{co_2}(t)}{V_{oil+co_2}(t)}. \tag{7.6}$$

Solving Equation 6 for $n_{co_2}(t)$ and substituting it in Equation 5 gives:

$$\rho_{co_2} = \frac{Mw_{co_2}\left[C_{co_2}(t)\right]_{ave}^{V} V_{oil+co_2}(t)}{V_{co_2}(t)}. \tag{7.7}$$

Rearranging Equation 7 results in:

$$V_{co_2}(t) = \frac{Mw_{co_2}}{\rho_{co_2}}[\left[C_{co_2}(t)\right]_{ave}^{V} V_{oil+co_2}(t)]. \tag{7.8}$$

Differentiating Equation 8 gives:

$$\frac{dV_{co_2}}{dt} = \frac{Mw_{co_2}}{\rho_{co_2}}\left[\left[C_{co_2}(t)\right]_{ave}^{V}\frac{dV_{oil+co_2}(t)}{dt} + V_{oil+co_2}(t)\frac{\partial\left[C_{co_2}(t)\right]_{ave}^{V}}{dt}\right], \tag{7.9}$$

Substituting from Equations 3 and 4, and rearranging the resultant equation gives:

$$\frac{dx(t)}{dt} = \frac{\frac{Mw_{co_2}}{\rho_{co_2}}[x(t)\frac{\partial\left[C_{co_2}(t)\right]_{ave}^{V}}{\partial t}]}{[1-\frac{Mw_{co_2}}{\rho_{co_2}}\left[C_{co_2}(t)\right]_{ave}^{V}]} = \frac{x(t)[\frac{\partial\left[C_{co_2}(t)\right]_{ave}^{V}}{\partial t}]}{[\frac{\rho_{co_2}}{Mw_{co_2}}-\left[C_{co_2}(t)\right]_{ave}^{V}]}, \tag{7.10}$$

$\left[C_{co_2}(t)\right]_{ave}^{V}$ and $\frac{\partial\left[C_{co_2}(t)\right]_{ave}^{V}}{\partial t}$ (the volumetric average of CO_2 concentration and its gradient with respect to time, at any time) are calculated using Equations 11 and 12, respectively.

$$\left[C_{co_2}(t)\right]_{ave}^{V} = \frac{\int_0^{x(t)} C_{CO_2}(t,x)dx}{x(t)}, \tag{7.11}$$

$$\frac{\partial\left[C_{co_2}(t)\right]_{ave}^{V}}{\partial t} = \frac{\int_0^{x(t)} \frac{\partial C_{CO_2}(t,x)}{\partial t}dx}{x(t)}, \tag{7.12}$$

7.4 Initial and Boundary Conditions

Equations 2 and 10 to 12 describe the dynamics of the swelling process. The aforementioned set of equations requires different sets of initial and boundary conditions for the two scenarios demonstrated in Figures 1 and 2.

In the case of the first scenario, direct contact of oil and CW, the initial and boundary conditions required to solve this set of equations are as follows:

***Initial Conditions*:**

At the beginning of the process, CO_2 concentration in the oil phase is equal to zero. Thus the first initial condition is given by:

$$C_{CO_2}(x,t=0)=0, \qquad 0 \le x \le L_o$$

The initial position of oil/CW interface (x_i) is also known.

$$x_i(t=0)=L_o$$

***Boundary Conditions*:**

For the left hand side boundary of the oil, the mass transfer flux at any time is equal to zero. Therefore the Neumann (second type) boundary condition can be applied as follows:

$$\frac{\partial C_{CO_2}(x=0,t)}{\partial x}=0 \qquad t \ge 0.$$

At the oil/CW interface, the right hand side boundary of the oil domain (Figure 2A), CO_2 concentration in the water phase is known and that of the oil phase is calculated using Equation 13.

$$C_{CO_2-O}(x_i,t)=K_{CO_2-w/o}C_{CO_2-W}(x_i,t), \qquad (7.13)$$

where $C_{CO2\text{-}O}$ (x_i, t) and $C_{CO2\text{-}W}$ (x_i, t) are the CO_2 concentration in the oil and water phases, at the water/oil interface, respectively, which are constants in the first scenario because the flowing stream of CW is always fully saturated with CO_2 and the two phases are at equilibrium at their interface.

For the second scenario, the required initial and boundary conditions are as follows:

***Initial Conditions*:**

At the beginning of the process, the CO_2 concentration in both oil and water are zero and the initial position of oil/W interface (x_i) is also known as in the first scenario. Hence one can write:

$$C_{CO_2}(x,t=0)=0, \qquad 0 \le x \le L_o$$

$$C_{CO_2}(x,t=0)=0, \qquad L_o \le x \le L_w$$

$$x_{i,o/w}(t=0)=L_o$$

***Boundary Conditions*:**

The left hand side boundary of the oil domain is a no-flow boundary without diffusion.

At the oil/water interface, the right hand side boundary of the oil domain (Figure 2B), the CO_2 concentration is calculated using Equation 13.

At the water/CO_2 source (CW) interface, the right hand side of the water domain (Figure 2B), CO_2 diffuses from a high CO_2 concentration, which is equal to the CO_2 concentration in the CO_2 source (CW) ($C_{CO_2-W}(x_{i,w/cw},t) = C_{CO_2,CW}$, where. $C_{CO2,CW}$ represents CO_2 solubility in water).

7.5 Solution Technique

The partial (Equation 2 for oil and water) and ordinary (Equation 10) differential equations together with two auxiliary equations (Equations 11 and 12) and the associated boundary and initial conditions described above were solved using COMSOL multi-physics mathematical modelling software which is based on the finite element method. The main difficulty in solving this set of equations is the dynamics of the oil-water interface, i.e., the dynamic nature of the mesh structure for the flow domain under study. This has been overcome using the moving mesh mode of the COMSOL package to dynamically track the position of the moving interface. Two diffusion application modes, one for the oil domain and one for the water domain, were used to solve Equation 2. The velocity of the moving mesh, i.e., that of the moving oil/CW boundary in the first scenario and the oil/water boundary in the second scenario is calculated by Equation 10. This equation was defined as an ODE (ordinary differential equation) in COMSOL. The volumetric average CO_2 concentration (Equation 11) and its gradient with respect to time (Equation 12) were obtained by defining two integration variables on the sub domain.

7.6 Estimation of Model Parameters

In this section, initially the integrity of the developed model is verified by simulating the experiment conducted by Campbell and Orr, et al. (1985), Figure 3. In this experiment, Soltrol 130, which is a synthetic mineral oil, was used as the oil trapped in

a dead end pore. Oil swelled (Figure 3B) as a result of CO_2 diffusion through the water layer (water blocking) separating oil and CO_2, and ultimately was recovered when oil expansion eliminated the water layer (Figure 3C).

The required parameters to simulate this experiment, i.e. CO_2 diffusion coefficient in oil, water, CO_2 solubility in water, partition coefficient and carbon dioxide density, were estimated as described below.

The empirical correlation of McManamey and Woollen (1973) (Equation 14) was used to estimate CO_2 diffusion coefficient in oil.

$$D_{co_2,oil} = 1.41\times10^{-10}\,\mu_{oil}^{-0.47} \tag{7.14}$$

In this equation μ_{oil}, viscosity of oil, is in Pa.s and $D_{co2,oil}$ in m^2s^{-1}. This equation has wide applications in the oil industry, as it relates CO_2 diffusivity in oil to its viscosity, which is usually available, in a simple way. The viscosity of Soltrol 130 is 1.45 mPa.s, at the conditions of the experiment of Campbell and Orr, giving a CO_2 diffusion coefficient of 3.04E-9 $m^2\,s^{-1}$.

Diffusion of CO_2 into oil reduces the oil viscosity and, based on Equation 14, the corresponding value of CO_2 diffusivity should increase. It is expected that this would be important for highly viscous oil, where the viscosity reduction is significant. In this model it was assumed that CO_2 diffusivity in water and oil is constant during the diffusion process. For the experiment conducted by Campbell and Orr, no significant variation of oil viscosity is expected; hence, the impact of this simplifying assumption on the results and conclusions is expected to be minimal.

Several researchers (Unver and Himmelblau, 1964; Thomas and Adams, 1965) have reported the CO_2 diffusion coefficient in water versus temperature at atmospheric pressure. These reported data are well correlated by the Stokes-Einstein equation (Grogan and Pinczewski, 1987):

$$D_{co_2,water} = 5.72\times10^{-12}\,\frac{T}{\mu_w}, \tag{7.15}$$

where T is in K, μ_w in centipoises (mPa.s) and $D_{co_2,water}$ in m^2s^{-1}.

If variation of water viscosity with temperature is assumed negligible, this equation expresses a linear relationship between the CO_2 diffusion coefficient in water and temperature, at atmospheric conditions. Hence one can correct the CO_2-diffusion coefficient in water for the effect of temperature using Equation 16.

$$\frac{\left(D_{co_2,water}\right)_2}{\left(D_{co_2,water}\right)_1} = \frac{T_2}{T_1}, \tag{7.16}$$

Wang et al. (1996) reported some experimental data on the diffusivity of CO_2 in water and brine for pressure values up to 5.178 MPa. Here, Wang's data, measured at 311 K is converted to 298 K, which is the temperature of the experiment of Campbell and Orr, using Equation 16. It is noted that, in this exercise, the effect of temperature on water viscosity was neglected. The diffusivity of CO_2 in water at the pressure of the experiment of Campbell and Orr (8.3 MPa) was estimated as 4.85E-9 m^2s^{-1} by extrapolating Wang's data, which had been corrected for the effect of temperature by Equation 16.

Balint (1971) and Daniel and Gaddy (1972) reported some measured values of the CO_2 partition coefficient between water and a crude oil. Grogan and Pinczewski (1987), who also simulated the Campbell and Orr experiment, interpolated between these data and estimated a value of 4.5 for the CO_2 partition coefficient between oil and water at Campbell and Orr's experimental conditions. Since, other measured data was not found for Soltrol 130, the value reported by Grogan and Pinczewski (1987) was used in this study.

The density of carbon dioxide at 8.3 MPa and 25 °C was estimated as 779 kg m^{-3}, based on the measured data of Zappe et al., (2000). CO_2 solubility in water at experimental conditions was estimated as 1.3 kmol m^{-3} (Dodds, et al., 1956). Table 1 shows a summary of all these input data.

7.7 Dimensional Analysis:

In the next section, where the results of the numerical modelling approach are discussed, we can benefit from a dimensional analysis exercise that is described in this section.

Following a dimensional analysis approach for the partial differential Equation 2, we can relate the CO_2 diffusion time to the oil thickness (L_o) and CO_2 diffusion coefficient in this 1-D oil system as follows:

$$t \propto \frac{L_o^2}{D_{CO_2}} \tag{7.17}$$

This relationship has been used by Grogan and Pinczewski (1987), for up-scaling purposes. Based on this relationship, the rate of oil swelling can be obtained by:

$$\frac{L_o}{t} \propto \frac{D_{CO_2}}{L_o} \tag{7.18}$$

Following the same dimensional analysis approach for Equation 10, the rate of oil swelling can also be obtained by:

$$\frac{L_o}{t} \alpha \frac{L_o[\frac{[C_{co_2}(t)]_{ave}^V}{t}]}{[\frac{\rho_{co_2}}{Mw_{co_2}} - [C_{co_2}(t)]_{ave}^V]} \tag{7.19}$$

Substituting from 18 into 19, gives:

$$\frac{D_{CO_2}}{L_o} \alpha \frac{L_o[\frac{[C_{co_2}(t)]_{ave}^V}{t}]}{[\frac{\rho_{co_2}}{Mw_{co_2}} - [C_{co_2}(t)]_{ave}^V]} \tag{7.20}$$

After some mathematical manipulation one can write:

$$t \propto \frac{L_o^2}{D_{CO_2}(\frac{\rho_{co_2}}{Mw_{co_2}[C_{co_2}(t)]_{ave}^V} - 1)} \tag{7.21}$$

In this relationship, at equilibrium conditions, $[C_{co_2}(t)]_{ave}^V$ is the CO_2 solubility. Compared to the relationship indexed 17, this is more representative as it also includes the impact of the CO_2 molar density and solubility, i.e. the swelling of the oil ganglion, on the diffusion process. Later, relationship indexed 21 will be used to interpret and support some of the results of the mathematical modelling of the CO_2 diffusion process.

7.8 Results

7.8.1 Validation of the model

Figure 4A shows an example of CO_2 concentration in the oil phase in the developed model after 3000 sec for the second scenario, indirect contact. This image also shows the amount of oil/water interface movement after this time. The corresponding CO_2 concentration in the water phase is shown in Figure 4B. After some preliminary checks on the integrity of the model, the experiment of Campbell and Orr (1985) was simulated.

As mentioned previously, Figure 3 shows the dead-end pore used in their experiment. Mirror images of this pattern were etched into two glass plates using a photofabrication technique and the mirror images were then aligned and annealed to bond the glass plates (Campbell and Orr, 1985). In this experiment, CO_2 diffuses into the oil phase through water and causes swelling of the oil phase. As a result, the water volume gradually reduces to zero and oil comes into direct contact with CO_2. Figure 3 shows that after 26.5 hours the 3 mm water layer was completely removed as a result of oil swelling.

Figure 5 shows both the dead-end pore of the experiment of Campbell and Orr and the corresponding geometry designed in the author's 2D model to simulate this test. In Figure 5A, the black and blue coloured areas represent the oil and water phases, respectively. The colourless CO_2 stream is flowing in a channel above the water phase. In Figure 5B, the blue coloured area represents the oil phase and the white rectangle is the water phase. The initial contact area between oil and water in the test was estimated at 5.17 mm. The corresponding value in the model was 5.00 mm. The initial ratio of the volume of water to oil in the experiment was estimated at 28.1% and the corresponding value in the model was 28.4 %. The initial thickness of the water layer and trapped oil were equal for both cases. Table 2 shows a summary of these data. As mentioned previously, in this model there is no diffusion at the boundaries except that through the water/oil interfaces, which causes the oil swelling and pushes the oil/water interface (Figure 5B) upward. In the model, the required time to remove the water phase entirely was estimated as 23.3 hr, which compares well with that in the experiment of Campbell and Orr, i.e. 26.5 hr.

This relatively small difference between these two values can be attributed to:

1) Uncertainty associated with some of the input parameters. This will be addressed later, in the next section,
2) Some of the simplifying assumptions (e.g., CO_2 concentration in oil at the oil/water interface was in equilibrium with that in water) made in the model. It should be noted that the data required to relax some of these simplifying assumptions are not available; therefore, the uncertainty in the estimated value could introduce larger errors,
3) Experimental errors in the experiment of Campbell and Orr (1985).

The minimal difference reported between the result of the experiment of Campbell and Orr (1985) and the model, was considered to confirm the integrity of the model. In the next section the source of error in this exercise will be further discussed and $K_{CO2\text{-}w/o}$, is identified as the most likely source of error, due to both high uncertainty in its estimated value and also its relative high sensitivity to the diffusion time.

7.8.2 Sensitivity of pertinent parameters

In this section, the sensitivity of pertinent parameters in the oil swelling process is investigated. The results are also used to find out the most likely source of error in simulating the experiment of Campbell and Orr (1985).

The parameters used in this study can be divided into two groups, based on their effects on oil swelling. CO_2 density (Den_{CO2}), equilibrium CO_2 concentration in carbonated water at the inlet ($C_{CO2\text{-}cw\text{-}in,}$), water/oil-$CO_2$ partition coefficient ($K_{CO2\text{-}w/o}$), equilibrium CO_2 concentration in oil (CO_2 solubility in oil) and initial oil volume (thickness of an oil droplet (L_o) in the 1D system) are parameters of the first group (referred to hereafter as Group I) and affect both the amount of swelling as well as the swelling rate. Diffusion coefficient of CO_2 in water ($D_{CO2\text{-}w}$) and oil ($D_{CO2\text{-}o}$) and the water layer thickness (L_w) are parameters of the second group (referred to, hereafter as Group II) and only affect the required time to reach to the final equilibrium conditions.

Figure 6 shows the effect of L_o, a parameter of Group I, on oil swelling. This figure demonstrates that as L_o is increased, both the amount of water/oil interface displacement and the time required reaching the final water/oil interface position increase.

Figure 7 shows the effect of initial thickness of the water layer (L_w), a parameter of Group II, on the diffusion time. The plotted data illustrate that, as for all the parameters of this group, a variation in water thickness does not affect the final position of the water/oil interface. However, an increase in the thickness of the water layer reduces the diffusion rate, i.e., the time required to reach to the final equilibrium position increases.

The sensitivity of pertinent parameters was investigated by two different evaluation methods for each (direct and indirect contact) scenario. In the first method (referred to, hereafter, as Method A), the time required for the interface to reach a specified position for different prevailing conditions is compared. In other words, the amount of oil swelling was fixed for all the cases and the impact of the parameters on the time required to reach to this fixed position was investigated. This fixed position was selected as that of 95% of the final equilibrium interface position of a base case. The parameters for the base cases corresponding to the first (direct contact) and second (indirect contact) scenarios are shown in Table 1. Since there is no water layer for the base case of the first scenario, diffusivity of CO_2 in water is not needed. Figure 7 also highlights the positions of the final equilibrium conditions (100%) and the abovementioned fixed position (95%) with horizontal lines, for the second scenario.

In the case of the second scenario, Method A helps to identify the uncertainty of input parameters of the model and the most likely source for the disagreement between the results of the model and Campbell and Orr's experimental results mentioned in the previous section. The initial thicknesses of oil and water layers in this study were selected as 0.7 and 0.4 mm, respectively. These values are typical values for oil and water layer thickness in the micromodel CWI and CO_2I experiments presented in the previous chapters.

In the second evaluation method (referred to, hereafter, as B), the required time for the interface to reach to 95% of its equilibrium position, in each case under study, is estimated and compared with that of the base case. The base case is the same as that used in evaluation Method A, and is different for the first and second scenarios.

It should be noted that the remaining 5% interface movement requires a significantly longer time, due to the reduced concentration gradient, i.e., driving force. Hence, 95%

of final equilibrium interface position (EIP) is considered as representing the final equilibrium conditions and the time required to reach to this position is referred to, hereafter, as the Equilibrium Diffusion Time (EDT). It should be noted that in the case of Method A, the times required to reach EIP of the corresponding base case (also referred to as EDT) are reported.

Based on these two definitions, both evaluation methods A and B give the same results for the parameters of Group II, which do not affect the interface position, i.e. amount of swelling.
As mentioned previously, the results of evaluation Method A are more useful when investigating the accuracy of pertinent parameters in the model simulating an experiment. They can also be useful for cases whereby the oil swelling has to reach a fixed position before being either mobilised or coalesced with another trapped oil droplet, before reaching the final equilibrium conditions.

The results of evaluation Method B are more relevant if the impact of the corresponding parameters is evaluated when a trapped oil droplet would need to reach its final equilibrium condition, either in a designed experiment or in the case of an isolated trapped oil droplet.

However, as was mentioned earlier, the results of Method A depend on the value selected for the fixed interface position. This makes Method B more independent. Furthermore, the impact of the thickness of an oil droplet (oil volume) can not be studied using Method A, as either the initial thickness of oil passes or the final EIP does not reach that of the fixed EIP of the base case.

The results of this sensitivity exercise, using both these two evaluation methods are shown in Tables 3 to 18 (to view these data in a clearer way, see the Tornado charts presented in a published journal paper, in Appendix E). In these tables, column one includes the deviation of the parameter under study from the corresponding base case value. The second and third columns contain the actual value of the pertinent parameter used in the model and the resultant predicted EDT, respectively. In each of these tables, column four shows the resultant change in EDT compared to the value for the corresponding base case. The relevant data for each base case are highlighted in bold.

First scenario, direct contact

The sensitivity of parameters, based on both evaluation methods, for the first scenario (Figure 2A), where oil was in direct contact with CW is shown in Tables 3 to 8. The EDT of the base case for this scenario was 350 sec.

Evaluation Method A

The impact of a change in the diffusion coefficient of CO_2 in oil ($D_{CO2\text{-}o}$), a parameter of Group II, is shown in Table 3. These data demonstrate that EDT is sensitive to the $D_{CO2\text{-}o}$ variation, i.e. if $D_{CO2\text{-}o}$ is overestimated by around 30%, the computed EDT decreases by 50%.

The impact of a change in equilibrium CO_2 concentration in CW at the inlet boundary ($C_{CO2\text{-}cw\text{-}in}$) and of a change in CO_2 density (Den_{CO2}) are shown in Tables 4 and 5, respectively. The former parameter affects how much CO_2 is diffused and the latter indicates how much added volume is gained. Both these parameters belong to Group I affecting both EIP and the corresponding EDT time. It should also be noted that a change in $C_{CO2\text{-}cw\text{-}in}$ is equivalent to that in the water/oil-CO_2 partition coefficient ($K_{CO2\text{-}w/o}$) or that in the equilibrium CO_2 concentration in oil ($C_{CO2\text{-}o}$), Equation 1, for both evaluation methods. It is noted that a small reduction (2%) in $C_{CO2\text{-}cw\text{-}in}$ or a small increase (2%) in Den_{CO2} significantly affects EDT. These data also highlight the non-symmetrical nature of the sensitivity of EDT to a change in these two parameters, using evaluation Method A. Furthermore, it is noted that both these two parameters affect EDT to a greater extent compared to $D_{CO2\text{-}o}$ (Table 3), i.e. a small 2% change results in an EDT deviation of up to 54%.

Evaluation Method B

As mentioned earlier, the results of the impact of variation of $D_{CO2\text{-}o}$ are similar using both evaluation methods, as $D_{CO2\text{-}o}$ only alters EDT but not EIP of the base case.

The impact of a change in $C_{CO2\text{-}cw\text{-}in}$, Den_{CO2} and L_o, based on evaluation Method B, is observed in Tables, 6, 7 and 8, respectively. It is noted that, for this method, the impact of a change in $C_{CO2\text{-}cw\text{-}in}$ (Table 6) or Den_{CO2} (Table 7) is slightly less pronounced compared to that in oil properties, i.e. $D_{CO2\text{-}o}$ (Table 3) or L_o (Table 8). These results are in good agreement with the results of the dimensional analysis relationship indexed

21 (Section 7). To verify this, the ratio of the equilibrium time (right hand side of the relationship) for each case compared to the base case was calculated for the data presented in Tables 3 and 6-8. The same ratio was also calculated using the results of the model. Columns five and six of these tables compare these data for $D_{CO2\text{-}o}$, $C_{CO2\text{-}cw\text{-}in}$, Den_{CO2} and L_o, respectively. As can be seen, the differences between these ratios for different cases are minimal, confirming the integrity of the results of the simulators and dimensional analysis approach.

Evaluation Method A versus B

A comparison of data of Tables 6 and 7 with those of Tables 4 and 5 show that EDT is more sensitive to $C_{CO2\text{-}cw\text{-}in}$ and Den_{CO2} using evaluation Method A rather than Method B. This is due to the fact that in Method A, the fixed EIP corresponds to that of the base case whilst in Method B it varies for each case, dampening the effect of the pertinent parameter. For example, 20% overestimation of $C_{CO2\text{-}cw\text{-}in}$, using Method A, decreases EDT by 60% but the same overestimation using Method B increases EDT by only 20%. Furthermore, the direction of changes of EDT for both parameters in Method A is in the opposite direction to that in Method B. For example, increasing $C_{CO2\text{-}cw\text{-}in}$ decreases EDT in Method A whereas increases EDT in Method B. This difference can be explained by looking at the definition of EDT for these two methods. That is, in Method A, increasing CO_2 concentration increases the driving force: hence, the model needs less time to reach the fixed EIP of the base case, whilst in Method B, the higher CO_2 concentration results in higher swelling value, in turn leading to a longer required time to reach its final EIP. The data in Tables 6 and 7 also demonstrate the more symmetrical nature of the effects of variation of parameters on EDT compared to those found in Tables 4 and 5, highlighting the more independent nature of evaluation Method B.

Second Scenario, Indirect Contact

Here, the sensitivity of parameters using these two evaluation methods for the second scenario, when oil indirectly contacts the CO_2 source (CW or CO_2), is studied. This exercise highlights the impact of the water layer on the effect of these parameters on the computed swelling time. The EDT of the base case for this scenario was 2380 sec.

Evaluation Method A

The impact of a change in $C_{CO2\text{-}cw\text{-}in}$, Den_{CO2} and the water/oil-CO_2 partition coefficient ($K_{CO2\text{-}w/o}$), which affect the amount of swelling, is shown in Tables 9 to 11, respectively. All these three parameters are of Group I, varying both EIP and the corresponding EDT time. It is noted that the sensitivity of EDT is more pronounced for a change in $C_{CO2\text{-}cw\text{-}in}$ and Den_{CO2} compared to a change in $K_{CO2\text{-}w/o}$. It is also noted that a small reduction in $C_{CO2\text{-}cw\text{-}in}$ and $K_{CO2\text{-}w/o}$ or a small increase in Den_{CO2} significantly affect EDT. It should be noted again that a change in $K_{CO2\text{-}w/o}$ is equivalent to that in $C_{CO2\text{-}o}$ (Equation 1).
The impact of the thickness of an oil droplet (oil volume) can not be studied here as either the initial thickness of oil passes or the final EIP does not reach that of the fixed EIP of the base case, which is the basis of the evaluation Method A.

The effects of a change in diffusion coefficient of CO_2 in water ($D_{CO2\text{-}w}$) and oil ($D_{CO2\text{-}o}$) and initial thickness of water (L_w) are shown in Tables 12 to 14 respectively. The impact of variation of these parameters on the results are similar using both evaluation methods, as they only alter EDT but not EIP of the base case; thus, the comparison of the sensitivity of these parameters will come in the next section.

Evaluation Method B

The impact of changes in $D_{CO2\text{-}w}$, $D_{CO2\text{-}o}$, L_w, L_o, $C_{CO2\text{-}cw\text{-}in}$, Den_{CO2} and $K_{CO2\text{-}w/o}$ are shown in Tables 12 to 18, respectively.

These data (Tables 12-18) reveal that EDT is most sensitive to the L_w variation, highly sensitive to $D_{CO2\text{-}w}$, $C_{CO2\text{-}cw\text{-}in}$ and Den_{CO2}, moderately sensitive to $K_{CO2\text{-}w/o}$ and least sensitive to $D_{CO2\text{-}o}$ and L_o.

Figure 8 shows the displacement of the oil/water interface versus swelling time for the base case and four other cases with two different $D_{CO2\text{-}w}$ and $D_{CO2\text{-}o}$ values. The plots at different diffusion coefficient values correspond to the same amount of deviation in $D_{CO2\text{-}w}$ or $D_{CO2\text{-}o}$ from the corresponding base case values. The last points in these curves correspond to EDT and EIP values found in Tables 12 and 13. This plot, like the tabulated data, shows that the swelling of the oil phase is much more sensitive to the

variation of $D_{CO2\text{-}w}$ than that of $D_{CO2\text{-}o}$. This point will be discussed later in Section 7.8.3.

Evaluation Method A versus B

The data reported in Tables 11 and 18 demonstrate that in the second scenario, similarly to the first scenario, the direction of changes in EDT for $K_{CO2\text{-}w/o}$ using evaluation Method A (Table 11) is in the opposite direction to that using evaluation Method B (Table 18). However, this trend was not observed for a change in $C_{CO2\text{-}cw\text{-}in}$ (Tables 9 and 16) and Den_{CO2} (Tables 10 and 17) because, in the second scenario, the adverse effect of the water layer weakened the changes due to these two parameters. A comparison of data in Tables 16 and 17 with those in Tables 9 and 10 shows that EDT is more sensitive to both parameters when using evaluation Method A rather than B.

First versus Second Scenario

There are three common parameters between the first (direct contact, Figure 2A) and the second (indirect contact, Figure 2B) scenarios; 1) $C_{CO2\text{-}cw\text{-}in}$ 2) Den_{CO2} 3) $D_{CO2\text{-}o}$. The role of water layer on the impact of these three parameters is discussed, below, in the following section.

Evaluation Method A

The impact of variation of $C_{CO2\text{-}cw\text{-}in}$ on EDT of the first and second scenarios is shown in Tables 4 and 9, respectively. A comparison of these data reveals that $C_{CO2\text{-}cw\text{-}in}$ is a more sensitive parameter in the former compared to that in the latter scenario. That is, for example, a 2% reduction in $C_{CO2\text{-}cw\text{-}in}$ increases, EDT by around 54% for the direct contact scenario (Table 4). The corresponding value for the indirect contact scenario is around only 13% (Table 9).

The sensitivity of EDT to Den_{CO2} for the first and second scenarios is shown in Tables 5 and 10, respectively. A comparison of these data demonstrates that similarly to $C_{CO2\text{-}cw\text{-}in}$, Den_{CO2} is a more sensitive parameter in the first compared to the second scenario. For example if Den_{CO2} is overestimated by just 2%, EDT increases by around 31% (Table 5) and 17% (Table 10) in the first and second scenarios, respectively.

The impact of variation of $D_{CO2\text{-}o}$ is similar using both evaluation methods, because this variation alters the EDT but not the EIP of the base case. This effect will be discussed in the next section.

Evaluation Method B

The sensitivity of the oil properties, i.e. $D_{CO2\text{-}o}$ and L_o in the first and second scenarios are shown in Tables 3, 8 and 13, 15, respectively. These data reveal that EDT is much more sensitive to the variation of those parameters when oil is in direct contact with CW compared to when there is a water layer between oil and the CO_2 source, dampening their impact.

As discussed earlier, the results of the model based on the first evaluation method, A, showed that Den_{CO2} is a more sensitive parameter in the first rather than second scenario. The sensitivity of this parameter based on Method B, is shown in Tables 7 and 17, for these two scenarios, respectively. These data demonstrate that Den_{CO2} is a more sensitive parameter in the second rather than first scenario.

As mentioned above the results based on evaluation Method A showed $C_{CO2\text{-}cw\text{-}in}$ to be a more sensitive parameter in the first rather than second scenario. The same study, based on evaluation Method B, with results given in Tables 6 and 16 for these two scenarios demonstrates that $C_{CO2\text{-}cw\text{-}in}$ in the second scenario (Table 16) is slightly more sensitive than that in the first scenario (Table 6). However, the extent of this difference is negligible and it can be concluded that $C_{CO2\text{-}cw\text{-}in}$ affects EDT for both these two scenarios, to almost the same extent.

A comparison of the data in Tables 6, 7 and 8 for the impact of $C_{CO2\text{-}cw\text{-}in}$, Den_{CO2} and $L_{o,}$ respectively, on EDT in the first scenario with the corresponding data in Tables 16, 17 and 15 for the second scenario, demonstrates that the effects of these three parameters on EDT are in opposite directions. That is, for example a 20% overestimation in the value of $C_{CO2\text{-}cw\text{-}in}$ results in a 20% increase in EDT for the direct contact scenario (Table 6) but a reduction of about 23% in EDT for the indirect contact scenario (Table 16). This is due to the adverse effect of the water layer and to the definition of EDT. Figure 9 shows these two different trends graphically. As was mentioned earlier and will be further explained, the water layer increases the required

EDT significantly. Therefore, if the negative impact of the water layer on CO_2 diffusion is reduced, for example by increasing the diffusion driving force, i.e., increasing $C_{CO2\text{-}cw\text{-}in}$, then EDT is reduced for the second scenario (Table 16). However, increasing $C_{CO2\text{-}cw\text{-}in}$ increases the amount of swelling and EDT for the first scenario (Table 6 and Figure 9). Similarly, a decrease in Den_{CO2} increases the EDT of the first scenario by increasing the oil volume whilst the negative impact of the water layer on EDT is reduced by a larger, faster reduction of the water layer (more increase in oil volume) for the same amount of CO_2 mass transfer, thus reducing EDT.

Uncertainty of the Model Simulating the Campbell and Orr's Experiment:

Using some of the results of the sensitivity studies of the parameters on oil swelling (evaluation Method A for the second scenario) the difference obtained between the required time to rupture the water layer in the authors' model and in Campbell and Orr's experiment can now be further discussed;

As shown previously, the estimated required time to rupture the water layer, based on the developed mathematical model, 23.3 hrs, is about 12% shorter than that reported by Campbell and Orr, 26.5 hrs. Assuming that there had not been any experimental error, the results of the above sensitivity study suggest that about 2% overestimation in $C_{CO2\text{-}cw\text{-}in}$ or underestimation in Den_{CO2} (Tables 9 and 10, respectively) could cause this disagreement. However, since the same values for these two quantities have been reported by many investigators, it is unlikely that the uncertainty in the values of these parameters could be the reason for this observed difference. An error in $D_{CO2\text{-}w}$ and $D_{CO2\text{-}o}$ (Tables 12 and 13, respectively) can not be the major source for the above mentioned difference, due to the low sensitivity of the diffusion process to these two parameters, i.e. the fact that a large deviation in the values of these two parameters would be required to justify a 12% difference in the time required to rupture the water layer. High accuracy in measuring L_w also suggests that this parameter could not be the source of this difference. Therefore, $K_{CO2\text{-}w/o}$, is the most likely source of error, due to both high uncertainty in its estimated value and also its relatively high sensitivity to diffusion time.

7.8.3 Effect of the water layer on swelling rate

In this section, the effect of the water layer on the oil swelling rate, based on the results of the first and the second scenarios, is studied.

Figure 10 shows the displacement of the oil/CW and oil/W interfaces versus time for the swelling process of the first scenario (direct contact of oil and CW), Figure 2A, and the second scenario (indirect contact of oil and CO_2 source), Figure 2B, respectively. This plot demonstrates that, as discussed in the previous chapters, visualisation micromodel experiments, the initial swelling rate is high but later slows down for the both cases.

There is an important point that can be highlighted when comparing the results of the first and second scenarios. It is noted that the swelling time for the second scenario (2380 seconds for the base case with 0.4 mm of water layer and 0.7 mm oil thickness) is significantly longer than that in the first scenario (350 seconds for the same base case with 0.7 mm oil thickness). In another exercise, it was noted that the swelling time of the second scenario (i.e. 2380 sec) was also longer than that corresponding to a case where water was replaced by oil and hence, oil had a thickness of 1.1 mm (i.e. 840 sec). Naturally, the amount of swelling and equilibrium time for the case with oil thickness of 1.1 mm is higher than that with oil thickness of 0.7 mm because of the increased oil volume.

Figure 10 also shows the swelling curve of the third case. Comparison of these curves indicates that the water layer is an important parameter in decreasing the CO_2 diffusion rate from carbonated water into oil. It should be noted that the equilibrium time for the third case is lower than that for the second case with water layer. This is because at early stages of the process, the CO_2 concentration at the fixed position of 0.7 mm in these two cases is lower for the latter compared to the former, i.e., there is a lower concentration gradient for the case with the water layer at the beginning of the process. The lower concentration gradient in water than that in oil is mainly due to the lower CO_2 solubility in water. These results highlight the major negative impact of the water layer on the CO_2 diffusion rate from a CO_2 source to oil.

7.8.4 Integrity of some of the assumptions

In this section the validity of some of the simplifying assumptions made in the model are investigated.

Convection due to diffusion

In the developed model, the mass transfer was considered only as a result of molecular diffusion and the convection term as a result of CO_2 diffusion through the oil phase was assumed to be negligible. In this part, the validity of this assumption is investigated. In this exercise, the model simulating Campbell and Orr's test (Table 1 and Figure 5B), was employed.

The general form of Fick's Law, which describes the diffusion and convection processes is derived directly from combining the continuity and flux equations as follows (Bird 1960):

$$\frac{\partial c_{co_2}}{\partial t} + \frac{\partial}{\partial x}(v.c_{co_2}) - \frac{\partial}{\partial x}(D_{co_2-B}\frac{\partial c_{co_2}}{\partial x}) = 0, \qquad (7.22)$$

where

c_{co_2} = Molar concentration of CO_2, mols/L^3.

c = Total molar concentration, mols/L^3.

D_{co_2-B} = Binary diffusivity for system CO_2-B, L^2/t.

t= Time, t.

v = molar average velocity, L/t.

In the above equation c and D_{co_2-B} are assumed to be constants.

This equation states that the mass transfer rate $\frac{\partial c_{co_2}}{\partial t}$ depends on the mass transfer driving force, which consists of the convection term $\frac{\partial}{\partial x}(v.c_{co_2})$ and the diffusion term $\frac{\partial}{\partial x}(D_{co_2-B}\frac{\partial c_{co_2}}{\partial x})$. Diffusion can induce convection in the system, with its magnitude proportional to the velocity of the interface as diffusion progresses. The convection due to the bulk fluid displacement is not considered here. To evaluate the impact of the convection as a result of diffusion on the results, the water/oil interface velocity was calculated and plotted in Figure 11. This figure shows that the velocity of

the interface reduces with time as the concentration gradient is reduced and the equilibrium conditions are approached. This velocity should be compared with an equivalent diffusion velocity. Based on the diffusion term, $\frac{\partial}{\partial x}(D_{co2-B}\frac{\partial c_{co2}}{\partial x})$, the ratio of diffusion coefficient and change in the thickness of the water/oil domain could be a representative term expressing the velocity of diffusion. D/L terms for the water and the oil phase using their corresponding CO_2 diffusion coefficients and their dynamic thickness values were estimated and are shown in Figure 12. The calculated water/oil interface velocity is also shown in this figure. The data in this plot indicate that the equivalent diffusion velocity (D/L) reduces (increases) with time, for oil (water). Since the diffusion coefficient has been assumed constant during the swelling process, this reduction (increase) is due to the swelling (shrinkage) of oil (water), respectively.

Comparison of the interface velocity and the diffusion velocity (Figure 12) reveals that the equivalent diffusion velocities are significantly higher than the interface velocity. These results confirm, to some extent, that neglecting the convection term as a result of the moving boundary is a valid assumption.

Variation of CO_2 diffusion coefficient in oil

As shown previously, the diffusion coefficient of CO_2 in the oil phase is a function of oil viscosity, which reduces with increased CO_2 concentration, as the CO_2 diffusion process progresses. In the model, such variation has been ignored. In this section, the validity of this assumption (having a constant CO_2 diffusion coefficient in oil during the diffusion process) is investigated.

The correction of the dead oil viscosity for dissolved gas, which was developed by Beggs and Robinson (1975), Equation 23, using experimentally measured data of more than 2000 live oils, was used in this exercise.

$$\mu = A\mu_{OD}^{B}, \tag{7.23}$$

where

$$A = 10.715(R_s + 100)^{-0.515} \tag{7.24}$$

$$B = 5.44(R_s + 150)^{-0.338} \tag{7.25}$$

R_s = Dissolved gas GOR, scf/STB

μ_{OD} = Viscosity of gas-free oil, cP

μ = Viscosity of gas-saturated oil, cP

Two methods were used to estimate the dissolved gas/oil ratio. The first method, which assumes Rs varies only with time, is based on an average dissolved CO_2 volume for the whole system at any time. It requires the gas compressibility factor, which was obtained using the Standing & Katz chart (1941). The following equation was used to estimate the average gas/oil ratio in the oil domain.

$$R_s(t) = \frac{5.615 \times P_2 T_1 V_{CO_2}(t)}{P_1 T_2 Z_2 V_{ini-oil}} \tag{7.26}$$

The second method, which assumes Rs varies with time and position, is based on CO_2 concentration at any time and location in the domain. In this method, Equation 27 was used to estimate the dissolved gas oil ratio.

$$R_s(t,x) = \frac{5.615 \times C_{co_2}(t,x) R T_1 V_{oil}(t)}{P_1 V_{ini-oil}}, \tag{7.27}$$

where

P_1= atmospheric pressure, 14.7 psia

P_2= model's pressure, 2000 psia

T_1= standard temperature, 298 K

T_2= model's temperature, 311 K

Z_2=CO_2 compressibility factor at T_2 and P_2, 0.37.

$V_{ini\text{-}oil}$=gas-free oil volume, m^3

V_{CO2} (t) = CO_2 volume at time t, m^3

V_{oil} (t) = gas saturated oil volume at time t, m^3

C_{co2} (t) = CO_2 concentration, mole m^{-3}

R= gas constant, 1.206245 m^3 psi K^{-1} mol^{-1}.

The empirical correlation of McManamey and Woollen (1973), Equation 28, was used to estimate CO_2 diffusion coefficient in oil, based on its updated viscosity value.

$$D_{co_2,oil} = 1.41 \times 10^{-10} \mu_{oil}^{-0.47} \tag{7.28}$$

In this equation μ_{oil}, viscosity of oil is in Pa.s and $D_{co_2,oil}$ in m^2s^{-1}.

The effect of viscosity change on diffusion rate in both the first (Figure 2A) and the second scenarios (Figure 2B) and for a wide range of initial oil viscosity were studied. It should be mentioned that in this exercise, the thickness of oil is 0.7 mm, in both scenarios, and the thickness of the water layer in the second scenario is 0.4 mm. The basic fluid properties and the prevailing temperature and pressure of the case under study are those of the micromodel experiments reported in the previous chapters. A summary of the parameters used in this study can be found in Table 19.

Figures 13-15 show the change in the solution gas/oil ratio (Rs), oil viscosity, and diffusion coefficient of the oil with initial viscosity of 16.5 cP, respectively, versus time for the second scenario. The Rs values in these plots were estimated using both Equations 26 and 27. In the case of Rs, which is based on Equation 27 and varies at each location, the corresponding trend for the right and left hand side boundaries, displaying the maximum and minimum extent of variation, have been included. It is noted that Rs of the right hand side boundary is higher than that of the left hand side boundary, Figure 13. This difference, as expected, could also be observed for the oil viscosity (although in the reverse direction) and diffusion coefficient of CO_2 in oil, Figures 14-15. In these figures it is noted that some time is required for the left hand boundary parameter to be affected by the CO_2 diffusion process. There is a minimal difference between the dynamic of the interface predicted by different Rs calculation methods. Furthermore, finally, at the equilibrium conditions, these curves overlap each other.

Figure 16 shows the reduction of oil viscosity (y-axis) within the oil domain (x-axis) at different time steps. This plot shows that the oil viscosity reduction at the initial times and closer to the CO_2 source is greater. This point is of significant importance as it suggests that the oil viscosity at the front of CW reduces significantly and, as a result, can favourably improve displacement efficiency by controlling the mobility ratio. As shown previously, CO_2 dissolution causes oil swelling as well as oil viscosity reduction.

The impact of viscosity change as a result of dissolved carbon dioxide in oil on diffusion rate and oil swelling was investigated for both the first (Figure 2A) and the second scenarios (Figure 2B) and for three typical (initial) oil viscosities of 0.83, 16.5

and 165 cP, which respectively correspond to the n-decane as a light oil, the viscous mineral oil as a medium viscous oil and the Crude Oil A as a highly viscous oil. For this purpose, two sets of data for each system were generated. In one of them diffusion coefficient was assumed constant and in the other one the variation of diffusion coefficient using Equations 23-28, as described above, was considered. The results are shown in Figures 17-19 for typical oil viscosity of 0.83, 16.5 and 165 cP, respectively. Thus, there are four curves, for the cases of constant and variable oil viscosity values two for the first scenario and two for the second scenario.

The results indicate that the swelling rate for the second case, viscosity reduction as a result of dissolved gas in oil, is higher than the case of a constant diffusion coefficient, i.e. the constant oil viscosity case. However, this difference is negligible and small for the typical oil with viscosity of 0.83 and 16.5 cP but considerable for the oil with viscosity of 165 cP. This behaviour is mainly due to higher viscosity reduction in the oil with higher viscosity. Therefore, it can be stated that, for the highly viscous oils, the impact of viscosity reduction on diffusion rate should be considered.

Comparison of the first scenario and the second scenario results shows that the water layer between the oil and the CO_2 source reduces this difference, i.e. the impact of viscosity reduction on the oil swelling rate reduces. This is consistent with the results of sensitivity analysis discussed previously, whereby the presence of the water layer in the second scenario dampened the impact of variation of pertinent parameters on the CO_2 diffusion process. It also shows the impact of the water layer on reduction of the swelling rate for both constant and non-constant CO_2 diffusion coefficient in oil.

Based on these results, it can be concluded that considering a constant diffusion coefficient of CO_2 in oil for the light oil and when there is a water layer between oil and CO_2 (as in the simulation of the Campbell and Orr test) is a valid assumption.

Figure 20 shows the viscosity reduction of different oil types versus time. In this plot the dimensionless viscosity (viscosity of oil at any time/initial oil viscosity) versus dimensionless time (time/equivalent equilibrium time for each case) has been plotted. As can be seen, the viscosity reduction and the rate of reduction are greater for the oil with higher viscosity. The rate of diffusion coefficient change for these oil types is

shown in Figure 21. This plot clearly shows that there is a larger variation of diffusion coefficient for the oil with higher viscosity. It also shows that the impact of initial oil viscosity on the molecular diffusion coefficient (Figure 21) is significantly more pronounced than that on the oil viscosity reduction (Figure 20).

7.8.5 A New equation to estimate diffusion coefficient of CO_2 in oil

As shown and discussed in the previous section, the diffusion coefficient of CO_2 in oil is a function of oil viscosity (Equation 28) which in turn depends on the solubility of CO_2 in oil (Equations 23-25). Combining these equations gives the following rather complex equation.

$$D_{co2,oil} = 1.41\times10^{-10} * (10.715(R_s + 100)^{-0.515}\,\mu_{OD}^{5.44(R_s+150)^{-0.338}})^{-0.47} \quad (7.29)$$

To develop a simpler equation, two more sets of data for oil with viscosity of 4 and 1650 cP were added to the previous three data sets. Using the developed mathematical model, the updated diffusion coefficient of CO_2 in oil as a function of dissolved CO_2 in oil for all five typical oil types and for both the first and the second scenario were plotted (Figure 22). As this plot shows, there is a linear relationship between these parameters. The intercept of this line with the y-axis ($D\text{-}_{CO2}\text{-o}$) gives the diffusion coefficient of the dead oil and the slope of the line varies for different oil types. Equation 30 expresses this dependency. This equation is more meaningful than Equation 29, since the effect of the oil viscosity (the first term) has been separated from the effect of the dissolved gas on diffusivity.

$$D_{co2,oil} = 1.41\times10^{-10} * \mu_{OD}^{-0.47} + mR_s \quad (7.30)$$

As mentioned above, the slope (m) of the line depends on the oil types. To find this dependency, the slopes of different lines in Figure 22 were plotted versus their corresponding initial oil viscosity (Figure 23). As Figure 23 shows, a power-law function adequately correlates these two parameters with the following equation:

$$m = 1\times10^{-12}\,\mu_{OD}^{-0.1725} \quad (7.31)$$

Substituting Equation 31 in Equation 30 results in:

$$D_{co2,oil} = 1.41\times10^{-10} * \mu_{OD}^{-0.47} + 1\times10^{-12}\,\mu_{OD}^{-0.1725} R_s \quad (7.32)$$

Rearranging Equation 32 gives:

$$D_{co2,oil} = 1.41\times10^{-10} * \mu_{OD}^{-0.47}(1 + 0.0071\mu_{OD}^{0.2975} R_s) \quad (7.33)$$

This equation is simpler than Equation 29. It should be noted that a limited amount of experimentation has been done to develop this equation but these data points cover a wide range of viscosity variation. Furthermore, the results are applicable in the context of assumptions made in the model, e.g. ideal solution.

7.8.6 Swelling of the viscous mineral oil, modelling vs. experimental results:

In this section, swelling of an oil ganglion recorded during CWI, Experiment No. 3 described in Chapter 3, is simulated using the developed mathematical model. Figure 24 shows the original shape of the oil ganglion at the beginning of the CWI period (Figure 24A) and that after 22.4 hrs of CWI (Figure 24B). Using the Photoshop image analysis computer software program the amount of oil swelling was quantified. A simple 2-D model was designed with the same diffusion contact area per volume ratio as that in the micromodel. It should be noted that due to the symmetry of the profile in the vertical direction, that is, in fact, a 1-D model with a thickness specified such that 1/L gives the same diffusion contact area per volume ratio as that in the micromodel.

Estimation of Model Parameters

The required parameters to simulate this experiment were estimated, as briefly described below.

In this model the variation of diffusion coefficient for the viscous mineral oil was considered to be variable.

Density of carbon dioxide at 2000 psi and 38 °C was estimated at 775.45 kg m^{-3}. (http://webbook.nist.gov/chemistry/fluid/). CO_2 solubility in water at experimental conditions was estimated at 1.235 mol m^{-3} (Dodds, et al., 1956). Table 20 shows a summary of data for these parameters.

The CO_2/oil partition coefficient, which determines the swelling factor, is a matching parameter in this study. It was estimated at 2.65, to obtain the swelling factor of 22.8% observed in the micromodel experiments. Since both the water and carbonated water phases in the micromodel are coloured blue, it was not possible to determine the water layer thickness separating the oil and flowing CW phases. Hence, the thickness of the water layer was altered to match the oil swelling rate. Figure 25 shows three cases with

different water thicknesses. Comparison of the experimental (blue curve) results with those of the model shows that the impact of the water layer on diffusion rate is not significant. This is due to the much lower CO_2 diffusion coefficient in oil than that in water for the viscous oil, compared to that for the light oil (the experiment of Campbell and Orr, 1985). The data in Figure 25 show that the pink curve for the case with 1 mm thickness of the water layer can be considered as the best match for the experimental results.

7.8.7 Swelling versus shrinkage process

In the micromodel experiments, there were some indications that the rate of oil shrinkage when CO_2 diffuses out of the oil was initially faster than that of swelling when CO_2 diffuses into the oil. The developed mathematical model was employed to compare the rate of swelling and shrinkage for both first and second scenarios. For the results presented in this section, the initial thickness of the oil droplet was 7E-4 m for both scenarios and the initial thickness of water in the second scenario was 4E-4 m. The physical properties presented in Table 19 for the viscous mineral oil were used in this study.

Initially, in the model, the CO_2 concentration was set to be at its maximum value at the right hand side boundary (i.e., oil/CW interface in the first scenario and water/CW interface in the second one). The simulation was allowed to progress whilst CO_2 is diffusing into oil increasing its volume until the oil is fully saturated with CO_2. Then the final conditions of the swelling process were used as the initial conditions for the shrinkage process, by reassigning the zero CO_2 concentration to the same boundary. In this exercise, the oil viscosity varies with time as CO_2 diffusion progresses, based on the discussion of the previous section.

Figure 26A shows the displacement of the viscous mineral oil/CW interface (in the form of the swelling and shrinkage factors) versus time for both swelling and shrinkage processes of the first scenario, direct contact of oil and CW(Figure 2A). It is noted that initial rates of both swelling and shrinkage (the tangent line on the curves) are high but later slow down as they approach equilibrium conditions. The absolute value of the interface displacement in the shrinkage process compared to its initial condition (oil fully saturated with CO_2) was then plotted, together with that of the swelling process, to

make a direct comparison between the two (Figure 26B). Figure 26B correctly shows that the absolute values of the initial and final displacement positions are similar. However, the shrinkage rate at the beginning of the process is higher than that of swelling rate, but later it slows down and becomes lower than the swelling rate. The higher shrinkage rate compared to swelling rate at the beginning of the process is attributed to the higher diffusion coefficient of CO_2 in oil ($D_{CO2\text{-}o}$) at the initial times of the shrinkage process, compared to the swelling process. That is, during the early stages of the shrinkage process, there is a higher $D_{CO2\text{-}o}$ (lower oil viscosity) resulting in faster transfer of CO_2 from oil into water. However as the process progresses, $D_{CO2\text{-}o}$ reduces in the former, which results in a lower shrinkage rate compared to the swelling rate at the end of the process.

The above procedure was repeated for the second scenario, indirect contact of oil and CW with a water layer, Figure 2B. Similarly to Figure 26B, Figure 27, shows that initial shrinkage rate is high but later slows down as it approaches the same final displacement value as that of swelling. However, the difference between shrinkage and swelling rates in this scenario is more pronounced than that observed for the first scenario. This is mainly due to the presence of the water layer in the second scenario. As shown previously (in Figures 17-19), the water layer thickness is an important parameter in delaying the CO_2 diffusion. Since the water layer thickness at the beginning of shrinkage is less than that at the beginning of the swelling process, the initial rate of shrinkage is faster than that of the swelling. However, later, this thickness reduces in the latter compared to the former, resulting in an increased swelling rate. To separate and compare the importance of the impact of the viscosity reduction (which was observed in the first scenario (Figure 26) and that of water layer, a new set of simulations were conducted using a constant value of $D_{CO2\text{-}o}$. Figure 28 compares swelling and shrinkage curves for this case. Since the diffusion coefficient was constant, the difference observed here is only attributed to the impact of the water layer. As can be seen and expected, the difference between swelling and shrinkage in this plot is less compared to that in Figure 27.

Figure 29 compares the observed difference between shrinkage and swelling (Shrinkage –Swelling, $d_{sh\text{-}sw}$) versus time, for the two recent cases. As can be seen, there is a major difference in the shape of the curves. That is, for the case of using a constant value of

$D_{CO2\text{-}o}$, consistent with the data in Figure 28, $d_{sh\text{-}sw}$ is positive during the entire process. However, in the second case (variable $D_{CO2\text{-}o}$) there are some negative values, which suggest that swelling is greater than the absolute value of shrinkage, which is consistent with the data in Figure 27. In addition to the change in $D_{CO2\text{-}o}$ and water layer thickness, the difference in the mass transfer driving force would also play a role in this process.

It should be noted that the CO_2 concentration in oil, which controls both the amount of viscosity reduction (which eventually determines the amount of $D_{CO2\text{-}o}$ alteration) and the thickness of the water layer, is an important parameter in dictating the degree of difference between swelling and shrinkage rates, (i.e. the shape of the $d_{sh\text{-}sw}$ curve versus time) during the mass transfer process.

Here, the effect of CO_2 concentration in oil was studied by increasing the CO_2 partition coefficient between oil and water ($K_{CO2\text{-}w/o}$) from 2.65, which corresponds to 23% oil swelling, to 3.98, which corresponds to 39% oil swelling. Figure 30 shows the swelling and shrinkage curves for this study with variable $D_{CO2\text{-}o}$. A comparison of this plot with Figure 27 highlights that the discrepancy between these two curves increases by increasing the swelling factor. Figure 31, which shows $d_{sh\text{-}sw}$ versus time for these two plots, clearly shows this further. The general trend of the results of the model discussed here is consistent with the experimental observations for n-decane. That is, the difference between the swelling and shrinkage of the n-decane with a higher swelling factor (Figure 3-21) was greater than the case of n-decane with a lower swelling factor (Figure 3-34).

Figure 31 shows a $d_{sh\text{-}sw}$ curve, which has been obtained by multiplying the $d_{sh\text{-}sw}$ curve corresponding to data for the lower $K_{CO2\text{-}w/o}$ of 2.65 by the ratio of the partition coefficients (3.98/2.65=1.5). As can be observed, this latter curve is lower than the one corresponding to the higher $K_{CO2\text{-}w/o}$ value of 3.98, highlighting that the variation is not linear. As mentioned previously, a change in $K_{CO2\text{-}w/o}$ or CO_2 concentration in water alters both CO_2 concentration in oil (Equation 1) and the final oil swelling to the same extent.

Figure 32 shows the variation of $D_{CO2\text{-}o}$ for the two different $K_{CO2\text{-}w/o}$ values. There is also another curve, which has been obtained by multiplying $D_{CO2\text{-}o}$ corresponding to data for the lower $K_{CO2\text{-}w/o}$ of 2.65 by the ratio of the partition coefficients (3.98/2.65=1.5). It is noted that $D_{CO2\text{-}o}$ has not changed to the same extent as $K_{CO2\text{-}w/o}$. In other words the change in $K_{CO2\text{-}w/o}$ has altered significantly the difference in swelling and shrinkage curves but not $D_{CO2\text{-}o}$. Therefore, it can be concluded that the variation of CO_2 concentration in oil affects the extent of oil swelling more than $D_{CO2\text{-}o}$.

7.8.8 Swelling vs. carbonation level

Here, to investigate the impact of carbonation level on the final oil swelling factor of oil, the CO_2 concentration in water ($C_{CO2\text{-}w}$), was changed.

The mathematical model simulating the first scenario, direct contact, was used in this study with fluid property parameters similar to those given in Table 19. Since the aim of this exercise is mainly investigation of the dependency of equilibrium amount of oil swelling on $C_{CO2\text{-}w}$, the second scenario is expected to give the same results. However it should be noted that it can also alter rate of oil swelling, which is different in these two scenarios. Figure 33 is a plot of final oil swelling versus $C_{CO2\text{-}w}$. This plot shows that an exponential trend (Equation 34) can describe this variation, highlighting that the incremental increase in the swelling factor is much more pronounced at higher CO_2 concentration. This result suggests that using a co-solvent in water improves the swelling factor significantly, which ultimately results in more mobilisations of oil ganglia and higher oil recovery by CWI.

$$SF = 8.0297e^{0.7428C_{CO_2-W}} \tag{7.34}$$

These results can be also analytically replicated by solving the ordinary differential Equation 10.

After simplification and elimination of dt from the either side of this ODE, we can obtain Equation 35.

$$dx(t) = \frac{x(t)d\left[C_{co_2}(t)\right]_{ave}^{V}}{\left[\frac{\rho_{co_2}}{Mw_{co_2}} - \left[C_{co_2}(t)\right]_{ave}^{V}\right]} \tag{7.35}$$

To solve this equation the dependent variable is changed as follows:

$$U = 1 - \frac{Mw_{co_2}}{\rho_{co_2}} \left[C_{co_2}(t) \right]_{ave}^{V} \tag{7.36}$$

Differentiating Equation 36 gives:

$$dU = -\frac{Mw_{co_2}}{\rho_{co_2}} d\left[C_{co_2}(t) \right]_{ave}^{V} \tag{7.37}$$

This equation is combined with Equation 35 to obtain:

$$\frac{dx}{x} = -\frac{dU}{U} \tag{7.38}$$

Integrating both sides of Equation 38 results in:

$$Lnx = -LnU + B_1 \tag{7.39}$$

where B_1 is a constant value.

Solving Equation 39 for x and substituting Equation 36 in this equation gives:

$$x = B_2 / U = B_2 / (1 - \frac{Mw_{co_2}}{\rho_{co_2}} \left[C_{co_2}(t) \right]_{ave}^{V}) \tag{7.40}$$

where B_2 is a constant value.

The coefficient of B_2 can be determined by solving it at t=0, initial conditions, which results in:

$$B_2 = X_{ini-oil} \tag{7.41}$$

Therefore, equation 40 takes the following form:

$$x = X_{ini-oil} / (1 - \frac{Mw_{co_2}}{\rho_{co_2}} \left[C_{co_2}(t) \right]_{ave}^{V}) \tag{7.42}$$

Equation 42 can be expressed in the form of swelling factor as follows:

$$x / X_{ini-oil} = (X_{ini-oil} + \Delta x) / X_{ini-oil} = 1 + SF = 1 / (1 - \frac{Mw_{co_2}}{\rho_{co_2}} \left[C_{co_2}(t) \right]_{ave}^{V}) \tag{7.43}$$

or,

$$SF = (\frac{1}{1 - \frac{mw_{CO_2}}{\rho_{CO_2}} \left[C_{co_2}(t) \right]_{ave}^{V}} - 1) * 100 \tag{7.44}$$

This equation was used to estimate the oil swelling factor for different CO_2 concentrations. Figure 34 compares the results of the model (blue points), which are numerical data, with the analytical data (pink points). As this plot shows, these two sets of data adequately match each other, indicating the accuracy of the numerical method.

In the micromodel experiments 95-100% oil swelling was observed for n-decane when fully saturated CW was used, whereas when the carbonation of CW was reduced to half, oil swelling reduced to 23.5%. This observation was simulated using the mathematical model. In the model, initially for fully saturated CW case the partition coefficient was varied to match the amount of swelling. Then, with the set partition coefficient, the swelling factor for the lower CO_2 concentration was estimated. Figure 35 shows the predicted data by the model and those measured from the image analysis of the micromodel experiments. As this plot shows, the experimental data was adequately matched by the mathematical model. The minimal difference between the model and the experiment can be attributed to the error of the image analysis and/or to the simplifying assumptions (i.e. assuming and ideal mixture for mixture of CO_2 and oil) made in the developed mathematical model.

7.9 Conclusions

The dynamic process of the swelling of an oil drop, both when it is separated from a CO_2 source by a water layer and when it is in direct contact with CW, was successfully simulated. The integrity of the mathematical model was verified by simulating the results of Campbell and Orr's experiment, which were reproduced with reasonable accuracy. Using a dimensional analysis technique a more representative relationship was developed.

The sensitivity of pertinent parameters was studied for both direct (oil/CW) and indirect (oil/W/CO_2 source) contact scenarios using two different evaluation methods (A and B). In the following conclusions, Method A refers to the first method, in which the time required for the interface to reach a specified position for different prevailing conditions was compared. Whereas, Method B refers to the second method, in which the required time for the interface to reach to 95% of its equilibrium position, was looked. Based on the sensitivity exercise conducted using both these methods for the two scenarios, it was demonstrated that:

- The impact of pertinent parameters of Group I that affect both the amount of swelling as well as the swelling rate (CO_2 concentration in CW at the inlet boundary, $C_{CO2\text{-}cw\text{-}in}$, CO_2 density, Den_{CO2}, water/oil-CO_2 partition coefficient, $K_{CO2\text{-}w/o}$,) was more pronounced based on evaluation Method A rather than B. This is due to the fact that the fixed interface position used in Method A corresponds to that of the base case, whilst in Method B it varies for each case, dampening the effect of the pertinent parameter.
- In contrast, for parameters of Group II that do not affect the amount of swelling (diffusion coefficient of CO_2 in water ($D_{CO2\text{-}w}$) and oil ($D_{CO2\text{-}o}$), water thickness (L_w)), both evaluation methods yielded the same results.
- The impact of pertinent parameters of Group I using evaluation Method A was non-symmetrical, i.e., the impact of an increase in a parameter was significantly different from that of a reduction in that parameter, highlighting the more independent nature of evaluation Method B, which did not follow this behaviour.
- In the first scenario (oil/CO_2 source (CW), direct contact) and based on the evaluation Method A, $C_{CO2\text{-}cw\text{-}in}$ (or $K_{CO2\text{-}w/o}$) and Den_{CO2} were the most sensitive parameters. Based on evaluation Method B, the impact of a change in $C_{CO2\text{-}cw\text{-}in}$ or Den_{CO2} was slightly less pronounced compared to that in oil properties, i.e. $D_{CO2\text{-}o}$ or L_o. These trends were consistent with those predicted for this case by the new relationship, which was developed based on a dimensional analysis technique.
- In the second scenario (oil/water/CO_2 source, indirect contact), the sensitivity of EDT, based on evaluation Method A, is more pronounced for a change in $C_{CO2\text{-}cw\text{-}in}$ and Den_{CO2} compared to a change in $K_{CO2\text{-}w/o}$. Based on evaluation Method B, EDT was most sensitive to the thickness of the water layer separating the oil and CO_2 source (L_w), highly sensitive to $D_{CO2\text{-}w}$, $C_{CO2\text{-}cw\text{-}in}$ and Den_{CO2}, moderately sensitive to $K_{CO2\text{-}w/o}$ and least sensitive to the value of $D_{CO2\text{-}o}$ and L_o.
- In the first scenario, the direction of changes of EDT for $C_{CO2\text{-}cw\text{-}in}$ and Den_{CO2} in Method A was in the opposite direction to that in Method B. This difference can be explained by looking at the definition of EDT for these two methods. That is, in Method A, increasing CO_2 concentration increases the driving force: hence, the model needs less time to reach the fixed EIP of the base case, whilst in

Method B, the higher CO_2 concentration results in higher swelling value, in turn leading to a longer required time to reach its final EIP.

- In the second scenario, the direction of the change in EDT by a change in $K_{CO2\text{-}w/o}$ using evaluation Method A was in the opposite direction of that using evaluation Method B. That is again due to the different definition of EDT for these two methods. However, this trend was not observed for a change in $C_{CO2\text{-}cw\text{-}in}$ or Den_{CO2}, because the adverse effect of the water layer weakened the changes due to these two parameters in the second scenario.
- Based on evaluation Method B, $C_{CO2\text{-}cw\text{-}in}$ and Den_{CO2} were more sensitive parameters in the second (indirect contact), rather than the first (direct contact), scenario.
- The impacts of a change in $C_{CO2\text{-}cw\text{-}in}$ or Den_{CO2} on EDT were in opposite directions for the first (direct contact) and second (indirect contact) scenarios. This was due to the fact that in the second scenario an increase in $C_{CO2\text{-}cw\text{-}in}$ or a decrease in Den_{CO2} reduces the dominant impact of the water layer, hence reducing the corresponding EDT values. However, in the first scenario, where there is no water, these changes increase the amount of swelling, hence increasing the corresponding EDT

The impact of the presence of a water layer separating the CO_2 source from the oil on swelling and shrinkage processes, the effect of CO_2 solubility in water on oil swelling and the validity of some of the simplified assumptions were studied with the following main conclusions:

- Although $D_{CO2\text{-}w}$ was higher than $D_{CO2\text{-}o}$, the swelling time (EDT) for the second scenario (2380 sec for the base case with 0.4 mm water layer thickness) was significantly longer than that for the first scenario (350 sec, for the same base case with 0.7 mm oil thickness). The EDT of the second scenario was also higher than that corresponding to the case with 1.1 mm oil thickness. This is because at early stages of the process, the CO_2 concentration at the fixed position of 0.7 mm is lower for the second scenario case compared to the latter case with 1.1 mm oil thickness, i.e., there is a lower concentration gradient for the case with the water layer at the beginning of the process. The lower concentration gradient in water than that in oil is mainly due to the lower CO_2

solubility in water. These results highlight the major negative impact of the water layer on the CO_2 diffusion rate from a CO_2 source to oil.

- The impact of convection due to diffusion on the results of the model was minimal. Therefore, neglecting convection as a result of the moving boundary as CO_2 diffuses and oil swells was a valid assumption.
- The swelling rates, considering viscosity reduction as a result of dissolved gas in oil, was higher than the case of a constant diffusion coefficient (constant oil viscosity). However, this difference was negligible and small for the typical oil with viscosity of 0.83 and 16.5 cP but considerable for the oil with viscosity of 165 cP. Comparison of the first scenario and the second scenario results (Figures 17-19) showed that the water layer between the oil and the CO_2 source reduced this difference, i.e. the impact of viscosity reduction on the oil swelling rate was reduced. This was consistent with the results of sensitivity analyses discussed previously, where the presence of the water layer in the second scenario dampened the impact of variation of pertinent parameters on the CO_2 diffusion process. Therefore, based on these results, it can be concluded that considering a constant diffusion coefficient of CO_2 in oil for the light oil and when there is a water layer between oil and CO_2 (as in the simulation of the experiment of Campbell and Orr) was a valid assumption.
- A simpler equation than the literature one was derived (Eq. 33) which can be used for simulation of diffusion processes. It should be noted that a limited number of experiments were performed to develop this equation but these data points cover a wide range of viscosity variation.
- The simulation of the dynamic process of the swelling of the viscous oil suggested that the water layer did not have a significant impact on the diffusion rate. This was due to the much lower CO_2 diffusion coefficient in oil than that in water for the viscous oil, compared to that for the light oil (the experiment of Campbell and Orr) where the water layer significantly delayed the CO_2 diffusion.
- Looking at the absolute value of the interface displacement compared to its initial conditions indicated that the shrinkage rate was initially higher (due to higher diffusion coefficient of CO_2 in oil (DCO_2-o), than that of swelling but later slowed down and became lower than the swelling rate.

- The difference between shrinkage and swelling rates in the second scenario was more pronounced than that observed for the first scenario. This was mainly due to the presence of a water layer in the second scenario. That is, the water layer thickness at the beginning of shrinkage was less than that at the beginning of the swelling process, resulting in faster initial rate of shrinkage than that of swelling.
- The plot of the oil swelling versus CO_2 concentration in water (carbonation level) followed an exponential trend, highlighting that the incremental increase in the swelling factor was much more pronounced at higher CO_2 concentration. This suggests that using a co-solvent in water improves the swelling factor significantly, which ultimately results in more mobilisations of oil ganglia and higher oil recovery by CWI.

7.10 References

Balint, V., 1971: ‘‘Method de prévision du comportemet d´un gisement d’huile balayé par du gaz carboniqe, Revue de L´Institut Francais du Pétrol’’, 26, No. 6, 473-94 (June)

Bijeljic B. R., Muggeridge A. H., Blunt M. J, 2002: ‘‘Effect of Composition on Waterblocking for Multicomponent Gas floods’’, SPE 77697, SPE annual Technical Conference and Exhibition held in San Antonio, Texas, 29 Sep-2 Oct.

Campbell B. T., Orr, Jr F. M., 1985: ‘‘Flow Visualization for CO_2/Crude-Oil Displacements’’, SPE 11958, Oct.

Daniel, R. and Gaddy V. L., 1972: ‘‘Natural Barriers Formed in the Region of Hydrocarbon Reservoirs’’, (Hungarian) Banyasz, Kohasz, lapok, Koolaj Floidgaz 5, No. 2, 37-45 (Feb. 1972).

Do, H.D., Pinczewski W.V.: ‘‘Diffusion controlled swelling of reservoir oil by indirect contact with injection gas’’, Chemical Engineering Science Vol.48, No18, PP. 3243-3252, (1993)

Dodds, W. S. Stutzman, L. F. and Sollami, B. J, 1956: ‘‘Carbon Dioxide Solubility in Water’’, Industrial and Engineering Chemistry Vol. 1, No. 1, (1956)

Grogan A.T., Pinczewski W.V., 1987: ‘‘The Role of Molecular Diffusion Processes in Tertiary CO_2 Flooding’’, JPT May and SPE 12706.

Grogan A.T., Pinczewski W.V., Ruskauff G. J., Orr Jr F.M., 1988: ‘‘Diffusion of CO_2 at Reservoir Conditions: Models and Measurements’’, SPE 14897.

McManamey, W.J. and Woolen, J.M., 1973: "The Diffusivity of Carbon Dioxide in Organic Liquids at 25 ^{o}C and 50 ^{o}C,'' AIChE J., May, 19, No. 3, 667-69.

Muller T., Lake L. W., 1991: ''Theoretical study of water blocking in miscible flooding'', SPE 20206.

National Institute of Standards and Technology Website: http://www.nist.gov/srd/, date accessed 23 April 2009.

Riazi, M. R., 1996: ''A new method for experimental measurement of diffusion coefficients in reservoir fluids'', Journal of Petroleum Science and Engineering 14, 235-250.

Tharanivasan, A. K., Yang, C. and Gu, Y., 2004: ''Comparison of three interface mass transfer models used in the experimental measurement of solvent diffusivity in heavy oil'', Journal of Petroleum Science and Engineering 44, 269-282.

Tharanivasan, A. K., Yang, C. and Gu, Y., 2006: ''Measurement of Molecular Diffusion Coefficient of Carbon Dioxide, Methane, and Propane in Heavy Oil under Reservoir Conditions.'', Energy & Fuels, 20, 2509-2517.

Thomas, W.J. and Adams, M.J., 1965: ''Measurement of the Diffusion Coefficient of Carbon Dioxide and Nitrous Oxide in Water and Aqueous Solution of Glycerol'', Transactions of the Faraday Society. 61, 668-73, (1965).

Unver, A.A. and Himmelblau, D.M., 1964: ''Diffusion Coefficient of CO_2, C2H4, C3H6, and C4H8 in Water from 6°C to 65°C'', Journal of Chemical & Engineering Data, 9, No. 3, 428.31 (July).

Wang, L.S., Lang, Z.X., and Guo, T. M., 1996: ''Measurement and correlation of the diffusion coefficients of carbon dioxide in liquid hydrocarbons under elevated pressures'', Fluid Phase Equilibria 117, 364-372.

Zappe, J., Wesch, A., and Ebert, K. H., 2000: ''Measurement of the Mass Transfer into Single Drops in the System of Water/Supercritical Carbon Dioxide'', Journal of Colloid and Interface Science 231, 1–7.

Parameter	Value	Description	Reference
μ_{oil}	1.45	Oil (Soltrol 130) viscosity, (m pa.s)	Campbell, and Orr. (1985).
ρ_{oil}	748	Oil (Soltrol 130) density (kg/m^3)	
$D_{CO2\text{-}o}$	3.04E-09	Diffusivity of CO_2 in oil (m^2/s)	Equation 14
$D_{CO2\text{-}w}$	4.85E-09	Diffusivity of CO_2 in water (m^2/s)	Equation 15 & Wang et al. (1996)
$K_{CO2\text{-}w/o}$	4.5	partition coefficient for CO_2 in oil and water	Grogan, and Pinczewski (1987)

Den_{CO2}	779	CO_2 density at 25° C and 8.3 M.Pa	Zappe, et al. (2000)
$C_{CO2\text{-}cw\text{-}in}$	1.3	CO_2 concentration in water at 25° C and 8.3 M.Pa [kmol/m^3]	Dodds, et al. (1956)
$C_{CO2\text{-}o}$	5.85	Maximum CO_2 concentration in oil (kmol/m^3)	Equation 13
$MW_{\text{-}CO2}$	44	CO_2 molecular weight (kg/kmol)	

Table 7-1: Estimated parameters for validation of the model by simulating Campbell and Orr's (1985) experiment.

Critical Parameters	Experiment	Model
Initial ratio of the volume of water to oil (%)	28.1	28.4
Initial contact area between oil and water (mm in 2D)	5.17	5.00
Initial thickness of water (mm)	3	3
Initial thickness of oil (mm)	3	3

Table 7-2: The reported parameters of Campbell and Orr's dead-end pore and the corresponding values used in our mathematical model.

Deviation in $D_{CO2\text{-}o}$ (%)	$D_{CO2\text{-}o}$ (m^2 sec^{-1})	EDT (sec)	Deviation in EDT (%)	EDT/ EDT_{bcase} -	EDT/ EDT_{bcase} Relationship 21 -
-30.00	2.13E-09	500	42.9	1.43	1.43
0.00	**3.04E-09**	**350**	**0.0**	**1.00**	**1.00**
30.00	3.95E-09	175	-50.0	0.50	0.77

Table 7-3: Impact of a change in diffusivity of CO_2 ($D_{CO2\text{-}o}$) in oil on the equilibrium diffusion time (EDT): first scenario (oil/CW, direct contact, Figure 2A), both evaluation Methods, A and B.

Deviation in $C_{CO2\text{-}cw\text{-}in}$ (%)	$C_{CO2\text{-}cw\text{-}in}$ (mole m^{-3})	EDT (sec)	Deviation in EDT (%)
-2	1.274	540	54.3
0	**1.300**	**350**	**0.0**
2	1.326	300	-14.3
10	1.430	200	-42.9
20	1.560	140	-60.0

Table 7-4: Impact of a change in the CO_2 concentration at the inlet boundary ($C_{CO2\text{-}cw\text{-}in}$) on the equilibrium diffusion time (EDT): first scenario (oil/CW, direct contact, Figure 2A), evaluation Method A.

Deviation in Den_{CO2}	Den_{CO2} (kg m^{-3})	EDT (sec)	Deviation in EDT (%)

(%)			
-10	701.10	190	-45.7
-2	763.42	295	-15.7
0	**779.00**	**350**	**0.0**
2	794.58	460	31.4

Table 7-5: Impact of a change in the CO_2 Density (Den_{CO2}) on the equilibrium diffusion time (EDT): first scenario (oil/CW, direct contact, Figure 2A), evaluation Method A.

Deviation in $C_{CO2\text{-}cw\text{-}in}$ (%)	$C_{CO2\text{-}cw\text{-}in}$ (mole m^{-3})	EDT (sec)	Deviation in EDT (%)	EDT/ EDT_{bcase} -	EDT/ EDT_{bcase} Relationship 21 -
-20	1.033	290	-17.1	0.83	0.72
-10	1.170	320	-8.6	0.91	0.86
0	**1.300**	**350**	**0.0**	**1.00**	**1.00**
10	1.430	380	8.6	1.09	1.16
20	1.560	420	20.0	1.20	1.33

Table 7-6: Impact of a change in the CO_2 concentration at the inlet boundary ($C_{CO2\text{-}cw\text{-}in}$) on the equilibrium diffusion time (EDT): first scenario (oil/CW, direct contact, Figure 2A), evaluation Method B.

Deviation in Den_{CO2} (%)	Den_{CO2} (kg m^{-3})	EDT (sec)	Deviation in EDT (%)	EDT/ EDT_{bcase} -	EDT/ EDT_{bcase} Relationship 21 -
-10	701.1	380	8.6	1.09	1.18
0	**779.0**	**350**	**0.00**	**1.00**	**1.00**
10	856.9	320	-8.6	0.91	0.87

Table 7-7: Impact of a change in the CO_2 Density (Den_{CO2}) on the equilibrium diffusion time (EDT): first scenario (oil/CW, direct contact, Figure 2A), evaluation Method B.

Deviation in L_o (%)	L_o (m)	EDT (sec)	Deviation in EDT (%)	EDT/ EDT_{bcase} -	EDT/ EDT_{bcase} Relationship 21 -
-20	5.60E-04	220	-37.1	0.63	0.64
-10	6.30E-04	280	-20.0	0.80	0.81
0	**7.00E-04**	**350**	**0.0**	**1.00**	**1.00**
10	7.70E-04	410	17.1	1.17	1.21
20	8.40E-04	480	37.1	1.37	1.44

Table 7-8: Impact of a change in the initial thickness of oil phase (L_o) on the equilibrium diffusion time (EDT): first scenario (oil/CW, direct contact, Figure 2A), evaluation Method B.

Deviation in $C_{CO2\text{-}cw\text{-}in}$ (%)	$C_{CO2\text{-}cw\text{-}in}$ (mole m^{-3})	EDT (sec)	Deviation in EDT (%)
-2	1.274	2680	12.6
0	**1.300**	**2380**	**0.0**
2	1.326	2160	-9.2
10	1.430	1680	-29.4
20	1.560	1340	-43.7

Table 7-9: Impact of a change in the CO_2 concentration in carbonated water ($C_{CO2\text{-}cw\text{-}in}$) on the equilibrium diffusion time (EDT): second scenario (oil/W/CO2 Source, indirect contact, Figure 2B), evaluation Method A.

Deviation in Den_{CO2} (%)	Den_{CO2} (kg m^{-3})	EDT (sec)	Deviation in EDT (%)
-10	701.10	1620	-31.9
-2	763.42	2160	-9.2
0	**779.00**	**2380**	**0.0**
2	794.58	2780	16.8

Table 7-10: Impact of a change in the CO_2 Density (Den_{CO2}) on the equilibrium diffusion time (EDT): second scenario (oil/W/CO2 source, indirect contact, Figure 2B), evaluation Method A.

Deviation in $K_{CO2\text{-}w/o}$ (%)	$K_{CO2\text{-}w/o}$ -	EDT (sec)	Deviation in EDT (%)
-2	4.41	2580	8.4
0	**4.50**	**2380**	**0.0**
2	4.56	2240	-5.9
10	4.95	2000	-16.0
20	5.40	1880	-21.0

Table 7-11: Impact of a change in the partition coefficient for CO_2 in oil and water ($K_{CO2\text{-}w/o}$) on the equilibrium diffusion time (EDT): second scenario (oil/W/CO2 source, indirect contact, Figure 2B), evaluation Method A.

Deviation in D_{CO2-w} (%)	D_{CO2-w} (m^2 sec^{-1})	EDT (sec)	Deviation in EDT (%)
-30.00	3.40E-09	3340	40.3
0.00	**4.85E-09**	**2380**	**0.0**
30.00	6.31E-09	1920	-19.3

Table 7-12: Impact of a change in the diffusivity of CO_2 in water phase (D_{CO2-w}) on the equilibrium diffusion time (EDT): second scenario (oil/W/CO2 source, indirect contact, Figure 2B), both evaluation Methods, A and B.

Deviation in D_{CO2-o} (%)	D_{CO2-o} (m^2 sec^{-1})	EDT (sec)	Deviation in EDT (%)
-30.00	2.13E-09	2480	4.2
0.00	**3.04E-09**	**2380**	**0.0**
30.00	3.95E-09	2320	-2.5

Table 7-13: Impact of a change in the diffusivity of CO_2 in the oil phase (D_{CO2-o}) on the equilibrium diffusion time (EDT): second scenario (indirect oil/W/CO_2 source, indirect contact, Figure 2B): both evaluation Methods, A and B.

Deviation in L_w (%)	L_w (m)	EDT (sec)	Deviation in EDT (%)
-15	3.40E-04	1680	-29.4
-10	3.60E-04	1900	-20.2
0	**4.00E-04**	**2380**	**0.0**
10	4.40E-04	2840	19.3
20	4.80E-04	3440	44.5

Table 7-14: Impact of a change in the initial thickness of the water barrier (L_w) on the equilibrium diffusion time (EDT): second scenario (oil/W/CO_2 source, indirect contact, Figure 2B), both evaluation Methods, A and B.

Deviation in L_o (%)	L_o (m)	EDT (sec)	Deviation in EDT (%)
-20	5.60E-04	2400	0.8
-10	6.30E-04	2400	0.8
0	**7.00E-04**	**2380**	**0.0**
10	7.70E-04	2340	-1.7
20	8.40E-04	2330	-2.1

Table 7-15: Impact of a change in the initial thickness of the oil phase (L_o) on the equilibrium diffusion time (EDT): second scenario (oil/W/CO_2 source, indirect contact, Figure 2B), evaluation Method B.

Deviation in $C_{CO2-cw-in}$ (%)	$C_{CO2-cw-in}$ (mole m^{-3})	EDT (sec)	Deviation in EDT (%)

-20	1.040	2950	24.0
-10	1.170	2670	12.2
-2	1.274	2420	1.7
-1	1.287	2400	0.8
0	**1.300**	**2380**	**0.0**
10	1.430	2080	-12.6
20	1.560	1840	-22.7

Table 7-16: Impact of a change in the CO_2 concentration in the carbonated water phase ($C_{CO2\text{-}cw\text{-}in}$) on the equilibrium diffusion time (EDT): second scenario (oil/W/CO_2 source, indirect contact, Figure 2B), evaluation Method B.

Deviation in Den_{CO2} (%)	**Den_{CO2} (kg m^{-3})**	**EDT (sec)**	**Deviation in EDT (%)**
-10	701.10	2040	-14.3
0	**779.00**	**2380**	**0.0**
2	794.58	2460	3.4
10	856.90	2600	9.2

Table 7-17: Impact of a change in the CO_2 Density (Den_{CO2}) on the equilibrium diffusion time (EDT): second scenario (oil/W/CO_2 source, indirect contact, Figure 2B), evaluation Method B.

Deviation in $K_{CO2\text{-}w/o}$ (%)	**$K_{CO2\text{-}w/o}$ -**	**EDT (sec)**	**Deviation in EDT (%)**
-20	3.60	1960	-17.7
-10	4.05	2240	-5.9
-2	4.41	2340	-1.7
0	**4.50**	**2380**	**0.0**
10	4.95	2560	7.6
20	5.40	2560	7.6

Table 7-18: Impact of a change in the partition coefficient for CO_2 in oil and water ($K_{CO2\text{-}w/o}$) on the equilibrium diffusion time (EDT): second scenario (oil/W/CO_2 source, indirect contact, Figure 2B), evaluation Method B.

Parameter	**Value**	**Description**
ρ_{CO2}	775.45	Density of CO_2 at 38 °C and 2000 psi-kg m^{-3}
Mw_{CO2}	44	CO_2 Molecular Weight-kg^1 $kmol^{-1}$
$D_{CO2-water}$	1E-08	Diffusivity of CO_2 in water-m^2 s^{-1}
$K_{CO2-w/o}$	2.65	Partition Coefficient (Will be discussed in the next section)
$x_{in-water}$	2.00E-04	Initial thickness of water layer in the second scenario-m
x_{in-oil}	7.00E-04	Initial thickness of oil domain-m
$C_{CO2-inletW}$	1.2357	CO_2 concentration in carbonated water-mol m^{-3}
P1	14.7	Standard Pressure in Psia

P2	2000	Experimental Pressure in Psia
T1	298	Standard Temperature 25 °C in K
T2	311	Experimental Temperature in K
Z2	0.37	Compressibility factor at 2000 Psia and 311 K
R	1.206245	Gas Constant m^3 psi K^{-1} mol^{-1}
μ_{oil}	0.83	Viscosity of gas-free oil (n-decane) at T2 and P2-cP
μ_{oil}	16.5	Viscosity of gas-free oil (Viscous mineral oil) at T_2 -cP
μ_{oil}	165	Viscosity of gas-free oil (A typical heavy oil)-cP

Table 7-19: The parameters used to study the effect of diffusion change as a result of dissolved CO_2.

Parameter Name	Value	Description	Reference
$D_{CO2\text{-}o}$	9.7E-10	Diffusivity of CO_2 in oil with viscosity of 16.5 cP (m^2/s) at initial time	Equation 23
$D_{CO2\text{-}w}$	1E-08	Diffusivity of CO_2 in water (m^2/s)	Order of magnitude from the previous chapter
($K_{CO2\text{-}w/o}$),	2.65	Partition Coefficient for CO_2 in Oil and Water	
Den_{CO2}	775.45	CO_2 density at 38° C and 2000 psi	http://webbook.nist.gov/chemistry/fluid/
$C_{CO2\text{-}cw\text{-}in}$	1.2357	CO_2 concentration in water at 38° C and 13.6 M.Pa [$kgmol/m^3$]	Dodds, et al. (1956)
$C_{CO2\text{-}o}$	3.273	Maximum CO_2 concentration in oil ($kgmol/m^3$)	Equation 1
$MW_{\text{-}CO2}$	44	CO_2 molecular weight (kg/kgmol)	
A/V_MM	6	Area/Volume in the micromodel (cm^{-1})	
X_oil_ini	0.167	Initial oil thickness (cm)	
A/V_M	5.988	Area/Volume in the mathematical model (cm^{-1})	

Table 7-20: Estimated model parameters for simulating the swelling of the viscous oil within the micromodel, during CWI, Experiment 3.

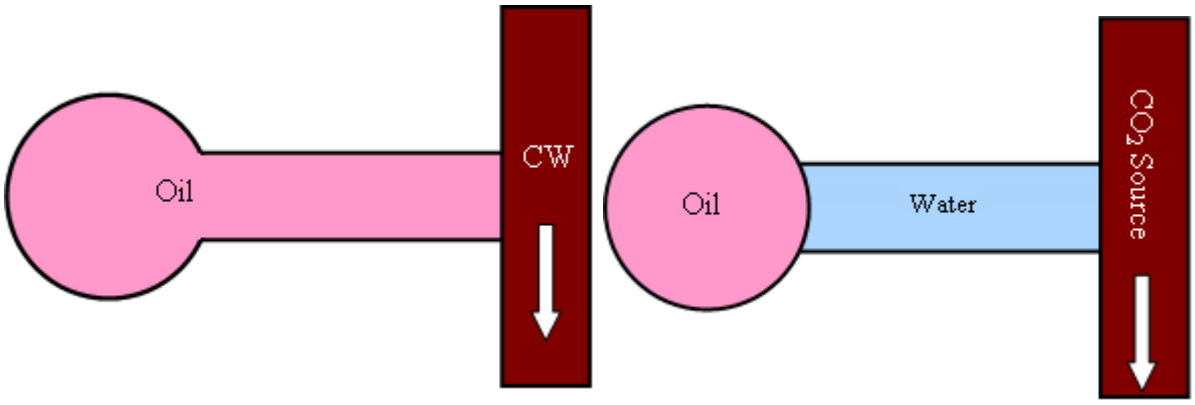

A B

Figure 7-1: An oil drop trapped in a dead-end pore is in contact with the (A) flowing carbonated water (CW) (direct contact) and (B) water, which in turn is in contact with the flowing CO_2 source (CW), indirect contact.

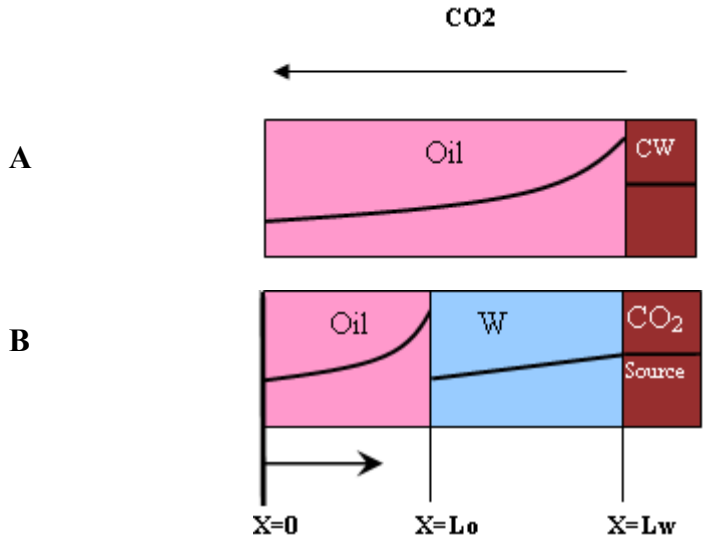

Figure 7-2: CO_2 concentration profiles for (**A**) first scenario (Figure 1.A), direct contact, and (**B**) second scenario (Figure 1.B), indirect contact.

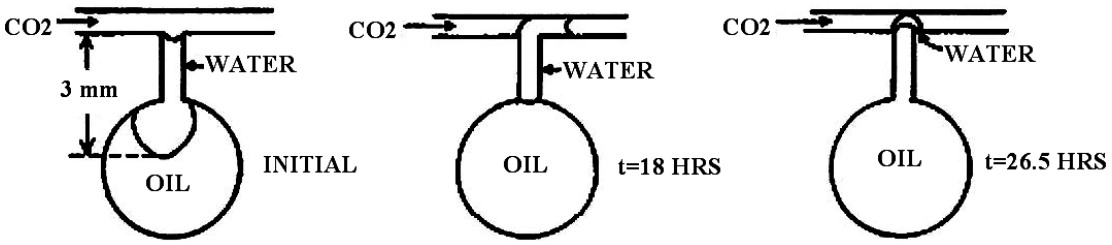

A B C

Figure 7-3: Swelling of the trapped oil in the dead end pore in the experiment reported by Campbell and Orr (1985).

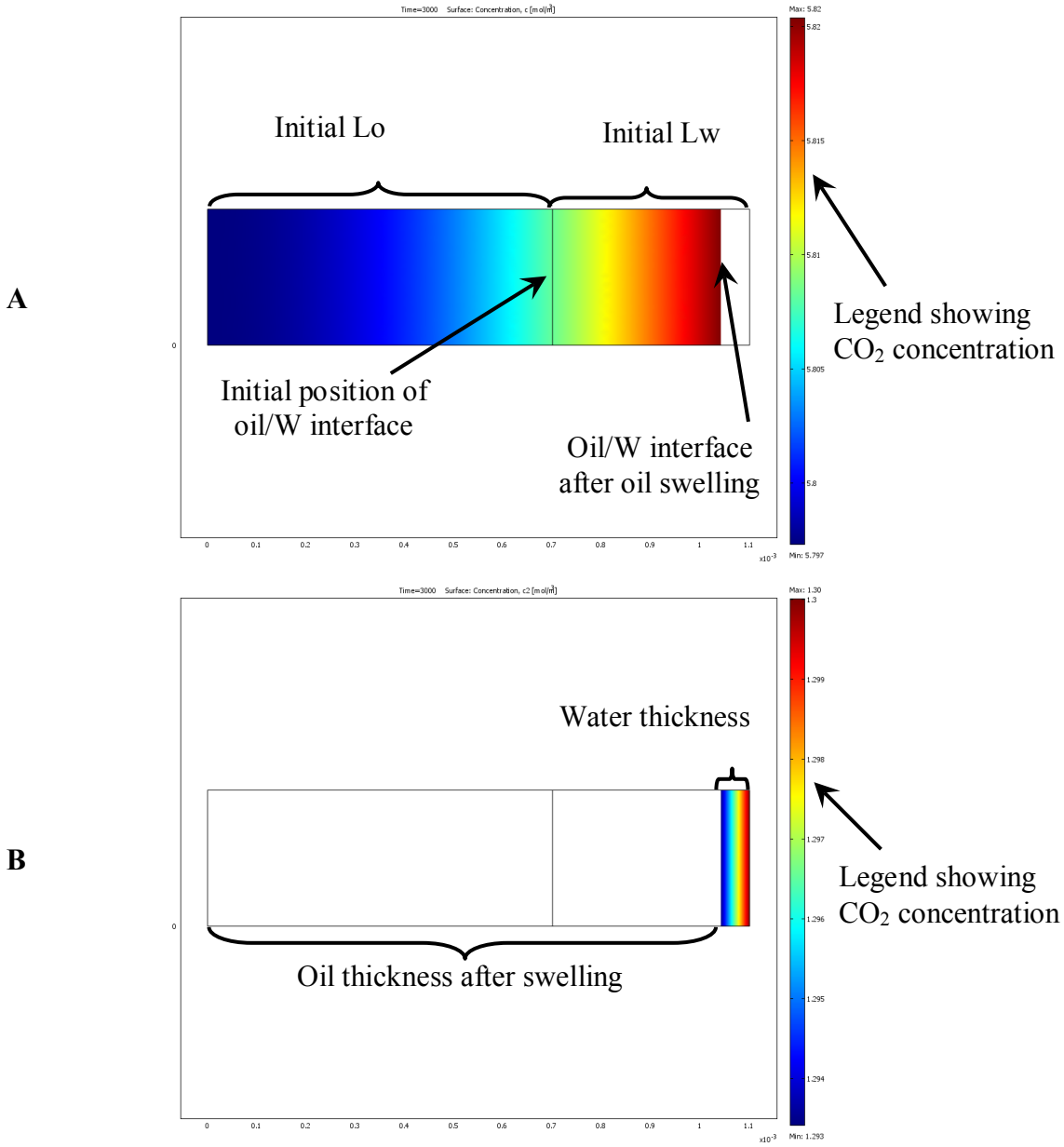

Figure 7-4: CO_2 concentration profile in the **A**) oil phase **B**) water phase, after 3000 sec. In this process oil has swollen due to diffusion of CO_2 from carbonated water, through the water layer, into the oil.

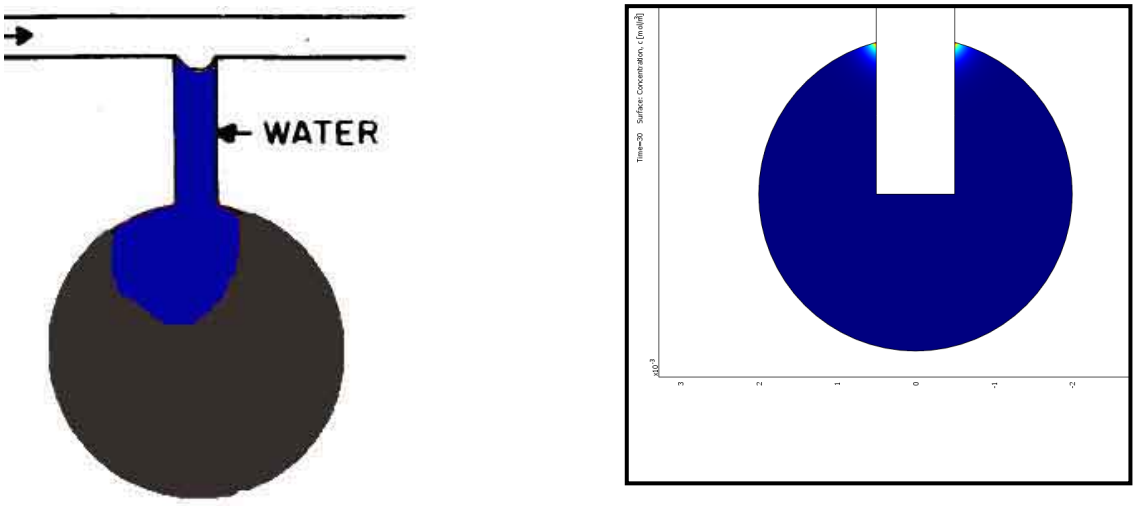

(A) (B)

Figure 7-5: A) Dead end-pore of Campbell and Orr's experiment and B) the developed mathematical model.

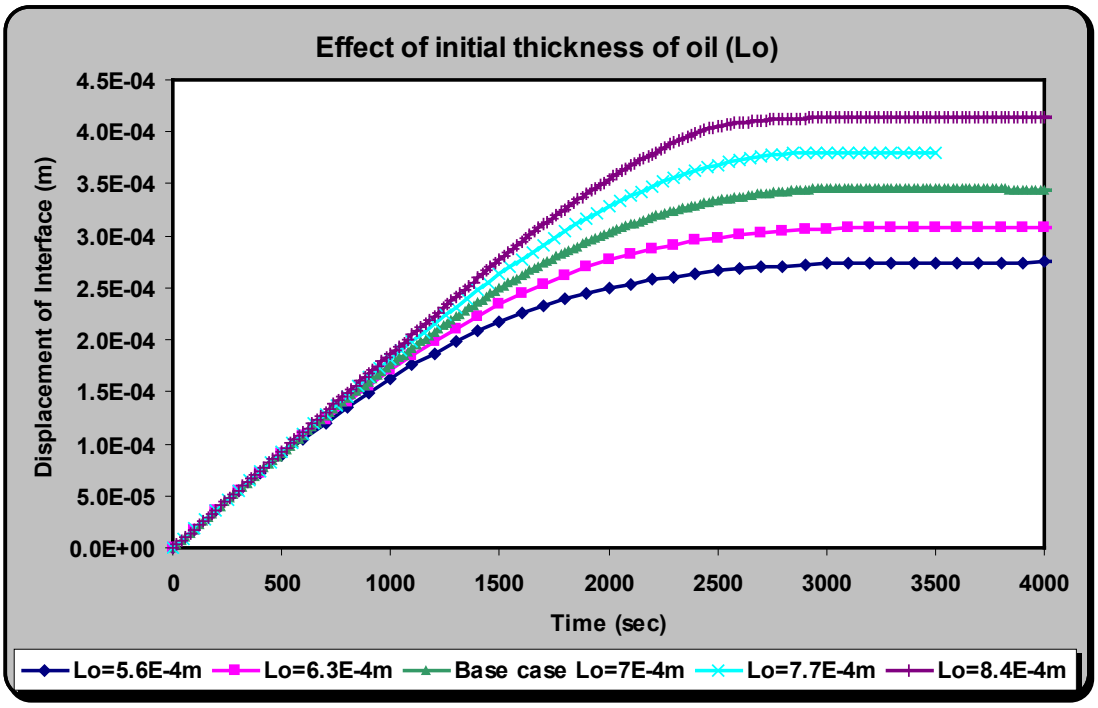

Figure 7-6: Displacement of oil water interface versus time at different initial oil thicknesses: second scenario (oil/CW, indirect contact, Figure 2B).

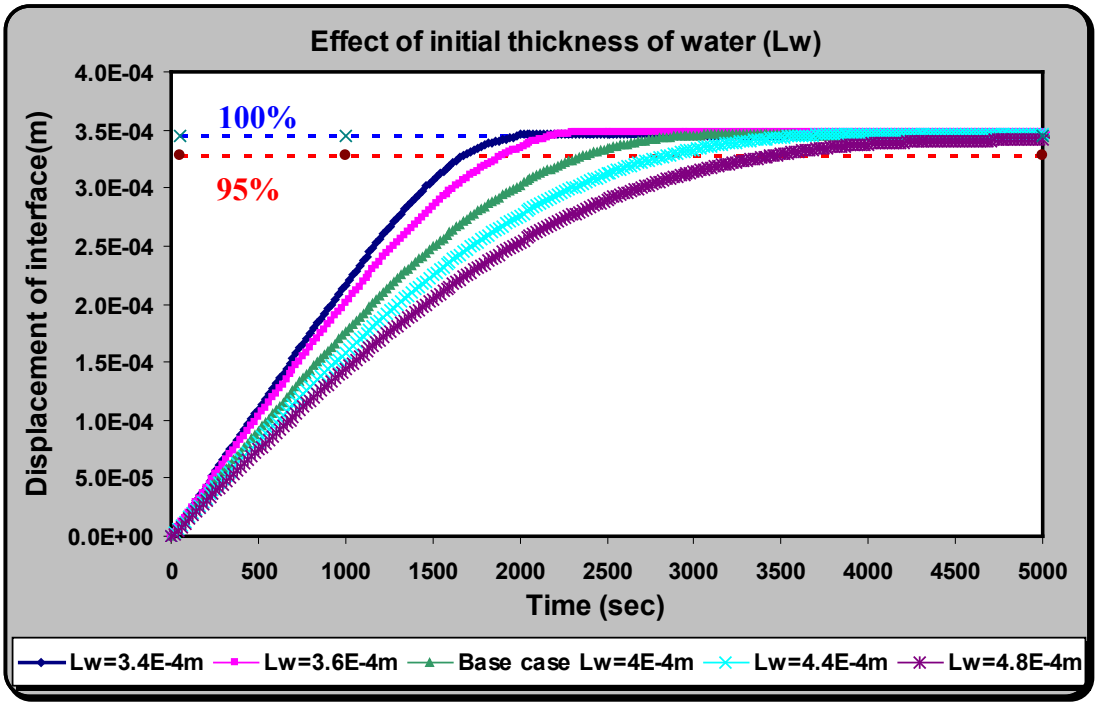

Figure 7-7: Displacement of oil water interface versus time at different initial water thicknesses: second scenario (oil/W/CO_2 source, indirect contact, Figure 2B).

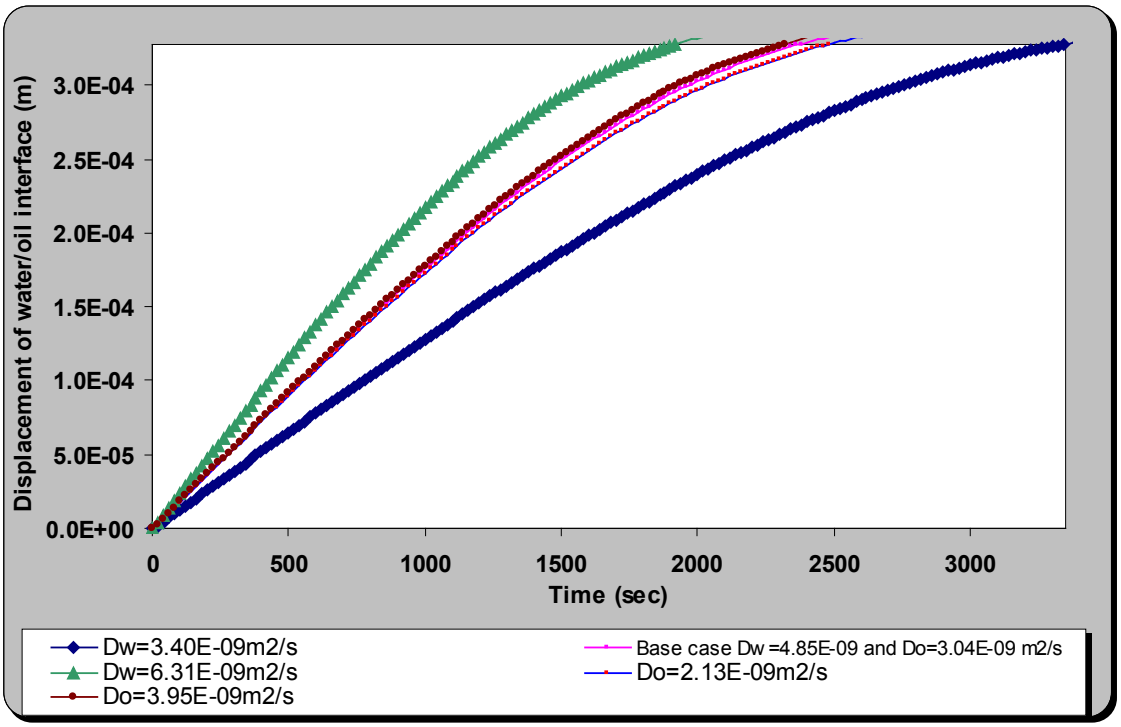

Figure 7-8: Displacement of interface versus time using different CO_2 diffusion coefficients in water and oil: second scenario (oil/W/ CO_2 source, indirect contact, Figure 2B).

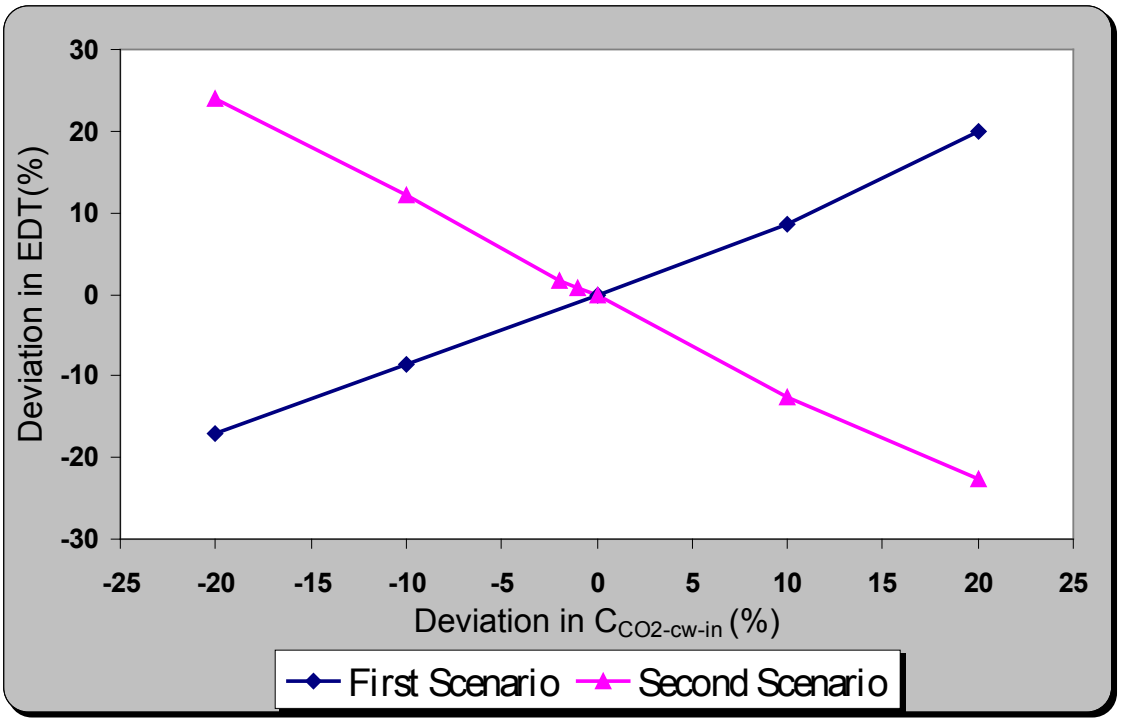

Figure 7-9: The impact of a change in equilibrium CO_2 concentration in CW at the inlet boundary ($C_{CO2\text{-}cw\text{-}in}$) on equilibrium diffusion time (EDT), for both direct contact (first scenario) and indirect contact (second scenario) cases, based on evaluation method B.

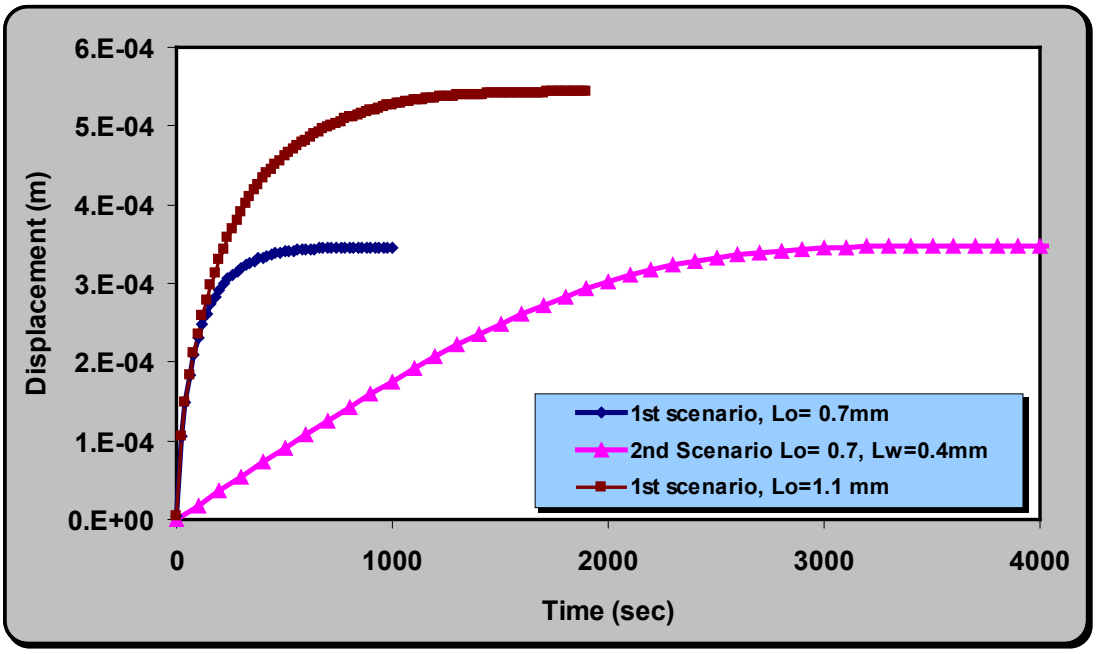

Figure 7-10: Swelling of oil in the first and second scenarios and the impact of the water layer on reduction of the swelling rate, Table 1 gives other data.

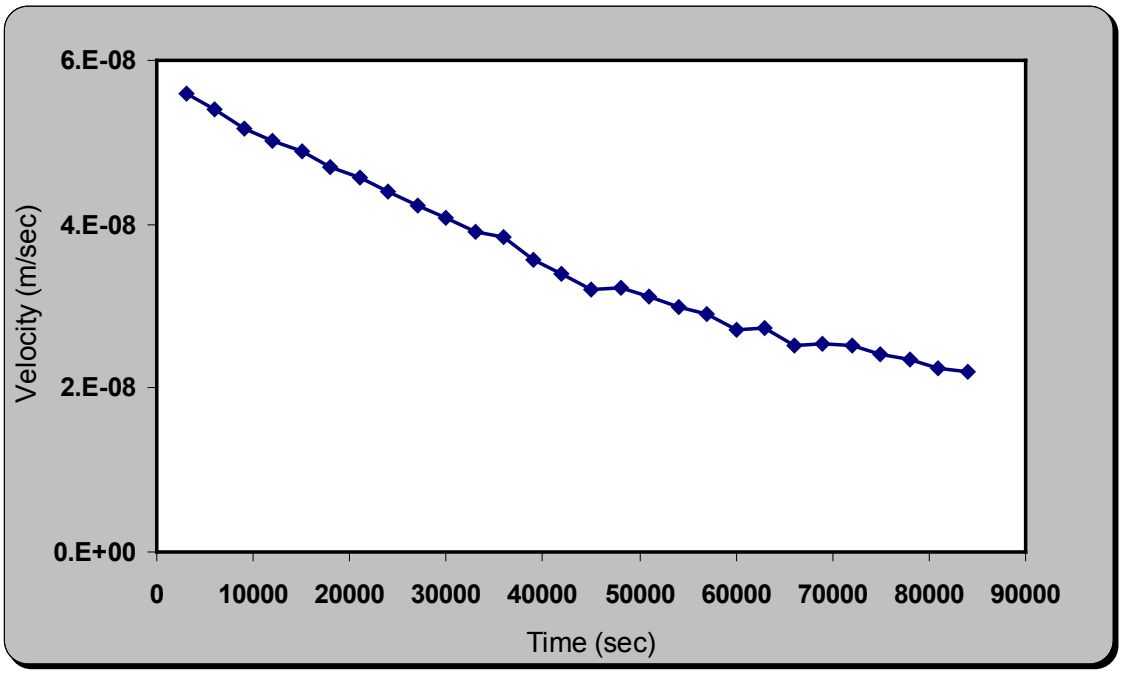

Figure 7-11: Oil-water interface velocity in the model simulating the experiment of Campbell and Orr, 1985.

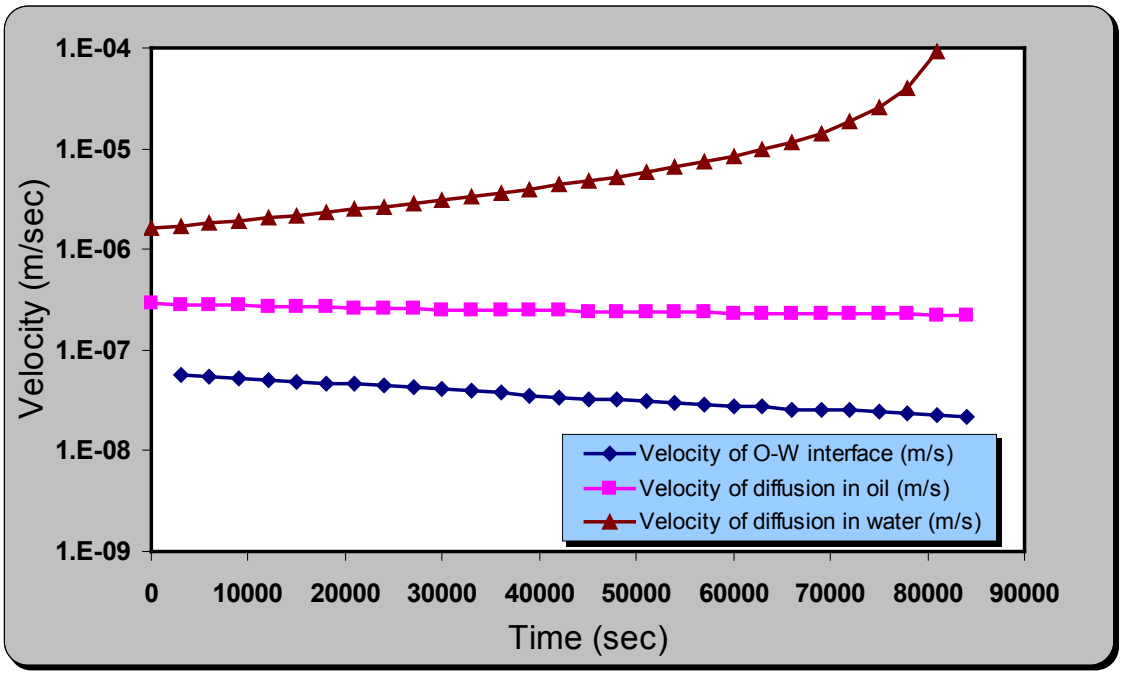

Figure 7-12: Oil-water interface velocity and the CO_2 diffusion rates in the oil and water phases in the model simulating the experiment of Campbell and Orr, 1985.

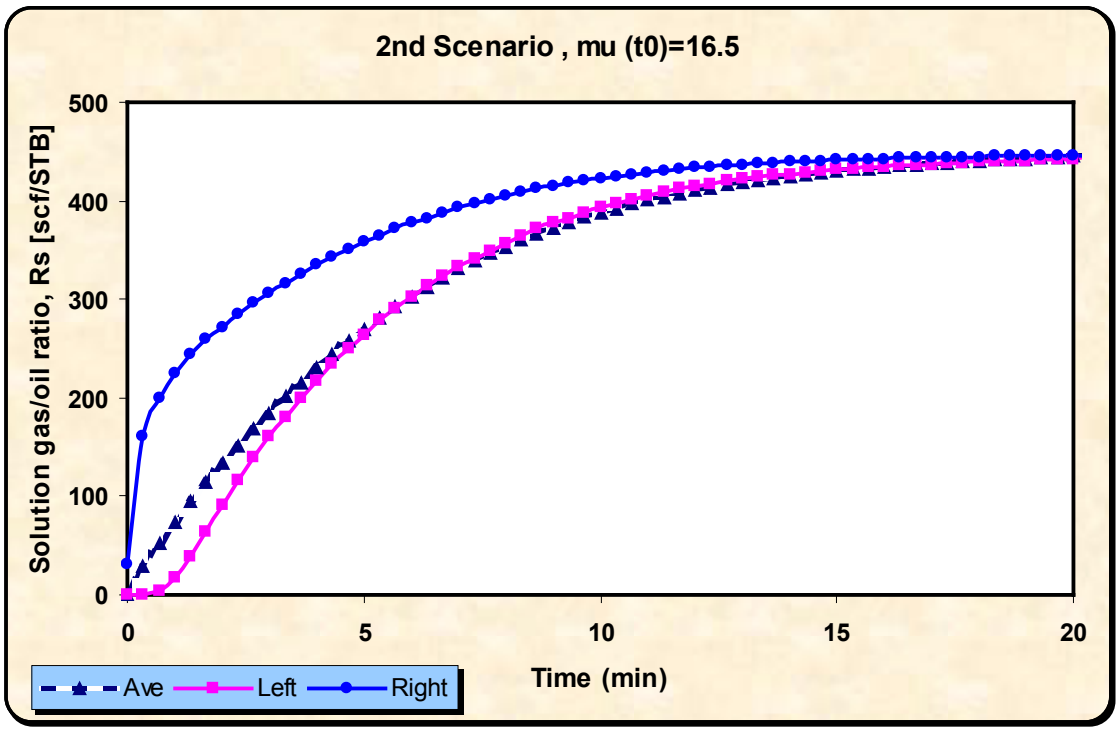

Figure 7-13: Variation of solution gas/oil ratio versus time as a result of dissolved CO_2 in the oil with initial viscosity of 16.5 cP for the second scenario, indirect contact between CO_2 source and oil, Figure 2B.

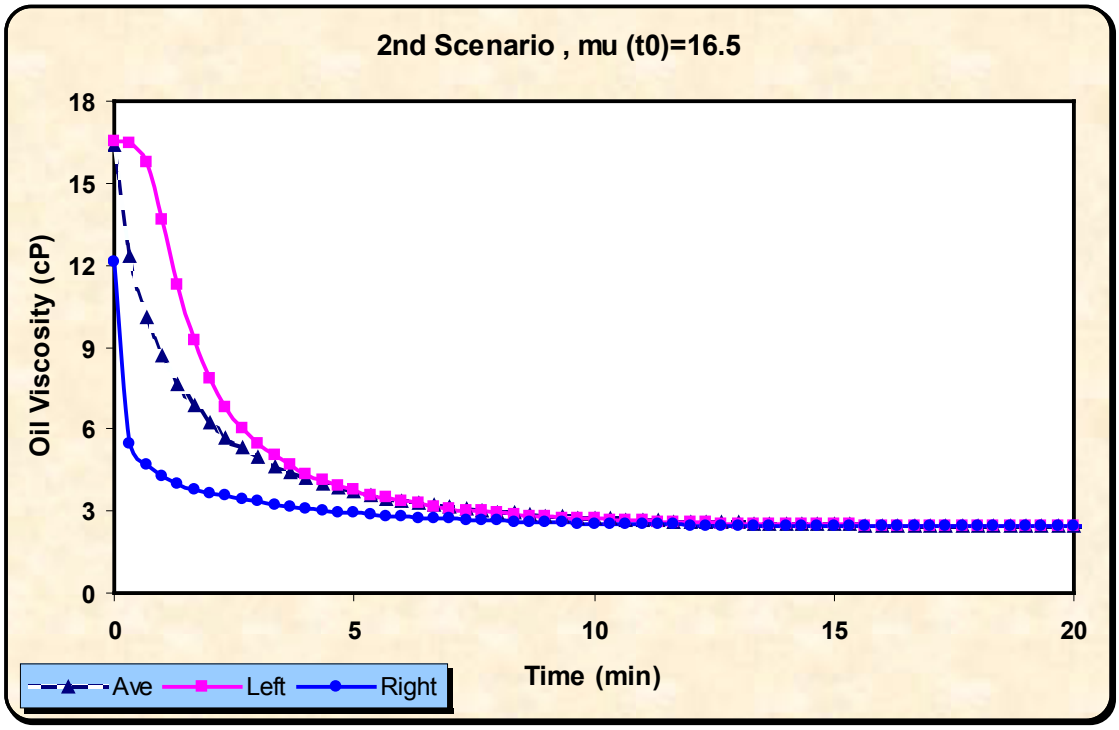

Figure 7-14: Variation of oil viscosity versus time as a result of dissolved CO_2 in the oil with initial viscosity of 16.5 cP for the second scenario, indirect contact between CO_2 source and oil, Figure 2B.

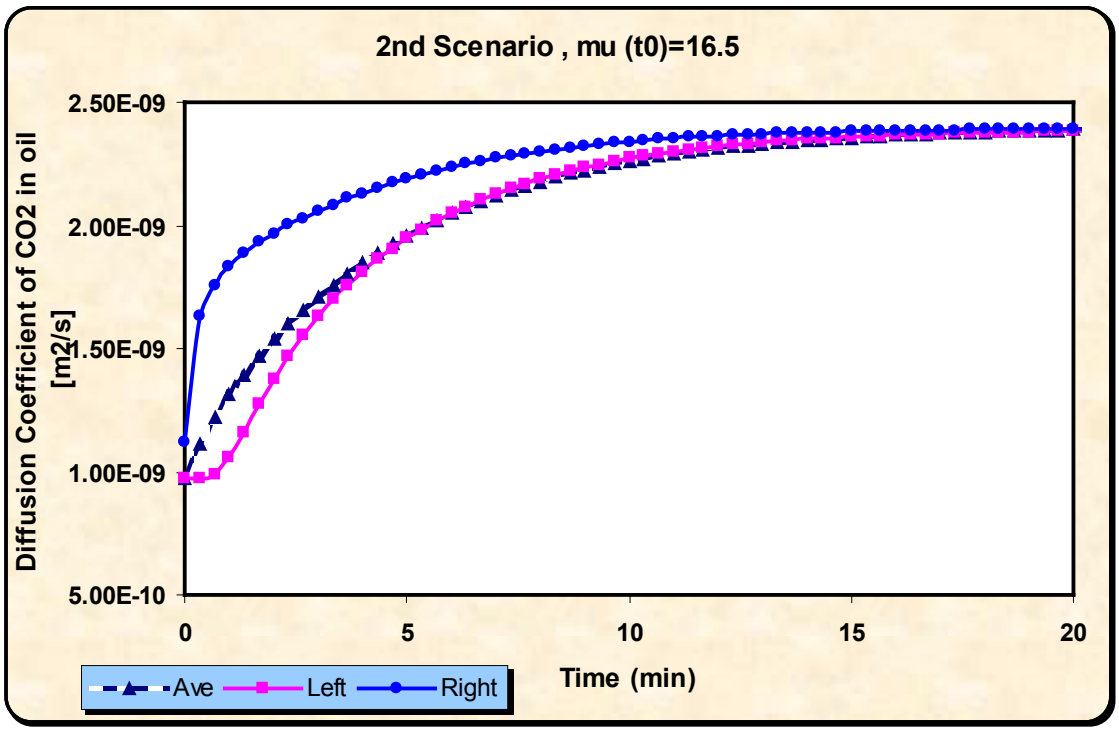

Figure 7-15: Variation of CO_2 diffusion coefficient in the oil phase with initial viscosity of 16.5 cP versus time for the second scenario, indirect contact between CO_2 source and oil, Figure 2B.

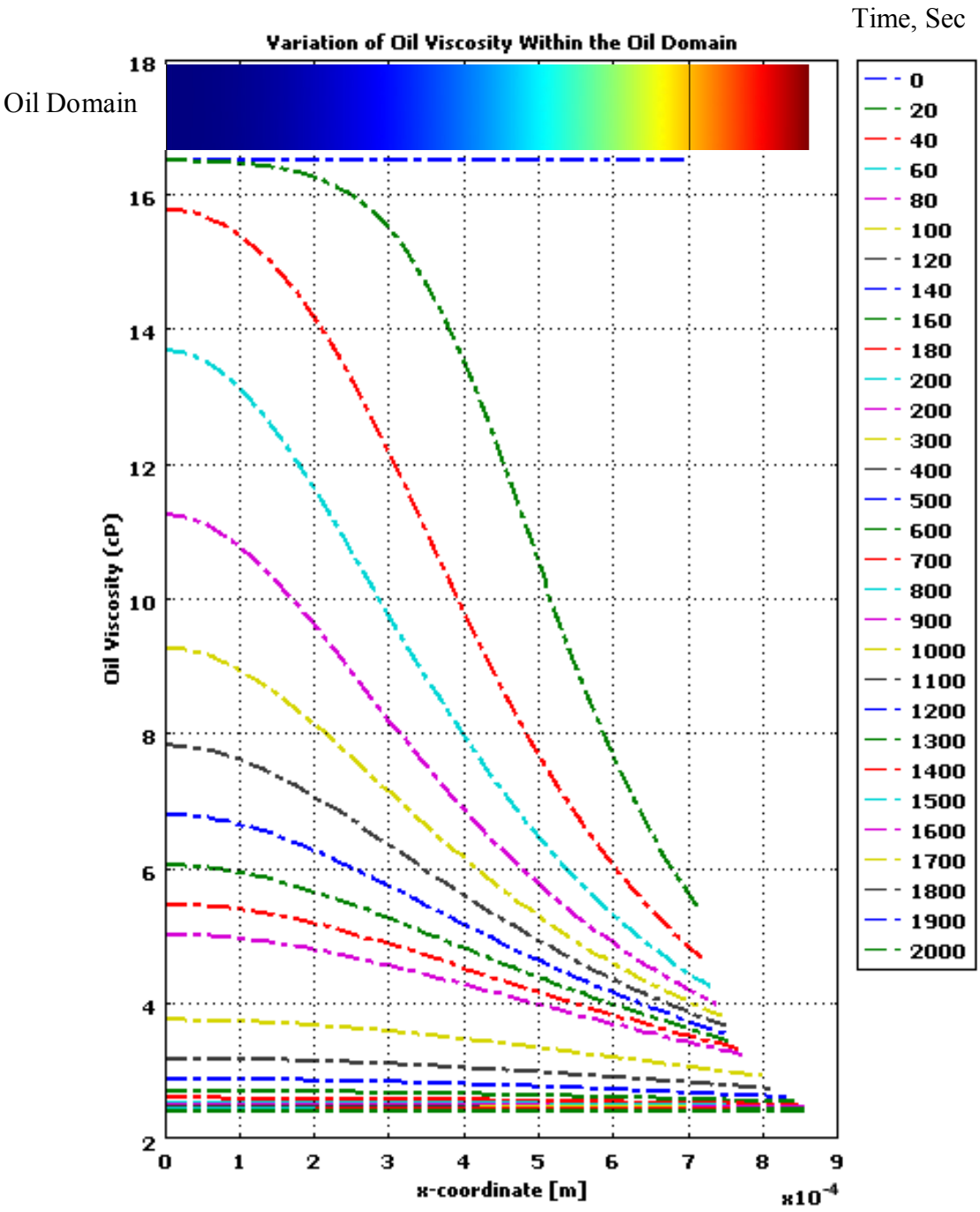

Figure 7-16: Variation of oil viscosity across the oil phase at different times, as a result of CO_2 dissolution in oil with initial viscosity of 16.5 cP: second scenario, indirect contact between CO_2 source and oil, Figure 2B.

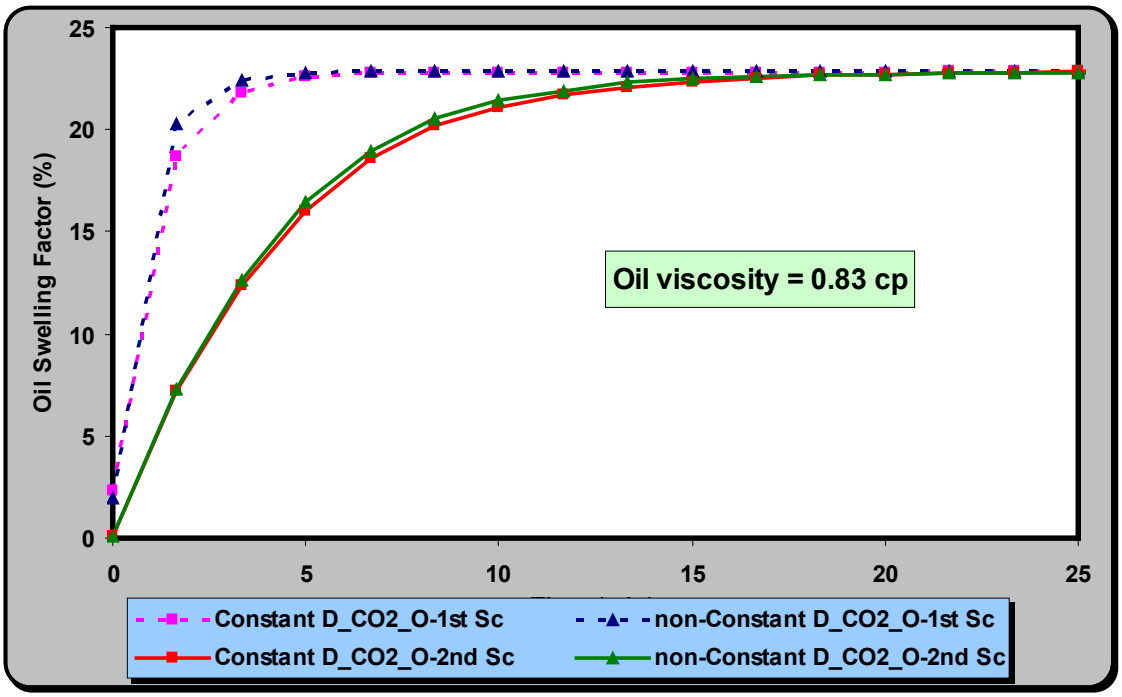

Figure 7-17: Diffusion rate for a typical oil with initial oil viscosity of 0.83 cp, both first scenario, direct contact between CO_2 source and oil, Figure 2A, and second scenario, indirect contact between CO_2 source and oil, Figure 2B. For both constant and non-constant CO_2 diffusion coefficient in oil

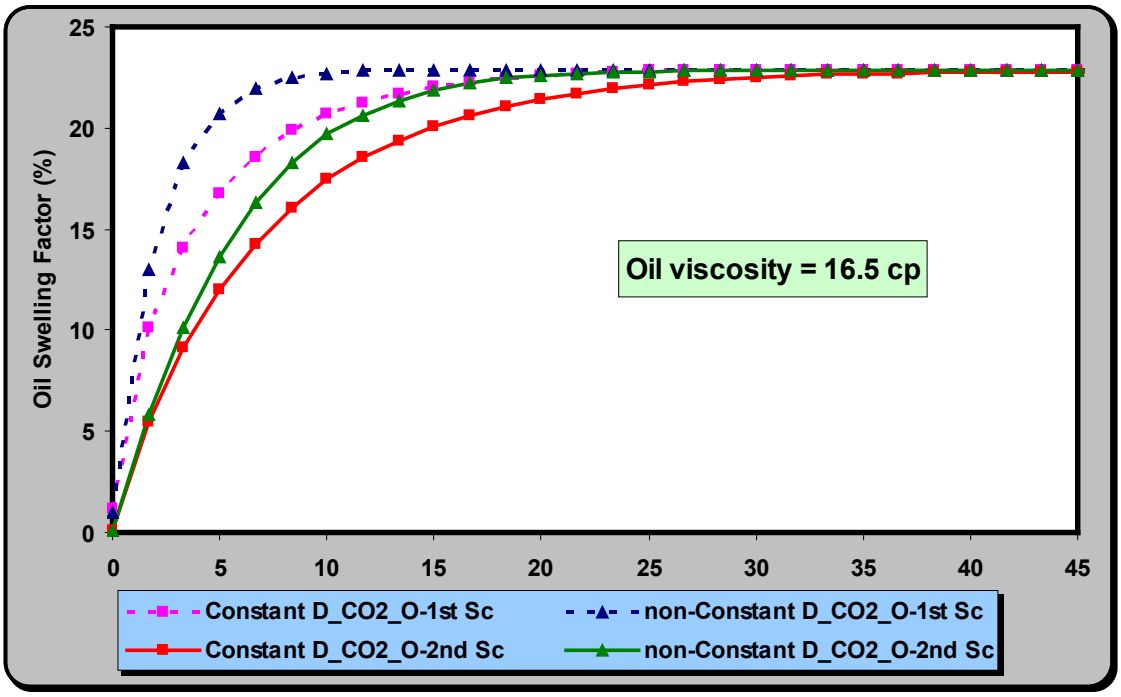

Figure 7-18: Diffusion rate for a typical oil with initial oil viscosity of 16.5 cp, both first scenario, direct contact between CO_2 source and oil, Figure 2A, and second scenario, indirect contact between CO_2 source and oil, Figure 2B. For both constant and non-constant CO_2 diffusion coefficient in oil

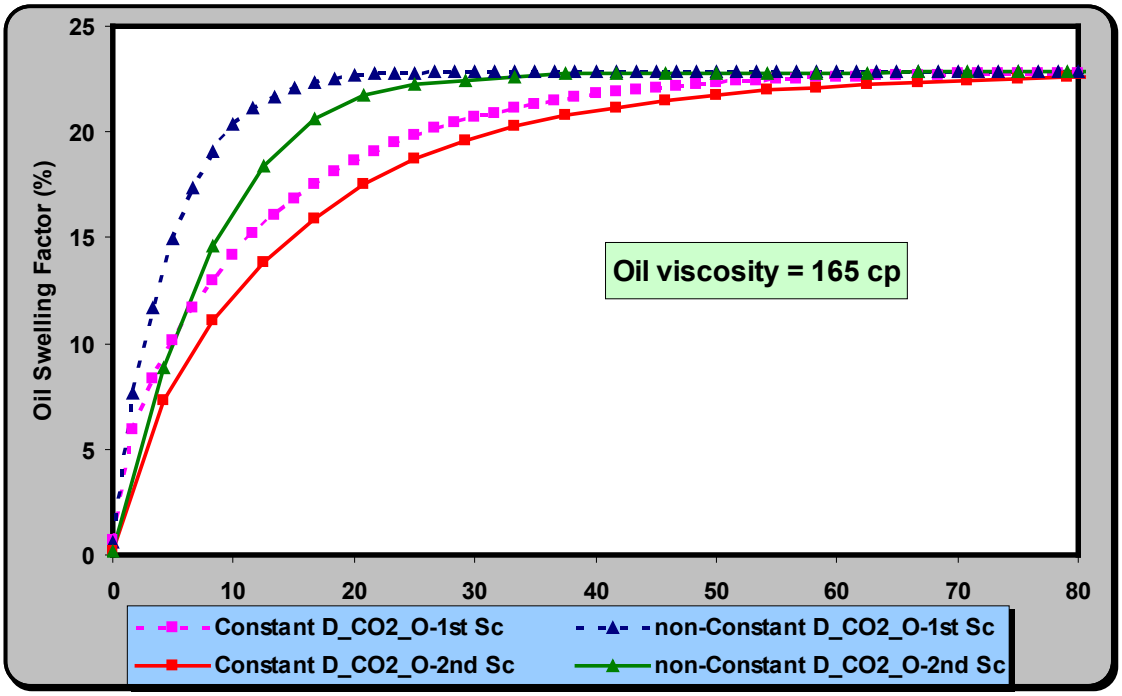

Figure 7-19: Diffusion rate for a typical oil with initial oil viscosity of 165 cp, both first scenario, direct contact between CO_2 source and oil, Figure 2A, and second scenario, indirect contact between CO_2 source and oil, Figure 2B. For both constant and non-constant CO_2 diffusion coefficient in oil

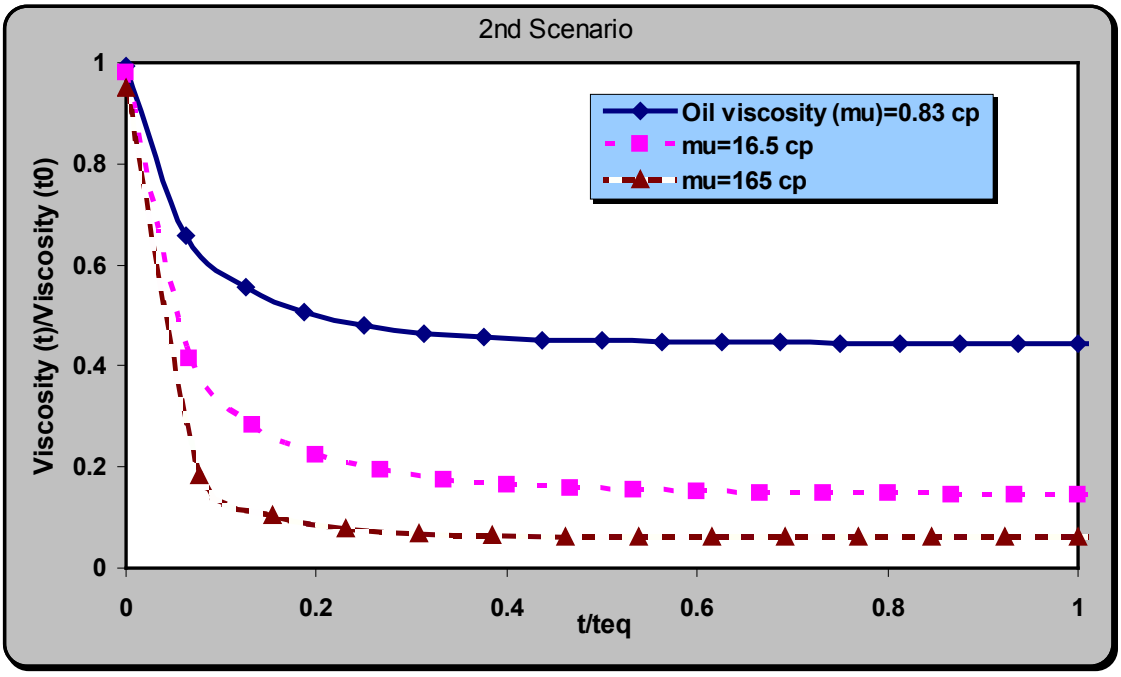

Figure 7-20: Rate of viscosity reduction during the CO_2 mass transfer process for oils with different initial viscosity.

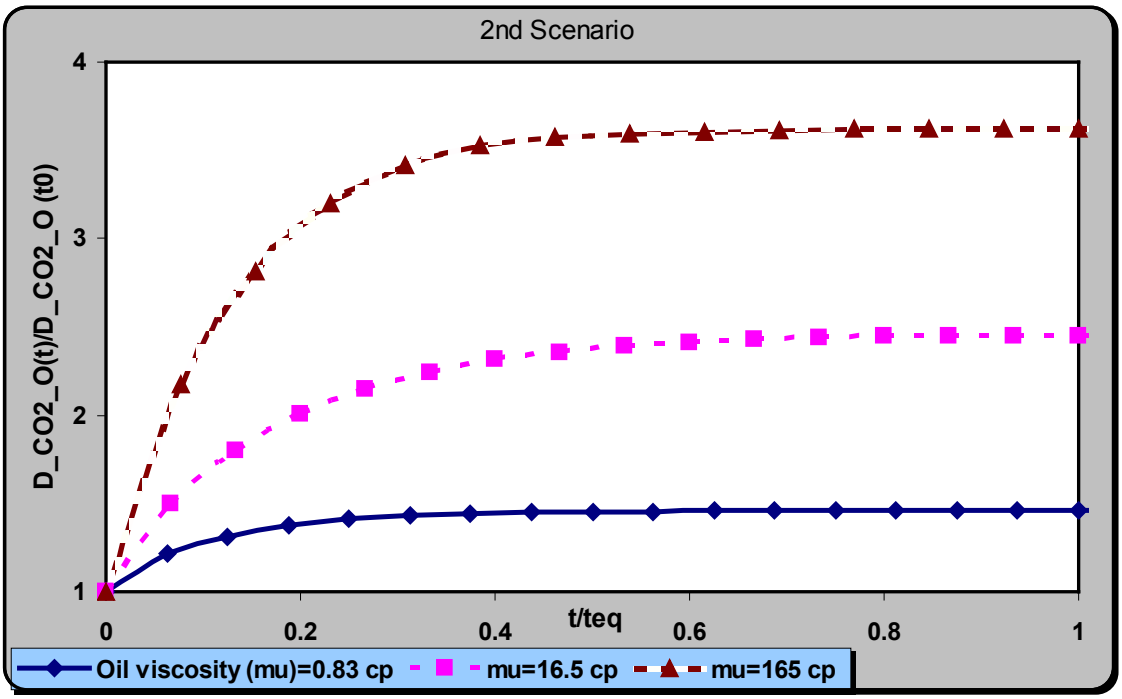

Figure 7-21: Rate of diffusivity (of CO_2 in oil) change during CO_2 mass transfer process for oils with different initial viscosity.

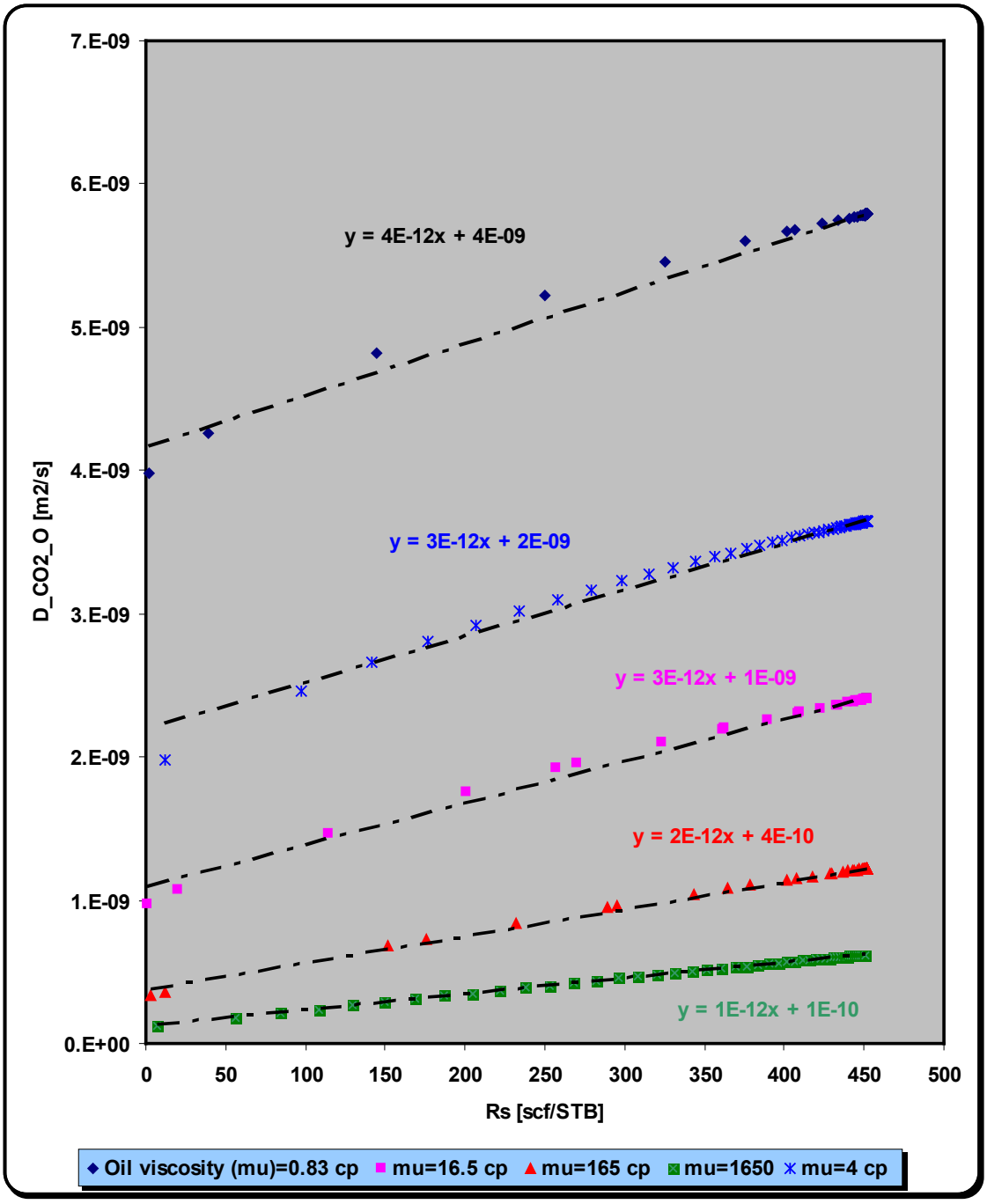

Figure 7-22: Diffusion coefficient of CO_2 in oil as a function of dissolved CO_2 in oil for different oil types.

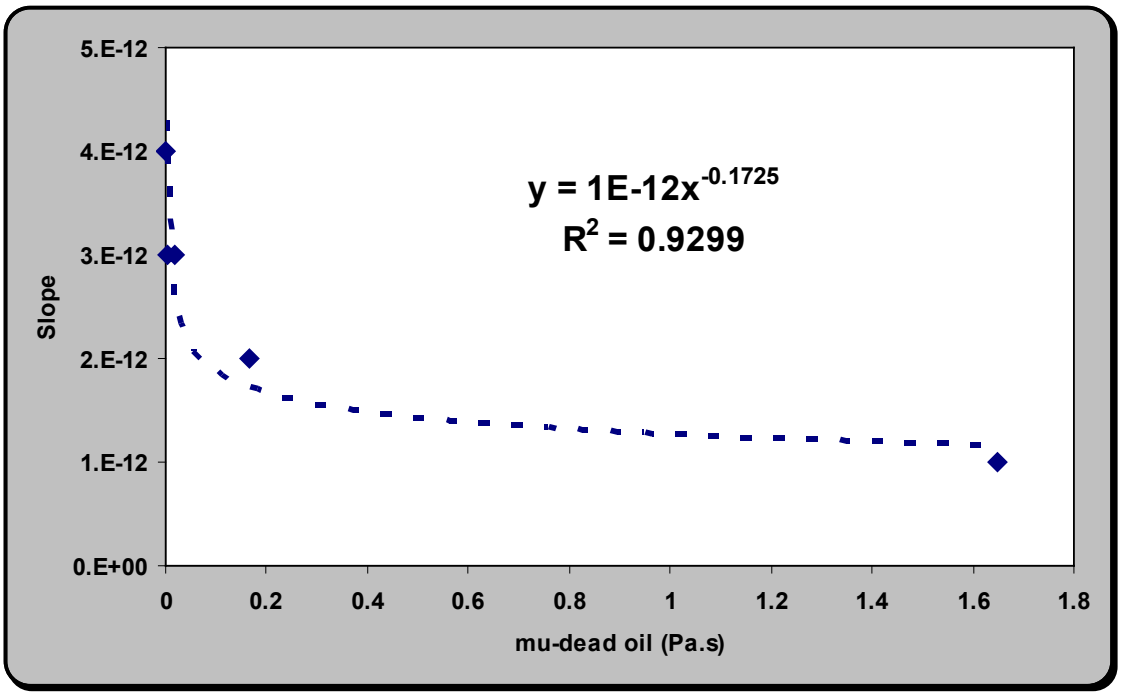

Figure 7-23: The slope (m) of the lines in Figure 22 as a function of initial oil viscosity (μ_{OD}).

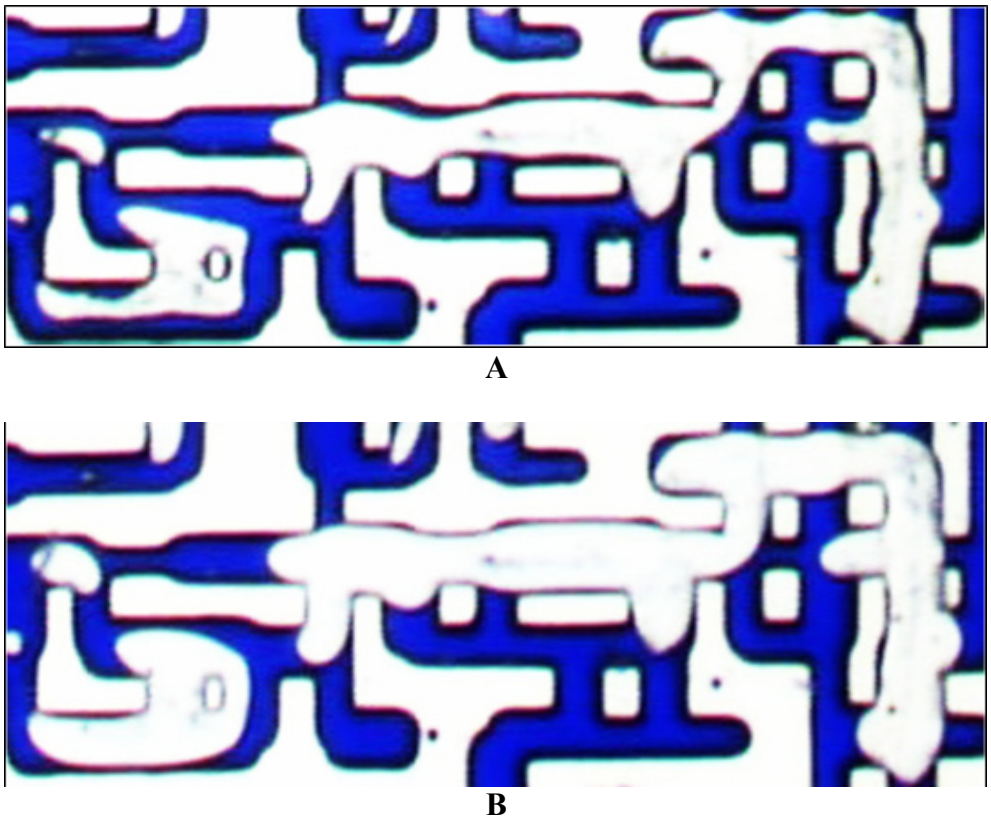

Figure 7-24: The selected oil ganglion in the micromodel, A) after WI B) after 22.4 hrs of CWI, Experiment No 3 of Chapter 3.

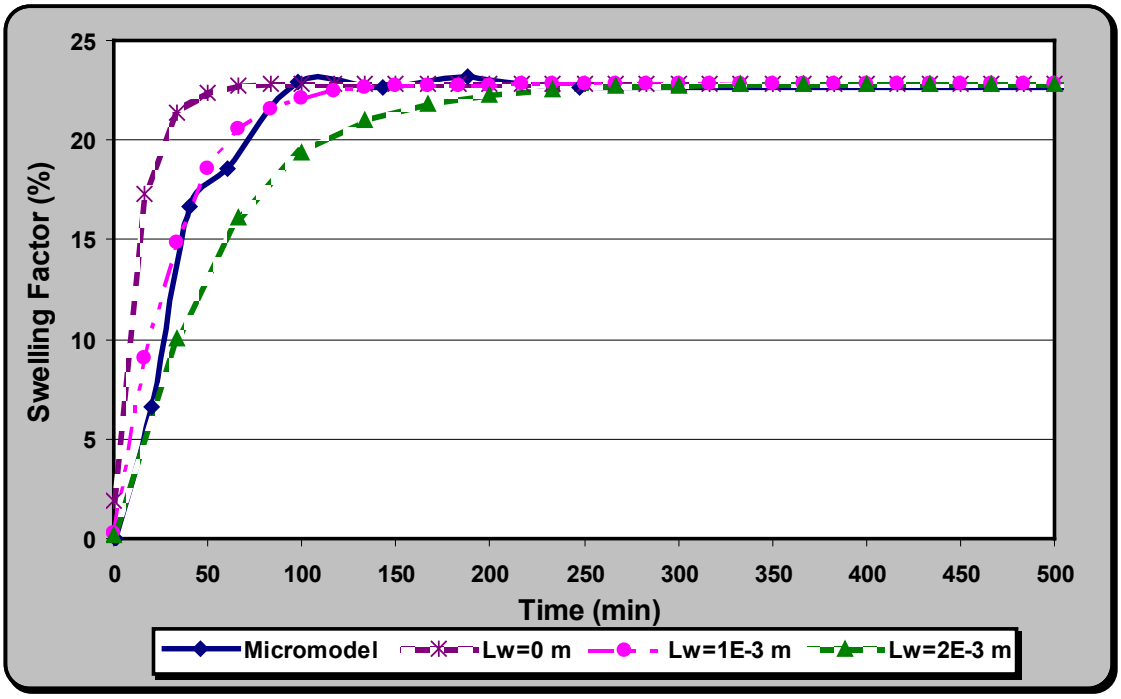

Figure 7-25: Swelling of the viscous oil ganglion versus time, as measured in the experiment (No.3) and predicted by the model, with different water thicknesses.

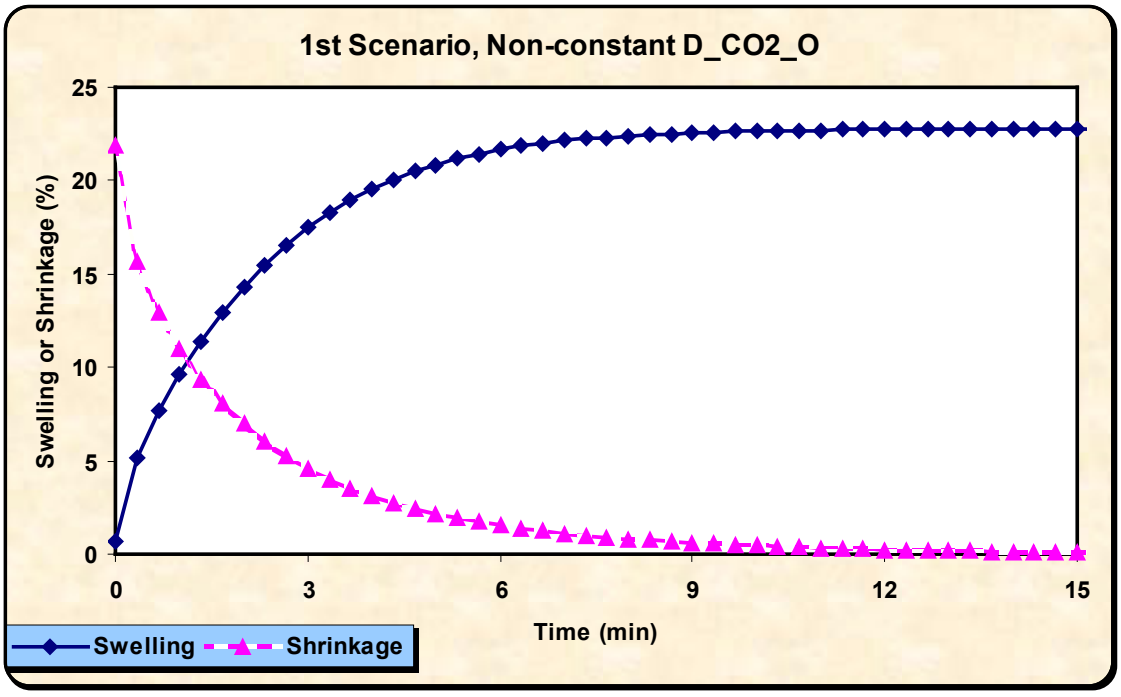

A

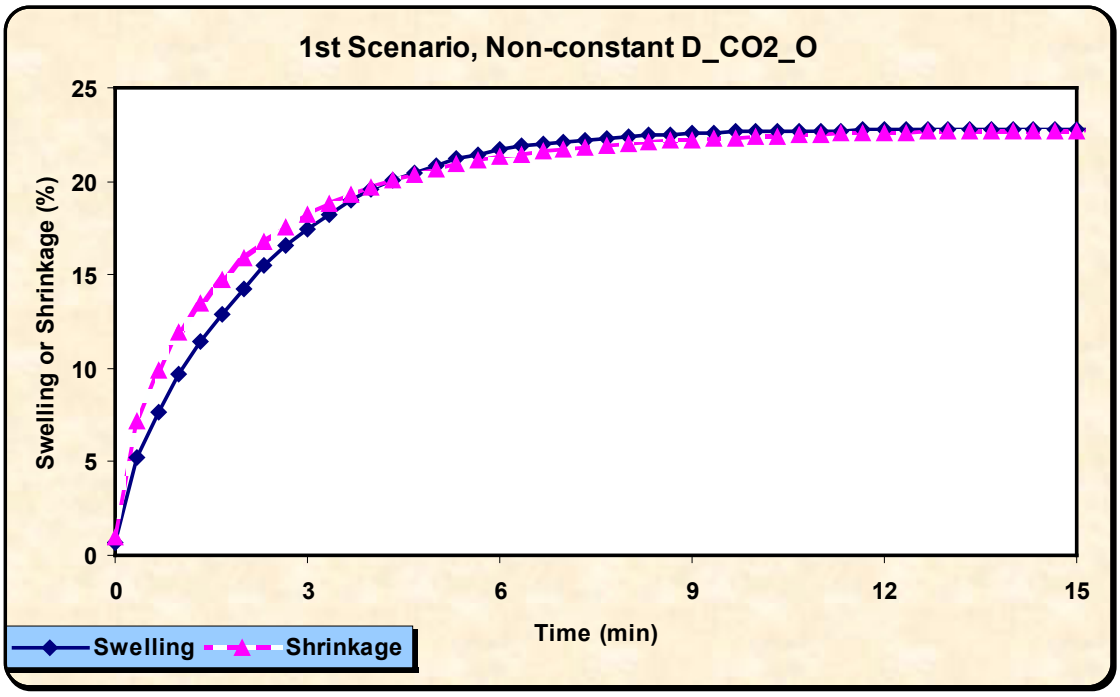

B

Figure 7-26: The swelling and shrinkage curves of an oil droplet versus time in the first scenario, Figure 2A, direct contact of oil and CW, **(A)** original data and **(B)** the absolute value of the displacement compared to the corresponding initial condition. The diffusion coefficient of CO_2 in oil changes with time as a result of CO_2 dissolution in oil.

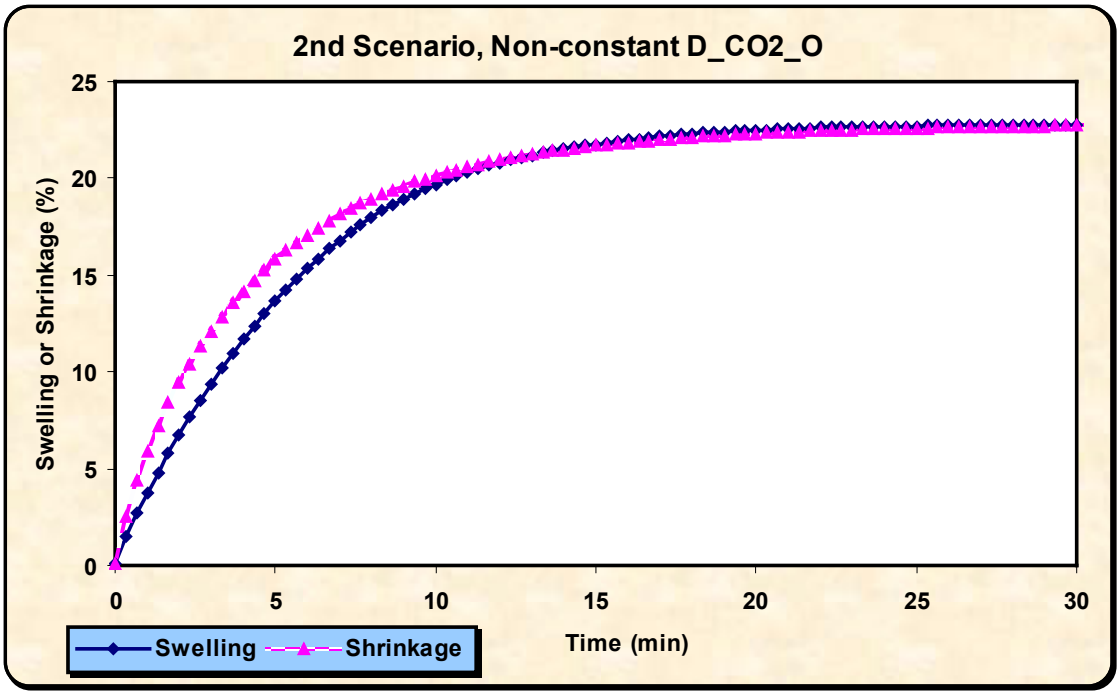

Figure 7-27: The absolute swelling and shrinkage values of an oil droplet versus time in the second scenario, Figure 2B, indirect contact of oil and CW. The diffusion coefficient of CO_2 in oil changes with time as a result of CO_2 dissolution in oil.

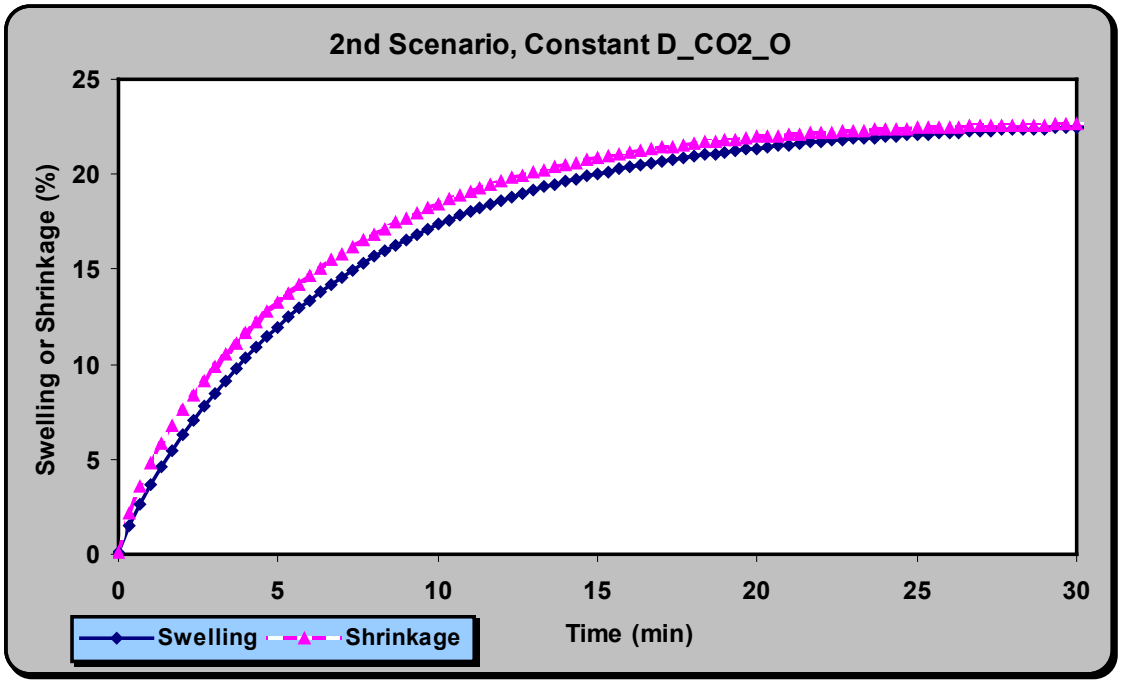

Figure 7-28: The absolute swelling and shrinkage curves of an oil droplet versus time in the second scenario, Figure 2B, indirect contact of oil and CW. The diffusion coefficient of CO_2 in oil is constant.

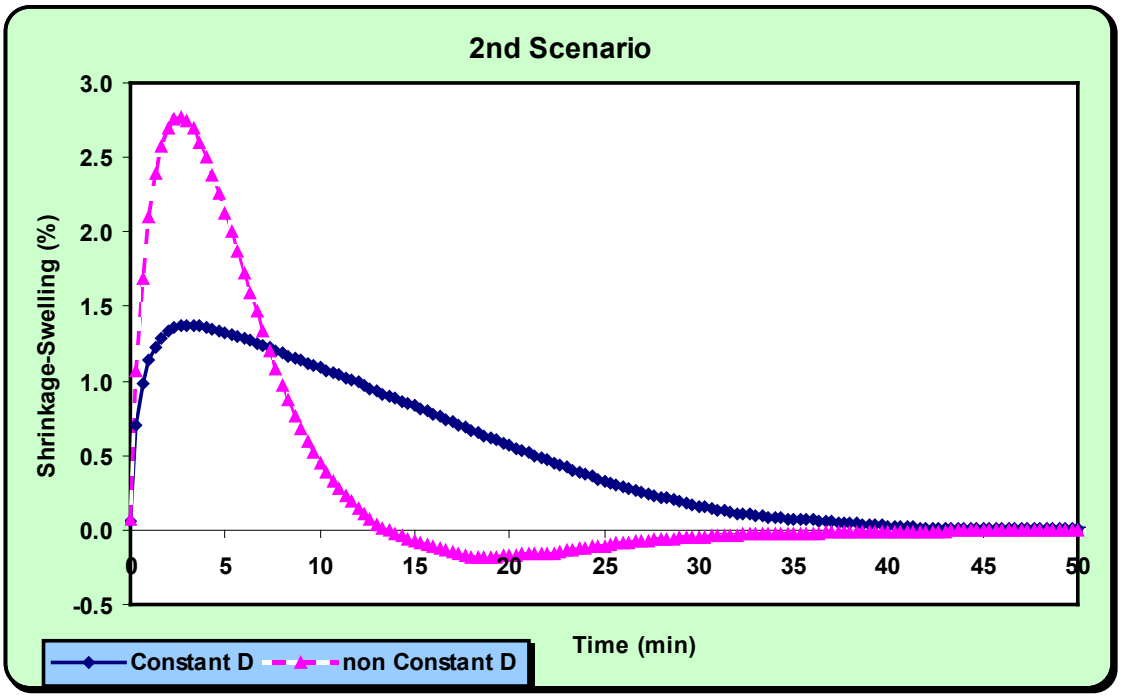

Figure 7-29: The difference between swelling and shrinkage curves shown in Figures 27-28 versus time for the second scenario.

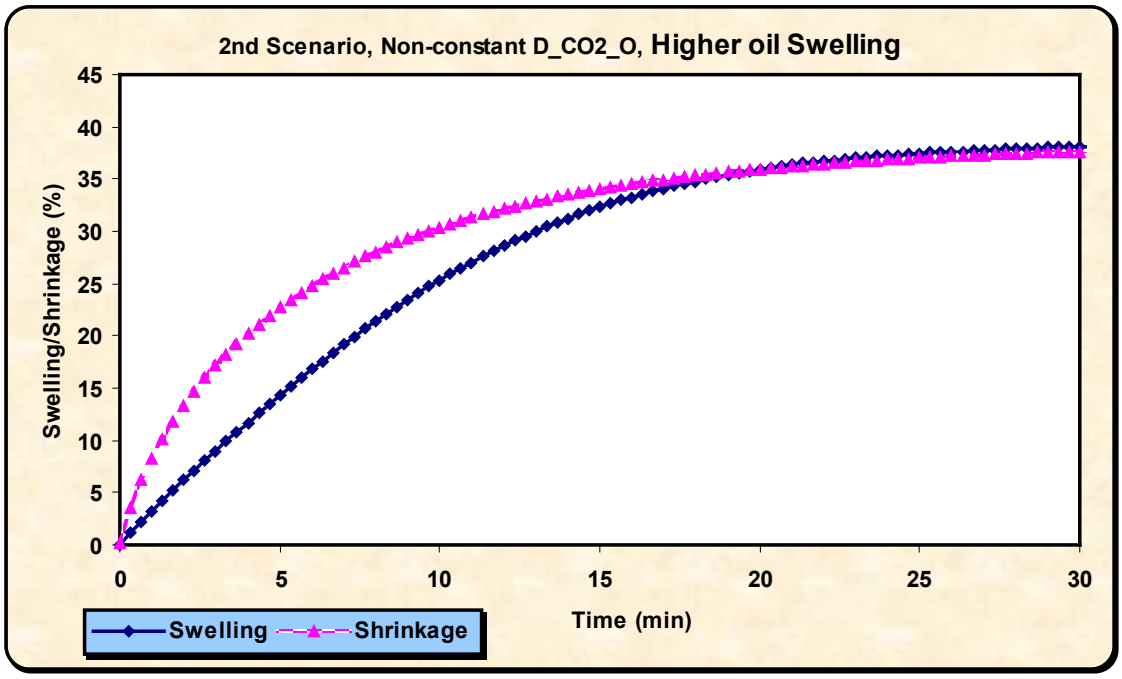

B

Figure 7-30: The absolute swelling and shrinkage values of an oil droplet versus time in the second scenario, Figure 2B, when the diffusion coefficient of CO_2 in oil varies as a result of dissolved CO_2 in oil, over time. When the partition coefficient is 3.98 (corresponding to 39% swelling)

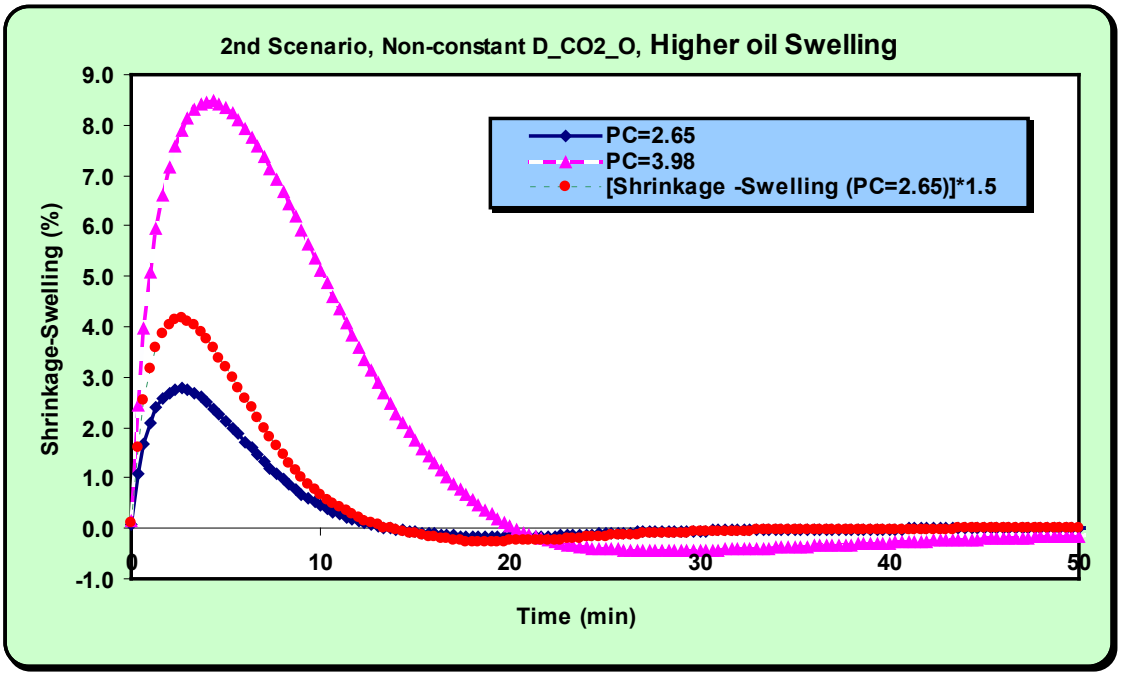

Figure 7-31: The discrepancy between swelling and shrinkage (Shrinkage –Swelling) curves versus time for the second scenario.

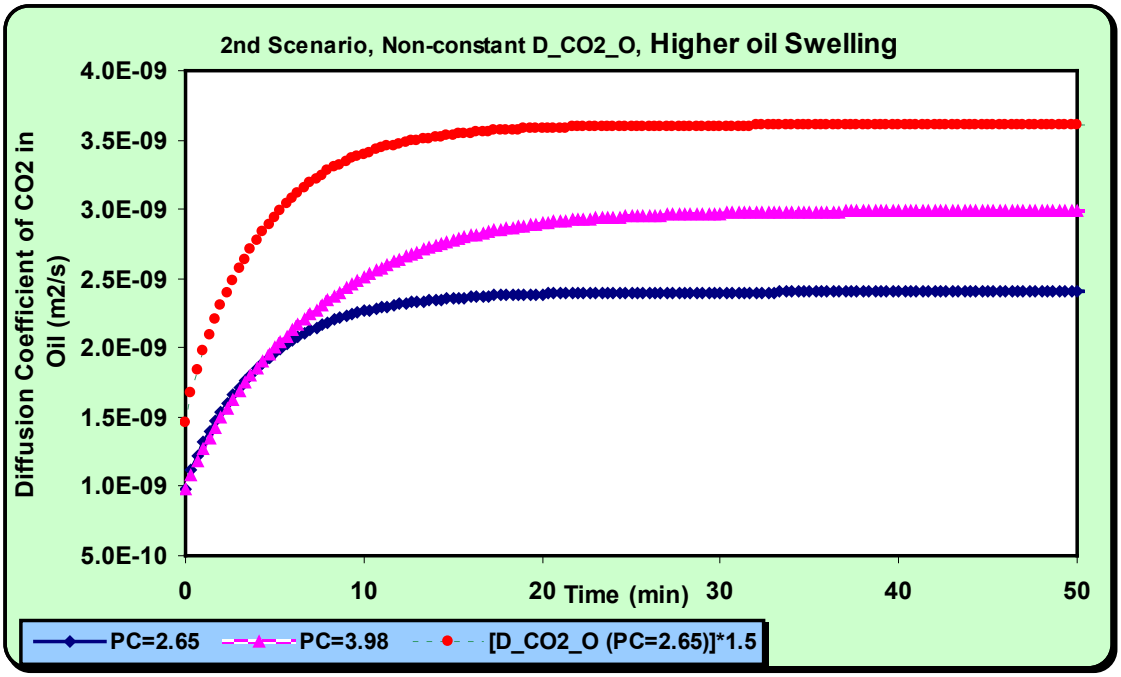

Figure 7-32: Variation of the diffusion coefficient of CO_2 in oil using different CO_2 partition coefficients.

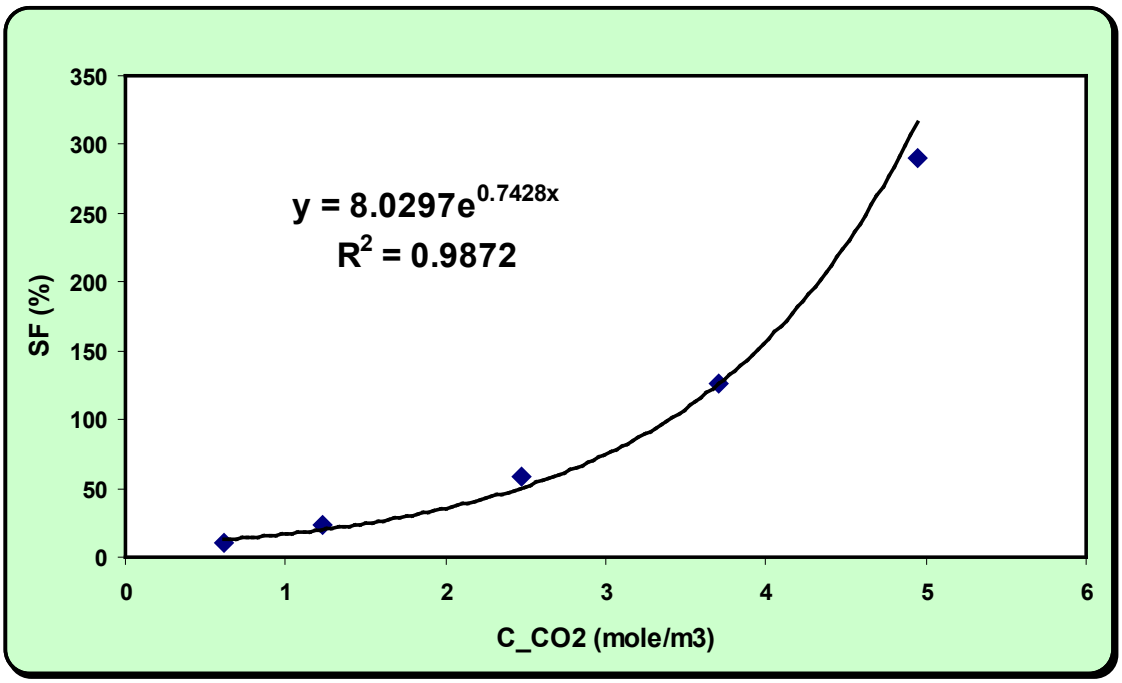

Figure 7-33: Equilibrium oil swelling factor versus CO_2 concentration in water.

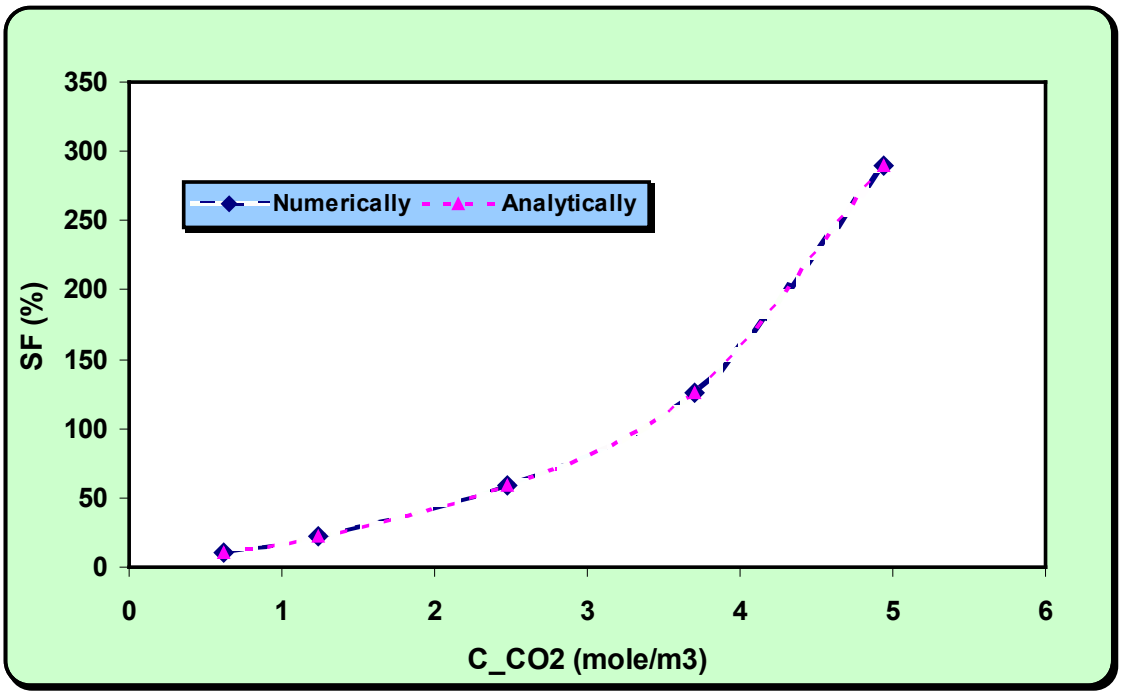

Figure 7-34: Equilibrium oil swelling factor versus CO_2 concentration in water, numerical versus analytical solution.

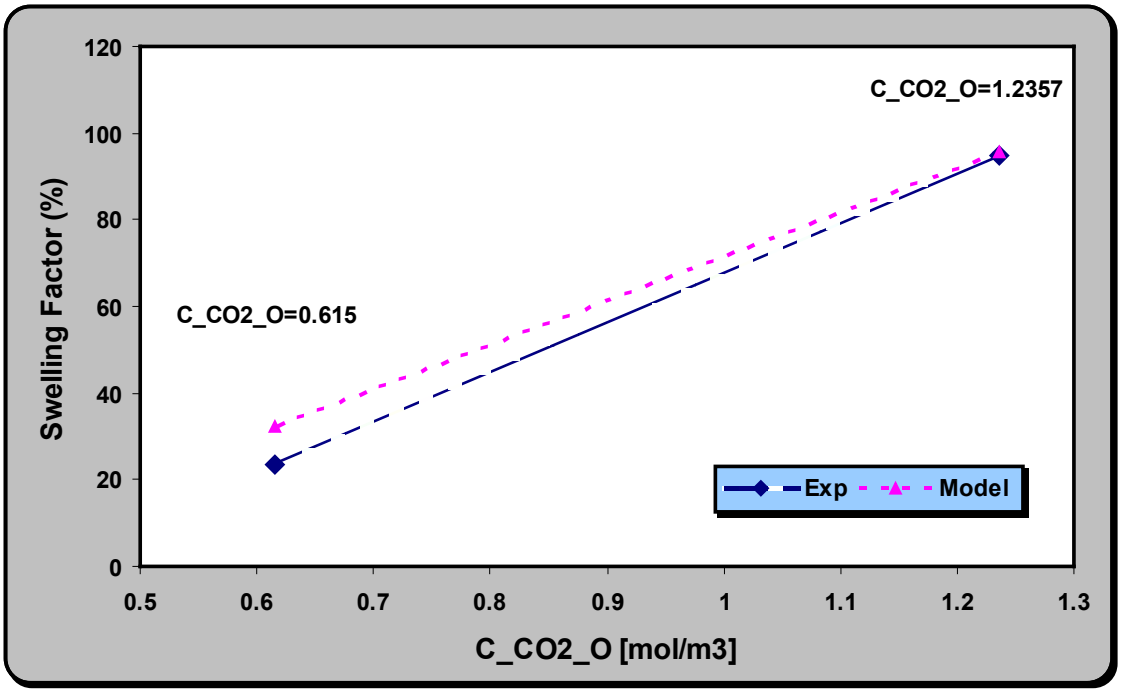

Figure 7-35: Equilibrium oil (n-decane) swelling factor versus CO_2 concentration in water for fully saturated (C_CO_2_W=1.2357 mol/m3) and partially saturated (C_CO_2 _W=0.615 mol/m3) carbonated water. Experimental results (blue) versus the results of the model (pink).

8 Chapter 8 Conclusions and Recommendations

8.1 Conclusions

In this study the main focus was on generating pore level information on carbonated water injection (CWI) by conducting pore scale visualisation experiments through which the underlying physical processes involved in CWI could be identified and studied. Mathematical models were also developed in order to simulate the important mechanisms of events during the CWI process.

The content of this research work can be divided into three main parts; 1) visualisation ''micromodel'' experiments (Chapters 3 and 4), 2) fluid/solid physical properties measurements (Chapters 5 and 6), 3) mathematical modelling of the dynamic process of oil swelling (Chapter 7). The main conclusions of each part are summarised in this chapter followed by some recommendations for future work.

8.1.1 Visualisation micromodel experiments (Chapters 3 and 4),

In the first part of this research programme the results of a series of high-pressure visualisation experiments of CWI, which provided a very useful tool to directly investigate and visualise the pore-scale mechanisms and events taking place during the flooding process, were reported and discussed in detail. Investigation of the pore-scale mechanisms of fluid-fluid, (i.e. fluid flow displacement mechanisms, mass transfer, oil swelling/reconnection, spreading/dewetting processes and fluid redistribution) and fluid-solid interactions (i.e. wettability alteration) during CWI, is essential in achieving an in-depth understanding of the impact of pertinent parameters in order to maximise the benefit of a CWI process. The main conclusions of this part based on the results of 19 micromodel experiments are summarised as follows:

- Three main observed mechanisms of oil recovery during CWI were; the swelling and subsequent coalescence of trapped oil ganglia, local flow diversion and reduction of the oil viscosity.

- CWI increases oil recovery, both as secondary and tertiary recovery method. However, this increase was higher in the secondary flood scenario. The poorer connectivity of the oil phase and lower oil saturation in the tertiary mode than the secondary one were the main reasons for this difference.
- The results have shown visually that a higher oil saturation before CWI in the porous medium causes higher additional oil recovery by CWI.
- CWI as a tertiary oil recovery method (post waterflood) increased oil recovery compared to the corresponding plain waterflooding both for the light (n-decane) and viscous oil. However this increase was higher for the light oil (32.7%) than the viscous oil (11.82%). This was mainly due to a higher swelling factor in n-decane.
- Alternating injection of water and CW brings about favourable fluid redistributions and more oil production; however, the additional oil recovery in the first cycle, was significantly higher than that in the second cycle.
- The results showed that oil swelling during CWI and oil shrinkage during the subsequent WI period do not happen at the same rate for both the first and the second cycle. This difference contributed to the oil redistribution during alternating injection of CW and water, which in one experiment resulted around 2% additional oil recovery during the WI period subsequent to CWI in the first test.
- Blow down of the porous medium (micromodel) subsequent to a period of CWI showed that the residual oil saturation could be further reduced and more oil can be recovered during this process.
- In the series of micromodel experiments using a real crude oil (crude A, see Table 2-3), there was clearly a tendency for the porous medium to become mixed-wet or weakly water-wet compared to the experiments in which mineral/model oil had been used. This demonstrates the ability of the crude oil to alter the wettability of the porous medium. As a result, the oil displacement mechanism with water and CW was mainly piston wise as opposed to layer and film flow, which was observed in the experiments with mineral oils.
- The colour of the crude oil was observed to change during both WI and CWI. In some locations, the oil colour became darker, which is believed to be due to the formation of small water droplets in the oil possibly linked to wettability

alteration. There was also oil with a lighter colour compared to the original oil colour which was caused by CO_2 dissolution in the oil phase.

- Comparison of the size of an oil ganglion after the first WI (before CWI) and the second WI period (after CWI) in Experiment No.10 showed that the oil did not return to the original size, even after stripping all the dissolved CO_2. The larger oil size, which was darker in colour at the end of the experiments, would support the idea of the formation of a micro emulsion of water in the oil phase.
- Injecting CW instead of plain water before CO_2 led to improved oil recovery, as the contact between CO_2 and oil increased and the CO_2 front invaded more oil-filled pores. The positive impact of CWI on the performance of CO_2I was verified by direct flow visualisation for both viscous mineral oil and crude oil A. This is mainly due to the changes of oil (and water) viscosity and IFT during CWI. It also seems that CO_2 ruptures the CW film separating oil and gas more easily, in Experiments No.15 and No.19 compared to Experiments No.14 and No.18, with a water film separating oil and CO_2 phases.

8.1.2 Physical properties measurements (Chapters 5 and 6)

In the second part of this thesis, some important physical properties pertinent to CWI, i.e. contact angle, CO_2 diffusion and CO_2 solubility in water, were experimentally measured. The main objective of the contact angle measurements was to study the impact of the dissolved CO_2 (in water) on the wettability of the system. Three different mineral substrates, i.e. glass, quartz and mica, were used in this study. Quartz was used because it is one of the main minerals of sandstones and mica was selected since it can be found in some shale and clay materials.

The impact of dissolved blue dye in the water (used in micromodel experiments) on the molecular diffusion rate and the amount of the dissolved CO_2 in water was also investigated by conducting bulk CO_2 diffusion coefficient and CO_2 solubility measurements for a number of systems. The CO_2 solubility measurements were conducted also to investigate the impact of carbonation level of CW on the enhanced oil recovery results of the micromodel experiments. The main conclusions of this part can be summarised as follows:

- CW makes the glass micromodel more water-wet compared to plain water at the conditions tested in the visualisation experiments (2000 psi and 38°C). Oil displacement by spontaneous imbibition was observed when CW was present but no evidence of spontaneous imbibition was observed for experiments with plain water.
- Compared to a CO_2-free system, dissolved CO_2 (carbonated water) makes the quartz slide more water wet at both 38 and 58 °C. However, contrary to the data obtained for quartz, dissolved CO_2 makes mica surface less water wet (at 38 °C).
- The variation of wettability (contact angle) for mica (43°-100.4°) with pressure compared to quartz (28°-36.7°) was considerably greater.
- The pressure drop of CO_2 in the PVT cell as a result of diffusion into the water phase was successfully simulated. The estimated diffusion coefficient of CO_2 in water and Henry's constant were in good agreement with the literature data.
- The results of the CO_2 solubility and the CO_2 diffusion coefficient measurement tests showed that the addition of the blue dye to water did not change these parameters considerably.

8.1.3 Mathematical modelling of the dynamic process of oil swelling (Chapter 7)

As a part of this research, a mathematical model was developed and used to study the impact of the key parameters on the CO_2 mass transfer during CWI. The model was also used to interpret some of the experimental observations. In this part, the dynamic process of the swelling of an oil drop, both when it is separated from a CO_2 source by a water layer and when it is in direct contact with CW, was successfully simulated. Using a dimensional analysis technique a more representative relationship was also developed. The sensitivity of pertinent parameters was studied for both direct (oil/CW) and indirect (oil/W/CO_2 source) contact scenarios using two different evaluation methods. In the first method (Method A), the time required for the interface to reach a specified position for different prevailing conditions was compared. In the second evaluation method (Method B), the required time for the interface to reach to 95% of its equilibrium position, in each case under study, was estimated and compared with that of the base case. The parameters used in the sensitivity studies were divided into two groups, based on their effects on oil swelling. CO_2 density (Den_{CO2}), equilibrium CO_2 concentration

in carbonated water at the inlet ($C_{CO2\text{-}cw\text{-}in}$,), water/oil-$CO_2$ partition coefficient ($K_{CO2\text{-}w/o}$), equilibrium CO_2 concentration in oil (CO_2 solubility in oil) and initial oil volume (L_o) are parameters of the first group (Group I) and affect both the amount of swelling as well as the swelling rate. Diffusion coefficient of CO_2 in water ($D_{CO2\text{-}w}$) and oil ($D_{CO2\text{-}o}$) and the water layer thickness (L_w) are parameters of the second group (Group II) and only affect the required time to reach to the final equilibrium conditions. Based on the sensitivity exercise conducted using both these methods for the two scenarios, it was demonstrated that:

- The impact of pertinent parameters of Group I that affect both the amount of swelling as well as the swelling rate was more pronounced based on evaluation Method A rather than B. In contrast, for parameters of Group II, which do not affect the amount of swelling, both evaluation methods yielded the same results.
- The impact of pertinent parameters of Group I using evaluation Method A was non-symmetrical, i.e., the impact of an increase in a parameter was significantly different from that of a reduction in that parameter, highlighting the more independent nature of evaluation Method B, which did not follow this behaviour.
- In the first scenario and based on the evaluation Method A, $C_{CO2\text{-}cw\text{-}in}$ (or $K_{CO2\text{-}w/o}$) and Den_{CO2} were the most sensitive parameters. Based on evaluation Method B, the impact of a change in $C_{CO2\text{-}cw\text{-}in}$ or Den_{CO2} was slightly less pronounced compared to that in oil properties, i.e. $D_{CO2\text{-}o}$ or L_o. These trends were consistent with those predicted for this case by the new relationship, which was developed based on a dimensional analysis technique.
- In the second scenario, the sensitivity of Equilibrium Diffusion Time (EDT), based on evaluation Method A, is more pronounced for a change in $C_{CO2\text{-}cw\text{-}in}$ and Den_{CO2} compared to a change in $K_{CO2\text{-}w/o}$. Based on evaluation Method B, EDT was most sensitive to the thickness of the water layer separating the oil and CO_2 source (L_w), highly sensitive to $D_{CO2\text{-}w}$, $C_{CO2\text{-}cw\text{-}in}$ and Den_{CO2}, moderately sensitive to $K_{CO2\text{-}w/o}$ and least sensitive to the value of $D_{CO2\text{-}o}$ and L_o.
- The impacts of a change in $C_{CO2\text{-}cw\text{-}in}$ or Den_{CO2} on EDT were in opposite directions for the first (direct contact) and second (indirect contact) scenarios. This was due to the fact that in the second scenario an increase in $C_{CO2\text{-}cw\text{-}in}$ or a decrease in Den_{CO2} reduces the dominant impact of the water layer, hence

reducing the corresponding EDT values. However, in the first scenario, where there is no water, these changes increase the amount of swelling, hence increasing the corresponding EDT

The impact of the presence of a water layer separating the CO_2 source from the oil on swelling and shrinkage processes, the effect of CO_2 solubility in water on oil swelling and the validity of some of the simplified assumptions were also studied with the following main conclusions:

- The results of the model highlighted the major negative impact of the water layer on the CO_2 diffusion rate from a CO_2 source to light oil.
- The swelling rates, considering viscosity reduction as a result of dissolved gas in oil, were higher than the case of a constant diffusion coefficient (constant oil viscosity). However, this difference was negligible and small for the typical oil with viscosity of 0.83 and 16.5 cP but considerable for the oil with viscosity of 165 cP. Comparison of the results of the first and second scenarios (Figures 7.17-7.19) showed that the water layer between the oil and the CO_2 source reduced this difference, i.e. the impact of viscosity reduction on the oil swelling rate was reduced. This was consistent with the results of sensitivity analyses, where the presence of the water layer in the second scenario dampened the impact of variation of the oil parameters on the CO_2 diffusion process. Therefore considering a constant diffusion coefficient of CO_2 in oil for the light oil and when there is a water layer between oil and CO_2 is a valid assumption.
- A simpler equation than the one available in the literature was derived (Eq. 7.33, page 223) which can be used for simulation of diffusion processes.
- The simulation of the swelling of the viscous oil (used in the micromodel experiments) suggested that the water layer did not have a significant impact on the diffusion rate. This was due to the much lower CO_2 diffusion coefficient in oil than that in water for the viscous oil, compared to that for the light oil where the water layer significantly delayed the CO_2 diffusion.
- The difference between shrinkage and swelling rates in the second scenario was more pronounced than that observed for the first scenario. This was mainly due to the presence of a water layer in the second scenario. That is, the water layer

thickness at the beginning of shrinkage was less than that at the beginning of the swelling process, resulting in faster initial rate of shrinkage than that of swelling.

- The plot of the oil swelling versus CO_2 concentration in water (carbonation level) followed an exponential trend, highlighting that the incremental increase in the swelling factor was much more pronounced at higher CO_2 concentration. This trend was the same as that observed in the experimental section.

8.2 Recommendations

During this study some aspects of CWI for oil recovery were experimentally and theoretically investigated. However, many aspects still remain to be studied. Here to further investigate this process and to improve our knowledge of this injection strategy some recommendations are made for future work.

8.2.1 Recommendations for the experimental work

- Formation of micro bubbles in the oil phase

In Experiments No.10 and 11 (See Chapter 3), formation of some micro bubbles in the oil phase was observed during carbonated water injection. As this important observation was beyond the scope of this study, further investigation of this issue is recommended to be carried out for future work. Some parameters, which are thought to be effective on formation of these bubbles, are concentration of CO_2, salinity of the water phase and the composition of the crude oil. The effect of these parameters, is recommended to be studied.

- Effect of wettability:

In this work a series of high-pressure visualisation experiments were conducted to study the process of CWI for oil recovery. The micromodel was strongly water wet and the experiments were conducted at 2000 psi and 38 °C. To cover a wider range of reservoir conditions and study the effect of initial wettability conditions on displacement mechanisms, it is recommended to perform tests using a mixed-wet and oil-wet micromodel at different temperature and pressure conditions.

- Effect of dissolved hydrocarbon gas in oil

In this study three different oil types, which correspond to three different IFT and oil viscosities, were used. However, the effect of dissolved natural gas in oil was not investigated. There are some contradictory reports on the impact of natural gas on CWI performance in the literature. For instance, Martin (1951) stated that ''*Carbon dioxide not only reacts with certain components of natural gas but also promotes the solubility of natural gas in crude oil. It appears possible that natural gas is more readily soluble in the hydrocarbon-carbon dioxide compounds than in the crude oil. The two gases thus complement each other in their effect on the removal of the oil from the sand''*. He also reported that the addition of certain organic compounds to the CW enhances the recovery of oil. Saxon et al. (1951) showed when natural gas is dissolved in the crude oil, a greater carbon dioxide saturation pressure is required to affect the same volume change, or in other words, as the natural bubble point of the crude oil is increased the solubility of carbon dioxide decreases significantly. Johnson et al. (1952) reported that as the percentage of light hydrocarbons (C_3 and higher) in the crude oil is increased the volume expansion becomes greater. Poettmann and Katz (1945) showed that carbon dioxide and gaseous hydrocarbon are mutually soluble at elevated pressure. Hence it is expected that the presence of gas improves the oil recovery from CO_2 flooding. Holm (1959), based on experimental work, showed that dissolved or free gas, up to 20% of hydrocarbon pore volume, does not have any appreciable effect on the efficiency of the CO_2-carbonated waterflooding. He also showed that neither the presence of methane (up to 15 vol%) in the CO_2 slug nor high gas saturation in the porous medium appreciably reduces the efficiency of the CO_2–carbonated water injection process.

To further investigate the impact of this parameter and also to reach a firm conclusion some experiments using live oil, oil with dissolved hydrocarbon gas, rather than dead oil, gas-free oil, are recommended.

- Effect of salinity with different compositions

In this work distilled water was used for both water injection and preparing CW. It is well known that added salt in water affects CO_2 solubility in water (Baviere, 1991), wettability alteration (Chiquet and Broseta, 2005) and oil expansion values (Saxon, et al., 1951). As another task for future work, it is recommended that brine with different salinities would be used instead of distilled water.

- The impact of CWI on properties of reservoir rock

Another important issue, which is recommended to be considered for future work, is the investigation of the geochemistry aspects of CWI through reactions with rock and petrophysical aspects of rock after reaction with CW which their impact on relative permeability could be important.

In the present work, contact angle measurements were carried out, to some extent, in Chapter 5. Further measurements using different minerals would further clarify the impact of CW on rock wettability.

In this study, the impact of CO_2 dissolved in water, which forms carbonic acid, on a reservoir rock was also examined by static treatment (i.e. no flow) of a piece of sandstone rock with CW prepared at 2000 psi and 38 °C. Figure 1 shows an ESEM (Environmental Scanning Electron Microscope) image of the rock sample before (1A) and after (1B) two weeks treatment with CW. As can be seen, CW has caused a part of rock surface to be dissolved. To obtain further information on such measurements, continuation of this line of research with different rock samples and for longer time scale is recommended.

- Effect of using co-solvents on the performance of CWI process

As discussed and shown in Chapter 1, CO_2 solubility in water compared to other gases such as C_1H_4, C_2H_4 and C_2H_6 is relatively high. However, if the CO_2 solubility in water is increased, more benefits will be achieved from CWI both in terms of enhanced oil recovery and also CO_2 storage. This can be achieved by adding chemicals, which act as co-solvents. As already mentioned, this reaction can be classified as a physical or chemical absorbent agent. Chemical absorption is characterized by the occurrence of a chemical reaction between the gas (CO_2) component and a component in the liquid (water). Use of such co-solvents (chemical absorption) is not in line with the objectives of CWI because it would not allow the absorbed CO_2 to dissolve into the oil phase. Physical absorbents, on the other hand, do not react chemically with the absorbed CO_2 and hence, allow partitioning of CO_2 when it comes in contact with oil.

In this study, two preliminary experiments were performed to investigate the impact of the co-solvent on the CWI process. The results of these experiments, which are discussed in Appendix D, showed a significantly improved swelling of oil due to the presence of co-solvents. It was shown in the previous chapters that oil swelling is one of the important key mechanisms on oil recovery during CWI. Hence, a full investigation of the application of using co-solvents is recommended as another element of the future work.

- IFT measurements

To quantitatively compare the spreading coefficient of CW/oil/CO_2 and W/oil/CO_2 systems, a series of IFT measurements need to be performed.

8.2.2 Recommendations for the modelling part

- Modelling in a single pore

Our mathematical model was developed based on some simplifying assumptions. Removing some of these simplifying assumptions is recommended to bring the results of the model closer to the real conditions. Examples of these assumptions are:

- ''The fluid system is an ideal mixture, that is, the total volume is the summation of volumes of oil and CO_2.'' In reality the system is not ideal. However, it should be noted that information on the partial volume of the components is also required, to modify the model and to account the non-ideal nature of the solution.
- ''Oil, water and CW are at equilibrium conditions at the interfaces.'' As known, in porous media, a mass transfer process, takes place across the fluid interfaces. The sensitivity of this assumption for mass transfer could be investigated, especially for the field scale, which is believed to be a kinetic process (Niessner and Hassanizadeh, 2009).

- Modelling in a multipore

The mathematical model was constructed for capturing the mass transfer process in only a single pore. This model can be further developed for multi pore scale to study the impact of properties of porous media such as tortuosity and aspect ratio on the diffusion process. In line with this task, developing a network model based on the physics

observed within the micromodel, is also recommended. The work can benefit from a network model to estimate some important parameters for up-scaling purposes such as relative permeabilities and capillary pressure curves relevant to CWI process.

- Modelling of the pressure decay experiments

Free convection due to gravity impact can be included to the model to further approach to the real conditions.

8.3 References

Baviere, M., 1991: ‘‘Basic concepts in enhanced oil recovery processes’’, Published for SCI by Elsevier Applied Science, in London and New York.

Chiquet, P. and Broseta, D., 2005: ‘‘Capillary Alteration of Shaly Caprocks by Carbon Dioxide.’’, SPE 94183.

Holm, L. W., 1959: ‘‘Carbon dioxide solvent flooding for increased oil recovery’’, SPE paper 1250-G.

Johnson, W. E., Macfarlane, R. M., Breston, J. N. and Neil, D. C., 1952: ‘‘Laboratory experiments with carbonated water and liquid carbon dioxide as oil recovery agents’’, Producers Monthly (Nov.) 17, No. 1, 15.

Martin J. W., 1951: ‘‘Additional oil production through flooding with carbonated water’’, Producers Monthly (July) 15, No. 9, 18.

Niessner, J. and Hassanizadeh S. M., 2009: ‘‘Modeling Kinetic Interphase Mass Transfer for Two-Phase Flow in Porous Media Including Fluid-Fluid Interfacial Area’’, Transport in Porous Media, Volume 80, Number 2 / November, P. 329-344.

Poettmann, F. H. and Katz, D. L., 1945: ‘‘Phase behaviour of binary carbon dioxide-paraffin system’’, Industrial and engineering chemistry, 37, 847

Saxon, J., Jr., Breston, J. N. and Macfarlane, R. M., 1951: ‘‘Laboratory tests with carbon dioxide and carbonated water as flooding mediums’’, Producers Monthly (Nov.) 16, N. 1, 8.

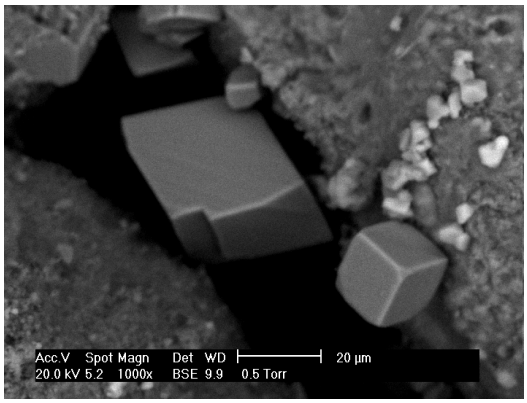

A

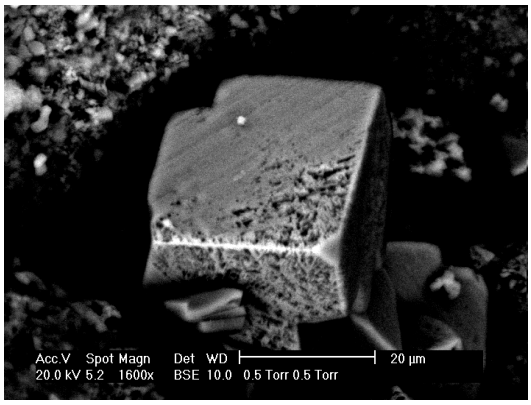

B

Figure 8-1: Microscopic image of a typical sandstone rock sample (SSK 2387), A) before treatment with CW and B) two weeks after contacting with CW at 2000 psi and 38 °C.

Appendix A: Experimental Data, Correlations and Theoretical Concepts

A.1 Introduction

CO_2 injection affects oil recovery by modifying physical properties of the fluids and rock such as density of oil and water, oil and water viscosity, interfacial tensions between fluids, CO_2 diffusion coefficient in oil and water and rock wettability.

Experimental data, correlations and theoretical concepts related to the above parameters collected from literature is presented in the following sections.

A.2 Fluid Density

A.2.1 Oil density

Miller and Jones (1981) conducted a series of experiments to determine oil viscosity, oil density (Figure A.1), saturation and swelling factor at three different values of temperature: 75°, 140° and 200° F (24°, 60° and 93° C). The effect of CO_2 on viscosity will be discussed in Section A.3. At each temperature, measurements were conducted at eleven pressures ranging from 200 to 5,000 psi (1400 to 34,500 kPa). Heavy oil samples with API gravity ranging from 10 to 17° (1.000 to 0.953 g/cm^3) were tested to determine these physical characteristics.

Experimental data shows that the presence of CO_2 may increase or decrease the oil density depending on temperature, pressure and oil type. Figure A.1 shows that density of Wilming oil (17 API) increases with pressure at any temperature from 75 to 200 °F. At temperatures below 200 °F, the slope of density vs. pressure ($d\rho/dP$) is always higher when CO_2 is present than in the case with no CO_2 in the oil. However, at 200 °F, the slopes are almost the same (Figure A.1). At temperature of 200 °F, the density of the oil with CO_2 in solution is less than the CO_2-free oil-density, at all values of pressure. This is not so at moderate and low temperature values.

Holm and Josendal (1974) presented density of Mead-Strawn stock-tank oil at 135 °F saturated with CO_2. They proposed that CO_2 injection affects oil recovery by increasing oil density, Figure A.2.

Bessieres, et al. (2001) experimentally measured the density of Decane at various values of pressure and temperature, at different CO_2 concentrations, Figures A.3 and A.4 respectively.

Zuniga-Moreno et al. (2005) also presented some experimental data and an empirical equation for calculation of the density of pure Decane and Decane saturated with CO_2 at different temperature and pressure values.

A.2.2 Water density

Most gases, when dissolved in water at reservoir conditions, reduce the density of the water but CO_2 is one of the few gases that shows the opposite trend

Hebach, et al. (2004) presented density data for carbonated water (water saturated with CO_2). They showed that for all isotherms, the density of CO_2-saturated water is higher than that of pure water. They demonstrated that the deviation between the densities of pure water and the CO_2-saturated water is large at low temperatures and high pressures (high solubility conditions of CO_2 in water), with a maximum of 1.9% at 284 K and 30 MPa. They divided the data set into two regions (data comprising CO_2 with densities below the critical density and above the critical density) and developed a correlation for each region:

Equation A.1 covers the data where the CO_2 phase is either liquid or compressed vapour, and exhibits densities of higher than 468 $kg.m^{-3}$, which is the critical density of pure CO_2.

$$\rho_{H_2O} = l_0 + l_1 p + l_2 T + l_3 p^2 + l_4 T^2 \qquad \text{(A.1)}$$

Equation A.2 is valid for densities lower than the critical density with respect to the CO_2-phase.

$$\rho_{H_2O} = g_0 + g_1 p + g_2 T + g_3 p^2 + g_4 T^2 + g_5 pT + g_6 p^3 + g_7 T^2 p + g_8 T p^2 \qquad \text{(A.2)}$$

In these regression functions, ρ_{H_2O} is the CO_2-saturated water density, T is the temperature in K, and p the pressure in MPa. $l_{0...4}$ and $g_{0...8}$ are coefficients; their units are given in Table A.1.

A.2.3 CO_2 density

The density of CO_2 at different temperatures and pressures was measured by Zappe et al. (2000). Their data set shows that the density of CO_2 increases with increasing pressure or decreasing temperature.

A.3 Fluid Viscosity

A.3.1 Oil viscosity

Lohrenz, et al. (1964) developed a correlation to calculate viscosity of oil based on its composition. This equation is capable of calculating viscosity of oil with dissolved CO_2 in the oil if CO_2 concentration is known and assumed to behave like a hydrocarbon constituent.

Simon and Graue (1964) also presented another correlation for calculation of viscosity of CO_2-Crude oil as a function of pressure, temperature and solubility of CO_2, Figure A.6.

Beggs and Robinson (1975) developed a correlation for calculation of oil viscosity variation with dissolved gas, based on 2000 experimentally measured data of live oil.

$$\mu = A\mu_{OD}^{B}, \qquad \text{(A.3)}$$

where

$A = 10.715(R_s + 100)^{-0.515}$

$B = 5.44(R_s + 150)^{-0.338}$

$R_s =$ Dissolved gas GOR, scf/STB

$\mu_{OD} =$ Viscosity of gas-free oil, cP

$\mu =$ Viscosity of gas-saturated oil, cP

Holm and Josendal (1974) were the first to propose that CO_2 injection affects oil recovery by reducing oil viscosity, Figure A.2.

As mentioned earlier, Miller and Jones (1981) performed a series of experiments to determine oil viscosity versus pressure (Figure A.5), at three different temperatures of 75°, 140° and 200° F (24°, 60° and 93° C).

Barrufet, et al. (1996) presented some experimental data for the viscosity of Decane and CO_2, for various temperatures and CO_2 concentrations. Their results show that by increasing both temperature and CO_2 concentration, the viscosity of (Decane and CO_2) binary mixture is reduced.

A.3.2 Water viscosity

Figure A.7 shows the viscosity of carbonated water as a function of carbon dioxide concentration. It is noted that similarly to density, the viscosity of water is increased by increasing CO_2 concentration in water.

Kumagai and Yokoyama (1998) measured and reported the viscosity of carbonated water along three isotherms at 273, 276 and 278 K at pressures up to 30 MPa. The measured data show that at constant temperature and pressure, the viscosity of the aqueous solutions increases with an increase in CO_2 content.

Recently, Uchida, et al. (2003) applied the dynamic light scattering method to measure the bulk viscosity of CO_2 solutions, to determine how the viscosity of carbonated water depends on time, temperature and pressure. They showed that viscosity of a water-CO_2 mixture increases with time until thermodynamic equilibrium conditions are reached, and is higher at higher pressures and lower temperatures. Based on these three trends, it can be concluded that the viscosity of carbonated water increases with increasing CO_2 concentration.

A.4 CO_2 Solubility

A.4.1 CO_2 solubility in oil

Simon and Graue (1964) developed a correlation to determine solubility of CO_2 in oil as a function of pressure and temperature based on some experimental data on seven crude oils and two refined oils with API density varying in the range of 11 to 33.

Figure A.8 shows CO2 solubility in a crude oil whose UOP (Universal Oil Products) characterization factor is 11.7. UOP characterization factors of crude oils can be determined from the charts proposed by Watson et al. (1935), if the viscosity and API gravity of the oil are known. This figure shows that with increasing pressure and decreasing temperature CO_2 solubility increases.

Simon and Graue (1964) also computed the swelling factor (ratio of oil volume with CO_2 content at pressure P and temperature T to that at atmospheric conditions) as a function of the amount of dissolved CO_2, as shown in Figure A.9. As can be seen, the swelling factor for the lighter oil, for the same CO_2 content, is greater. This plot also shows an exponential trend between oil swelling and CO_2 content. The same trend was observed in this study and discussed in the previous chapters, experimentally and theoretically.

Welker and Dunlop (1963) developed a number of correlations for calculation of the solubility of CO_2 in oil and the swelling factor of oil, with various API gravities at 80 °F. Figure A.10 shows that the solubility of CO_2 in oil falls for heavier oil, as API gravity is reduced. They also presented viscosity values of various dead oils saturated with CO_2, which were measured based on the Darcy equation at various P and T.

A.4.2 CO_2 solubility in water

Dodds, (1956) collected all the available data published up to that data and reported them in the form of Figure A.11.

Yih-Bor et al. (1998) presented a correlation to estimate the solubility of CO_2 in water and brine. In their correlation, solubility of CO_2 in water is directly related to pressure, and is inversely proportional to temperature and salinity. Figure A.12 compares the result of their correlation with experimentally measured data, at the same conditions.

Figure A.13 also shows the effect of pressure, temperature and salinity on the solubility of CO_2 in water, (Baviere, 1991). This figure shows that the increase in CO_2 solubility is more pronounced at lower pressures.

Figure A.14 also shows a series of measurements on the solubility of CO_2 in water at high pressure and temperature, reported by Diamond and Akinfiev (2003).

Koschel, et al. (2006) presented another data set for CO_2 solubility in water and brine; Figure A.15 shows their data.

A.5 Interfacial Tension of Fluids

A.5.1 Water-CO_2 interfacial tension

Chalbaud, et al. (2006) presented a correlation to determine the IFT of CO_2-brine systems. This correlation was developed on the basis of the Parachor model, also accounting for the effect of the presence of salt. In their regression more than one hundred experimental data for IFT were used. Figure A.16 shows IFT of Brine-CO_2 system vs. pressure for different temperatures.

Massoudi and King (1975) presented an empirical equation for the interfacial tension of water with different salinities and CO_2 concentrations.

The variation of water-CO_2 IFT with pressure ranging from 0.1 to 20 MPa and temperature from 278 to 335 K was studied by Hebach, et al. (2002).

Yang and Gu (2004b) studied the effects of temperature and pressure on IFT for crude oil-CO_2, Brine-CO_2 and Brine-crude oil-CO_2 systems. The density and viscosity of the crude oil in their experiments were 0.911 g/cm^3 and 6.83 cP at the atmospheric pressure and 25 °C conditions, respectively, with the density of brine being 1.003 g/cm^3 at 15 °C. Figure A.17 and A.18 show their results, for both oil-CO_2 and Brine-CO_2 systems, respectively. It is noted that by increasing pressure and decreasing temperature, IFT decreases for both systems.

Yang et al. (2005), in another publication, reported a set of dynamic IFTs (i.e., IFT is measured versus time before it reaches its stable value) for the following systems:

1. Reservoir brine+CO_2
2. Crude oil +CO_2
3. Reservoir water +Crude oil
4. Reservoir water +Crude oil+CO_2

The density and viscosity of the crude oil and density of brine in these experiments were the same as those in the previous publication.

Figure A.19 and Figure A.20 show the effect of CO_2 on the IFT of crude oil and reservoir brine at the same temperature but different pressure conditions. It is noted that the presence of CO_2 has reduced the IFT between brine and oil by about 5 mN/m.

A.5.2 Oil-CO_2 interfacial tension

Yang and Gu (2004a) also measured the IFT of CO_2 and a crude oil with density of 0.911 g/cm^3 at atmospheric pressure and 25 °C. They showed that equilibrium IFT increases as temperature increases, however it reduces as the pressure increases. They attributed those observations to a decreased CO_2 solubility at a higher temperature and an increased CO_2 solubility at a higher pressure.

A.5.3 Water-oil interfacial tension

Zeppieri et al. (2001) presented IFT of alkanes and water (Figure A.21).

Bi-Yu, et al. (1996) presented similar graph for IFT between alkanes and water vs. pressure. Figure A.22 shows that the interfacial tension of n-alkane + water systems increases slightly with pressure, with an approximately linear relationship.

A.6 CO_2 Diffusion Coefficient

A.6.1 CO_2 diffusion coefficient in oil

Aguilera et al. (2002) presented two different diffusion coefficient values for n-decane-carbon dioxide, corresponding to cylindrical and square capillary tubes. Figure A.23 and Figure A.24 show the diffusion coefficient of n-decane-carbon dioxide as a function of temperature and pressure for these two systems. It is noted that there is a major

difference between calculations based on cylindrical or square capillary tubes. Please note that the maximum value of the y axis should read 12.E-10 in Figure A.23 and 12.E-8 in Figure A.24.

Grogan, et al. (1988) presented CO_2 diffusion coefficients in Pentane, Decane and Hexadecane at 25 °C and 6000 kPa. Figure A.25 shows these data.

An empirical correlation was developed by McManamey and Woollen (1973), Equation A.4, to estimate the CO_2 diffusion coefficient in oil, based on the viscosity of oil.

$$D_{co2,oil} = 1.41 \times 10^{-10} \mu_{oil}^{-0.47} \qquad \text{(A.4)}$$

In this equation μ_{oil}, viscosity of oil is in Pa.s and $D_{co2,oil}$ in m^2s^{-1}. This equation has wide application in the oil industry, as it relates CO_2 diffusivity in oil to its viscosity in a simple way.

A.6.2 CO_2 diffusion coefficient in water

Several researchers (Unver and Himmelblau, 1964; Thomas and Adams, 1965) reported the change in the CO_2 diffusion coefficient in water with temperature at atmospheric pressure. These reported data are well correlated by the Stokes-Einstein equation (Grogan and Pinczewski, 1987):

$$D_{co2,water} = 5.72 \times 10^{-12} \frac{T}{\mu_w}, \qquad \text{(A.5)}$$

where T is in K, μ_w in centipoises (mPa.s) and $D_{co2,water}$ in m^2s^{-1}.

Wang et al. (1996) reported some experimental data on the diffusivity of CO_2 in water and brine for pressure values up to 5.178 MPa.

Experimentally measured diffusion coefficients were also reported for CO_2 in decane and in 0.25 M NaCl brine up to 850 psia and 100°F (Renner, 1988). Statistical analysis of the data indicated that water viscosity and gas viscosity were both related to the diffusion coefficient. Renner recommends a correlation (Equation A.6) developed based on these data and two more series of literature data all measured at atmospheric pressure

and a range of temperature. However our experience has shown that this equation is only valid for the data used and cannot predict satisfactory results for brine at different pressure and temperature conditions.

$$D_{ij} = 6.391 \times 10^{3} \mu_{i}^{-0.1584} \mu_{j}^{6.911}, \quad \text{(A.6)}$$

where

$D_{ij} =$ Diffusion coefficient of gas (i) in liquid j /ft^{2}s^{-1}

$\mu_i =$ Viscosity of gas i /cp.

$\mu_j =$ Viscosity of water or brine j /cp

Figure A.26 shows the diffusion coefficient data that satisfy this equation.

A.7 CO_2 Effect on pH (Water Acidity) and Contact Angle

Toews et al. (1995) presented some measured and predicted data for the pH of water in equilibrium with supercritical CO_2 at various temperatures and pressures. The pH was analyzed under pressures of 70-200 atm and temperatures of 25-70 °C. Figure A.27 shows that pH increases with increasing temperature and decreases with increasing pressure, a trend consistent the level of solubility of CO2.

Chiquet et al., (2005) studied the wettability alteration effect when CO_2 comes into contact with the caprock containing water. They reported water-rock-CO_2 contact angle measurements on quartz and mica at various brine salinities, at pressures up to 100 bar and temperature of 35 °C. A significant increase in the contact angle was observed; in other words, quartz and mica became less water-wet at higher pressures. Such contact angle variation with CO_2 is primarily caused by the change in brine pH, i.e., the decrease in pH changes the balance of electrical charges on the rock surface. Therefore the (repulsive) electrostatic interactions between the mineral/brine and brine/CO_2 interfaces, which tend to stabilize the brine film and favour water-wettability, are less effective at high CO_2 pressure or lower pH. They suggested this wettability alteration reduces threshold pressure of CO_2 resulting in its leakage from cap rock. Figure A.28 and A.29 show contact angle measurements for mica and quartz in brines (dissolved

CO_2) for various salt concentrations. The impact of CO_2 on contact angle and wettability has been investigated in the present study, as described in Chapter 5.

A.8 References

Aguilera, M. E., Cerro, R.L. and Lopez de Ramos, A. 2002: ''Enhanced CO_2 diffusion in wedges.'', Chemical Engineering Journal 87, 31–40.

Barrufet M. A., Said El-Sayed K., Tantawy S. M., Gustavo A. and Iglesias-Silva, 1996: ''Liquid viscosities of carbon dioxide + hydrocarbons from 310 K to 403 K'', Journal of Chemical and Engineering Data, Vol. 41, No. 3.

Baviere, M., 1991: ''Basic concepts in enhanced oil recovery processes'', Published for SCI by Elsevier Applied Science, in London and New York.

Beggs, H. D. and Robinson, J. R., 1975: ''Estimating the viscosity of crude oil systems'', JPT, **9** (1975), pp. 1140–1141.

Bessieres D., Saint-Guirons H., and Daridon J.L., 2001: ''Volumetric behavior of decane + carbon dioxide at high pressures: measurement and calculation'', Journal of Chemical and Engineering Data, Vol. 46, No. 5.

Bi-Yu C., Ji-Tao Y., and Tian-Min G., 1996: ''interfacial tension of hydrocarbon + water/brine systems under high pressure'', Journal of Chemical and Engineering Data, 41, 493-496.

Campbell B. T., Orr, Jr F. M., 1985: ''Flow visualization for co_2/crude-oil displacements'', SPE 11958, Oct 1985.

Chalbaud, C. Robin, M. Egermann, P., 2006: ''interfacial tension data and correlations of brine/CO_2 system under reservoir conditions'', SPE 102918 Sep 2006.

Chiquet, P., Broseta, D., and Thibeau, S., 2005: ''Capillary alteration of shaly caprocks by carbon dioxide.'', SPE 94183, Proceedings of the SPE Europec/EAGE Annual Conference held in Madrid, Spain, 13-16 June 2005.

Diamond, L. W. and Akinfiev, N. N., 2003: ''Solubility of CO_2 in water from−1.5 to 100 ◦C and from 0.1 to 100 MPa: evaluation of literature data and thermodynamic modelling'', Fluid Phase Equilibria 208, 265–290.

Do H.D., Pinczewski W.V.: ''Diffusion controlled swelling of reservoir oil by indirect contact with injection gas'', Chemical Engineering Science Vol. 48, No. 18, PP. 3243-3252, (1993)

Dodds, W. S. Stutzman, L. F. and Sollami, B. J., 1956: ‘‘Carbon dioxide solubility in water, ’’Industrial and Engineering Chemistry Vol. 1, No. 1.

Ennis-King J, Paterson L., 2003: ‘‘Role of convective mixing in the long-term storage of carbon dioxide in deep saline formations.’’ SPE 84344 Oct 2003.

Grogan A.T., Pinczewski W.V., 1987: ‘‘The role of molecular diffusion processes in tertiary CO_2 flooding’’ JPT May 1987 and SPE 12706,

Grogan, A.T. Pinczewski, W.V. Gregory, J. R. Orr Jr, F. M., 1988: ‘‘Diffusion of CO_2 at reservoir conditions: models and measurements’’, SPE 14897 Feb 1988.

Hebach A., Oberhof A., Dahmen N., Kogel A., Ederer H., and Dinjus E., 2002: ‘‘Interfacial tension at elevated pressures: measurements and correlations in the water + carbon dioxide System’’, Journal of Chemical and Engineering Data, Vol. 47, No. 6, 2002.

Hebach, A., Oberhof, A. and Dahmen, N., 2004: ‘‘density of water + carbon dioxide at elevated pressures: measurements and correlation’’, Journal of Chemical and Engineering Data, Vol. 49, No. 4, 2004.

Holm, L. W. and Josendal, V. A., 1974: ‘‘Mechanisms of oil displacement by carbon dioxide’’, SPE 4736, Dec 1974.

Koschel D., Coxam J. Y., Rodier L., Majer V., 2006: ‘‘Enthalpy and solubility data of CO_2 in water and NaCl(aq) at conditions of interest for geological sequestration’’, Fluid Phase Equilibria Vol. 247, P. 107–120.

Kumagai A., and Yokoyama C., 1998: ‘‘Viscosity of aqueous solution of CO_2 at high pressures’’, International Journal of Thermophysics, Vol. 19, No. 5.

Lohrenz, J., Barry B. G., Aime M., and Clark C. R., 1964: ‘‘Calculating viscosity of reservoir fluids from their compositions.’’, SPE 915, Oct 1964.

Massoudi, R. and King, A. D. Jr, 1975: ‘‘Effect of pressure on the surface tension of aqueous solutions. adsorption of hydrocarbon gases, carbon dioxide, and nitrous oxide on aqueous solutions of sodium chloride and tetra-n-butylammonium bromide at 25°C’’, The Journal of Physical Chemistry, Vol. 79, No. 16.

McManamey, W.J. and Woollen, J.M., 1973: ‘‘The diffusivity of carbon dioxide in organic liquids at 25°C and 50°C’’, AIChE J. (May 1973) Vol. 19, No. 3, 667-69

Miller, J. S. and Jones, R. A., 1981: ‘‘A laboratory study to determine physical characteristics of heavy oil after CO_2 saturation’’, SPE/DOE 9789 April 1981.

Renner, T.A., 1988: ‘‘Measurement and correlation of diffusion coefficients for CO_2 and rich gas application’’, SPE 15391, May 1988.

Simon, R and Graue, D. J., 1964: ‘‘Generalized correlations for predicting solubility, swelling and viscosity behaviour of CO_2-crude oil systems’’, SPE 917, Oct 1964.

Thomas, W.J. and Adams, M.J., 1965: ‘‘Measurement of the diffusion coefficient of carbon dioxide and nitrous oxide in water and aqueous solution of glycerol.’’, Trans. Faraday Soc., 61, 668-73.

Toews, K. L., Shroll R. M., and Wai C. M., Smartt, N. G., 1995: ‘‘pH-defining equilibrium between water and supercritical CO_2. influence on SFE of organics and metal chelates’’, Analytical Chemistry, Vol. 67, No. 22, November 15.

Tumasyan, A. B., Panteleev, V. G. and Meinster, G. P., 1969: ‘‘Influence de l’anhydride carbonique sur les proprietes physiques du petrole et de l’eau’’. Nefteprom. dela, 2 pages 20-3.

Uchida, T., Ohmura, R., Nagao, J., Takeya, S., Ebinuma, T. and Narita, H., 2003: ‘‘Viscosity of aqueous CO_2 solution measured by dynamic light scattering’’, Journal of Chemical and Engineering Data, Vol. 48, P. 1225-1229.

Unver, A.A. and Himmelblau, D.M., 1964: ‘‘Diffusion coefficient of CO_2, C_2H_4, C_3H_6, and C_4H_8 in water from 6°C to 65°C’’, Journal of Chemical and Engineering Data (July) Vol. 9, No. 3, P. 428-431.

Wang, L.S., Lang, Z.X., and Guo, T. M., 1996: ‘‘Measurement and correlation of the diffusion coefficients of carbon dioxide in liquid hydrocarbons under elevated pressures.’’, Fluid Phase Equilibria Vol. 117, P. 364-372.

Watson. K. M., Nelson, F. F. and Murphy, G. B., 1935: ‘‘characterization of petroleum fraction’’, IEU, Vol. 27, 1460.

Welker, J.R and Dunlop, D.D., 1963: ‘‘Physical properties of carbonated oils’’, SPE 567 August 1963.

Wiebe, R., 1941: ‘‘The Binary System Carbon Dioxide-Water under Pressure’’ Chemical Reviews 29, 475.

Yang, D. and Gu, Y., 2004a: ‘‘Visualization of interfacial tension of crude oil-CO_2 systems under reservoir conditions’’, SPE 89366 April.

Yang, D. and Gu, Y., 2004b: ‘‘Interfacial interactions of crude oil-brine-CO_2 systems under reservoir conditions’’, SPE 90198, Sep.

Yang, D. Tontiwachwuthikul, P and Gu, Y., 2005: ‘‘Interfacial Tensions of the Crude Oil + Reservoir Brine + CO_2 Systems at Pressures up to 31 MPa and Temperatures

of 27 °C and 58 °C'', Journal of Chemical and Engineering Data, Vol. 50, No. 4, 2005.

Yih-Bor C., Coats B.K. and Nolen J.S., 1998: ''A Compositional Model for CO_2 Floods Including CO_2 Solubility in Water'', SPE 35164, April 1998.

Zappe J., Wesch A., and Ebert K. H., 2000: ''Measurement of the Mass Transfer into Single Drops in the System of Water/Supercritical Carbon Dioxide'', Journal of Colloid and Interface Science 231, 1–7.

Zeppieri S., Rodríguez J., and López de Ramos A. L., 2001: ''Interfacial Tension of Alkane + Water Systems'', Journal of Chemical and Engineering Data, Vol. 46, P. 1086-1088.

Zuniga-Moreno A., Galicia-Luna L. A., and Camacho-Camacho L. E., 2005: ''Compressed Liquid Densities and Excess Volumes of CO_2 + Decane Mixtures from (313 to 363) K and Pressures up to 25 MPa'', Journal of Chemical and Engineering Data, Vol. 50, No. 3.

coefficient	value
I_0/kg·m^{-3}	949.7109
I_1/kg·m^{-3}·MPa^{-1}	0.559 684
I_2/kg·m^{-3}·K^{-1}	0.883 148
I_3/kg·m^{-3}·MPa^{-2}	−0.000 97
I_4/kg·m^{-3}·K^{-2}	−0.002 28
g_0/kg·m^{-3}	805.1653
g_1/kg·m^{-3}·MPa^{-1}	44.126 85
g_2/kg·m^{-3}·K^{-1}	1.573 145
g_3/kg·m^{-3}·MPa^{-2}	−1.450 73
g_4/kg·m^{-3}·K^{-2}	−0.003 13
g_5/kg·m^{-3}·MPa^{-1}·K^{-1}	−0.196 58
g_6/kg·m^{-3}·MPa^{-3}	6.27×10^{-5}
g_7/kg·m^{-3}·MPa^{-1}·K^{-2}	0.000 209
g_8/kg·m^{-3}·MPa^{-2}·K^{-1}	0.004 204

Table A.1. Coefficients of the Regression Function (Eqs. A.1 and A.2), Hebach, et al. (2004).

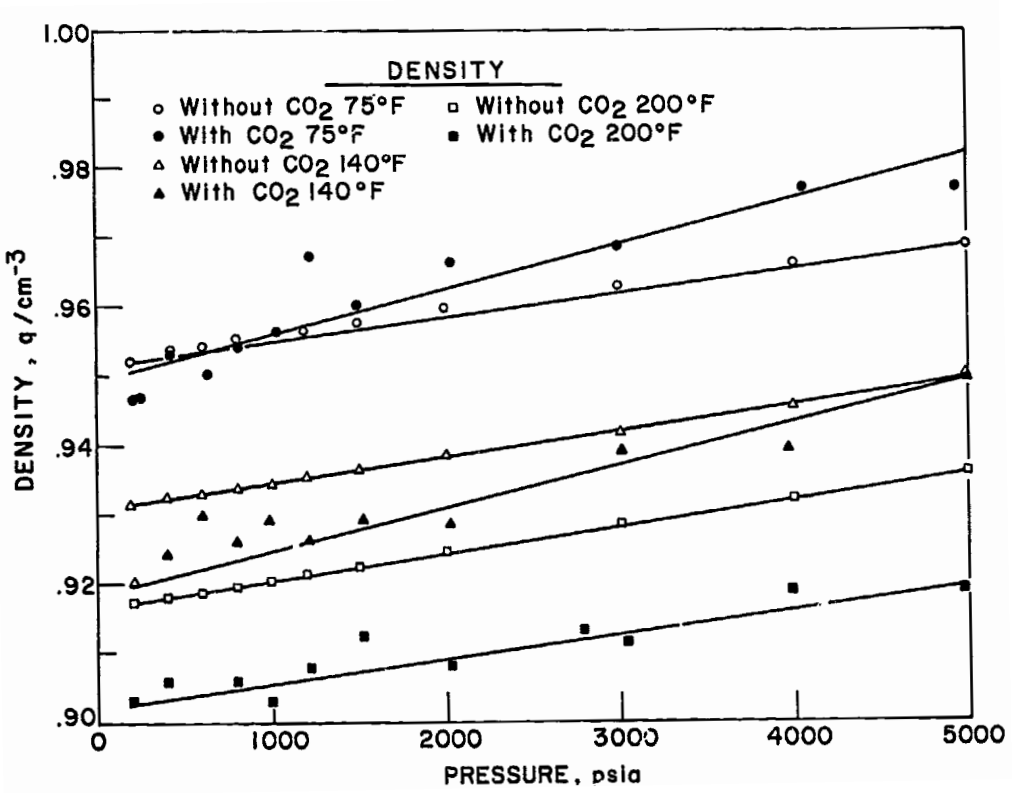

Figure A.1: Density of Wilmington oil (17 API gravity) at 75 °F, 140 °F and 200 °F, (Miller and Jones, 1981).

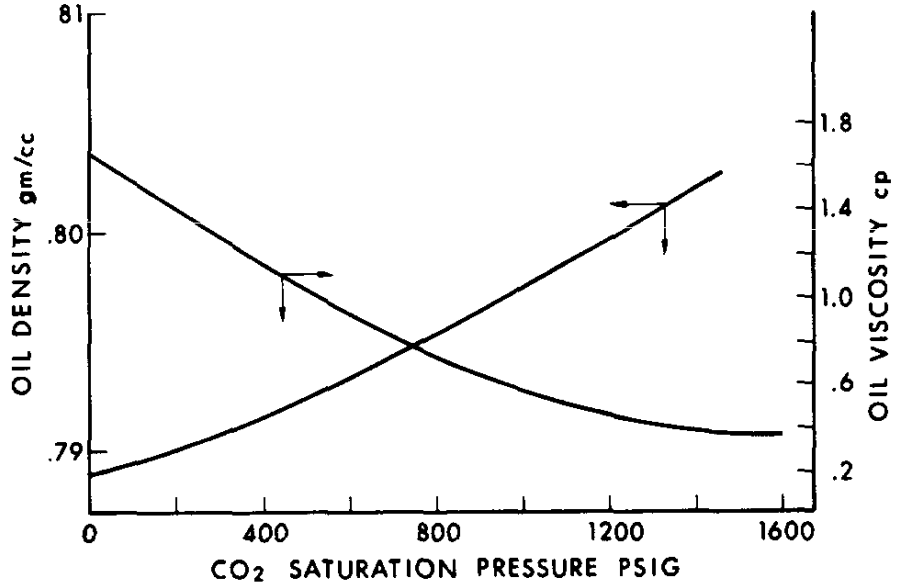

Figure A.2: Oil density and viscosity of CO_2-saturated Mead-Strawn stock-tank oil versus pressure at 135F, (Holm and Josendal, 1974).

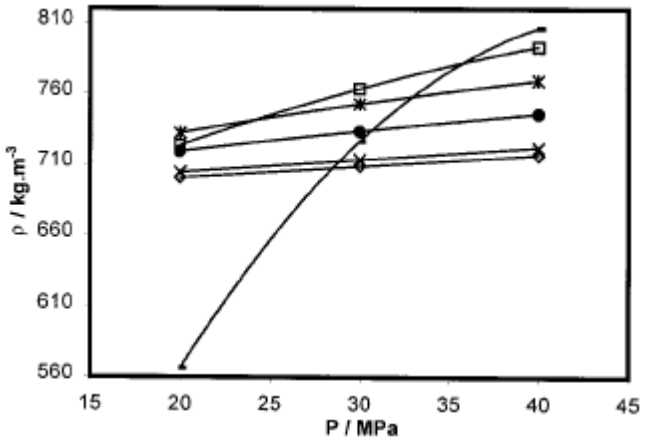

Figure A.3: Variation of decane density with pressure at different concentrations x_1, ◇ 0; × 0.15; ● 0.51; * 0.66; □, 0.84; – 1, (Bessieres, et al., 2001).

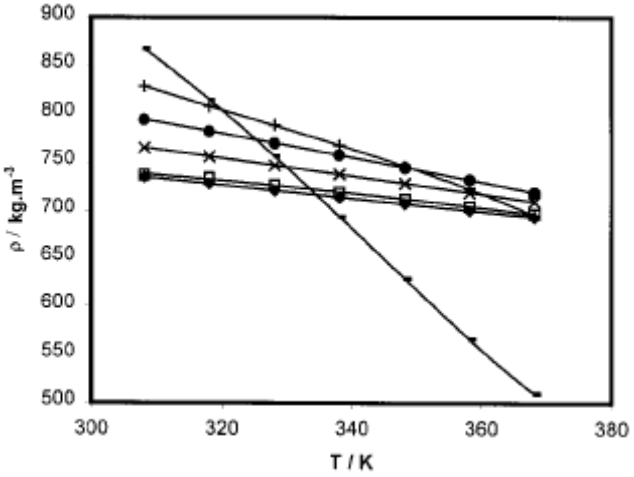

Figure A.4: Variation of decane density with temperature at different CO_2 concentrations x1: ◆ 0; □ 0.15; × 0.51; ● 0.66; +, 0.84; - 1, (Bessieres, et al., 2001).

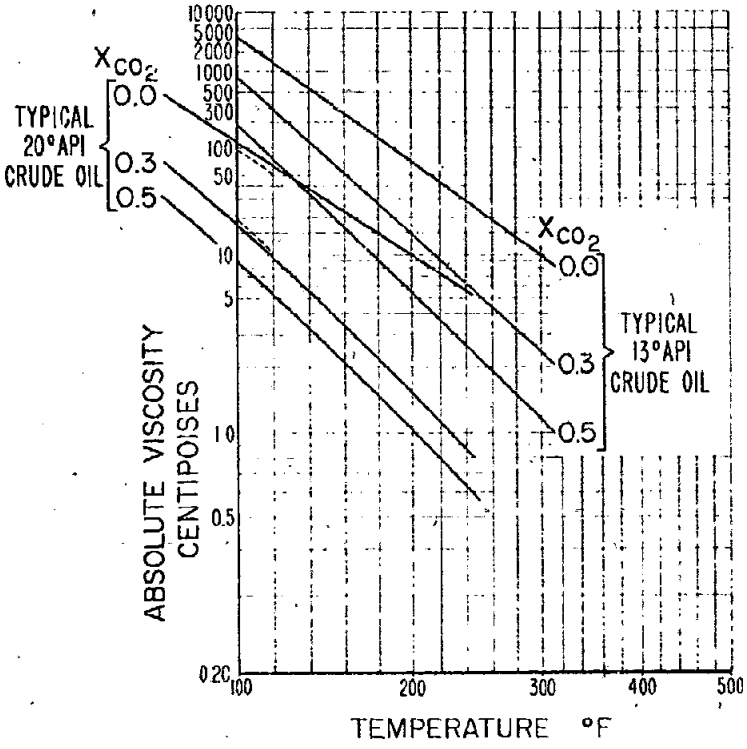

Figure A.5: Viscosity versus temperature chart for a number of crude oils, (Simon and Graue, 1964).

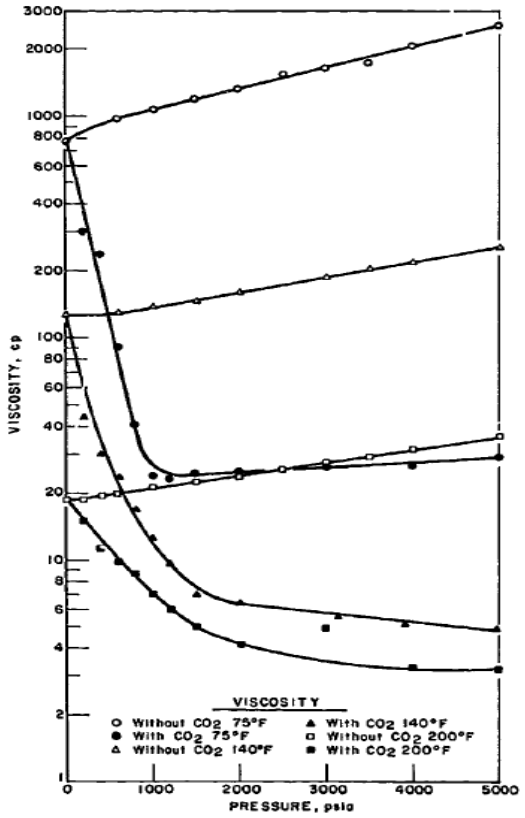

Figure A.6: Viscosity of Wilming oil (17° API Gravity) versus pressure at 75 °F, 140 °F, and 200 °F, (Miller and Jones, 1981).

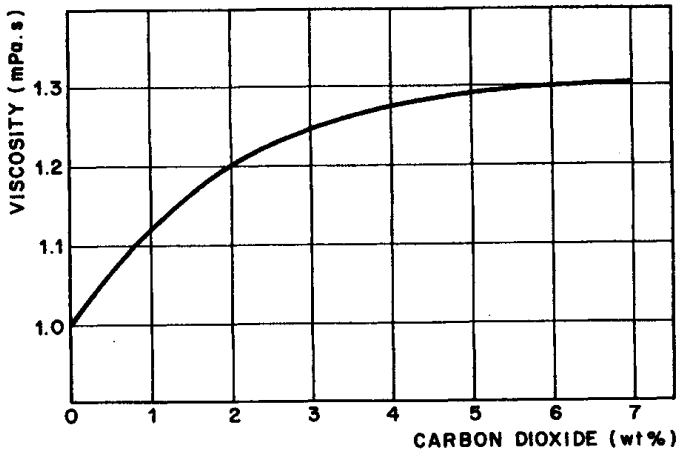

Figure A.7: Viscosity of carbonated water as a function of CO_2 concentration, Tumasyan, et al. (1969).

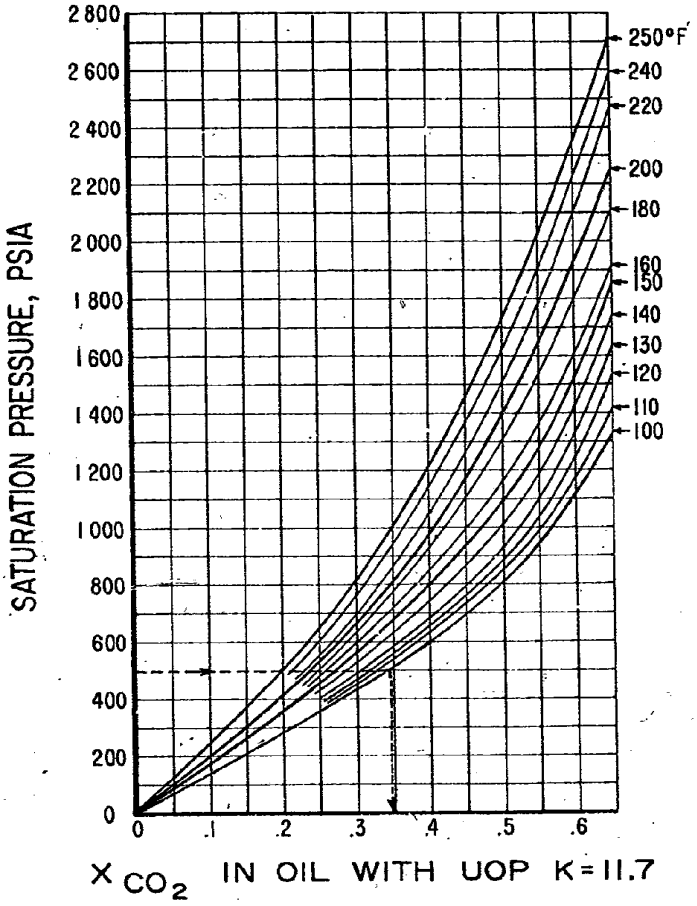

Figure A.8: CO_2 Solubility in an oil whose UOP characterization factor is 11.7, at different temperature and pressure values, (Simon and Graue, 1964).

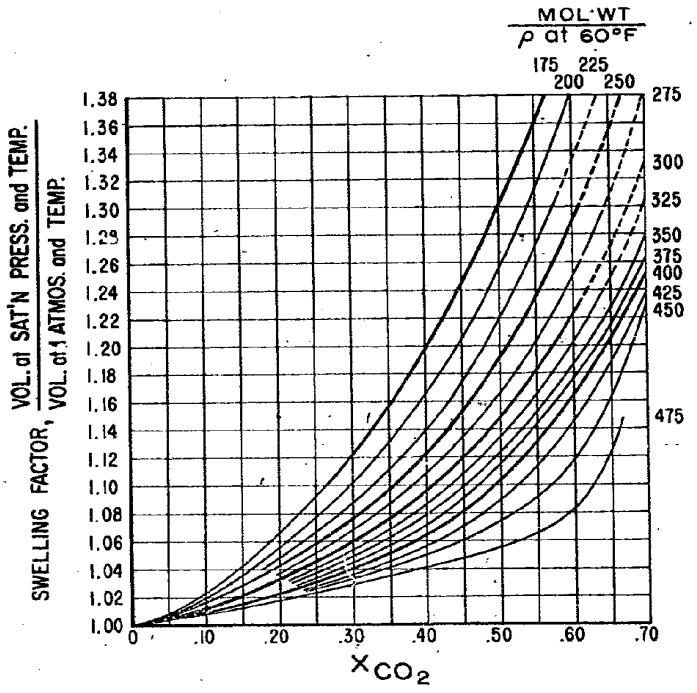

Figure A.9: Swelling factor versus mole fraction of CO_2, (Simon and Graue, 1964).

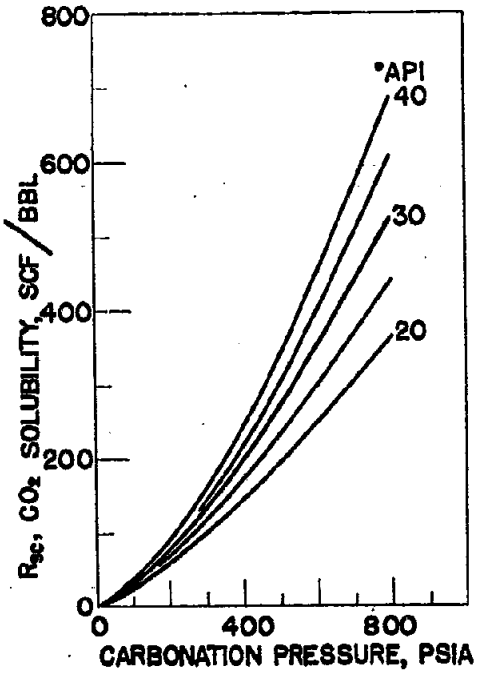

Figure A.10: Solubility of CO_2 in Crude oils at 80 F, (Welker and Dunlop, 1963).

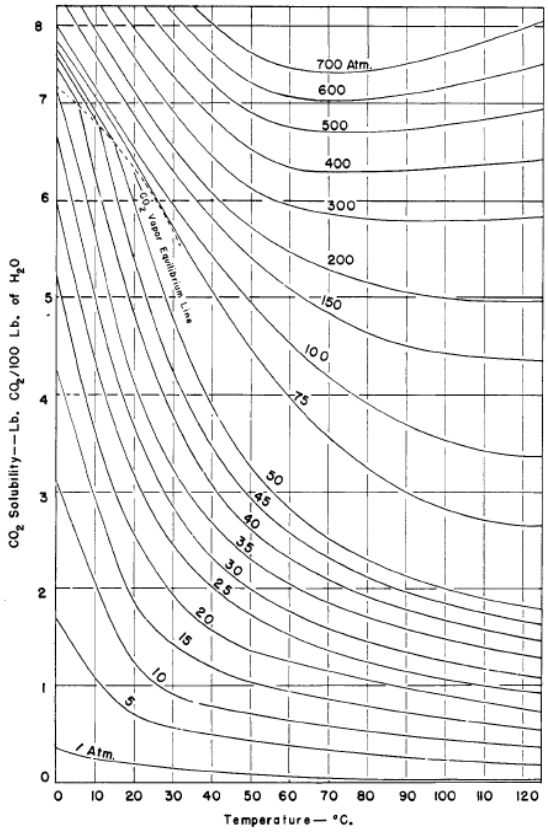

Figure A.11: Effect of temperature and pressure on the solubility of CO_2 in water, (Dodds, et al., 1956).

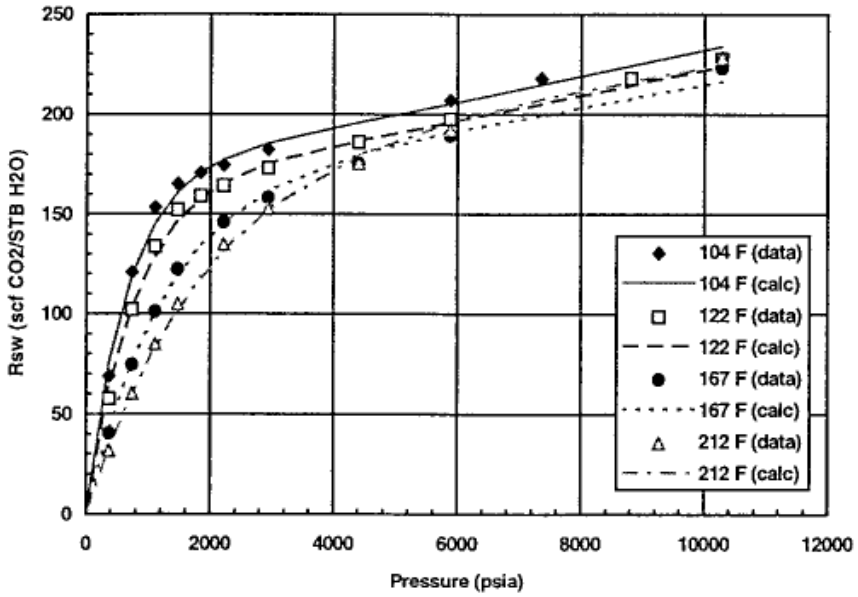

Figure A.12: Comparison of measured (Wiebe, 1941) and calculated (Yih-Bor, et al., 1998) CO_2 solubility in distilled water.

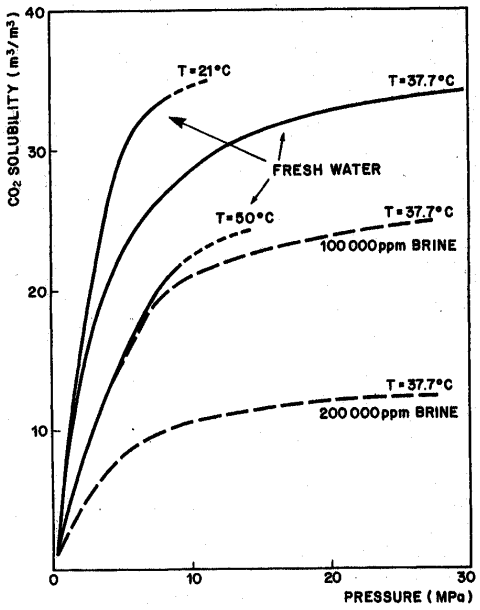

Figure A.13: effect of pressure, temperature and salinity on CO_2 solubility in water, (Baviere, 1991).

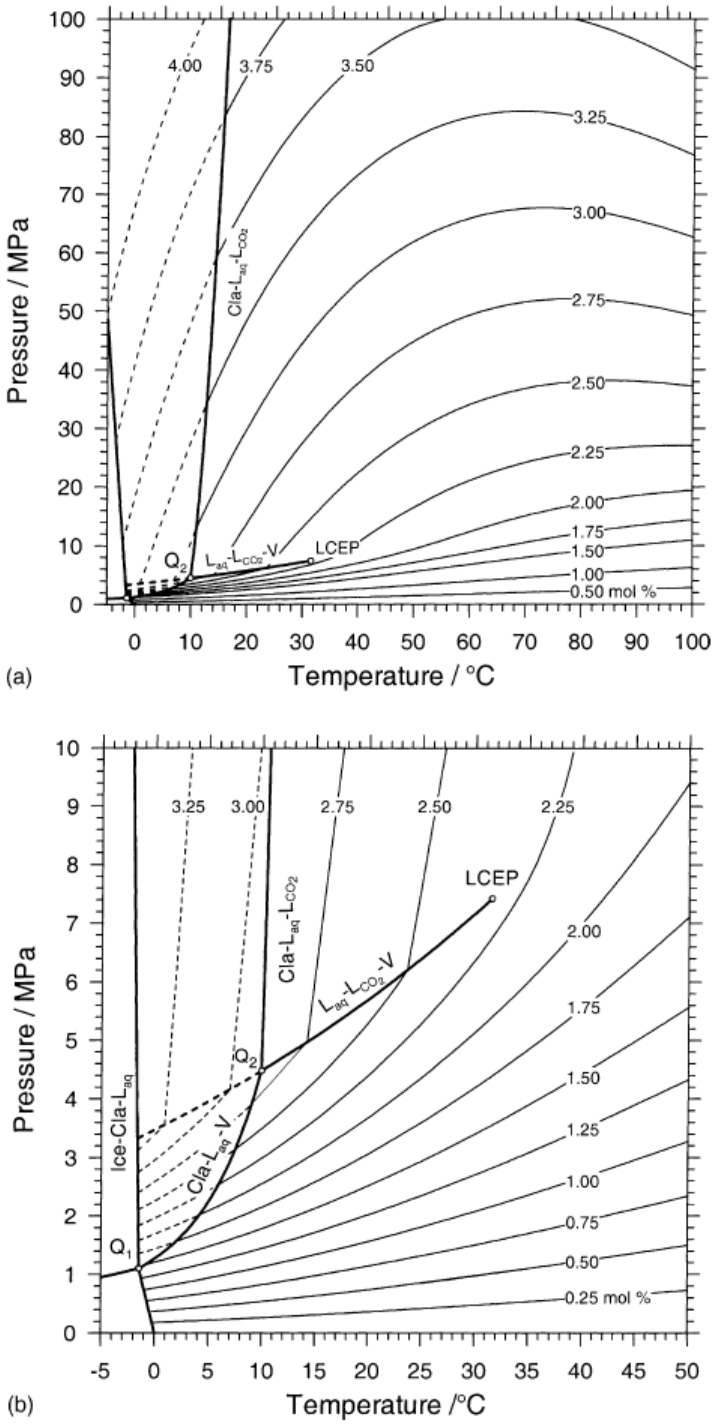

Figure A.14: P–T diagram showing selected solubility isopleths of $xCO_2(aq)$ between 0.25 and 4 mol%, Water is stable over the entire contoured area. Metastable isopleths and phase boundaries within the clathrate stability field are shown dashed. (a) Entire P–T region of model validity; (b) details of low-P, low-T region, (Diamond and Akinfiev, 2003)

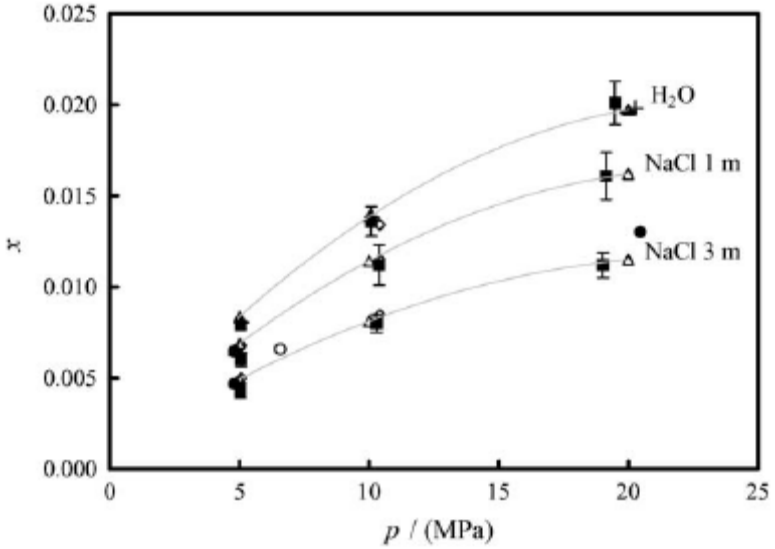

Figure A.15: Solubility of CO_2 at 373.1K and pressure range from 5 to 20MPa, in water and aqueous solution of NaCl 1 and 3 M, (Koschel, et al., 2006).

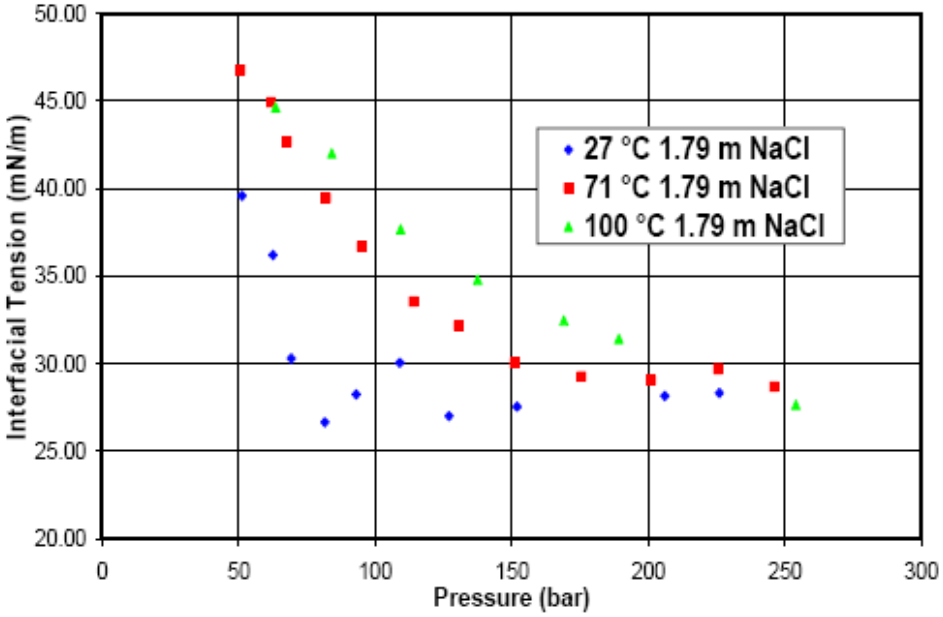

Figure A.16: Brine-CO_2 interfacial tension as a function of pressure at different temperature and 1.79 M (100,000 ppm) NaCl concentration, (Chalbaud, et al., 2006).

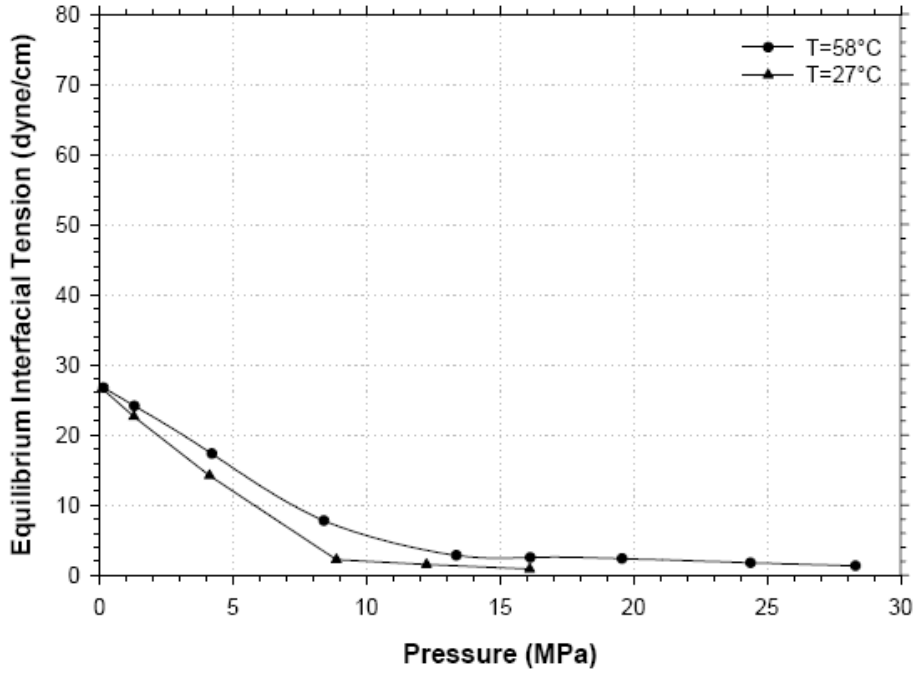

Figure A.17: Measured IFT of the crude oil-CO_2 system versus pressure at two different temperatures, (Yang and Gu, 2004b).

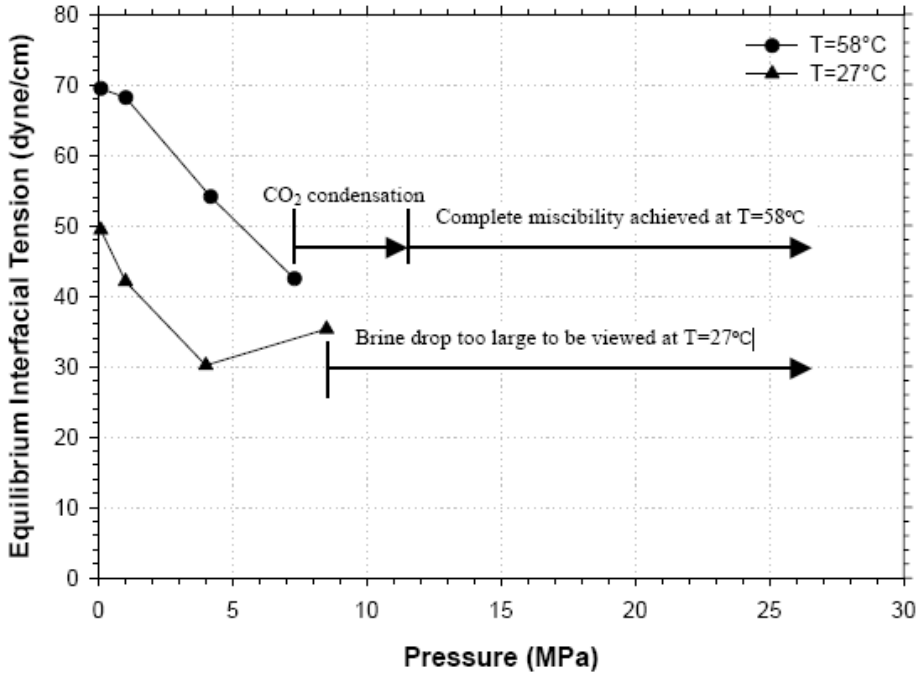

Figure A.18: Measured IFT of the brine-CO_2 system versus pressure at two different temperatures, (Yang and Gu, 2004b).

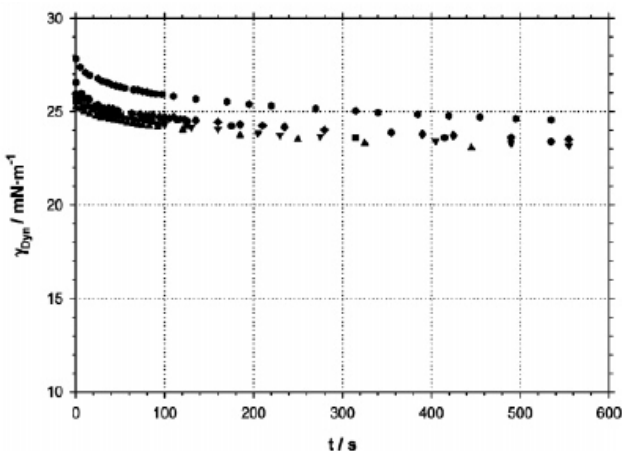

Figure A.19: measured dynamic IFT of crude oil+ reservoir brine system as a function of time at 58 °C for different pressures, (Yang, et al., 2005).

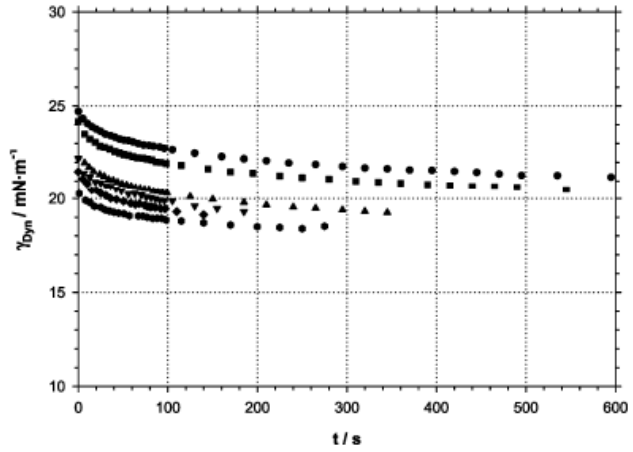

Figure A.20: measured dynamic interfacial tensions of crude oil+ reservoir brine+ CO_2 systems as a function of time at 58 °C for different pressures, (Yang, et al., 2005).

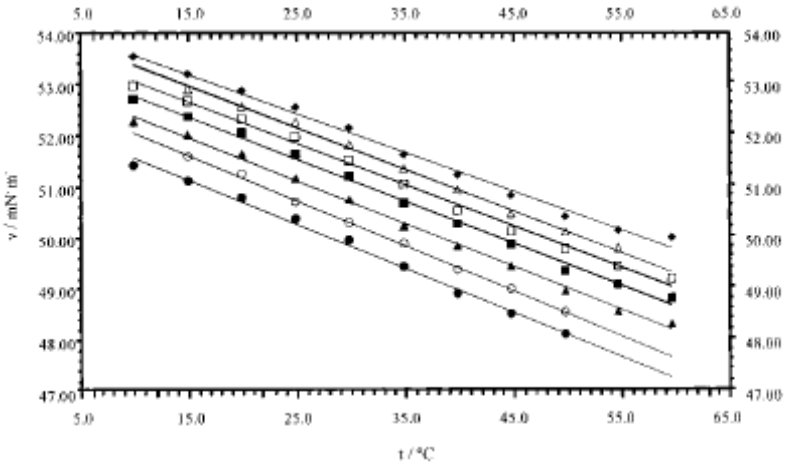

Figure A.21: IFT values as a function of temperature for water-n-alkane systems (at atmospheric pressure): ●hexane; O heptane; ▲ octane;■ nonane; □ decane; △ undecane;◆ dodecane, (Zeppieri, et al., 2001).

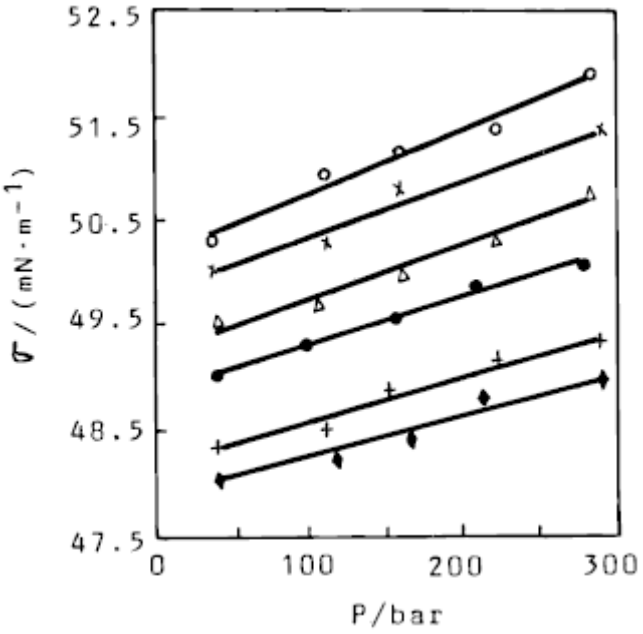

Figure A.22: Pressure effect on the IFT of n-alkane+ water systems at 50.0 °C: O C16; × C14; △ C12; ●. C10; + C8; ◆ C6, (Bi-Yu, et al., 1996).

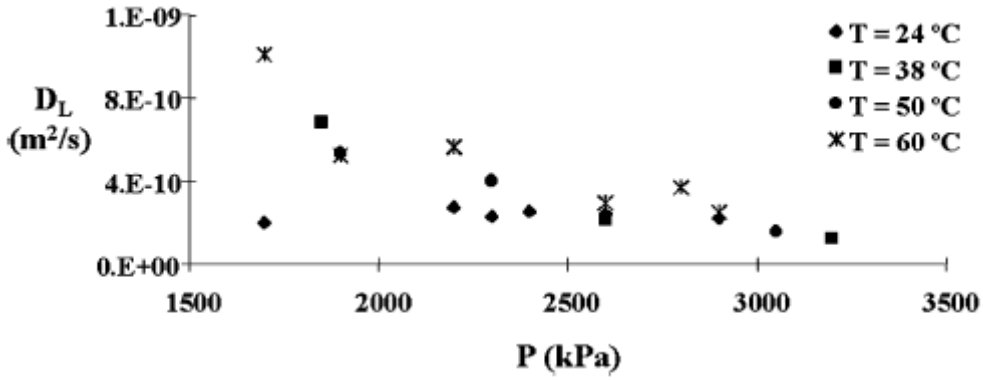

Figure A.23: Diffusion coefficient of liquid phase at different values of temperature and pressure for n-decane–carbon dioxide system (0.8 mm cylindrical capillary), (Aguilera, et al., 2002).

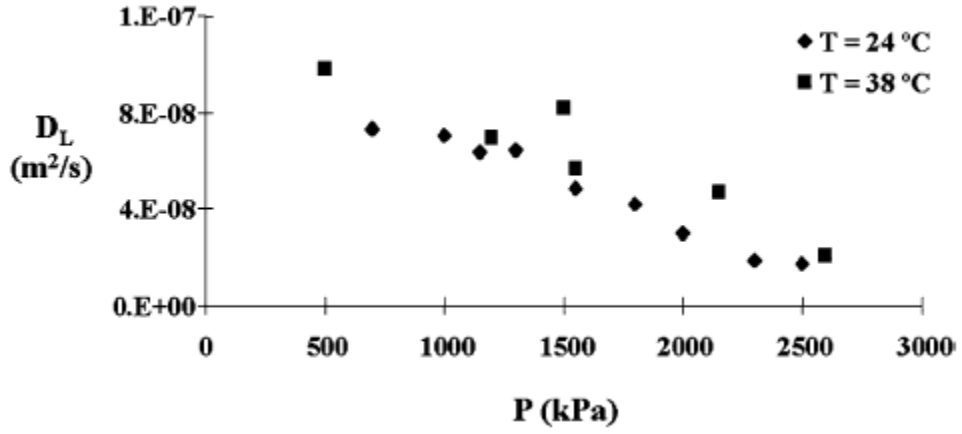

Figure A.24: Diffusion coefficient of liquid phase at different values of temperature and pressure for n-decane–carbon dioxide system (2 mm square capillary), (Aguilera, et al., 2002).

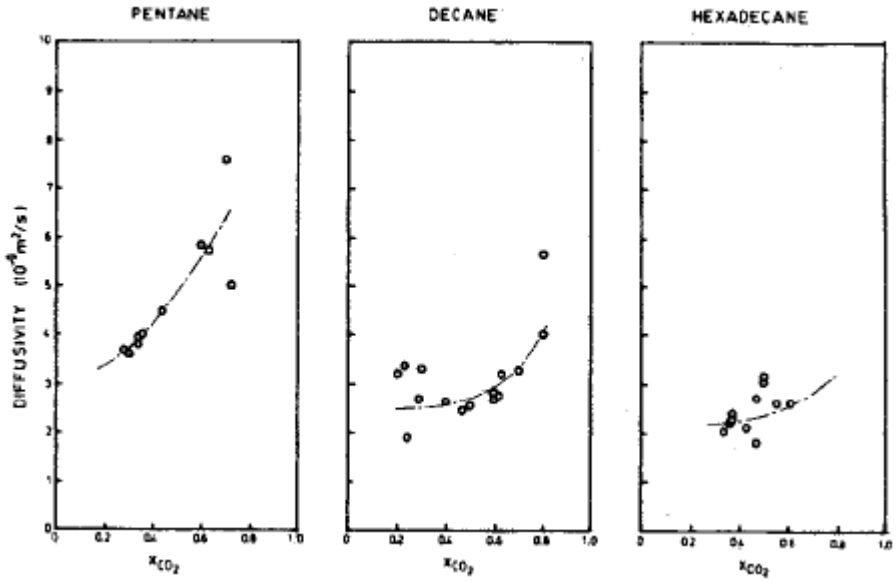

Figure A.25: Diffusion coefficient for CO_2 in three normal paraffins at 25 °C and 6000 kPa, (Grogan, et al., 1988).

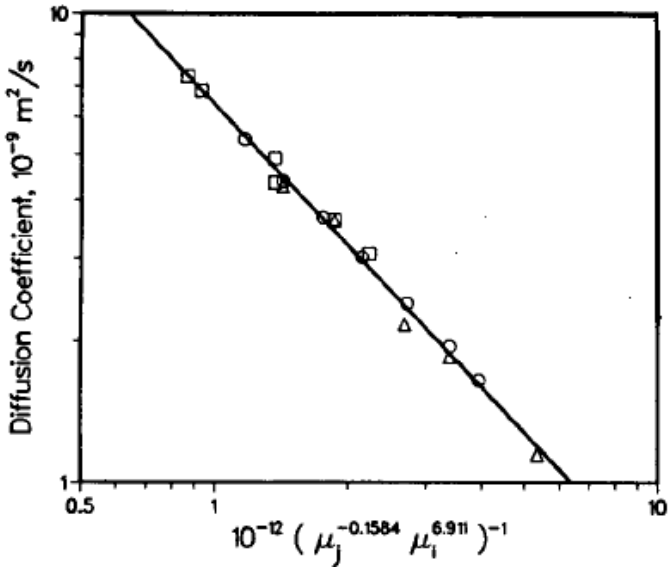

Figure A.26: Diffusion coefficient for CO_2 in water/ brine correlated as a function of both water/brine viscosity and CO_2 viscosity, (Renner, 1988).

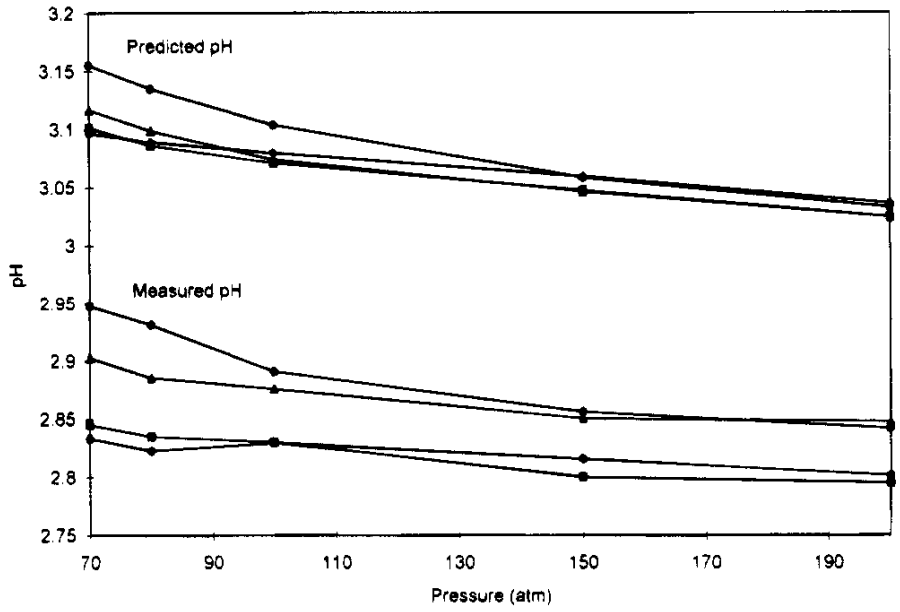

Figure A.27: Variation of pH of water in equilibrium with supercritical CO_2 at temperatures of of (◆) 25, (■) 40, (▲) 50, and (●) 70 C and pressures of 70, 80, 100, 150, and 200 atm, (Toews, et al., 1995).

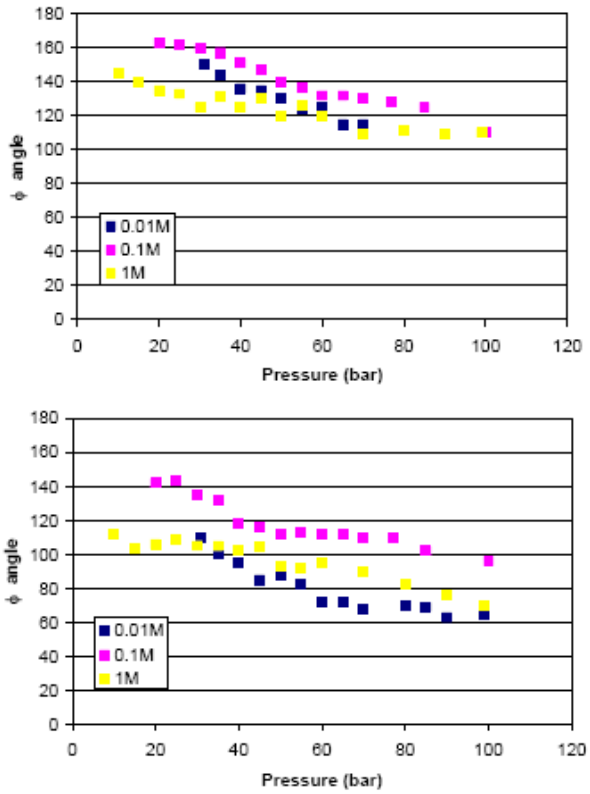

Figure A.28: Advancing (top) and receding (bottom) contact angles on mica in brines with various salt contents (0.01, 0.1 and 1 M NaCl), (Chiquet, et al., 2005).

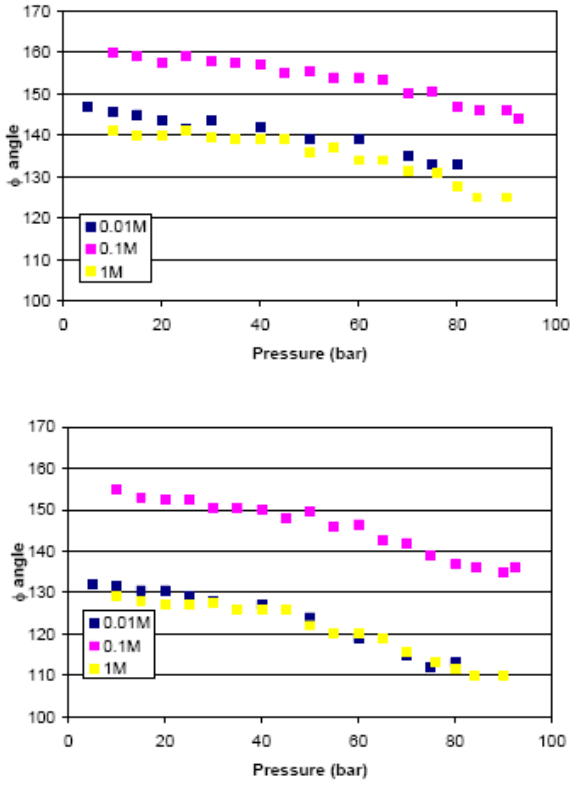

Figure A.29: Advancing (top) and receding (bottom) contact angles on quartz in brines with various salt contents (0.01, 0.1 and 1 M NaCl). (Chiquet, et al., 2005).

Appendix B: Visualisation Results of the Micromodel Experiments-CWI

EXP No.	Oil type	Flooding Procedure	CW* type
P*1	n-C_{10}	OI	-
P2	n-C_{10}	T-CWI	-
P3	n-C_{10}	OI	-
1	n-C_{10}	T-CWI	Fully saturated
2	n-C_{10}	S-CWI	Fully saturated
3	Viscous oil	T-CWI	Fully saturated
4	Viscous oil	T-CWI	Partially saturated
5	n-C_{10}	T-CWI	Partially saturated
6	n-C_{10}	S-CWI/BD	Partially saturated
7	n-C_{10}	S-CWI/BD	Partially saturated
8	CW	BD	Partially saturated
9	Crude oil	S-CWI	Fully saturated
10	Crude oil	T-CWI	Fully saturated
11	Crude oil	T-CWI	Fully saturated
12	W	CO_2I	-
13	Viscous oil	CO_2I	-
14	Viscous oil	WI/CO_2I	-
15	Viscous oil	CWI/CO_2I	Fully saturated
16	R14	WI/CO_2I	-
17	R15	CWI/CO_2I	Fully saturated
18	Crude oil	WI/CO_2I	-
19	Crude oil	CWI/CO_2I	Fully saturated
20	n-C_{10}	W	-
21	n-C_{10}	CW	Fully saturated
22	Viscous oil	GMI	-
23	Viscous oil	LMI	-

Table B-1: List of the micromodel experiments in this study.

*__BD__: Blow down (depressurisation), __CO_2__: Carbon dioxide, __CW__: Carbonated water

__I__: injection, __O__: oil, __P__: Preliminary test, __R__: Repeat, __S__: Secondary, __T__: Tertiary,

__W__: Water

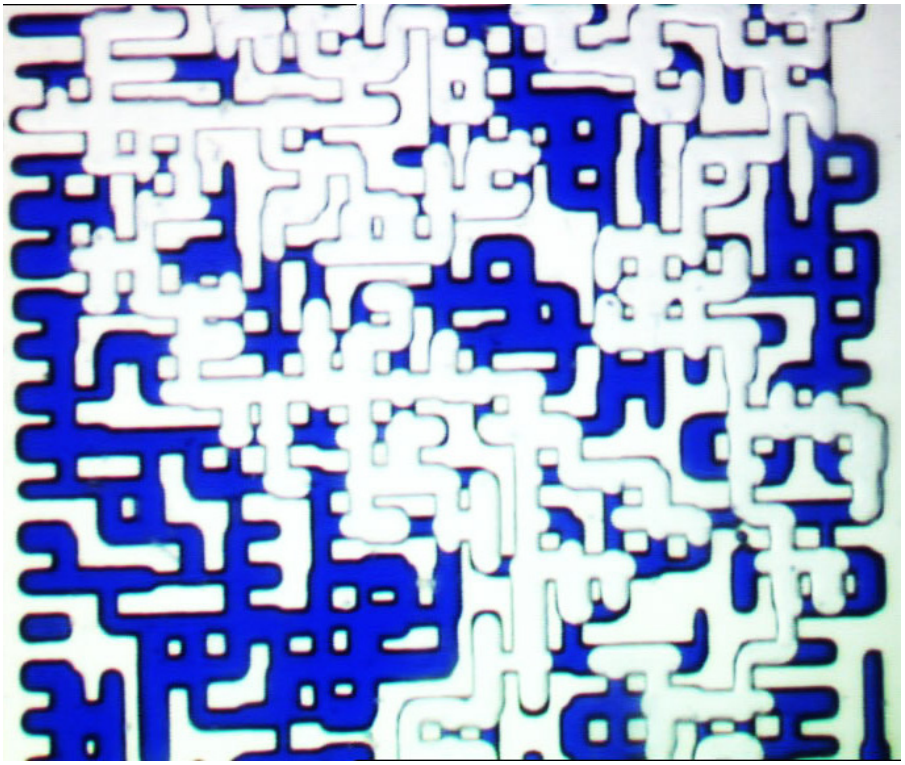

Figure B-1: Initial oil saturation after the first drainage stage in a selected frame of the micromodel, Experiment No.2 (Secondary CWI- Decane).

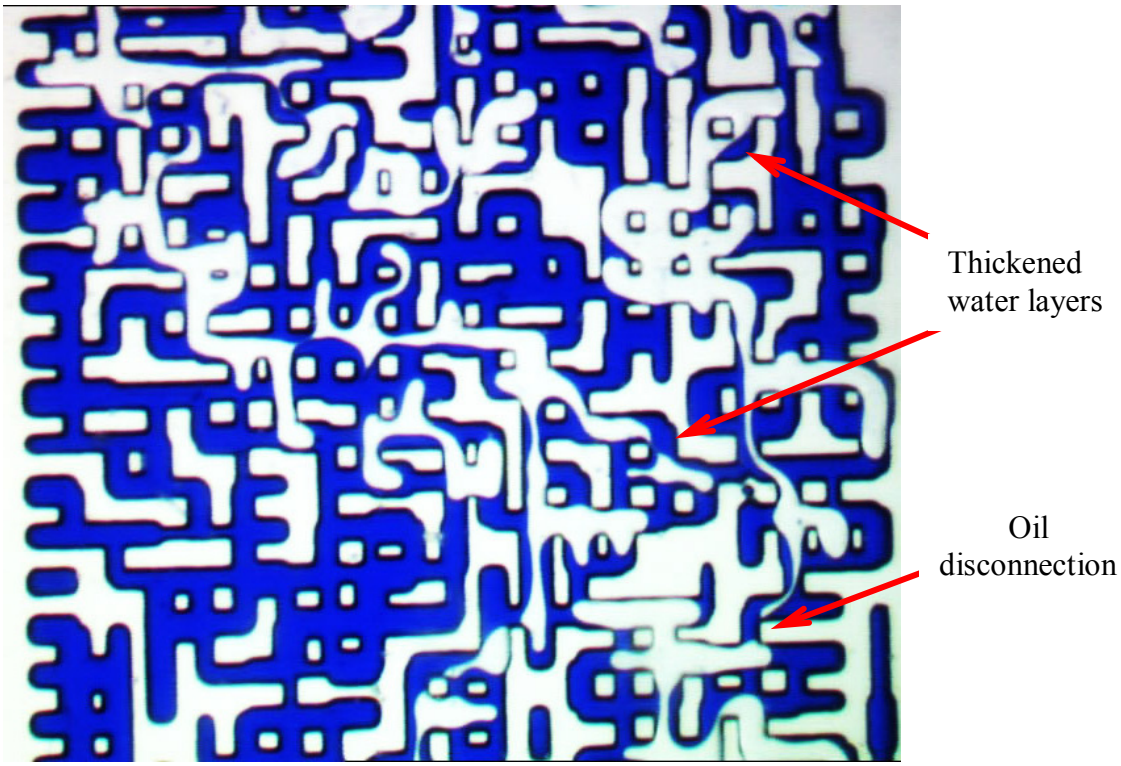

Figure B-2: Fluid distribution in the same selected frame (as in Figure B-1) at breakthrough (BT) of carbonated water (CW), Experiment No.2 (Secondary CWI-Decane).

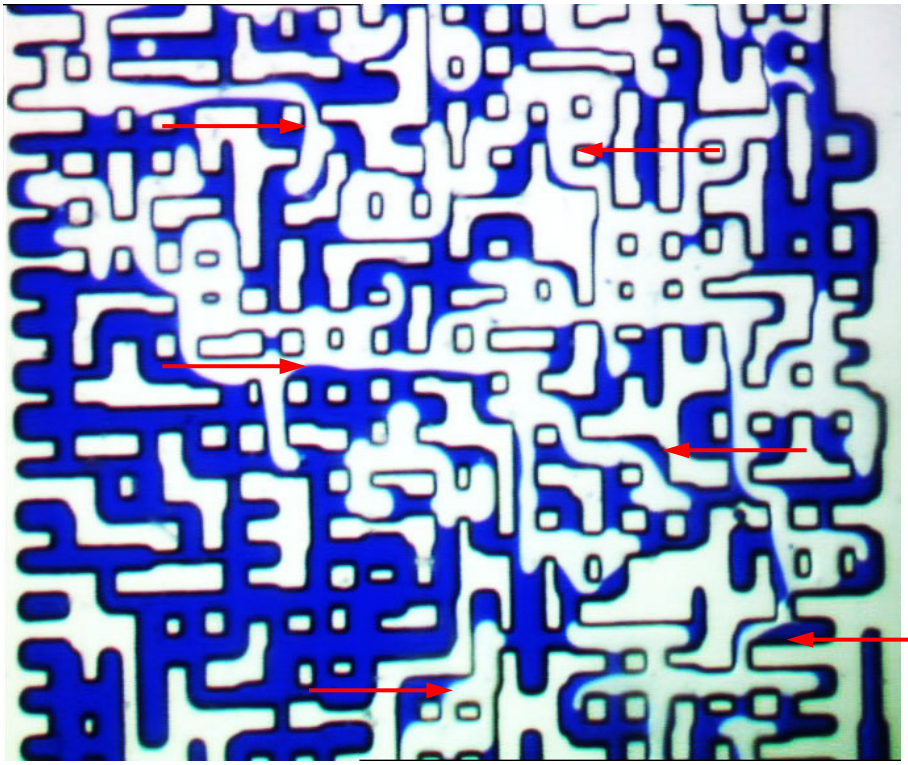

Figure B-3: Fluid distribution in the same selected frame (as in Figure B-1), 42 hrs after CWI, Experiment No.2 (Secondary CWI- Decane).

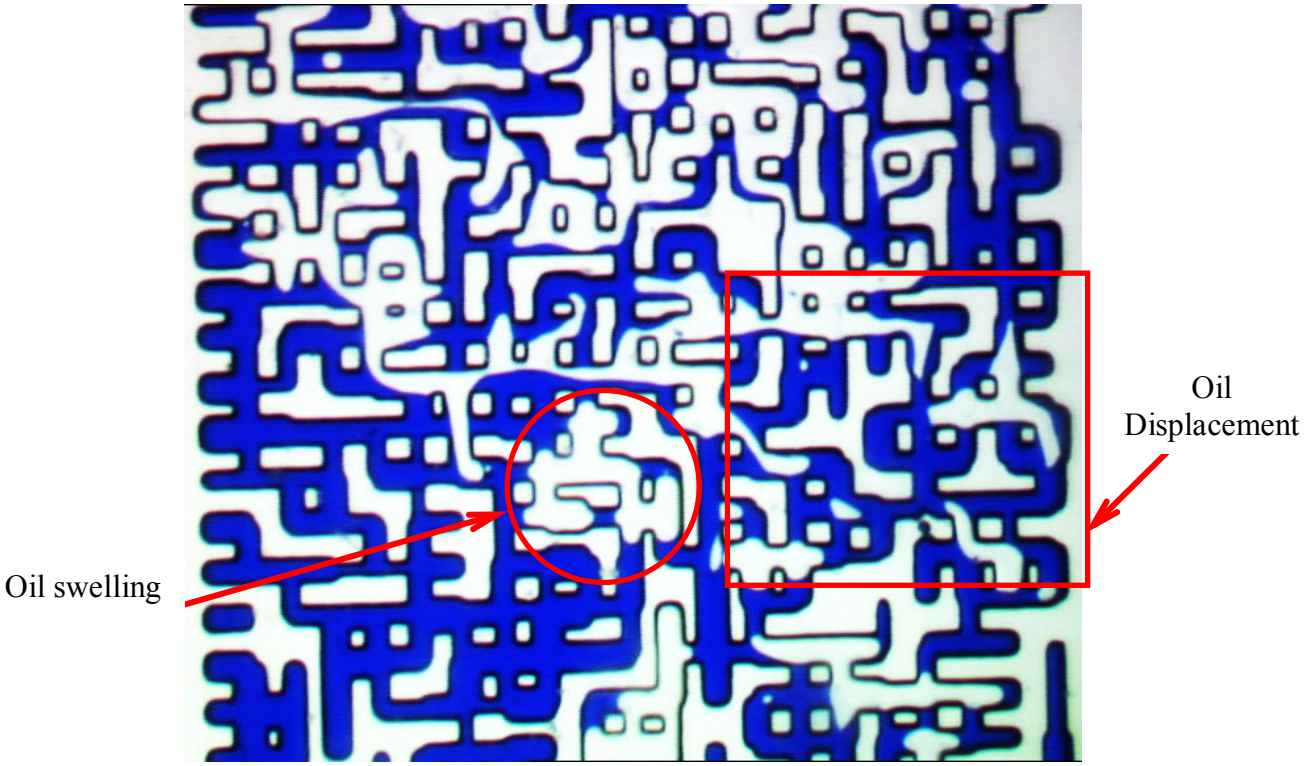

Figure B-4: Fluid distribution in the same selected frame (as in Figure B-1) after 138 hrs of CWI, Experiment No.2 (Secondary CWI- Decane).

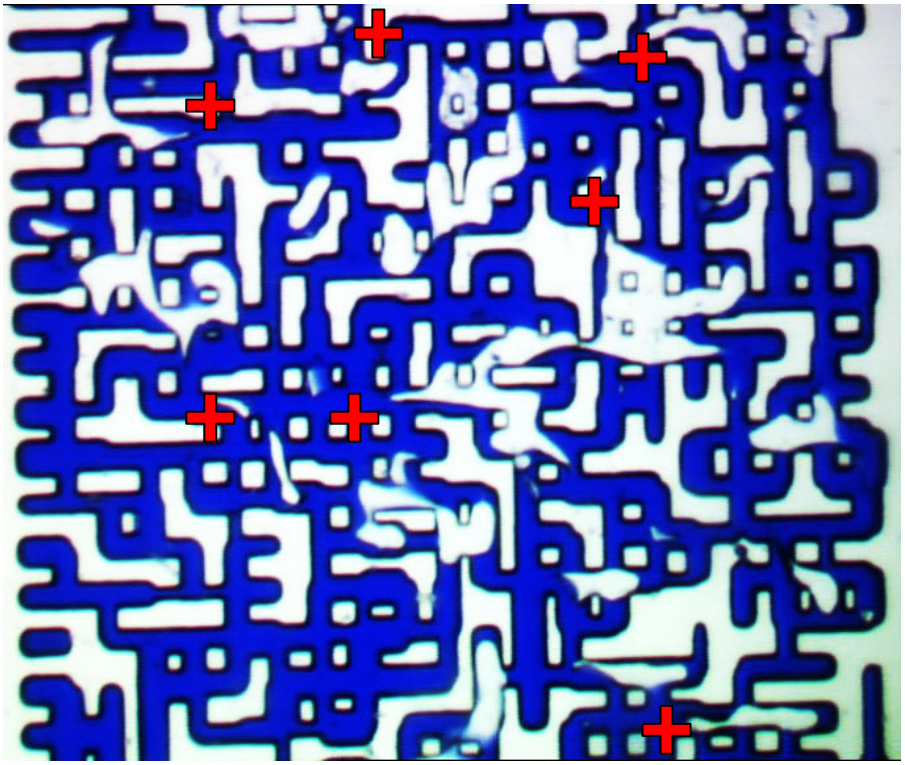

Figure B-5: Shrinkage and disconnection (+ sign) of oil ganglia as a result of stripping CO_2 away by plain water in the same selected frame (as in Figure B-1), after 24 hrs of WI, Experiment No.2 (Secondary CWI- Decane).

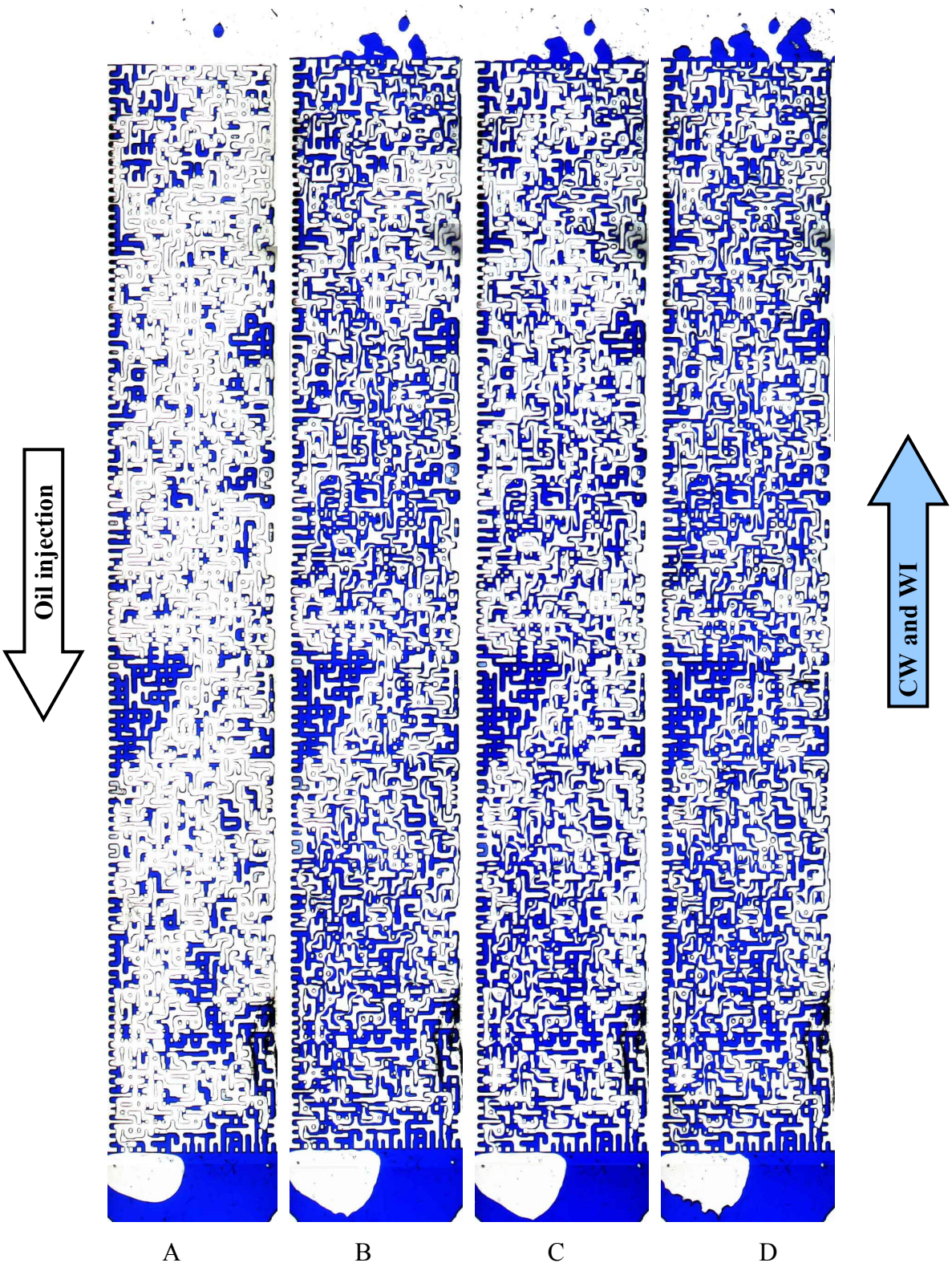

Figure B-6: Fluid distribution in Experiment No.3 (Tertiary CWI- Viscous oil) at different stages: A) Soi (initial oil saturation); B) residual oil saturation after the first water injection; C) First CWI (30 hrs); D) Second WI.

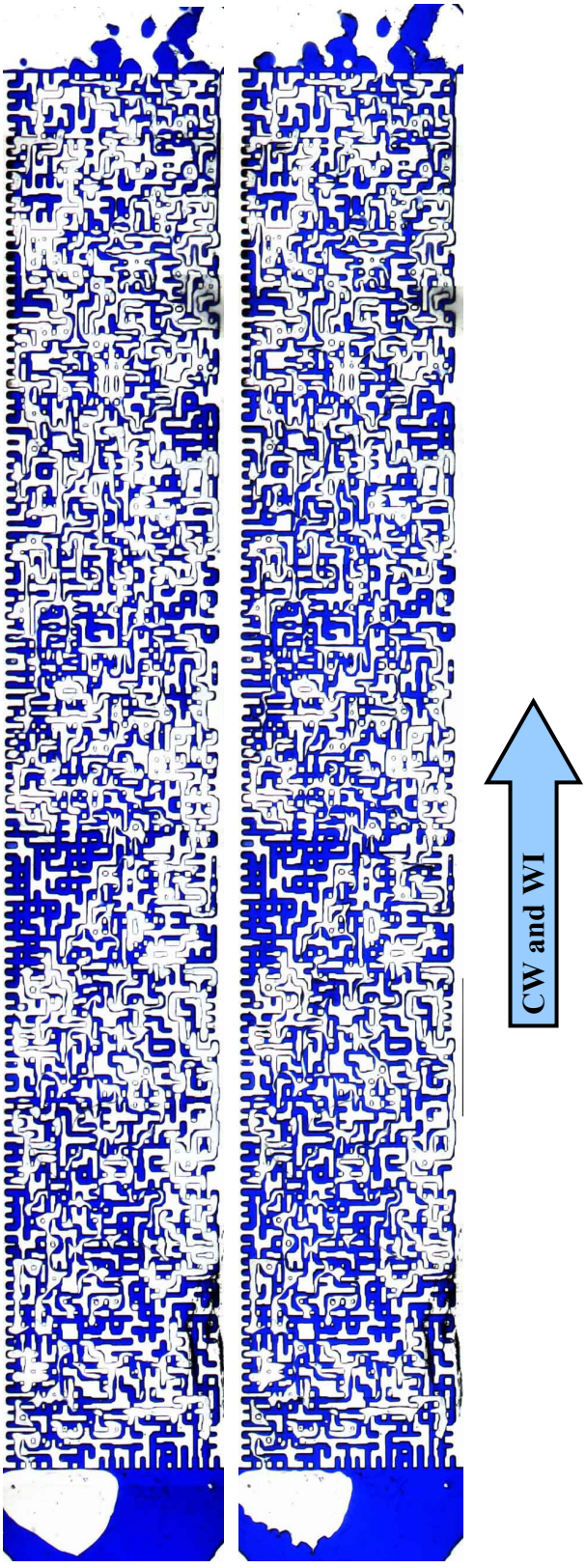

Figure B-6 (cont.): E) Second CWI (24 hrs); F) Third WI, Experiment No.3 (Tertiary CWI- Viscous oil).

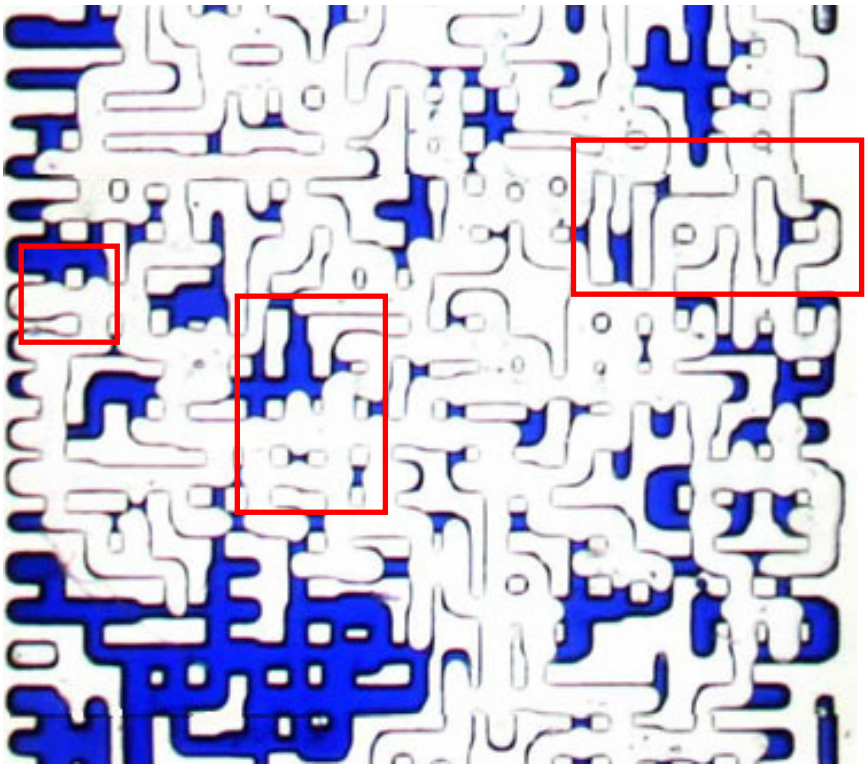

Figure B-7: Initial oil saturation in a selected frame of the micromodel, Experiment No.3 (Tertiary CWI- Viscous oil).

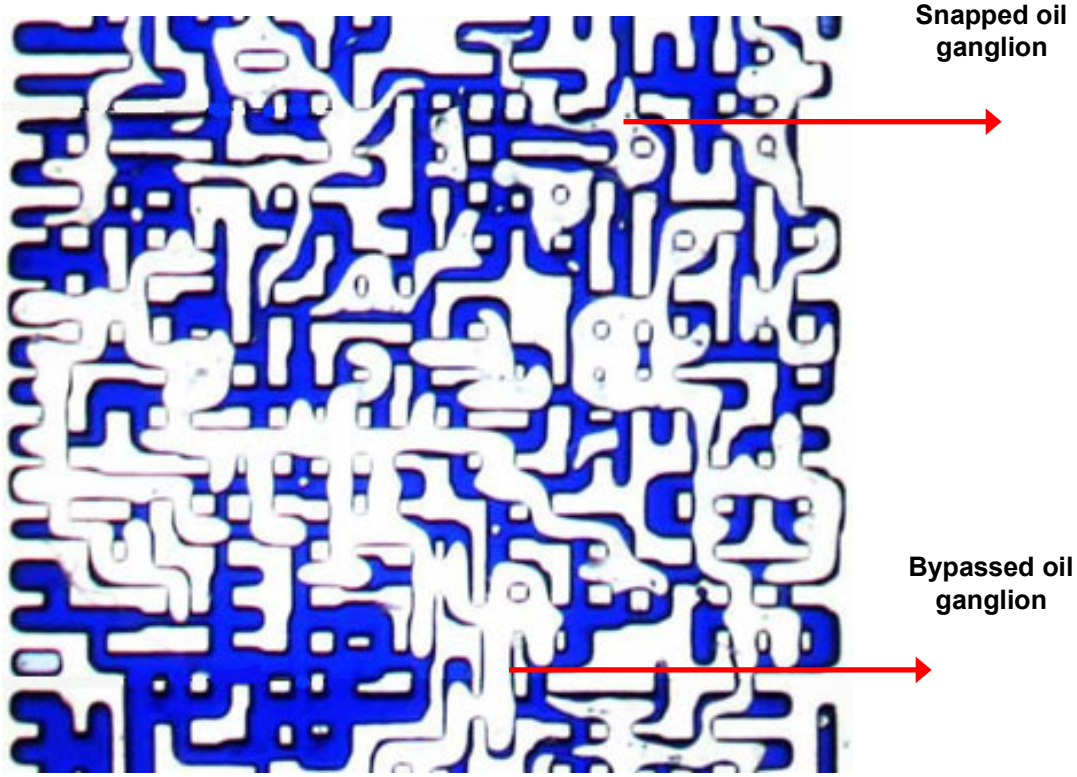

Figure B-8: Fluid distribution in the same selected frame (as in Figure B-7), after the first WI.

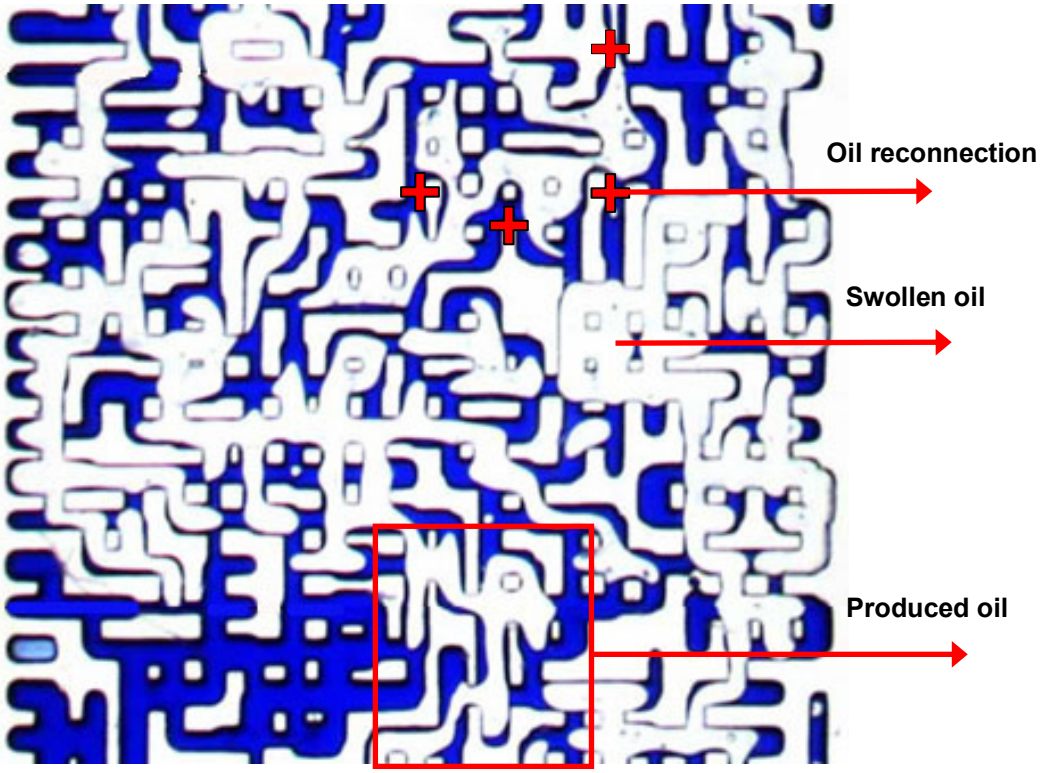

Figure B-9: Fluid distribution in the same selected frame (as in Figure B-7), after the first CWI.

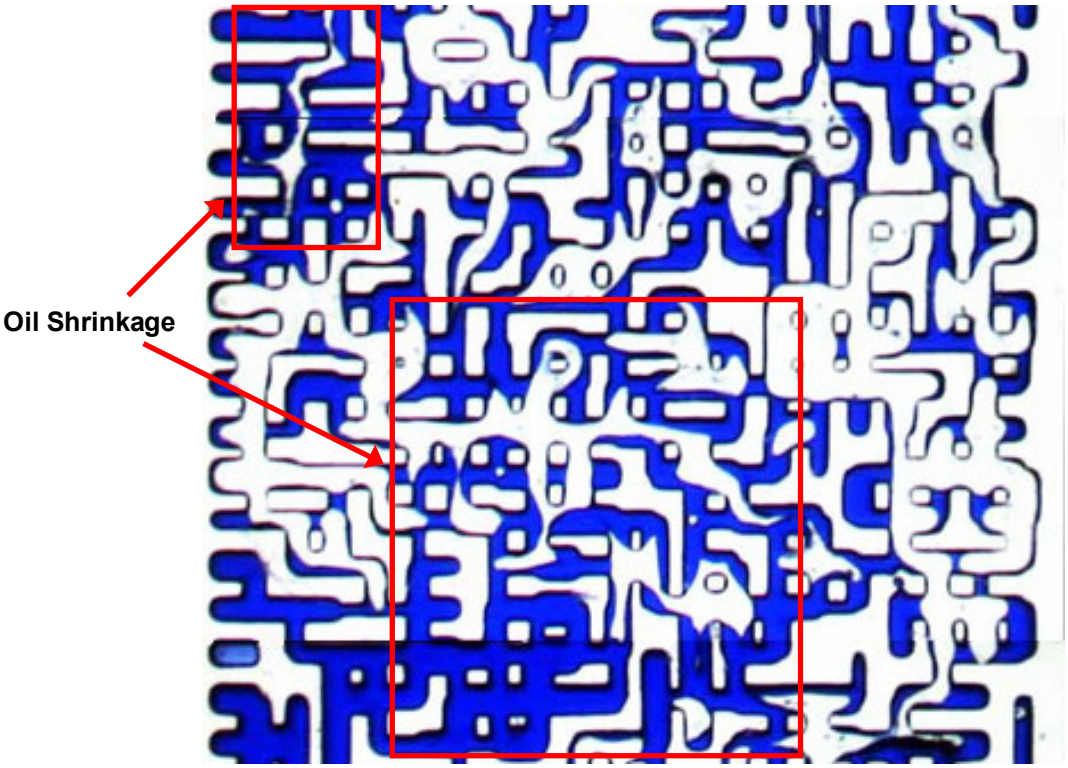

Figure B-10: Fluid distribution in the same selected frame (as in Figure B-7), after the second WI.

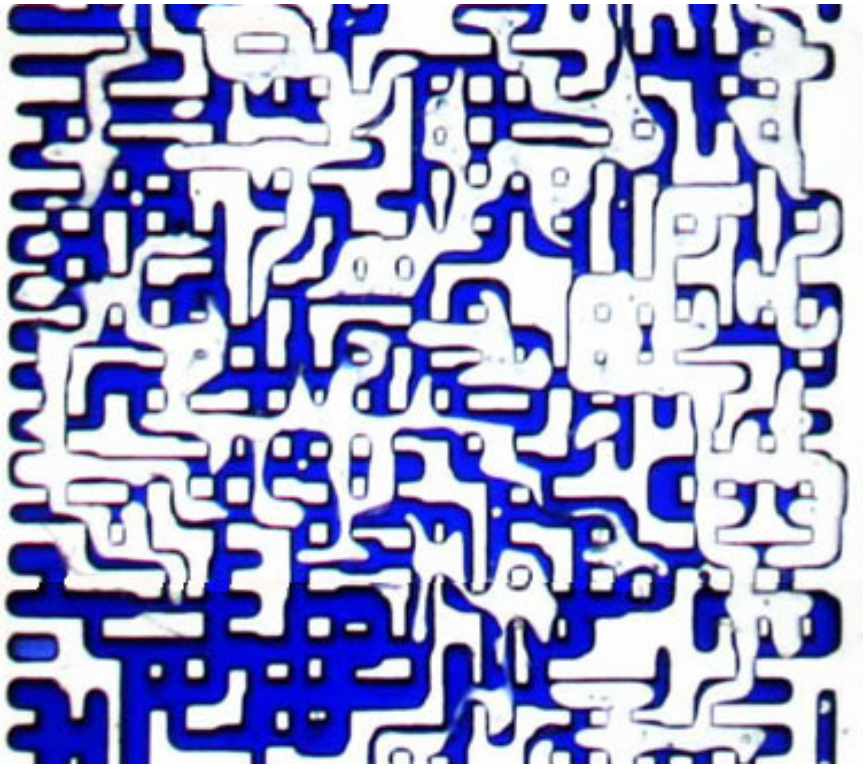

Figure B-11: Fluid distribution in the same selected frame (as in Figure B-7), after the second CWI.

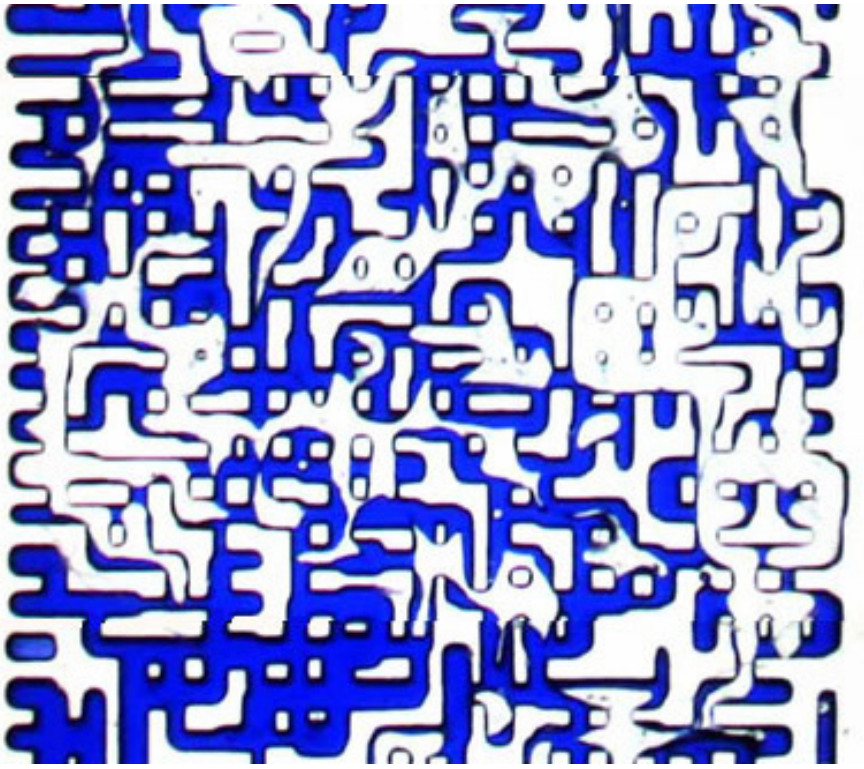

Figure B-12: Fluid distribution in the same selected frame (as in Figure B-7), after the third WI.

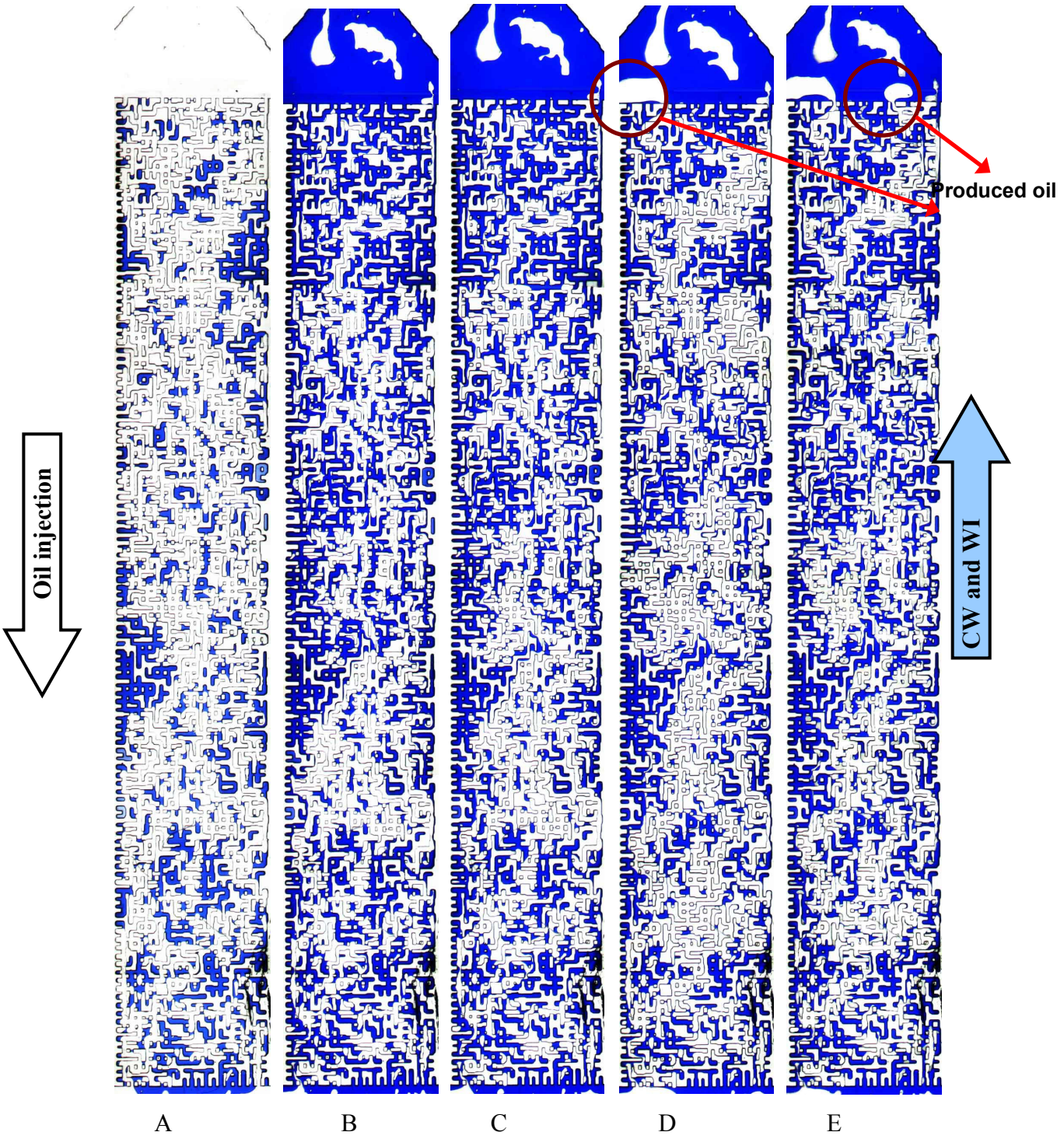

Figure B-13: Fluid distribution in Experiment No.5 (Tertiary CWI- Decane- Low CO_2 Concentration in CW): A) Decane with irreducible water saturation (S_{wi}); B) fluid saturation after the first water injection; C) and D) are subsequent fluid distribution after 5 and 100 hrs of CWI, respectively; E) fluid saturation after the second water injection.

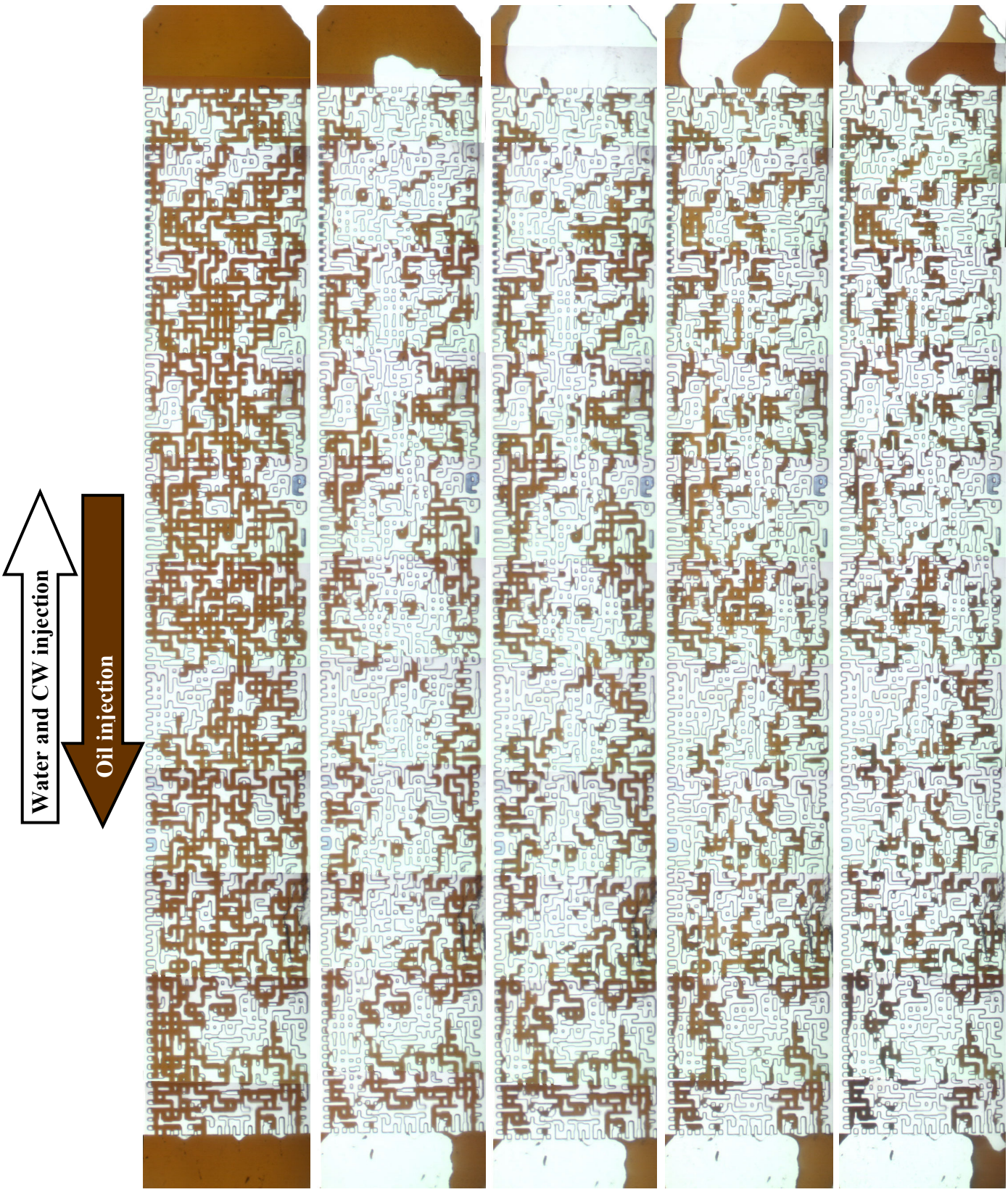

Figure B-14: The full length images of the micromodel during Experiment No.9 (Secondary CWI -Crude oil): A) is the initial oil saturation; B), C) and D) are the fluid distribution at BT and after 48 hrs and 67 hrs of CWI, respectively; E) is the residual oil saturation after 22 hrs of WI.

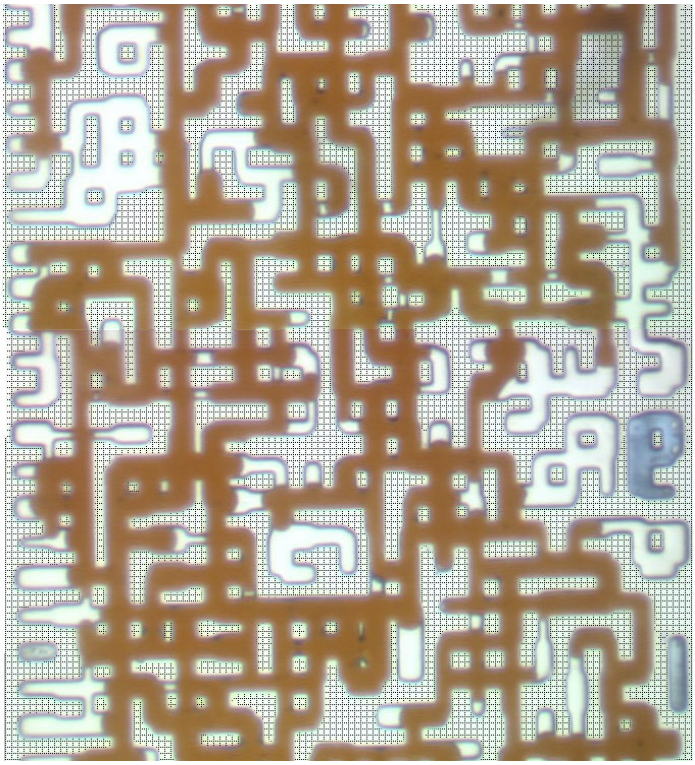

Figure B-15: Initial oil saturation at S_{wi} in a selected section of the micromodel after the first drainage stage, Experiment No.9 (Secondary CWI -Crude oil).

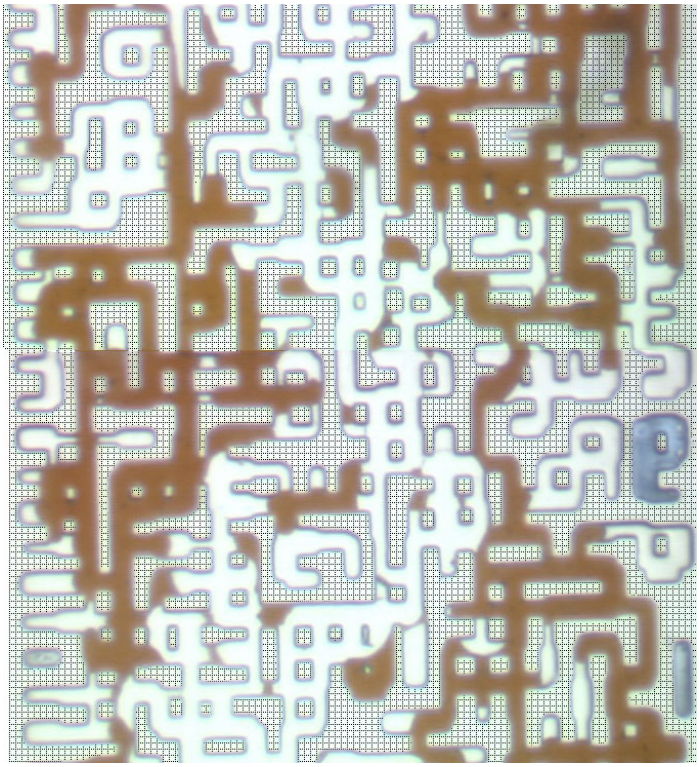

Figure B-16: Fluid distribution at the BT time of CWI, in the same section of the micromodel as that in Figure B-15, Experiment No.9 (Secondary CWI -Crude oil).

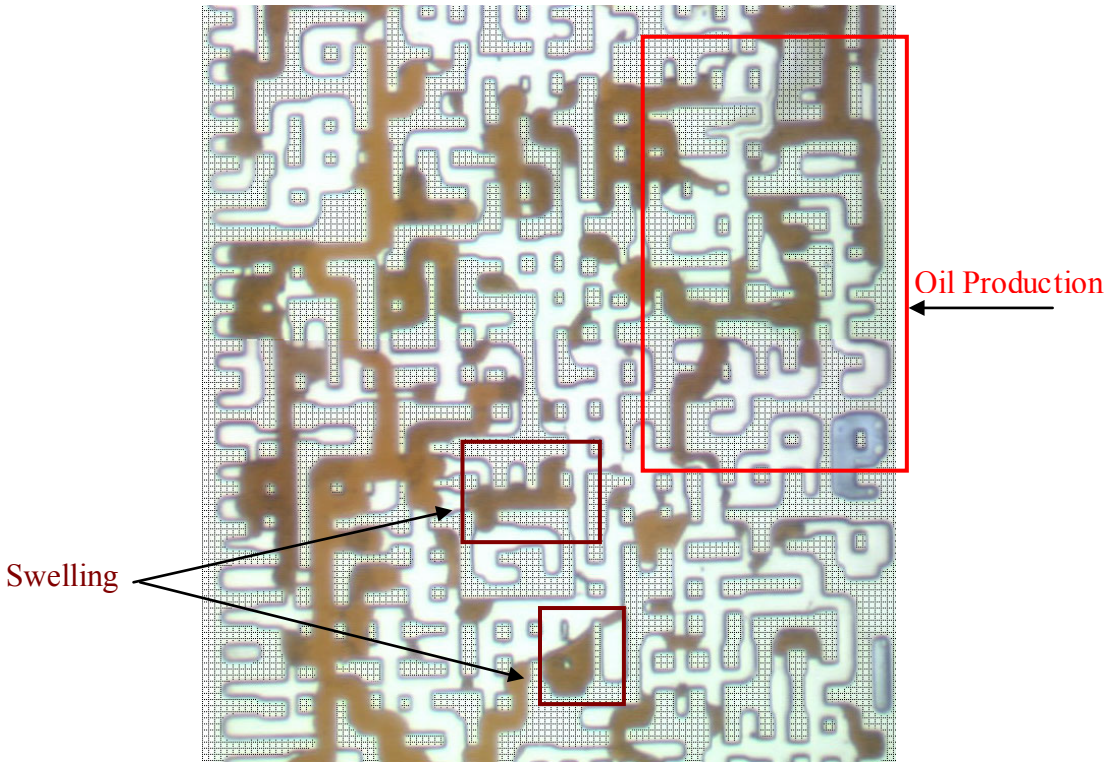

Figure B-17: Fluid distribution after 67 hrs of CWI, in the same section of the micromodel as that in Figure B-15, demonstrating swelling and displacement of oil, Experiment No.9 (Secondary CWI -Crude oil).

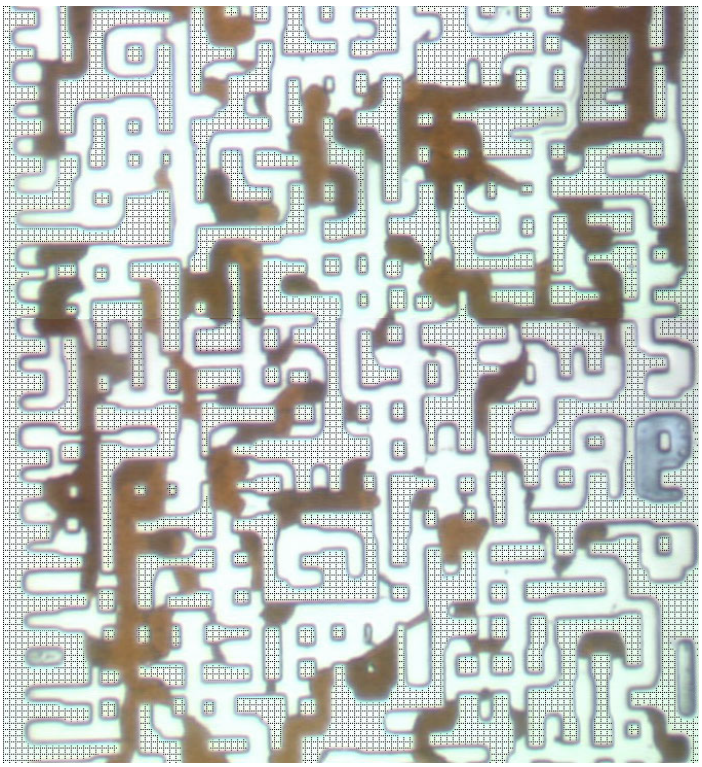

Figure B-18: Fluid distribution after 22 hrs of WI, in the same section of the micromodel as that in Figure B-15, demonstrating shrinkage and disconnection of oil ganglia as a result of stripping CO_2 away by plain water, Experiment No.9 (Secondary CWI -Crude oil).

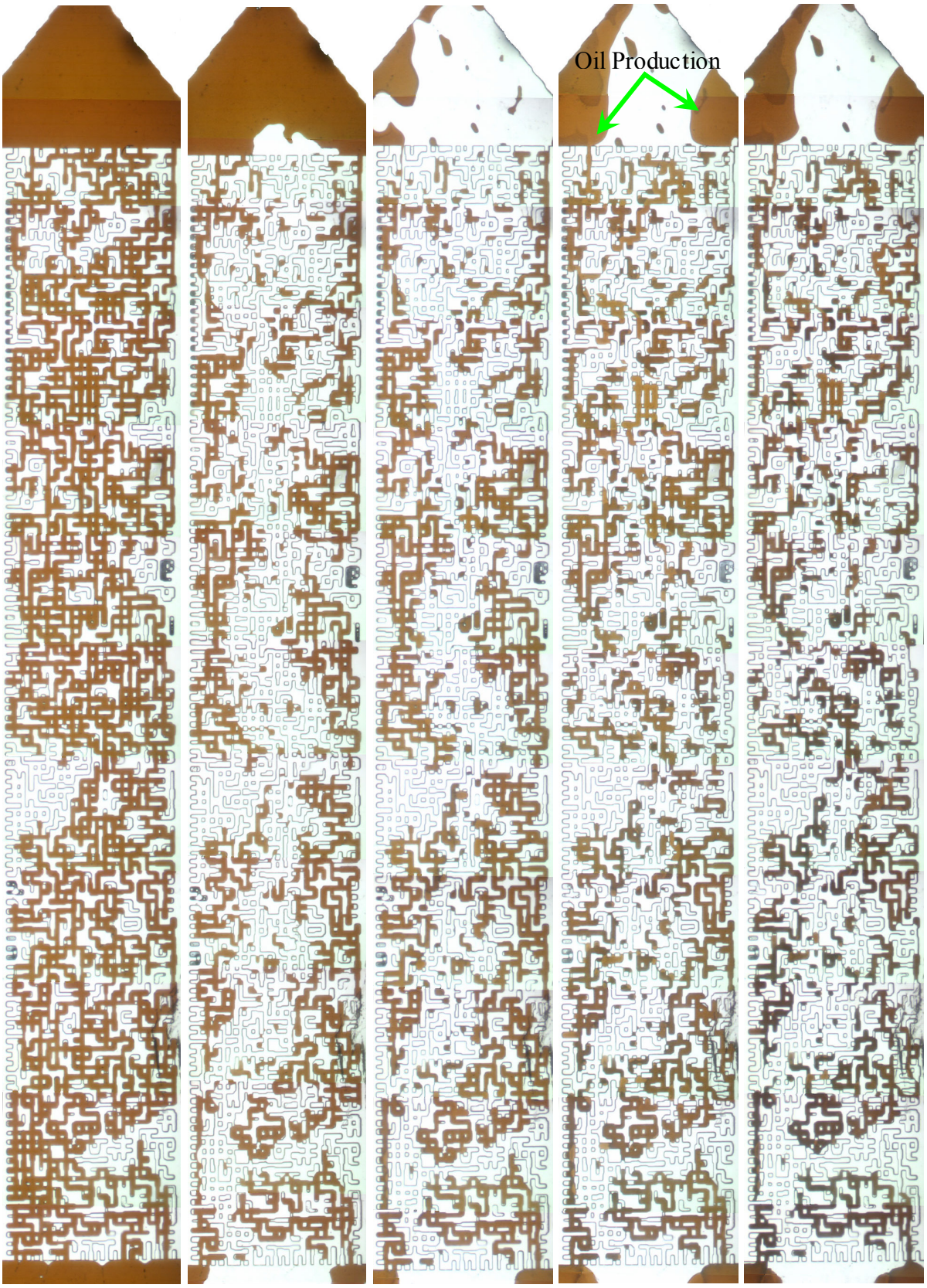

Figure B-19: The fluid distribution in the micromodel during Experiment No.10 (Tertiary CWI -Crude oil): A) Initial oil saturation condition; B) S_{or} after the first WI; C) and D) Fluid distribution after 20.5 hrs and 93 hrs of CWI, respectively; E) Residual oil saturation after the 2nd WI, 18 hrs.

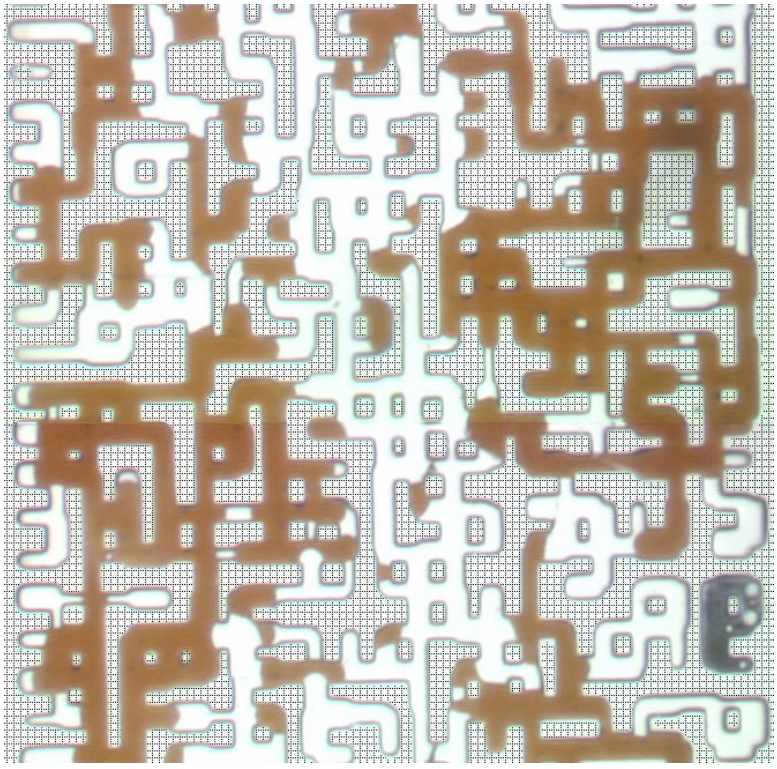

Figure B-20: Waterflood residual oil saturation condition after the 1st WI, Experiment No.10 (Tertiary CWI -Crude oil).

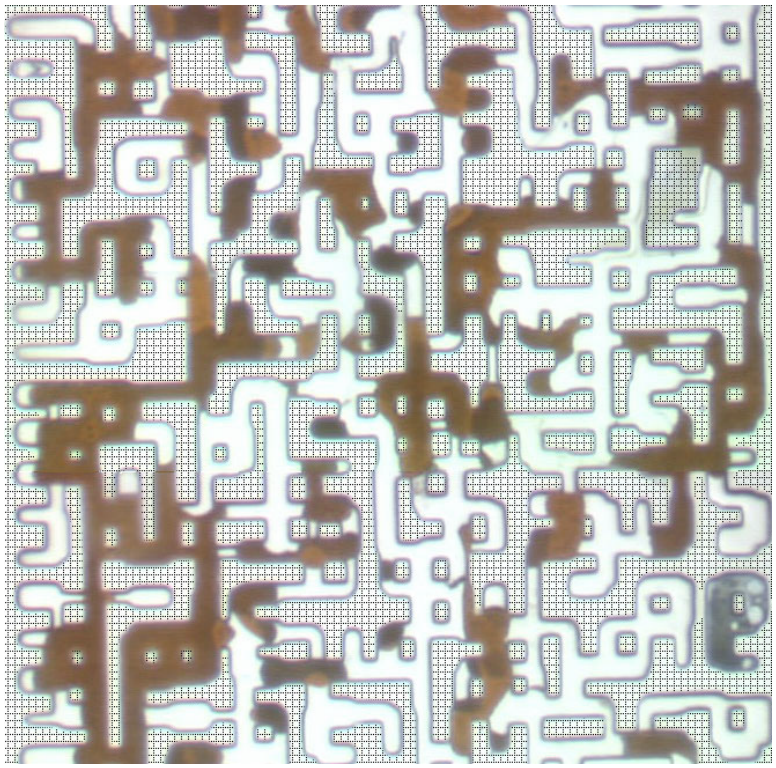

Figure B-21: Waterflood residual oil saturation condition after the 2nd WI, Experiment No.10 (Tertiary CWI -Crude oil).

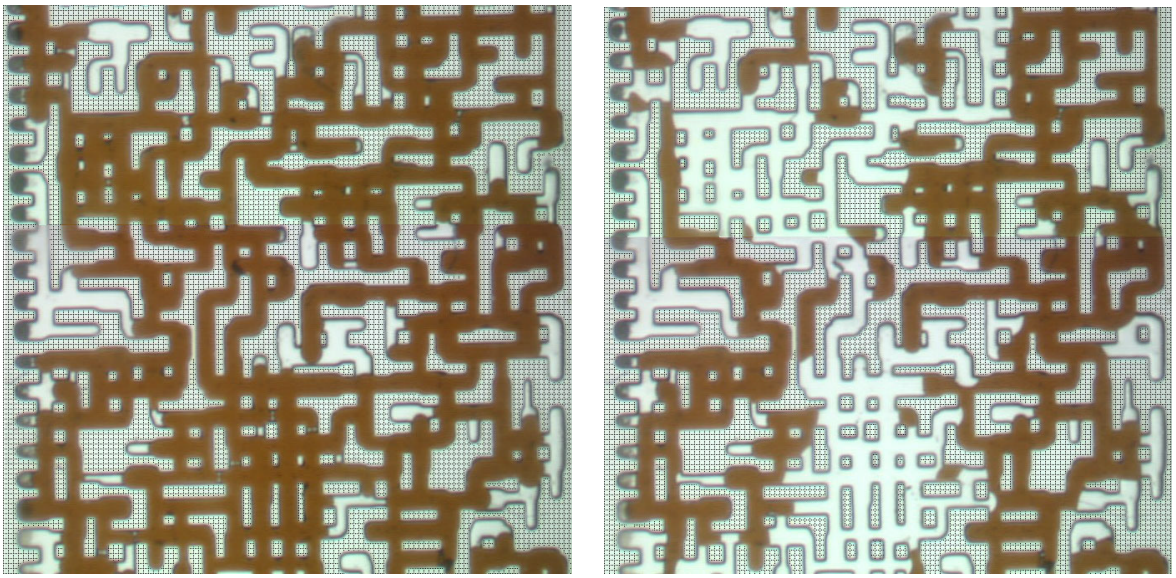

A B

Figure B-22: A) Initial oil saturation; B) Fluid distribution after the first WI, Experiment No.11 (Tertiary CWI -Crude oil- low oil saturation at BT).

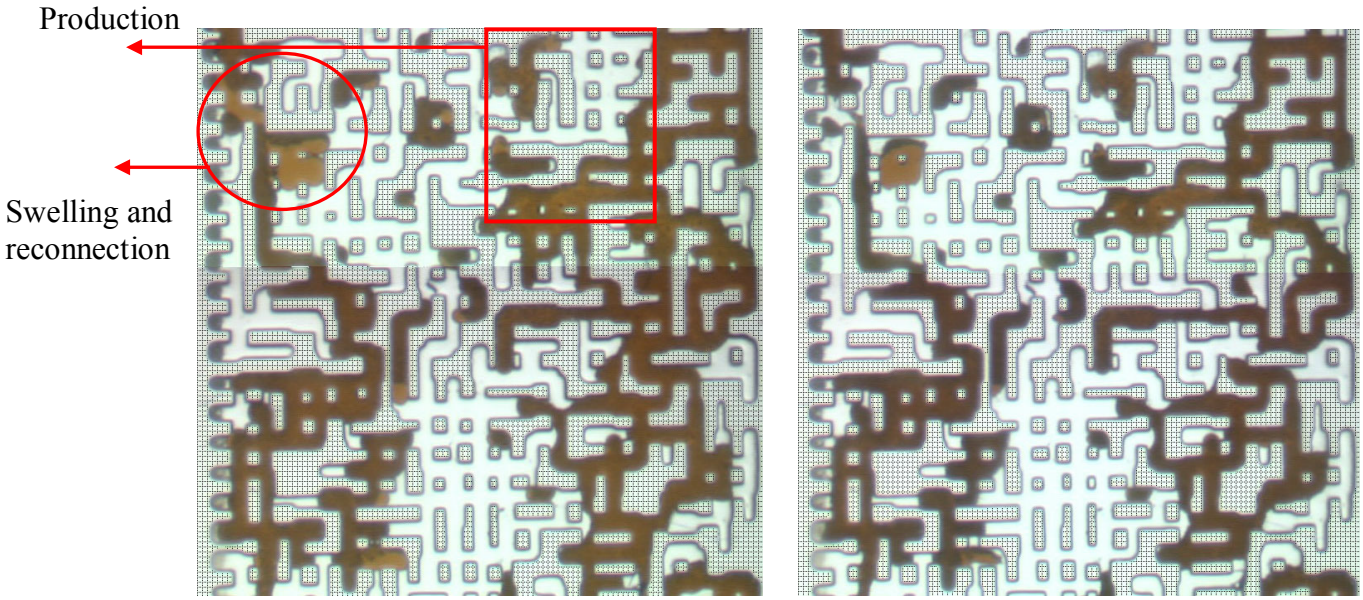

A B

Figure B-23: Fluid distribution: A) after 140 hrs CWI; B) after the second WI, Experiment No.11 (Tertiary CWI -Crude oil- low oil saturation at BT).

Appendix C: Visualisation Results of Micromodel Experiments-Blow Down

As discussed in Chapter 3, the purpose of depressurising the fluid system in Experiment No.6 was investigating the feasibility of blowdown mode, subsequent to the CWI stage, on additional oil recovery. However, another experiment (Experiment No.7), similar to Experiment No.6, was carried out with the main purpose of monitoring the gas nucleation and detecting the exact pressure of liberation of the gas from the liquids (oil and water) within the porous medium during the depressurisation period.

Experiment No.7- Depressurisation of CW-oil system with lower CO_2 content

In this experiment, the first gas nucleation was observed to take place at 431 Psia (and 38 °C). There are some interesting issues, such as location of gas nucleation and density of gas bubbles that can be investigated during depressurisation period. Since that is beyond the scope of this study, here, only some visual observations are illustrated:

Figure 1 shows a sequence of images depicting the formation of a gas bubble in the water phase and its subsequent movement from water into the oil phase. Figures 1C-D show the gas bubble breaking through the water-oil interface and becoming enclosed within the oil phase. The subsequent images show that, while in the oil phase, the gas bubble expands rapidly.

Figure 2 shows gas nucleation and growth in both oil and water at the same pressure range as Figure 1. This figure shows that major growth of the gas bubbles took place in the oil phase. Figure 2C has 5 numbered gas bubbles. Bubbles 4 and 5 were produced in oil and grew mainly due to CO_2 liberation from oil to gas bubble. Bubble 1 broke through the water-oil interface and came into contact with the oil phase. This bubble, like the one in Figure 1, grew fast in the oil phase.

Figure 2F shows that the size of bubbles 2 and 3 remained unchanged compared to that of bubble 1. This observation could have two explanations, 1) bubble 1 has initially a larger surface area for diffusion and 2) the initial thickness of the water layer separating CO_2-enriched oil and bubble 1 is less than that separating bubbles 2 and 3 from the CO_2 source.

In the pressure blowdown period, some of the mobilised gas bubbles moved and connected up to the stationary gas bubbles. Figure 3 shows this phenomenon which took place in the 431-429 psia pressure range. This figure shows how oil is displaced by time as a result of gas bubbles growing and displacing.

Experiment No.8- Depressurisation of CW with lower CO_2 content

The previous discussed experiment and Experiment No.6 show that gas liberation takes place at very low pressures (between 400 and 500 psi). This very low pressure range for gas nucleation was initially below what was expected, since the CO_2 content was only reduced by half the value of the fully saturated CW at 2000 Psia. This experiment was therefore designed to determine the bubble point of the CW. In this experiment, the system (micromodel and all the pipes and lines) was saturated with CW. During depressurisation a saturated liquid with gas reaches supersaturated state before any gas nucleation takes place, so the term critical supersaturation is defined as the difference of pressure at which the first bubble is formed and the saturation pressure ($\Delta P = P(equilibrium) - P(gas\ formation)$). Shahabi-Nejad et al. (2005) showed that ''*increasing the depletion rate, that is lowering the time at which a certain level of supersaturation is maintained, will increase the value of critical supersaturation*''. Thus, to trim down the effect of supersaturation the decline in pressure in this experiment was rather lower than those in Experiments No.6 and 7 (i.e. 10 psi/hr rather than 50 psi/hr).

Figure 4 shows a sequence of images of the whole micromodel after gas nucleation. In this figure the gas positions have been indicated by red arrows.

The first bubble in the micromodel was observed at 463 Psia (Figure 4A). Figures 4B and 4C show the consecutive formation of gas bubbles at 457 and 446 psia,

respectively. The appearance of bubbles over a period of time during depressurisation has been reported elsewhere by Yousfi, et al. (1997).
During the gas growing process, which consists of expansion as a result of pressure drop and CO_2 diffusion (CO_2 transfer from CW into the bubble), gas bubbles were observed to move toward the bigger pores because gas, as the non-wet phase, prefers to fill the big pores with less capillary pressure. The red circles in Figure 4A and 4B show such a displacement for one of the gas bubbles.

Based on the bubble point pressure estimated in this experiment (neglecting the super-saturation pressure), 463 psi, the CO_2 concentration in water was checked using the literature data. Table 1 shows experimental data collected and reported by Dodds (1956) for CO_2 solubility in water at 40°C for different pressure conditions. The plot presented by Baviere (1991) (see Appendix A) shows an almost linear dependency of pressure on CO_2 solubility at high and low pressure ranges but with different slopes. So assuming a linear dependency between CO_2 solubility and pressure, CO_2 solubility at two different pressure values of 463 psi (saturation pressure for CW with lower CO_2 content) and 2000 psi (equilibrium pressure for CW with fully saturated CO_2) was estimated by interpolating the experimental data. As the estimated value in Table 1 reveals, the CO_2 content of the CW used in Experiments No.4-8 is about half of that used in Experiments No.1-3. These estimated data are in quite good agreement with the experimentally measured data of 17.8 CO_2 m^3/water m^3 Vs. 33 CO_2 m^3/water m^3 (see Chapter 6 for more details).

The in-house measured experimental data for the CO_2 concentration of the CW with low CO_2 content, was estimated, as 3.072 lb/100 lb water (5.695/33*17.8=3.072), which based on data of Table 1 corresponds to the saturation pressure of 537 psi. The difference between this estimated pressure (537 psi for saturation pressure) and the observed bubble point pressure (463 psi) can be either due to the supersaturation pressure and/or the error of the estimations.

References:

Baviere, M., 1991: ‘‘Basic Concepts in Enhanced Oil Recovery Processes’’, Published for SCI by Elsevier Applied Science, in London and New York.

Dodds, W. S., Stutzman, L. F. and Sollami, B. J., 1956: ''Carbon Dioxide Solubility in Water'', Industrial and Engineering Chemistry vol. 1, no. 1.

Shahabi-Nejad K., Danesh A., Cordelier P., and Hamon G., 2005: ''Pore-Level Investigation of Heavy-Oil Depressurisation'', SPE/PS-CIM/CHOA 97894 PS -402.

Yousfi, A. El., Zarcone, C. Bories, S., 1997: ''Physical Mechanisms for Bubble Growth during Solution Gas Drive.'', SPE annual technical conference and exhibition in San Antonia, Texas, SPE paper 38921.

Pressure (psi)	Pressure (bar)	CO_2 solubility (Lb/100 Lb water)	Method
	25.0	2.281	Experimental data
	50.0	3.995	Experimental data
463	31.5	2.726	Estimated linear interpolation
537	36.5	3.072	Estimated linear interpolation
	125.0	5.636	Experimental data
	150.0	5.769	Experimental data
2000	136.1	5.695	Estimated linear interpolation

Table C-1: CO_2 solubility in water at 40 °C and different pressures: experimental data reported by Dodds, (1956).

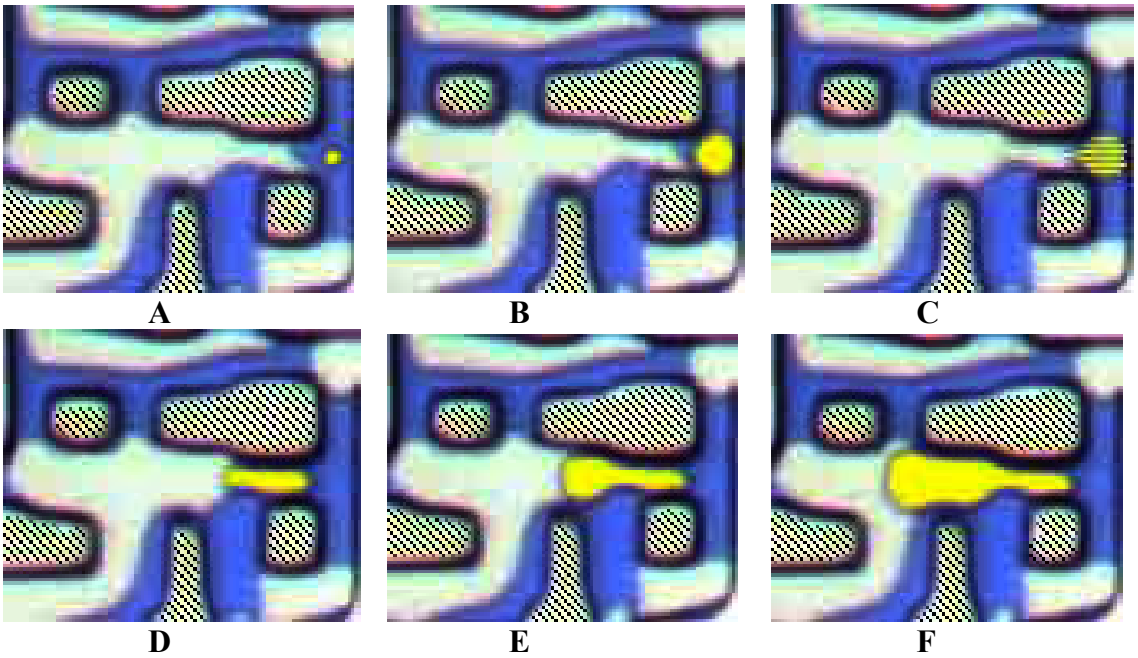

Figure C-1: Gas nucleation in water, growth and migration into oil (took place between 431-429 psia pressure range).

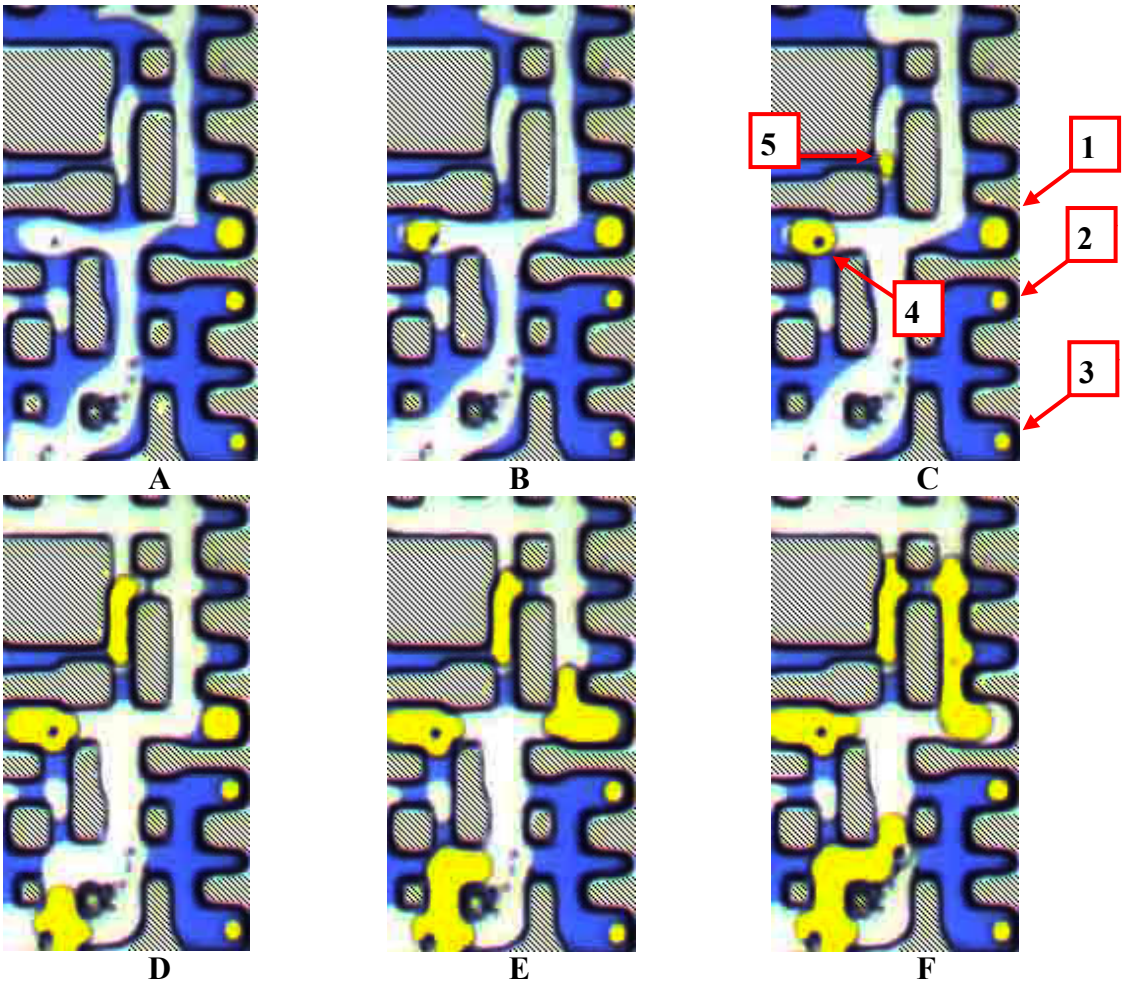

Figure C-2: Gas nucleation in both water and oil. (nucleation took place between 431-429 psia pressure range).

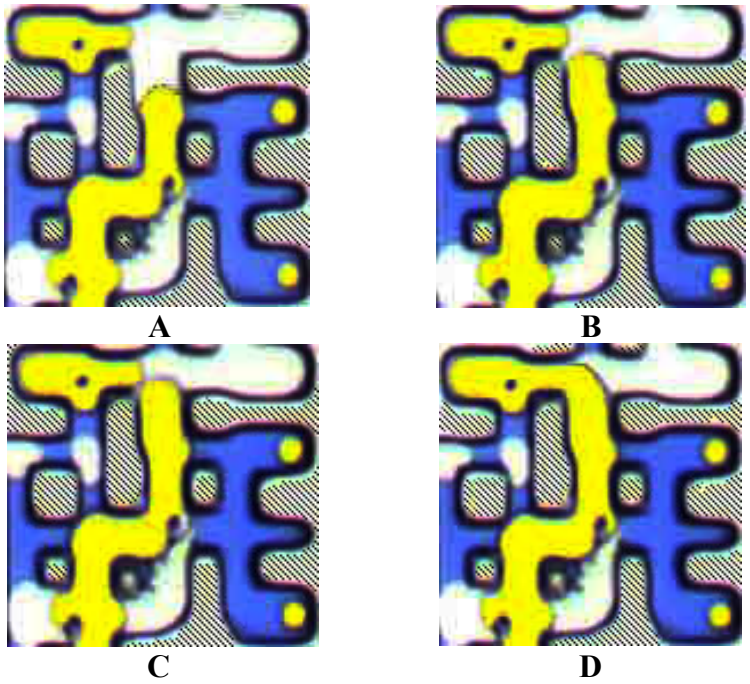

Figure C-3: A growing and moving gas bubble connecting to a stationary and slowly growing gas bubble.

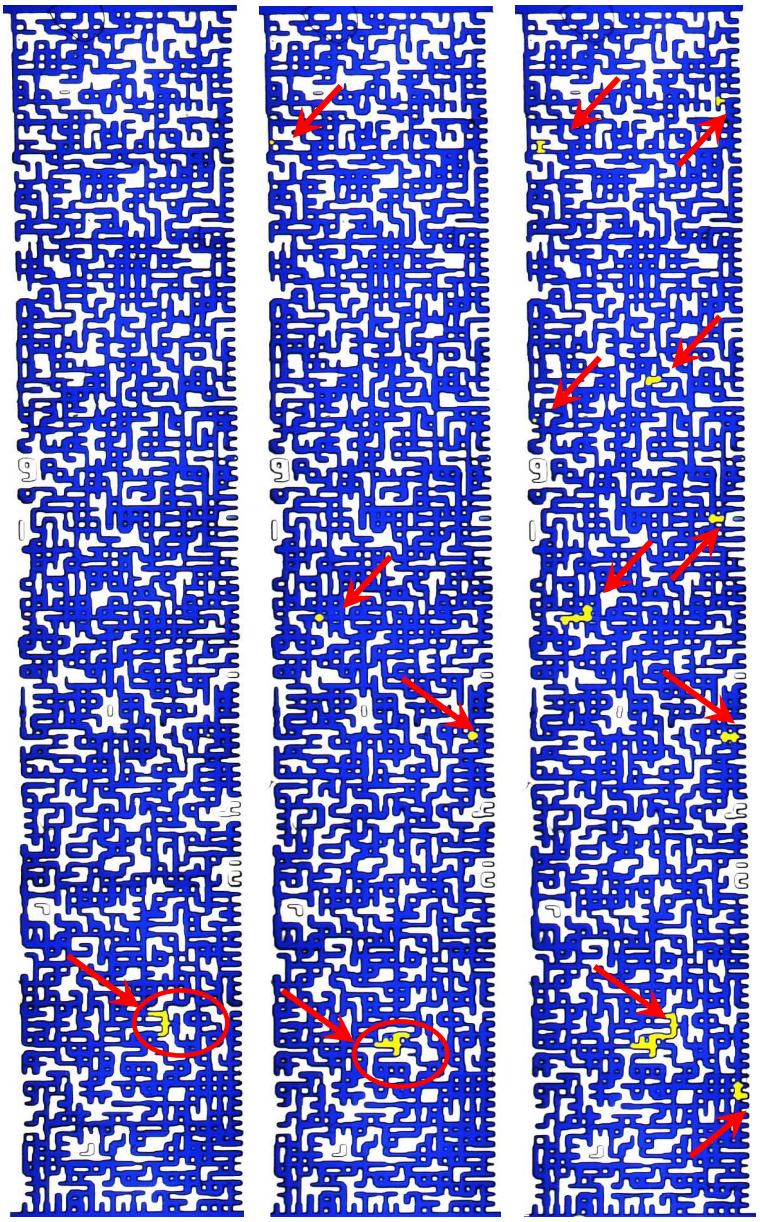

Figure C-4: Fluid distribution in Experiment No.8 at different pressures: A) 463 Psia; B) 457 Psia; C) 446 Psia.

Appendix D: Effect of Using Co-solvent on the Performance of CWI Process

In this study, two preliminary experiments were performed to investigate the impact of the co-solvent on the CWI process. Jodecke et al. (2007), in a very recent paper showed that the presence of acetone in water could increase CO_2 solubility significantly. Therefore, in this study the use of acetone for increasing CO_2 solubility in water was examined. The fluid system used in the experiments consisted of distilled water, a viscous mineral oil, carbon dioxide and acetone. Mixtures of CO_2/acetone (Experiment No.22) or water/acetone (Experiment No.23) were prepared under the same conditions (i.e. at 2000 psi and 38 °C) and following the same procedure as that for preparing CW described in Chapter 2. In both of the aforementioned experiments, the micromodel orientation (horizontal) and directions of injection were similar to those reported in Chapter 3 and 4.

Experiment No.22-WI followed by gas mixture injection (GMI)

The aim of this test was to investigate the effect of the co-solvent on swelling of oil ganglia shielded by water. A gas mixture (GM) of 90 wt% CO_2 and 10 wt% acetone was prepared. The initial procedure of this test was exactly the same as that of Experiment No.14. Figure 1A and 1B show the initial saturation and residual oil saturation after waterflooding, respectively. Figure 1C reveals the fluid distribution after injection of the CO_2+acetone gas mixture.

Figure 1D shows fluid distribution after 4 hours of GMI in this test. Comparison of this image with that at the beginning of the test, Figure 1C, reveals more oil production as test progressed. This figure also reveals the swelling of those water shielded oil ganglia.

Figure 2 shows the magnified images of a section of the micromodel highlighted by the red rectangle in Figure 1C. The position and the size of oil drops before GMI are

shown in Figure 2A. The swelling of these two oil ganglia after about 4 hours of GMI is shown in Figure 2B. The last image, Figure 2C, shows the coalescence of these two separated oil ganglia after 14 hrs of GMI. The area of these two oil ganglia was estimated based on the number of oil pixels at different times. Table 1 and Figure 3 show these values versus time. Based on these data, the swelling of the oil is estimated to be 44% of the dead oil volume, whereas the maximum swelling estimated during the CO_2I test for this oil was only 19.4%. Figure 4 compares the swelling curves of these two experiments. This significantly improved swelling is due to the presence of co-solvents (acetone).

To establish whether this swelling was as a result of diffusion of acetone from the gas mixture through the water layer into oil or as a result of improved CO_2 concentration in the oil phase, Experiment No.23 was designed and performed.

Experiment No.23: WI followed by liquid mixture injection (LMI)

The purpose of this test was to investigate the impact of the presence of the co-solvent in water rather than in the gas, which was the case in the previous experiment. A liquid mixture (LM) of 70 wt% blue water and 30 wt% acetone was prepared. After establishing initial oil saturation and WI, LMI was performed. Figures 5A-B illustrate the fluid distribution at different stages after LMI. Comparison of these images revealed that there was no significant swelling or extraction. It should be mentioned that prior to performing this test, a series of experiments with test tubes had been also carried out at ambient pressure and temperature conditions. The results of this set of tests confirmed the micromodel's results, i.e., there was no considerable mass transfer.

Although a significant amount of water/acetone mixture was injected, there was only a little change in the results. The result of this test confirmed that the significantly improved swelling observed in Experiment No.22 is due to the improved CO_2 concentration in the oil phase.

It should be noted that the amount of CO_2 in the oil phase could be increased as a result of improving the CO_2 concentration in the water layer and/or improving the partition coefficient. Based on the literature data (Jodecke et al., 2007), adding

acetone to water increases the CO_2 solubility in water. These results also suggest a possible change in partition coefficient. To quantify the amount of change in partition coefficient further tests are needed to be performed. Hence, in Chapter 8, a full investigation of the application of using co-solvents was recommended as another element of the future work.

References:

Jodecke M., Kamps A. P-S, and Maurer G., 2007: ''Experimental Investigation of the Solubility of CO_2 in (Acetone + Water)'', Journal of Chemical and Engineering Data, Vol. 52, No. 3, P 1003-1009.

Time (hrs)	pixel number of the both oil spots
0.0	6521
0.5	6685
1.3	7054
4.1	8063
9.2	8758
14.2	9228
19.2	9389
29.2	9390

Table D-1: Volume of the oil droplets in Figure 2 at different times.

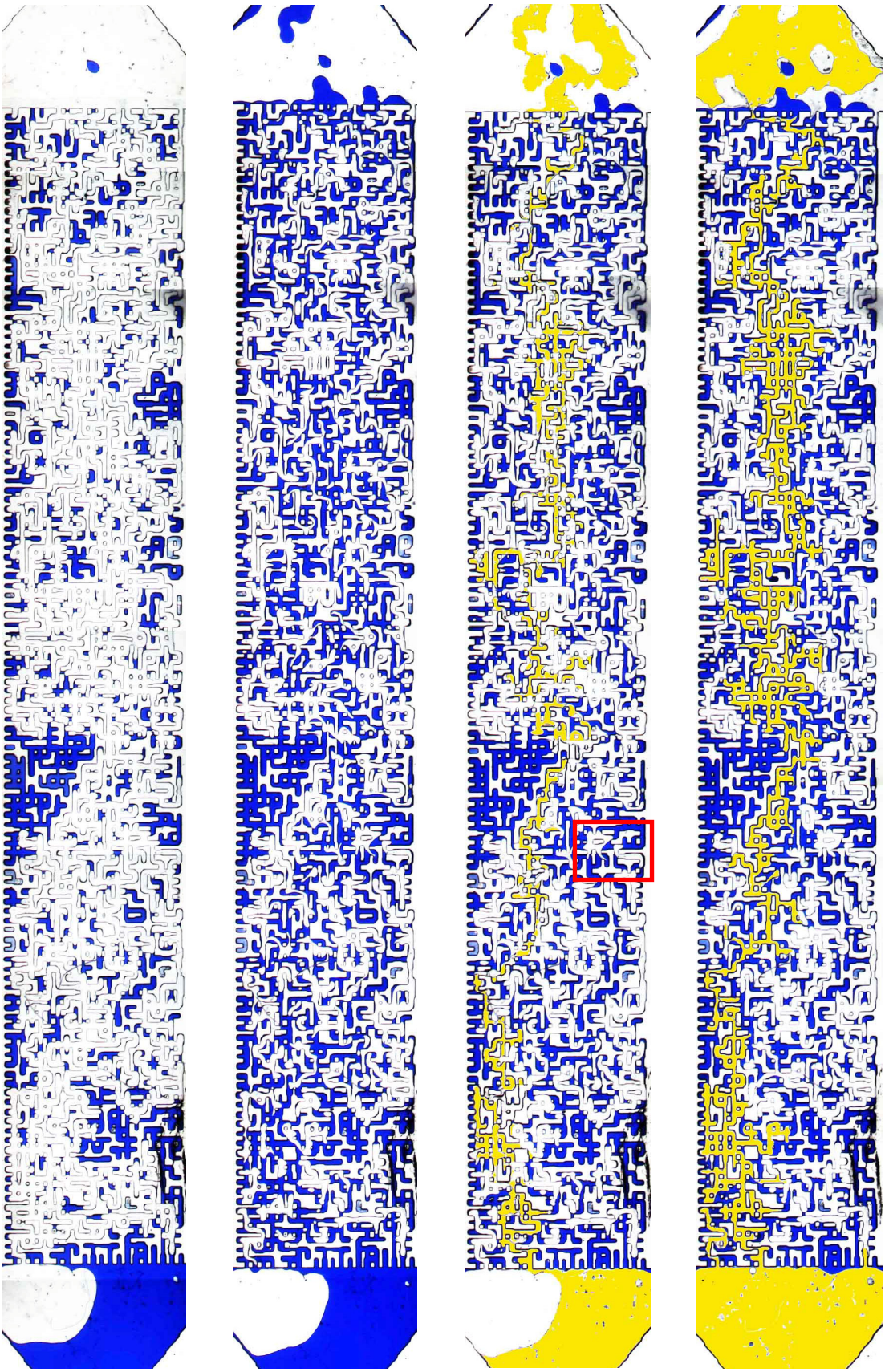

Figure D-1: Fluid distribution in Experiment No.22: A) initial oil saturation with S_{wi}; B) residual oil saturation condition after water flooding; C) and D) are subsequent fluid saturation after GMI at 0.45, and 4.1 hrs respectively.

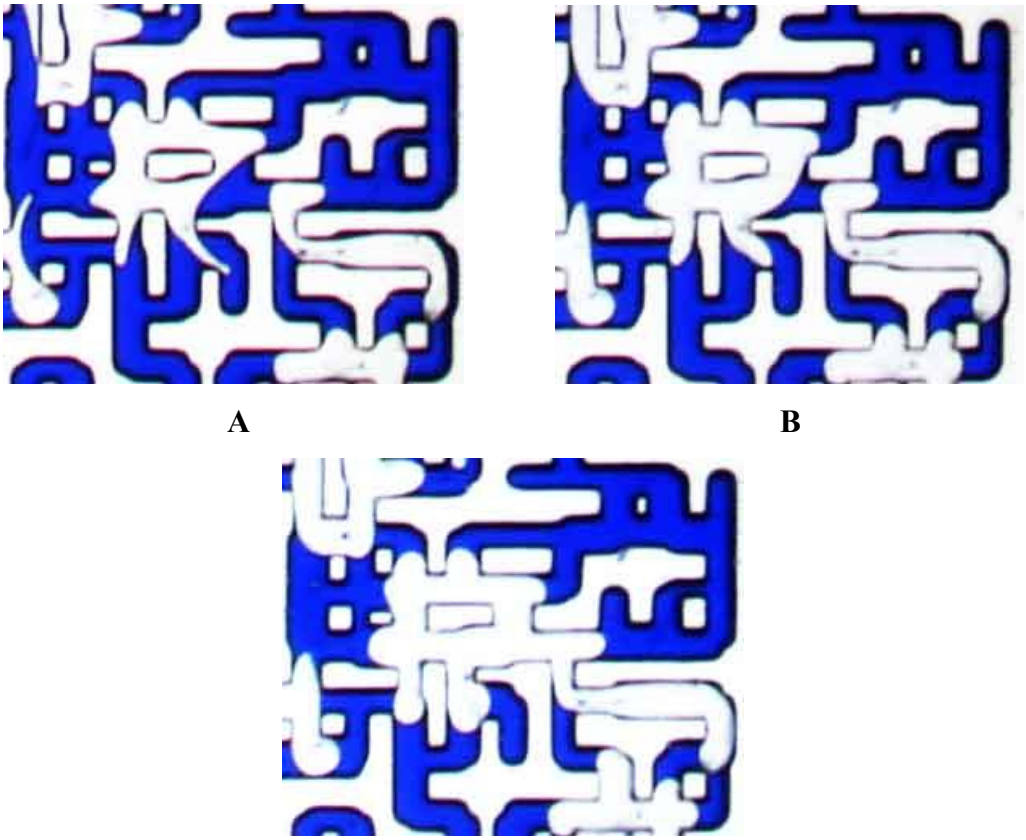

Figure D-2: A subsequent of oil swelling in a magnified section of micromodel A) before GMI; B) swelling of oil ganglia 4 hrs after GMI; C) reconnection of oil ganglia 14 hrs after GMI.

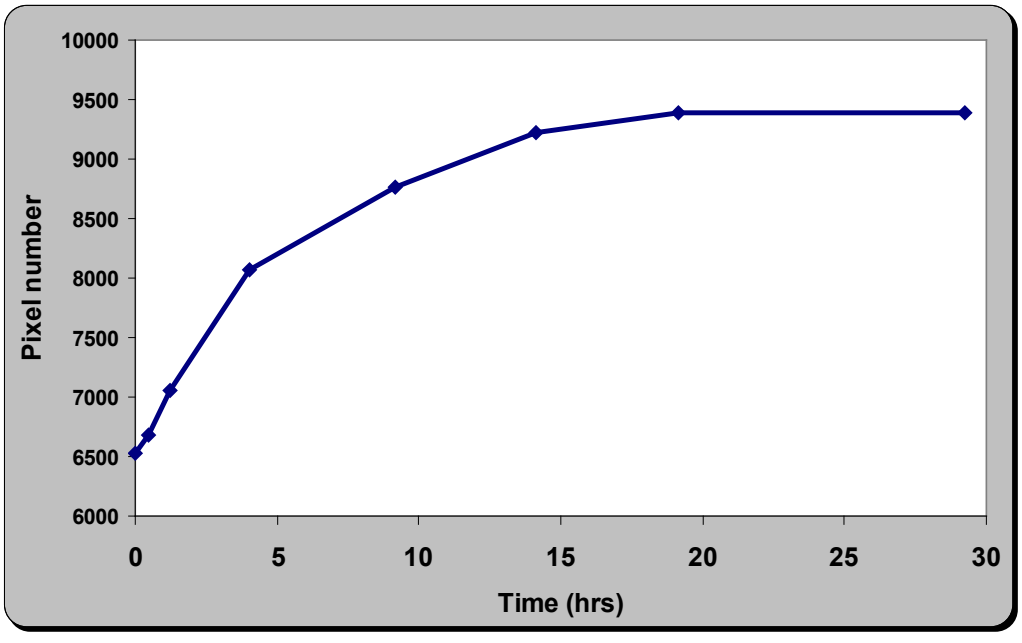

Figure D-3: Volume of the oil droplets in Figure 2 versus time

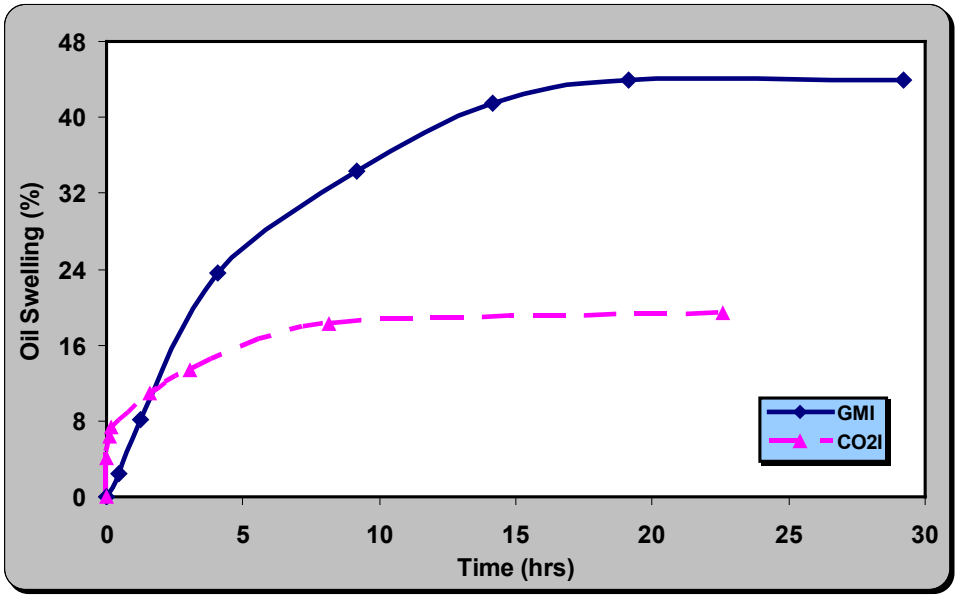

Figure D-4: Swelling of the viscous mineral oil during CO_2 injection (pink curve) and during GMI (blue curve).

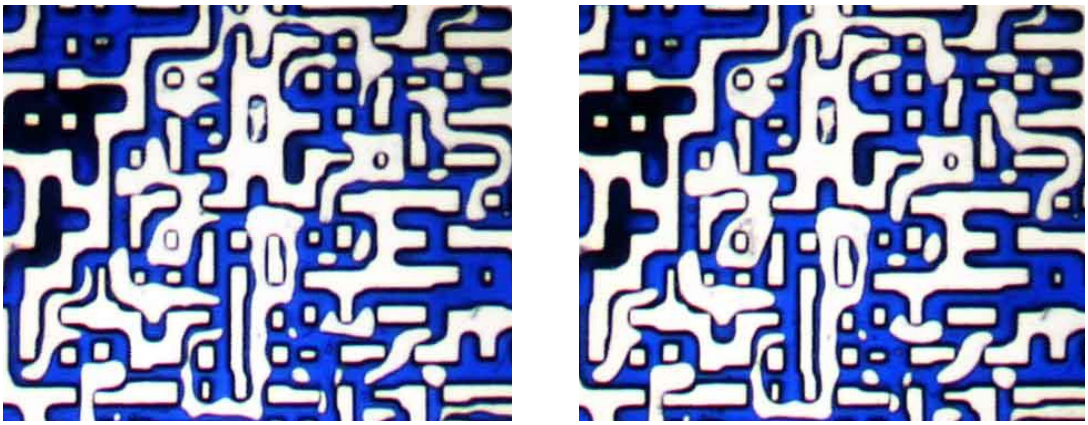

A **B**

Figure D-5: A section of the micromodel during LMI in Experiment No.23: A) and B) residual oil shape and distribution after 1 and 18 hours of LMI, respectively.

Appendix E: Publication of this Research Work

The research material in this thesis was part of the research program of the first phase of a three year joint industrial project (JIP) referred to as carbonated water injection (CWI) studies. The results of this publication have been reported, presented and discussed every six months in the corresponding steering committee meetings during Dec 2006-2009, the duration of the first phase of CWI JIP. Hence, in total, six progress reports and a final report were prepared for its five industrial sponsors.

Furthermore, parts of the results of this study have been presented (and submitted) as technical papers in different international conferences (and peer reviewed journals).

A list of these publications is as follows:

2011

1. **Riazi, M.**, Sohrabi, M., Jamiolahmady, M.: "Experimental Study of Pore-Scale Mechanisms of Carbonated Water Injection (CWI)", In Press, Journal of Transport in Porous Media, (2011) 86:73-86, DOI 10.1007/s11242-010-9606-8.

2. **Riazi**, **M.,** Jamiolahmady, M., Sohrabi, M.: "Theoretical investigation of pore-scale mechanisms of carbonated water injection", In press, Journal of Petroleum Science and Engineering, Volume 75, Issues 3-4, January 2011, Pages 312-326.

2010

1. **Riazi, M.**, Sohrabi, M., Jamiolahmady, M., Irland, S. and Brown, C.: "Oil Recovery Improvement Using CO_2-Enriched Water Injection", Submitted to SPEJ for publication.

2. **Riazi, M.,** Sohrabi, M., Bernstone, C., Jamiolahmady, M., Ireland S.: "Visualisation of Mechanisms Involved in CO_2 Injection and Storage under Various Reservoir Conditions", Accepted for publication in Journal of IChemE.

3. Sohrabi, M., **Riazi M.**, Jamiolahmady M., Ireland, S and Robertson, G.: "Safe Storage of CO_2 Together With Improved Oil Recovery by CO_2-Enriched Water Injection", submitted to IChemE (Institution of Chemical Engineers) Journal for publication in a special issue on Carbon Capture and Storage, May 2010.

4. Sohrabi, M., Kechut, N., **Riazi**, **M.**, Jamiolahmady, M., Ireland, S., Brown C., and Robertson, G.: "Coreflooding Studies to Investigate the Potential of Carbonated Water Injection as an Injection Strategy for Improved Oil Recovery and CO_2 Storage", Submitted for publication to Journal of Transport in Porous Media.

5. Sohrabi, M., Kechut, N., **Riazi**, **M.**, Jamiolahmady, M., Ireland, S., and Robertson, G. : "Carbonated Water Injection (CWI) for Improved Oil Recovery and CO_2 Storage", DEVEX 2010, 7th European Production & Development Conference & Exhibition, 12-13 May 2010, Aberdeen, UK. ***Presented by Dr Sohrabi.***

6. Mehran Sohrabi, **Masoud Riazi**, Mahmoud Jamiolahmady, Nor Idah Kechut, Shaun Ireland, Graeme Robertson and Chris Brown: "Carbonated Water Injection (CWI) – A Productive Way of Using CO_2 for Oil Recovery and CO_2 Storage", International Conference on Greenhouse Gas Technologies (GHGT), 19-23 September 2010, RAI Amsterdam, The Netherlands. ***Presented by Dr Sohrabi.***

7. Nor Idah Kechut, **Masoud Riazi**, Mehran Sohrabi, Mahmoud Jamiolahmady: "Tertiary Oil Recovery and CO_2 Sequestration by Carbonated Water Injection (CWI)", SPE paper 139667, SPE International Conference on CO_2 Capture, Storage and Utilization held in New Orleans, Louisiana, USA, 10-12 November 2010. ***Presented by Ms Nor Idah Kechut.***

2009

1. **Riazi, M.**, Sohrabi, M., Jamiolahmady, M., Irland, S. and Brown, C.: "Direct Observation of CO_2 Transport and Oil Displacement Mechanisms in CO_2/Water/Oil Systems", 15th European Symposium on Improved Oil Recovery, 27-29 April 2009 Paris, France. ***Presented by the author***.

2. Sohrabi, M., **Riazi, M.**, Jamiolahmady, M., Irland, S. and Brown, C.: "Enhanced Oil Recovery and CO_2 Storage through Carbonated Water Injection", DEVEX 2009, The Production & Development Conference & Exhibition, Aberdeen, UK, 12-13 May 2009. ***Presented by Dr Sohrabi***.

3. **Riazi, M.**, Sohrabi, M., Jamiolahmady, M., Irland, S. and Brown, C.: "Oil Recovery Improvement Using CO_2-Enriched Water Injection", SPE 121170, Proceedings of the 2009 SPE EUROPEC/EAGE Annual Conference and Exhibition, Amsterdam, The Netherlands, 8-11 June 2009. ***Presented by the author***.

4. **Riazi, M.**, Sohrabi, M., Jamiolahmady, M., Irland, S. and Brown, C and Kechut, N.: Poster "Enhanced Oil Recovery Using Carbonated Water Injection", SPE Forum: CO_2 Capture and Storage: "Can the Oil and Gas Industry Support its Development and Deployment?", 13-18 September 2009, Cadiz, Spain, ***Presented by Dr Sohrabi***.

5. Sohrabi, M., **Riazi, M.**, Jamiolahmady, M., Irland, S. and Brown, C: "Mechanisms of Oil Recovery by Carbonated Water Injection", International Symposium of the Society of Core Analysts, held in Noordwijkaan Zee, The Netherlands 27-30 September, 2009. ***Presented by Dr Sohrabi***.

6. Sohrabi, M., **Riazi, M.**, Jamiolahmady, M., Irland, S. and Brown, C: "Enhanced Oil Recovery and CO2 Storage by Carbonated Water Injection", International Petroleum Technology Conference (IPTC 14070) in Doha, Qatar, 7-9 December 2009. ***Presented by Dr Sohrabi.***

2008

1. Sohrabi, M., **Riazi, M.**, Jamiolahmady, M., Irland, S. and Brown, C.: "Carbonated Water Injection for Oil Recovery and CO_2 Storage", Sustainable Energy UK: Meeting the science and engineering challenge, Oxford, UK 13-14 May 2008. ***Presented by the author***.

2. Sohrabi, M., **Riazi, M.**, Jamiolahmady, M., Irland, S. and Brown, C.: "Carbonated Water Injection (CWI) Studies", 29th Annual Workshop & Symposium, IEA Collaborative Project on Enhanced Oil Recovery, Beijing, China, 3-5 Nov. 2008. ***Presented by Dr Sohrabi***.